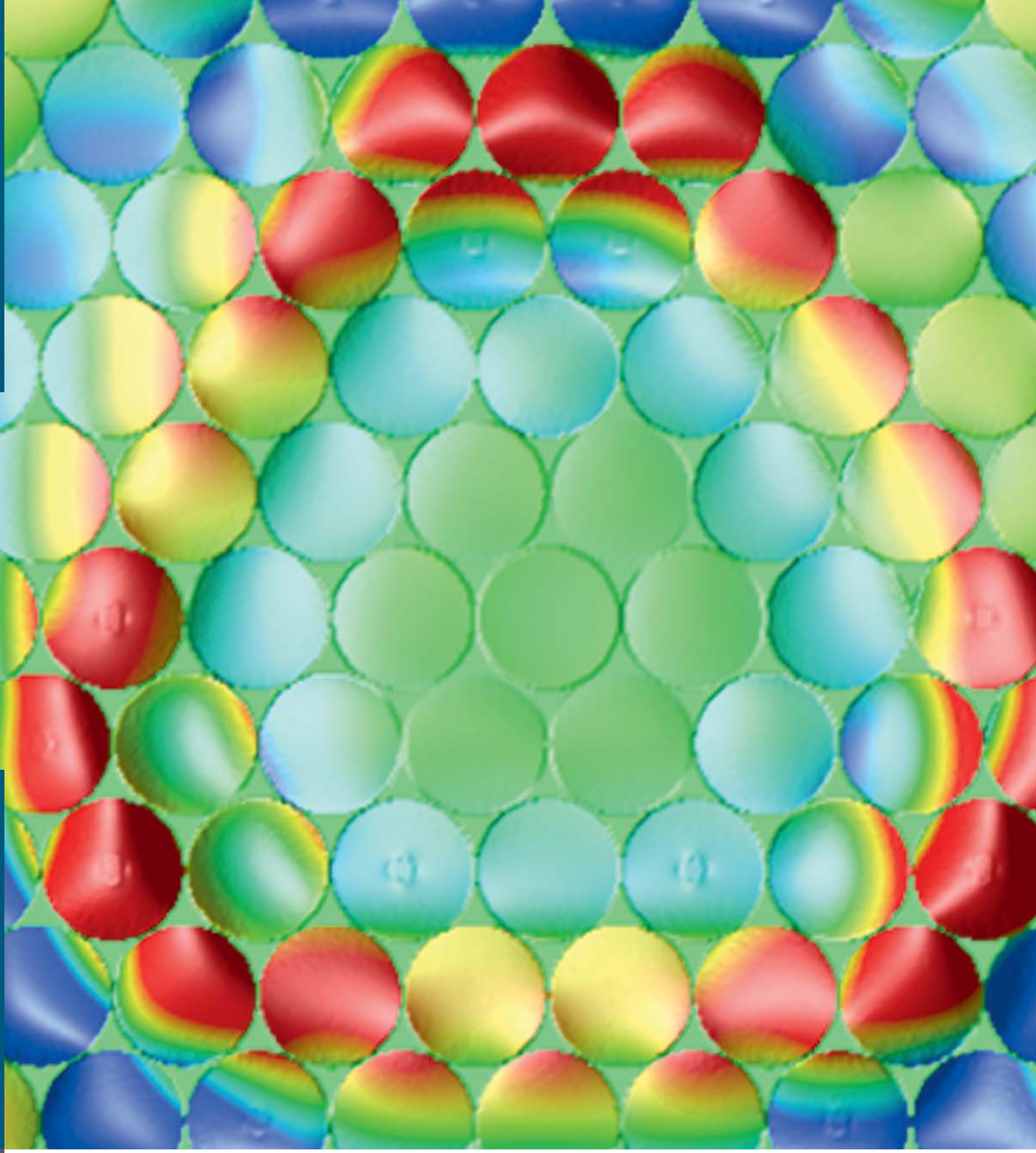

Scientific Report 2009

Institut für Festkörperforschung
Institute of Solid State Research

JÜLICH
FORSCHUNGSZENTRUM

Member of Helmholtz Association

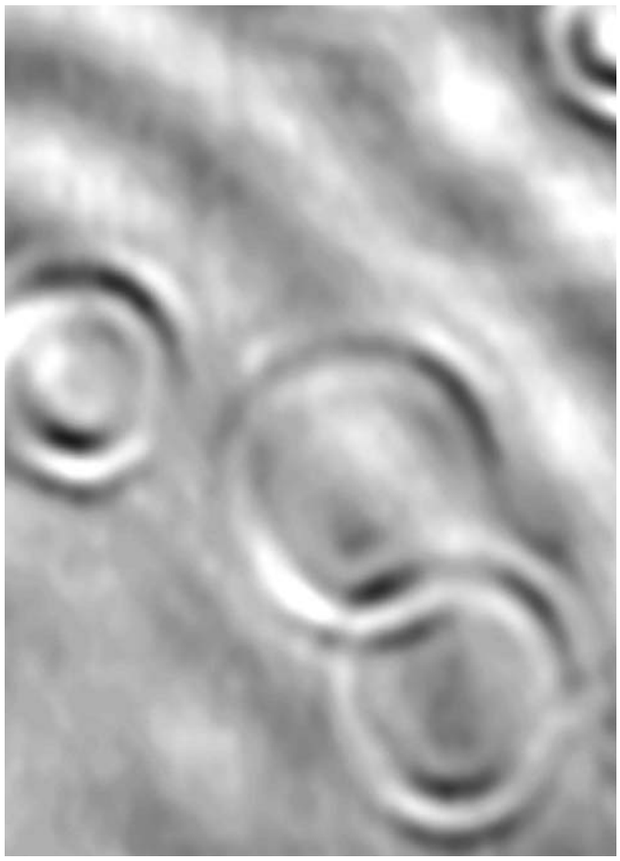

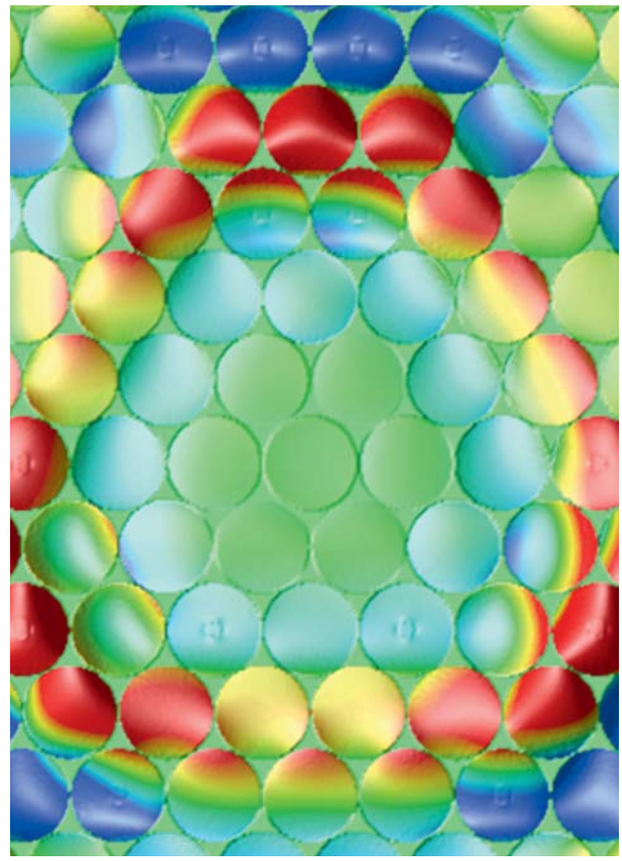

Just as sonar sends out sound waves to explore the hidden depths of the ocean, electrons can be used by scanning tunnelling microscopes to investigate the hidden properties of the atomic lattice of metals. Researchers from Göttingen, Halle and the Institute of Solid State Research succeeded in making inner Fermi surfaces visible in this manner. Fermi surfaces determine the most important properties of metals.

Left: A scanning tunnelling microscope recognises spherical patterns on a copper surface (image section approx. nine times nine nanometres). These irregularities in electron distribution are caused by cobalt atoms deep inside the copper.

Right: Simulation of the structure.

Original publication:

Seeing the Fermi Surface in Real Space by Nanoscale Electron Focusing;
Alexander Weismann, Martin Wenderoth, Samir Lounis, Peter Zahn, Norbert Quaas, Rainer G. Ulbrich, Peter H. Dederichs, Stefan Blügel;
Science, 27 February 2009, Vol. 323. no. 5918, pp. 1190 – 1193;
DOI: 10.1126/science.1168738

Scientific Report 2009

Institut für Festkörperforschung
Institute of Solid State Research

Directors of the Institute of Solid State Research (IFF) from left:

Prof. Dr. Jan K. G. Dhont (IFF-7: Soft Condensed Matter)
Prof. Dr. Knut Urban (IFF-8: Microstructure Research
Prof. Dr. Heiner Müller-Krumbhaar (IFF-3: Theory of Structure Formation)
Prof. Dr. Dieter Richter (IFF-5: Neutron Scattering)
Prof. Dr. Thomas Brückel (IFF-4: Scattering Methods)
Prof. Dr. Stefan Blügel (IFF-1: Quantum Theory of Materials)
Prof. Dr. Rainer Waser (IFF-6: Electronic Materials)
Prof. Dr. Claus M. Schneider (IFF-9: Electronic Properties)
Prof. Dr. Gerhard Gompper (IFF-2: Theoretical Soft Matter and Biophysics)

Contents

Research reports

Foreword

The annual report 2009 is intended to inform the international scientific community, including our scientific advisory board and the Helmholtz Association (Helmholtz-Gemeinschaft, HGF) about the research activities of the Institute of Solid State Research (IFF) during the past year. With this report, we have attempted to present a typical cross section through the research conducted at the IFF in 2009, within the Helmholtz research programmes "Condensed Matter Physics", "Information Technology with Nanoelectronic Systems", and "Large-scale Facilities for Research with Photons, Neutrons, and Ions".

2009 has been a very eventful year for the IFF. 40 years ago, on 12 December 1969, the supervisory board of the former Nuclear Research Centre Jülich, Forschungszentrum Jülich today, agreed to the formation of the IFF. However, the official constitution did not happen until 4 May, 1970. Approaching this 40th anniversary, we are looking back to fruitful years, crowned by the Nobel price 2007 that has been awarded to Professor Peter Grünberg. To name but some highlights of 2009:

Forschungszentrum Jülich officially opened the Peter Grünberg Centre in March. This Centre is operated jointly with the colleagues from the Institute of Bio- and Nanosystems" (IBN) within the new programme "Fundamentals of Future Information Technology". It constitutes the central platform for basic research in the field of nanoelectronics in the Jülich-Aachen region, and the first research institution in the field of nanoelectronics in Germany that is fully open to external users. Forschungszentrum Jülich named the centre in honour of its Nobel Prize Laureate Professor Peter Grünberg. As is explained below, the Peter Grünberg Centre will transcend into yet another larger entity, the Peter Grünberg Institute in conjunction with the reorganization of the research areas and departments in the Forschungszentrum Jülich.

Work in 2009 began with a groundbreaking ceremony for an extension to the Ernst-Ruska-Centre (ER-C) on the campus of Forschungszentrum Jülich in November. Under the umbrella of the Jülich-Aachen Research Alliance (JARA), from 2010 the Centre for Microscopy and Spectroscopy with Electrons, founded jointly by RWTH Aachen University and Forschungszentrum Jülich, will be operating a unique electron microscope with a world-beating resolution of 50 billionths of a millimetre, which will be housed in the new building.

Our neutron researchers have secured funding worth around € 1.1 million as part of the 7th EU Framework Programme for the exploitation and further development of neutron scattering for European science. With this funding, the Jülich Centre for Neutron Science (JCNS) is able to offer European neutron researchers from science and industry another 102 measuring days with Jülich research instruments at the Heinz Maier Leibnitz research neutron source (FRM II) in Garching near Munich. In 2009, 140 external proposals for external beam time with a request for 854 beam days were received at the JCNS. 99 proposals by users have been allocated 489 beam days at the instruments of JCNS at FRM II, ILL, and SNS, 304 beam days have been allocated to internal proposals. At the SNS in Oak Ridge, Tennessee, the strongest neutron source in the world, a state-of-the-art neutron spin echo (NSE) spectrometer was inaugurated by the JCNS in November. The NSE spectrometer enables detailed observations to be made of the motion of proteins and polymers. It will thus help to develop improved plastics or to understand metabolic processes in cells.

The synchrotron radiation research in Jülich profited from the stimulus fund activities of the German government and was able to start with the construction of the Nanospectrosopy Facility. This facility comprises two mutually complementary state-of-the-art immersion lens microscopes with energy-filtering and aberration-correction. The instruments, which will be operated at BESSY in Berlin provide a unique access to electron-spectroscopic characterizations on a nanoscale and will be made available to users soon.

The quality of our research is widely appreciated and respected by the scientific community as well as the public, as reflected by awards like, for example, the Walter Hälg Prize to Professor Dieter Richter, Head of the Institute of "Neutron Scattering" and Vice Director of the JCNS, in recognition of his "coherent work towards understanding the dynamics of polymers and biological macromolecules", or by the induction of our Nobel laureate, Professor Peter Grünberg, into the new German Research Hall of Fame. The jury thus paid tribute to his discovery of giant magnetoresistance. A very special honour was the visit of Forschungszentrum Jülich by President Horst Köhler in March. His visit was devoted to Peter Grünberg, whose places of research were at the centre of the two-hour programme.

Last, but not least, the "IFF Spring School" celebrated its 40th year running. Every year since 1970, the IFF has held this very successful course for students and young researchers. For a full two weeks, everything revolved around "Spintronics – from GMR to Quantum Information". Among the highlights were presentations by the founders of this pioneering technology: Nobel Laureates in Physics 2007, Professor Peter Grünberg and Professor Albert Fert.

For many years now, we have experienced changes and we have carved our research area accordingly at the Forschungszentrum Jülich and the Helmholtz Association. Since 2002, the research strategies are planned in a more global manner by the Helmholtz programmes. The Helmholtz research programmes are shaped and formulated by the scientists and reflect their long-term research interests and competences. In 2009, in order to support the effort of the Forschungszentrum Jülich to become the European supercomputer centre, the "Institute for Advanced Simulation" (IAS) was founded. The three theory institutes of the IFF are co-jointly members of the IAS and the IFF. For the new funding period starting in 2010, there are now four Helmholtz programmes "Fundamentals of Future Information Technology" (FIT), "Macromolecular Structures and Biological Information Processing" (BioSoft), and "Large-scale Facilities for Research with Photons, Neutrons, and Ions" (PNI). These long-term programmes run across four Institutes, the IFF, the IBN, the Institute of Structural Biology and Biophysics (ISB), and the IAS.

In order to better prepare ourselves for future challenges we decided to rebuild our departmental structure. After careful discussions within the institutes, the board of directors initiated a reorganization, according to which the IFF, IBN, and ISB will merge into two new institutes, the "Peter Grünberg Institute" and the "Institute for Soft Matter and Life Science" (working title). In addition, the JCNS will ascend into the status of an institute. This transformation will immediately increase the visibility and impact of the programmes by representing them through Institutes. We are convinced that this reorganization will further strengthen our activities in both fundamental research as well as technological innovations. In this spirit, the IFF will inherit and expand its power in cutting-edge research into the newly formed institutes.

In this sense, this will most probably be the last report named "IFF Scientific Report". But our research activities will continue in the expanded environment and – perhaps – under even better, more efficient boundary conditions. We will for sure keep you informed about our highlights as you are used to.

I hope you will enjoy reading the report and learning about our activities.

Prof. Dr. Rainer Waser
Managing Director of IFF in 2010
Director of IFF-6 "Electronic Materials"
March 2010

Snapshots 2009

Peter Grünberg Centre on the Jülich campus opened on 12 March

This is the central platform for basic research in the field of nanoelectronics in the Jülich-Aachen region, and the first research institution in the field of nanoelectronics in Germany that is also open to external users. Forschungszentrum Jülich named the centre in honour of its Nobel Prize Laureate Peter Grünberg (third from the left). In the opening ceremony, the Nobel Laureate was presented with a symbolic key to the new centre bearing his name. You will find more information on this topic on the right.

9-20 March
Nobel Laureates speak at "IFF Spring School"

The "IFF Spring School" celebrated its 40th anniversary. Every year since 1970, the Institute of Solid State Research (IFF) has held this very successful course for students and young researchers. For a full two weeks, everything revolved around the hot topic of "Spintronics – From GMR to Quantum Information". Among the highlights were presentations by the founders of this pioneering technology: Nobel Laureates in Physics 2007 Professor Peter Grünberg and Professor Albert Fert.

Not an everyday experience: Proessor. Albert Fert, Nobel Laureate in Physics, holds a lecture during the IFF Spring School.

IBM scientist Dr. Stuart Parkin gives a lecture on MRAM technology.

12 March
Peter Grünberg Centre opened

Forschungszentrum Jülich officially opened the Peter Grünberg Centre. It is the central platform for basic research in the field of nanoelectronics in the Jülich-Aachen region, and the first research institution in the field of nanoelectronics in Germany that is also open to external users. Forschungszentrum Jülich named the centre in honour of its Nobel Prize Laureate Professor Peter Grünberg.

The Peter Grünberg Centre unites research, technological developments and designs for innovative instruments. At this Centre, strong basic research in solid-state physics and material sciences forms the foundation for the discovery and use of novel and unexpected phenomena. An essential feature of the research is interdisciplinary collaboration between physics, chemistry and biology. On this basis, novel instrument concepts and manufacturing processes will be developed, which will also play a part in other fields such as energy technology and medicine.

The Peter Grünberg Centre is integrated in the cooperation between Forschungszentrum Jülich and RWTH Aachen University as part of the Jülich Aachen Research Alliance (JARA). It enhances joint research in the field of future information technology.

Together with Parliamentary State Secretary Thomas Rachel (3rd from the left), the guests at the opening ceremony visited the facility for new gate materials and strained silicon operated by Professor Siegfried Mantl's (far right) research team.

25 March
German President Horst Köhler visits IFF

Federal President Horst Köhler (centre) and Proessor Claus M. Schneider (left) from IFF discuss innovative research strategies for future information technology.

President Horst Köhler visited Forschungszentrum Jülich on 25 March. His visit was devoted to the Nobel Laureate for Physics, Professor Peter Grünberg, whose places of research at the IFF were at the centre of the two-hour programme. "Science needs persistence. Forschungszentrum Jülich gives me reason to believe that we will continue to make constant progress in the scientific area," said Köhler. "My aim is to help ensure that the framework conditions are right for conducting research in Germany."

Horst Köhler also gained insights into innovative forms of information processing when he visited the "nano-spintronics cluster tool" of Professor Claus M. Schneider, head of IFF institute 9 "Electronic Properties". This apparatus serves to study the structure of magnetic layer systems. Researchers hope to considerably reduce the energy consumption of information technology in future. The aim is, for example, to produce smaller, economical, but more powerful processors for notebooks or mobile phones.

President Köhler was accompanied by Thomas Rachel (Member of the German Bundestag), Parliamentary State Secretary in the German Federal Ministry of Education and Research, and Dr. Michael Stückradt, State Secretary from the Ministry of Innovation, Science, Research and Technology of North Rhine-Westphalia.

8 April
European research prize for neutron researcher Dieter Richter

Professor Dieter Richter

The 2009 Walter Hälg Prize was awarded to Professor Dieter Richter, Head of the Institute of "Neutron Scattering" (IFF-5) and Vice Director of the Jülich Centre for Neutron Science (JCNS), in recognition of his "coherent work towards understanding the dynamics of polymers and biological macromolecules". Every two years, the European Neutron Scattering Association (ENSA) awards the Prize to a European scientist for pioneering research in the field of neutron scattering. The prize is worth around € 6,600 and was awarded to Richter at the International Conference for Neutron Scattering in Knoxville, USA.

28 April
Neutron research: € 1.1 million in EU funding for Jülich

Neutron researchers have secured funding worth around € 1.1 million as part of the 7th EU Framework Programme for the exploitation and further development of neutron scattering for European science. With this funding, the Jülich Centre for Neutron Science (JCNS) is able to offer European neutron researchers from science and industry another 102 measuring days with Jülich research instruments at the Heinz Maier Leibnitz research neutron source (FRM II) in Garching near Munich. This is the strongest neutron source in Germany where JCNS operates its German branch lab. The measuring time on the Jülich research instruments, some of which are unique, is determined by an international panel of independent experts.

€ 450,000 will be spent on the development of new neutron scattering methods. In this context, JCNS coordinates a development network in which seven European research groups are involved to further develop possible applications of polarized neutrons for the investigation of magnetic properties in solid-state physics or for the investigation of the dynamics of individual molecules in polymer physics and biology. The funding covers a period of four years.

A view into the neutron guide hall at FRM II in Garching.

Photo: Wenzel Schürmann, Munich University of Technology

2 – 5 August
International conference "Polarized Neutrons and Synchrotron X-rays for Magnetism 2009"

Around 120 scientists from Germany as well as from Europe and abroad met at the Gustav Stresemann Institute in Bonn to exchange information and views regarding the impact of polarized neutrons and X-ray scattering methods for investigating magnetic phenomena. To this end, the Institute of Solid State Research (IFF-4, Scattering Methods) organized the second international conference "Polarized Neutrons and Synchrotron X-rays for Magnetism 2009", PNSXM 2009 for short. PNSXM 2009 took place as a satellite conference of the well-known International Conference on Magnetism – ICM 2009.

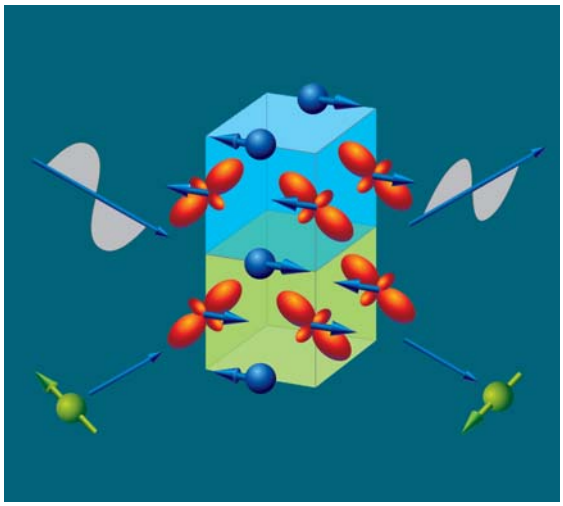

6 September
Open day: IFF opens its doors to the public

Around 40,000 people visited Forschungszentrum Jülich on Open Day 2009. Many curious and interested members of the public also visited the Institute of Solid State Research (IFF), where a varied selection of research topics awaited them from the wide range of fields represented at the institute. Remaining true to the IFF motto "phenomena, materials and methods", visitors had the opportunity to learn about topics such as high-temperature superconductors and the flow behaviour of red blood cells, the growth of single crystals and the fabrication of thin films in sputtering facilities, as well as the application of scattering methods and electron microscopy for research purposes. With lectures, presentations, and interactive hands-on exhibits, younger visitors were entertained as well as the grown-ups.

The exhibits at IFF attracted a large number of visitors on Open Day.

Photo: Dieter Triefenbach

22 September
Peter Grünberg inducted into Hall of Fame

In a ceremony on 22 September, Professor Peter Grünberg, 2007 Nobel Laureate for Physics, was inducted into the German Research Hall of Fame. The jury thus paid tribute to his discovery of giant magnetoresistance, which is used for computer hard disc drives. The address at the ceremony in Berlin was given by Annette Schavan, Federal Minister of Education and Research, in the presence of 150 representatives of industry, politics and science.

From left: Dr. Arno Balzer (Chief Editor "Manager-Magazin"), Nobel Laureate for Physics Professor Peter Grünberg (IFF), Professor Jürgen Kluge (McKinsey Germany and Franz Haniel & Cie. GmbH)

4 November
Work begins on laboratory for world's strongest microscope

Groundbreaking ceremony for an extension to the Ernst Ruska-Centre (ER-C), from left to right: Professor Knut Urban (Director ER-C), Professor Achim Bachem (Chairman of the Board of Directors of Forschungszentrum Jülich), Thomas Rachel (Federal Ministry of Education and Research), Professor Ernst Schmachtenberg (Rector of RWTH Aachen University), and Professor Joachim Mayer (Director ER-C).

Work began with a groundbreaking ceremony for an extension to the Ernst Ruska-Centre (ER-C) on the campus of Forschungszentrum Jülich. Under the umbrella of the Jülich-Aachen Research Alliance (JARA), from 2010 onwards the Centre for Microscopy and Spectroscopy with Electrons, founded jointly by RWTH Aachen University and Forschungszentrum Jülich, will be operating a unique electron microscope with a world-beating resolution of 50 billionths of a millimetre. This will enable Jülich and Aachen to maintain their position as the frontrunners in ultrahigh-resolution microscopy worldwide.

4 November
Neutron scientists inaugurate unique device in the USA

A unique large-scale research device from Jülich went into operation in the USA. At the strongest neutron source in the world, the spallation source SNS in Oak Ridge, Tennessee, the Jülich Centre for Neutron Science (JCNS) inaugurated a so-called neutron spin echo (NSE) spectrometer. The NSE spectrometer enables detailed observations to be made of the motion of proteins and polymers. It will thus help to develop improved plastics or to understand metabolic processes in cells.

Inauguration of the Jülich NSE spectrometer at Oak Ridge, USA. From left to right: Dr. Ian S. Anderson, head of SNS, Christian Jörgens, head of the Science and Technology Department at the German Embassy in Washington, Beatrix Vierkorn-Rudolph, head of the Subsection for Large Facilities, Energy and Basic Research of the German Federal Ministry of Education and Research, Prof. Sebastian M. Schmidt, member of the Board of Directors of Forschungszentrum Jülich, Dr. Jost Liebich, personal assistant to the Board of Directors, Forschungszentrum Jülich, and representing the Jülich team operating the NSE spectrometer: Dipl.-Ing. Tadeusz Kozielewski, head engineer at NSE, Dipl.-Ing. Christoph Tiemann, Jülich Central Technology Division, Dr. Michael Ohl, NSE project leader, and Dipl.-Ing. Guido Vehres, Institute of Solid State Research (IFF-5 Neutron Scattering).

Photo: Oak Ridge National Laboratory

26 November
Focus on neutron research

Neutron researchers at the Jülich Centre for Neutron Science (JCNS) in Garching opened their doors for a journalists' workshop. The programme included a tour of the experimental hall, examples of exciting research and, of course, background information on the Jülich Centre for Neutron Science and also on activities at the pioneering spallation neutron source (SNS) in Oak Ridge, USA, and the European Spallation Source (ESS) in Lund, Sweden. The 27 journalists who took part in the workshop found it extremely interesting.

Photos: W. Schürmann, Munich University of Technology

1 December
European Network of Excellence "SoftComp" now self-supporting

A new future was on the cards for the successful work conducted by the European Network of Excellence "Soft Matter Composites – An approach to nanoscale functional materials" (SoftComp). From 1 December, the network coordinated by IFF physicist Prof. Dieter Richter has been supporting itself having received EU funding for a total of 66 months. 35 partners in twelve countries signed an agreement to support the network until at least the end of 2012.

In 2004, 29 groups from scientific institutions and European companies had joined forces in an effort to concentrate and consolidate multidisciplinary European research in the field of soft matter. Permanent common structures had been created for this purpose – both in the area of scientific infrastructure and for the exchange of information and findings.

Soft matter is part and parcel of our everyday life and it carries with it a high potential for innovation. SoftComp know-how, for example, is used in the development of biosensors for medical purposes and fuel-saving car tyres with a lower rolling resistance. The IFF partners, for example, are working on environmentally friendly cleaning solutions for the printing industry and they also conduct research on the flow behaviour of red blood cells.

A brochure published in October presents work conducted by the research network up to 2009 and prospects for the following years.

Honours and appointments

1 December
Intensified cooperation in the field of life sciences and soft matter

Forschungszentrum Jülich, the German Electron Synchrotron (DESY) in Hamburg, the Society for Heavy Ion Research (GSI) in Darmstadt, the GKSS Research Centre Geesthacht and the Helmholtz-Zentrum Berlin (HZB) are intensifying their research cooperation in the field of life sciences and soft matter. The five research centres from the Helmholtz Association agreed upon these measures at a workshop on the topic of "Soft Matter and Life Science" held at the Gustav Stresemann Institute in Bonn from 30 November to 1 December.

Joint scientific projects were arranged as well as the construction of a joint web portal including a sample database. In future, the workshop will be held every two years, and other meetings on specific scientific topics are also planned. As part of the Helmholtz Programme "Research with Photons, Neutrons and Ions (PNI)", the five research centres operate large-scale research devices and pursue their own research projects with the aim of fully exploiting and optimizing the potential of these devices and providing the most effective possible support for external users.

76 delegates from research centres in the Helmholtz Association spent two days in Bonn discussing life sciences and soft matter.

Mr **Markus Betzinger**
(Institute: Quantum Theory of Materials/Institute for Advanced Simulation-1) was awarded a Springorum Memorial Medal by RWTH Aachen University.

Ms **Tania Claudio Weber**
(Institute: Scattering Methods) received a prize for the best presentation during the annual meeting of PhD students of the Belgian graduate college on "MAIN – Science and Engineering for Materials, Interfaces and Nanostructures".

Dr. **Benjamin Grushko**
(Institute: Microstructure Research) received a prize for the best poster at the CALPHAD XXXVIII Meeting in Prague in May.

Dr. **Raphael Hermann**
(Institute: Scattering Methods) was appointed visiting professor by the University of Liège.

Dr. **Hermann Kohlstedt**
(Institute: Electronic Materials) was offered a chair at the University of Kiel.

Mr **Boris Lorenz**
(Institute: Quantum Theory of Materials) was awarded a prize for the best poster at the WE-Heraeus Seminar "Physics of Tribology – Understanding Friction and Wear Processes in Technical Systems".

Dr. **Matvey Lyatti**
(Institute: Microstructure Research) received a Young Researcher Award for impressive achievement and the presentation entitled "Liquid Identification by Hilbert Spectroscopy" at the 12th International Superconductive Electronics Conference 2009 at Fukuoka, Japan.

Two publications by Dr. **Bo Persson**
(Institute: Quantum Theory of Materials) were selected among the 27 best articles published in the "Journal of Physics: Condensed Matter" in 2008.

Dr. **Christina Schindler**
(Institute: Electronic Materials) was awarded the Günther Leibfried Prize for successful scientific communication.

Mr **Alexander Thiess**
(Institute: Quantum Theory of Materials/Institute for Advanced Simulation-1) received a prize for the best poster at ISMFS.

Dr. **Simon Woodford**
(Institute: Quantum Theory of Materials/ Institute for Advanced Simulation-1) was awarded the Borchers Medal by RWTH Aachen University.

Institute of Solid State Research (IFF)

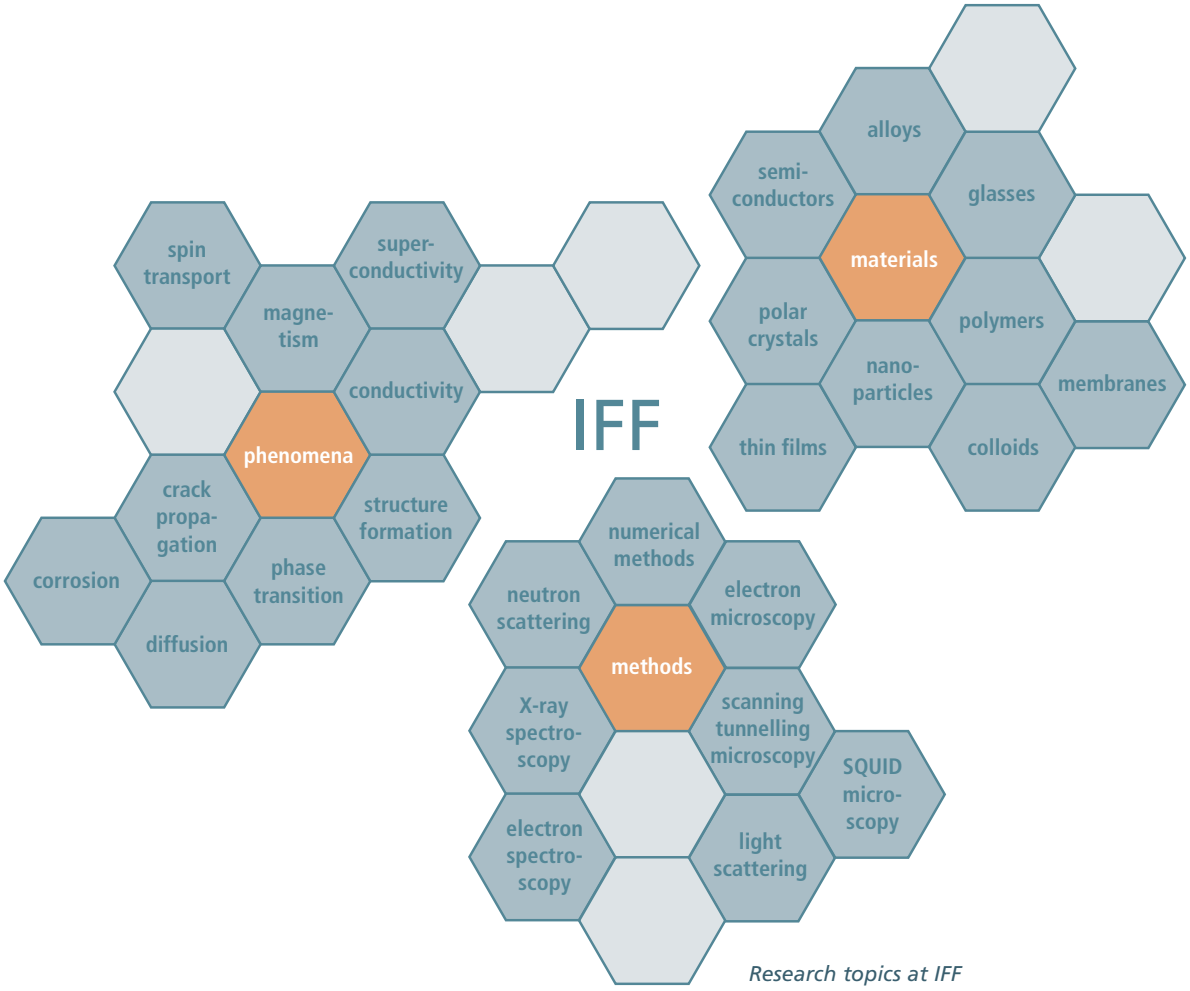

Research topics at IFF

Founded in 1969, the scientific reputation of the Institute of Solid State Research (Institut für Festkörperforschung – IFF) still owes much to the conception of its founders that new discoveries are made at the boundaries of disciplines. This is as true today as it was forty years ago. In this spirit, the IFF has pioneered new research fields and set trends towards multi- and cross-disciplinary activities in both fundamental research as well as technological innovations. This is highlighted by the 2007 Noble Prize in Physics, awarded to Prof. Dr. P. Grünberg, – jointly with Prof. Dr. A. Fert, Paris – for the discovery of Giant Magnetoresistance (GMR), an activity which triggered the new research field of spintronics.

Today, the IFF is engaged in investigating a multitude of condensed matter phenomena with special emphasis on three prime objectives:

- studies of fundamental physical mechanisms and phenomena of condensed matter,
- the development and improvement of experimental and theoretical analysis methods, as well as
- the elucidation and utilization of new material properties in complex systems.

The corresponding research programs exploit the full scale of analytical and numerical methods to elucidate relations between structural, electronic, magnetic and functional properties of condensed matter, and to achieve a description of the underlying physical mechanisms. Research efforts are directed at obtaining a detailed understanding of phenomena, ranging from microscopic and atomistic interactions in the solid state to the competition of entropic and energetic forces in macromolecular fluids.

Research at the IFF rests firmly on the two pillars of quantum mechanics and statistical physics. On a microscopic scale, we describe the interactions of electrons and atomic building blocks and determine how these entities respond to external influences. Particular strengths encompass the theory of electronic structures, clusters, micro-mechanics of lattice imperfections, the dynamics of structure formation and phase transitions, materials and phenomena of magneto- and nanoelectronics, spintronics, spin dynamics, and strongly correlated electron systems. On the mesoscopic scale, we study soft matter systems, such as polymer solutions and melts, colloidal dispersions, surfactants, membranes, vesicles, and cells. Important questions concern self-assembly and structure formation, the competition of entropic and enthalpic forces, geometric and topological interactions, the complexity of multi-component systems, systems far from equilibrium, as well as the behavior under external fields. In all cases, the instrumentation of electron, neutron, and synchrotron radiation sources and their application is essential to the study of condensed matter.

The experimental portfolio together with an acknowledged expertise enables the IFF to tackle complex problems in close cooperation with scientists and industry worldwide. Special state-of-the-art laboratories exist for thin film deposition and growth of bulk crystals, for nanostructuring as well as for the preparation of soft matter materials. In addition to standard methods for materials characterization, highly specialized techniques ranging from superconducting microscopy and spin-polarized microscopies to femtosecond laser spectroscopy are available at the IFF and are being constantly improved in performance.

The Jülich Centre for Neutron Science (JCNS) operates advanced neutron scattering instruments at the worldwide most modern and highest flux neutron sources. As a complement to local research opportunities, instruments are designed and operated at external national and international neutron sources, such as the FRM II in Munich, the Institut Laue-Langevin in Grenoble or the neutron spallation source in Oak Ridge.

Ernst Ruska-Centre for Microscopy and Spectroscopy with Electrons ER-C

With the Ernst Ruska-Centre for Microscopy and Spectroscopy with Electrons (ER-C) the IFF operates a national user facility housing several of the world's most advanced electron microscopes and tools for nanocharacterization. In-house research programs cover topical issues in

condensed matter physics and – as a matter of course – future developments of subångström and sub-electronvolt microscopy.

The newly founded Peter Grünberg Centre provides the competence and method platform for the research on fundamentals of future information technology. It is operated jointly by the institutes IFF and IBN in the framework of the Jülich-Aachen Research Alliance JARA. The Grünberg Centre houses several units. The Helmholtz Nanoelectronic Facility (HNF) provides manifold means to prepare complex material systems and nanoelectronic structures in combination with an in-depth characterization. In the Synchrotron Radiation Laboratory (SRL) a broad variety of spectroscopy, microscopy, and scattering experiments at various synchrotron radiation facilities are designed and realized. The lab also provides expertise for the development of new beamlines and experimental concepts and, thus, acts as a valuable partner for synchrotron radiation laboratories throughout the world.

JARA|FIT
Fundamentals of Future Information Technology

The international networking of the IFF is a main pillar of its success; the institute initiated two EU Networks of Excellence (NoE), and co-founded the section "Fundamentals of Future Information Technology (FIT)" of the Jülich-Aachen Research Alliance (JARA). JARA-FIT is the center of excellence for nanoelectronics research in the Jülich-Aachen region and is jointly operated by the Forschungszentrum Jülich and the RWTH Aachen University. It provides an excellent basis for future developments of nanoelectronics and information technology. To identify technology-drivers the research areas cover

quantum-electronics, magneto-electronics, ferro-electric and molecular nanostructures as well as Terahertz-electronics and bioelectronic signal processing. The IFF is partner of more than one hundred universities and research institutions from all around the world.

The IFF puts particular emphasis on the support of young scientists and has successfully established a number of Young Investigator Groups in the fields of quantum transport, spinelectronics, thermoelectrics, complex liquids and multifunctional materials.

Last but not least, the IFF has a long tradition in teaching and training of students, not only through the approximately 30 IFF staff scientists steadily giving lectures at universities, but in particular through the annual IFF Spring Schools and Neutron Laboratory Courses. Dissemination of knowledge to students and scientist is provided through the organisation of workshops and conferences, in particular the yearly Jülich Soft Matter Days or JCNS workshops. In addition, the IFF is involved in the German Research School for Simulation Science (GRS) established together with the RWTH Aachen University.

The IFF is a department, which comprises six experimental and three theoretical divisions as well as joint service facilities. As part of the Forschungszentrum Jülich – a member of the Hermann von Helmholtz Association of German Research Centres (HGF) – in 2009 the IFF provided key contributions to the strategic mission of the HGF within three research programs:

- Condensed Matter (pages 36 – 137),
- Information Technology with Nanoelectronic Systems (pages 138 – 169),
- Large-scale Facilities for Research with Photons, Neutrons and Ions (pages 170 – 199).

The success of the IFF rests upon the inventiveness and initiative of its more than 300 members. The IFF supports independent research by encouraging the responsibility of individual scientists – a philosophy that contributes greatly to the stimulating atmosphere in the department. In order to sustain this level on the long run, special encouragement is given to young scientists.

Read more:

Institute of Solid State Research:
www.fz-juelich.de/iff/e_iff/

Forschungszentrum Jülich:
www.fz-juelich.de

Ernst Ruska-Centre: www.er-c.org

Jülich Synchrotron Radiation Laboratory:
www.fz-juelich.de/iff/d_iee_jsrl/

Jülich Centre for Neutron Science:
www.jcns.info/

Jülich-Aachen Research Alliance:
www.jara-excellence.de

Helmholtz Association:
www.helmholtz.de/en/

Department IFF

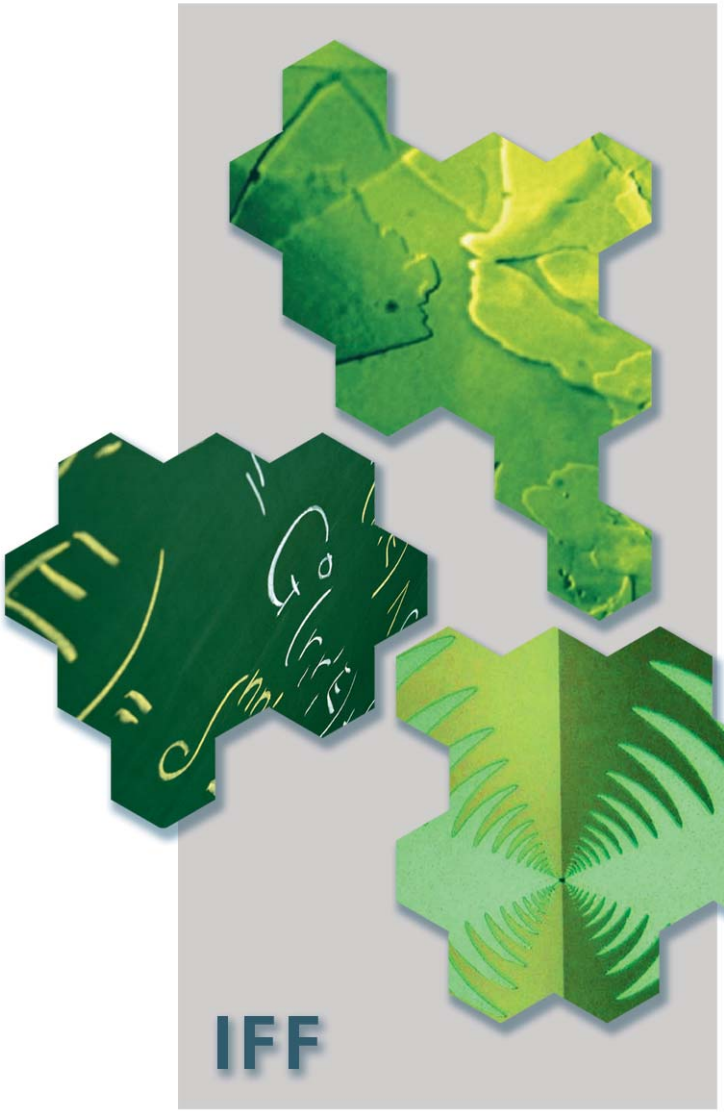

comprising the Institutes

IFF-1:	Quantum Theory of Materials	Prof. Dr. Stefan Blügel
IFF-2:	Theoretical Soft Matter and Biophysics	Prof. Dr. Gerhard Gompper
IFF-3:	Theory of Structure Formation	Prof. Dr. Heiner Müller-Krumbhaar
IFF-4:	Scattering Methods	Prof. Dr. Thomas Brückel
IFF-5:	Neutron Scattering	Prof. Dr. Dieter Richter
IFF-6:	Electronic Materials	Prof. Dr. Rainer Waser
IFF-7:	Soft Condensed Matter	Prof. Dr. Jan K. G. Dhont
IFF-8:	Microstructure Research	Prof. Dr. Knut Urban
IFF-9:	Electronic Properties	Prof. Dr. Claus M. Schneider

IFF-1: Quantum Theory of Materials

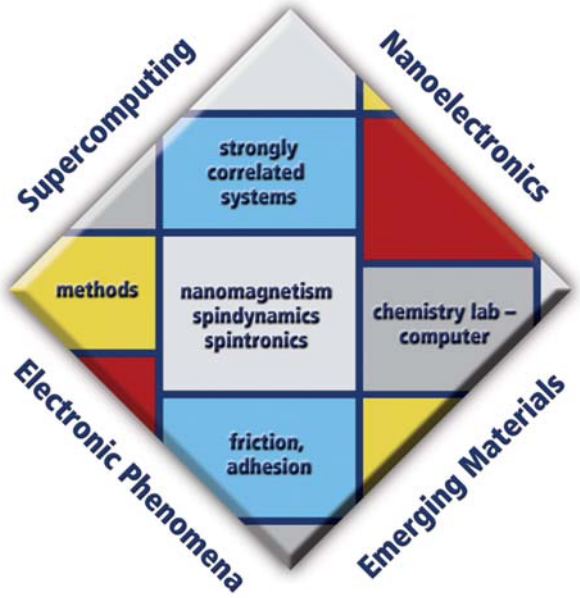

A major focus at "Quantum Theory of Materials" is the analysis and computation of structural, electronic, magnetic, transport and chemical properties and processes in molecules and solids, in terms of both basic research and practical applications. The goal is to achieve a microscopic understanding of such complex phenomena.

Our research covers key areas of condensed matter theory, computational materials science, nanoelectronics and supercomputing. We explore the electronic and structural properties of systems from large organic (including biological) molecules, low-dimensional magnets, and magnetic multilayers, to complex solids. We consider transport properties across interfaces and molecules as relevant for spintronics and molecular electronics. We investigate the electronic excitations, and dynamical properties of atomic and molecular clusters, solids, and solid surfaces, as well as the quasiparticle behaviour of semiconductors, oxides and transition metals that results from electronic correlations. We analyze the physics of strongly correlated materials such as transition-metal oxides and molecular crystals paying particular attention to complex ordering phenomena. Other areas include nanoscale tribology, including friction, plastic deformation, adhesion, and brittle fracture, as well as nonlinear processes in the atmosphere and agrosphere.

A major asset of our institute is the competence in developing conceptual and computational methods based on density functional theory, molecular dynamics simulations, and Quantum Monte Carlo methods.

IFF-2: Theoretical Soft Matter and Biophysics

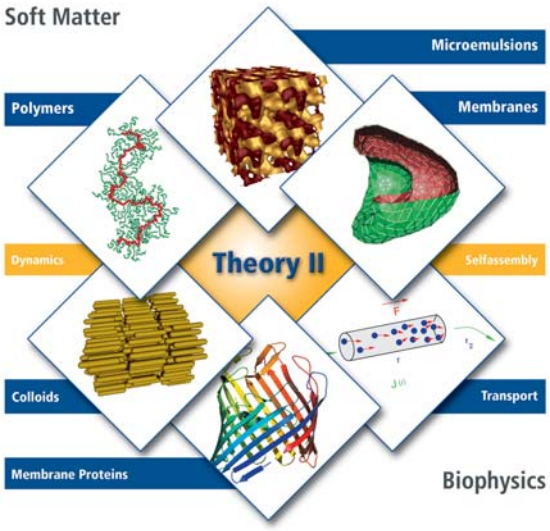

The main research topic of the Institute "Theoretical Soft Matter and Biophysics" is the theory of macromolecular systems. Soft matter physics and biophysics are interdisciplinary research areas encompassing statistical physics, materials science, chemistry, and biology. Our systems of interest include polymer solutions and melts, colloidal suspensions, membranes, vesicles and cells, but also composite systems ranging from colloids in polymer solutions to mixtures of surfactants and amphiphilic block copolymers. A major focus is the hydrodynamic behaviour of complex fluids and biological systems, both in equilibrium and under flow conditions.

At IFF-2, a large variety of methods are applied. In fact, a combination of analytical and numerical methods is often required to successfully characterize the properties of these complex systems. In particular, simulation methods (Monte Carlo, molecular dynamics), mesoscale hydrodynamic simulation techniques, field theory, perturbation theory, and exact solutions are employed. Since the building blocks of soft matter systems often contain a large number of molecules, "simplified" mesoscale modelling is typically required, which is then linked to the molecular architecture.

A characteristic feature of soft-matter research is the fruitful interaction between theory and experiment. IFF-2 closely cooperates with the Institute for Neutron Scattering (Prof. Richter) and the Institute for Soft Condensed Matter (Prof. Dhont) to successfully tackle many of the essential aspects of the systems investigated.

IFF-3: Theory of Structure Formation

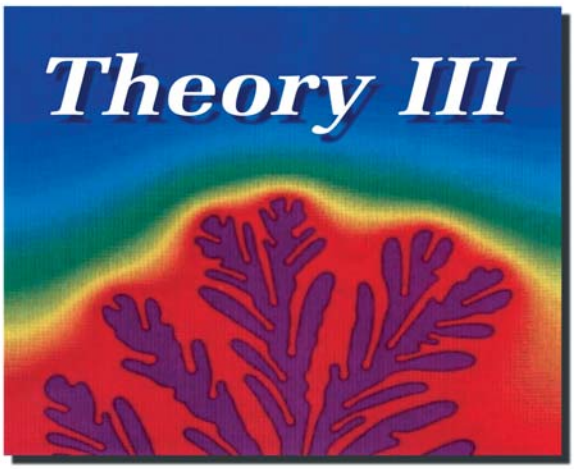

The research of the Institute "Theory of Structure Formation" is concerned with the mechanisms of the formation of structures and their consequences in condensed matter. The investigations start from electronic properties which define the shortest length and time scales, but they also encompass the macroscopic consequences. The analytical and numerical studies are in many ways closely connected to experimental research performed in other groups of the IFF, but also to activities in other Jülich institutes. The institute contributes mainly to the research programmes "Condensed Matter Physics" and "Information Technology with Nanoelectronic Systems" of the Research Centre.

Central points of interest for the research at IFF-3 are in the field of electronic structure of solids, in particular effects of strong electronic correlations. A specific interest concerns materials relevant for Information technology. A second mainstream is formed by cooperative phenomena in condensed matter. Questions here aim at the dynamics of structure and pattern formation and the statistical mechanics of order and disorder processes. Specific activities concern the effect of long-range interactions like elastic effects in solids, friction and fracture phenomena, or hydrodynamic interactions in solid-liquid systems.

The research of IFF-3 employs all analytical and numerical techniques applicable to many-body problems of equilibrium and non-equilibrium phenomena in condensed matter. In addition, the development of new methodological concepts and numerical procedures is part of our research interest. The development of parallel programme codes adapted to massively parallel computers has received special attention in recent years.

IFF-4: Scattering Methods

At the Institute for Scattering Methods, we focus on the investigation of structural and magnetic order, fluctuations and excitations in complex or nanostructured magnetic systems and highly correlated electron systems. Our research is directed at obtaining a microscopic atomic understanding based on fundamental interaction mechanisms and relating this microscopic information to macroscopic physical properties and functionalities.

The systems studied have a high potential for applications in future information technologies. In the field of nanomagnetism and Spintronics they range from magnetic molecules, via magnetic nanoparticles and magnetic thin film systems to laterally patterned superlattices. Among the correlated electron systems, we focus on transition metal oxides and -chalcogenides with unusual properties, such as colossal magnetoresistance or multiferroicity. Transition metal oxide superlattices, also laterally patterned, combine the aspects of correlated electron systems and nanomagnetism. Thermoelectric materials are being explored in the form of bulk and nanostructures.

Our emphasis lies in the application of most advanced synchrotron X-ray and neutron scattering methods. We place great emphasis on the complementary use of these two probes. Some of our efforts are devoted to dedicated sample preparation, from the synthesis of nanoparticles via physical thin film deposition techniques to single crystal growth. For sample characterisation, several ancillary techniques such as magnetometry, specific heat, conductivity etc. are being used to complement the scattering methods.

A significant part of our activity is devoted to the development of novel scattering techniques and the construction and continuous improvement of instruments at large scale neutron and synchrotron radiation facilities. Our strength lays in polarization analysis techniques. The Institute for Scattering Methods is partner in the Jülich Centre for Neutron Science JCNS, which operates instruments at some of the leading facilities: the research reactor FRM II in Garching, the Institut Laue-Langevin ILL in Grenoble, France and the Spallation Neutron Source SNS in Oak Ridge, USA. Moreover, we contribute to the operation of a sector at the Advanced Photon Source APS (Argonne, USA).

IFF-5: Neutron Scattering

The Institute for Neutron Scattering is concerned with neutron research placing major emphasis on soft condensed matter, i.e. materials that react strongly to weak forces. Neutron scattering is a valuable tool for these systems because it reveals structure and dynamics of Soft Matter on the relevant length- and timescales.

A major part of the Soft Matter studies is done on polymers. Apart from their structure, we are interested in the dynamics of polymers in melts and solutions (e.g. gels, rubbery networks, aggregates) also under nanoscopic confinement. These polymers often have a complex architecture (copolymers, star-polymers etc.) or are modified by filler materials to tailor them for industrial applications. In addition, biological materials (e.g. proteins) are studied concerning their structure and dynamics. Another field of interest are complex liquids such as microemulsions or colloid systems.

The institute has modern chemical laboratories for the synthesis, characterisation, and modification of Soft Matter. In order to complement neutron scattering experiments several ancillary techniques are used in the institute: rheology, computer simulation, impedance spectroscopy, light scattering, calorimetry, and x-ray scattering.

The Institute for Neutron Scattering is partner in the Jülich Centre for Neutron Science JCNS. In this position it operates several neutron scattering instruments at the research reactor FRM II in Munich, at the Institut Laue-Langevin in Grenoble, and at the Spallation Neutron Source in Oak Ridge, USA. These instruments are available to guest researchers on request. Another focus of research is the development of neutron instrumentation for research reactors and future spallation sources worldwide.

IFF-6: Electronic Materials

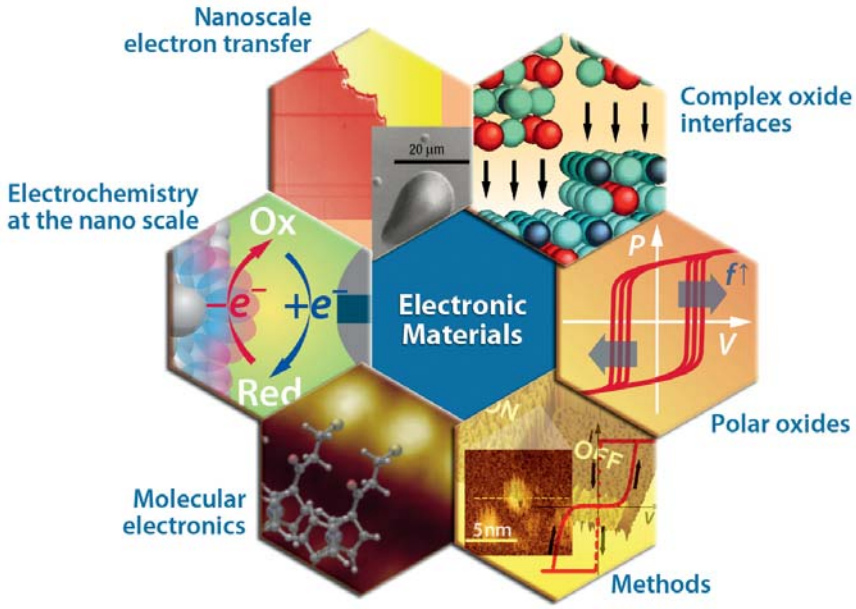

Progress in information technology and related fields such as energy storage and sensors originates to a large extent from novel electronic phenomena in functional materials as well as advances in the processing technology of these materials.

In this sense, at the Institute "Electronic Materials" we focus on the physics and chemistry of electronic oxides and electronically active organic molecules, which are promising for potential memory, logic, and sensor functions. Our research aims at the fundamental understanding of functional effects based on nano-scale electron transfer, electrochemical redox processes, space charge formation, electron/ion conduction in reduced dimensions, as well as ferro- and piezoelectricity, and at the elucidation of their potential for future device application. For this purpose, our institute provides a broad spectrum of facilities reaching from atomically controlled film deposition methods for heteroepitaxial oxide thin films, molecular self-assembly routes, and dedicated integration technologies. In addition, our institutes are equipped with tools for the characterisation of processes, structures, and electronic properties with atomic resolution. Circuit design is utilized for the development of hybrid and integrated circuits which comprise new electronic functions as well as advanced measurement systems. This is complemented by numerical simulation and modelling methods which aim at the theoretical explanation of the electronic phenomena and materials under study as well as the corresponding devices.

IFF-7: Soft Condensed Matter

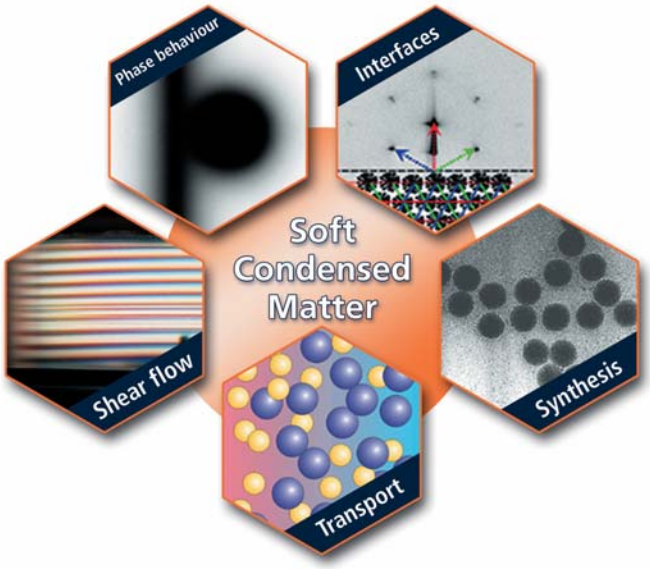

The Soft Condensed Matter group investigates the chemistry and physics of colloidal systems. Colloidal systems can be regarded as solutions of very large molecules which exhibit phase transitions and show non-equilibrium phenomena that are also found for simple molecular systems. Due to the slow dynamics of colloids and the tuneable interactions between the colloidal particles, however, there are many transitions and non-equilibrium phenomena that do not occur in simple molecular systems, like gellation and shear-band formation. The aim is to understand structure, dynamics and non-equilibrium phenomena on a microscopic basis with an open eye for possible technological applications.

The main topics that are studied include,

- the phase behaviour, pattern formation, phase separation kinetics and dynamics of suspensions of spherical and rod-like colloids under shear flow,
- mass transport induced by temperature gradients,
- dynamics and micro-structural properties of colloidal systems near walls and interfaces,
- the effects of pressure on interactions, the location of phase transition lines and gellation transitions and the dynamics of colloids and polymers,
- response of colloids to external electric fields,
- the equilibrium phase behaviour of mixtures of colloids and polymer-like systems,
- dynamics of various types of colloidal systems in equilibrium, and
- the synthesis of new colloidal model particles, with specific surface prop erties, interaction potentials and particle geometries.

IFF-8: Microstructure Research

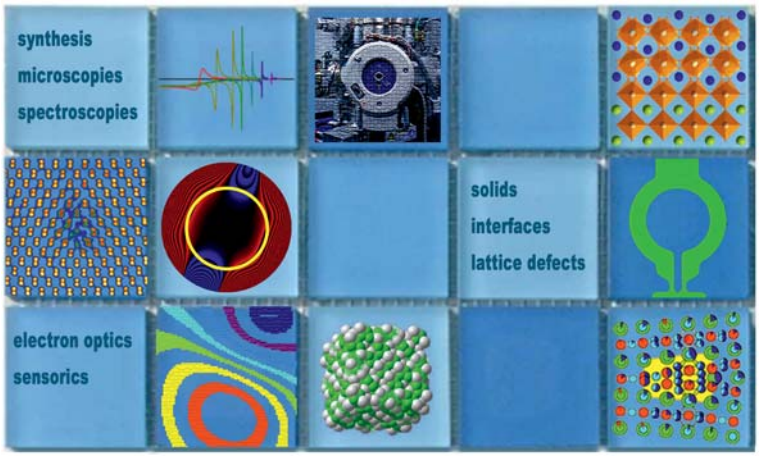

A major focus at "Microstructure Research" is the in-depth investigation of atomic-scale phenomena in crystalline solids with a special emphasis on electroceramics, complex metal alloys, and nanostructured semiconductors. Relevant issues cover the understanding of structural and electronic properties associated with heterointerfaces and lattice imperfections via a multidisciplinary research approach making use of a broad portfolio of microscopic and spectroscopic analysis techniques.

For the above purposes, IFF-8 continuously complements competence in the fields of single crystal growth, sputtering deposition technology, Josephson admittance and Hilbert spectroscopy as well as scanning tunnelling microscopy. In some of these fields, the competence covers the whole range from basic research via materials synthesis to the design and manufacturing of technical devices. In other fields, access to novel material classes and intricate problems are provided by qualified collaborations targeting on the application of ultra high-resolution transmission electron microscopy techniques accompanied by the development of novel analysis methods.

Over and above general solid state and technology-related activities, IFF-8 operates the Ernst Ruska-Centre for Microscopy and Spectroscopy with Electrons (ER-C) on a pari passu base with the Central Facility for Electron Microscopy (GFE) of RWTH Aachen University. Representing one of the world's foremost establishments in the field of electron optics research, ER-C features several unique tools for nanocharacterisation complemented by a strong expertise in the development of advanced methods provided also to external researchers within the framework of ER-C user services. Pushing the limits in the field of fundamental electron optical research is, hence, accompanied by the application of advanced techniques to the investigation of a variety of solid state phenomena taking place on the atomic scale.

IFF-9: Electronic Properties

At the Institute "Electronic Properties" we explore the multifaceted interrelations between the electronic structure and the physical properties of matter. Our current research focus lies on magnetism, magnetic phenomena, and their exploitation in nanoscience and information technology. Systems of interest range from ultrathin films and thin film layer stacks through quantum wires and dots to clusters and molecules.

Magnetism displays a complicated interplay of competing interactions taking place on different length, energy, and time scales. We are particularly interested in the influence of the reduced dimensionality and the formation of quantum effects in nanoscale magnetic structures. The crosslinks between electronic structure and magnetism are addressed by a variety of spin-resolving spectroscopic techniques, such as spin-polarized photoemission and x-ray magnetooptics. These studies are carried out at dedicated beamlines at the synchrotron radiation facilities BESSY and DELTA.

The second line of research addresses the response of magnetic systems on short (magnetodynamics) and ultrashort timescales (spin dynamics). The magnetodynamics is experimentally accessed by pump-probe schemes and interpreted via micromagnetic simulations. Laser-based techniques provide high time-resolution, whereas time-resolved photoemission microscopy combines high lateral resolution with large magnetic sensitivity and element selectivity. In the realm of spin dynamics, we study energy and angular momentum transfer processes between the electron, spin, and lattice subsystems. Such experiments are performed by femtosecond pump-probe methods.

The third topic in the IFF-9 is Spintronics, i.e. the physics of spin-dependent transport processes. Resting on a long-standing experience with magnetoresistive phenomena, the current studies focus on the fundamental physics of spin transfer phenomena. This includes the development of new magnetic material systems and nanoscale devices. Particular emphasis lies on the exploration of smart magnetic switching alternatives involving spin-polarized electrical currents and photons.

International Helmholtz Research School of biophysics and soft matter

The International Helmholtz Research School of Biophysics and Soft Matter (IHRS BioSoft) provides intensive training in biophysics and soft matter. It also offers a comprehensive framework of experimental and theoretical techniques that will enable PhD students to gain a deeper understanding of the structure, dynamics, and function of complex systems.

The IHRS BioSoft is located at Forschungszentrum Jülich, run in cooperation with the universities in Cologne and Düsseldorf and caesar Bonn, and funded by the Helmholtz Association. The research school brings together PhD students who work on soft matter and biophysics.

The fellows of IHRS BioSoft are members of institutes that participate in the new PoF program "BioSoft" (IBN-2, IBN-4, IFF-2, IFF-5, IFF-7, ISB-1, ISB-2, ISB-3), of the Institute for the Chemistry and Dynamics of the Geosphere: Phytosphere (ICG-3), and of groups of Prof. Egelhaaf, Prof. Seidel, and Prof. Willbold at Heinrich-Heine-Universität Düsseldorf, the group of Prof. Strey at Universität zu Köln, and the group of Prof. Kaupp at Forschungszentrum caesar Bonn. In particular, the IFF institutes "Theoretical Soft Matter and Biophysics" (IFF-2), "Neutron Scattering" (IFF-5), and "Soft Condensed Matter" (IFF-7) actively participate in the school's activities. The IHRS BioSoft is jointly headed by Prof. Gompper (IFF-2) and Prof. Merkel (Institute of Bio- and Nanosystems, IBN-4).

Fellows of the IHRS BioSoft are admitted after an application talk and an interview in front of a committee of faculty members. In 2009, the school had more than 20 highly qualified fellows that originated from 7 countries: China, Germany, Great Britain, Greece, France, India, and the United States of America. Four fellows have successfully finished their PhD thesis and ten students have been admitted as new fellows of the school for their three-year PhD project.

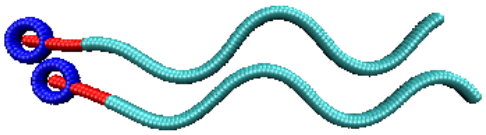

Students benefit not only from lectures, seminars, and lab courses given by experts in the field, but also from courses in transferable skills that are conducted by Imperial College London. In 2009, the courses of the IHRS BioSoft in Jülich have attracted approximately 50 students from different institutes.

In the beginning of 2009, students were offered the one-semester introductory lecture course on *'Cell Biology'* by Prof. Müller and Prof. Baumann that included lab demonstrations, and the advanced lecture courses on *'Complex Fluids'* by Prof. Strey and *'Rheology'* by Prof. Vermant (Leuven). These courses have also been attended by postdocs with special interest in the specific topic. In the summer, the lecture *'Introduction to Optical Microscopy'* has been taught jointly by Prof. Merkel and Prof. Egelhaaf and a block course *'Macromolecular Physics and Chemistry'* has been taught by Prof. Richter, Dr. Zorn, and several other colleagues from the Institute for Neutron Scattering. In winter 2009/2010, the introductory lecture course *'Statistical Mechanics I'* by Prof. Dhont and Prof. Gompper and the lecture series *'Molecules of Life I'* (coordinated by J. Fitter and in 2009 with lectures of A. Baumann, R. Merkel, J. Fitter, and C. Seidel) have started.

Several complementary laboratory courses have been organized: a four-day course on *'Electron Microscopy'* by the group of Prof. Strey coordinated by M. Baciu and conducted by L. Belkoura, a one-day course on *'NMR'* offered by B. König, and a four-day course *'Introduction to Optical Microscopy'* offered by the groups of Prof. Merkel, Prof. Egelhaaf, and Prof.

Seidel. The two-week course on *'Neutron Scattering'* (organized by T. Brückel, G. Heger, D. Richter, and R. Zorn) was again open for students of the IHRS BioSoft.

The scientific course program equips the students with basic and interdisciplinary knowledge for their research projects. From a physics point of view, entropy and statistical physics have a large influence on the behaviour of the systems that are often mesoscopic. The biological lectures cover systems from amino acids to the structure and dynamics of entire cells together with appropriate methods such as X-ray crystallography, fluorescence spectroscopy, force measurement techniques, and electrophysiology.

In addition to the scientific program, Prof. Kaupp taught a course on Scientific Writing on the Jülich campus. Furthermore, the fellows have participated in the Transferable Skills courses that were appropriate for their stage of the PhD project. On this occassion, they also had the chance for networking with PhD students from other Helmholtz Research Schools located at different centres all over Germany.

Many fellows and faculty members participated in the retreat in La-Roche-en-Ardenne, Belgium. Besides social activities, the program contained a discussion about the educational activities of the school, and a journal club. Talks in the journal club were grouped around three major topics – viruses, chemotaxis, and protein aggregation – that are interesting from a biological, physical, and chemical point of view and ranged from "How is a DNA packed into a virus?" to "H1N1 2009 - swine flu", from "sperm" to "cellular slime mold", and from "diffusion limited aggregation" to "Alzheimer".

The PhD projects that are conducted within the IHRS BioSoft cover a wide rangs of topics in Biophysics and Soft Matter and are mirrowed by the talks in the Student's Seminar. This seminar provides a major platform for the scientific exchange between groups and the talks need to be prepared for an interdisciplinary audience. Therefore a talk in the Student's Seminar is very challenging. Topics of talks that were given in 2009 include:

- Photo-control of cell networks for extracellular recording systems (V. Maybeck, Bioelectronics)
- Microstructure and short-time viscosity of suspensions of Yukawa-like colloidal particles (M. Heinen, Soft Condensed Matter)
- Self-assembly in a binary $H_2O-C_{12}E_4$ system (I. Savić, Physical Chemistry, Cologne)
- Squeezing actin: a TIRF microscopy study (A. Tsigkri, Soft Condensed Matter)
- Delayed greening in Theobroma cacao (A. Czech, Phytosphere)
- Towards single molecule studies of a multidomain protein (T. Rosenkranz, Molecular Biophysics)
- Structure and dynamics of balanced supercritical CO_2 microemulsions (M. Klostermann, Physical Chemistry, Cologne)
- Binding studies of CLE peptides and their receptors in plant stem cells (S. Grabowski, Molecular Physical Chemistry)
- Expression and composition of pacemaker channels in the mouse brain (A. Aho, Molecular Sensory Systems, Bonn)
- Self-propelled rods near surfaces: MPC simulations (K. Marx, Theoretical Soft Matter and Biophysics)
- Production and characterization of Au-nanopillar-electrodes for electrical coupling with neurons (M. Jansen, Bioelectronics)
- Mini structural genomics project of SARS coronavirus accessory proteins (J. Lecher, Structural Biochemistry)
- Star-like block copolymer micelles (S. Gupta, Neutron Scattering)
- Phosphorylation-dependent vinculin exchange dynamics during focal adhesion maturation (K. Küpper, Biomechanics)

In addition to the advertisement by its scientific output – the publications and presentations of the fellow PhD students – the school has been advertized in Physics World and on naturejobs.com. The school was also presented at larger events, such as the Jülich Soft Matter Days and the fair for young academics at the open day at Forschungszentrum Jülich.

40^{th} IFF Spring School – Nobel laureates held lectures

Forschungszentrum Jülich's "IFF Spring School" celebrated its 40th year running. Every year since 1970, the Institute of Solid State Research (IFF) had held this very successful course for students and young researchers. From 9 until 20 March 2009, everything revolved around the hot topic of "Spintronics – From GMR to Quantum Information". Among the highlights were presentations by the founders of this pioneering technology: Nobel Laureates in Physics 2007, Prof. Peter Grünberg and Prof. Albert Fert.

Twenty years ago, Peter Grünberg and Albert Fert laid the foundation for Sprintronics. Their discovery of the Giant Magnetoresistance (GMR) was honoured by the 2007 Nobel Prize in Physics. Today Spintronics is one of the most dynamic research fields in condensed matter physics, exploring the fundamentals and applications of spin-dependent transport and transfer processes.

The 40th IFF Spring School focused on the recent development in this field, such as spin torque transfer, spin Hall effect, molecular spintronics, or the exploitation of the spin in quantum information.

At the same time the School provided the students with a solid basis in spin-dependent transport, micro- and nanomagnetism, and magnetization and spin dynamics.

The discovery of Giant Magnetoresistance (GMR) in 1988 laid the foundation to a whole new and very active research field – Spinelectronics or Spintronics – which strives to exploit the electron spin as a state variable in electronic devices. The pioneering work of Peter Grünberg (IFF) and Albert Fert (Université Paris Sud), changed our view of the role of the electron spin in electrical transport and has been honoured by the 2007 Nobel Prize in Physics, partly also because of its enormous technological and economical impact. Only ten years after the discovery of the effect in the laboratory, GMR-based hard disk read heads hit the market as first generation spintronic devices and revolutionized the magnetic mass storage industry. Since its advent 20 years ago, Spintronics continues to provide us with a wide variety of spin-dependent transport processes, novel materials and many open questions and challenges. The emphasis in current spintronics research is threefold.

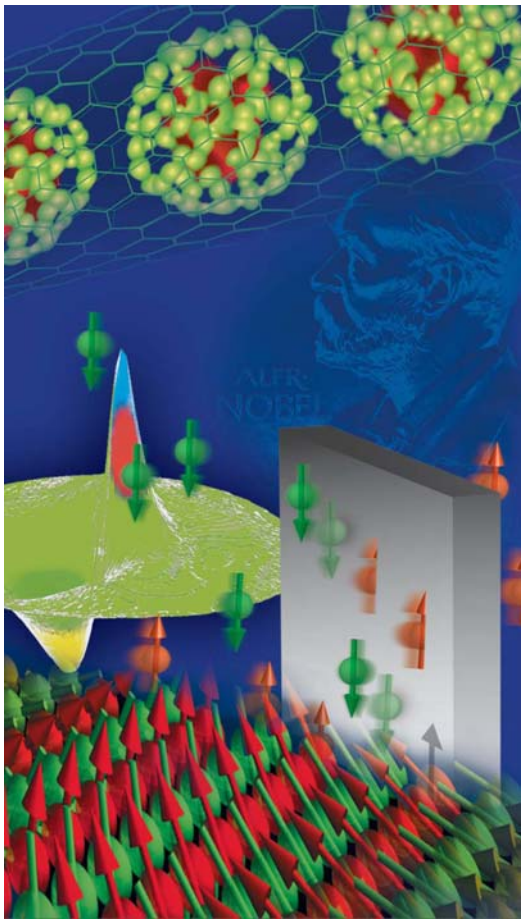

The 40th IFF Spring School focused on "Spintronics - from GMR to Quantum Information".

- First, it aims to achieve a control of spin transport on very small length scales down to the level of single spins, which will open a pathway to quantum information applications. This control also includes the active switching of the magne tization by means of spin-polarized currents.
- Second, in order to obtain the best of both worlds, spinelectronics may be combined with advanced semiconductor nanoelectronics. A crucial step in this direction is the realization of an efficient electrical spin-injection into semiconductors.

253 students and young scientists from 29 countries registered for the 40th IFF Spring School in 2009.

- Third, the next generation of spintronic devices should combine passive and active functionalities, thereby enabling magnetologic circuits and even magnetoprocessors.

On the way to meet these challenges many fundamental questions have to be solved and many materials-related issues have to be addressed. Among others this concerns the microscopic interactions and mechanisms leading to spin dephasing, the manipulation of spins by spin-orbit interactions, the understanding of spin transfer torque mechanisms, or the utilization of the spin Hall effect. On the material side, dilute magnetic semiconductors, highly spin-polarized oxides and half-metals, but also graphen and multiferroics are currently in the focus of interest.

The IFF Spring School 2009 addressed the fundamentals and new developments in spintronics on a graduate student level. The lectures were designed to first build a basis for the understanding of the major fundamental phenomena and aspects in magnetism and spin-dependent transport, including the theoretical framework for a quantitative description. The School then advanced to contemporary aspects of spin transfer processes at interfaces and in nanostructures down to the quantum level. Exchange interactions and spin effects in highly correlated materials were another important topic. Finally, current and future technological applications of spintronic concepts were discussed.

The topics of the lectures covered:

- Fundamentals of Magnetism
- Spin-dependent Interactions
- Quantum Transport
- Spin Transport Phenomena
- Spin Injection and Coherence
- Spin Transfer Torque
- Electronic Correlations
- Magnetization and Spin Dynamics
- Multiferroics
- Spin Hall Effect
- Magnetic Storage, Memory and Logics
- Quantum Information Processing

The Spring School offered about 50 hours of lectures plus discussions, as well as the opportunity to take part in practical courses and visits to the participating institutes at the Forschungszentrum Jülich. For the first time, the Spring School has been organised under the roof of the Jülich Aachen Research Alliance, section "Fundamentals of Future Information Technology" (JARA-FIT), together with the “2. Physikalisches Institut” of RWTH Aachen University.

The organizers in Jülich und Aachen:

- IFF-1: Quantum Theory of Materials
- IFF-6: Electronic Materials
- IFF-9: Electronic Properties
- RWTH Aachen University: 2. Physik. Inst. B

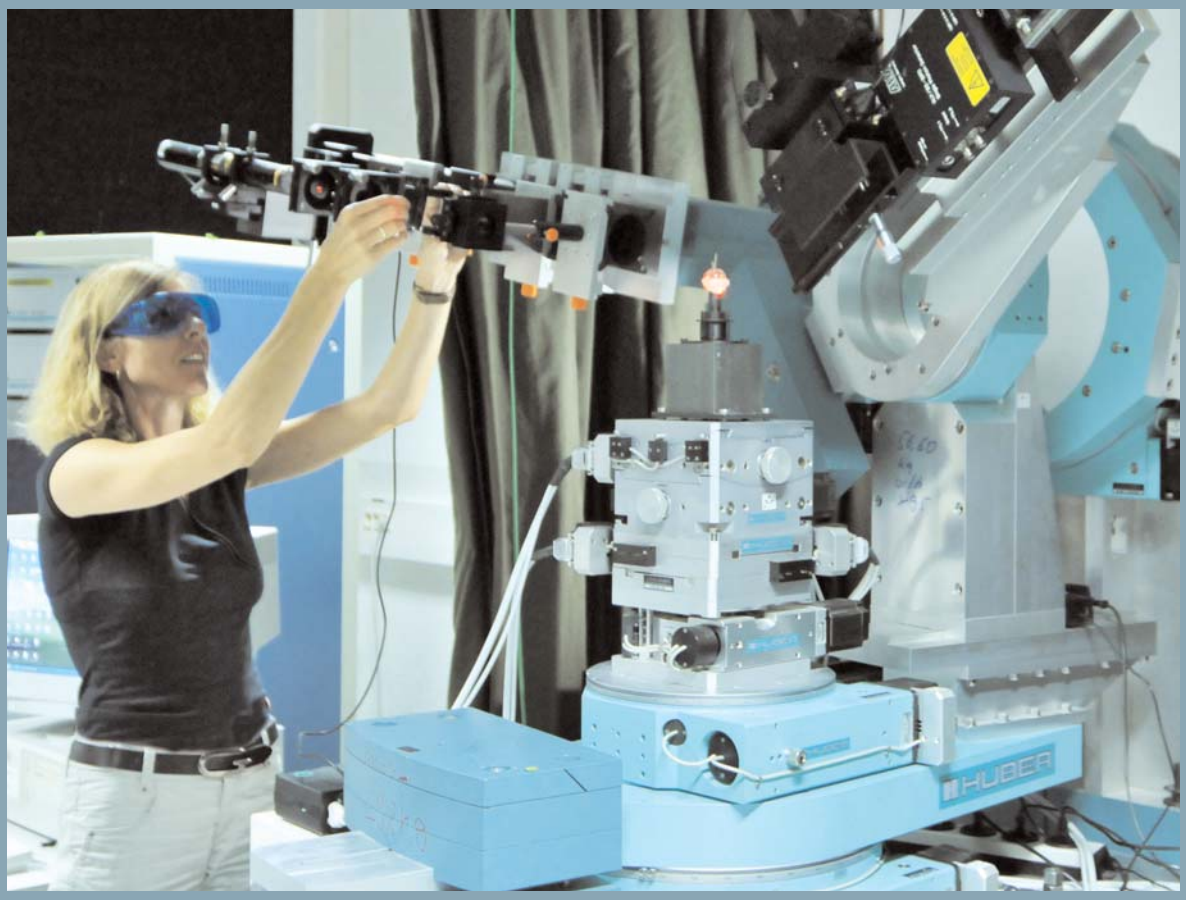

A triple-axis goniometer apparatus is used to study dynamics of colloids near fluid-solid interfaces by means of evanescent-wave scattering. The sample is contained in the small semi-spherical container in the center of the set up.

Condensed matter physics

Research in condensed matter is concerned with the complex interplay of the myriads of atoms in a solid or a liquid. Research in this field can thus be understood as the exploration of the „third infinity“, being on equal footing with the exploration of the very small scales of elementary particle physics and the very large scales of astrophysics. The conceptual framework of quantum physics and statistical physics forms the basis for our understanding of condensed matter. The cooperation of the electrons and atoms within a many-body system is responsible for the different properties of the substances and determines why they are solid, fluid or gaseous, soft or hard, transparent or opaque, magnetic, metallic or even superconducting. Extreme length and time scales give rise to the characteristic complexity of condensed matter, ranging from subatomic sizes up to macroscopic measures, from electronic reaction times in the femtosecond range up to geological periods.

Our activities focus, in particular, on multi-scale phenomena in solid state and liquid phases and are organized in three topics:

- Electronic and Magnetic Phenomena,
- From Matter to Materials, and
- Soft Matter and Biophysics.

The studies in the first topic encompass electronic and magnetic quantum states and their properties. This includes problems in highly-correlated materials, superconductivity, magnetism in low dimensions and on short time scales. The second topic deals with phase transitions and transport processes, glass-like states, and complex metallic alloys, and finally structure formation and self-organization. In the third topic, structure formation and self-organization, mesoscopic dynamics and driven systems, as well as biology-inspired physics are addressed.

The spectrum of the materials investigated covers a wide range from metals, semiconductors and ceramics, through macromolecular systems up to biological systems and cells. For this purpose, a broad portfolio of theoretical and experimental techniques is utilized, which are constantly improved and progressed. The experimental emphasis lies on neutron scattering, synchrotron-radiation methods and ultrahigh resolution electron microscopy, whereas the theoretical treatments range from quantum theory to statistical physics and involve both analytical and numerical procedures.

Origin of Jahn-Teller distortion and orbital-order in $LaMnO_3$

E. Pavarini[1,2], E. Koch[3,4]

[1] IFF-3: Theory of Structure Formation
[2] IAS: Institute for Advanced Simulation
[3] IFF-1: Quantum Theory of Materials
[4] German Research School for Simulation Sciences, Forschungszentrum Jülich and RWTH Aachen

The origin of the cooperative Jahn-Teller distortion and orbital-order in $LaMnO_3$ is central to the physics of the manganites. To clarify the situation we use the LDA+dynamical mean-field method to disentangle the effects of super-exchange from those of lattice distortions. We find [1] that super-exchange alone would yield $T_{\mathrm{KK}} \sim 650$ K. The tetragonal and $GdFeO_3$-type distortions, however, reduce T_{KK} to ~ 550 K. Thus electron-phonon coupling is essential to explain the persistence of local Jahn-Teller distortions to $\gtrsim 1150$ K and to reproduce the occupied orbital deduced from neutron scattering.

The insulating perovskite $LaMnO_3$ is the parent compound of the colossal magneto-resistance manganites and it is considered a text-book example of a cooperative Jahn-Teller (JT) orbitally-ordered material. Two distinct mechanism have been proposed to explain the cooperative distortion: many-body Kugel-Khomskii (KK) super-exchange (SE) [2] and one-electron electron-phonon (EP) coupling [3]. Determining the relative strength of these mechanisms will provide a measure of the importance of strong correlation effects for the orbital physics in the manganites. Unfortunately the situation is complicated by the simultaneous presence of tetragonal and $GdFeO_3$-type distortions as well as a strong Hund's rule coupling between the Mn e_g and t_{2g} electrons.

In $LaMnO_3$ the Mn^{3+} ions are in a $t_{2g}^3\, e_g^1$ configuration. Due to strong Hund's rule coupling the spin of the e_g electron is parallel to the spin of the t_{2g} electrons on the same site, $\mathbf{S}_{t_{2g}}$. Above $T_N = 140$ K the spins on neighboring sites are disordered. The crystal structure is orthorhombic (Fig. 1). It can be understood by starting from an ideal cubic perovskite structure with axes $\mathbf{x}$, $\mathbf{y}$ and $\mathbf{z}$: First, a tetragonal distortion reduces the Mn-O bond along $\mathbf{z}$ by 2%. The La-O and La-Mn covalencies induce a $GdFeO_3$-type distortion resulting in an orthorhombic lattice with axes $\mathbf{a}$, $\mathbf{b}$, and $\mathbf{c}$, with the oxygen-octahedra tilted about $\mathbf{b}$ and rotated around $\mathbf{c}$ in alternating directions. Finally, the octahedra distort, with long (l) and short (s) bonds alternating along $\mathbf{x}$ and $\mathbf{y}$, and repeating along $\mathbf{z}$. This is measured by $\delta_{JT} = (l-s)/((l+s)/2)$. The degeneracy of the e_g orbitals is lifted and the occupied orbital, $|\theta\rangle = \cos\frac{\theta}{2}|3z^2-1\rangle + \sin\frac{\theta}{2}|x^2-y^2\rangle$, is $\sim |3l^2-1\rangle$, i.e. it points in the direction of the long axis. Thus orbital-order (OO) is d-type with the sign

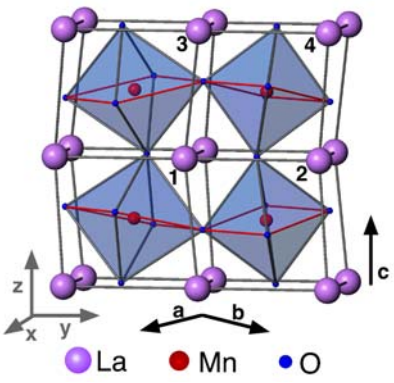

FIG. 1: Structure of $LaMnO_3$ at 300 K. For sites 1 and 3 the long (short) bond l (s) is $\sim$ along $\mathbf{y}$ ($\mathbf{x}$), vice versa for sites 2 and 4 (d-type pattern). All Mn sites are equivalent. The symmetries that transform them into a site of type 1 are: $x \leftrightarrow y$ (site 2) $z \to -z$ (site 3), $x \leftrightarrow y$, $z \to -z$ (site 4).

of θ alternating along $\mathbf{x}$ and $\mathbf{y}$ and repeating along $\mathbf{z}$. At 300 K the JT distortion is substantial, $\delta_{JT} = 11\%$, and $\theta \sim 108^o$ was estimated from neutron scattering data. Above $T_{OO} \sim 750$ K a strong reduction to $\delta_{JT} = 2.4\%$ was reported, accompanied by a change in θ to $\sim 90^o$. Recently this was, however, identified as an order-to-disorder transition: Due to orientational disorder, the crystal appears cubic on average, while, within nano-clusters, the MnO_6 octahedra remain fully JT distorted up to $T_{JT} \gtrsim$1150 K.

To identify the driving mechanism for OO in $LaMnO_3$, it is mandatory to account for both the realistic electronic structure and many-body effects. To understand the mechanism one has to disentangle the contribution of KK SE from that of the JT or the $GdFeO_3$-type and tetragonal distortions. In the present work [1] we do this by calculating directly the Kugel-Khomskii super-exchange transition temperature, T_{KK}. We adopt the method used successfully for $KCuF_3$ [4], and based on the LDA + dynamical mean-field theory (DMFT) or LDA + cluster DMFT (CDMFT) approach (implemented as in [5]). We consider several structures: (i) the room temperature structure, R_{11} with $\delta_{JT} = 11\%$, and a series of hypothetical structures, $R_{\delta_{JT}}$, with reduced JT distortion δ_{JT}, (ii) the (average) structure found at 800 K, $R_{2.4}^{800\mathrm{K}}$, which has a slightly larger volume than R_{11} and a smaller $GdFeO_3$-type distortion, and (iii) the

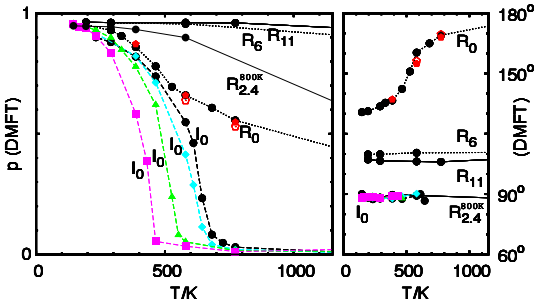

FIG. 2: Orbital polarization p (left) and (right) occupied state $|\theta\rangle$ for sites 1 as a function of temperature. Solid line: 300 K (R_{11}) and 800 K ($R_{2.4}^{800K}$) structures. Dots: same structure with half (R_6) or no (R_0) JT distortion. Pentagons: 2 (full) and 4 (empty) sites CDMFT. Dashes: ideal cubic system (I_0) for U (eV) 5 (circles), 5.5 (diamonds), 6 (triangles), 7 (squares). Crystal-field splitting (meV): 840 (R_{11}), 495 (R_6), 219 (R_0), 168 ($R_{2.4}^{800K}$), and 0 (I_0).

ideal cubic structure, I_0, with the same volume as R_{11}. For all structures we find that at each site the e_g spins align to $\mathbf{S}_{t_{2g}}$. We calculate the orbital polarization p as a function of temperature by diagonalizing the DMFT (or CDMFT) occupation matrix and taking the difference between the occupation of the most ($|\theta\rangle$) and least ($|\theta+\pi\rangle$) filled orbital.

For the 300 K structure (R_{11}) the e_g states split by ~ 840 meV, in good agreement with experiments. We find an insulating solution in the full range $U = 4-7$ eV. For $U = 5$ eV, suggested by recent estimates, the Hubbard bands are at ~ -1.5 and 2 eV, gap and spectra are in line with experiments. We find that even at 1150 K the system is fully orbitally polarized ($p \sim 1$), the occupied state is $|\theta\rangle \sim |106^o\rangle$ at site 1 and and the OO is d-type. We find that things hardly change when the JT distortion is halved (R_6). Even for the average 800 K structure ($R_{2.4}^{800K}$) OO does not disappear: Although the JT distortion is strongly reduced to $\delta_{JT} = 2.4\%$, the crystal-field splitting is ∼168 meV and the orbital polarization at 1150 K is as large as $p \sim 0.65$, while θ is now close to 90^o. For all these structures, OO is already determined by the distortions via the crystal-field splitting.

To find the temperature $T_{\rm KK}$ at which Kugel-Khomskii super-exchange drives orbital-order we consider the zero crystal-field limit, i.e. the ideal cubic structure, I_0. Removing the $GdFeO_3$-type distortion sizably increases the e_g band-width; for $U = 5$ eV the ideal-cubic system is a Mott insulator (with a tiny gap) only below $T \sim 650$ K. To check how strongly $T_{\rm KK}$ changes when the gap opens, we increase U. For $U = 5.5$ eV we find an insulating solution with a small gap of ~ 0.5 eV and $T_{\rm KK}$ still close to ~ 650 K. For $U = 6$ eV, $E_g \sim 0.9$ eV and $T_{\rm KK} \sim 550$ K. Even with an unrealistically large $U = 7$ eV, giving $E_g \sim 1.8$ eV, $T_{\rm KK}$ is still as large as ~ 470 K. Thus, despite the small gap, $T_{\rm KK}$ decreases as $\sim 1/U$, as expected for SE. For a realistic $U \sim 5$ eV, the calculated $T_{\rm KK} \sim 650$ K is surprisingly close to the order-disorder transition temperature, $T_{OO} \sim 750$ K, though still much smaller than $T_{JT} \gtrsim 1150$ K. The occupied state at site 1 is $|\theta\rangle \sim |90^o\rangle$ for all U.

It remains to evaluate the effect of the orthorhombic distortion on the transition. For this we perform calculations for the system R_0 with no JT distortion, but keeping the tetragonal and $GdFeO_3$-type distortion of the 300 K structure. This structure is metallic for $U = 4$ eV; for $U = 5$ eV it has a gap of ~ 0.5 eV. We find a large polarization already at 1150 K ($p \sim 0.45$). Such polarization is due to the crystal-field splitting of about 219 meV, with lower crystal-field states at site 1 given by $|1\rangle \sim |x^2 - y^2\rangle$. Surprisingly the most occupied state $|\theta\rangle$ is close to $|1\rangle$ ($\theta \sim 180$) only at high temperature (~ 1000 K). The orthorhombic crystal-field thus competes with SE, analogous to an external field with a component perpendicular to an easy axis. On cooling the occupied orbitals rotate to $|\theta\rangle \sim |132^o\rangle$ (see Fig. 2). This effect of SE, occurs around a characteristic temperature $T_{\rm KK}^{\rm R} \sim 550$ K; still surprisingly large, but reduced compared to $T_{\rm KK}$ for the ideal cubic system I_0 and much smaller than the experimental $T_{JT} \gtrsim 1150$ K. Short-range correlations could reduce $T_{\rm KK}^{\rm R}$ or modify θ. To estimate this effect we perform CDMFT calculations; our results (Fig. 2) remain basically unchanged.

In conclusion, we find [1] that $T_{\rm KK}^{\rm R}$ in orthorhombic $LaMnO_3$ is ~ 550 K. We have shown that two elements are crucial: the super-exchange mechanism, which yields a transition temperature as high as 650 K, and the tetragonal plus $GdFeO_3$-type distortion, which, due to the reduced hopping integrals and the competing orthorhombic crystal-field, reduces $T_{\rm KK}$ to 550 K. Experimentally, an order-to-disorder transition occurs around $T_{OO} \sim 750$ K, but a local Jahn-Teller distortion persists in the disordered phase up to $T_{JT} \gtrsim 1150$ K. The Kugel-Khomskii mechanism alone cannot account for the presence of such Jahn-Teller distortions above 550 K ($T_{\rm KK}^{\rm R} \ll T_{JT}$). It also cannot justify the neutron scattering estimate $\theta = 108^o$. Thus electron-phonon coupling is a crucial ingredient, both for making the Jahn-Teller distortions energetically favorable at such high temperatures and in determining the occupied orbital.

[1] E. Pavarini and E. Koch, arxiv:0904.4603.

[2] K. I. Kugel and D. I. Khomskii, Zh. Eksp. Teor. Fiz. **64**, 1429 (1973) [Sov. Phys. JETP **37**, 725 (1973)].

[3] J. Kanamori, J. Appl. Phys. **31**, S14 (1960).

[4] E. Pavarini, E. Koch, and A. I. Lichtenstein, Phys. Rev. Lett. **101**, 266405 (2008).

[5] E. Pavarini *et al.*, Phys. Rev. Lett. **92**, 176403 (2004); E. Pavarini, A. Yamasaki, J. Nuss and O. K. Andersen, New J. Phys. **7** 188 (2005). M. De Raychaudhury, E. Pavarini, O. K. Andersen, Phys. Rev. Lett. **99**, 126402 (2007).

Ordering phenomena in lightly hole-doped $La_{1-x}Sr_xMnO_3$ single crystals

H.-F. Li[1], Y. Su[1,2], Y. G. Xiao[1], J. Persson[1], P. Meuffels[3], Th. Brückel[1,2]

[1] IFF-4: Scattering Methods
[2] JCNS: Jülich Centre for Neutron Science
[3] IFF-6: Electronic Materials

The ordering phenomena have long been of great interest in CMR manganites. Herein reports a detailed study of the structural and magnetic transitions by neutron powder diffraction (NPD) and magnetization measurements and the charge/orbital ordering (CO/OO) phenomena by resonant x-ray scattering (RXS) in single-crystal $La_{\frac{7}{8}}Sr_{\frac{1}{8}}MnO_3$. The NPD study shows that the sample belongs to orthorhombic ($Pnma$, O) above the Jahn-Teller (JT) transition [T_{JT} = 270(1) K] and monoclinic ($P12_1/c1$, M') below the JT regime. At 5 K, a small *A*-type antiferromagnetic moment [0.54(2) μ_B/Mn] is imbedded in a larger ferromagnetic matrix [3.43(5) μ_B/Mn], indicating a possible electronic phase separation. The RXS results present strong resonant enhancements of the CO/OO (0 0.5 0) reflection ($Pnma$) at the Mn L_{III}-edge and the oxygen *K*-edge, but not at the Mn *K*-edge, providing an experimental evidence of the hole ordering below $T_{CO/OO}$ = 150(1) K.

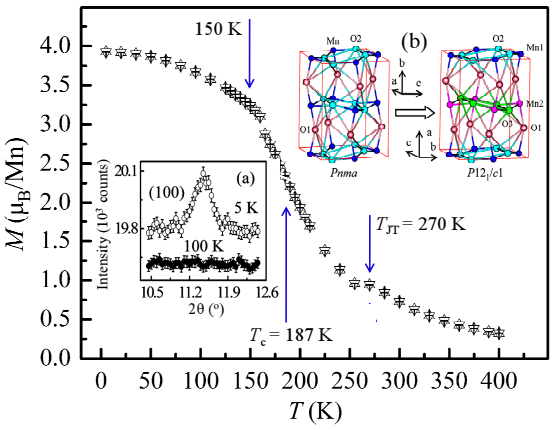

FIG. 1: Temperature dependence of the ZFC (up triangles) and FC (down triangles) magnetization at 70 kOe. Inset (a) shows the presence of an A-AFM (1 0 0) peak in $P12_1/c1$ symmetry at 5 K. Inset (b) illustrates the lattice unit cells of Pnma (left) and $P12_1/c1$ (right) symmetries. The detailed characterizations and phase transitions were reported in Ref. [3].

The parent compound $LaMnO_3$ is an antiferromagnetic (AFM) insulator with an orbital order induced by the cooperative Jahn-Teller (JT) effect of Mn^{3+} ions below the JT transition. With Sr doping, the JT distortion is gradually suppressed, which leads to a ferromagnetic insulator (FMI) and finally to a FM metal (FMM) state. The classical double-exchange mechanism originally formulated by Zener and the strong Hund's coupling are able to qualitatively explain the FMM phase observed at intermediate hole-doping levels. However, the nature of the unusual FMI state in lightly doping levels has attracted much attention and given rise to many controversies. $La_{\frac{7}{8}}Sr_{\frac{1}{8}}MnO_3$ is one of the outstanding examples to tackle the complex ordering phenomena in highly correlated electrons. Up to now, the detailed actual structure of this compound in the FMI regime has not been solved. Although the importance of the charge/orbital ordering (CO/OO) phenomena on understanding the microscopic origin of the FMI phase has been realized, the exact and detailed CO/OO model is till a puzzle just because of the bewildering structures.

High-quality single crystals of $La_{1-x}Sr_xMnO_3$ were grown by an optical floating-zone method at Research Center Jülich GmbH, Germany. The dc magnetization was measured on a Quantum Design MPMS-7 superconducting quantum interference device (SQUID) magnetometer. For the neutron powder diffraction (NPD) measurements performed on the SPODI at the FRM-II, Germany, a suitable piece was cut from the center of a big single crystal and was lightly ground into powder. The resonant x-ray scattering (RXS) studies were carried out on the two-circle UHV ALICE diffractometer at the UE56/1-PGM-b beamline at BESSY, Germany, and the 6 ID-B beamline at APS, Argonne, USA.

We first tried to solve the crystal structure of $La_{\frac{7}{8}}Sr_{\frac{1}{8}}MnO_3$ as a function of temperature. Our previous studies show that slightest deviations from nominal stoichiometry can affect the physical properties of these manganites drastically [1, 2]. In addition, single-crystalline and ceramic samples show different behaviours, and these crystals are heavily twinned with an increasingly complex twining pattern as the symmetry is reduced in subsequent phase transitions. Therefore, we investigated a well defined single crystal. The magnetization measurements at 70 kOe (Fig. 1) show the clear indications of the JT, FM and CO/OO transitions at 270(1) K, 187(1) K and 150(1) K, respectively, indicating the high quality of the single crystal. The detailed characterizations and

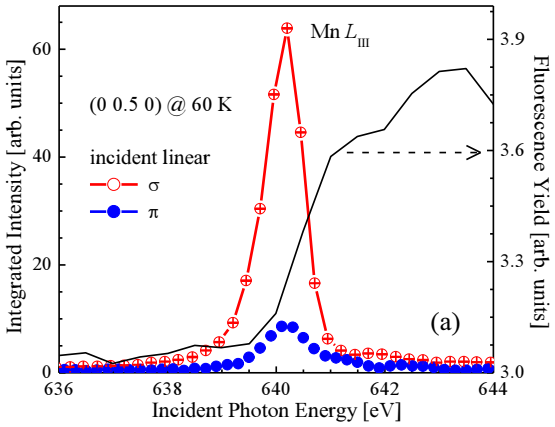

FIG. 2: Resonances of the CO (0 0.5 0) reflection (Pnma) with σ and π polarizations at the Mn L_{III}-edge and 60 K.

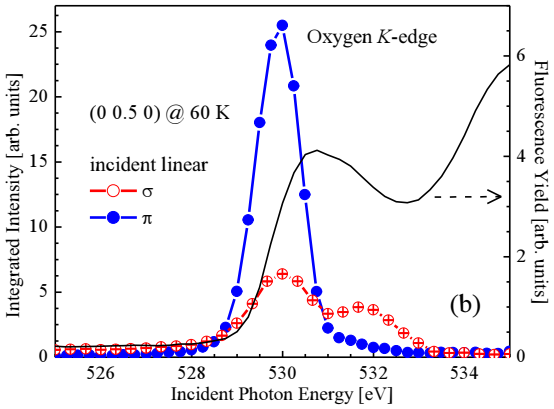

FIG. 3: Resonances of the CO (0 0.5 0) reflection (Pnma) with σ and π polarizations at the oxygen K-edge and 60 K.

phase transitions were reported in Ref. [3].

We confirmed that the sample has an O ($Pnma$) structure above the T_{JT} = 270(1) K and a monoclinic ($P12_1/c1$, M') one between T_{JT} and $T_{CO/OO}$ = 150(1) K by comparing the two competing models [3]. We have also refined the NPD data below $T_{CO/OO}$ with the $P12_1/c1$ symmetry because the experimental resolution was insufficient to clearly identify the triclinic ($P\bar{1}$) structure. The unit cells of $Pnma$ (left) and $P12_1/c1$ (right) symmetries are illustrated in the inset (b) of Fig. 1, where the Mn and O2 sites in $Pnma$ symmetry split into Mn1, Mn2 sites and O2, O3 sites in the $P12_1/c1$ symmetry, respectively, while O1 still retains one site. We find that short-range *A*-AFM domains indicated by an appearance of a broad (1 0 0) peak [inset (a) of Fig. 1] are embedded in the long-range ordered FM domains at 5 K. This peak disappears at 100 K, indicating the melting of the AFM domains. In addition, the AFM and FM moments have the same orientation indicative of a possible phase separation. The BVS's results show no obvious charge disproportion between the two distinct Mn1 and Mn2 sites in spite of a big difference existing between their JT distortion sizes. The detailed results in this part was published in [3].

The interesting FMI phase in $La_{\frac{7}{8}}Sr_{\frac{1}{8}}MnO_3$ below $T_{CO/OO}$ has been usually related to the CO/OO phenomena. The proposed orbital-polaron model has more or less evidenced the occurrence of OO. However, the above calculated charge disproportion between Mn1 and Mn2 [maximum is 0.11(5) e^-] [3] falls into the shade in contrast with the traditionally proposed integral charge difference one e^- between Mn^{3+} and Mn^{4+} ions. In order to solve the puzzle of CO in this compound, we performed the RXS studies.

In the classic ionic scenario, the CO in manganites occurs with Mn^{3+} and Mn^{4+} ions being arranged periodically. This ordered pattern can be detected by a measure of the chemical shift in 1*s* core level, since this chemical shift will lead to an occurrence of the resonance at the Mn *K*-edge via the 1*s*$\longrightarrow$4*p* dipolar transition. However, we did not observe this kind of resonance in the hard x-ray range indicative of the failure of the classic ionic CO scenario.

In contrast, in the soft x-ray region, the resonance at the Mn $L_{II,\ III}$-edges corresponds to 2*p*$\longrightarrow$3*d* excitations, which is believed to be the direct experimental evidence for the 3*d* valence states, orbitals, spins, etc. We observed the resonant enhancement of the CO (0 0.5 0) reflection at the Mn L_{III}-edge ($\sim$640.0 eV) at 60 K as shown in Fig. 2, indicating the occurrence of the CO at the Mn sites. Surprisingly, this reflection also displays a strong resonance at the oxygen *K*-edge (Fig. 3). Both resonances have a strong polarization (σ and π) dependence. Their temperature dependences coincide with the FMI phase transition in this compound. These results provide a strong evidence that due to the oxygen 2*p*-Mn 3*d* hybridization, the holes due to doping are partly localized on the oxygen sites. This situation is similar to the so-called Zhang-Rice singlets proposed for high T_c cuprates.

These results reveal the importance of spin, charge and lattice interactions in manganites. Theoretically modeling these resonances are indispensable for further understanding the physics behind.

Acknowledgements: The authors would like to thank the Neutron Source at FRM-II (Garching, Germany) and the Synchrotron Radiation Sources at BESSY (Berlin, Germany) and APS (Argonne, USA) for providing excellent conditions of the corresponding beamlines.

[1] H.-F. Li, Y. Su, J. Persson, P. Meuffels, J. M. Walter, R. Skowronek, and Th. Brückel, J. Phys.: Condens. Matter **19**, 176226 (2007).

[2] H.-F. Li, Y. Su, J. Persson, P. Meuffels, J. M. Walter, R. Skowronek, and Th. Brückel, J. Phys.: Condens. Matter **19**, 016003 (2007).

[3] H.-F. Li, Y. Su, Y. G. Xiao, J. Persson, P. Meuffels, and Th. Brückel, Eur. Phys. J. B **67**, **149** (2009).

Non-Fermi-liquid behavior in cuprates: a cluster dynamical mean field study

A. Liebsch[1], N.-H. Tong[2]

[1] IFF-1: Quantum Theory of Materials
[2] Department of Physics, Renmin University of China, 100872 Beijing, China

The effect of doping in the two-dimensional Hubbard model is investigated within finite temperature exact diagonalization combined with cluster dynamical mean field theory. To evaluate the phase diagram, the transition from Fermi-liquid to non-Fermi-liquid behavior is studied as a function of Coulomb energy and temperature. The self-energy component $\Sigma_{X=(\pi,0)}(\omega)$ is shown to exhibit a collective mode above E_F whose energy and strength varies with doping. As the hole doping decreases below a critical value δ_c, this low-energy excitation gives rise to non-Fermi-liquid behavior, opening of a pseudogap, and particle-hole asymmetry, in agreement with recent photoemission data. For electron doping, the collective mode and the concomitant pseudogap are located below E_F.

The nature of the metal insulator transition as a function of doping is one of the key issues in strongly correlated materials, such as high-T_c cuprates. Experimental studies reveal a rich phase diagram, with conventional Fermi-liquid behavior in overdoped metals and an anomalous non-Fermi-liquid pseudogap phase in underdoped systems close to the Mott insulator. One of the most challenging aspects of the non-Fermi-liquid phase is the observation of highly non-isotropic behavior in momentum space. Whereas along the nodal direction ΓM well-defined quasiparticles exist, in the vicinity of $X = (\pi, 0)$ strong deviations from Fermi-liquid behavior occur. In particular, below a critical doping a pseudogap appears which becomes more prominent close to the Mott insulator.

In [1] we use cluster dynamical mean field theory (CDMFT) [2] in combination with exact diagonalization (ED) to investigate the two-dimensional Hubbard model on a square lattice for 2×2 clusters:

$$H = -\sum_{\langle ij\rangle\sigma} t_{ij}(c^+_{i\sigma}c_{j\sigma} + \text{H.c.}) + U\sum_i n_{i\uparrow}n_{i\downarrow}. \quad (1)$$

The band dispersion is given by $\epsilon(\mathbf{k}) = -2t[\cos(k_x) + \cos(k_y)] - 4t'\cos(k_x)\cos(k_y)$. To represent hole-doped cuprate systems, the nearest and next-nearest neighbor hopping integrals are defined as $t = 0.25$ and $t' = -0.3t$. The local Coulomb interaction is $U = 10t$ so that, at half-filling, the system is a Mott insulator.

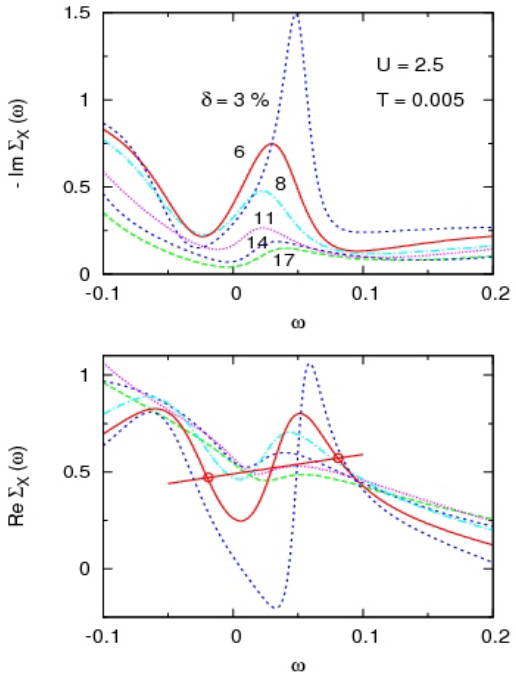

FIG. 1: Self-energy $\Sigma_X(\omega)$ for several hole doping concentrations δ. Upper panel: imaginary part; lower panel: real part; $U = 2.5$, $T = 0.005$. The outer intersections of $Re\Sigma_X$ with the straight lines $\omega + \mu - \epsilon_k$ yield the approximate width of the pseudogap Δ.

Within CDMFT the interacting lattice Green's function is given by

$$G_{ij}(i\omega_n) = \sum_{\mathbf{k}} [i\omega_n + \mu - t(\mathbf{k}) - \Sigma(i\omega_n)]^{-1}_{ij} \quad (2)$$

where the $\mathbf{k}$ sum extends over the reduced Brillouin Zone, $\omega_n = (2n+1)\pi T$ are Matsubara frequencies and μ is the chemical potential. $t(\mathbf{k})$ denotes the hopping matrix for the superlattice. For the purpose of perfoming the ED calculation the impurity cluster Green's function $G_0(i\omega_n) = [G(i\omega_n)^{-1} + \Sigma(i\omega_n)]^{-1}$ is projected onto a larger cluster consisting of 4 impurity levels and 8 bath levels. The cluster self-energy matrix $\Sigma_{ij}(i\omega_n)$ is derived by making use of the Arnoldi algorithm to calculate low-lying excited states. An important advantage of ED is the accessibility of large

Coulomb energies and low temperatures, and the absence of sign problems. This scheme has recently also been used to evaluate the phase diagram of the partially frustrated Hubbard model for triangular lattices.[3] Further details are given in [4].

The key quantity which exhibits the change from Fermi-liquid to non-Fermi-liquid behavior most clearly is the self-energy component Σ_X associated with $X = (\pi, 0)$. As shown in Fig. 1, for hole doping $\delta \leq 15 \ldots 20$ %, spatial fluctuations within the cluster give rise to a low-energy collective mode in $\mathrm{Im}\,\Sigma_X(\omega)$, whose energy and strength exhibit a characteristic variation with doping. The real part of $\Sigma_X(\omega)$ then exhibits a positive slope above E_F, implying removal of spectral weight from electron states and the opening of a pseudogap in the density of states. These results are consistent with earlier work performed within quantum Monte Carlo (QMC) and ED at $T = 0$ [5].

As a result of the pseudogap, the density of states acquires a very asymmetric shape. At large doping the Fermi level is located at a peak in the density of states, and quasiparticle broadening varies quadratically near E_F. For decreasing doping the pseudogap shifts downwards, giving rise to a marked particle-hole asymmetry in the spectral distributions $A(\mathbf{k}, \omega)$ due to enhanced quasi-particle damping predominantly above E_F. Moreover, with decreasing doping the pseudogap appears first along the antinodal direction before it opens across the entire Fermi surface.

To make contact to recent ARPES measurements on $Bi_2Sr_2CaCu_2O_{8+\delta}$ [6] we have calculated the spectral distributions $A(\mathbf{k}, \omega)$ defined as

$$A(\mathbf{k}, \omega) = -\frac{1}{\pi} \mathrm{Im}\,[\omega + \mu - \epsilon(\mathbf{k}) - \Sigma(\mathbf{k}, \omega)]^{-1}, \quad (3)$$

where $\Sigma(\mathbf{k}, \omega)$ represents an interpolation between Σ_Γ, Σ_M, and Σ_X [2]. These spectra are shown in Fig. 2 for the same cuts through the Brillouin Zone as in the experiment: cut 1 corresponds to the nodal direction and has the lowest relative weight from $\Sigma_X(\omega)$, whereas cuts 2 and 3 are parallel to this line at 25 and 50 % towards $X = (\pi, 0)$. Thus, along these cuts the X component becomes more prominent.

For large doping, the system is a Fermi liquid. Thus, the spectral weight at all three cuts is largest at E_F and decays symmetrically for increasing and decreasing ω. Particle-hole asymmetry is then limited to energies far from E_F. Below critical doping ($\delta = 0.14$, top panel), the particle-hole symmetry initially persists along the nodal direction, but gets weaker along cut 3. At $\delta = 0.11$, this asymmetry begins to extend to the nodal direction, until at $\delta = 0.08$ (lower panel) the particle-hole asymmetry is complete throughout the Brillouin zone. These spectral distributions reveal that the particle-hole asymmetry is a direct consequence of the pseudogap which gradually develops with doping in the region $\omega \approx 0.02 \ldots 0.05$ above E_F, and which is driven by the $(\pi, 0)$ component of the self-energy. The momentum dependent opening of the pseudogap above E_F, and the particle-hole

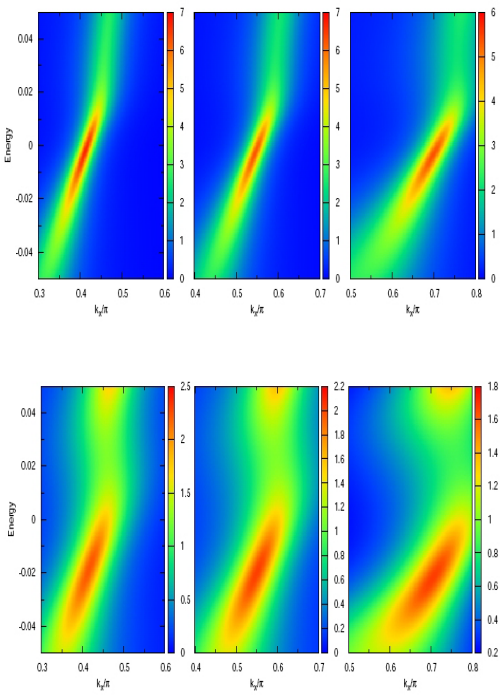

FIG. 2: Spectral function $A(\mathbf{k}, \omega)$ along cuts 1, 2, 3 (from left to right, see text); upper panel: doping $\delta = 0.14$; lower panel: $\delta = 0.08$; $U = 2.5$, $T = 0.005$.

asymmetry caused by the collective mode seen in $\mathrm{Im}\,\Sigma_X(\omega)$, are in qualitative agreement with ARPES data [6].

The T/U phase diagram shows that for hole doping $\delta_c \approx 0.15 \ldots 0.20$ for various system parameters, i.e., near the optimal doping observed in many high-T_c cuprates. For electron doping, the resonance of $\Sigma_X(\omega)$ and the corresponding pseudogap are located below E_F. The critical doping which marks the onset of non-Fermi-liquid behavior is systematically smaller than for hole doping. Moreover, the Mott transition induced via electron doping exhibits first-order hysteresis, while the hole doping transition appears to be continuous or weakly first-order. The consistency of these results with previous work demonstrates that finite-temperature cluster ED/DMFT is a highly useful and accurate method that complements alternative cluster DMFT approaches.

[1] A. Liebsch and N.-H. Tong, Phys. Rev. B **80**, 165126 (2009).

[2] G. Kotliar, S. Y. Savrasov, G. Palsson, and G. Biroli, Phys. Rev. Lett. **87**, 186401 (2001).

[3] A. Liebsch, H. Ishida, and J. Merino, Phys. Rev. B **79**, 195108 (2009).

[4] C. A. Perroni, H. Ishida, and A. Liebsch, Phys. Rev. B **75**, 045125 (2007).

[5] M. Jarrell *et al.*, Europhys. Lett. **56**, 563 (2001); B. Kyung *et al.*, Phys. Rev. B **73**, 165114 (2006).

[6] H.-B. Yang *et al.*, Nature **456**, 77 (2008).

Phonon dynamics in parent and superconducting FeAs compounds

R. Mittal[1,2,3], Y. Su[1,2], L. Pintschovius[4], M. Zbiri[5], S. Rols[5], Y. Xiao[2], H. Schober[5], S. L. Chaplot[3], T. Chatterji[1], R. Heid[4], Th. Brueckel[1,2]

[1] JCNS: Jülich Centre for Neutron Science
[2] IFF-4: Scattering Methods
[3] Solid State Physics Division, Bhabha Atomic Research Centre, Trombay, Mumbai 400 085, India
[4] Forschungszentrum Karlsruhe, Institut für Festkörperphysik, P.O.B. 3640, D-76021 Karlsruhe, Germany
[5] Institut Laue-Langevin, BP 156, 38042 Grenoble Cedex 9, France

We have carried out extensive measurements of the phonon dispersion relation and phonon density of states for the newly discovered parent and superconducting FeAs compounds using inelastic neutron scattering technique. The phonon spectra are analyzed using ab-initio and empirical model calculations giving density of states and dispersion relation. We found strong temperature dependence of some phonons in $CaFe_2As_2$ near the structural phase transition around 172 K, which may indicate strong electron phonon coupling and/or anharmonicity. Furthermore, measurement of phonon density of states in $CaFe_{1-x}Co_xAsF$ compounds (x = 0, 0.06, 0.12) support coupling of electrons and phonons in Co doped CaFeAsF compounds.

The discovery of superconductivity in fluorine-doped RFeAsO (R = rare earth) and K-doped $BaFe_2As_2$has stimulated enormous interest [1–10] in the field of condensed matter physics. It is important to note that these compounds have high superconducting transition temperatures without requiring the presence of copper oxide layers. Electron or hole doping suppresses structural and magnetic phase transitions and induces superconductivity at lower temperatures. At present, it remains unclear whether the change of the electron concentration by doping is essential for achieving superconductivity or whether the suppression of the phase transition into a magnetically ordered state is the main effect.

Theoretical electronic structure calculations for FeAs compounds show that superconductivity in these compounds is mainly due to the structural and electronic states of the Fe-As layers. The mechanism of superconductivity, and in particular the role of lattice dynamics in superconducting pair formation in these newly discovered compounds is still to be settled. Meanwhile it is necessary to study phonon dynamics carefully in these materials. This has motivated us to carry out measurements of phonon dynamics [4–10] in parent and superconducting FeAs compounds.

We have extensively carried out [4] inelastic neutron scattering measurements of phonons on a single crystal of $CaFe_2As_2$. The measurements allowed us to establish a fairly complete picture of phonon dispersions in the main symmetry directions. The experiment was carried out on the 1T1 triple-axis spectrometer at the Laboratoire Léon Brillouin, Saclay. The phonon spectra were also calculated by density functional theory (DFT) in the local density approximation (LDA). There are serious discrepancies between calculations done for the optimized structure and experiment, because the optimised structure is not the ambient pressure structure but is very close to the “collapsed” structure reached at p = 3.5 kbar. However, if the experimental crystal structure is used the calculation gives correct frequencies of most phonons. We also observed strong temperature dependence of some phonons near the structural phase transition near 172 K. We have also carried out spin-polarized DFT-GGA calculations in the orthorhombic phase of $CaFe_2As_2$. The calculated phonon spectra for non-magnetic/spin-polarized structures are shown as dashed lines in Fig. 1. It appears that the calculated line widths of phonon modes are larger in the orthorhombic phase because the orthorhombic distortion leads to a splitting of modes. The agreement between our experimental results and the calculation is poor, which further suggest anomalous phonons in $CaFe_2As_2$. Our findings indicate that the interplay between magnetism and the lattice is in some way responsible for the anomalous phonons in $CaFe_2As_2$. That is to say, the coupling of the vibrational and the electronic degrees of freedom is

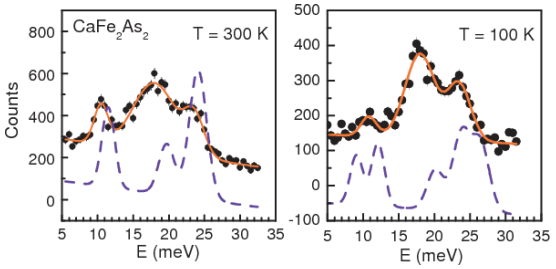

FIG. 1: Energy scans [4] taken at Q = (2.5,1.5,0) at room temperature and at a temperature far below the structural phase transformation temperature of 172 K. The full lines are fit curves to the data. The dashed lines show phonon intensities calculated from density functional theory convoluted with the experimental resolution. The calculations were based on the experimental room temperature structure (which is non-magnetic, left hand side) and the orthorhombic low temperature structure (right hand side). For better visibility the calculated profiles (dashed lines) in the left and right panels are shifted down by 200 counts.

stronger than calculated by DFT, and hence phonons might play an important role in superconductivity in the doped compounds.

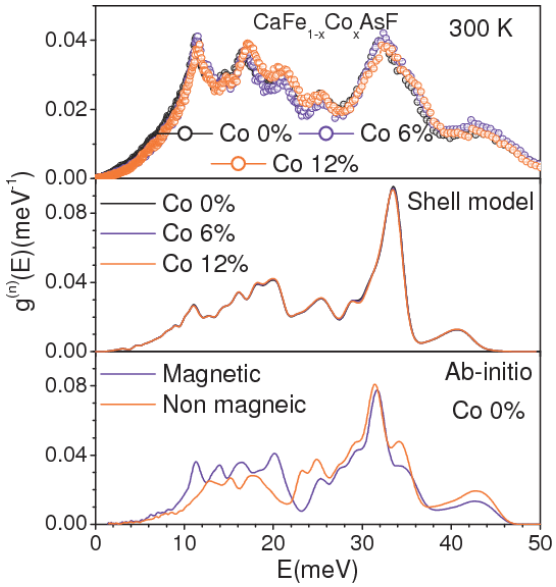

FIG. 2: Comparison of experimental phonon spectra [10] for $CaFe_{1-x}Co_xAsF$ (x = 0, 0.06, 0.12). The phonon spectra are measured with incident neutron wavelength of 5.12 Å using the IN6 spectrometer at ILL. The calculated phonon spectra using the shell model and ab-initio are also shown. The calculated spectra have been convoluted with a Gaussian of FWHM of 5% of the energy transfer in order to describe the effect of energy resolution in the experiment.

Further, we have measured [10] composition as well as temperature dependence of the phonon density-of-states in FeAs compounds with composition $CaFe_{1-x}Co_xAsF$ (x= 0, 0.06, 0.12). The electronic structure calculations for these compounds show that bands near the Fermi level are mainly formed by Fe 3d states, which is quite different from other 122 and 1111 FeAs compounds, where both Fe and As are believed to be related to superconductivity. The difference in electronic structure for fluorine based compounds may cause phonon spectra to behave differently as a function of composition and temperature in comparison with our phonon studies [5, 6, 9] on parent and superconducting MFe_2As_2 (M=Ba, Ca, Sr). The composition as well as temperature dependence of phonon spectra for $CaFe_{1-x}Co_xAsF$ (x= 0, 0.06, 0.12) compounds have been measured (Fig. 2) using time of flight IN4C and IN6 spectrometers at ILL, France. The comparison of phonon spectra at 300 K in these compounds shows (Fig. 2) that acoustic phonon modes up to 12 meV harden in the doped compounds in comparison to the parent CaFeAsF. While intermediate energy phonon modes from 15 meV to 25 meV are also found to shift towards high energies only in the 12 % Co doped CaFeAsF compound. The experimental results for $CaFe_{1-x}Co_xAsF$ (x= 0, 0.06, 0.12) are quite different from our phonon studies [5, 6, 9] on parent and superconducting MFe_2As_2 (M=Ba, Ca, Sr) where low-energy acoustic phonon modes do not react with doping, while the phonon spectra in the intermediate range from 15 to 25 meV are found to soften in these compounds. We argue that stronger spin phonon interaction play an important role for the emergence of superconductivity in these compounds. The lattice dynamics of $CaFe_{1-x}Co_xAsF$ (x= 0, 0.06, 0.12) compounds is also investigated using the ab-initio as well as shell model phonon calculations. We show that the nature of the interaction between the Ca and the Fe-As layers in CaFeAsF compounds is quite different compared with our previous studies on $CaFe_2As_2$.

In conclusion, we have carried out extensive measurements of the temperature dependence of phonon spectra for parent and superconducting compounds using the inelastic neutron scattering technique. Our work on FeAs parent and superconducting compounds shows that electron-phonon coupling is present in these compounds but it can not be solely responsible for the superconductivity.

[1] Y. Kamihara et al, J. Am. Chem. Soc. **130**, 3296 (2008).

[2] H. Takahashi et al, Nature **453**, 376 (2008).

[3] M. Rotter et al, Phys. Rev. Lett. **101**, 107006 (2008).

[4] R. Mittal, et al, Phys. Rev. Lett. **102**, 217001 (2009).

[5] R. Mittal et al, Phys. Rev. B **78**, 104514 (2008).

[6] R. Mittal et al, Phys. Rev. B **78**, 224518 (2008).

[7] R. Mittal et al., arXiv:0911.1665.

[8] R. Mittal et al., arXiv:0912.1782.

[9] R. Mittal et al, Phys. Rev. B **79**, 144516 (2009).

[10] R. Mittal et al, Phys. Rev. B **79**, 214514 (2009).

Signatures of spin-canting in a single-molecule transistor

M. R. Wegewijs, S. Herzog

IFF-3: Theory of Structure Formation

We predict the basic experimental signatures of chiral spin states in a single-molecule transistor. Such states occur when two electrons spins are coupled by anti-symmmetric Dzyaloshinskii-Moriya (DM) exchange interaction induced by relativistic spin-orbit coupling. The predicted transport effects can be used to completely characterize the DM effect in a single-molecule junction which is a key prerequisite for using the spin degrees of freedom in single-molecule spintronics.

Insight into the interplay of magnetic degrees of freedom and transport processes has become a key issue in nanoscale electronics. Nowadays even relativistic spin-orbit effects can be resolved in electrical transport experiments on nanoscale devices, for instance, using STM on atomic chains or even single magnetic atoms on a surface. Intrinsic effects of spin-orbit coupling in magnetic molecules have also been investigated in three terminal devices [1] allowing for the electric control over magnetism at the single-molecule level. In the latter work easy-axis magnetic anisotropy has been investigated, an effect induced in second order in the spin-orbit interaction (SOI). The so-called Dzyaloshinskii-Moriya (DM) interaction, in contrast, can give rise to effects in linear order in the SOI and favors spiraling spin-structures. This antisymmetric exchange interaction, first identified by Dzyaloshinskii based on symmetry arguments , and later derived from a microscopic model by Moriya , is fundamental to the understanding of weak ferromagnetism in materials like $\alpha - \mathrm{Fe_2O_3}$. In single molecules the DM interaction is known to have a large effect on the magnetism of dimers and plays an important role in various single molecular magnets such as $\mathrm{Mn_6}$, $\mathrm{Mn_{12}}$ and $\mathrm{V_{15}}$. The DM-interaction is dominant in systems with broken inversion symmetry, which is generically the case for a molecule placed on a surface [2] or in a three-terminal junction. It is therefore of interest to identify the characteristic transport signatures of this “spin-canting”. A novel aspect here is that multiple molecular charge states with different magnetic ground states can be addressed. Furthermore non-equilibrium magnetic excitations are induced by the transport, dominating over slow magnetic relaxation processes. Clearly these are key issues for the future application of molecular magnets in classical- or quantum information storage or processing devices.

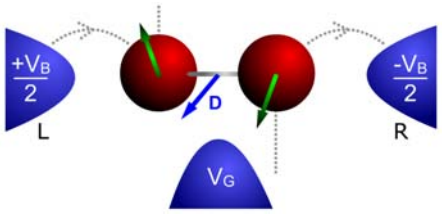

FIG. 1: Dimer with localized spins, which are slightly canted due to interplay between DM interaction and isotropic exchange coupling J. The grey vertical lines indicate the spin orientation without DM interaction. The dimer is probed in a three terminal junction (V_B: bias voltage, V_G: gate voltage). Tunneling of single-electrons is only possible between monomers and from one monomer to the adjacent lead.

The DM interaction arises in its most elementary form in a molecular dimer where two localized electrons interact via Coulomb and hybridization terms, in combination with local spin-orbit scattering into excited orbitals. As a result, an effective spin-spin interaction arises between the spin 1/2 localized at the monomers labelled by $i = 1, 2$ (see Fig. 1):

$$H_{\mathrm{eff}} \quad = \quad J\mathbf{S}_1 \cdot \mathbf{S}_2 + \mathbf{D} \cdot (\mathbf{S}_1 \times \mathbf{S}_2) + \mathbf{B} \cdot (\mathbf{S}_1 + \mathbf{S}_2)$$

The isotropic exchange typically dominates, resulting in a singlet and triplet split in energy by J. The antisymmetric exchange interaction is specified by a vector $\mathbf{D}$ which is, like J, an intrinsic property of the molecule. Although typically it presents a weak perturbation, it can mix two multiplets of different total spin length, $S = 0$ and 1. The magnetic field $\mathbf{B}$ (in energy units, where $g\mu_B = 1$) enhances this mixing by bringing one triplet component close to the singlet, resulting in an energy level anticrossing at $|\mathbf{B}| \approx J$. Interestingly, this mixing strongly depends on the orientation of the field $\mathbf{B}$ relative to the DM vector $\mathbf{D}$. For $\mathbf{B} \parallel \mathbf{D}$ the singlet state does not mix with the lowest triplet and the states can cross, since in this case the Zeeman and DM terms commute (they contain three different spin-components). In contrast, for $\mathbf{B} \perp \mathbf{D}$ the singlet and $S_z = \pm 1$ triplet states are mixed. Furthermore, the relative orientation of the two spins shows an interesting field dependence: For example, in case of the ground state the antiparallel spins are slightly canted at zero field and rotate towards each other with increasing field, until they are almost perpendicular at the anticrossing point $\mathbf{B} \approx J$. For

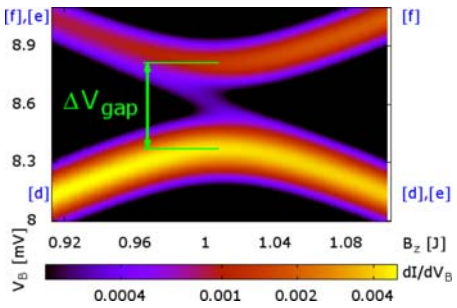

FIG. 2: Differential conductance dI/dV_B (in units of the tunnel rate Γ) versus bias voltage V_B and the magnetic field magnitude B_z for fixed direction $\mathbf{B} \perp \mathbf{D}$. The microscopic parameters are chosen such that the effective exchange anti-ferromagnetic, $J = 4\,\mathrm{meV}$ and $\mathbf{D} = -(0.32, 0, 0)\,\mathrm{meV}$ and the electron thermal energy $T = 0.02\,\mathrm{meV}$ is sufficiently low to resolve the DM-anticrossing.

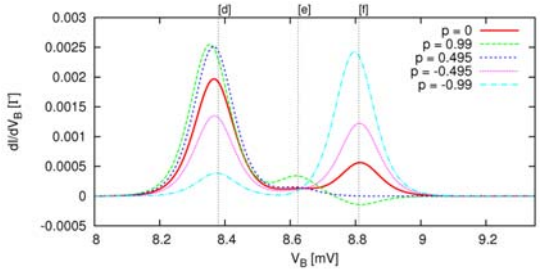

FIG. 3: Conductance dI/dV_B as function of V_B for fixed magnetic field $\mathbf{B} \perp \mathbf{D}$ and $B_z \approx J$ i.e. a vertical trace through Fig. 2. The electrodes have antiparallel spin polarization and dI/dV_B is shown for several degrees and signs of the spin-polarization p. The transition energies are marked by green vertical lines.

higher fields $\mathbf{B} > J$ they become aligned by the external field This "canting" of the spins is quantified by the expectation value $\langle \mathbf{S}_1 \times \mathbf{S}_2 \rangle$, whose sign indicate the chirality of the intra-molecular spin structure.

We have studied the single electron transport signatures of this most elementary realization of DM interaction in detail [3] for a molecular dimer placed in a three terminal junction (see Fig. 1). We have used a microscopic many-body model which captures the basic physics discussed above while incorporating all electron charge, orbital and spin degrees of freedom, which are required for a full calculation of the transport current as function of the applied voltages and the magnetic field. The corresponding effective DM interaction for the two-electron charge state can be derived perturbatively giving

$$\mathbf{D} \;=\; 2\frac{\mathrm{i}\lambda_1 \mathbf{l}_{1'1}}{\epsilon_{1'} - \epsilon_1}\left(\frac{t_{12}\, t_{21'}}{U} + v_{1221'}\right) - (1 \leftrightarrow 2)$$

where $1 \leftrightarrow 2$ denotes the same term with the roles of the monomers interchanged. Clearly, a non-vanishing DM vector will arise if the two monomers show any asymmetry in their excitation spectra $(\epsilon_i, \epsilon_{i'})$ Coulomb interaction matrix elements (v), spin-orbit couplings (λ_i) and imaginary matrix elements of the quenched orbital moments $\mathbf{l}_{i'i}$. We now highlight the most characteristic transport feature of the DM interaction [3]. Experimentally, due to the Coulomb blockade effects, one is able to tune the gate voltage such that only two successive charge states of the molecule are involved, which are here states with $N = 1$ and $N = 2$ extra electrons on the dimer. In Fig. 2 we show the differential conductance dI/dV_B as the bias V_B and the magnetic field is swept, for the field direction $\mathbf{B} \perp \mathbf{D}$. A clear spin-allowed conductance peak approaches the boundary line of the single-electron tunneling (SET) and Coulomb-blockade (CB) regimes and the *transport* spectrum displays a pronounced anticrossing. This maps out the anticrossing in the $N = 2$ *energy* spectrum, allowing the *magnitude* of the DM vector to be read off:

$$\Delta V_{\mathrm{gap}} = \frac{1}{\sqrt{2}}|\mathbf{D}| \qquad (1)$$

However, in contrast to the energy spectrum, Fig. 2 reveals an additional transport resonance running straight through the anticrossing gap. This indicates non-equilibrium occupation of magnetic $N = 1$ electron states induced by the non-linear transport. If the external magnetic field is rotated, the size of the gap in the transport spectrum shows pronounced oscillations, in particular for $\mathbf{B} \parallel \mathbf{D}$ the anticrossing in the energy spectrum vanishes. Based on this we have formulated a magneto-transport measurement scheme [3] by which the *axis* of the $\mathbf{D}$-vector can be determined.

However, to determine the sign of spin-chirality of the molecular ground state, i.e.whether $\mathbf{D}$ is aligned antiparallel or parallel to this above found axis, ferromagnetic electrodes are needed. These can nowadays be attached a single molecule to create a spin-valve device [4]. Here we orient both spin-polarization axes of the electrodes perpendicular to the plane spanned by the external magnetic field and the $\mathbf{D}$-vector for a maximal effect. Then a clear signature of the definite spin-chirality induced by the DM interaction is that for antiparallel electrode polarizations the monomer spins in the $N = 2$ ground state will both be oriented either favorably or both unfavorably for the transport. Fig. 3 indeed shows that the ground-state conductance peak [d] is clearly enhanced for $p > 0$ and suppressed for $p < 0$, whereas the peak [f] involving the $N = 2$ excited state with opposite chirality shows the opposite behavior. From a measurement resembling Fig. 3 one can thus experimentally infer the ground state spin structure [3] i.e. the microscopic canting of spins in a single-molecule device is accessible by transport measurements.

[1] H. Heersche, et. al., Phys. Rev. Lett. 96, 206801 (2006)

[2] M. Bode, et. al. Nature 447, 190 (2007)

[3] S. Herzog and M. R. Wegewijs, Nanotechnology, in press, (2009)

[4] Hauptmann, J. R. and Paaske, J. and Lindelof, P. E., Nat. Phys. 4, 373, (2008)

Observation of the underscreened Kondo effect in a molecular transistor

N. Roch[1], S. Florens[1], T. A. Costi[2], W. Wernsdorfer[1], F. Balestro[1]

[1] Institut Néel, associé à l'UJF, CNRS, BP 166, 38042 Grenoble Cedex 9, France
[2] IFF-3: Theory of Structure Formation

We present first quantitative experimental evidence for the underscreened Kondo effect, an incomplete compensation of a quantized magnetic moment by conduction electrons in an even charge spin $S = 1$ molecular quantum dot, obtained by electromigration of C_{60} molecules into gold nanogaps. The persistence of logarithmic singularities in the low temperature conductance is demonstrated by a comparison to the fully screened configuration obtained in odd charge spin $S = 1/2$ Coulomb diamonds.

When a magnetic impurity is inserted in a piece of metal, its magnetic moment can be completely screened by the conduction electrons, owing to their quantized spin $1/2$. This general phenomenon, the Kondo effect, has been thoroughly studied in diluted magnetic alloys [1] and has attracted considerable attention in the more recent quantum dot systems [2]. Clearly, impurities carrying a spin S greater that $1/2$ need to bind several electronic orbitals in order to fully quench their magnetism, and Nature seems to conspire in always providing enough screening channels for that situation to occur in general [3]. Therefore, the possibility that screening may happen to be incomplete, as initially proposed on theoretical grounds by Nozières and Blandin [5], has remained elusive for almost thirty years, despite the great experimental control that one can achieve with artificial quantum dot setups. The observation of the underscreened Kondo effect is also especially appealing since it constitutes one of the simplest cases where standard Fermi Liquid Theory is violated.

We report here [6] on the first observation of the anomalous logarithmic behavior in the temperature and bias voltage dependent conductance in a spin $S = 1$ quantum dot below the Kondo scale as previously predicted for underscreened impurities [7], and successfully confront our results with quantitative numerical renormalization group (NRG) calculations. Our C_{60} molecular transistor [8] is described by two orbital levels $(-1, +1)$ coupled to two metallic leads (L, R) (see figure 1.b), resulting in two Kondo scales T_{K1}, T_{K2} associated to each of the two channels. Moderate left/right asymmetries in the tunneling amplitudes leads to vastly different Kondo scales, because of the exponential behavior of the Kondo scale

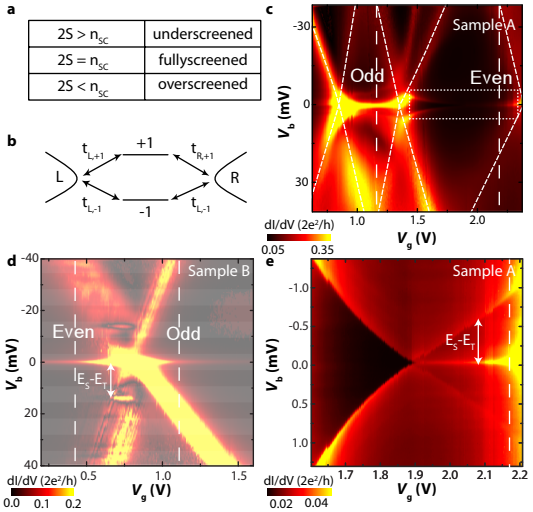

FIG. 1: ***a.*** *Summary of the different types of Kondo effects according to impurity spin S and number of screening channels n_{sc};* ***b.*** *Tunneling model of our single molecule transistor: two orbital levels couple to two leads;* ***c.*** *Conductance map of sample A recorded at $T = 35$mK. Dashed lines are positioned at the gate voltages where more detailed studies where performed;* ***d.*** *Conductance map for sample B;* ***e.*** *Zoom inside the dotted rectangle defined in the even diamond of sample A. The white arrows represents the singlet-triplet splitting in both samples.*

on tunneling amplitudes, a situation that naturally occurs with electromigration, as the molecule tends to stay preferably closer to one of the electrodes. Fig. 1 shows indeed that our conductance maxima, here shown for two different devices, are much lower than the quantum value $2e^2/h$, with e the electron charge and h Planck's constant. It is then possible to have a large range of temperatures $T_{K1} << T << T_{K2}$ over which underscreened behavior prevails. A further crucial condition for the realization of the underscreened Kondo effect is the formation of a spin $S = 1$ unit itself, which is evidenced in our devices via the spectroscopically resolved singlet-triplet excitations see figure 1.d-e.

We now present the study of our two different devices (see figure 1.c-d), both showing fully screened and underscreened Kondo anomalies. In the fully screened Kondo effect, the conductance versus lowering the temperature has a logarithmic increase

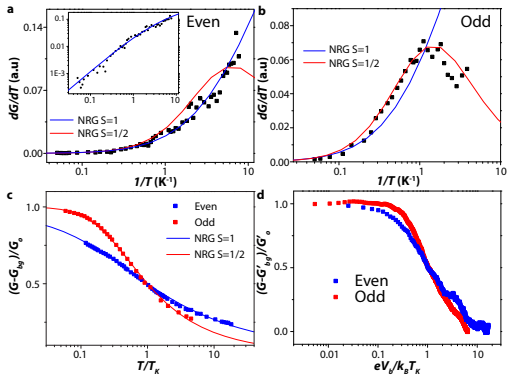

FIG. 2: ***a.*** *Derivative of the conductance at gate $V_g = 2.17V$ and bias $V_b = 0V$ in the even Coulomb diamond of sample A The best fit is obtained for an underscreened Kondo model (blue) and gives $G_o = 0.14$ (in units of $2e^2/h$) and $T_K = 1.1K$;* ***b.*** *Derivative of the conductance at $V_g = 1.2V$ and $V_b = 0V$ in the odd Coulomb diamond. The best fit is obtained for a fully screened Kondo model (red) and gives $G_o = 0.34$ and $T_K = 4.4K$;* ***c.*** *Conductance data of a and b compared to the relevant NRG curves.* ***d.*** *Differential conductance at the base temperature rescaled in universal form, with $G'_o = G(T_{\rm base})$, and G'_{bg} such that the conductance is $G'_o/2$ at $eV_b = k_BT_K$.*

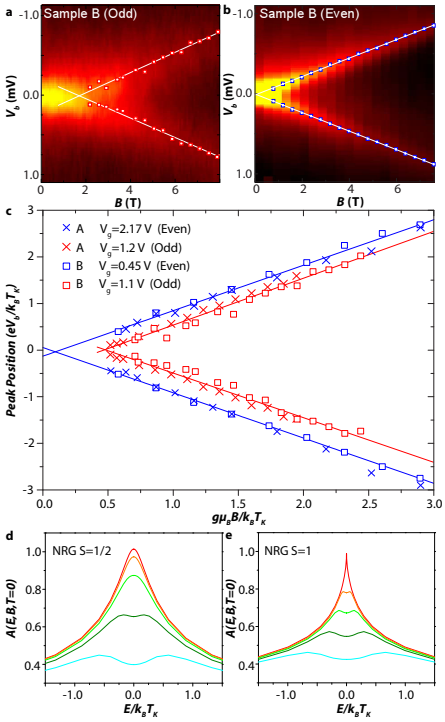

FIG. 3: ***a.*** ***b.*** *Differential conductance versus bias voltage and magnetic field for sample B in the odd and even diamonds;* ***c.*** *Positions of the Zeeman peaks of both samples and odd/even diamonds, as extracted from above.* ***d.*** ***e.*** *NRG calculations of the energy E dependent equilibrium local density of states $A(E, B, T = 0)$ at zero temperature, normalized to its $E = B = 0$ value, for the spin $S = 1/2$ and $S = 1$ single-channel Kondo models and magnetic field values $g\mu_B B/k_BT_K = 0, 1/8, 1/4, 1/2, 1$ (top to bottom).*

above the Kondo temperature, and then saturates in a quadratic, Fermi-liquid like fashion. On the other hand, the underscreened Kondo effect is expected to show two distinct logarithmic behaviors [7], above and below the highest Kondo temperature T_{K2}. This is best seen by plotting the derivative of conductance with respect to temperature as a function of inverse temperature, as suggested in [7]. Our data in the inset of figure 2a, taken for the even diamond of sample A, clearly display two distinct $1/T$ regimes. Another way to discriminate both Kondo effects is to perform a fit to NRG results [3, 4] of single channel spin $S = 1/2$ and $S = 1$ Kondo models. The obvious qualitative differences, namely the apparent divergence in $dG(T)/dT$ at low temperature T for spin $S = 1$ and the presence of a maximum for spin $S = 1/2$, in addition to the quantitative agreement with the NRG predictions are strong indications of two remarkably different Kondo states, see Fig. 2a-b.

The evolution of the Kondo peak as a function of magnetic field, as seen in the bias spectrum of Fig. 3.a-b, displays even more dramatic effects, showing anomalous sensitivity of the underscreened Kondo rsonance to a magnetic field, as confirmed also by the numerical solution indicating that the underscreened Kondo resonance starts to unveil its magnetic excitations for Zeeman energies as low as $k_BT_K/16$, see figure 3.d-e.

In conclusion, we have given comprehensive experimental evidence for the occurence of Nozières and Blandin underscreened Kondo effect in even charge molecular quantum dots. Our analysis, based on the stark differences with respect to regular transport properties of fully screened impurities, was strenghtened by NRG calculations. An unexpected magnetic field sensitivity of partially screened Kondo impurities was also discovered, that we could confirm theoretically. This work illustrates the striking versatility of molecular electronics for the investigation of fundamental aspects in quantum magnetism.

[1] A. C. Hewson, The Kondo Problem to Heavy Fermions, (Cambridge University Press, Cambridge, 1993).

[2] D. Goldhaber-Gordon et al. Nature, **391**, 156 (1998).

[3] T. A. Costi et al, Phys. Rev. Lett. **102**, 056802 (2009).

[4] F. Mallet et al, Phys. Rev. Lett. **97**, 226804 (2006).

[5] P. Nozières and A. Blandin, J. Phys. **41**, 193 (1980).

[6] N. Roch, S. Florens, T. A. Costi, W. Wernsdorefer and F. Balestro, Phys. Rev. Lett. **103**, 197202 (2009).

[7] A. Posazhennikova and P. Coleman, Phys. Rev. Lett. **94**, 036802 (2005).

[8] N. Roch et al., Nature **453**, 633 (2008).

Ferromagnetism in $MgO_{1-x}N_x$

P. Mavropoulos[1,2,3], M. Ležaić[1,2,3], S. Blügel[1,2,3]

[1] IFF-1: Quantum Theory of Materials
[2] IAS: Institute for Advanced Simulation
[3] JARA-FIT: Jülich Aachen Research Alliance - Fundamentals of Future Information Technology

Ferromagnetism in semiconductors and insulators has attracted strong attention due to possible applications in spintronics. After the discovery of diluted magnetic semiconductors, where a small fraction of transition element atoms is dissolved in nonmagnetic semiconductors creating a ferromagnetic state, it has recently been realized that ferromagnetism can also be targeted for in oxides by dissolving non-transition-elements, so-called sp-atoms [1]. In this respect, Nitrogen-doped MgO has been proposed as a candidate for sp-magnetism. As we find via ab-initio calculations, ferromagnetic order can be established, but the Curie temperature, T_C, is rather low, of the order of 30 K for 10% N concentration [2].

Our approach is based on the local density approximation (LDA) to density-functional theory. For the solution of the Kohn-Sham equations we use the Korringa-Kohn-Rostoker Green-function method (KKR) [3], while the disorder at the Oxygen site is described within the coherent potential approximation (CPA). After calculating the electronic structure self-consistently, we employ the method of infinitesimal rotations [4] to extract the inter-atomic exchange-coupling parameters $J_{nn'}$ of the Heisenberg Hamiltonian $H = -\sum_{nn'} J_{nn'} \hat{e}_n \cdot \hat{e}_{n'}$; here, $\hat{e}_n$ and $\hat{e}_{n'}$ are the directions of magnetic moments at sites n and n'. The stability of the ferromagnetic state is quantified by solving the Heisenberg Hamiltonian for the Curie temperature within the random-phase approximation (RPA) [5].

The electronic structure of $MgO_{1-x}N_x$ is best understood through an analysis of the spin-dependent density of states (DOS), shown in Fig. 1 for a concentration $x = 5\%$. The energy range of choice is around the valence band, dominated by the Oxygen p-states; the conduction band, where the Mg states dominate, is much higher in energy (MgO has a gap of 8 eV), and is therefore irrelevant. When Nitrogen impurities are dissolved in MgO, the impurity-induced p-levels are positioned in the gap, approximately 0.5 eV above the valence band edge. This is because N is to the left of O in the periodic table, and is therefore less electronegative. In addition, since N has one less electron, one of the impurity p-states is empty, resulting in an unpaired electron and therefore a spin moment of 1 μ_B. As the concentration increases, the impurity gap-states interact,forming impurity bands. However, because the 2p states are rather localized, Hund's rule is still applicable and the atomic moments remain strong also at high concentrations. The exchange splitting is of the order of 1 eV, while the system shows a half-metallic character: the majority-spin states are fully occupied, and the Fermi level cuts through the minority-spin impurity states at $2/3$ filling. The spin moment is unchanged, at 1 μ_B per impurity atom.

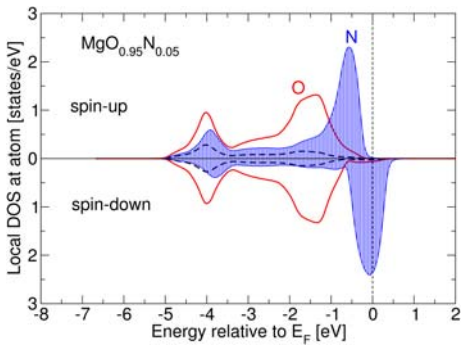

FIG. 1: Atom-resolved density of states of $MgO_{0.95}N_{0.05}$. Red line: Oxygen DOS. Blue, shaded area: spin-split Nitrogen DOS. Black, dashed line: Magnesium DOS.

The positioning of the impurity band compared to the Fermi energy suggests a ferromagnetic interaction via Zener's double-exchange mechanism. This acts in the following way. If two N impurities are aligned ferromagnetically, then the hybridization between the half-occupied states results in an impurity-band broadening; the occupied part of the band shifts to lower energies, and energy is gained.

The strength of the ferromagnetic coupling can be seen more clearly by examining the distance-dependent pair exchange interactions. These are presented in Fig. 2 for concentrations 1%, 3% and 5%. A strong concentration dependence of $J_{nn'}$ is seen, characteristic of the double-exchange mechanism: smaller concentrations amount to stronger interaction. However, the most important effect is the exponential decay of $J_{nn'}$ with distance R. This is a result of the spin-up band gap at the Fermi energy (see Fig. 1). As a result of this decay, the stronger interactions at low concentrations (e.g. 1%) are ir-

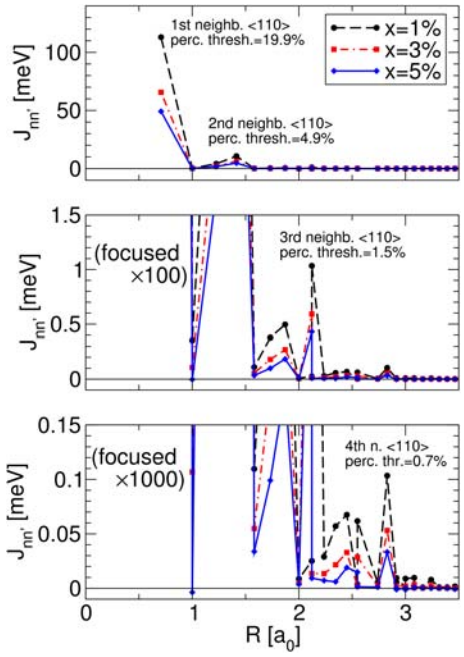

FIG. 2: Pair exchange interactions $J_{nn'}$ as a function of distance (measured in lattice parameters a_0) for several N concentrations in $MgO_{1-x}N_x$.

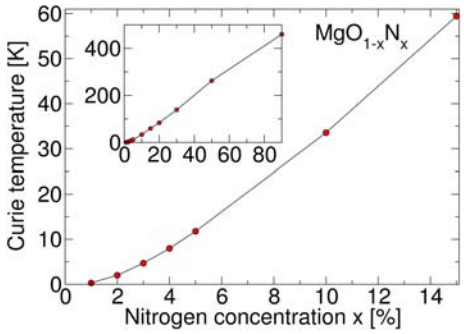

FIG. 3: Calculated Curie temperature as a function of N concentration in $MgO_{1-x}N_x$.

relevant for T_C, since the average inter-impurity distance so large that the interaction is practically zero. This effect is known as *magnetic percolation* [6]. If we approximate the exponential decay of $J_{nn'}(R)$ by setting $J_{nn'} = 0$ after a certain cutoff radius R_c, then there we find a *percolation threshold*, i.e. a characteristic concentration, depending on R_c, under which $T_C = 0$. In Fig. 2 we also show the percolation threshold for certain inter-impurity distances corresponding to peaks in the value of $J_{nn'}(R)$. These peaks appear predominantly in the $\langle 110 \rangle$ direction, along which the impurity wavefunction has its largest extent. We see, for example, that a concentration of at least 4.9% is needed, for the second-neighbour along $\langle 110 \rangle$ to start playing a role for T_C (corresponding to the peak of $J_{nn'}$ at $R = 1.41$ a_0). For concentrations under 1.5%, the interactions that play a role are of the order of 0.1 meV or less, and we consider them negligible. Therefore we conclude that the overall percolation threshold for the appearance of a ferromagnetic state in $MgO_{1-x}N_x$ is 1.5%.

Next we turn to the calculation of T_C as a function of concentration. This is calculated within the RPA, after creating a supercell with randomly placed impurity atoms, with their interactions taken from the CPA calculation (as in Fig. 2). The results for the concentration-dependent T_C are shown in Fig. 3 for concentrations up to 15%. We see that, after the percolation threshold of about 1.5%, T_C increases linearly as a function of concentration. This behavior is brought about by the decrease of the average inter-impurity distance, which improves the quality of magnetic percolation. However, we find that the Curie temperature is rather low, certainly too low for applications: even at a high concentration of 10%, T_C is only 30 K. As we see in the inset of Fig. 3, one would have to reach concentrations of 50% to achieve room-temperature ferromagnetism; unfortunately such concentrations are experimentally unrealistic.

We believe that there can be two types of "engineering" in order to increase the Curie point. One is a co-doping by another type of impurity, that could assist the impurity-gap states of N to become more long-ranged, e.g. by shifting the N impurity band. Our tries in this direction have not been met with success. The second way would be the engineering of concentrated nano-structures in the MgO matrix, such as delta-doped layers, nano-columns or nano-dots. The high local concentration at such inclusions could be sufficient to achieve a magnetic state at room temperature.

[1] K. Kenmochi, V. A. Dinh, K. Sato, A. Yanase, and H. Katayama-Yoshida, J. Phys. Soc. Jpn. 73, 2952 (2004); A. Droghetti, C. D. Pemmaraju, and S. Sanvito, Phys. Rev. B **78**, 140404(R) (2008).

[2] P. Mavropoulos, M. Ležaić, and S. Blügel, Phys. Rev. B **80**, 184403 (2009).

[3] The SPR-TB-KKR package, H. Ebert and R. Zeller, http://olymp.cup.uni-muenchen.de/ak/ebert/SPR-TB-KKR.

[4] A. I. Liechtenstein, M. I. Katsnelson, V. P. Antropov, and V. A. Gubanov, J. Magn. Magn. Mater. **67**, 65 (1987).

[5] S. Hilbert and W. Nolting, Phys. Rev. B **70**, 165203 (2004).

[6] K. Sato, W. Schweika, P. H. Dederichs, and H. Katayama-Yoshida, Phys. Rev. B **70**, 201202(R) (2004); L. Bergqvist, O. Eriksson, J. Kudrnovsky, V. Drchal, P. Korzhavyi, and I. Turek, Phys. Rev. Lett. **93**, 137202 (2004).

The surface electronic structure of ferromagnetic Fe(001)

L. Plucinski[1], Y. Zhao[2], B. Sinkovic[2], E. Vescovo[3], C. M. Schneider[1]

[1] IFF-9: Electronic Properties
[2] Department of Physics, University of Connecticut, Storrs, CT, USA
[3] National Synchrotron Light Source, Brookhaven National Laboratory, Upton, NY

A thorough investigation of the surface electronic structure of ferromagnetic Fe(100) films, epitaxially grown on single crystal W(100), has been conducted using spin- and angle-resolved photoemission combined with *state-of-the-art* density functional theory slab-computations. The dispersion of the surface state emission close to the Fermi level has been assessed quantitatively. The experimental results are in a good agreement with the calculations. In particular the presence of a minority surface state with d_{xz+yz} character along the $\overline{\Gamma X}$ high-symmetry direction is unambiguously established. Additionally, the calculations predict the existence of an unoccupied surface state localized at $\overline{\Gamma}$. The presence of the related minority interface resonance near the Fermi edge and outside of the surface-Brillouin-zone center $\overline{\Gamma}$ is believed to control the tunneling magneto-resistance in Fe/MgO/Fe(001) for very thin MgO spacers. Our results indirectly confirm these predictions.

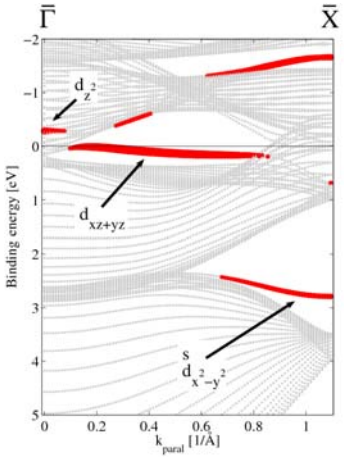

FIG. 1: Minority-spin band structure of Fe(001) along $\overline{\Gamma X}$ calculated using WIEN2k [4] for a 30 atoms slab. Adjacent slabs were separated by 29.8 Å of vacuum. States with more than 20% charge located on the surface atom are emphasized as thicker (red) lines. Only even states with respect to the emission plane are plotted since only these states are accessible in our experimental geometry.

The nature of the surface states in iron has been an area of intense research spanning several decades. Due to their high localization, surface states of magnetic materials have been closely scrutinized for signs of surface-enhanced electronic correlation, surface-dominated magnetic anisotropies, and surface-enhanced magnetism. Methods of choice to investigate these surface states have been angular-resolved photoemission (ARPES) and its spin-polarized version SP-ARPES, yielding detailed insights into the spin-split electronic structure and the symmetry of the occupied and unoccupied electronic states. In spite of these efforts, the determination of the surface photoemission contribution from a seemingly simple system like ferromagnetic Fe(001) is still somewhat unclear. One of the reasons for this is the interplay of exchange and spin-orbit interaction, which tend to split and mix states particularly in the vicinity of the Fermi level. Another reason for this is the insufficient description of electronic correlations in standard density functional theory approaches.

The mechanism of tunneling in Fe/MgO/Fe(001) magnetic tunnel junctions (MTJs) may be understood on the basis of band structure theory [1]. In real devices only local atomic order is mandatory, thus textured interfaces are often sufficient, being easier in preparation. Photoemission is a laterally averaging approach, thus capturing what happens *locally* in the real MTJ requires preparation of *long-range* atomically ordered films under UHV.

In this study we examine the Fe(001) surface emission by using SP-ARPES [2]. Although being limited to sampling occupied states – contrary to STM studies – these type of measurements probe the k-dependence and spin-character of the occupied electronic bands directly, together with their energy distribution. Furthermore, by adjusting photon energy and emission angle, several distinct points in the bulk Brillouin zone can be sampled. We compare a new set of experimental data to a state-of-the-art band structure computation. The minority surface state is observed to cross the Fermi level and to become unoccupied in the proximity of $\overline{\Gamma}$ as predicted by the calculations. We also examine the effects of oxygen adsorption on the relative intensities of various features in valence band spectra, which provides an additional evidence whether they are bulk- or surface-related.

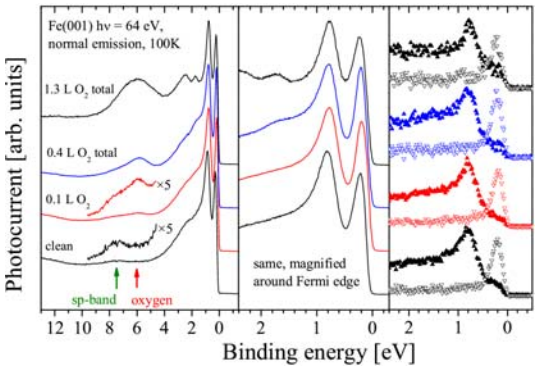

FIG. 2: Oxygen adsorption on Fe(001): normal emission spectra at hν = 64 eV. Both spin-integrated (left and center panels) and spin-polarized (right panel) spectra are shown; ▲ - majority states, ▽ - minority states.

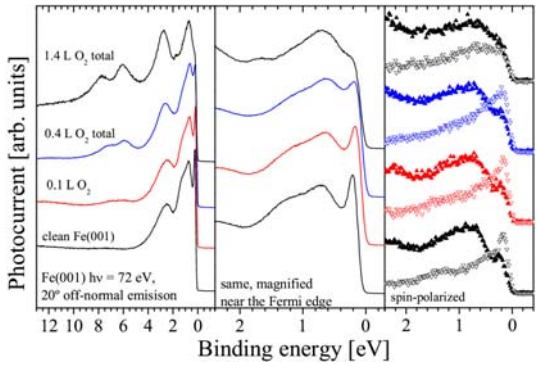

FIG. 3: Oxygen adsorption on Fe(001): 20° off-normal emission spectra at hν = 72 eV probing states in the bulk BZ where a strong minority peak appears near the Fermi edge [2]. See caption of Fig. 2 for details.

We have grown relatively thick Fe(001) films (~ 30 Å) on a W(001) single crystal at 100 K at a rate of ~ 8 Å per minute by electron beam evaporation. The base pressure in the chamber was 5×10^{-11} Torr and rose to about 1×10^{-10} Torr during Fe deposition. After deposition the sample was flashed to 400 K to improve crystallinity and subsequently cooled down again to 100 K. Low energy electron diffraction (LEED) observations indicate that above a few monolayers thickness, such a procedure yields epitaxial films with a relaxed bulk-Fe lattice constant.

Figure 2 compiles normal emission data taken at 64 eV photon energy for the clean and oxygen exposed Fe(001) surface. Adopting the usual free-electron-like final-state, bulk states close to the Γ point are excited at this photon energy. In order to test for any surface related emission in these spectra, experiments with carefully controlled oxygen exposures were performed. The region near the Fermi edge is dominated by a strong minority feature, which, however, is not influenced by oxygen exposure. This indicates that the electronic origin of this feature is rather of a bulk than surface nature.

In order to find the occupied surface state described in the calculations above, we have continued the search by mapping the band structure along ΓH in off-normal emission and sharp emission features near the Fermi edge were observed especially for 67 eV, 12° and 72 eV, 20° (actually both having minority character) [2]. The latter parameters have been chosen for more detailed spin-polarized measurements. Figure 3 presents the results of the oxygen absorption test for the off-normal emission condition. This time the minority emission close to the Fermi level is strongly suppressed by the presence of adsorbed oxygen, clearly indicating its surface origin. It should, however, be noted that in order to completely quench this state relatively high oxygen exposures (1.4 Langmuir) are needed. By contrast, for smaller doses (up to 0.4 L) it remains practically unaffected. Oxygen is known to form epitaxial crystalline overlayers on the Fe(001) surface, and indeed a single broad feature is observed in normal emission, while two distinct features are seen in the spectra 20° off-normal emission, which indicates a dispersive character. Possibly the surface state is pushed above the Fermi level only when a certain fraction of the surface is covered with oxygen.

In summary we have established details of the occupied minority spin surface state in Fe(001). The minority spin surface state of d_{xz+yz} symmetry lies in the gap of the projected bulk spin-down band structure of even symmetry. It is occupied for the major part of the $\overline{\Gamma X}$ distance and disappears both near $\overline{\Gamma}$ and near $\overline{X}$. Around $\overline{\Gamma}$ there exists another unoccupied surface state of d_{z^2} character, which was previously observed [3]. Adsorption of an ordered monolayer of oxygen quenches the surface state, however, without removing the surface ferromagnetism [5]. Our results provide new important information regarding the details of the electronic states which are believed to play an essential part in the functionality of Fe/MgO/Fe(001)-based MTJs. Further off-normal emission experimental results and detailed theoretical calculations are needed to establish how MgO overlayers influence the minority surface state of Fe(001).

This work was supported by NSF Grant No. ECS-0300235. NSLS is funded by the U.S. DoE, Office of Science, Office of Basic Energy Sciences, under Contract No. DE-AC02-98CH10886.

[1] W. H. Butler, X.-G. Zhang, T. C. Schulthess, and J. M. MacLaren, Phys. Rev. B 63, 054416 (2001).

[2] L. Plucinski, Y. Zhao, C. M. Schneider, B. Sinkovic, and E. Vescovo, Phys. Rev. B 80, 184430 (2009) .

[3] J. A. Stroscio, D. T. Pierce, A. Davies, R. J. Celotta, and M. Weinert, Phys. Rev. Lett. 75, 2960 (1995).

[4] P. Blaha, K. Schwarz, G. K. H. Madsen, D. Kvasnicka, and J. Luitz, http://www.wien2k.at/.

[5] A. Winkelmann, D. Hartung, H. Engelhard, C.-T. Chiang, and J. Kirschner, Rev. Sci. Instrum. 79, 083303 (2008).

Wannier-function approach to spin excitations in itinerant ferromagnets

E. Şaşıoğlu[1,2], A. Schindlmayr[3], C. Friedrich[1,2], S. Blügel[1,2]

[1] IFF-1: Quantum Theory of Materials
[2] IAS: Institute for Advanced Simulation
[3] Department Physik, Universität Paderborn, 33095 Paderborn, Germany

We developed a computational scheme to study spin excitations in magnetic materials from first principles using Wannier functions. The main quantity of interest is the dynamical transverse spin susceptibility, from which magnetic excitations, including single-particle spin-flip Stoner excitations and collective spin-wave modes, can be obtained. In order to describe spin waves we include appropriate vertex corrections in the form of a multiple-scattering T-matrix, which describes the coupling of electrons and holes with different spins. Our implementation is based on the full-potential linearized augmented-plane-wave (FLAPW) method. As an illustration, we present spin-wave spectra and dispersions for the elementary ferromagnet bcc Fe.

Spin excitations in solids are of fundamental interest for a wide variety of phenomena. For example, in magnetic materials at low temperatures collective spin excitations, so-called spin waves or magnons, leave a mark on the transport, dynamical, and thermodynamical properties [1]. Another interesting example is high-temperature superconductivity, in which spin waves have been proposed as a possible mediator for the attractive electron-electron interaction [2]. Spin excitations play also a very important role in the field of magneto-electronics. The writing process of magnetic information in a giant magneto-resistance or tunnel-magneto-resistance device is closely related to the rotation of the magnetization, a process generating and radiating spin waves at all wave lengths, whose damping rate is an important parameter determining the writing time [3].

The properties and physics of spin waves evidently comprise an unusually rich area of research. A lot of information about the spin dynamics in solids can be obtained from the dynamical spin susceptibility. The spectrum of magnetic excitations corresponds to the poles of the dynamical susceptibility and can be directly compared with experiments such as inelastic neutron scattering. In this way it provides insight into the nature of the exchange coupling and the complex magnetic order. The dynamical spin susceptibility is thus a central quantity for the theoretical description of magnetic materials.

So far most theoretical studies of magnetic excitations in solids were based on an adiabatic treatment of the spin degrees of freedom in which the slow motion of the magnetic moments and the fast motion of the electrons are separated by mapping the complex itinerant electron problem onto the classical Heisenberg Hamiltonian with exchange parameters obtained from constrained density-functional theory calculations [4]. Within this approach the spin-wave excitations can be calculated efficiently, whereas the single-particle Stoner excitations are neglected. Furthermore, the spin-wave life times are not accessible. From a fundamental point of view, the Heisenberg model is justified only for local-moment systems like insulators and rare earths, which possess well-defined spin-wave modes over the entire Brillouin zone, so that the adiabatic approximation is reliable. For itinerant-electron magnets the adiabatic approximation yields reasonable results only in the long-wave-length region.

First-principles calculations of the dynamical spin susceptibility using realistic energy bands and wave functions are very rare. Only very few works were reported so far [5, 6]. The difficulty is two-fold: As the magnetic behavior originates in localized *d* or *f* orbitals of transition-metal and rare-earth elements, an all-electron scheme is mandatory. Furthermore, the treatment of spin waves requires dynamic exchange-correlation effects. To study excitation spectra of magnetic materials from first principles we develop a practical computational scheme within the FLAPW method and implement it in the SPEX code [7, 8]. The magnetic response function is calculated within a many-body context. To study collective spin-wave excitations we include vertex corrections in the form of ladder diagrams, which describe the coupling of elec-

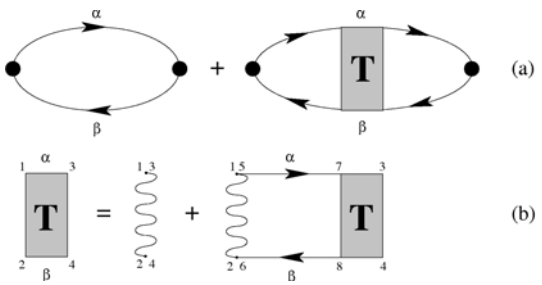

FIG. 1: Diagrammatic representation of (a) the dynamical spin susceptibility and (b) the T-matrix.

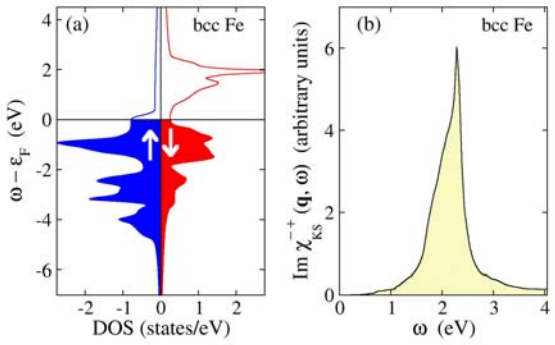

FIG. 2: (a) Density of states for the majority (up) and minority (down) spin channel of ferromagnetic bcc Fe. (b) Imaginary part of the non-renormalized Kohn-Sham spin susceptibility for $\mathbf{q} = (0.1, 0.1, 0)2\pi/a$.

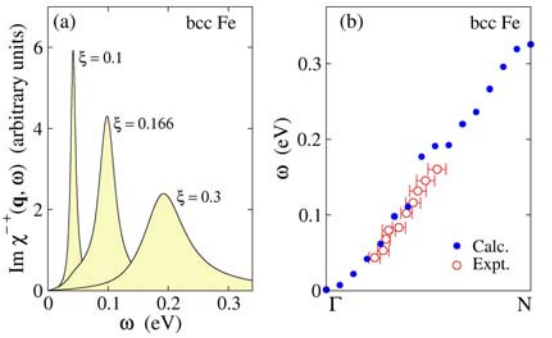

FIG. 3: (a) Imaginary part of the renormalized spin susceptibility of bcc Fe for wave vectors $\mathbf{q} = (\xi, \xi, 0)2\pi/a$ *and (b) calculated spin-wave dispersion along the* $[110]$ *direction compared to experimental data from Ref. [11].*

trons and holes with opposite spins via the screened Coulomb interaction. In analogy to the T-matrix that describes the particle-particle scattering channel, here we use the same term for the electron-hole channel. In contrast to earlier treatments, the matrix elements of the screened Coulomb potential are calculated entirely from first principles employing the random-phase approximation. In order to reduce the numerical cost for the calculation of the four-point T-matrix we exploit a transformation to maximally localized Wannier functions, which provide a more efficient basis to study local correlations than extended Bloch states [9].

The dynamical spin susceptibility can be schematically written as $\chi^{-+} = \chi^{-+}_{\mathrm{KS}} + \chi^{-+}_{\mathrm{KS}} T^{-+} \chi^{-+}_{\mathrm{KS}}$, where the first term represents the response of the noninteracting system, i.e., the Kohn-Sham spin susceptibility. The second term contains the T-matrix, which describes dynamic correlation in the form of repeated scattering events of particle-hole pairs with opposite spins and is responsible for the occurrence of collective spin-wave excitations. The Feynman diagrams for the dynamical spin susceptibility χ^{-+} and the T-matrix are displayed in Fig.1.

As an example we show results for bcc Fe, obtained with $30 \times 30 \times 30$ mesh points in the full Brillouin zone [10]. Figure 2 shows the transverse spin susceptibility of the non-interacting Kohn-Sham system. As there is no dynamic correlation in this case, only single-particle spin-flip Stoner excitations exist. As a consequence, the spectral function $\mathrm{Im}\chi^{-+}_{\mathrm{KS}}(\mathbf{q}, \omega)$ exhibits a peak around 2 eV, which equals the exchange splitting visible in the density of states and corresponds to spin-flip transitions between occupied majority and unoccupied minority states. When dynamic correlation is included in the form of the screened Coulomb interaction, an additional spin-wave peak appears at low energies as illustrated in Fig. 3(a). Plotting the peak positions as a function of the wave vector yields the spin-wave energies as displayed in Fig. 3(b) for the $[110]$ direction in bcc Fe. The dispersion obtained in this way, with no empirical parameters, is in excellent agreement with experimental data [11].

In summary, we present a computational scheme to study spin excitations in magnetic materials from first principles. The central quantity is the transverse spin susceptibility, which treats both collective spin-wave excitations and single-particle spin-flip Stoner excitations on an equal footing. The susceptibility is derived from many-body perturbation theory and includes dynamic correlation through a summation over ladder diagrams that describe the coupling of electrons and holes with opposite spins. In contrast to earlier treatments, the matrix elements of the screened Coulomb potential are calculated entirely from first principles. To reduce the numerical cost for the calculation of the four-point scattering matrix we perform a projection onto maximally localized Wannier functions, which allows us to truncate the matrix efficiently by exploiting the short spatial range of electronic correlation in the partially filled *d* or *f* orbitals. As an illustration, we present spin-wave spectra and dispersions for the elementary ferromagnet bcc Fe calculated with our scheme. The results are in good agreement with available experimental data.

[1] T. Moriya, *Spin Fluctuations in Itinerant Electron Magnetism* (Springer, Berlin, 1985).

[2] D. J. Scalapino, Phys. Rep. **250**, 329 (1995).

[3] B. C. Choi, M. Belov, W. K. Hiebert, G. E. Ballentine, and M. R. Freeman, Phys. Rev. Lett. **86**, 728 (2001).

[4] L. M. Sandratskii, Adv. Phys. **47**, 91 (1998).

[5] S. Y. Savrasov, Phys. Rev. Lett. **81**, 2570 (1998).

[6] K. Karlsson and F. Aryasetiawan, Phys. Rev. B **62**, 3006 (2000).

[7] E. Şaşıoğlu, A. Schindlmayr, C. Friedrich, F. Freimuth, and S. Blügel, Phys. Rev. B **81**, 054xxx (2010).

[8] C. Friedrich, A. Schindlmayr, and S. Blügel, Comput. Phys. Commun. **180**, 347 (2009); C. Friedrich, S. Blügel, and A. Schindlmayr, Phys. Rev. B (to be published).

[9] F. Freimuth, Y. Mokrousov, D. Wortmann, S. Heinze, and S. Blügel, Phys. Rev. B **78**, 035120 (2008).

[10] A. Schindlmayr, C. Friedrich, E. Şaşıoğlu, and S. Blügel, Z. Phys. Chem. (to be published).

[11] C.-K. Loong, J. M. Carpenter, J. W. Lynn, R. A. Robinson, and H. A. Mook, J. Appl. Phys. **55**, 1895 (1984).

Kondo decoherence: realistic models for iron impurities in gold and silver

T. A. Costi[1], L. Bergqvist[1], A. Weichselbaum[2], J. von Delft[2], T. Micklitz[3], A. Rosch[3], P. Mavropoulos[4], P. H. Dederichs[1], F. Mallet[5], L. Saminadayar[5], C. Bäuerle[5]

[1] IFF-3: Theory of Structure Formation
[2] Physics Department, LMU, München, 80333 München, Germany
[3] Institute for Theoretical Physics, University of Cologne, 50937 Cologne, Germany
[4] IFF-1: Quantum Theory of Materials
[5] Institut Néel - CNRS, 38042 Grenoble, France

We use Kondo decoherence of electrons to resolve a basic open question concerning the classic Kondo systems of Fe impurities in gold and silver: which Kondo-type model yields a realistic description of the relevant multiple bands, spin and orbital degrees of freedom? Our ab-initio and model calculations suggest a $S = 3/2$ fully screened Kondo model, which we show provides a consistent explanation of the measured resistivity and decoherence rates.

The Kondo effect of magnetic impurities in non-magnetic metals, e.g. Mn, Fe or Co in Cu, Ag or Au, first manifested itself in the early 1930's as an anomalous rise in resistivity with decreasing temperature, leading to a resistivity minimum [1]. In 1964 Kondo explained this effect [2] as resulting from an antiferromagnetic exchange coupling between the spins of localized magnetic impurities and delocalized conduction electrons.

However, for many dilute magnetic alloys, including Fe impurities in Au and Ag, with the former being the very first magnetic alloy known to exhibit the Kondo effect, the basic question of deriving the correct effective low-energy model for a quantitative understanding of experiments has remained open [3]. Attempts to fit experimental data on, for example, AgFe, with theoretical results for thermodynamics, by assuming a fully screened low-energy effective Kondo model [4], have been inconclusive.

Here [7] we address the above problem by using density functional theory calculations to derive effective low energy models which we then solve for transport quantities using the numerical renormalization group, comparing the results to available experiments.

Fig. 1 shows the d-level local density of states (LDOS) of substitutional Fe in Ag and Au, obtained by spin-polarized calculations using a 108 atom supercell. The cubic local symmetry leads to e_g (doublet) and t_{2g} (triplet) components with a e_g-t_{2g} splitting, $\Delta \gtrsim 0.15$ eV in LDA (Fig. 1(a-b)).

Within spin-polarized LDA a large spin moment μ_S of approximately 3-3.1 μ_B forms spontaneously, consistent with Mösbauer measurements that give 3.1-3.2 μ_B for the spin moment for Fe in Ag [5]. In contrast, there is no tendency for a sizable orbital moment (or a Jahn-Teller distortion). We conclude that

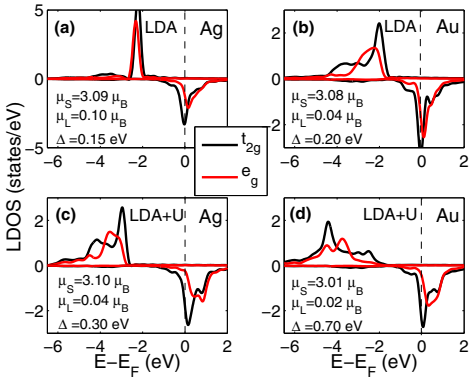

FIG. 1: The d-level local density of states (LDOS) of substitutional Fe in Ag and Au within spin-polarized LDA (a,b) and LDA+U (c,d), with inclusion of spin-orbit interactions, and showing the e_g (red) and t_{2g} (black) components of the d-level LDOS of FeAg (left panels) and FeAu (right panels). Majority/minority contributions are shown positive/negative. Legends give the spin (μ_S) and orbital (μ_L) magnetic moments in units of the Bohr magneton μ_B, and the splitting (Δ) between the e_g and t_{2g} components of the d-level LDOS.

the orbital degree of freedom is quenched on an energy scale set by the width $\Gamma_{t_{2g}}$ of the t_{2g} orbitals.

The above results justify formulating an effective low-energy model in terms of the spin-degree of freedom only. The large spin moment μ_S of 3-3.1 μ_B suggests an effective spin $S = 3/2$. Our LDA results thus imply as effective model a spin-3/2 3-channel Kondo model, involving local and band electrons of t_{2g} symmetry.

We thus describe Fe in Ag and Au using the following fully screened Kondo model:

$$H = \sum_{k\alpha\alpha} \varepsilon_k c^\dagger_{k\alpha\sigma} c_{k\alpha\sigma} + J \sum_\alpha \mathbf{S} \cdot \mathbf{s}_\alpha \, . \qquad (1)$$

It describes n channels of conduction electrons with wave vector k, spin σ and channel index α, whose spin density $\Sigma_\alpha \mathbf{s}_\alpha$ at the impurity site is coupled antiferromagnetically to an Fe impurity with spin $S = n/2$. Whereas our LDA results suggest $n = 3$, we shall also consider the cases $n = 1$ and 2.

We have calculated the resistivity $\rho_m(T)$ and decoherence rate $\gamma_m(T)$ by using the NRG [9, 10]. The results are compared to measurements of $\rho_m(T)$ and

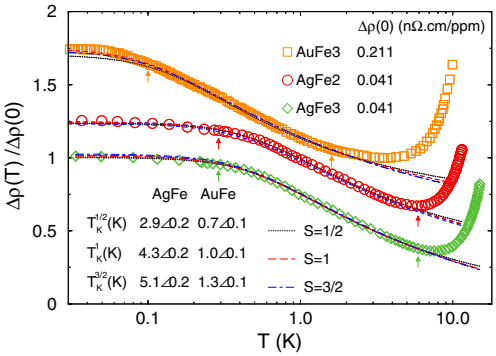

FIG. 2: Measured resistivities $\Delta\rho(T)$ (symbols) fitted to equation (2) (lines), for $n = 2S = 1, 2$ and 3, in the range below the onset of the phonon contribution, but above $100 - 200\,\mathrm{mK}$. Specifically, we used $0.1 - 1.6\,\mathrm{K}$ for AuFe and $0.29 - 5.9\,\mathrm{K}$ for AgFe (arrows). The curves for AgFe 2 and AuFe 3 have been offset vertically by 0.25 and 0.75, respectively. The inset gives the Kondo scales T_K^S for AgFe and AuFe extracted from the fits. Estimates of the unitary Kondo resistivities for $n = 1, 2$ and 3 (in units of nΩ.cm/ppm) yield $\rho_\mathrm{m}(0) = 0.041$, 0.047 and 0.049 for AgFe (averaged over the two samples), and 0.23, 0.26 and 0.27 for AuFe, respectively.

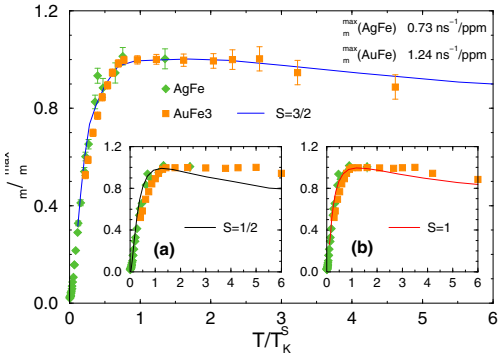

FIG. 3: Comparison of the measured (symbols) and theoretical (lines) results for the dimensionless decoherence rate $\gamma_\mathrm{m}(T)/\gamma_\mathrm{m}^\mathrm{max}$ as function of T/T_K^S, using $S = 3/2$. Insets show comparisons to $S = 1/2$ (a) and $S = 1$ (b). T_K^S for AgFe and AuFe was extracted from the resistivities (inset of Fig. 2), while $\gamma_\mathrm{m}^\mathrm{max}$ was determined as the average plateau height in the region $T/T_\mathrm{K}^{3/2} \in [0.7, 1.35]$. Typical error bars are shown for $S = 3/2$. They grow with increasing temperatures due to the increasing difficulty of subtracting the growing phonon contribution to the decoherence rate.

$\gamma_\mathrm{m}(T)$ on quasi 1-dimensional, disordered wires, for two AgFe samples [6], (AgFe 2 and AgFe 3 having 27 ± 3 and 67.5 ± 7 ppm Fe impurities in Ag, respectively), with a Kondo scale $T_\mathrm{K} \approx 5\mathrm{K}$ (for $S = 3/2$, see below).

Fig. 2 illustrates how we extract the Kondo scale T_K^S and $\rho_\mathrm{m}(0)$ from the experimental data, by fitting the Kondo-dominated part of $\Delta\rho(T)$ in a fixed temperature range to the NRG results of using the Ansatz

$$\Delta\rho(T) \approx \delta + (\Delta\rho(0) - \delta) f_S(T/T_\mathrm{K}^S)\,. \qquad (2)$$

Such fits are made for each of the fully screened Kondo models, using T_K^S and δ as fit parameters. All three models fit the Kondo contribution very well, as shown in Fig. 2, so a determination of the appropriate model from resistivity data alone is not possible.

To break this impasse, we exploit the remarkably S-dependent sensitivity of the decoherence rate $\gamma_m(T)$. Fig. 3 shows the measured dimensionless decoherence rate $\gamma_\mathrm{m}(T)/\gamma_\mathrm{m}^\mathrm{max}$ for Ag and Au samples (symbols) as function of T/T_K^S for $S = 1/2, 1$ and $3/2$, using the T_K^S values extracted from the resistivities, together with the corresponding parameter-free theoretical predictions (lines). The agreement between theory and experiment is poor for $S = 1/2$, better for $S = 1$ but excellent for $S = 3/2$, confirming the conclusion drawn above from ab initio calculations.

In this Letter we addressed one of the fundamental unresolved questions of Kondo physics: that of deriving and solving the effective low-energy Kondo model appropriate for a realistic description of Fe impurities in Au and Ag. Remarkably, for both Ag and Au samples, the use of a fully screened $S = 3/2$ three channel Kondo model allows a quantitatively consistent description of both the resistivity and decoherence rate with a single T_K (for each material). Our results set a benchmark for the level of quantitative understanding attainable for the Kondo effect in real materials.

[1] W. J. de Haas, J. de Boer, and G. J. van den Berg, Physica (Amsterdam) **1**, 1115 (1934).

[2] J. Kondo, Prog. Theor. Phys. **32**, 37 (1964).

[3] P. Nozières and A. Blandin, J. Phys. (Paris) **41**, 193 (1980).

[4] A. C. Hewson, *The Kondo Problem To Heavy Fermions*, Cambridge Studies in Magnetism (Cambridge University Press, Cambridge, England, 1997).

[5] P. Steiner and S. Hüfner, Phys. Rev. B **12**, 842 (1975).

[6] F. Mallet et al., Phys. Rev. Lett. **97**, 226804 (2006).

[7] T. A. Costi et al., Phys. Rev. Lett. **102**, 056802 (2009).

[8] T. Micklitz et al., Phys. Rev. Lett. **96**, 226601 (2006).

[9] A. Weichselbaum and J. von Delft, Phys. Rev. Lett. **99**, 076402 (2007).

[10] R. Bulla, T. A. Costi, and T. Pruschke, Rev. Mod. Phys. **80**, 395 (2008).

Ultrafast and element-selective demagnetization dynamics

P. Grychtol[1], R. Adam[1], C. La-O-Vorakiat[2], M. Siemens[2], S. Mathias[2,3], J. Shaw[4], H. Nembach[4], T. Silva[4], M. Aeschlimann[3], M. Murnane[2], H. Kapteyn[2], C. M. Schneider[1]

[1] IFF-9: Electronic Properties
[2] Department of Physics and JILA, University of Colorado, Boulder
[3] University of Kaiserslautern and Research Center OPTIMAS, Kaiserslautern
[4] Electromagnetics Division, National Institute of Standards and Technology, Boulder

We employ higher harmonics generated by a table-top femtosecond laser amplifier to detect element-selectively the ultrafast demagnetization in Permalloy at the M absorption edge of Fe and Ni in the soft X-ray regime. The magnetic signal at both edges is reduced simultaniously by about 60% within the first 300 fs after pump pulse excitation. This behaviour points towards a strong exchange coupling between Fe and Ni.

The study of magnetism, magnetic materials, and dynamics in magnetic systems is not only a topic of fundamental interest in our understanding of correlated systems, but also is it directly relevant to technology and information storage. In recent years, magnetism at the ultrafast timescale has been a topic of increasing interest. A thorough understanding of femtosecond magnetism will address the important question of how fast the magnetization can be modified in a material and what physical processes present fundamental limits to this speed. This consideration has motivated a variety of studies using magneto-optical effects with ultrafast light pulses.

Most magneto-optical studies of magnetization dynamics currently make use of either visible wavelength range from ultrafast lasers, or X-rays from large-scale synchrotron radiation facilities. Ultrafast lasers produce short pulses (around 50 fs), thereby attaining a time resolution in the femtosecond range [1, 2, 3], but with a spatial resolution that is generally limited by the wavelength of the probe light. X-rays, on the other hand, allow for a high spatial resolution, high contrast and element specificity by probing ferromagnetic materials at their absorption edges. However, the available time resolution to-date has been too slow (at the order of ps) to resolve the fastest domain reorientation dynamics. Because of this, significant efforts have been devoted to using laser pulses to select short bursts (less than 100 fs) of X-rays from a synchrotron light source (so-called femtosecond slicing) [4]. However, these experiments are time-consuming and challenging, due to the low flux of the sliced photons and the complexity of the technique.

In our work [5], we show for the first time that XUV light generated using high-harmonic generation [6, 7] can be used to observe magnetization dynamics of magnetic materials, exploiting the transverse magneto-optic Kerr effect. In this so-called T-MOKE geometry (Fig. 2b), the reflectivity of the material changes depending on the magnetization of the sample. In our experiment, we periodically reverse the magnetization direction of a grating structure made of Permalloy ($Ni_{80}Fe_{20}$), using an externally applied magnetic field from a Helmholtz coil (Fig. 2a). The strength of the magnetic signal is commonly quantified by the asymmetry, which is defined as $\frac{I_+ - I_-}{I_+ + I_-}$, where I_+ and I_- denote the reflected intensities recorded for two opposite magnetization directions. It can be shown that the asymmetry as a first approximation is linearly proportional to the magnitude of the magnetization [8].

A typical HHG spectrum is displayed in Fig. 1. It shows discrete harmonics diffracted off the Permalloy grating which are recorded by a X-ray CCD camera. The strong absorption at 72 eV is due to Al filters used to block the laser light co-propagating with the harmonics. We can map the magnetic asymmetry of the sample over the entire region around the Ni (67 eV) and Fe (54 eV) M absorption edge. We measured asymmetries of up to 4 % and 6 % at the Fe and Ni edge, respectively, depending on the angle of incidence on the sample. Due to the high photon flux and the high magnetic contrast in this spectral region, a good signal-to-noise ratio (more than 30) could be obtained in an acquisition time of only 100 seconds.

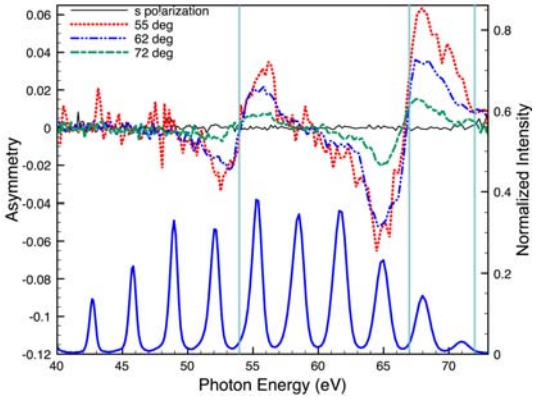

FIG. 1: Experimental data showing the HHG spectrum (bottom, right axis) and measured magnetic asymmetry (bottom, left axis). No asymmetry is measured with s-polarized light. The vertical lines denote Fe, Ni and Al M absorption edges.

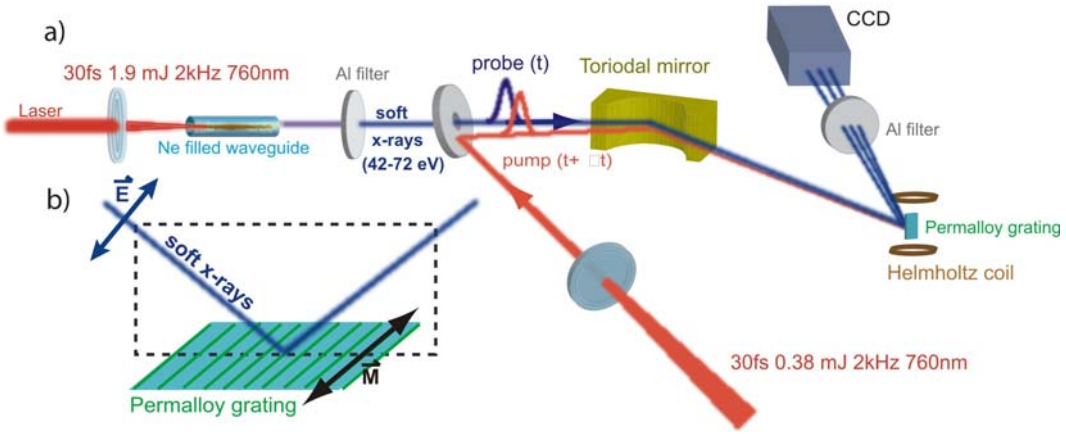

FIG. 2: a) Experimental setup: Intense light from an ultrafast laser amplifier is split by a beamsplitter (not shown). Most of the beam (about 80 %) is used to generate XUV higher harmonics, which are focused with a toriodal mirror onto a Permalloy grating. The diffracted light is recorded by a X-ray sensitive CCD. The rest of the beam is used as a pump to excite the sample. b) T-MOKE geometry: the large blue arrow depicts the polarization of the incident soft X-ray light (p-polarized light) whose plane of incidence is shown by the dashed black box. Black arrows indicate two directions of magnetization rotation, which are perpendicular to the plane of incidence of the probe light.

We demonstrate the use of a high harmonic beam from a table-top setup as an element-specific probe of ultrafast demagnetization processes after laser pulse excitation which demagnetizes the sample. Initially, the ultrafast intense pump pulse coherently interacts with the electron and spin system within the duration of the laser pulse [9]. Then, thermalization of the electron and spin system take place by means of incoherent scattering processes, resulting in a subsequent reduction/re-orientation of the magnetization vectors [1, 2, 3]. The data shown in Fig. 3 was obtained with a pump fluence of about $1\ \frac{mJ}{cm^2}$. We used harmonics around the Ni and Fe M absorption edge to measure the element-selective asymmetry as a function of the delay between pump and probe pulse. Fig. 3 shows clearly the simultanious reduction of the magnetic asymmetry for Ni and Fe within 300 fs after heating the sample by the pump beam. This behaviour points towards a tight exchange coupling of both elements and is in agreement with past measurements in the visible regime [3].

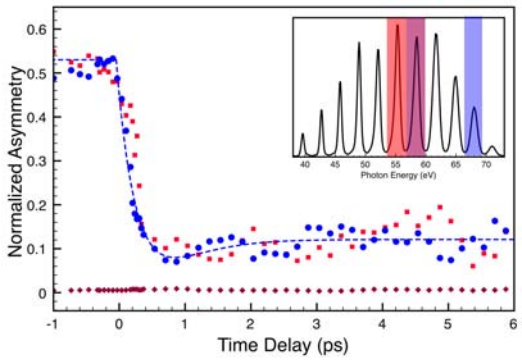

FIG. 3: Time-resolved measurement of the femtosecond laser-pulse induced demagnetization of the Permalloy film by high-harmonic photons around the Ni (blue circle), Fe (red square) M edge, and off-resonance (diamond). The dashed line corresponds to a fit of the expected response [3].

In summary, we exploit the T-MOKE to measure the magnetization dynamics of Permalloy at the M absorption edges of Fe and Ni using HHG light from a table-top laser. By using photon energies near absorption edges of the materials, element specific information about magnetic materials can be obtained with a high signal-to-noise ratio within short acquisition times. This experiment demonstrates the feasibility to investigate coherent magnetization dynamics [9] in the low femtosecond-to-attosecond regime using high-harmonic light with element specificity, and with the potential of a spatial resolution below 100 nm if coherent diffractive imaging techniques are employed [10].

[1] E. Beaurepaire, *et al.*, PRL, **76**, 4250 (1996)

[2] M. Cinchetti, *et al.*, PRL, **97**, 177201 (2006)

[3] I. Radu, *et al.*, PRL, **102**, 117201 (2009)

[4] C. Stamm, *et al.*, Nature Materials, **6**, 740 (2007)

[5] C. La-O-Vorakiat, *et al.*, PRL, **103**, 257402 (2009)

[6] H. C. Kapteyn, *et al.*, Physics Today, **58**, 39 (2005)

[7] A. Rundquist, *et al.*, Science, **280**, 1412 (1998)

[8] H. Höchst, *et al.*, JAP, **81**, 7584 (1997)

[9] J. Bigot, *et al.*, Nature Physics, **5**, 515 (2009)

[10] R. Sandberg,*et al.*, PNAS, **105**, 24 (2008)

Efficient all-electron implementation of the GW approximation: the Spex code

C. Friedrich[1,2], S. Blügel[1,2], A. Schindlmayr[3]

[1] IFF-1: Quantum Theory of Materials
[2] IAS: Institute for Advanced Simulation
[3] Department Physik, Universität Paderborn, 33095 Paderborn, Germany

We have implemented the GW approximation for the electronic self-energy within the full-potential linearized augmented-plane-wave (FLAPW) method. The algorithm uses a mixed product basis for the representation of response matrices and related quantities. We demonstrate how the algorithm can be made very efficient by exploiting spatial and time-reversal symmetry as well as by applying an optimization of the mixed product basis that retains only the numerically important contributions of the electron-electron interaction. We show results for prototype semiconductors and insulators and demonstrate that the SPEX code can deal with large supercells containing more than one hundred atoms.

The excitation energies of a system of interacting electrons corresponding to direct and indirect photoemission spectroscopy can be obtained from the solution of the quasiparticle equation. This equation contains the complex self-energy operator, which incorporates all exchange and correlation effects. Many-body perturbation theory allows to construct approximations for this complicated quantity from first principles. The GW approximation [1] treats electronic exchange exactly, while screening is treated at the level of the random-phase approximation, where electron-hole ring diagrams are summed to all orders. This makes the GW approximation particularly suited for weakly to moderately correlated systems. Mathematically it is given by a frequency convolution of the one-particle Green function with the dynamically screened Coulomb interaction.

In recent years the GW approximation was successfully applied to a large variety of materials [2]. However, most codes still rely on the pseudopotential approximation, which restricts the range of materials that can be examined considerably. Technologically interesting systems, such as transition-metal compounds and oxides, cannot be treated efficiently in this approach. Only few all-electron implementations exist today [3, 4, 5, 6].

We report an implementation within the full-potential linearized augmented-plane-wave (FLAPW) method, which offers a highly accurate basis set for all kinds of materials – the SPEX code [7]. The code is part of the Jülich FLAPW software package FLEUR [8]. In contrast to the pseudopotential approach the core and valence electrons are treated on the same footing. We employ density-functional theory in the local-density approximation (LDA) as the starting point for the perturbation theory.

Numerical realizations of the GW approximation typically suffer from the high computational expense required for the evaluation of the non-local and frequency-dependent self-energy. However, the scientific community is more and more interested in larger and more complex systems, such as multi-component materials, artificial heterostructures, defects, interfaces, surfaces, clusters, and nanowires. In codes using periodic boundary conditions these must be treated in a supercell geometry often exceeding 100 atoms. Therefore, we payed particular attention to making the implementation as efficient as possible, while retaining the accuracy of the all-electron formulation.

The fundamental process of two electrons interacting with each other involves two pairs of incoming and outgoing electron states. These pairs can be described by products of wave functions. An accurate description of such processes thus requires an auxiliary basis that is particularly designed for the representation of wave-function products. Such a basis is given by the so-called mixed product basis (MPB) [4] that is derived from products of FLAPW basis functions. The whole numerical procedure is then formulated in terms of this basis.

We found that the MPB can be made very efficient by a systematic removal of linearly dependent combinations of basis functions, such that the resulting basis for the wave-function products is only a little larger than the basis for the wave functions themselves.

Furthermore, we proposed a procedure to reduce the basis set further by taking only the dominant part of the bare electron-electron interaction into account. Mathematically this can be achieved by a diagonalization of the Coulomb matrix and retaining only those eigenfunctions whose eigenvalues exceed a given threshold value. This reduces the basis set and the computational demand considerably.

The non-locality of the self-energy and the polarization function is mainly responsible for the large computational demand in GW calculations, as their evaluation at any point in $\mathbf{k}$ space requires an additional summation over the entire Brillouin zone (BZ).

In practical calculations the BZ is sampled by a finite set of $\mathbf{k}$ points. Spatial and time-reversal symmetries allow to divide this set into groups of equivalent $\mathbf{k}$ points. The summations can then be restricted to only one member of each group, while the contribution of the others is obtained by a cheap symmetry transformation.

Due to the long-range nature of the Coulomb interaction its Fourier transform diverges at the BZ center. The calculation of the self-energy involves a three-dimensional integration over this singularity, which is of second order and therefore gives rise to a finite but quantitatively important contribution. In previous implementations this problem was either circumvented by using a shifted $\mathbf{k}$ point set and thus avoiding the divergence altogether [4] or by reverting to a less accurate plane-wave basis set, which simplifies the treatment of the singularity [3]. In our implementation we use a recently developed exact reformulation of the MPB Coulomb matrix [9] that allows a treatment similar to a pure plane-wave basis, while retaining the full accuracy of the all-electron description. In this way the integrand can be subdivided into a divergent and a non-divergent part, which are integrated analytically and numerically, respectively.

While the frequency convolution of the exchange self-energy can be performed analytically by summing over the residues of the known poles of the Green function, the correlation self-energy contains the screened interaction, whose poles are in general unknown. Hence, one must perform the frequency convolution explicitly. Unfortunately, the integrand has a lot of structure along the real frequency axis, which makes a direct evaluation difficult. There are two methods that avoid the integration over real frequencies and use the imaginary axis instead: analytic continuation [10] and contour integration [11]. The former allows a faster and easier implementation, but contains a badly controlled fitting procedure, which can be tested with the more accurate contour-integration method. We have implemented both algorithms and found that they give similar results for the systems considered here.

In Tab. 1 we list the fundamental LDA and GW band gaps for a variety of semiconductors and insulators, together with experimental and other theoretical values for comparison. The latter are calculated with the projector-augmented-wave (PAW) method. Our own results for the fundamental band gaps are converged to within 0.01 eV. We found that an accurate description of semicore states and high-lying unoccupied states with local orbitals is crucial for properly converged GW results. Overall our results agree very well with those of Ref. [6].

In order to demonstrate the efficiency of the code we examine the computational time for calculating quasiparticle shifts for diamond in the conventional unit cell ($1\times1\times1$) containing two atoms as well as in $2\times2\times2$ and $4\times4\times4$ supercell geometries containing 16 and 128 atoms, respectively. While the calculation of the quasiparticle shifts takes only five seconds on a single CPU (Intel Xeon 2.66 GHz) for the conventional unit cell, the treatment of supercells containing 16 and 128 atoms only consumes affordable 0.24 and 34.2 hours of computation time, respectively.

	This work		Ref. [6]		
	LDA	GW	LDA	GW	Expt.
Ge	0.02	0.75	—	—	0.74
Si	0.62	1.11	0.62	1.12	1.17
GaAs	0.29	1.31	0.49	1.30	1.63
CdS	1.17	2.18	1.14	2.06	2.58
GaN	1.67	2.83	1.62	2.80	3.27
$SrTiO_3$	1.80	3.36	—	—	3.25
$BaTiO_3$	2.18	3.18	—	—	3.3
CaSe	2.04	3.63	—	—	3.85
C	4.15	5.62	4.12	5.50	5.48
BN	4.35	6.20	4.45	6.10	5.97
MgO	4.64	7.17	4.76	7.25	7.83
NaCl	4.90	7.53	—	—	8.5

TAB. 1: Fundamental GW band gaps for a variety of semiconductors and insulators as calculated for the experimental lattice constant compared with experimental and theoretical values from the literature. We also exhibit the LDA eigenvalue gaps. All values are in eV.

In conclusion, we have described an implementation of the GW approximation for the electronic self-energy within the all-electron full-potential linearized augmented-plane-wave method. As all-electron GW calculations have so far been prohibitive for large systems due to the computational cost, we presented ways to speed up the calculations considerably, so that supercell calculations for defect systems, nanowires, interface or surface structures become feasible. As a demonstration we showed that the SPEX code can treat 128 carbon atoms in a diamond supercell.

[1] L. Hedin, Phys. Rev. 139, A796 (1965).

[2] W. G. Aulbur, L. Jönsson, and J. W. Wilkins, Solid State Physics 54, 1 (2000).

[3] W. Ku and A. G. Eguiluz, Phys. Rev. Lett. 89, 126401 (2002).

[4] M. Usuda, N. Hamada, T. Kotani, and M. van Schilfgaarde, Phys. Rev. B 66, 125101 (2002).

[5] B. Arnaud and M. Alouani, Phys. Rev. B 62, 4464 (2000).

[6] M. Shishkin and G. Kresse, Phys. Rev. B 75, 235102 (2007).

[7] C. Friedrich, S. Blügel, and A. Schindlmayr, submitted to Phys. Rev. B.

[8] http://www.flapw.de

[9] C. Friedrich, A. Schindlmayr, and S. Blügel, Comput. Phys. Commun. 180, 347 (2009).

[10] H. N. Rojas, R. W. Godby, and R. J. Needs, Phys. Rev. Lett. 74, 1827 (1995).

[11] R. W. Godby, M. Schlüter, and L. J. Sham, Phys. Rev. B 37, 10159 (1988).

Uniqueness of magnetotomography for fuel cells and fuel cell stacks

H. Lustfeld[1], J. Hirschfeld[1], M. Reißel[2], B. Steffen[3]

[1] IFF-1: Quantum Theory of Materials
[2] Aachen University of Applied Science, Jülich section
[3] JSC: Jülich Supercomputing Centre

The criterion for the applicability of any tomographic method is its ability to reconstruct the desired inner structure of a system from external measurements, i.e. to solve the inverse problem. Magnetotomography applied to fuel cells and fuel cell stacks aims at determining the inner current densities from measurements of the external magnetic field. Still the question remained unsolved over nearly ten years, how uniquely the inverse problem could be solved. Now we have presented a proof that by exploiting Maxwell's equations extensively the inverse problem of magnetotomography becomes unique under rather mild assumptions and we have shown that these assumptions are fulfilled in fuel cells and fuel cell stacks. Our proof is probably equally important for certain other problems e.g. medical magnetic imaging.

Over the last decades fuel cells and fuel cell stacks (the arrangement of many fuel cells in series) have attracted much attention because their efficiency, not limited by Carnot's law, can in principle be close to 1. However, they are very complex devices: From a theoretical point of view, since their functioning is still not well understood in detail, and from a practical point of view, since the efficiency of today's fuel cells is far below its theoretical value. Moreover they tend to become unstable [1, 2]. Under such circumstances good diagnostics is essential. At the same time it is desirable to avoid direct measurements in the inner of these devices, since any local manipulation in the interior may change the internal state. Thus tomographic methods are favoured and magnetotomography [3] seems to be one option, because the current densities in fuel cells and fuel cell stacks are large: several hundreds mA per cm^2 .

Reconstructing inner currents from external magnetic fields is a problem not solvable in all cases. Examples are ideal toroidal coils or very long coils whose external magnetic fields are vanishing although the internal electric currents may be strong. That was why for a long time it remained an open question, how unique the magnetotomography really is [3, 4, 5, 6].

We have recently shown, however, that by use of magnetotomography the internal electric current densities of fuel cells and fuel cell stacks can indeed be uniquely determined [7]. The assumptions are rather mild:

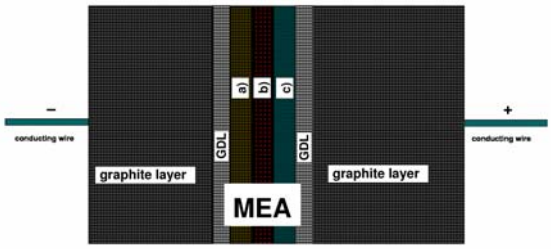

FIG. 1: Schematic representation of the MEA in a fuel cell. The MEA consists of two **G***as* **D***iffusion* **L***ayers (GDL) the catalytic layer at the anode denoted by a), the electrolytic layer denoted by b) and the catalytic layer at the cathode denoted by c). The layers containing the channels for the fuel and the exhaust gas are fabricated e.g. from graphite. Note that the scales in depth, width and height are not identical: Typical height is* 20 *cm, typical depth is* 20*cm as well, typical thickness of the layers a), b) and c) is* 0.06*mm each, typical thickness of the GDL is* 0.2*mm each and the thickness of the graphite layers is* 1*mm each or less.*

The cells must consist of nonmagnetic and nonparamagnetic material. In other words, the relative permeability μ must be close to 1. This is fulfilled in the fuel cells being used at present. And as far as we know there is no urgent necessity of changing this in the future.

The proof rests on the assumption that the real **M**embrane **E**lectrode **A**ssembly (MEA) of a fuel cell (cf Fig. 1) can be replaced by another one that avoids taking into account the very complex chemical and physical processes and currents occurring on a *microscopig scale*. The MEA is composed of two **G**as **D**iffusion **L**ayers (GDL) constituting its external surfaces. Between those are a) the catalytic layer at the anode where chemical reactions (e.g. $H_2 \rightarrow 2H^+ + 2e^-$) as well as transport of ions and electrons take place, b) the electrolytic layer, through which the ions are migrating and c) the catalytic layer at the cathode where again chemical reactions (e.g. $2H^+ + 1/2O_2 + 2e^- \rightarrow H_2O$) as well as transport of ions and electrons take place. In these 3 layers Ohm's law is not valid. On a *non-microscopic scale* the state of the MEA is well described by the normal current density $j_n(\mathbf{r})$ going through it. Moreover the three layers together have a thickness of about 0.2 mm - a scale that is below the resolution magnetotomography can achieve [8, 9]. Therefore the three layers can be replaced by i) A boundary layer in the mid-

dle of these three layers to which the normal current densities on the MEA now refer to. ii) Two small layers of about 0.1mm thickness located on both sides of this boundary layer with transverse and longitudinal conductivities obtained from an operating point of the MEA. In this way the MEA, in which complicated mixed chemical and transport processes occur, has been replaced by an equivalent MEA. We think that our approximation of the MEA (we call it the thin MEA approximation) *is a mild one, realistic and yet avoids very small scales*.

Using the two mentioned approximations we have succeeded in proving the uniqueness of magnetotomography for fuel cells and fuel cell stacks.

A disadvantage of our proof is a practical one: There is no estimate in the proof how precisely magnetic fields have to be determined for guaranteeing uniqueness. We believe that a final answer to this question can only be found numerically, estimates for fuel cells have been worked out already [8, 9]. Estimates for fuel cell stacks are in progress.

We would like to point out that our proof is not restricted to fuel cells and fuel cell stacks but is valid whenever the properties listed in ref. [7] are given.

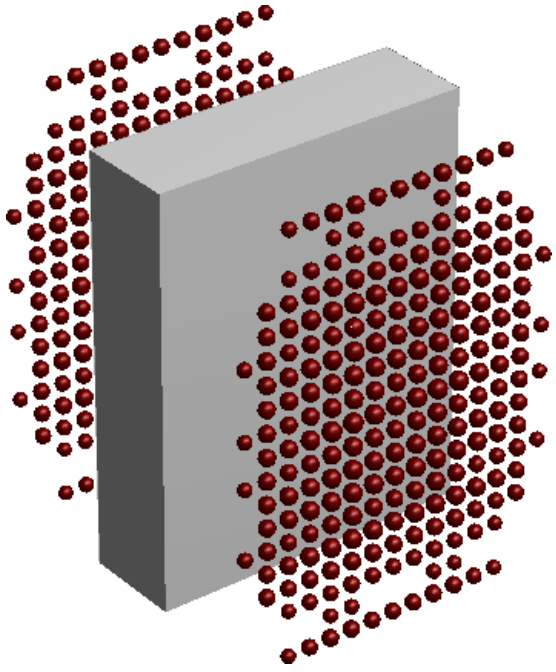

FIG. 2: For a fuel cell with nearly quadratic transverse section 458 relevant measuring points (lying on only two surfaces) are shown. Dimensions of the fuel cell used here are similar to fuel cells investigated in IEF-3 of the FZJ: Dimensions of MEA: 0.6 mm $\times$ 13.8 cm $\times$ 17.8 cm, dimensions of flowfield in bipolar plates: 2.0 mm $\times$ 13.8 cm $\times$ 17.8 cm, dimensions of steel plates: 2.0 mm $\times$ 13.8 cm $\times$ 17.8 cm. Note that in the figure the scales in depth, width and height are not identical. Available resolution in this arrangement is about $1.5\,cm$ on the surface of the MEA.

[1] Y. G. Yoon, W. Y. Lee, T. H. Yang, G. G. Park, and C. S. Kim: J. Power Sources **118**, 193 (2003).

[2] M. Noponen, T. Mennoloa, M. Mikkola, T. Hottinen, and P. Lund: J. Power Sources **106**, 304 (2002).

[3] K.-H. Hauer, R. Potthast, T. Wüster and D. Stolten: J. Power Sources **143**, 67 (2005).

[4] R. Kress, L. Kühn and R. Potthast: Inverse Problems **18**, 1127 (2002).

[5] L. Kühn: Magnetic Tomography - On the Nullspace of the Biot-Savart Operator and Point Sources for Field and Domain Reconstruction, Dissertation Göttingen 2005.

[6] R. Potthast and M. Wannert: SIAM J. Appl. Math. **70**, 563 (2009).

[7] H. Lustfeld, J. Hirschfeld, M. Reißel, and B. Steffen: J. Phys. A: Math. Theor. **42**, 495205 (2009).

[8] H. Lustfeld, M. Reißel, U. Schmidt and B. Steffen: J. Fuel Cell Sci. Technol. **6**, 021012 (2009).

[9] H. Lustfeld, M. Reißel, and B. Steffen: Fuel Cells **9**, 474 (2009).

Phase change memory materials: an update

R. O. Jones[1], J. Akola[1,2]

[1] IFF-1: Quantum Theory of Materials
[2] Nanoscience Center, University of Jyväskylä, Finland

Phase change (PC) materials remain leading candidates for future computer random access memory (RAM) and rewritable storage devices. The battle to replace the current standard in the world of optical recording material, the digital versatile disk (DVD), was decided in 2008, when the Blu-ray Disk (BD) became the *de facto* world standard. The recording medium of all BD products comprise PC materials, where a write/erase cycle involves the reversible switching between amorphous and ordered states in nanosized "bits" in a polycrystalline layer. The state can be identified by monitoring the optical or electrical properties. The transition between different *structures* is crucial, and we have used density functional methods to simulate several materials in widespread use. As in other areas of materials science, improving our understanding of the processes that occur on an atomistic length scale should result in materials that are better or can be prepared more cheaply. Crucial to our studies of amorphous and ordered alloys has been the availability of the BlueGene/P (Jugene) and Juropa supercomputers.

Phase change (PC) materials are familiar to us all as rewritable media (CD-RW, DVD-RW, DVD-RAM, and now BD). Many know that laser light is involved, but fewer seem to know how the information is recorded and read. The "active" parts of all these devices comprise thin layers of an alloy (often containing Ge, Sb, and/or Te) that undergo a rapid and reversible transition between the crystalline and amorphous forms of nanoscale bits ($\lesssim$ 100 nm) that arise from quenching after a localized and short ($\sim$ 1 ns) laser annealing to a temperature above the melting point. Longer laser heating ($\lesssim$ 50 ns) to above the glass transition temperature but below the melting point leads to a metastable crystalline form.

Many alloys used in PC storage and memory materials can be seen in Fig. 1. Alloys along the $(GeTe)_{1-\gamma}(Sb_2Te_3)_\gamma$ are widely used, including $Ge_2Sb_2Te_5$ (GST, $\gamma = \frac{1}{3}$). Numerous alloys used in BD applications also belong to this family, including $Ge_8Sb_2Te_{11}$ ($\gamma = \frac{1}{9}$). Binary alloys of Sb and Te near the eutectic composition ($Sb_{0.70}Te_{0.30}$) are also in common use, particularly in DVD-RW systems. We discuss alloys from both of these regions of Fig. 1.

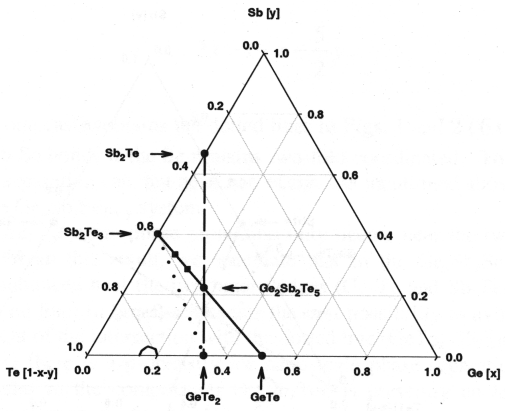

FIG. 1: Alloy diagram for $Ge_xSb_yTe_{1-x-y}$.

The Blue Gene supercomputers in Jülich have enabled us to perform simulations for a unit cell with hundreds of atoms over several hundred picoseconds. Starting from a high temperature liquid in order to avoid any structural bias, we showed that amorphous GST has many structural units ("ABAB squares", A: Ge or Sb, B: Te) that are also present in the ordered state. Substantial numbers of cavities (vacancies, voids) provide the space needed for the structural phase change to occur in a few nanoseconds. The original calculation showed good agreement with x-ray diffraction measurements of researchers at SPring-8, the world's most powerful x-ray source [1]. Together with our Japanese colleagues [2], we have developed a procedure for refining our structure to reproduce even better the measured structure factors and radial distribution functions (Fig. 2).

There is good contrast between the optical properties of the amorphous and ordered phases near the GeTe end of the pseudobinary line GeTe-Sb_2Te_3, but the crystallization process is slow. The reverse is true at the Sb_2Te_3 end: short crystallization times, but poor optical contrast. $Ge_2Sb_2Te_5$ has been adopted by many as a compromise, but alloys nearer to GeTe appear to be even better. $Ge_8Sb_2Te_{11}$ is used in Blu-ray Disc applications, and we have simulated it with 630 atoms in the unit cell over 400 picoseconds [3]. The properties of $Ge_8Sb_2Te_{11}$ are generally similar

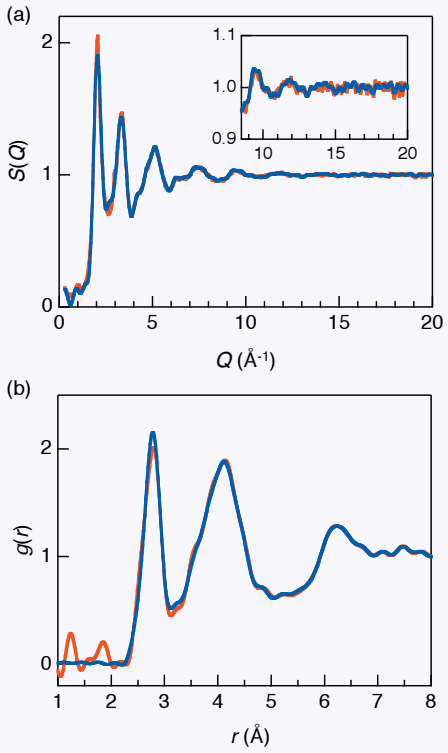

FIG. 2: (a) Structure factor $S(Q)$ in amorphous GST. Red; x-ray diffraction, blue: calculated. (b) Total radial distribution function $g(r)$.

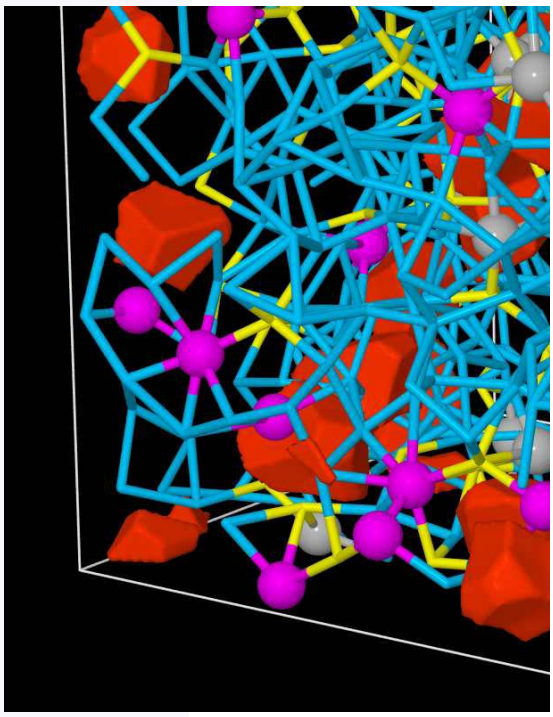

FIG. 3: Snapshot of ℓ-AIST (Ag: silver, In: magenta, Sb: blue, Te: yellow). Ag and In are depicted with small spheres, the cavities are shown in red.

to those of $Ge_2Sb_2Te_5$, but it crystallizes even more rapidly. The addition to GeTe of a small amount of Sb has a remarkable effect, and such "GeTe-rich" alloys are much favoured by manufacturers such as Panasonic.

Alloys of Sb and Te with compositions near the eutectic ($Sb_{0.70}Te_{0.30}$) are used for CD-RW and DVD-RW applications, usually including small amounts of Ag and In. Here the amorphous marks crystallize by growth from the edge (rather than nucleation from inside, as in GST alloys). We have simulated the liquid phase of a common composition of this alloy ($Ag_{3.5}In_{3.8}Sb_{75.0}Te_{17.7}$), and the comparison with new experimental data from SPring-8 was very encouraging [4]. A snapshot of part of the structure is shown in Fig. 3, and the work (experimental and theoretical) is being extended to the amorphous phase.

Almost all of the alloys used commercially as optical storage materials contain tellurium, which itself has properties that are no less remarkable: it crystallizes rapidly, and it has a very unusual density maximum just above its melting point. Te shares this behaviour with water, the most important liquid on Earth, and the structure of Te in the supercooled phase could shed light on the (still controversial) structure of water. A detailed study of Te is almost complete, and you should come back to these pages next year for a report.

The Jülich supercomputers allow us to perform calculations on length and time scales that are much closer to physical reality than were previously possible. Nevertheless, materials science and condensed matter physics play much smaller roles on Jugene than elementary particle physics. One of the most eminent elementary particle physicists, Steven Weinberg, noted that this field "has no direct applications that anyone can foresee" [5]. By contrast, materials scientists are challenged on a daily basis by problems with direct applications. Our experiences with PC materials and the work of many others show just how exciting such applications can be.

[1] J. Akola and R. O. Jones, Phys. Rev. B **76**, 235201 (2007); J. Phys.: Condens. Matter **20**, 465103 (2008).

[2] J. Akola, R. O. Jones, *et al.* Phys. Rev. B **80**, 020201(R) (2009).

[3] J. Akola and R. O. Jones, Phys. Rev. B **79**, 134118 (2009).

[4] J. Akola and R. O. Jones, Appl. Phys. Lett. **94**, 251905 (2009).

[5] S. Weinberg, New York Review of Books, **56**, Number 16, 19-22, 2009. *"Although surprises are always possible, my own main research area, elementary particle physics, has no direct applications that one can foresee."*

A thermal memory cell

M. Feuerbacher[1], M. Heggen[1], J. Dolinsek[2], M. Jagodic[3], Z. Jaglicic[3]

[1] IFF-8: Microstructure Research
[2] J. Stefan Institute, Jamova 39, SI-1000 Ljubljana, Slovenia
[3] Institute of Mathematics, Physics and Mechanics, University of Ljubljana, Jadranska 19, SI-1000 Ljubljana, Slovenia

We present the concept of a thermal memory cell, storing a byte of digital information into the storage medium by purely thermal manipulation. Thermal inscription of information employs a specific temperature–time profile that involves continuous cooling and isothermal waiting time periods in the absence of any external magnetic or electric field. Our storage media are magnetically frustrated solids. We succeeded to thermally write arbitrary ASCII characters into the Taylor-phase $T-Al_3$(Mn,Fe) complex intermetallic compound. Besides for data storage, the concept may be employed for secure data transfer and for retrieving cosmological information from extraterrestrial dust particles.

A bit, short for binary digit, is a basic unit of information storage taking two values e.g. 0 and 1, and corresponds to the quantity of information required to distinguish two mutually exclusive equally probable states from each other. A byte is an ordered collection of eight bits and represents the smallest unit of binary data on which meaningful computation can be performed. Bits can physically take many forms, e.g. electrical levels in digital circuits or pits and grounds on a CD ROM. In hard disks, a ferromagnetic layer is conceptually divided into many sub-micrometer-sized magnetic regions, each forming a magnetic dipole, which is magnetized directionally "up" or "down" by a write head. Common to all the known memory cells is the fact that digital information is inscripted by an external field, either electric (DRAM), magnetic (hard disks) or electromagnetic (laser light on CDs). The thermal memory cell (TMC) presented here, is a conceptually different way of digital data storage, taking place by purely thermal manipulation in the absence of any external field.

Thermal information storage is based on the memory effect (ME) in frustrated systems with broken ergodicity [1, 2]. The interaction between particles in these systems is such that no configuration can simultaneously satisfy all bonds and minimize the energy at the same time. Examples are magnetically frustrated systems such as spin glasses. Their dynamics is characterized by a broad spectrum of correlation times. At the freezing temperature T_f, the system undergoes an ergodic–nonergodic phase transition, below which, thermal fluctuations can no longer maintain an equilibrium on experimentally accessible time scales. The system exhibits an out-of-equilibrium dynamics, which is responsible for the appearance of the ME.

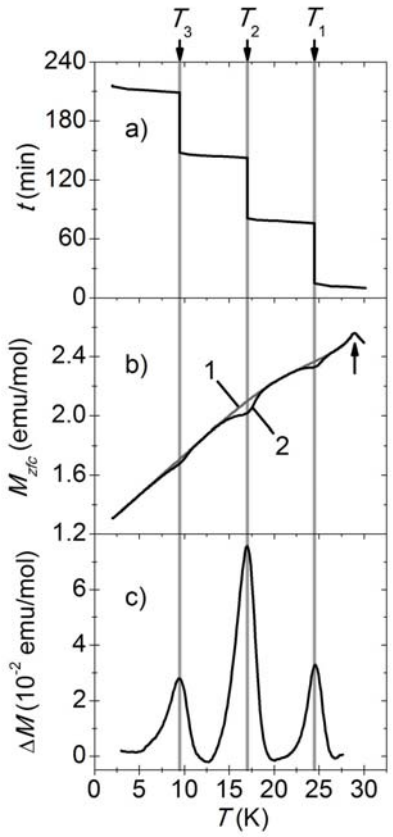

FIG. 1: a) Temperature-time protocol for the thermal inscription of information in a zfc run. The information is stored by isothermal aging for t_w = 1 h at temperatures $T_1 = 24.5\ K$, $T_2 = 17\ K$, and $T_3 = 9.5\ K$. b) zfc electronic magnetization for two thermal histories: the reference zfc run (curve 1) and the zfc run with three consecutive stops at the above temperatures (curve 2). The freezing temperature $T_f = 29K$ is defined from the cusp in M_{zfc} (arrow). c) magnetization difference ΔM between curves 1 and 2, exhibiting peaks at T_1, T_2, and T_3.

Here we demonstrate the TMC phenomenon in a single crystal of the complex metallic Taylor-phase T-Al_3(Mn,Fe) with composition $Al_{72.5}Mn_{21.5}Fe_6$ and dimensions 2×1×1 mm^3. The Mn and Fe atoms represent a network of predominantly antiferromagneti-

cally (AFM) coupled localized spins. The nonergodic phase occurs below T_f = 29 K (Fig. 1b). The information is stored by employing a specific temperature–time profile (Fig. 1a), involving continuous cooling in the absence of any external magnetic or electric field (a so-called zero-field cooling (zfc) procedure) and isothermal waiting (or "aging") time periods at three temperatures T_i. Reading the thermally stored information is conveniently (but not necessarily) done by employing a low static magnetic field of about 4 Oe at the lowest temperature and then recording the electronic magnetization M_{zfc} in a continuous heating run. While in the temperature intervals where the preceding zfc cooling was continuous M_{zfc} builds up continuously, it shows anomalies in the vicinity of the stop temperatures. The thermally stored information is best retrieved by performing two complementary experiments (Fig. 1b): (i) a zfc *reference* cooling run without any stop to the lowest temperature and then recording the zfc magnetization in a subsequent heating run and (ii) a zfc run with stops at the desired temperatures. The difference ΔM then appears in the form of resonant peaks on the baseline, located at the stop temperatures (Fig. 1c). A peak in ΔM is considered as a logic 1, whereas "ground" (no peak) means the absence of stored information, corresponding to a logic 0. For reading the entire information, the TMC has to be heated to a temperature above T_1, which leads to erasure of the stored information.

The thermal memory cell is established [3] by dividing the temperature range below T_f into eight intervals, each representing one single-bit memory section. Digital information is inscripted into each memory section during a cooling run, employing either continuous cooling over the associated temperature interval, equivalent to writing a 0, or stopping within the interval for a given time thus creating a peak in ΔM, thus writing a 1.

An eight-bit byte with all bits set to 1 is displayed in Fig. 2a, showing that all eight peaks in are clearly recognizable. Further data manipulation by taking the negative second derivative and clipping the negative parts yields a pattern with well defined peaks and baseline (Fig. 2b). We have successfully written ASCII characters into the $T - Al_3$(Mn,Fe) complex metallic alloy but also into other spinglasses, e.g. polygrained $Cu_{92}Mn_8$ [3]. The stability of the encrypted information was demonstrated to be stable over durations of several weeks.

Thermal writing is as yet time-consuming, but at least ten times shorter writing times are feasible. Currently, the read-out employs a minute magnetic field since the electronic magnetization is measured to read the information. In principle, purely thermal read-out without any external field, e.g. by calorimetry is feasible as well.

The information stored in a TMC can be read only once, i.e. the data is unavoidably erased during reading. This feature prompts for the application in data security and secure data transfer issues. We furthermore point out that the TMC concept can be em-

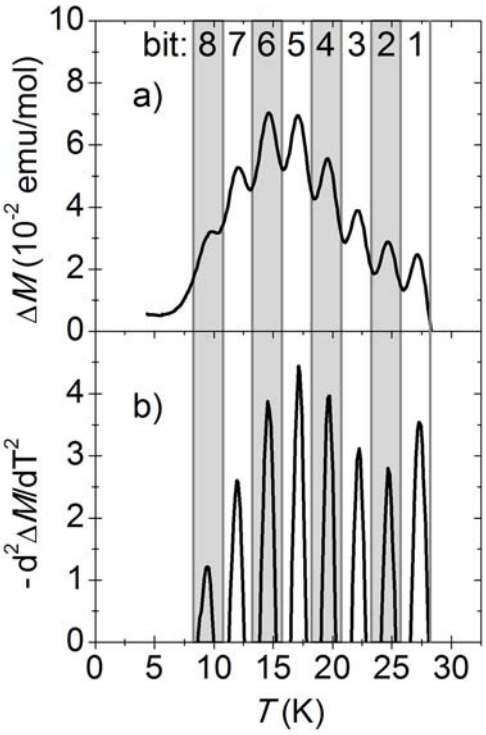

FIG. 2: An eight-bit byte of thermally inscripted digital information with all bits set to high, i.e., 11111111. a) raw ΔM data. b) data processed by taking the negative second derivative and subsequent clipping of the negative parts to give a digital pattern, consisting of peaks (1) and base line (0). The units are 10^{-2} emu/mol K^2.

ployed in other scientific disciplines: cold transition-metal-rich particles, contained in interstellar and interplanetary dust may be understood as pristine TMCs. Read-out of particles of suitable chemical composition may enable retrieving their thermal history and provide valuable information e.g. on the formation of late-type stars or Jupiter-like planets, and on early stages of the galaxy.

This work was done within the activities of EU Network of Excellence “Complex Metallic Alloys” (Contract No. NMP3-CT-2005-500140)

[1] K. Jonason, E. Vincent, J. Hammann, J. P. Bouchaud, and P. Nordblad, Phys. Rev. Lett. **81**, (1998), 3243.

[2] J. Dolinsek *et al.*, *Phys. Rev.* B **77,** (2008), 064430.

[3] J. Dolinsek, M. Feuerbacher, M. Jagodic, Z. Jaglicic, M. Heggen, and K. Urban. J. Appl. Phys. **106** (2009), 043917.

Anomalous hyperfine interaction in Co-compounds

T. Chatterji[1], G. J. Schneider[2]

[1] JCNS, Forschungszentrum Jülich Outstation at Institut Laue-Langevin, B.P. 156, 38042 Grenoble Cedex, France
[2] JCNS: Jülich Centre for Neutron Science

We investigated previously nuclear spin excitations in several Nd-based compounds and established that the energy of nuclear spin excitations is linearly proportional to the moment of Nd ions in Nd-compounds. We wished to check whether a similar relationship exists also for the Co-compounds. The Fe-group transition-metal ions have more extended d electrons compared to that of the rare earth ions, which are well shielded. Also the Co metal and the Co-compounds are known to have unquenched orbital moments and therefore may behave differently. We therefore investigated nuclear spin excitations in Co metal and several Co-compounds viz. CoO, CoF_2 and Co_2SiO_4. The results of the present investigations showed that although Co metal, Co-P alloys and CoO show a linear relationship, CoF_2 and Co_2SiO_4 deviate strongly from the linear behaviour. We ascribe the deviation from the linear behaviour to be due to the presence of different unquenched orbital moments in these compound.

The method of investigating hyperfine interaction by spin-flip scattering of neutrons is now well established [1, 2]. We performed inelastic neutron scattering experiments on CoF_2 [3] powder samples by using the high resolution back-scattering neutron spectrometer SPHERES of the Jülich Centre for Neutron Science located at the FRMII reactor in Munich. We observed inelastic signals in CoF_2 at energies $E = 0.728 \pm 0.008\mu$eV on both energy gain and loss sides at $T = 3.5$ K. The energy of the inelastic signal decreases continuously as the temperature is increased and finally merges with central elastic peak at $T_N \approx 37$ K. Figure 1 shows typical energy spectra of CoF_2 at several temperatures. The inelastic signals have resolution limited widths at least at low temperatures. The inelastic peaks move towards the central elastic peak as the temperature is increased and at the ordering temperature they just merge with the central elastic peak. We interpret the inelastic signal observed in CoF_2 due to the excitations of the ^{59}Co nuclear spins $I = \frac{7}{2}$. We also investigated nuclear spin excitations in Co metal [4] and other two Co-compounds, CoO and Co_2SiO_4 [5, 6] and have found similar results.

Figure 2(a) shows the temperature variation of the energy of the inelastic peak of CoF_2 both in the heating and in the cooling cycles. The absence of any appreciable hysteresis and also the continuous variation of the energy as a function of temperature shows that the antiferromagnetic phase transition in CoF_2 is of the second order.

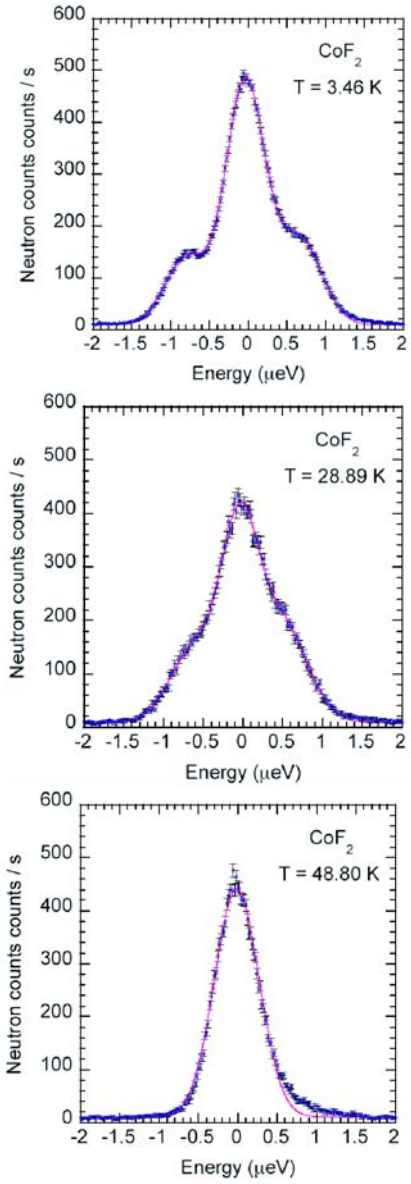

FIG. 1: Typical energy spectra of CoF_2 at several temperatures.

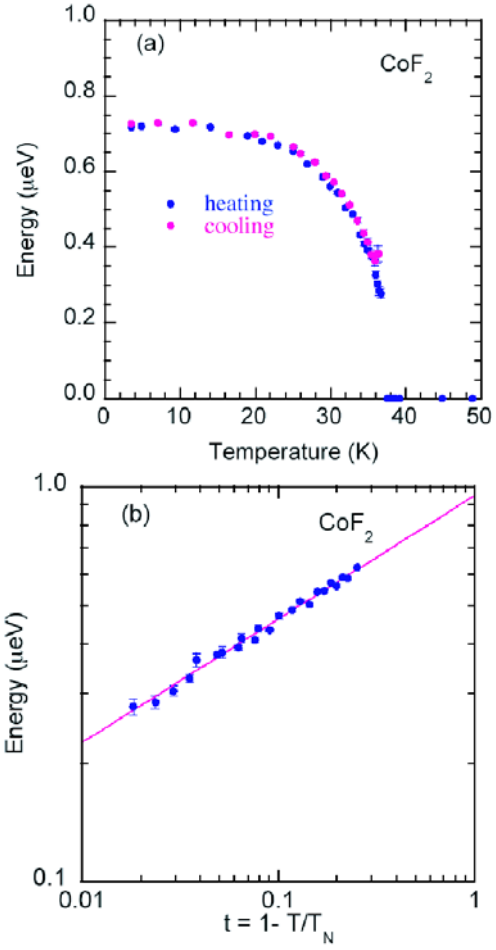

FIG. 2: (a)Temperature variation of the energy of the inelastic peak of CoF_2. (b) Log-log plot of the energy of the inelastic peak vs. reduced temperature $t = (T_N - T)/T_N$ that yield the critical exponent $\beta = 0.313 \pm 0.007$.

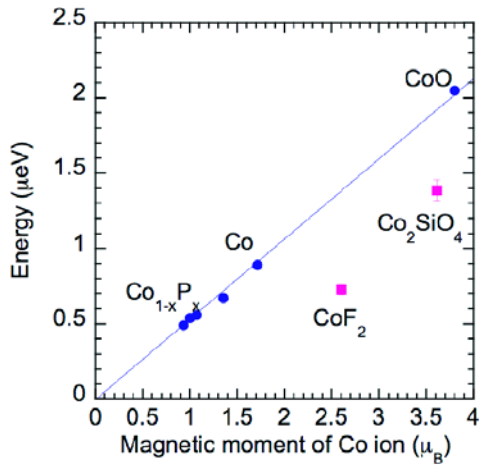

FIG. 3: Plot of energy of the inelastic signals vs. the corresponding electronic magnetic moment of Co compounds.

We checked whether the energy of the inelastic peak or the hyperfine splitting can be considered to be the order parameter of the phase transition. We therefore attempted to determine the critical exponent β assuming the validity of the proportionality of the energy of inelastic peak with the sublattice magnetisation of CoF_2. From the least squares fit of the data close to the Néel temperature to the power law $E(T) = E(0)\,(1 - T/T_N)^{\beta}$ gave $T_N = 37.2 \pm 0.2$ K and $\beta = 0.313 \pm 0.007$. Figure 2(b) shows a log-log plot of the energy vs. reduced temperature. The critical exponent determined $\beta = 0.313 \pm 0.007$ is close to the three-dimensional Ising value $\beta = 0.326$ in consistence with the known results. This shows that the energy of the nuclear spin excitations can be considered to be the order parameter of the phase transition. We also investigated the magnetic phase transitions in Co metal [4] and also CoO and Co_2SiO_4 [5, 6] by determining the temperature variation of the energy of nuclear spin excitations and have found that the energy can be considered to be the order parameter of the phase transition.

Figure 3 shows a plot of energy of inelastic peaks observed in CoF_2 along with that reported in Co metal [4], CoO [5], Co-P alloys [7] and also Co_2SiO_4 [6] vs. the corresponding saturated electronic magnetic moment of Co in these compounds. The data corresponding to all of these compounds except for CoF_2 and Co_2SiO_4 lie approximately on a straight line showing that energy of inelastic peak or the hyperfine splitting of the nuclear level is approximately proportional to the electronic magnetic moment. The slope of the linear fit of all data without that of CoF_2 Co_2SiO_4 gives a value of $0.531 \pm 0.006 \mu eV/\mu_B$. The dramatic departure from the linear behaviour in CoF_2 and Co_2SiO_4 is likely related to the unquenched orbital moments of Co ions in these compounds. The orbital moment in Co metal is known to produces hyperfine field that has opposite sign to that generated by the spin moment [8]. So the orbital moments in CoF_2 and Co_2SiO_4 may be the cause for the reduction of the hyperfine field and splitting compared to that in CoO, Co and Co-P amorphous alloys and hence the deviation from the linear relationship.

In conclusion we have investigated the low energy excitations in CoF_2 and other Co-compounds by inelastic neutron scattering with a backscattering neutron spectrometer. The present results have shown that the hyperfine fields are significantly smaller than that expected from the ordered magnetic moment of 2.60 μ_B and 3.61 μ_B of CoF_2 and Co_2SiO_4, respectively. This is likely related to the presence of significant unquenched orbital moment of Co in CoF_2 and Co_2SiO_4.

[1] A. Heidemann, Z. Phys. **238**, 208 (1970)

[2] T. Chatterji et al., Phys. Rev. B **79**, 132408 (2009).

[3] T. Chatterji et al., J. Phys.: Condens. Matter **21**, 436008 (2009)

[4] T. Chatterji and J. Wuttke (unpublished results).

[5] T. Chatterji et a., Phys. Rev. B **79**, 212409 (2009).

[6] T. Chatterji et al., (unpublished results).

[7] A. Heidemann, Z. Phys. B **20**, 385 (1975)

[8] A.J. Freeman and R.E. Watson, in *Magnetism* ed. G.T. Rado and H. Suhl, Academic Press, New York, London, vol. II A (1965).

Magnetic structure of $EuFe_2As_2$: an x-ray and neutron scattering study

Y. Xiao[1], Y. Su[2], J. Herrero-Martín[3], M. Meven[4], A. Thamizhavel[5], Th. Brückel[1,2]

[1] IFF-4: Scattering Methods
[2] JCNS: Jülich Centre for Neutron Science
[3] European Synchrotron Radiation Facility, Grenoble, France
[4] FRM II, Technische Universität München, Garching, Germany
[5] Tata Institute of Fundamental Research, Mumbai, India

The recent discovery of pnictide superconductors has drawn extensive attention because it provides a new opportunity to investigate the mechanism of superconductivity [1]. Since magnetism and superconductivity appears to be intimately related in iron pnictides, it is therefore important to understand their magnetism. Among various parent compounds of iron pnictide superconductors, $EuFe_2As_2$ stands out due to the presence of both spin density wave of Fe and antiferromagnetic ordering of the localized Eu^{2+} moment. Both resonant x-ray scattering and neutron diffraction experiments have been carried out to determine the magnetic structure of this compound and investigate the coupling between two magnetic sublattices. The determination of magnetic structure of $EuFe_2As_2$ parent compound is significant to understand the relationship between superconductivity and magnetism in pnictide superconductors.

Most of the research on pnictide superconductors has focused on RFeAs($O_{1-x}F_x$) (with R = La, Nd or Sm etc.) and $A$$Fe_2As_2$ (with A = Ba, Ca, or Sr etc.), the so called '1111' and '112' families. These two families are closely related since both of them adopt a layered structure with a single FeAs layer in the unit cell of '1111' and two such layers in the unit cell of '122'. The superconducting state can be achieved either by electron or hole doping of the parent compounds. Considering that the electronic states near the Fermi surface are dominated by contributions from Fe and As, it is believed that the FeAs layers are responsible for superconductivity in these compounds.

$EuFe_2As_2$ is a peculiar member of $A$$Fe_2As_2$ family since the A site is occupied by Eu^{2+}, which is an S-state rare-earth ion possessing a $4f^7$ structure with the electron spin S = 7/2. However, the magnetic ordering and the details of magnetic structure of $EuFe_2As_2$ have not been clarified so far via neutron diffraction due to the extremely large neutron absorption cross-section of Eu. Therefore, the element-specific resonant x-ray scattering acts as an attractive complement to neutron diffraction methods for magnetic structure determination. Here we report the magnetic structure determination of $EuFe_2As_2$ by using the combination of resonant x-ray scattering and neutron diffraction methods.

The single crystals of $EuFe_2As_2$ with typical dimensions $5\times5\times1mm^3$ were grown by the high temperature solution growth method using a fourth element, Sn as the solvent. Single crystal neutron diffraction measurement was performed on hot-neutron four-circle diffractometer HEIDI at FRM II (Garching, Germany). A Cu (220) monochromator was selected to produce a monochromatic neutron beam with the wavelength at 0.868 Å. X-ray scattering data were collected on ID20 beamline at ESRF (Grenoble, France) by using both horizontal (π-incident light) and vertical (σ-incident light) diffraction configurations. The beamline optics was optimized close to Eu L_3 absorption edge (6.97 keV) for resonant measurements.

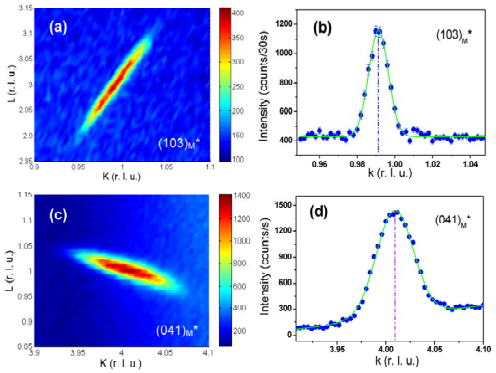

FIG. 1: (a)(c) The contour maps show the Q dependence of the (103) and (041) magnetic reflections. (b)(d) Q scans of (103) and (041) magnetic reflections. The (103) reflection is observed in k scan because of the existence of twinned domains.

The crystal structure of $EuFe_2As_2$ can be described within the framework of tetragonal symmetry at 300 K. Upon cooling down, the crystal structure distortion from tetragonal (S.G. *I4/mmm*) to orthorhombic (S.G. *Fmmm*) structure was revealed by the splitting of the tetragonal (220) reflection into the orthorhombic (400) and (040) reflections. To clarify the magnetic structure of $EuFe_2As_2$ at low temperature, extensive search of magnetic reflections was performed in the reciprocal space. In addition to the expected nuclear reflections, two sets of magnetic superstruc-

ture reflections can be clearly identified with two magnetic propagation wave vectors (1,0,1) and (0,0,1) respectively. The neutron diffraction contour map of (103) and (401) reflections fully illustrated the intensity distribution as shown in Fig. 1(a) and Fig. 1(c). In Fig. 1.(b), the Q scan of (103) reflection can be fitted by a single Gaussian function with k = 0.991. This strongly indicates that the $(h0l)$ type reflections (with h and l equal to odd number) are associated with the $(h00)$ domain and they can thus be described with the propagation wave vector **k** = (1,0,1), which is related to the antiferromagnetic order of Fe^{2+} moments. Consequently, the magnetic reflections with a propagation wave vector **k** = (0,0,1) (with h even and l odd) are due to the long range order of the localized Eu^{2+} moments. The moment direction of Eu^{2+} can be determined as along the a direction since the Q scan on (041) reflection (Fig. 1(d)) giving a peak position of k = 4.01. By taking into account of twinned components properly, the refinement on both Fe^{2+} and Eu^{2+} magnetic sublattices was carried out and the magnetic structure of $EuFe_2As_2$ is unambiguously determined as illustrated in Fig. 3(a). The magnitudes of Eu^{2+} and Fe^{2+} moments are deduced to be 6.8(3) and 0.98(8) μ_B, respectively. The antiferromagnetic configuration of Fe^{2+} moments is also observed in other iron pnictides that we have investigated, such as $BaFe_2As_2$ [2] and CaFeAsF [3]. It should be noted that the Fe moment is quite small (less than 1 μ_B) in all iron pnictides and the origin of that small iron moment in these compounds can be explained as the result of the itinerant character of iron spins or the nearest and next nearest neighbour superexchange interactions between Fe ions which give rise to a frustrated magnetic ground state.

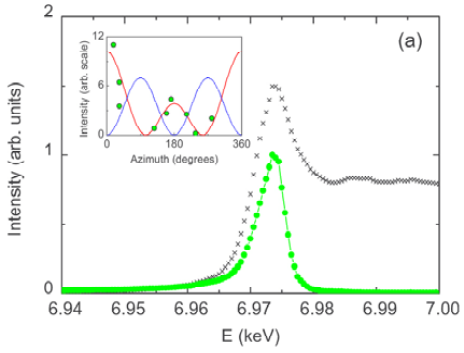

FIG. 2: A energy dependence of $\sigma - \pi$' channel of (209) reflection (filled circles) at 10 K. Fluorescence is shown for comparison (crosses). The inset shows the experimental azimuth behavior of the (209) reflection (circles) compared to calculated evolution in case of Eu moments along crystal a (solid line) or b (dashed) axis.

Fig. 2 shows the resonant x-ray scattering spectra of the (209) reflection in the $\sigma - \pi$' channel at 10 K in the vicinity of the Eu L_3 edge. At resonance, there is no component in the $\sigma - \sigma$' channel as expected. In the inset of Fig. 2 measured resonant intensity in the $\sigma - \pi$' channel as a function of the azimuth angle is plotted together with the expected dependences. The resonant x-ray scattering data confirmed that the Eu moments are aligned along the crystallographic a axis.

Fig. 3(b) shows the temperature dependence of the (112) and (003) magnetic reflections attributed to the ordering of Eu^{2+} moments. The onset temperature of Eu^{2+} magnetic order is deduced to be 19 K. The magnetic ordering temperature of Fe^{2+} moment is estimated to be 190 K based on the temperature dependence of the (101) and (103) magnetic reflections (see Fig. 3(c)). The tetragonal-orthorhombic structural phase transition also takes place at 190 K as revealed by the sharp change of full width at half maximum in (040) nuclear reflection, which indicated the existence of the strong coupling between the structural and magnetic phase transitions in $EuFe_2As_2$.

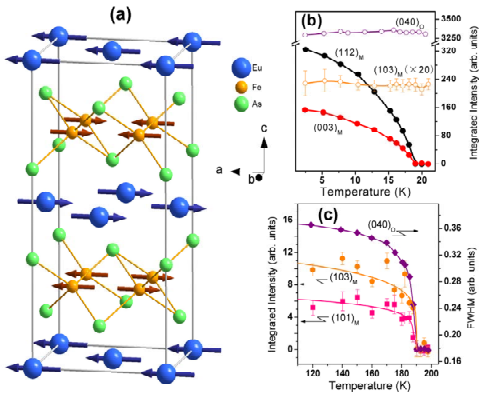

FIG. 3: (a) Illustration of the magnetic structures of $EuFe_2As_2$ at 2.5 K. (b) Temperature dependence of integrated intensity of (040) nuclear reflection as well as the (103), (112) and (003) magnetic reflections below 22 K. (c) Temperature dependence of integrated intensity of (103) and (101) reflections; temperature dependence of FWHM of (040) reflection.

In summary, both single crystal neutron diffraction and resonant x-ray scattering experiments were performed to investigate the crystal and magnetic structure of $EuFe_2As_2$. With decreasing temperature, the antiferromagnetic order of Fe^{2+} moments set in at 190 K with the propagation vector **k** = (1,0,1). Below 19 K, the Eu^{2+} moments order antiferromagnetically with the propagation vector **k** = (1,0,1) and are aligned along the a axis. Our studies also suggest a weak coupling between the Fe^{2+} and Eu^{2+} magnetic sublattices [4, 5].

[1] Y. Kamihara et al., J. Am. Chem. Soc. **130**, 3296 (2008).

[2] Y. Su et al., Phys. Rev. B **79**, 064504 (2009).

[3] Y. Xiao et al., Phys. Rev. B **79**, 060504(R) (2009).

[4] Y. Xiao et al., Phys. Rev. B **80**, 174424 (2009).

[5] J. Herrero-Martín et al., Phys. Rev. B **80**, 134411 (2009).

Monolayer resolved EEL spectroscopy for high-resolution interface analysis

M. Heidelmann[1,3], J. Barthel[2,3], L. Houben[1,3]

[1] IFF-8: Microstructure Research
[2] Gemeinschaftslabor für Elektronenmikroskopie, RWTH Aachen
[3] ER-C: Ernst Ruska-Centre for Microscopy and Spectroscopy with Electrons

The physical properties of materials can be controlled by compositional and bonding fluctuations on the nanoscale. Resolving such fluctuations on the atomic scale has been a long standing challenge in analytical microscopy. Electron energy loss (EEL) spectroscopy with a high-energy electron probe focussed to atomic size in a scanning transmission electron microscope (STEM) is an essential approach to this problem. Here, a simple and powerful technique for monolayer resolved spectrometry of interfaces or 1-dimensional nanostructures is demonstrated. Contrary to the common approach, a precise synchronization of measurement location and spectral information is possible. Electron dose control in combination with atomic-scale resolution and quantitative accuracy opens unique possibilities for studying the local composition of chemically abrupt interfaces.

The commonly used technique for gathering spatially resolved EEL data in a STEM is to record spectra for a series of raster points. If this is done in one spatial dimension it is called the line profile technique while spectrum imaging (SI) refers to a mapping over two dimensions. For each raster point, either full EEL spectra are available for fine structure analysis or elemental maps can be extracted by spectrum integration over an energy window at the onset of a characteristic core-loss. The EEL spectrum acquisition is disrupted periodically to take a high-angle annular dark-field (HAADF) image of a reference area. The image of the reference area is used to counteract the unavoidable specimen and beam drift by applying a compensating shift of the scan frame. The SI and the line profile technique share disadvantages: The recording of an EEL spectrum with a sufficient signal-to-noise ratio (SNR) usually requires a dwell time during which instrumental instabilities are hardly negligible, even for a single beam position. The consequential loss of control over the measurement position due to inherent specimen and beam drift becomes most perceivable at atomic resolution. Small probe displacements on the Ångstrom scale sensitively affect the excitation probability of am inelastic core-loss scattering event, meaning that quantitative spectroscopic data must be considered with caution.

In order to overcome the inherent uncertainties connected with the common procedures we propose a simple technique which is most suited for atomic scale spectroscopy of 1-dimensional nanostructures or planar interfaces [1]. The technique, named StripeSTEM, is based on an isochronous collection of a series of EEL spectra while an HAADF image is taken in a continuous, undisrupted scan. Fig. 1 shows the schematic procedure for the case of a crystalline sample. While the electron probe scans successively along lattice planes aligned to the x-direction, EEL spectra are recorded in sequence as a function of the y-coordinate of the scan. Spectrometer readout times are set such that several EEL spectra are recorded per traversed lattice plane and that each spectrum relates to several scan lines along the y-direction.

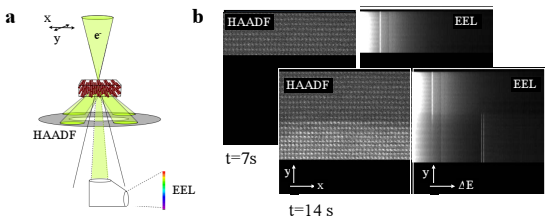

FIG. 1: StripeSTEM measurement. High-resolution HAADF data and EEL data are recorded isochronously while the electron probe with a diameter of less than 1 Å scans the sample. The HAADF image reveals the spatial origin of the energy-loss signal alongside any distortions related to inavoidable specimen and beam drift. The corresponding EEL spectrum stack image reveals the chemical compositon as a function of one spatial coordinate.

Since specimen and beam drift during the experiment, the raw spectral intensity collected shows variations even for equivilant lattice planes in a crystalline sample. However, in a StripeSTEM experiment the effective beam dwell time for a certain monolayer can be calculated using the HAADF-image as a log of the instabilities. Details of the according signal normalization and a practical example are described in [1]. The post-correction of signals leads to an improved accuracy of compositional data compared to the commonly used techniques.

Monolayer resolution is achieved for core loss EEL signals. An experimental proof is shown in fig. 2. Monolayer precipitates of octahedrally coordinated In_2O_3 in ZnO served as an atomically sharp reference structure. In the StripeSTEM experiment, the

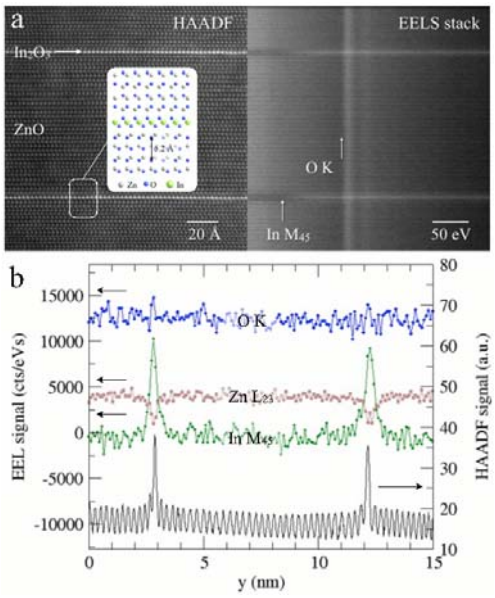

FIG. 2: Monolayer resolution in a StripeSTEM measurement on a reference sample containing monolayer precipitates of In_2O_3 in a ZnO matrix. (a) StripeSTEM data, a model of the defect is superimposed onto the HAADF image. (b) HAADF and EEL chemical profiles orthogonal to the basal plane precipitates.

In_2O_3 monolayers are resolved with a spatial resolution of 1.8 Å in the HAADF profile and 2.7 Å in the In M_{45} core loss signal.

The spatial resolution of the energy loss data is affected by three principal factors: (1) the delocalization of the inelastic scattering process, for core-losses this is typically 1-2 Å, (2) the dynamical dispersion of the electron beam in the sample, and (3) the "geometrical source width" of the probe at high beam current [1]. The first two factors are of physical nature and represent the ultimate limit for the attainable resolution. The last factor is connected to the brightness of the electron emitter. With modern Schottky field emitter microscopes in combination with aberration corrected probe formation the ultimate limit of the spatial resolution can be achieved for strong energy loss signals, like the white lines of transition metals. For weak signals, e.g. the core loss of oxygen, it is necessary to adjust for a high beam current in order to achieve a sufficient SNR for accurate quantification, on the expense of spatial resolution.

StripeSTEM was applied to the analysis of an interface between La_2CuO_4 and $SrTiO_3$. The interface is of the polar/non-polar type and structural or electronic reconstruction is required to avoid a 'polar catastrophe' [2]. The HAADF image in fig. 3 reveals two perovskite blocks in the atomic coordination at the interface. According to the ionic model an abrupt chemical termination would give rise to a net electrostatic field. Previous work based on the quantification of the phase of a reconstructed wavefunction in high-resolution TEM suggested intermixing in the cation sub-lattice, in contrast to electronic reconstruction and free charge carrier accumulation [3]. The

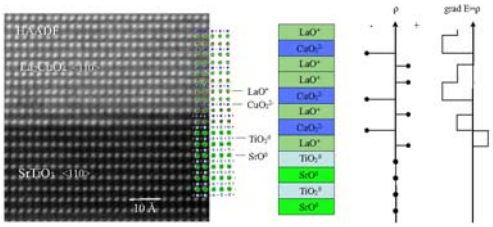

FIG. 3: Atomic coordination at the $SrTiO_3/La_2CuO_4$ interface ([001]STO || [001]LCO). Left: The multiexposure HAADF image shows two intermediate perovskite blocks. A tentative model is depicted. Right: According to the to the ionic model an abrupt chemical termination would give rise to a net electrostatic field and diverging potential in the LCO.

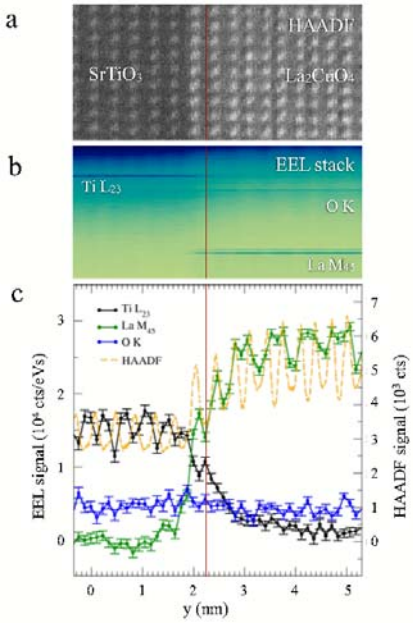

FIG. 4: StripeSTEM analysis of the chemical compositon of the interface between STO and LCO. (a) HAADF image and (b)stack of EEL spectra. (c) Quantitative signal of core losses of Ti, O, and La after background subtraction. Error bars indicate the 1σ uncertainty due to noise and background extrapolation. The HAADF signal is displayed for comparison. The substitution of Cu by Ti in the interfacial perovskite layer introduces an excess positive charge which aids in avoiding a fictitional 'polar catastrophe'.

StripeSTEM experiment shown in fig. 4 now prooves that a considerable Ti concentration is present in the intermediate perovskite-like La(Cu,Ti)O_3 layers. The substitution of Cu^{2+} in the CuO_2^{2-} plane with a high fraction (50%) of Ti^{4+} provides the extra positive charge required to avoid an interface charge: Accumulation of free charge carriers is not a necessity, ionic reconstruction averts a diverging electrostatic potential.

[1] M. Heidelmann, J. Barthel, and L. Houben, Ultramicroscopy, **109** (2009) 1447 – 1452.

[2] N. Nakagawa, H. Y. Hwang, and D. A. Muller, Nature Materials **5** (2006), 204 – 209

[3] L. Houben, J. Mater. Sci. **41** (2006), 4413–4419

Facts and fancy – basic truths about atomic resolution transmission electron microscopy

K. Urban[1,2], C. L. Jia[1,2], L. Houben[1,2], M. Lentzen[1,2], S. B. Mi[1,2], K. Tillmann[1,2]

[1] IFF-8: Microstructure Research
[2] ER-C: Ernst Ruska-Centre for Microscopy and Spectroscopy with Electrons

Transmission electron microscopy has taken a great step forward with the introduction of aberration-corrected electron optics. An entirely new generation of instruments enables studies to be performed at a resolution well below 100 picometres, and the accuracy of spatial measurements has reached a few picometres. These new possibilities are meeting the growing demand of nanosciences for an atomic understanding of materials and device properties together with the validation of the expected functionaltities. However, understanding the results is generally not straightforward and only possible with extensive quantum mechanical calculations. Actually, in order to be able to appreciate the progress that has been achieved it is essential to be aware of three basic facts about electron microscopic imaging.

The **first fact** is that atomic structures are not imaged in electron microscopy in any way comparable to light microscopy where the information is primarily obtained by exploiting the locally varying absorption of the sample. The atomic world is that of quantum mechanics and none of the electrons entering the sample is actually absorbed, but an electron wave field is interacting with the interatomic potential. On account of the high electron energies this interaction has to be described by the Dirac equation which for the conditions applying to TEM adopts a Schrödinger form with relativistically corrected electron wavelength and mass. Solving this equation for a given interatomic potential gives us the exit plane wave function (EPWF) at the lower specimen surface. The basic task in atomic-resolution TEM is not to calculate the scattering problem but instead, since we have to conclude "backward" from images on structure, to invert it.

In electron microscopy, 'images" recorded are wave-interference patterns. In general the way to derive from the images the underlying structure includes two steps. In the first the EPWF is computed since this is the actual object of our optics and it contains all the information on the specimen we can get. Unfortunately, typically about 20 images are required which are recorded by varying e.g. the objective lens focus over a certain range. Since varying the focus induces phase shifts into the electron wave field this technique has similarities to interferometry. This means that by this technique we are probing the wave function; actually we are measuring it. The second step is to conclude from the EPWF to the specimen structure. Since no technique is known as yet that allows to directly calculate the potential and on this basis the structure "backwards" from the EPWF, the only solution is to do a "forward" calculation. For this purpose a model structure based on a first guess is constructed and iteratively improved to obtain a best fit between the calculated and experimental EPWF. This procedure is, however, hampered by the fact that there is no direct access to imaging parameters as sample thickness and the precise direction of the incident electrons. There is no other possibility but to treat these parameters as variables that also

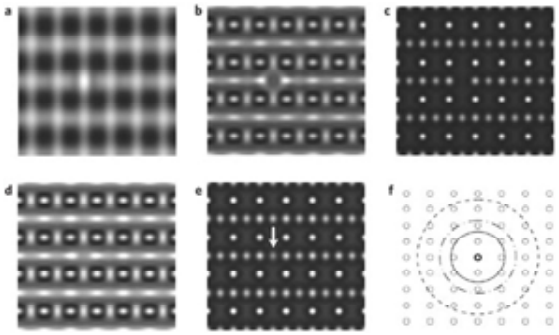

FIG. 1: Computer-simulated images for a $SrTiO_3$ crystal viewed along a [110] zone axis. (a-c): Images corresponding to different aperture radii in the back focal plane of the microscope's objective lens (f) selecting the beams that contribute to image formation. In sequence (a) to (c), the sample contains an empty atom column. With the smallest aperture (full circle in (f)), only the transmitted and four diffracted beams are used to form the image. This situation corresponds to uncorrected electron microscopy where wider apertures cannot be tolerated because of the effect of lens aberrations. Superficially, (a) appears to show an atomic lattice, but this bears little resemblance to the real lattice imaged in (c) with the widest aperture setting. Atomic resolution is only provided in (c). Note the artefacts in (b) taken with the intermediate aperture size. Two "atomic maxima" appear on both sides of the hole. Images (d) and (e), corresponding to the smallest and the largest aperture size, respectively, show simulations for a 30% reduction in occupancy of the atomic position marked with an arrow in (e). To reveal this reduction in occupancy, the large aperture used in an aberration-corrected instrument is essential [1].

have to be determined by means of the fitting procedure. Therefore, the result generally is not an image in the conventional sense but a computer model of the structure that gives the atomic species and coordinates.

The **second fact** is that imaging in the fully aberration corrected mode, although technically feasible, is never ever used in TEM. The background for the need to operate the microscope at a certain value of residual aberration arises from the fact that atomic-resolution TEM is mainly based on phase contrast. This means that the information on the specimen structure is encoded in the EPWF in terms of a locally varying phase shift. Since phases cannot be "seen", a technique analogous to Zernike phase contrast in light microscopy, i.e. converting phase into amplitude information, needs to be applied in TEM as well. Unfortunately a Zernike type phase shifter is not available for TEM. Therefore, the necessary phase shift has to be introduced by exploiting the aberration-induced phase shifting properties of the microscope's objective lens by tuning the lens' spherical aberration parameter for a certain residual value. Since also a deviation from exact focus contributes to the desired phase shift, this is combined with a certain amount of defocusing. In colloquial language one could say that the cost for seeing anything is that one has to accept that the images become "unsharp" to a certain extent.

The **third fact** characterising atomic-resolution TEM is that it is generally not a "snap shot" or "single image" technique. The reason for this is that there is also no way to know a priori the exact focus of the lens nor can the focus be judged reliably by visual inspection. Again the image series obtained at varying lens defocus provides us with a solution to this problem. Following an iterative procedure we obtain the correct focus values while solving for the EPWF. With the EPWF and the eventual sample structure available it is certainly no problem to select from a series of images that one whose image intensity distribution fits best to the measured atomic structure. Now we can "believe", at least to a certain extent, what we are "seeing". However, without the described thorough investigation regarding their background such single images are of very limited value.

How then should "atomic resolution" be defined? The answer is simple as can be: The information must be entirely local on the atomic level. Any change in the position or occupancy of an atomic site in the sample must show up in the image as an individual signal localised only at the corresponding atomic position. In this stringent sense only the images obtainable in modern aberration-corrected instruments are matching the standards of genuine "atomic" resolution. As a matter of fact, the first images showing contrast resembling that of atomic structures were published more than 50 years ago. These images were obtained by placing an aperture in the back focal plane of the objective lens by which only a few low-angle reflections were selected to form the image. This is equivalent to constructing an image taking into account the basic Fourier components only

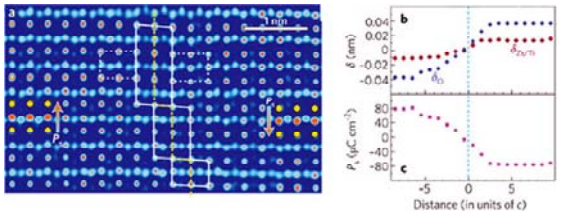

FIG. 2: Polarisation domain wall in PZT. (a) Atomic structure. The shifts of the oxygen atoms (blue circles) out of the Ti/Zr-atom rows (red circles) can be seen directly, as can the change in separation between Ti/Zr and Pb (yellow circles). Arrows give the direction of the spontaneous polarisation, which can be directly inferred from the local atom displacements. (b) Atomic-resolution measurements of the shifts of oxygen (O), and titanium/zirconium (Ti/Zr) atoms as a function of distance from the wall centre in a longitudinal-inversion domain wall. (c) The value of the local polarisation P_S that can be calculated from these data [3].

(Fig. 1a). Although such an image shows a periodic structure consisting of contrast dots, which superficially resemble an atomic lattice, it is entirely inadequate with respect to atomic resolution in the sense just defined. Atomic "individuality" requires high-order Fourier components (Fig. 1b-c) which in early days could not be allowed to contribute to the image due to the detrimental influence of lens aberrations.

In contrast, today's aberration corrected instruments yield images of such quality that we can virtually put our finger on individual atomic positions. For illustration purposes Fig. 2 displays a ferroelectric domain boundary in PZT. Not only that all the different atomic positions are well resolved, we can even measure the individual lateral shifts of the atoms, in the order of 40 pm, out of their symmetry positions which induce electronic lattice polarisation [2]. An investigation employing Gaussian regression analyses reveals that such position measurements can be carried out at a precision of better than $\pm$ 5 pm [3]. Such a precision is by far superior to that of any other state-of-the-art microscopic technique including STEM and STM. Although resolution is defined by the minimum separation of two optically broadened intensity peaks at which these can just be separated in the image, the distance between two well isolated peaks can be measured at a precision more than an order of magnitude higher.

[1] K. Urban, Nature Materials **8** (2009), 260-262.

[2] K. Urban, C. L. Jia, L. Houben, M. Lentzen, S. B. Mi, and K. Tillmann, Phil. Trans. R. Soc. A **367** (2009), 3735-3753.

[3] K. Urban, L. Houben, C. L. Jia, M. Lentzen, S. B. Mi, K. Tillmann, and A. Thust, in: *Advances in imaging and electron physics*, ed. by P. Hawkes, vol. **153** (2008), pp. 439-480, Academic Press, Oxford (UK).

High-resolution transmission electron microscopy on an absolute contrast scale

A. Thust[1,2]

[1] IFF-8: Microstructure Research
[2] ER-C: Ernst Ruska-Centre for Microscopy and Spectroscopy with Electrons

A quantitative approach to high-resolution transmission electron microscopy requires a satisfactory match between image simulations and experiments. While an almost perfect image match is routinely achieved on a relative contrast level, a huge mutual discrepancy in the absolute image contrast by a factor of three has been frequently reported. It is shown that a major reason for this well known contrast discrepancy, which is called Stobbs-factor problem, lies in the neglect of the correct detector modulation-transfer-function in image simulations.

The technique of high-resolution transmission electron microscopy (HRTEM) offers nowadays the possibility to study the atomic configuration of solid state objects with a resolution of around 0.08 nm. Highly accurate information about atomic positions and chemical occupancies at lattice defects and interfaces can be obtained by the quantitative use of this technique.

Due to the quantum-mechanical nature of the electron diffraction inside the object and due to the subsequent electron-optical imaging process, any quantitative extraction of object information from HRTEM images requires a justification by accompanying image simulations. Since the introduction of digital image comparison to HRTEM in the early 1990s, a satisfactory agreement between simulation and experiment could be established only on a relative basis by disregarding the absolute magnitude of the image contrast. The reason for this still common practice was first published by Hÿtch and Stobbs in 1994, who found a remarkably strong discrepancy between the magnitude of the simulated and the experimental image contrast [1]. In their experiment, the image contrast was found to be by a factor of three too low when compared to image simulations. Since the image motifs were nevertheless widely consistent between simulation and experiment, the problem was regarded mainly as a scaling problem, and became prominent as Stobbs-factor problem, factor-of-three problem, or contrast-mismatch problem. An explanation for this prominent and long standing problem, which has been meanwhile frequently reproduced and investigated, has not been found so far.

The electron microscopic imaging process can be subdivided into three stages, of which each can be potentially responsible for the contrast-mismatch problem: (i) the diffraction of the incoming electron wave by the object, (ii) the subsequent electron optical transfer of the diffracted wave by the electromagnetic lenses, and (iii) the final image acquisition by a camera. Concerning the diffraction part, plasmon and phonon scattering were explicitly ruled out as a reason for the problem, and moreover, a remarkable discrepancy between measured and simulated diffraction data was not found. Concerning the electron optical part, the measurement of coherent aberrations and of partially coherent contrast dampening functions is possible with high accuracy and did not reveal inconsistencies. However, little attention has been paid to the final image recording step, which involves the frequency-transfer properties of the image recording device.

In the work of Hÿtch and Stobbs the modulation transfer-function (MTF) of the photographic film plates used at that time was not considered [1]. It is also remarkable that the most popular image simulation software packages, EMS and MacTempas, do not allow to incorporate actually measured MTFs. In all, the actual MTFs of the meanwhile used CCD (charge coupled device) cameras were often not considered in the literature related to the Stobbs-factor problem. Concerning the very rare implementation of actually measured MTFs into image simulations, criticism is allowed: Earlier MTF measurements were often based on the so-called noise method, which is known to yield too optimistic results when compared to the knife-edge method, which is the state-of-the art technique for MTF measurement.

A generalization of the knife-edge method towards a 2-dimensional evaluation of the MTF was developed for this work [2]. This improved method uses as input a shadow image of the microscope's beam stop and is designed to avoid artifacts due to image noise, aliasing, and periodic continuation. Fig. 1 displays (a) the shadow image of the beam stop, (b) a line scan through the shadow image, (c) the rotationally symmetric part of the MTF, and (d) the corresponding point-spread function. The strong fall-off of the measured MTF, which is reflected by a considerably low and broad point-spread function, indicates a strong contrast-dampening effect of the CCD camera in use.

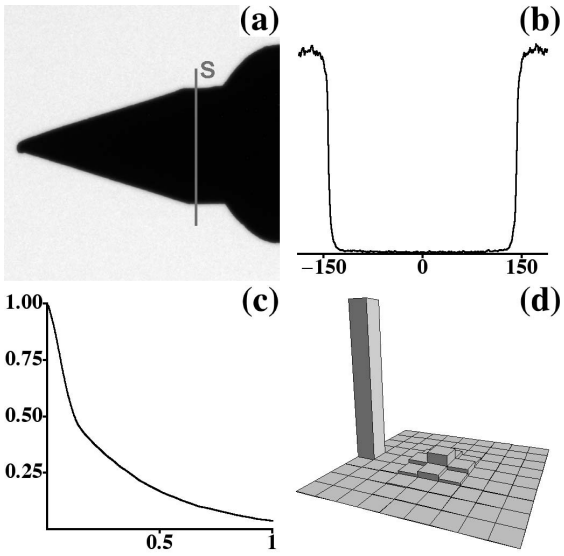

FIG. 1: (a) Shadow image of beam stop acquired with 300 kV electrons by a Gatan UltraScan 1000 camera. (b) Linescan through the vertical section labeled by "S" in the shadow image. Abscissa in pixel units. (c) 1-dim. section of modulation transfer-function $\mathrm{MTF_S}$ derived from shadow image. Abscissa in units of the Nyquist frequency. (d) Central 9 × 9 "pixels" of the related point-spread function $\mathrm{PSF_S}$. The bar at the edge shows the height of an ideal δ-like PSF.

A focal series of [110]-oriented $SrTiO_3$ was acquired with a spherical-aberration corrected FEI Titan 80-300 microscope operated at 300 kV and is compared with image simulations including the measured MTF. The series of 30 images was acquired with a spherical aberration of $C_S = -25\,\mu m$ at an excessively high sampling rate of 9.71 pixels/Å.

The main steps of the accompanying image simulation are visualized in Fig. 2, which highlights four exemplary images belonging to the focal series of 30 images. Column (a) shows ideal images simulated for an object thickness of 2.8 nm. In column (b) residual optical aberrations, which cannot always be avoided during experiment, have been added to the simulation. Column (c) displays the simulated images after the additional application of the measured MTF, and column (d) shows the experimentally acquired images. Simulation (c) and experiment (d) are displayed on the same grey level scale, and are in almost perfect agreement, not only with respect to the similarity of the image motifs, but – what is most important here – also with respect to the occupied absolute contrast range.

A quantitative contrast comparison for the complete series is shown in Fig. 3. It can be seen that the residual aberrations, which change the image motifs in a drastic way, have a comparatively small impact on the simulated image contrast. The major contrast reducing effect is clearly due to the MTF. Only after the application of the correctly measured MTF in simulation (dashed line in Fig. 3) an almost perfect absolute contrast match to experiment (squares in Fig. 3) is possible.

In summary, the existence of a general contrast-mismatch problem of remarkable size in HRTEM can not be confirmed. On the contrary, an almost perfect consistency between simulation and experiment is found when including the correct detector MTF in image simulations.

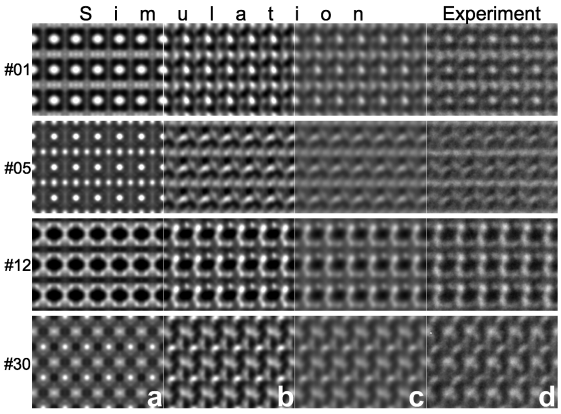

FIG. 2: Image patches comprising 3×3 $SrTiO_3$ unit cells projected along the [110] zone axis. The patches 1, 5, 12, and 30, belong to different focal values and are shown exemplarily for a series of 30 images. All patches are displayed on the same grey scale extending between intensity values 0.35 (black) and 2.2 (white). (a) Simulation for an object thickness of 2.8 nm, (b) simulation including additionally residual lens aberrations, (c) simulation including residual aberrations and additionally the measured MTF, (d) experimental images.

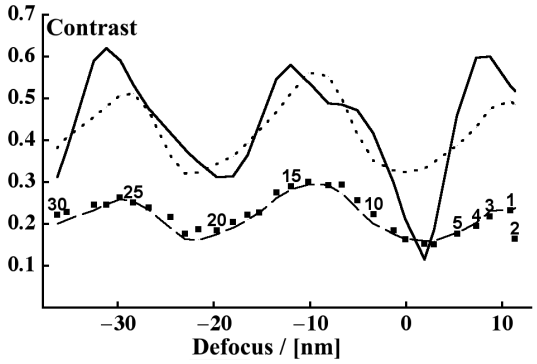

FIG. 3: Solid line: Image contrast simulated for an object thickness of 2.8 nm and for the focal values of the experimental $SrTiO_3$ series. Dotted line: Simulated contrast including additionally residual lens aberrations. Dashed line: Simulated contrast including residual aberrations and additionally the MTF. Squares: Experimental image contrast. Image numbers within focal series are indicated.

[1] M. J. Hÿtch and W. M. Stobbs, Ultramicroscopy 53, (1994) 191.

[2] A. Thust, Phys. Rev. Lett. 102, (2009) 220801.

Constitutions of the Al-Cu-Ir and Al-Ni-Ir alloy systems

B. Grushko[1], D. Kapush[1,2], T. Ya. Velikanova[2]

[1] IFF-8: Microstructure Research
[2] I. N. Frantsevich Institute for Problems of Materials Science, Kyiv, Ukraine

The Al-rich parts of the Al-Cu-Ir and Al-Ni-Ir constitutional diagrams were determined in the temperature ranges up to 1100 °C and 1150 °C, respectively. The study was carried out using powder XRD, DTA, SEM/EDX and TEM. Both alloy systems exhibit formation of complex intermetallic phases.

Al–Cu–Ir and Al-Ni-Ir belong to a group of the Al-based alloy systems exhibiting the formation of quasicrystals and structurally related periodic phases [1]. Using the updated Al-Ir phase diagram [2], the former was studied in a compositional range of Al >30 at.%, the later in a range of Al >50 at.%.

In Al-Cu-Ir congruent equiatomic AlIr extends at quite constant Al concentration up to 35 at.% Cu, cubic C-$Al_{2.7}Ir$(C-phase) up to 13 at.% Cu and hexagonal Al_3Ir up to 8.5 at.% Cu. The solubility of the third element in other binaries was below 3 at.%. The formation of a stable ternary decagonal phase and four ternary periodic phases (Table 1) was revealed [3, 4]. The decagonal phase exhibited a periodicity of ∼0.4 nm in the specific direction (D_1-structure). The Al–Cu–Ir ω-phase is isostructural to Al_7Cu_2Rh, also observed at similar compositions in Al–Cu–Co (Fe, Ru) [1] (Co, Rh and Ir belong to the same column of the periodic table, while Fe and Ru belong to a neighboring column). The C_2-phase, structurally related to the binary C-$Al_{2.7}Ir$, is also formed in Al–Cu–Rh and a number of other ternary aluminum-transition metal alloy systems [1], while the so-called ε_6-phase is known to be formed in the binary Al–Rh and Al–Pd alloy systems [1]. The Al_2CuIr phase belongs to a new structural type. Its detailed structural investigation will be published in [5].

The low-temperature Al_2CuIr phase congruently transforms to the β-phase at 1063 °C. Subsequently, the low-temperature boundary of the β-phase has a bell-like shape with a maximum at Al_2CuIr. With the decreasing temperature the low-Cu and high-Cu regions of the β-phase are formed.

At 1000 °C the high-Cu region was only observed in a small compositional region around $Al_{48}Cu_{35}Ir_{17}$, while at 980 °C this composition corresponded to a three-phase equilibrium (Fig.1).The low-Cu β-phase region extends up to ∼7 at.% Cu at 800 °C. The other ternary phases are formed incongruently in reactions involving the liquid phase. For example, the decagonal phase is formed close to 1000 °C and exists in a compositional range from $Al_{61.5}Cu_{20}Ir_{18.5}$to $Al_{59}Cu_{25.5}Ir_{15.5}$. The corresponding data on the other phases are included in Table 1. Although only the ε_6 structural variant was revealed in TEM examinations, other known variants of this phase [1] are not excluded.

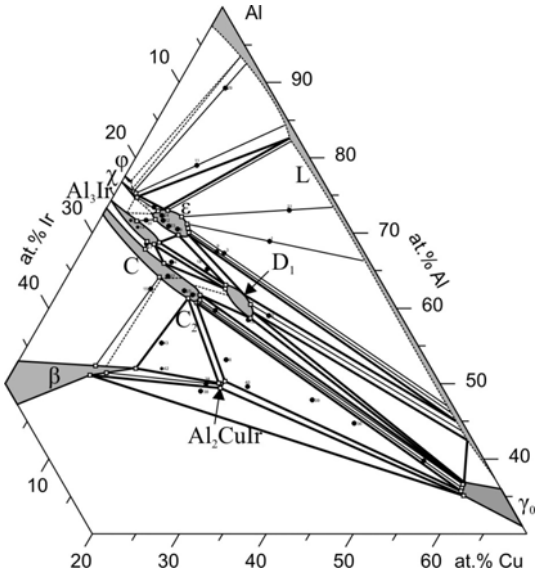

FIG. 1: Partial isothermal 980 °C section of Al-Cu-Ir. The compositions of the studied samples are shown by spots. Provisional tie-lines are shown by broken lines.

Partial 1100, 1000, 980, 900, 800, 700, 600 and 540 °C isothermal sections of Al-Cu-Ir were determined [4].

In Al-Ni-Ir equiatomic congruent AlIr and AlNi form a continuous region of solid solutions. The C-$Al_{2.7}Ir$, $Al_{28}Ir_9$ (χ-phase) and Al_9Ir_2 dissolve up to 6, 10.5 and 2.5 at.% Ni, respectively, while the solubility of Ni in Al_3Ir and $Al_{45}Ir_{13}$ (ϕ-phase) is below 1 at.%. The dissolution of Ni results in a decrease of the melting temperatures of the Al–Ir phases.

In contrast to Al-Cu-Ir and Al-Ni-Rh(Co) containing stable decagonal phases, no quasicrystals were observed in Al-Ni-Ir. The only ternary orthorhombic ε_6-phase was found (see Table 1). Partial 1150, 1000, 900 and 800 °C isothermal sections of Al-Ni-Ir were

Phase	Space group	Lattice parameters, nm			Composition, at.%	Melting T, °C
		a	b	c		
ACI-ε_6	*Pnma*	2.34	1.65	1.24	$Al_{71.5}Cu_6Ir_{22.5}$ to $Al_{68}Cu_{12.5}Ir_{19.5}$.	1200
ANI-ε_6					$Al_{74}Ni_4Ir_{22}$ to $Al_{72.5}Ni_{17}Ir_{10.5}$	1342
C_2	$Fm\overline{3}$	1.5393	–	–	around $Al_{63}Cu_{13}Ir_{24}$	> 1400
ω	$P4/mnc$	0.6414	–	1.4842	around $Al_{70}Cu_{20}Ir_{10}$	683
Al_2CuIr	Cmma	0.8120	0.5065	0.5185	$Al_{50}Cu_{25}Ir_{25}$	1063

TAB. 1: Crystallographic data, compositions and maximal melting temperatures of the ternary periodic AlCu-Ir and Al-Ni-Ir phases.

determined. The overall compositions of the phases in Al-Cu-Ir and Al-Ni-Ir are shown in Fig.2.

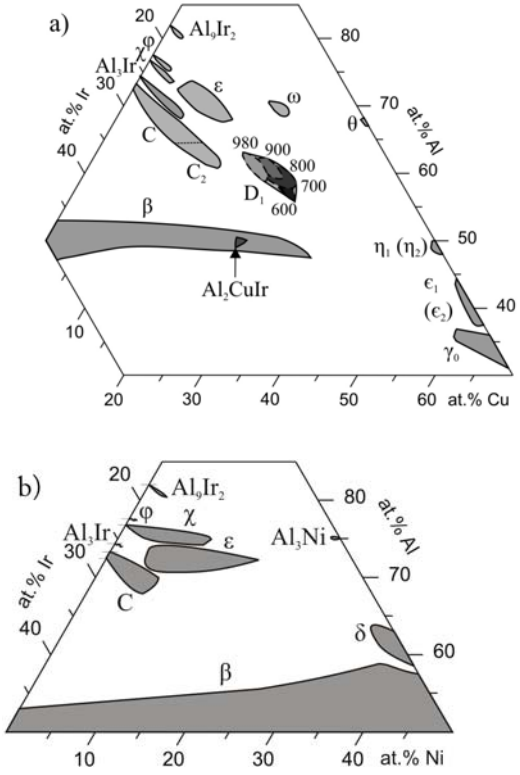

FIG. 2: Overall compositions of the Al-Cu-Ir (a), and AlNi-Ir (b) phases. The compositional regions of the D_1-phase are shown in (a) at the mentioned temperatures.

The Al-Ir C and χ phases dissolve noticeable percentages of Cu and Ni, which results in some decrease of their Al concentration. This decrease is less pronounced in Al-Ni-Ir than in Al-Cu-Ir. Considering the shapes of the compositional regions of the C and χ phases, Ni replaces rather Ir than Al, while Cu rather replaces Al in these phases. This is consistent with the suggestion of the importance of the electron concentration for the stability of Al-TM phases [1]. Some widening of the phase regions in ternary compositions was observed similar to that in many other systems [1].

Formation of the ternary ε-phases in the title systems is in favor of the stabilization of a metastable Al–Ir ε-phase by a third element. The extrapolations of the ε-regions in Al-Ni-Ir, Al-Cu-Ir and Al-Pd-Ir towards Al-Ir intersect close to Al_3Ir, the composition corresponding to that of the stable ε-phase in Al-Rh [1]. The stability region of the ε-phase phase in Al–Ni–Ir is at somewhat higher-Al concentrations than in Al–Cu–Ir. This is similar to the above-mentioned ternary extensions of the C and χ phases and has similar nature.

No stabilization of the metastable Al–Ir decagonal quasicrystals by Ni was observed, in contrast to the stabilizing effect of Cu. This also is in contrast to the metastable Al–Co and Al–Rh quasicrystals, which are stabilized by both Ni and Cu [1]. In Al–Ni–Co the decagonal quasicrystals are formed in a wide compositional range and exhibit several structural modifications. In a smaller compositional range around $Al_{70}Ni_{15}Co_{15}$ the decagonal phase is stable at least down to 800 °C, while at lower temperatures its stability is unclear due to sluggish equilibration. In Al–Ni–Rh a D_1-phase is only formed at elevated temperatures and in very narrow temperature and concentration regions [1]. Subsequently, the decagonal region completely vanishes in Al–Ni–Ir, which follows the same tendency.

[1] B. Grushko and T. Velikanova, CALPHAD, **31**, 217 (2007).

[2] D. Pavlyuchkov, B. Grushko and T. Ya. Velikanova, Intermetallics. **16**, 801 (2008).

[3] B. Grushko, D. Pavlyuchkov, Powder Diffraction, **23**, 356 (2008).

[4] D. Kapush, B. Grushko and T. Ya. Velikanova, J. Alloys Comp. in press
DOI :10.1016/j.jallcom.2009.12.070

[5] L. Meshi, V. Ezersky, D. Kapush, B. Grushko, (to be published).

Determination of screened Coulomb repulsion energies in organic molecular crystals: a real space approach

A. Dolfen[1], E. Koch[1,2], L. Cano-Cortés[3], J. Merino[4]

[1] German Research School for Simulation Sciences, Forschungszentrum Jülich and RWTH Aachen
[2] IFF-1: Quantum Theory of Materials and IAS: Institute for Advanced Simulation
[3] Departamento de Física Universidad Autónoma de Madrid, Madrid 28049, Spain

We present a general method for determining screened Coulomb parameters in molecular assemblies, in particular organic molecular crystals. This allows us to calculate the interaction parameters used in a generalized Hubbard model description of correlated organic materials. In such a model only the electrons in levels close to the Fermi level are included explicitly, while the effect of all other electrons is included as a renormalization of the model parameters. For the Coulomb integrals this renormalization is mainly due to screening. For molecular materials we can split the screening into intra- and inter-molecular screening. Here we demonstrate how the inter-molecular screening can be calculated by modeling the molecules by distributed point-polarizabilities and solving the resulting self-consistent electrostatic screening problem in real space. For the example of the quasi one-dimensional molecular metal TTF-TCNQ we demonstrate that the method gives remarkably accurate results.

The minimal model to describe the low-energy electronic properties of low-dimensional organic systems is the Hubbard model [1], where transfer integrals between neighboring sites and on-site Coulomb interactions are taken into account. Such a simple Hubbard model is, however, usually not sufficient to describe strongly correlated organics, as long-range Coulomb repulsion energies can rarely be neglected [2, 3]. In the generalized model

$$H = -t\sum_{\langle ij\rangle,\sigma}(c^{\dagger}_{i,\sigma}c_{j,\sigma}+h.c.)+U\sum_{i} n_{i\uparrow}n_{i\downarrow}+\sum_{i,j} V_{ij}n_i n_j,$$

we include hopping integrals between nearest neighbors, t, on-site Coulomb energies, U, and longer-range Coulomb interactions, V_{ij}. While transfer integrals can be obtained from *ab-initio* DFT calculations [4], Coulomb parameters are more difficult to obtain, as they include the screening correction due to different high-energy processes inside the crystal, the main mechanism being the polarization of the surrounding, usually highly polarizable, molecules. By realizing that organic molecules preserve their identity inside the crystal, we may estimate the screening energy, by describing the molecular interactions through classical electrostatics.

In BEDT-TTF and TTF-TCNQ families of organic conductors, flat molecules crystallize forming low-dimensional anisotropic structures. Considering such a lattice of organic molecules, we ask what happens when a charge is added to one molecule. The electric field of that charge will induce a dipole moment in the surrounding highly polarizable molecules. Solving this electrostatic problem assuming fixed polarizabilities, we obtain the screening of the charged molecule in linear response. This gives the screening contribution of the lattice that is needed for renormalizing the bare Coulomb integral.

Modelling each molecule in the crystal as a polarizable point with polarizability α_i, we can express the electrostatic interaction between the dipoles using the interaction matrix [5]

$$\Gamma_{i\mu,j\nu} = \frac{3r_{ij\mu}r_{ij\nu} - \delta_{\mu\nu}r_{ij}^2}{r_{ij}^5}, \qquad (1)$$

where $i \neq j$ are the lattice sites and μ, ν are the cartesian coordinates (x,y,z). The field created by a fixed arrangement of dipoles on the molecules is then given by $|\mathbf{E}^{dip}\rangle = \Gamma|\mathbf{p}\rangle$. The energy of the system in an external field is thus given by

$$W = \frac{1}{2}\langle\mathbf{p}|\alpha^{-1} - \Gamma|\mathbf{p}\rangle - \langle\mathbf{p}|\mathbf{E}^{ext}\rangle. \qquad (2)$$

By applying the variational principle, $\delta W = 0$, we obtain the expression for the set of dipoles which minimize the energy of the whole lattice,

$$|\mathbf{p}\rangle = \left(\alpha^{-1} - \Gamma\right)^{-1}|\mathbf{E}^{ext}\rangle. \qquad (3)$$

Inserting into (2) yields:

$$\delta W = -\frac{1}{2}\langle\mathbf{E}^{ext}|\left(\alpha^{-1} - \Gamma\right)^{-1}|\mathbf{E}^{ext}\rangle. \qquad (4)$$

Therefore, placing two charges at a lattice point or two different lattice points, we are able to calculate the correction to the total energy due to the polarization of the rest of the molecules in the crystal. Defining the external field as the composition of two fields, corresponding to charges placed at points n and m in the lattice, $\mathbf{E}^{ext} = \mathbf{E}_n + \mathbf{E}_m$, the energy of the system then gives for $n = m$ te on-site Coulomb screening and for $n \neq m$ the screening of the inter-site Coulomb

interaction. Thus, defining $|n-m| = l$, the general equation for the screening Coulomb parameters reads:

$$\delta V^l = -\langle \mathbf{E}_0 | \left(\alpha^{-1} - \Gamma\right)^{-1} | \mathbf{E}_l \rangle \quad \Rightarrow \quad V^l = V_0^l + \delta V^l,$$

where δU corresponds to $l = 0$, δV to $l = 1$, ... and V_0^l are the Coulomb parameters for a single molecule/dimer, calculated with DFT [4].

To illustrate the method we apply it to a cubic lattice of polarizable point dipoles, in which an antiferroelectric instability occurs [6], due to the anisotropy in the dipole interactions. Such instability influences the screening of a charge in the lattice. For small polarizabilities α the induced dipoles simply arrange along the field-lines of the central point charge. Increasing α we, however, observe quite unconventional dipole arrangements. This reflects the fact that for this lattice the matrix $(\alpha^{-1} - \Gamma)$ becomes singular at a critical polarizability α_c, with the eigenvector of the vanishing eigenvalue having non-zero momentum (in this case $(\pi, \pi, 0)$). Hence the ferroelectric instability happens before the critical value α_{CM} obtained from the Clausius-Mossotti relation [5].

In a real molecular crystal the molecules typically form stacks, i.e., they are quite closely packed. Consequently, approximating the polarizability of a molecule by just one point-polarizability is not a good approximation. It only works outside a sphere containing the charge density of the molecule, which for typical π-bonded molecules will intersect the neighboring molecules, but it becomes accurate at large distances. To obtain a better description of the molecular response, we model it as point-polarizabilities distributed over the non-hydrogen atoms of the molecule. The accuracy of this submolecular approach is tested for TTF-TCNQ salts.

We consider a small system of only 3 or 5 molecules of a TTF chain. For such small systems we can perform constrained density-functional calculations [4], constraining the added charge to the central molecule. This gives us the screening due to the molecules in this small assembly. We compare to the results of the screening calculated using the distributed point-polarizability approach. Since this approach works least well in the near-field, this is a critical test of the method. Nevertheless, both approaches agree within 5%. If we included more distant molecules, for which the computational cost of constrained density-functional calculations would be prohibitive, the agreement would improve further, as the multipole approximation becomes exact in the far-field. Thus, using polarizability tensors obtained with DFT [4] in our submolecular approach essentially reproduces the results of full quantum mechanical treatment of the screening.

To obtain the screened parameters for a TTF-TCNQ crystal, we perform calculations for crystal fragments (clusters) of increasing sizes to extrapolate to the infinite-size limit. To obtain the parameters for the extended Hubbard model we consider the Coulomb screening between two charges at the same or at

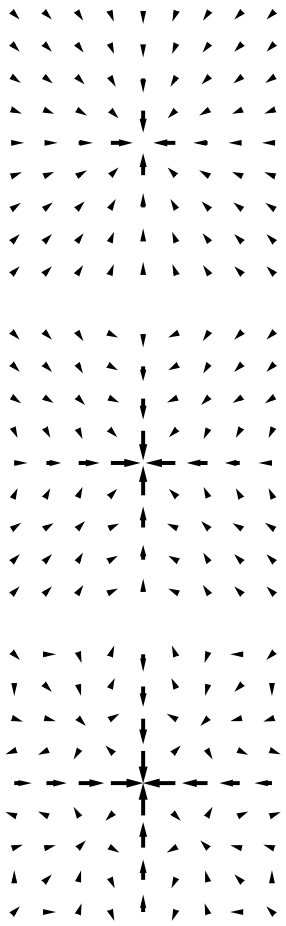

FIG. 1: Dipole arrangement in the x-y-plane of a simple-cubic lattice of point dipoles to a charge added at the center. As the polarizability increases from $\alpha = 0.5\alpha_{CM}$ (top), $0.75\alpha_{CM}$ (middle) to $\alpha = 0.8\alpha_{CM}$ (bottom), the dipoles start to deviate strongly from pointing along the field-lines of the external field.

neighbor molecules placed in the center of the cluster. For simplicity, the clusters of N molecules are constructed as spheres of radius R, where R is the distance between the doped molecule (or center of the pair of molecules) and the farthest neighbor in the cluster, hence $\Omega = \frac{4\pi}{3} R^3$ being the volume of the sphere. For large enough R we can linearly extrapolate the screening energy δU or δV, respectively, versus $1/R$ to the thermodynamic limit ($R \to \infty$).

[1] P. W. Anderson, Science **235**, 1196 (1987); J. Hubbard, Proc. R. Soc. Lond. A **276**, 238 (1963).

[2] J. Hubbard, Phys. Rev. B **17**, 494 (1978).

[3] M. Mayr, P. Horsch, Phys. Rev. B **73**, 195103 (2006).

[4] L. Cano-Cortés *et al.*, Eur. Phys. J. B **65**, 173 (2007).

[5] P. B. Allen, J. Chem. Phys. **120**, 2951 (2004).

[6] J. M. Luttinger and L. Tisza, Phys. Rev. B **70**, 954 (1946).

Heat transfer between elastic solids with randomly rough surfaces

B. N. J. Persson, B. Lorenz

IFF-1: Quantum Theory of Materials

We study the heat transfer between elastic solids with randomly rough surfaces. We include both the heat transfer from the area of real contact, and the heat transfer between the surfaces in the non-contact regions. We apply a recently developed contact mechanics theory, which accounts for the hierarchical nature of the contact between solids with roughness on many different length scales. For elastic contact, at the highest (atomic) resolution the area of real contact typically consists of atomic (nanometer) sized regions, and we discuss the implications of this for the heat transfer. For solids with very smooth surfaces, as is typical in many modern engineering applications, the interfacial separation in the non-contact regions will be very small, and for this case we show the importance of the radiative heat transfer associated with the evanescent electromagnetic waves which exist outside of all bodies.

The heat transfer between solids is a topic of great importance. Classical applications include topics such as cooling of microelectronic devices, spacecraft structures, satellite bolted joints, nuclear engineering, ball bearings, tires and heat exchangers. Other potential applications involve microelectromechanical systems (MEMS). Heat transfer is also of crucial importance in friction and wear processes, e.g., rubber friction on hard and rough substrates depends crucially on the temperature increase in the rubber-countersurface asperity contact regions [1].

A large number of papers have been published on the heat transfer between randomly rough surfaces[2]. However, most of these studies are based on asperity contact models such as the model of Greenwood and Williamson (GW) [3]. Recent studies have shown that the GW-model (and other asperity contact models) are very inaccurate, mainly because of the neglect of the long-range elastic coupling [4]. That is, if an asperity is pushed downwards somewhere, the elastic deformation field extends a long distance away from the asperity, which will influence the contact involving other asperities further away. This effect is neglected in the GW theory, but it is included in the contact mechanics model of Persson, which we have used in the study presented in Ref. [5]. In addition, in the GW model the asperity contact regions are assumed to be circular (or elliptical) while the actual contact regions (at high enough resolution) have fractal-like boundary lines, see Fig. 1. Thus, because of their complex nature, one should try to avoid to directly involve the nature of the contact regions when studying contact mechanics problems, such as the heat or electric contact resistance. The approach we use in Ref. [5] does not directly involve the nature of the contact regions. Finally, we note that for elastically hard solids the area of real (atomic) contact A may be a very small fraction of the nominal or apparent contact area A_0, even at high nominal squeezing pressures.

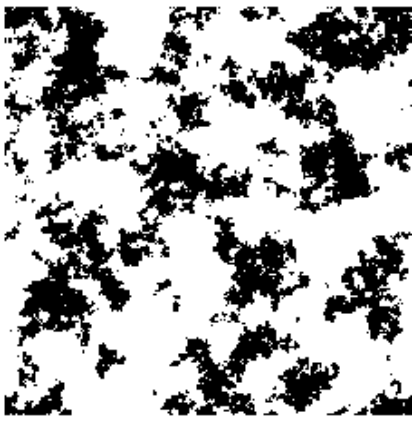

FIG. 1: The black area is the contact between two elastic solids with randomly rough surfaces. For surfaces which have fractal-like roughness the whole way down to the atomic length scale, the contact at the highest magnification (atomic resolution) typically consists of nanometer-sized atomic clusters. The result is obtained using Molecular Dynamics (MD), but since there is no natural length scale in elastic continuum mechanics the picture could also be the contact observed between two macroscopic elastic solids.

Another important discovery in recent contact mechanics studies is that for elastic contacts, the contact regions observed at atomic resolution may be just a few atoms wide, i.e., the diameter of the contact regions may be of the order of ~ 1 nm. The heat transfer via such small junctions may be very different from the heat transfer through macroscopic sized contact regions, where the heat transfer usually is assumed to be proportional to the linear size of the contact regions (this is also the prediction of the macroscopic heat diffusion equation), rather than the contact area. In particular, if the typical

phonon wavelength involved in the heat transfer becomes larger than the linear size of the contact regions (which will always happen at low enough temperature) the effective heat transfer may be strongly reduced. Similarly, if the phonons mean free path is longer than the linear size of the contact regions, ballistic (phonon) energy transfer may occur which cannot be described by the macroscopic heat diffusion equation. These effects are likely to be of crucial importance in many modern applications involving micro (or nano) sized objects, such as MEMS, where just a few atomic-sized contact regions may occur. However, for macroscopic solids the thermal (and electrical) contact resistance is usually very insensitive to the nature of the contact regions observed at the highest magnification, corresponding to atomistic (or nanoscale) length scales (see Ref. [5]). In fact, the heat transfer is determined mainly by the nature of the contact regions observed at lower magnification where the contact regions appear larger, see Fig. 2. For example, in Ref. [5] we show that for self-affine fractal surfaces the contact resistance depends on the range of surface roughness included in the analysis as $\sim r(H) - (q_0/q_1)^H$, where q_0 and q_1 are the smallest and the largest wavevector of the surface roughness included in the analysis, respectively, and H is the Hurst exponent related to the fractal dimension via $D_{\rm f} = 3 - H$. The number $r(H)$ depends on H but is of the order of unity. In a typical case $H \approx 0.8$, and including surface roughness over one wavevector decade $q_0 < q < q_1 = 10q_0$ results in a heat resistance which typically is only $\sim 10\%$ smaller than obtained when including infinitely many decades of length scales (i.e., with $q_1 = \infty \times q_0$). At the same time the area of real contact approaches zero as $q_0/q_1 \to 0$. Thus, there is in general no relation between the area of real contact (which is observed at the highest magnification, and which determines, e.g., the friction force in most cases), and the heat (or electrical) contact resistance between the solids. One aspect of this in the context of electric conduction was pointed out a long time ago: if an insulating film covers the solids in the area of real contact, and if electrical contact occurs by a large number of small breaks in the film, the resistance may be almost as low as with no film. Similarly, the thermal contact resistance of macroscopic solids usually does not depend on whether the heat transfer occur by diffusive or ballistic phonon propagation, but rather the contact resistance is usually determined mainly by the nature of the contact regions observed at relative low magnification.

Note that as H decreases towards zero (or the fractal dimension $D_{\rm f} \to 3$) one needs to include more and more decades in the length scales in order to obtain the correct (or converged) contact resistance, and for $H = 0$ (or $D_{\rm f} = 3$) it is necessary to include the roughness on the whole way down to the atomic length scale (assuming that the surfaces remain fractal-like with $H = 0$ the whole way down to the atomic length scale). Most natural surfaces and surfaces of engineering interest have (if self-affine fractal) $H > 0.5$ (or $D_{\rm f} < 2.5$), e.g., surfaces prepared by crack propagation or sand blasting typically have $H \approx 0.8$, and in these cases the contact resistance can be calculated accurately from the (apparent) contact observed at relatively low magnification. However, some surfaces may have smaller Hurst exponents. One interesting case is surfaces (of glassy solids) with frozen capillary waves (which are of great engineering importance), which have $H = 0$. The heat transfer between such surfaces may be understood only by studying the system at the highest magnification corresponding to atomic resolution.

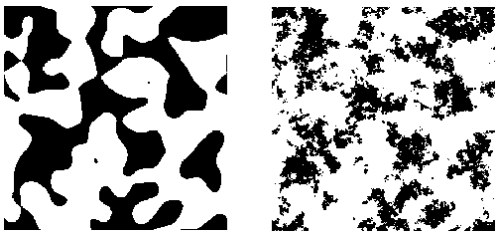

FIG. 2: The contact region (black area) between two elastic solids observed at low (left) and high (right) magnification. The contact resistance depends mainly on the long-wavelength roughness, and can usually be calculated accurately from the nature of the contact observed at low magnification (left).

In Ref. [5] we considered the heat transfer between (macroscopic-sized) solids in the light of recent advances in contact mechanics. We studied both the contribution to the heat transfer not just from the area of real contact (observed at atomic resolution), but also the heat transfer across the area of non-contact, in particular the contribution from the fluctuating electromagnetic field, which surrounds all solid objects. For high-resistivity materials and for hard and very flat surfaces, such as those involved in many modern applications, e.g., MEMS applications, this non-contact radiative heat transfer may in fact dominate in the total heat transfer (at least under vacuum condition). We note that for flat surfaces (in vacuum) separated by a distance d larger than the thermal length $d_{\rm T} = c\hbar/k_{\rm B}T$, the non-contact heat transfer is given by the classical Stefan-Boltzman law, and is independent of d. However, for very short distances the contribution from the evanescent electromagnetic waves to the heat transfer will be many orders of magnitude larger than the contribution from propagating electromagnetic waves (as given by the Stefan-Boltzman law).

[1] B. N. J. Persson, J. Phys.: Condensed Matter **18**, 7789 (2006).

[2] M. Bahrami, J. R. Culham, M. M. Yanavovich and G. E. Schneider, Applied Mechanics Reviews **59**, 1 (2006).

[3] J. A. Greenwood and J. B. P. Williamson, Proc. Roy. Soc. London A**295**, 300 (1966).

[4] B. N. J. Persson, J. Phys.: Condens. Matter **20**, 312001 (2008).

[5] B. N. J. Persson, B. Lorenz and A. I. Volokitin, European Journal of Physics E, (2010).

Nonlinear two-dimensional Green's function in smectics

E. Brener[1], V. I. Marchenko[2], D. Pilipenko[1]

[1] IFF-3: Theory of Structure Formation
[2] Kapitza Institute for Physical Problems, Russian Academy of Sciences, ul. Kosygina 2, Moscow, 119334 Russia

The problem of the strain of smectics subjected to a force distributed over a line in the basal plane has been solved.

The asymptotic expressions for strains around isolated defects in smectics at long distances are characterized by the exponent α [1]. If $\alpha < 0$, the linear theory is applicable. If $\alpha = 0$, (edge dislocation [2, 3], Green's function [4]), the linear solution is valid at small action amplitudes, whereas nonlinear effects become important at larger amplitudes. If $\alpha > 0$, nonlinear effects should be taken into account even for extremely weak actions. In this paper, we report the solution of the nonlinear problem of the two-dimensional Green's function ($\alpha = 1/2$) [1]. Let us consider a smectic sample with the thickness L that is sandwiched between solid undeformable walls parallel to smectic layers (see figure). A force uniformly distributed along the y axis (normal to the figure plane) with the linear density F is applied at the center ($x = z = 0$) of the smectic sample. The energy of the small strains of the smectic sample is given by the expression (see Eq. (44.13) in [5])

$$E = \frac{A}{2}\int\left\{\left(\partial_z u - \frac{(\partial_x u)^2}{2}\right)^2 + \lambda^2(\partial_x^2 u)^2\right\}dV, \quad (1)$$

where u is the displacement of the layers along the smectic axis z, A is the elastic modulus, and λ is the microscopic length parameter. In our problem, the maximum displacement u_0 is reached in the force application line. In terms of the new function $f = u/u_0$ and new coordinates $\tilde{z} = z/L$ and $\tilde{x} = x/L$, where $\varepsilon = u_0/L$, Eq. (1) is represented in the form

$$E = 2^{-1}AL^2\varepsilon^{5/2}\int\left(\sigma^2 + \beta(f'')^2\right)d\tilde{z}d\tilde{x}, \quad (2)$$

where $\beta = (\lambda/\varepsilon L)^2$, $\sigma = \dot{f} - (f')^2/2$, and the dot and prime mean differentiations with respect to $\tilde{z}$ and $\tilde{x}$ respectively. Thus, it is necessary to determine the function f that provides the minimum of energy (2), is equal to unity at $\tilde{x} = \tilde{z} = 0$, and is equal to zero at the edges of the smectic layer $\tilde{z} = \pm 1/2$. The force is given by the expression $F = F_+ - F_-$, where

$$F_\pm = \mp\int\sigma_{zz}dS = \mp AL\varepsilon^{3/2}\int\sigma d\tilde{x}. \quad (3)$$

In the macroscopic problem, curvature $\propto \beta$ can be neglected even for the case of a negligibly small force

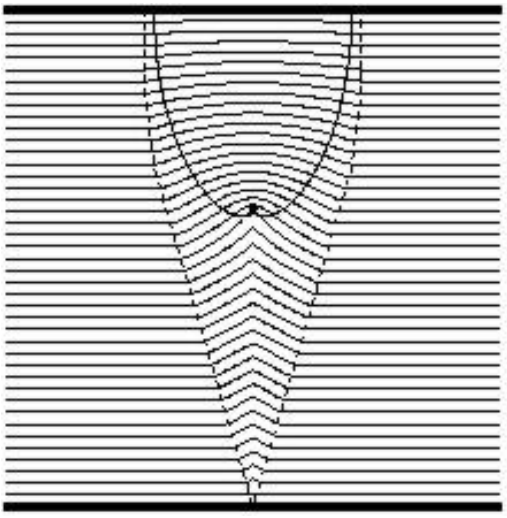

FIG. 1: Strain of the smectic layer subjected to the linearly distributed force($\varepsilon = 0.1$)applied at the thick point. The dashed line is the boundary of the region, where a noticeable strain appears. The thin line is the boundary of the compression region($\sigma < 0$).

$F \sim \lambda A\sqrt{\lambda/L}$, where the amplitude u_0 is larger than the distance between smectic layers $\sim \lambda \ll L$. It is interesting that integrals (2) and (3) can be calculated in this case even without the complete solution, because the strain field is divided into two regions. In the first region, where the material is compressed, the problem can be solved analytically. In the second region, owing to the Helfrish instability (see the problem in Section 44 in [5]), rotary states almost without stresses appear instead of tension. Here, noticeable stresses exist only inside microscopically thin twin boundaries [6].

The figure shows the strain pattern in the smectic layer obtained by numerically solving the problem. In the compression region, the function f is a quadratic function of the variable $\tilde{x}$: $f(\tilde{x},\tilde{z}) = f_0(\tilde{z}) + f_2(\tilde{z})\tilde{x}^2$. It is easy to verify that the equilibrium equation $\dot{\sigma} - (f'\sigma)' = 0$ corresponding to the extremum of energy (2) has such an exact solution satisfying the necessary conditions. It can be represented in the parametric form

$$f_0 = 1 - \frac{2\varphi}{\pi}, f_2 = -\frac{\pi\cos\varphi}{2\sin^3\varphi}, \tilde{z} = \frac{\varphi - \sin\varphi\cos\varphi}{\pi}. \quad (4)$$

The compression region $\sigma < 0$ corresponds to the range $-\tilde{x}_m < \tilde{x} < \tilde{x}_m$, at $\tilde{z} > 0$, where $\tilde{x}_m = 2\sin^2\varphi/\pi$. The thin line in the figure is the boundary taking into account the displacement of smectic layers, where σ is zero. Under this line, down to the dashed line, strains result in the appearance of two twins [6] in which inhomogeneous strains increase in the direction to the force application level. Here, stresses are small and are likely caused by the finiteness of the grid used for the calculation.

When the tension of the twin boundaries is disregarded (at $\beta = 0$) [6], $F_- = 0$. Then, $F = F_+ = = (8/3\pi)AL\varepsilon^{3/2}$. Correspondingly,

$$u_0 = \left(\frac{3\pi a}{8}\right)^{2/3} L^{1/3},\ a = \frac{F}{A}. \qquad (5)$$

At $\tilde{z} \ll 1$, according to (4), $u = u_0 + \delta u$, where

$$\delta u = -3\left(\frac{a^2 z}{16}\right)^{1/3} - \frac{x^2}{3z},\ \delta u \ll u_0. \qquad (6)$$

Let us assume that the displacement near the force application point has the form $\delta u = -z^{1/3}a^{2/3}\psi(v)$, where $v = xa^{-1/3}z^{-2/3}$. Note that $\delta u$is independent of L. In this case, the equilibrium equation is the ordinary differential equation

$$\left(\left(2\psi - 4v\psi' + 3(\psi')^2\right)\left(3\psi' - 2v\right)\right)' = 0, \qquad (7)$$

where the prime means differentiation with respect to v, and has a trivial first integral. The integration constant is zero, because the expression in the second parentheses in Eq. (7) is zero for solution (6). The expression in the first parentheses is proportional to stress σ. It is convenient to represent the solution of the equation $\sigma = 0$ in the parametric form $\psi = (4 + t^3)/2t$, and $v = (1 + t^3)/t^2$. The intervals $-1 < t < 0$ and $0 < t < 2^{1/3} \to z > 0$ correspond to the regions $z < 0$ and $z > 0$ respectively. The integration constant is chosen from the condition $\psi\left(3/2^{2/3}\right) = 3/2^{1/3}$ at $t = 2^{1/3}$ (matching with solution (6) on the line $x_m(z) \simeq 3(az^2/4)^{1/3}$). Near the $z = 0$ line ($|v| \to \infty$),

$$\delta u = -2\sqrt{a|x|} + \frac{az}{2|x|}.$$

At the $x = 0$ line at $z < 0$ ($|v| \to 0$)

$$\delta u = -\frac{3}{2}a^{2/3}|z|^{1/3} - \frac{a^{1/3}|x|}{|z|^{1/3}}.$$

If $a \ll \lambda$, onlinear asymptotic expressions are valid at $|z| \gg \lambda^3/a^2$, and $|x| \gg \lambda^2/a$, and the GreenÕs function of the linear approximation is applicable at smaller distances [1]. If $a \gg \lambda$, small-strain approximation (1) is violated at $|z| \sim |x| \sim a$.

Stresses in the problem under consideration exist only in the smectic compression region and rotary adjustment in a certain bounded region occurs instead of tension. Such a character of nonlinear response implies that the compression field and, correspondingly, the u_0 value (with the change $L \to 2L_+$), as well as the asymptotic expression for δu, remain unchanged in the general case, where the force is applied not to the center, but at any distance L_+ in the direction of the force action from the undeformable wall. The boundary conditions on the opposite side and, generally speaking, beyond the compression region affect only the adjustment structure at distances of about the sample sizes.

[1] E. A. Brener and V. I. Marchenko, PisÕma Zh. Eksp. Teor. Fiz **86**, 446 (2007) [JETP Lett. 86, 389 (2007)]

[2] E. A. Brener, V. I. Marchenko, Phys. Rev. **E59**, R4752 (1999)

[3] T. Ishikawa, O. L. Lavrentovich, Phys. Rev. **E60**, R5037 (1999)

[4] E. A. Brener and V. I. Marchenko, PisÕma Zh. Eksp. Teor. Fiz **90**, 153 (2009)

[5] L. D. Landau and E. M. Lifshitz, Course of Theoretical Physics, Vol. 7: Theory of Elasticity (Nauka, Moscow, 1982; Pergamon, New York, 1986).

[6] V. I. Marchenko, PisÕma Zh. Eksp. Teor. Fiz. **86**, 841 (2007)[JETP Lett. 86, 730 (2007)]

Dynamical properties of RNA polymerase motors

T. Tripathi[1], G. M. Schütz[2], D. Chowdhury[1]

[1] Physics Department, Indian Institute of Technology, Kanpur 208016, India
[2] IFF-2: Theoretical Soft Matter and Biophysics

Polymerization of RNA from a template DNA is carried out by a molecular machine called RNA polymerase (RNAP). It also uses the template as a track on which it moves as a motor utilizing chemical energy input. The time it spends at each successive monomer of DNA is random; we derive the exact distribution of these "dwell times" in our model. The inverse of the mean dwell time satisfies a Michaelis-Menten-like equation. Often many RNAP motors move simultaneously on the same track. Incorporating the steric interactions among the RNAPs in our model, we also plot the three-dimensional phase diagram for RNAP traffic using an extremal current hypothesis.

RNA polymerase (RNAP) is a molecular motor [1]. It moves on a stretch of DNA, utilizing chemical energy input, while polymerizing a messenger RNA (mRNA). The sequence of monomeric subunits of the mRNA is dictated by the corresponding sequence on the template DNA. This process of template-dictated polymerization of RNA is usually referred to as *transcription*. It comprises three stages, namely, initiation, elongation of the mRNA and termination.

We report analytical results on the characteristic properties of single RNAP motors. In our approach [3], each RNAP is represented by a hard rod while the DNA track is modelled as a one-dimensional lattice whose sites represent a nucleotide, the monomeric subunits of the DNA. The mechano-chemistry of individual RNAP motors is captured by assigning m distinct "chemical" states to each RNAP and postulating the nature of the transitions between these states. The dwell time of an RNAP at successive monomers of the DNA template is a random variable; its distribution characterizes the stochastic nature of the movement of RNAP motors. We derive the *exact* analytical expression for the dwell-time distribution of the RNAPs in this model.

We also report results on the collective movements of the RNAPs. Often many RNAPs move simultaneously on the same DNA track; because of superficial similarities with vehicular traffic, we refer to such collective movements of RNAPs as RNAP traffic.

For every RNAP, the dwell time is measured by an imaginary "stop watch" which is reset to zero whenever the RNAP reaches the chemical state 2, *for the first time*, after arriving at a new site (say, $i+1$-th from the i-th). Let P_μ be the probability of finding a RNAP in the chemical state μ at time t. The time evolution of the probabilities P_μ are given by

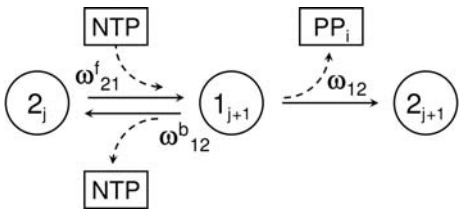

FIG. 1: The mechano-chemical cycle of a RNAP in our model. In the chemical state 1 the RNAP is bound to pyrophosphate (PP_i) whereas no PP_i is bound to it in the state 2. The integer subscript j labels the position of the RNAP motor on its track.

$$\frac{dP_1}{dt} = \omega^f_{21} P_2 - \omega_{12}\, P_1 - \omega^b_{12}\, P_1 \qquad (1)$$

$$\frac{dP_2}{dt} = \omega_{12}\, P_1 - \omega^f_{21}\, P_2 + \omega^b_{12}\, P_1 \qquad (2)$$

Following the trick commonly used in the calculation of the dwell time distributions, we insert a hypothetical intermediate state $2*$ between the states 1 and $2*$: the state $(i+1,1)$ makes an irreversible transition to the state $(i+1,2*)$ which is essentially an "excited" state of the RNAP. From the state $(i+1,2*)$ it relaxes to the state $(i+1,2)$ at a rate δ. At the end of the calculation we take the limit $\delta \to \infty$ so that the states $(i+1,2*)$ and $(i+1,2)$ become practically indistinguishable. Then, in addition to the equation for $P_1(t)$, we need the equation

$$\frac{dP_{2*}}{dt} = \omega_{12}\, P_1 \qquad (3)$$

for P_{2*}. The probability that an RNAP arrives at the state $2*$ between times t and $t+\delta t$ is $\omega_{12} P_1(t)\ \delta t$. Therefore, the dwell time distribution $f(t)$ is given by

$$f(t) = \omega_{12} P_1(t). \qquad (4)$$

Adapting standard techniques we get

$$f(t) = \frac{\omega^f_{21}\,\omega_{12}}{A} \mathrm{e}^{-Bt} \sinh(At) \qquad (5)$$

where

$$A = \sqrt{\frac{(\omega_{12} + \omega_{12}^b + \omega_{21}^f)^2}{4} - \omega_{12}\omega_{21}^f} \qquad (6)$$

$$B = \frac{\omega_{12} + \omega_{12}^b + \omega_{21}^f}{2} \qquad (7)$$

From equation (5) we get the inverse mean dwell time

$$\frac{1}{\langle t \rangle} = \frac{\tilde{V}_{max}}{1 + \frac{\tilde{K}_M}{[NTP]}} \qquad (8)$$

where $\tilde{V}_{max} = \omega_{12}$ and $\tilde{K}_M = (\omega_{12} + \omega_{12}^b)/\tilde{\omega}_{21}^f$. There is a close formal similarity between the mechano-chemical cycle of an RNAP in our model (see Fig.1) and the catalytic cycle of an enzyme in the Michaelis-Menten scenario. Indeed, the form of the expression (8) is identical to the Michaelis-Menten formula for the average rate of an enzymatic reaction. It describes the slowing down of the "bare" elongation progress of an RNAP due to the NTP reaction cycle that it has to undergo. The unit of velocity is $nucleotide/second$.

We also obtain the diffusion coefficient

$$D = \frac{\omega_{12}\omega_{21}^f}{\omega_{12} + \omega_{12}^b + \omega_{21}^f} \times \left[\frac{\left(\omega_{12} + \omega_{12}^b + \omega_{21}^f\right)^2 - 2\omega_{12}\omega_{21}^f}{2\left(\omega_{12} + \omega_{12}^b + \omega_{21}^f\right)^2} \right] \qquad (9)$$

which is in agreement with the general expression for the effective diffusion constant of a molecular motor with unbranched mechano-chemical cycle which was first reported by Fisher and Kolomeisky [2].

Now we take into account the hard core steric interaction among the RNAPs which are simultaneously moving on the same DNA track. Our model of RNAP traffic can be regarded as an extension of the totally asymmetric simple exclusion process (TASEP) [4] for hard rods where each rod can exist at a location in one of its m possible chemical states. The movement of an RNAP on its DNA track is coupled to the elongation of the mRNA chain that it synthesizes. Naturally, the rate of its forward movement depends on the availability of the monomeric subunits of the mRNA and the associated "chemical" transitions on the dominant pathway in its mechano-chemical cycle. This cycle leads to a hopping process with a dwell time distribution that is not a simple exponential. The initiation and termination of transcription can be captured by imposing open boundary conditions (OBC). Due to the steric interactions between RNAP's their stationary flux (and hence the transcription rate) is not limited solely by the initiation and release at the terminal sites of the template DNA.

We calculate the resulting phase diagram under OBC by utilizing the extremal current hypothesis (ECH) [4] in a 3-dimensional space where the additional dimension corresponds to the concentration of the monomeric subunits of the mRNA. In the special case where the dominant pathway is that shown in Fig. 1 (ω_{12}^b = 0 for further calculation as $\omega_{12} \gg \omega_{12}^b$), we have for the stationary flux of RNAP traffic within mean field approximation

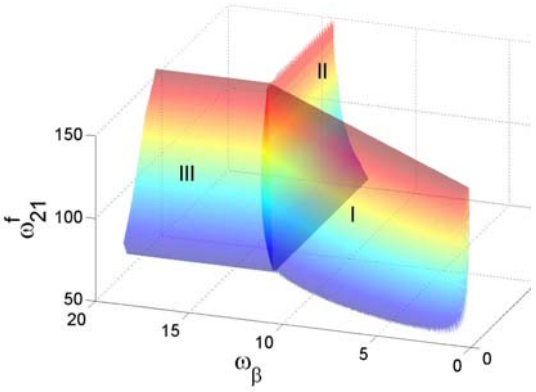

FIG. 2: The 3-d phase diagram of our model for RNAP traffic. The LD and HD phases coexist on the surface I. The surfaces II and III separate the MC phase from the HD and LD phases, respectively.

$$J(\rho) = \frac{\omega_{12}\,\omega_{21}^f\,\rho\,(1-\rho\,\ell)}{\omega_{12}\,(1-\rho\,(\ell-1))\;+\;\omega_{21}^f\,(1-\rho\,\ell)} \qquad (10)$$

From (10) one expects three phases, viz. a maximal-current(MC) phase with with bulk density ρ^*, a low-density phase (LD) with bulk density ρ_-, and a high-density phase (HD) with bulk density ρ_+. We get [3]

$$\rho_- = \frac{\omega_\alpha\,\left(\omega_{12} + \omega_{21}^f\right)}{\omega_{12}\,\omega_{21}^f\;+\;\omega_\alpha\left(\omega_{12} + \omega_{21}^f\right)(\ell - 1)} \qquad (11)$$

and

$$\rho_+ = \frac{\omega_{12}\,\omega_{21}^f\;-\;\omega_\beta\,\left(\omega_{12} + \omega_{21}^f\right)}{\omega_{12}\,\omega_{21}^f\,\ell\;-\;\omega_\beta\,\left(\omega_{12} + \omega_{21}^f\right)(\ell\;-\;1)}. \qquad (12)$$

The presence of a coexistence line between LD and HD suggests the occurrence of RNAP "traffic jams" when stationary initiation and release of RNAP at the terminal sites of the DNA track are able to balance each other. This traffic jam would perform an unbiased random motion, as argued earlier on general theoretical grounds in the context of protein synthesis by ribosomes from mRNA templates [4]. We also observe that the collective average rate of translation as given by the stationary RNAP current (10) is reduced by the need of the RNAP to go through the pyrophosphate bound state. This is a prediction that is open to experimental test.

[1] M. Schliwa, (ed.) *Molecular Motors*, (Wiley-VCH, 2003).

[2] M. E. Fisher and A. B. Kolomeisky, PNAS **96**, 6597 (1999).

[3] T. Tripathi, G. M. Schütz and D. Chowdhury. J. Stat. Mech. P08018 (2009).

[4] G. M. Schütz, in: *Phase Transitions and Critical Phenomena*, vol. 19 (Acad. Press, 2001).

Lipid membranes with transmembrane proteins in shear flow

A. Khoshnood[1,2], H. Noguchi[3,2], G. Gompper[2,4]

[1] Sharif University of Technology, Tehran, Iran
[2] IFF-2: Theoretical Soft Matter and Biophysics
[3] University of Tokyo, Chiba, Japan
[4] IAS: Institute for Advanced Simulation

The effects of embedded proteins on the dynamical properties of lipid bilayer membranes are studied in shear flow. In thermal equilibrium, rigid protein-like molecules aggregate in a membrane of flexible lipids, while flexible proteins do not aggregate. In shear flow parallel to the membrane, the monolayers of lipid bilayer slide over each other. The presence of transmembrane proteins enhances the intermonolayer friction. The friction coefficient is found to increase with protein length (with positive mismatch, i.e. proteins which are longer than the membrane thickness) and protein cluster size. In flow, proteins get oriented in the flow direction to reduce friction.

Biomembranes are the main building blocks of biological cells. Besides playing the role of an envelope for the cell itself, it is a major ingredient in many organelles inside the cell. These membranes are in the fluid phase, and dynamically change their shapes to achieve their functions, in particular in the endoplasmic reticulum (ER) and the Golgi complex, where lipids and proteins are transported via vesicle budding and fusion. In the Golgi complex, a new stack of cisternae (closed disk-shaped membranes) is formed at the cis face and an old trans stack is divided into vesicles at the opposite face for vesicular transport. The tubular network of the ER frequently reforms their network junctions. These changes of membrane shape and topology often require the monolayers of a membrane to slide across each other.

In fact, there are various other conditions that induce slippage of monolayers of biological membranes across each other. Relative motion of membrane layers occurs when the membrane is under shear, *e.g.* when red blood cells (RBCs) and fluid vesicles perform a tank-treading membrane rotation under flow [1]. A sliding between leaflets can also be induced by local-curvature change, for example when an RBC is creeping through a microvessel with a smaller diameter than of the cell itself, and the RBC is squeezed into a parachute shape [2]. Another example is the formation of membrane tubes of the ER by molecular motors, which can grab the membrane and pull it as they walks along the filaments of the cytoskeleton. Finally, we want to mention that many kinds of cells exhibit crawling, where the plasma membrane is under shear force.

Biomembranes contain a large number of proteins attached to or embedded in the lipid bilayer. Here, transmembrane proteins interact with each other mediated by the membrane. When the length of the hydrophobic region of a protein has a mismatch with that of the lipid bilayer, the bilayer is locally deformed to match the lengths. This induces an attraction between the proteins in order to reduce the contact between proteins and lipids. Proteins with asymmetric shapes interact by modifying the local membrane curvature. Proteins with a barrel- or hourglass-like shape tilt the surrounding lipids, and this tilt induces

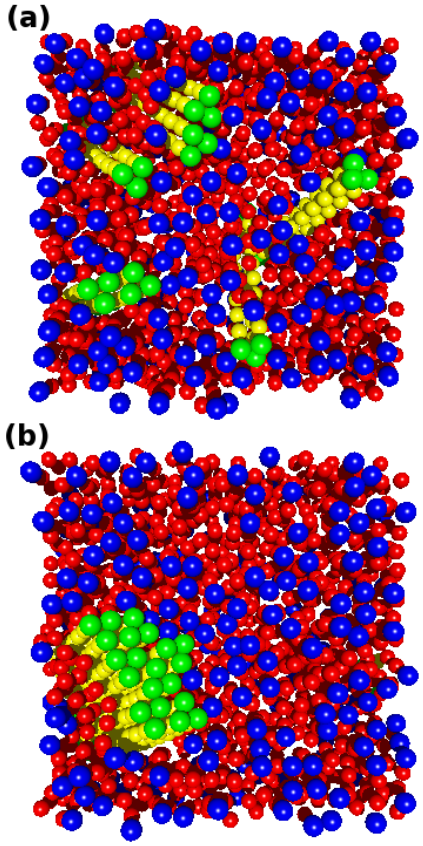

FIG. 1: Snapshots of a bilayer contains 246 *lipids of type* ht_4 *and seven* h_6t_{24} *rigid proteins in thermal equilibrium, (a) after* 150τ *and (b) after* 1750τ*. The dark blue and red spheres are lipid heads and tails, respectively. The hydrophobic and hydrophilic particles of the proteins are shown by yellow and green spheres, respectively.*

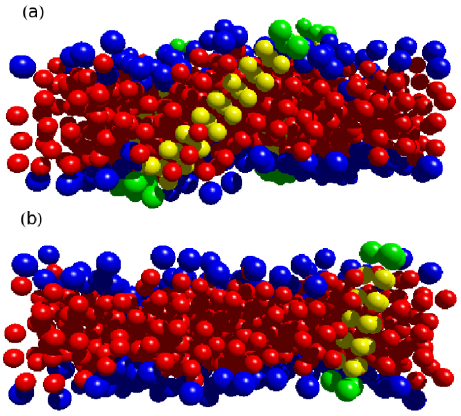

FIG. 2: Snapshots of a lipid bilayer with embedded rigid proteins, in thermal equilibrium. Side view (a) with 270 lipid molecules ht_4 and seven proteins h_6t_{24} (after 135τ) and (b) with 280 lipid molecules ht_4 and one protein h_6t_{15} (after 825τ). The dark blue and red spheres are lipid heads and tails, respectively. The hydrophobic particles of the proteins are yellow, the hydrophilic parts green.

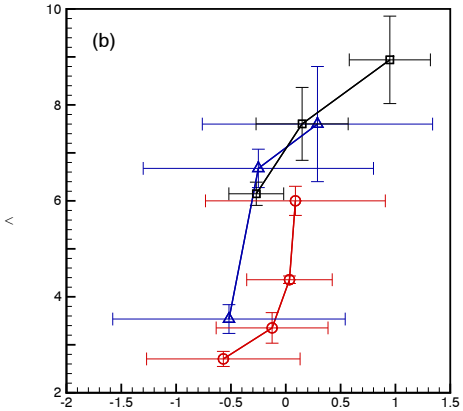

FIG. 3: Friction coefficient of a membrane, $\hat{\xi}$, as a function of surface tension ζ. Results are shown for three different systems, a membrane with no protein (○), a membrane with flexible proteins of type h_4t_{16} (△), and a membrane with rigid proteins of type h_6t_{24} (□). All lipids are of the type ht_4. The protein concentration is about $5-10\%$. The simulations are carried out for three different shear rates $\dot{\gamma} = 0.1$, 0.05 and $0.03\tau^{-1}$.

interaction between proteins. In living cells, such membrane-mediated interactions can induce protein-enriched domains "rafts".

Particle-based computer simulations are a very powerful tool to study the structure and dynamics of membranes at the molecular level. Atomistic-level simulations are available only for short time dynamics and small length scales with typical current computational resources. To overcome this problem, coarse-grained descriptions have been developed, in which clusters of atoms are grouped together to form a single super-site, compare Fig. 1. This significantly reduces the number of degrees of freedom, but also the number of interactions to be determined.

We simulate lipid membrane with embedded proteins based on the lipid model of Ref. [3]. Lipid, protein and solvent molecules are made up of two types of particles: hydrophilic and hydrophobic. Head groups of lipid and protein molecules, and also water or solvent molecules, are hydrophilic; tail groups of lipid and protein molecules are hydrophobic. Different arrangements of hydrophilic and hydrophobic particles enable us to model all molecules of interest [4]. h and t denote head (hydrophilic) and tail (hydrophobic) particles, respectively. For example, ht_4 denotes a lipid made up of one hydrophilic and four hydrophobic particles. Other types of molecules are built by changing the number of hydrophobic particles in the chains of lipid or protein. Particles of the same type (either hydrophobic or hydrophilic) interact via an attractive Lennard-Jones potential, while hydrophilic and hydrophobic particle interact via a repulsive soft-core potential. We use $\tau = \sqrt{m\sigma^2/\epsilon}$ as the natural time scale in MD simulations with Lennard-Jones potentials, where m is the mass of each particle, σ the particle diameter, and ϵ the potential strength.

Figures 1 shows two snapshots of the system with rigid proteins. The snapshot of Fig. 1(a) is taken at the beginning steps of simulation; it shows that three proteins are still separate, while the others have formed pairs. After more than 1500τ, all proteins aggregate (see Fig. 1(b)) and make a rigid cluster which remains stable over the subsequent simulation time. Rigid proteins h_6t_{24} have a strong positive mismatch, while proteins h_6t_{15} have a very weak mismatch in a bilayer of the type ht_4, see Fig. 2. Our simulations show that initially separated h_6t_{15} proteins also make stable cluster in membrane consisting of ht_4 lipids [4]. Thus, protein rigidity is required for membrane-induced attractive interaction between proteins when there is no hydrophobic mismatch.

The friction coefficient ξ for the sliding of the two monolayers across each other increases with increasing lateral tension ζ, see Fig. 3. Thus, the slippage of the two leaflets of a compressed membrane over each other is easier than of a stretched membrane [4]. With increasing lipid density, the membrane thickness increases and forces lipid molecules to be more extended. Therefore, lipids in one layer interact less strongly with molecules in the other layer, which results in the reduction of ξ. The friction coefficient ξ increases sharply with increasing tension near $\zeta = 0$. Stiff and flexible proteins have nearly the same effect on ξ for fixed tension. The main contribution of membrane proteins on ξ occurs near zero lateral tension. Proteins shift the location of the sharp increase of ξ to negative surface tension.

[1] H. Noguchi and G. Gompper, Phys. Rev. Lett. **93**, 258102 [1-4] (2004).

[2] J. L. McWhirter, H. Noguchi, and G. Gompper, Proc. Natl. Acad. Sci. USA **106**, 6039–6043 (2009).

[3] R. Goetz, G. Gompper, and R. Lipowsky, Phys. Rev. Lett. **82**, 221–224 (1999).

[4] A. Khoshnood, H. Noguchi, and G. Gompper, J. Chem. Phys. **132**, 025101 [1-10] (2010).

Self-propelled rods near surfaces

J. Elgeti[1], G. Gompper[1,2]

[1] IFF-2: Theoretical Soft Matter and Biophysics
[2] IAS: Institute for Advanced Simulation

The behavior of self-propelled nano- and micro-rods confined between parallel walls is studied by mesoscale simulations and scaling arguments. Self-propelled rods are found to display a strong surface excess in confined geometries. An analogy with semi-flexible polymers is employed to derive scaling laws for the dependence on the wall distance, the rod length, and the propulsive force. The simulation data are in good agreement with the scaling predictions.

Both in soft matter and in biology, there are numerous examples of swimmers and self-propelled particles. With a typical size in the range of a few nano- to several micro-meters, both low-Reynolds-number hydrodynamics [1] and thermal fluctuations are essential to determine their dynamics. Well-known biological examples are sperm cells which are propelled by a snake-like motion of their tail [2], and bacteria like *E. coli* which move forward by a rotational motion of their spiral-shaped flagella. In soft matter systems, synthetic self-propelled particles have been designed to perform directed motion. Examples are bimetallic nanorods which are driven by different chemical reactions at the two types of surfaces.

Both in soft matter and in biological systems, surfaces and walls are ubiquitous. For example, bacteria in wet soil, near surfaces or in microfluidic devices, or sperm in the female reproductive tract find themselves in strongly confined geometries. Already in 1963, Lord Rothschild found that sperm accumulate at surfaces. Thus surfaces strongly affect the dynamics of swimmers and self-propelled particles.

We study here the dynamics of self-propelled rod-like particles confined between two planar walls at distance d, see Fig. 1. Such particles capture the elongated geometry of most of the swimmers mentioned above. In the vicinity of a wall, the rod-like geometry of the particles is important, since it favors parallel orientation — both with and without hydrodynamic interactions. We consider rods which are small enough for thermal fluctuations to play an important role. Thermal fluctuations induce a persistent-random-walk behavior of the trajectories in the bulk, and an entropic repulsion near the wall.

We model the rod of length l as a crane-like structure [3, 4]. Three filaments, each consisting of N_m monomers, are arranged in a triangular cross section. The distances between the filaments and between monomers within a filament are the same bond length l_b, so that $l = (N_m - 1)l_b$. The effect of the fluid on a self-propelled particle is described by a Stokes friction and thermal fluctuations. Propulsion is achieved by applying a forward thrust

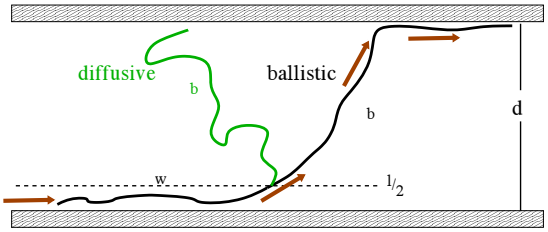

FIG. 1: Schematic representation of the different regimes of rod motion, near a wall for time τ_w, and in the bulk for time τ_b, either in the ballistic or in the diffusive regime.

$$\mathbf{F}_i = f_t \hat{\mathbf{r}}_{i,i-1} \quad \text{for } i > 1, \tag{1}$$

on each monomer i of the rod, where $\hat{\mathbf{r}}_{i,i-1}$ is the unit vector connecting monomers i and $i-1$, and f_t is the force strength per monomer. In a Brownian dynamics simulation, the velocity v of the rod is $v \simeq f_t/\gamma_0$, with friction coefficent γ_0. This leads to the Peclet number

$$Pe = \frac{lv}{D} = \frac{6l^2 f_t}{k_B T}, \tag{2}$$

with diffusion constant $D = k_B T/(6\gamma_0 l)$. For $Pe \gg 1$, propulsion dominates and the rod should have a persistent directed motion, while for $Pe \ll 1$ thermal noise dominates and leads to a diffusive behavior.

The main result of our simulations is that self-propelled rods accumulate at a wall, both with and without hydrodynamic interactions, in contrast to passive rods which are depleted near a wall due to entropic reasons [3]. The rod accumulation at a wall is illustrated in Fig. 2, which shows the probability density $P(z)$ to find the center of mass of a rod at distance z from the wall for various propulsive forces f_t. Passive rods show a depletion layer of thickness $l/2$; however, with increasing propulsion force f_t, a pronounced peak develops near the wall.

To quantify the surface localization, we define the surface excess

$$s = \int_0^{d/2} \big[P(z) - P_b\big] \mathrm{d}z \tag{3}$$

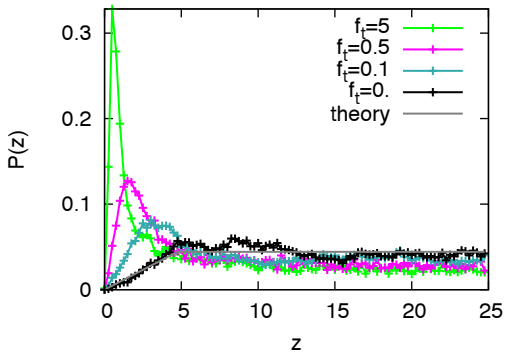

FIG. 2: Probability density $P(z)$ as function of the distance z from the surface, for various propelling forces f_t. The corresponding surfaces excesses are $s = -0.11$, $s = 0.07$, $s = 0.21$, and $s = 0.33$ for increasing f_t. The rod length is $l = 9.5a$, the walls are located at $z = 0$ and $z = 50a$. Here and below, we use the length scale $a = 2l_b$. A solid gray line shows the density profile of passive rods.

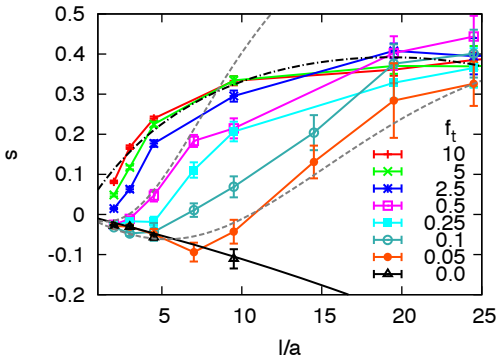

FIG. 3: Surface excess s as a function of scaled rod length l/a, for various propelling forces f_t, as indicated. The (black) dashed-dotted line is the scaling result in the ballistic regime, the (gray) dashed lines are scaling results in the diffusive regime for $f_t = 0.5$ and $f_t = 0.05$. The length scale is $a = 2l_b$, the wall distance is $d = 50a$.

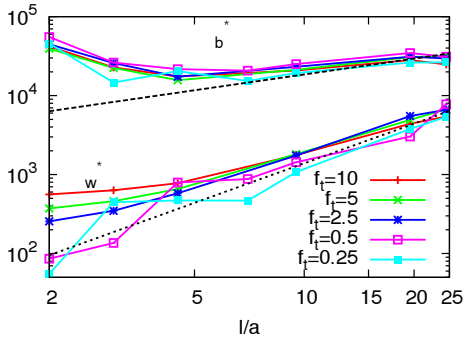

FIG. 4: Rescaled wall time $\tau_w^* = \tau_w f_t^{2/3}$ and bulk time $\tau_b^* = \tau_b f_t^{2/3}/10$ for different propulsive forces f_t, as indicated. Dashed lines are scaling predictions $\tau_w \sim l^{5/3}$ and $\tau_b \sim l^{2/3}$. The wall separation is $d = 50a$.

where P_b is the bulk probability density. A homogeneous distribution corresponds to $s = 0$, while full absorption at the wall corresponds to $s = 1$. For a passive rod, $P(z)$ increases linearly for $0 < z < l/2$, and $s = -1/(2d/l - 1)$. The surface excess is shown in Fig. 3 as a function of the rod length l for various propulsive forces f_t. Passive rods with $f_t = 0$ show the expected negative surface excess due to entropic repulsion, in good agreement with the analytical equilibrium result. Long propelled rods show a strong surface excess, which decreases for smaller rod lengths ($l/a < 10$). Short and weakly-propelled rods behave like passive rods (with negative s), but with increasing length, they show a crossover to a positive surface excess, with a minimum of the surface excess at intermediate rod lengths. This minimum occurs at a Peclet number $Pe \simeq 10$.

In order to understand the mechanism which is responsible for the effective surface adhesion of self-propelled rods, and to predict their behavior as a function of rod length, propulsive force, and wall separation, we exploit the analogy of the trajectories of self-propelled rods with the conformations of semi-flexible polymers [3]. In the bulk, the rotational diffusion constant of a rod is $D_r \sim k_B T/(\eta l^3)$, with viscosity η, which implies a persistence length

$$\xi_p \sim v/D_r \sim \eta v l^3/k_B T \qquad (4)$$

of the trajectory. The probability to find the self-propelled rod in a layer of thickness $l/2$ near the wall can be expressed as $p = \tau_w/(\tau_w + \tau_b)$, where τ_w is the time the rod remains within this layer and τ_b is the time it is located in the bulk (with $l/2 < z < d - l/2$). The surface excess s is easily obtained from p [3].

To estimate τ_w, we consider a rod, which at time $t = 0$ is oriented parallel to the wall, and located very close to the wall with $0 < z \ll l/2$. As the rod moves forward, it is reflected when is hits the wall, and is thereby constrained to the positive half-space $z > 0$, see Fig. 1. This situation is very similar to a semi-flexible polymer, which is fixed at one end near the wall with tangent vector parallel to the wall; its bending rigidity κ is determined by the persistence length, $\xi_p = \kappa/k_B T$. In this case, the distance of the polymers from the wall increases as $\langle z \rangle \sim (k_B T/\kappa)^{1/2} x^{3/2}$ and the orientation angle as $\langle \theta \rangle \sim (k_B T/\kappa)^{1/2} x^{1/2}$, where $x = vt$ is the distance traveled parallel to the wall. The condition $\langle z \rangle = l/2$ at $t = \tau_w$ then implies [3]

$$\tau_w \sim \frac{1}{v}\left(l^2 \xi_p\right)^{1/3} \sim \left(\frac{\eta}{k_B T}\right)^{1/3} l^{5/3} v^{-2/3}. \qquad (5)$$

The scaling result (5) is compared in Fig. 4 with the simulation data. The agreement is very good.

[1] E. M. Purcell, Am. J. Phys. **45**, 3 (1977).

[2] Y. Yang, J. Elgeti and G. Gompper, Phys. Rev. E **78**, 061903 [1-9] (2008).

[3] J. Elgeti and G. Gompper, EPL **85**, 38002 [1-6] (2009).

[4] J. Elgeti and G. Gompper, Proceedings of NIC Symposium 2008, edited by G. Münster, D. Wolf, and M. Kremer, NIC series Vol. 39, p. 53–61 (Neumann Institute for Computing, Jülich, 2008).

Vesiculation and budding induced by conical membrane inclusions

T. Auth[1], G. Gompper[1,2]

[1] IFF-2: Theoretical Soft Matter and Biophysics
[2] IAS: Institute for Advanced Simulation

Conical inclusions in a lipid bilayer generate an overall spontaneous curvature of the membrane, which depends on concentration and geometry of the inclusions. Examples are integral and attached membrane proteins, viruses, and lipid domains. We propose an analytical model to study budding and vesiculation of the lipid bilayer membrane, which is based on the membrane bending energy and the translational entropy of the inclusions. If the inclusions are placed on a membrane with similar curvature radius, their repulsive membrane-mediated interaction is screened. Therefore, for high inclusion density the inclusions aggregate, induce bud formation and finally vesiculation.

Cell membranes contain large amounts of proteins within or attached to the lipid bilayer. The distribution of the proteins is not necessarily homogeneous, which can have important functional consequences. For example, proteins with an intrinsic curvature couple to the bilayer conformation; on the one hand, such proteins are preferably found on similarly curved parts of the membrane, on the other hand, the proteins deform the membrane locally. The conical inclusions in our model can mimick asymmetric proteins within the bilayer, proteins or polymers attached to the membrane [1], curved domains [2], or viruses that bind to the membrane.

The deformation-induced, pairwise interaction of curved inclusions is usually repulsive. For a planar membrane, the interaction energy decays like d^{-2} for large distances, d, between the inclusions. However, the repulsive interaction can be strongly screened if the average curvature of the membrane and the protein curvature are similar. One obvious example for such strongly screened interactions are inclusions that are placed on a vesicle with similar curvature radius. Screening can also be achieved by many-body interaction in clusters of inclusions, e. g. in an early stage of bud formation.

We study budding induced by curved inclusions on a vesicle using a model that represents the lipid bilayer as a mathematical surface with a finite bending rigidity, κ. We estimate the bending energy using cylindrically symmetric membrane patches around each inclusion, see Fig. 1.

The boundary conditions are set by the inclusion geometry and the surface density of inclusions, σ, as well as the vesicle radius, R. The bending energy for one cylindrical membrane patch is

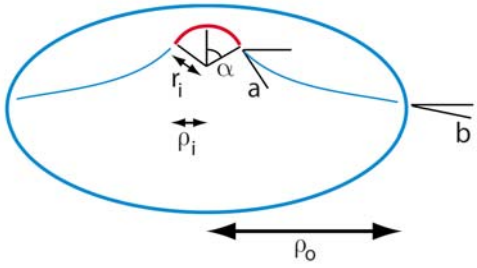

FIG. 1: Curved inclusion (red) and resulting bilayer deformation (blue). The inclusion geometry is characterized by the curvature radius, r_i, the opening angle, α, and the projected inclusion radius, $\rho_i = r_i \sin(\alpha)$. The size of the corresponding membrane patch is ρ_o, the slope of the membrane at the inclusion is $a = -\tan(\alpha)$, and the slope of the membrane at the outer boundary is b ($b = 0$ for inclusions on a planar membrane).

$$\mathcal{E} = \frac{2\pi\kappa(b\rho_o - a\rho_i)^2}{(\rho_o^2 - \rho_i^2)}\,, \qquad (1)$$

where $\rho_o = d/2 \approx 1/(\pi\sigma)^{1/2}$ is the outer radius of the patch, $b = -\tan(\beta)$ is the slope of the membrane at the outer boundary (with $\beta = \arccos((n-2)/n)$ and n inclusions per vesicle), and a and ρ_i are given by the inclusion geometry. For a single inclusion in an infinite planar membrane, $b = 0$ and $\rho_o \to \infty$, the bending energy vanishes and the membrane deformation is catenoid-like, $h(\rho) = a\rho_i \ln(\rho/\rho_i)$.

The membrane shape and the minimal bending energy around each inclusion (assuming that the inclusions have maximal mutual distances) can be calculated using our model [3]. We find that for $b\rho_o = a\rho_i$ the membrane around the inclusion has almost catenoid shape; the catenoid is a minimal surface with vanishing bending energy. If the entire vesicle is covered with inclusions and catenoids such that the bending energy is zero (Fig. 2 (b)), the inclusions have optimal density.

For lower inclusion densities, in a first approximation the catenoid shape borders on a spherical shape with the curvature radius of the vesicle. The bending energy of a vesicle that is decorated with curved inclusions is reduced by the fraction of the sphere's surface area that is covered by the inclusions and the

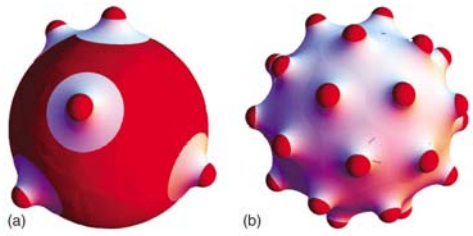

FIG. 2: (a) Vesicle decorated with curved inclusions. Around each inclusion, the membrane can be modeled by patches of the catenoid minimal surface with vanishing bending energy (white). (b) Vesicle decorated with inclusions at optimal density; the bending energy of the lipid bilayer membrane vanishes.

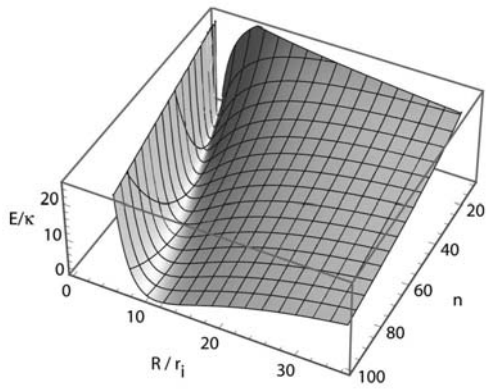

FIG. 3: Normalized bending energy, E/κ, of a vesicle with radius R and n inclusions ($r_i \approx 5.5nm$, $\alpha \approx 0.64$). There is a region of low inclusion density at large R with $0 < E < 8\pi\kappa$, which is delineated by a line of zero-energy ground states from a region of high inclusion density at small R, where also bending energies $E > 8\pi\kappa$ can be found. (The high energies that are cut off at small n and large R mark the breakdown of the small-curvature expansion of the bending energy.)

catenoid-shaped membrane segments (Fig. 2 (a)). A vesicle that consists only of lipid bilayer has the bending energy $8\pi\kappa$, therefore for low inclusion density the bending energy of the decorated spherical vesicle is in the range $0 < E < 8\pi\kappa$.

For inclusion densities that are higher than the optimal density, due to the boundary conditions no solution can be constructed by matching of catenoids to spherical patches. In this case, the bending energy always has a finite value that can exceed the bending energy of a bare vesicle. The minimal bending energy of a vesicle with inclusions is shown in Fig. 3 as function of the number of inclusions, n, and the vesicle radius, R. We find degenerate zero-energy ground states that have optimal inclusion density with an approximately linear dependence $R(n)$.

The same value for the inclusion density can be high, optimal, or low, depending on the radius of the vesicle on which the inclusions are placed. The smaller the radius of the vesicle, the larger the value of the optimal density. In a planar membrane, the slopes of two adjacent catenoid-like deformations cannot be matched for any finite distance between the inclusions and therefore the inclusions are always in the high-density regime.

Bud formation does not occur for a vesicle with low inclusion density and bending energies $0 < \mathcal{E} < 8\pi\kappa$, because this would lead to an increase of the total bending energy. For high inclusion densities, $n > 4R/(|a|\rho_i)$, the system can always reach a state of lower bending energy if small vesicles bud from the main vesicle. However, the number and the sizes of the smaller vesicles into which a large vesicle splits up is not uniquely determined from bending energy alone, because the states of vanishing bending energy are degenerate.

Note that the results of our analytical model so far do not depend on the value of the bending rigidity κ of the bilayer, which is a constant factor for the bending energy. The value of κ becomes important if thermal fluctuations are included into the model. Because of the degeneracy of the states with vanishing bending energy, thermal fluctuations and the budding pathway play a decisive role to determine how a large vesicle with high inclusion density splits up into smaller vesicles [3].

We take thermal fluctuations into account via the positional entropy of the inclusions that can be found in a fluid and in a crystalline phase. In the crystalline phase, we construct the free energy per inclusion from the membrane bending energy and the fluctuation free energy of a harmonic crystal. In the fluid phase, we obtain the free energy from the sum of the membrane bending energy and the translational entropy of the inclusions that are modeled as effective hard discs. Usually the translational entropy favors a homogeneous distribution of particles. However, because in our case the effective hard-disc radius depends on the membrane curvature, a homogeneous distribution of inclusion does not need to be the preferred state and a higher density on the bud can be favourable.

Not only free energy minimization, but also dynamics plays an important role for bud formation. The relaxation time for membrane fluctuations with a given wavelength is much shorter than the time for the diffusion of the inclusions within the membrane over a comparable distance. Already small fluctuations of the inclusion density can lead to the onset of bud formation. Once a neck with an opposite sign of the curvature has formed, it acts as a barrier for the diffusion of inclusions and prevents further inclusions to enter the bud.

[1] T. Auth and G. Gompper, Phys. Rev. E **72**, 031904 (2005).

[2] S. Schneider and G. Gompper, Europhys. Lett. **70**, 136 (2007).

[3] T. Auth and G. Gompper, Phys. Rev. E **80**, 031901 (2009).

Mesoscale hydrodynamic simulations of colloid sedimentation

A. Wysocki[1,2], R. G. Winkler[2,3], H. Löwen[1], G. Gompper[2,3]

[1] Institut für Theoretische Physik II, Heinrich-Heine-Universität Düsseldorf, 40225 Düsseldorf
[2] IFF-2: Theoretical Soft Matter and Biophysics
[3] IAS: Institute for Advanced Simulation

The sedimentation of an initially inhomogeneous distribution of hard-sphere colloids confined in a slit is simulated using the multiparticle collision dynamics scheme which takes into account hydrodynamic interactions mediated by the solvent. The system is an example for soft matter driven out of equilibrium where various length and time scales are involved. The initial laterally homogeneous density profiles exhibit a hydrodynamic Rayleigh-Taylor-like instability. Solvent backflow effects lead to an intricate non-linear behavior which is analyzed via the solvent flow field. The growth rate of the Rayleigh-Taylor instability is in agrement with the prediction of a linear stability theory. Excellent agreement is found between theory, simulations, and experimental results.

Sedimentation under gravity of dispersed particles is a common phenomena in colloidal systems and is exploited in isolation of cells from blood, separation of macromolecules, and industrial filtration. The understanding of the time evolution of a given initial state towards sedimentation-diffusion equilibrium is a challenging problem due to the presence of disparate time and length scales and requires careful multiscale modelling. The dynamics of a molecular solvent takes place on the picosecond level, while the time a colloid needs to diffuse over its own radius is in the second time scale for micron-sized colloids. Hydrodynamic interactions between the colloidal particles are mediated by the solvent flow on an intermediate time scale and are of long-range and many-body nature. Hydrodynamic interactions can only be neglected at very low colloidal volume fractions. The recently developed multiparticle collision (MPC) dynamics approach is well suited to gain insight into the non-equilibrium behavior of a colloidal system taking hydrodynamic interactions into account [1].

The motion of a colloid is characterized by the Peclet number $Pe = \tau_D/\tau_S$, which is the ratio between the time τ_D it takes a particle to diffuse its own radius and the time τ_S it takes to sediment the same distance. A Peclet number of order unity is the dividing line between colloidal ($Pe \leq 1$) and granular systems ($Pe \gg 1$), i.e., Pe measures the importance of Brownian motion. Most attempts at a quantitative description of sedimentation to date considered a homogenously distributed dispersion as the initial state. For preparative purposes, on the other hand, starting with a particle-rich layer on top of a pure solvent is more relevant as it enables the separation of particles depending on their sedimentation coefficient. However, this configuration is unstable with respect to gravity. The particle velocities become correlated, which leads to emergent density fluctuations and consequently more rapid sedimentation than Stokes' flow alone. It is well known that many practical relevant particle concentrations develop this Rayleigh-Taylor (RT) like instability. The 'original' Rayleigh-Taylor instability, which occurs if a heavy, immiscible fluid layer is placed on top of a lighter one has been intensively studied. Here we consider a suspension of colloidal hard spheres (without surface tension), in which we have access to all relevant length scales, from the single-particle level to the full system [2, 3].

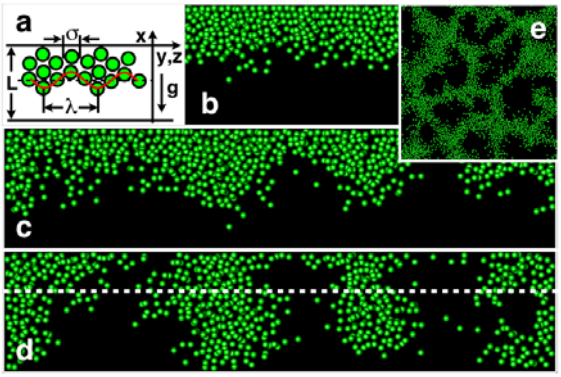

FIG. 1: (a) Schematic illustrating the spatial parameters σ, λ and L. (b-e) Simulation snapshots of a system which contains $N = 33858$ colloidal particles and $Ns = 32118397$ solvent particles (not displayed) in a simulation box with dimensions $L/\sigma = 18$ and $L_y/\sigma = L_z/\sigma = 81$. The value of the Peclet number is $Pe = 1.6$. (b-d) Time series of the system at time $t/\tau_s = 3.2$ (b), 6.4 (c), 9.6 (d). The snapshots are slices of thickness 2σ done in the xy plane. (e) Slice of thickness 2σ in the yz plane at time $t/\tau = 9.6$. The height of the yz plane is $x/L = 2/3$, as indicated by the dashed line in (d).

An initial state with a heavy fluid on top of a lighter one is mechanically unstable. Under the influence of the gravitational force, the initially flat interface starts to develop perturbations with a characteristic wavelength $\lambda = 2\pi/k$, where k is the wave number. Figure 1 shows snapshots of the time evolution of the system [2, 3]. The appearance of an instability with a

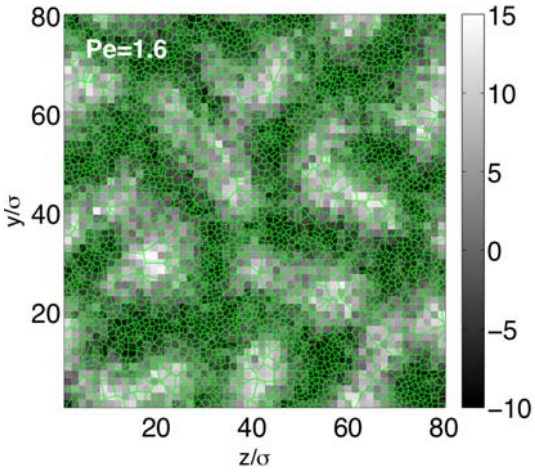

FIG. 2: Solvent velocity field in the yz plane at the height $x/L = 1/2$ and time $t/\tau_S = 11.2$ for $Pe = 1.6$ and $L/\sigma = 18$. The gray scale represents the magnitude of the solvent velocity $v_x(y,z)/V_s$ in gravity direction, where V_s is the sedimentation velocity at infinite dilution. The Voronoi diagram of the colloid positions in this plane is indicated by green lines.

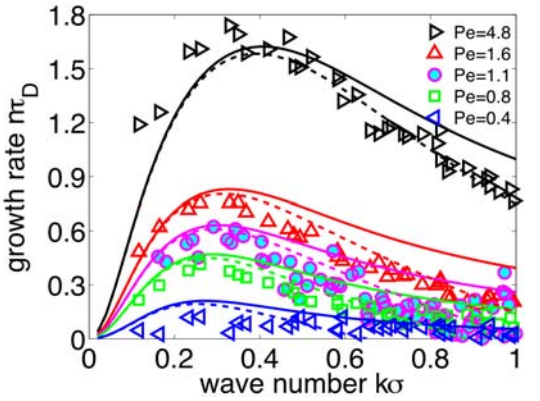

FIG. 3: Simulation (open symbols) and experimental (closed symbols) result of the growth rate $n\tau_D$ for various Peclet numbers and $L/\sigma = 18$. The solid lines are the results of the linear stability analysis; the dashed lines are obtained by taking diffusion corrections into account.

characteristic wavelength $\lambda_{\max}$ is evident. While snapshots along the direction of gravity (Fig. 1b, c, d) illustrate the overall process of sedimentation, snapshots in the horizontal yz plane show the formation of a transient pattern or network-like structure that results from the instability (Fig. 1e). At later times, the network structure decays and a laterally homogenous density profile develops, where the colloids start to form a layer at the bottom of the cell which becomes more compact with time.

The network-like structure of Fig. 1e is associated with a hydrodynamic backflow: colloid-rich regions move downwards and solvent-rich regions move upwards. In Fig. 2 a, the solvent velocity field in the yz plane perpendicular to the driving force is shown at the intermediate height $x = L/2$. Inhomogeneities are revealed on the same length scale $\lambda_{\max}$ as in the colloidal density profile. This is clearly evident by the Voronoi tessellation of the colloid concentration. Again, the structures exhibit the characteristic length scale $\lambda_{\max} = 2\pi/k_{\max}$, the fastest growing wavelength in the linear regime [2, 3].

A linear stability analysis predicts a fastest growing wavelength in the RT instability [2]. The dimensionless growth rate $n\tau_D$ is displayed in Fig. 3 for various Peclet numbers. Without diffusion, fluctuations grow at all wave numbers as indicated by the solid lines. Diffusion leads to a suppression of the growth rate at larger wave vectors, i.e., diffusion destroys the RT instability at sufficiently small wavelengths. We find excellent agreement between the theory with diffusion and both simulations and experimental data up to $k\sigma \approx 1$.

With decreasing wall separation L, the growth rate $n_{\max}$ decreases and $k_{\max}$ increases. Since the fluid velocity in the gravity direction decreases as e^{-kx}, where x is the distance from the interface, only long wavelength undulations feel the presence of the walls. Figure 3 shows that for a fixed L an increase in the Peclet number leads to an increase in the wavenumber of the fastest growing undulation $k_{\max}$ and the corresponding growth rate $n_{\max}$. So far we have considered only the linear regime of the instability, which is valid at small times, when the amplitude of the fluctuations is smaller than the wavelength. Our simulations permit detailed access to all relevant time- and length-scales in the non-linear regime, where the colloids form foam-like structures in the (confined) xz plane (Fig. 1c) and a network-like structure in the yz plane (Fig. 1e) appears. Apparently, both continue to exhibit the characteristic length scale $\lambda_{\max} = 2\pi/k_{\max}$ of the fastest growing wavelength of the linear regime.

By calculating the first moment $\langle x \rangle$ of the center-of-mass density distribution, three distinct regimes can be identified in sedimentation [2]. At short times, we find the linear regime in which the flat interface develops undulations and hence $\langle x \rangle$ slowly decreases. This time regime is followed by a nonlinear regime where 'droplets' of colloid-rich material fall to the bottom and therefore $\langle x \rangle$ sharply decreases. Finally, a regime appears, where colloids start to form a layer at the bottom of the cell which becomes more compact with time as is reflected in a slow decrease of $\langle x \rangle$. This behavior is in quantitative agreement with experimental results obtained by confocal microscopy [2].

[1] G. Gompper, T. Ihle, D. M. Kroll, R. G. Winkler, Adv. Polym. Sci. **221**, 1 (2009)

[2] A. Wysocki, C. P. Royall, R. G. Winkler, G. Gompper, H. Tanaka, A. van Blaaderen, H. Löwen, Soft Matter **5**, 1340 (2009)

[3] A. Wysocki, C. P. Royall, R. G. Winkler, G. Gompper, H. Tanaka, A. van Blaaderen, H. Löwen, Faraday Discuss. **144**, 245 (2010)

Mesoscale simulations of polymer dynamics in microchannel flows

R. G. Winkler[1,2], L. Cannavacciuolo[1], G. Gompper[1,2]

[1] IFF-2: Theoretical Soft Matter and Biophysics
[2] IAS: Institute for Advanced Simulation

The non-equilibrium structural and dynamical properties of flexible polymers confined in a square microchannel and exposed to a Poiseuille flow are investigated by mesoscale simulations. The chain length and the flow strength are systematically varied. Two transport regimes are identified, corresponding to weak and strong confinement. For strong confinement, the transport properties are independent of the polymer length. For weak confinement or sufficiently strong flow and far from the channel center, the local stretching is similar to that of a polymer in simple shear flow, but in the central part the polymer exhibits a different behavior.

Confinement fundamentally alters the properties of dilute polymer solutions – compared to the bulk behavior – when either the polymer radius of gyration is on the order of the characteristic dimensions of its proximity, and/or an external field is applied, e.g., in shear or pressure-driven flow. In the first case, geometrical constraints lead to a stretching of the polymer parallel to the confining surfaces. In the second case, in addition to flow-induced deformations, polymer-surface hydrodynamic interactions determine the polymer dynamics and lead to, e.g., cross-streamline migration [1]. These aspects are important in emergent microfluidic devices and their application in chemical and biological analyses. As a particular example, we mention emerging technologies for single-molecule analysis of DNA in such micro- and nanometer scale devices. The understanding of the DNA conformational, dynamical, and transport properties is fundamental for the conception and design of such devices.

The proper account of hydrodynamic interactions is essential in simulation studies of fluid flows in channels as is emphasized by the appearance of cross-streamline migration. We employ the multiparticle collision (MPC) dynamics method, which is able to bridge the length- and time-scale gap between the solvent and solute degrees of freedom [2].

The polymer behavior in Poiseuille flow strongly depends on its size compared to the (square) channel cross section. Scaling considerations based on the blob model yield an equilibrium stretch of a flexible polymer in a microchannel when its bulk radius of gyration $r_{g0} \equiv \langle r_g^2 \rangle^{1/2} \sim aN^{3/5}$, where a is the bond length and N the number of monomers, exceeds the lateral channel dimension L, i.e., for $r_{g0} \gg L$. Here, the channel width becomes the characteristic length scale and the blob relaxation time τ_L, which is determined by L, the relevant time scale. For $r_{g0} \ll L$, the conformations are unaffected by confinement and the characteristic length- and time-scales are given by the bulk values of the polymer. The ratios $2r_{g0}/L$ for the considered polymer lengths cover the range $0.36-1.3$, corresponding to the crossover regime between weak and strong confinement. The snapshots of Fig. 1 illustrate the preferred average alignment and extension of a polymer along the flow direction.

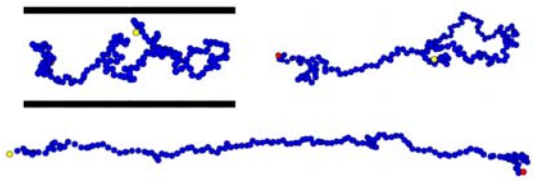

FIG. 1: Conformations of a polymer of length $N = 160$ in a channel of width $L = 15a$ for weak ($Pe_L = 10$, top two images) and strong ($Pe_L = 100$, bottom) flow. The latter yields close to fully stretched polymers. The channel walls are indicated in the top left image by solid lines.

Figure 2 shows radial monomer distributions P_m, where r is the distance transverse to the flow direction from the channel center, for various Peclet numbers Pe_L. Since the polymer radius of gyration is comparable with the channel width, the effective shear rate $\dot{\gamma}$ is determined by L, i.e, $\dot{\gamma} = gL\varrho/(2\eta)$, with η the solvent viscosity, ϱ the fluid mass density, and g the strength of the applied gravitational field. The blob diameter yields the blob relaxation time τ_L such that $Pe_L \equiv \dot{\gamma}\tau_L, \;\; \text{with} \;\; \tau_L = \eta(L/2)^3/(3k_BT)$. With increasing Peclet number, the distribution P_m develops a maximum at a finite distance from the center. At large Pe_L migration towards the channel center sets in, which is caused by hydrodynamic interactions between the polymer and the confining wall and leads to a shift of the maximum to smaller radii. The widths of the radial distribution functions for the various chain lengths are shown as inset in Fig. 2. They are independent of the Peclet number for small Pe_L and decay for large Pe_L. For $N \gtrsim 40$, there seems to be only a weak dependence on the chain length. The widths start to decrease at approx-

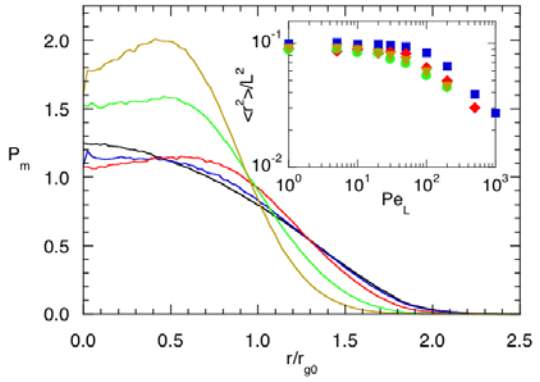

FIG. 2: Radial monomer distribution functions P_m for the Peclet numbers $Pe_L = 0,\ 10,\ 50,\ 100,\ 200$ (right to left for $r/r_{g0} > 1.5$), $N = 40$, and $L/a = 15$. Inset: Widths of the distribution functions for the chain lengths $N = 20$, $r_{g0} = 2.7a$ (squares), $N = 40$, $r_{g0} = 4.1a$ (diamonds), $N = 80$, $r_{g0} = 6.3a$ (bullets), and $N = 160$, $r_{g0} = 9.5a$ (triangles).

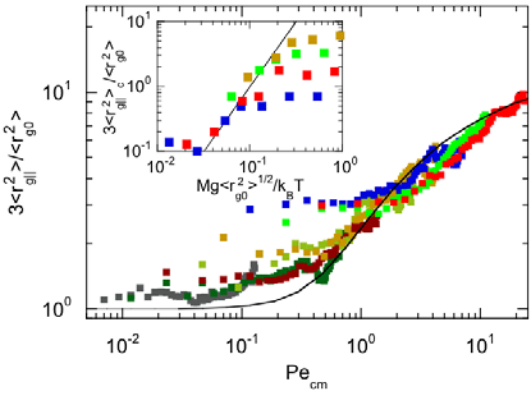

FIG. 3: Mean square radii of gyration parallel to the channel for the Peclet numbers $Pe_L = 1,\ 5,\ 10,\ 20,\ 30,\ 50,\ 100,\ 200$ (left to right), $L = 15a$, and $N = 40$ as a function of the Peclet number Pe_{cm}. The solid line is an analytical result for a semiflexible chain in simple shear flow [3]. Inset: Mean square radius of gyration in the central part of the channel for the chain lengths $N = 20,\ 40,\ 80$, and 160 (bottom to top). The solid line is proportional to $(gr_{g0})^2$.

imately the same Peclet number. This is consistent with our assumption that blobs determine the polymer properties.

Migration towards the wall is observed by studying the center-of-mass distribution of a polymer. Our centers-of-mass distributions for the various polymer lengths exhibit an increase in the probability close to a wall with increasing flow rate in the range $10 \lesssim Pe_L \lesssim 100$. This is accompanied by an increases of the widths of these distributions with a maximum at $Pe_L \approx 50$, which grows with increasing polymer length. However, for larger Peclet numbers, the widths of the centers-of-mass distributions decrease in a similar way as those of the monomer distributions displayed in the inset of Fig. 2 as a consequence of the polymer migration towards the channel center. The broadening of the center-of-mass distribution is caused by stretching and preferred alignment of the polymer along the flow direction. Since the monomer distribution for sufficiently long and hence strongly confined polymers is only weakly affected by flow for $Pe_L < 50$, we conclude that there is only a very weak migration for such Peclet numbers. Flow leads to an alignment of the polymer but hydrodynamic interactions, which are fundamental for migration, do not contribute to the broadening of the center-of-mass distribution. Only for Peclet numbers $Pe_L > 50$, we find a decrease in the width of the monomer distributions for the various chain lengths, which we associate with migration.

Aside from properties averaged over the the cross-section of the channel, we can defined a local shear rate which changes linearly with the radial distance for the parabolic velocity profile. This leads to the local Peclet number $Pe_{cm} = \varrho g r_{g0}^3 r_{cm}/(3k_BT)$, where r_{cm} is the radial chain center-of-mass position, and can be related to Pe_L via $Pe_{cm} = 2\,(2r_{g0}/L)^3\, Pe_L r_{cm}/L$. Note that Pe_{cm} is independent of the system size L. As long as the local radial polymer deformation due to the non-linearity of the flow profile is not too strong, we might expect that the polymer radius of gyration exhibits a dependence on Pe_{cm} similar to the dependence on the Weissenberg number in simple shear flow [3]. Figure 3 shows the mean square radius of gyration parallel to the channel as function of Pe_{cm}. For a given Pe_L, an individual curve indicates the conformational changes as a function of the center-of-mass position. For small Pe_{cm}, i.e., in the central part of the channel, we find a position-independent stretching of the polymer. The inset of Fig. 3 shows that in this regime the radius of gyration increases approximately quadratically with g, within the accuracy of our results, as should be expected due to symmetry reasons (flow reversal), and saturates for strong flows. Interestingly, the stretching seems to be a universal function of Mgr_{g0}/k_BT, with M the monomer mass, which we adopted as scaling function for the various polymer lengths. Thus, in the central part, the channel flow is different from a simple shear flow – the extended polymer never experience a linear velocity profile only. At larger radial distances, the polymer is even stronger stretched, particulary for large flow velocities. More importantly, the various data sets approach a limiting curve for sufficiently large r_{cm} (depending on Pe_L), which is close to the mean square radius of gyration as a function of the shear rate of the same polymer in simple shear flow. The solid line is calculated using a semiflexible polymer model for a polymer in shear flow [3]. Thus, a polymer in Poiseuille flow sufficiently far from the center behaves locally as a polymer in simple shear with a shear rate given by the local velocity gradient.

[1] L. Cannavacciuolo, R. G. Winkler, G. Gompper, EPL **83**, 34007 (2008)

[2] G. Gompper, T. Ihle, D. M. Kroll, R. G. Winkler, Adv. Polym. Sci. **221**, 1 (2009)

[3] R. G. Winkler, Phys. Rev. Lett. **97**, 128301 (2006)

Modelling DNA looping by proteins

A. G. Cherstvy

IFF-2: Theoretical Soft Matter and Biophysics

We study the energetics of DNA loop formation and calculate optimal shapes for DNA loops formed by DNA-looping proteins, with the emphasis on electrostatic interactions along the looped DNA.

DNA looping and ring formation is ubiquitous in biophysics. DNA looping is an essential feature in controlling gene regulatory processes both in pro- and eu-karyotes, with typical lengths of DNA loops l =0.5-5 l_p, where DNA persistence length is $l_p \approx 500$Å or ≈150 bp of DNA. DNA looping occurs in DNA complexes with large structural proteins such as nucleosomes, where the wrapped fragment of negatively charged DNA maintains close contacts with basic groups on the histone proteins. Proteins can also loop DNA without direct contacts with the helix. Particularly, DNA-binding proteins with two binding domains to DNA such as lac repressor (LR) provoke DNA loop formation, controlling thereby lactose metabolism in the cell.

Forming a complex, two LR dimers make a template for DNA loop formation, Fig. 1. Minimal DNA length for stable LR-DNA complexes is l ≈100 bp, due to a high penalty of DNA elastic deformations involved. The maximum LR-DNA binding constants are achieved for loop lengths l =2-3 l_p. The energy of ∼100 bp long LR-DNA loops is estimated as 20-25 k_BT [1]. Although the conformations of LR-bound DNA fragment and DNA-binding protein domains are well resolved by the x-ray studies, there exists no data on the shape of LR-induced DNA loops. This presents a challenge for theoretical investigations.

Both the nucleosomal stability [2] and LR-DNA binding [3] are extremely sensitive to salinity of buffer solutions, indicating the importance of electrostatic interactions. The LR-DNA affinity originates partly from electrostatic contacts of positively charged amino acids in LR head domains to negative DNA phosphate groups. Within a fragment of looped DNA, the repulsion of charges along the contour results in electrostatic energy penalty for loop formation. This effect is similar to end-closure probability upon cyclization of short DNA fragments that is also suppressed at low-salt conditions.

Previous theoretical studies have focused on equilibrium spatial configurations of twisted elastic rods in application to DNA looping. Several of them contain

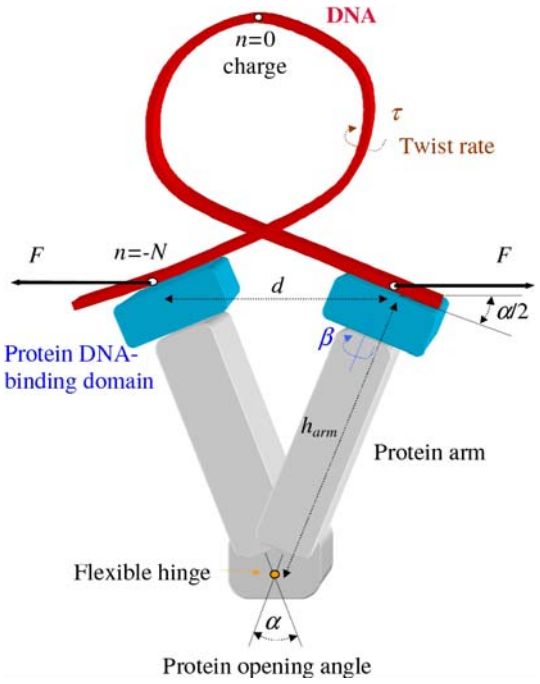

FIG. 1: Geometry of lac-repressor DNA binding with one possible conformation of DNA loop shown.

numerical and analytical treatments of electrostatic effects along looped or ring polyelectrolytes [4]. The exact analytical treatment of optimal loop shapes preferred by a charged filament under arbitrary external forces and torques is however a complicated problem. It involves interplay of long-ranged electrostatic forces and local equations of general elasticity theory resulting in integro-differential equations for the boundary value problem. For charged filaments, the conditions of looping instability have also not been analyzed in details.

First, we derived the analytical expression for the loop shapes formed by long twisted neutral filaments stretched by parallel end forces. Using this solution, we calculated electrostatic energies stored in long charged looped filaments upon changes in solution salinity and in torques applied to cable ends [5]. We analyzed the looping behavior of thin charged filaments using the solution of general elasticity theory equations [6] for buckling instability of twisted neutral filaments. In application to DNA, we accounted

for Manning-like renormalization of DNA charge. We argued that standard theories of electrostatic persistence are only applicable in a limited range of loop parameters, when loop curvature radii and loop close-contact distances are much larger than Debye screening length λ_D. We predict that larger twist rates τ are required to trigger loop formation on long charged cables, as compared to neutral ones.

We also analyzed the shape of charged loops formed on filaments of finite length at different salt amounts, via minimizing the sum of DNA elastic, DNA-DNA ES, and protein elastic energies. We have shown that at low salt concentrations more open loops are favored due to enhanced electrostatic repulsion of DNA charges. This loop opening is consistent with the results of recent computer simulations on LR-induced DNA loops [1]. Even for well-neutralized DNA with ≈20%, for 100-300 bp long loops, we show that electrostatic forces are capable of loop opening at low salt.

Then, we modelled [5] the precise geometry of DNA binding by the LR, Fig. 1, and explored the evolution of geometrical shapes of DNA loops formed, Fig. 2, using as trial functions the set of loop shapes formed by neutral cable. We scanned different DNA lengths clamped on the ends by protein domains and vary protein hinge angles α that define DNA tangents on the loop ends. The loop energetic properties were obtained, such as the loop total energy of 15-22 k_BT for loop lengths l=70-230 bp at λ_D =100Å, that are in good agreement with the results of more elaborate numerical calculations for DNA loops [1, 4]. Loop bending energy was in this case ≈7-15 k_BT, being a non-monotonous function of loop length. We have calculated the loop-length dependence of the protein hinge angle α, filament twist rate τ required, end force F to be applied, loop height, width, and separation between DNA-binding protein domains. Electrostatic energies for the loops shown in Fig. 2 vary in the range 3-10 k_BT for λ_D =100Å, 0.3-1 k_BT for λ_D =30Å, 0.03-0.1 k_BT for λ_D =10Å, and 0.003-0.01 k_BT for λ_D =3Å, for the loop lengths l=70-230 bp.

The results obtained can be applicable in biological systems involving protein-induced DNA looping. In particular, they can be relevant to salt-dependent DNA looping by DNA-binding proteins such as LR as well as to DNA wrapping in nucleosomes. The nucleosome unwrapping process, for instance, might require smaller DNA stretching forces at low salinities because of intrinsic ES-induced opening of DNA superhelical turns. For LR-DNA system, at low-salt conditions we predict a dramatic increase of loop electrostatic energy that would disfavor the loop formation and trigger loop opening. Extreme DNA deformations in loops pave a way for various proteins to bind the deformed DNA sequences with affinities that are different from those onto a straight DNA fragment with the same bp sequence.

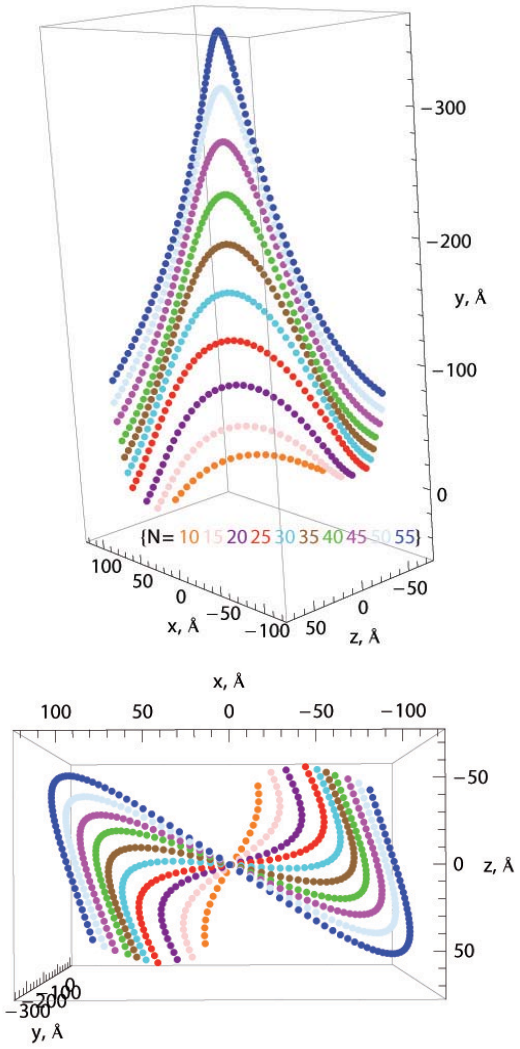

FIG. 2: Loop shapes for different DNA lengths $l = 2Nl_B$, with parameter N indicated and $l_B = 7.1Å$.

[1] A. Balaeff et al., PRE, **73** 031919 (2006).

[2] A. G. Cherstvy, J. Phys. Chem. B, **113** 4242 (2009).

[3] A. G. Cherstvy et al., ibid., **112** 4741 (2008).

[4] D. Swigon et al., PNAS, **103** 9879 (2006).

[5] A. G. Cherstvy, J. Phys. Chem. B, submitted.

[6] J. Coyne, IEEE J. Ocean. Ing., **15** 72 (1990).

Globular protein under denaturing conditions

V. Lacroix[1,2], M.-S. Appavou[1], P. Cayot[2], C. Loupiac[2], D. Richter[1,3]

[1] JCNS: Jülich Centre for Neutron Science
[2] Equipe EMMA, AGROSUP Dijon, Université de Bourgogne, Dijon, France
[3] IFF-5: Neutron Scattering

The isolation of protein folding intermediates is somehow crucial to understand protein misfolding and protein aggregation for example. The process of protein unfolding is driven by the balance between protein-protein, protein-water and water-water interactions. Pressure denaturation studies provide fundamental thermodynamic parameters for protein unfolding: the volume change $\Delta V^{\circ}/V^{\circ}$. We have observed by SANS whether the ligand of beta-lactoglobulin (BLG) can stabilize its structure upon chemical and pressure denaturating conditions.

Proteins acquire the three-dimensional native structure related to their functions in few seconds probably because they do not explore all the space conformations. Indeed, some parts of the proteins fold more quickly than others and lead to folding intermediates [1]. High pressure is more and more used in food industries for sterilization process since this procedure has less influence on texture and taste than thermal sterilization. In the frame of understanding the folding of proteins, we have investigated the unfolding of a whey protein: the Beta-lactoglobulin (BLG). BLG is mainly beta-strand protein which naturally binds the retinol (Vitamine A). Guanidinium hydrochloride (GdmCl) was used as denaturing agent at several concentrations in order to get some of the folding intermediates of this protein. Its structure is similar to peptide bond and enters in competition with protein for hydrogen bonding. As a salt, GdmCl induces also electrostatic interactions leading to protein unfolding. Using the scattering length density contrast between hydrogenated protein and deuterated solvent in SANS techniques, we can access these folding intermediates. These folding intermediates can be characterized by applying polymer physics theory. For instance, we present here results at low q with the radius of gyration extrapolated at null concentration in the Guinier regime.

In a first step we have focused on the chemical denaturation of beta-lactoglobulin without and with retinol in the Guinier Regime.

Figure 1 represents a Debye plot of the scattering pattern for BLG without and with Retinol at different concentration of guanidinium hydrochloride.

From the measurement in the Guinier regime for the Retinol-free BLG, we have found an increase of the

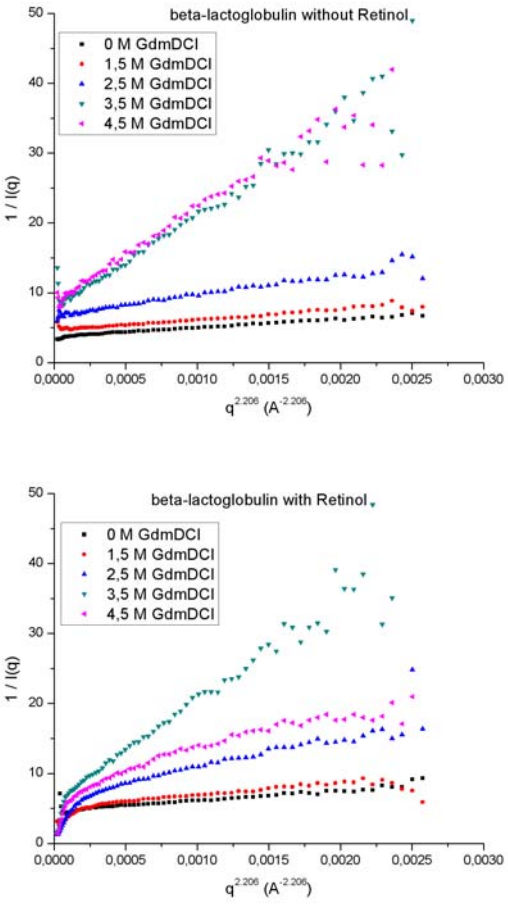

FIG. 1: Debye representation of the scattering pattern for beta-lactoglobulin solution at 5 mg/mL at different GdmDCL concentration without (Top) and with (bottom) retinol binding.

radius of gyration extrapolated at null concentration from Rg(0) = 21,1± 0,2 Å in the native state up to Rg(0) = 32,6 ± 1,5 Å in the denatured state. However, we can observe a destabilization effect of the ligand binding on BLG respect to GdmDCL addition according to the spectra related to the Retinol-bound BLG; some aggregation phenomena occur when we add the GdmDCl.

We have then investigated the pressure denaturation of beta-lactoglobulin without and with Retinol in the Guinier Regime. The table 1 presents the evolution

of the radius of gyration extrapolated at null concentration of beta-lactoglobulin without and with Retinol in the Guinier Regime before and after pressurization.

	Rg(0) without Retinol (Å)	Rg(0) with Retinol (Å)
P atmospheric	21,2 ± 0,2	24,3 ± 0,8
P 1500 bar	30,2 ± 1,5	27,3 ± 1,7
$\Delta V^{\circ}/ V$ (%)	42,5 ± 0,1	12,4 ± 0,1

TAB. 1: Evolution of the radius of gyration extrapolated at null concentration of beta-lactoglobulin without and with Retinol in the Guinier Regime before and after pressurization.

Pressure induces same increase of the null concentration extrapolated radius of gyration of the Retinol-free BLG from Rg(0) = 21.1± 0.2 Å in the native state up to Rg(0) = 30,2 ± 1,5 Å in the denatured state. The volume of the ligand-free protein has increased by 42.5 ± 0.1%.

Ligand bound to BLG induces a slight increase of the Rg(0) by 14.6 % without unfolding the protein.

We can observe a smaller increase of the radius of gyration from Rg(0) = 24.3± 0.8 Å in the native state up to Rg(0) = 27.3 ± 1.7 Å as far as the protein was pressurized at 1.5 kbar before being measured at atmospheric pressure. The volume of the ligand-bound protein have increased by 12.4 ± 0.1%. (The detailed results and interpretations are presented in [3]).

Using SANS spectroscopy, we have investigated the stabilization effect of retinol binding on beta-lactoglobulin protein. We have seen that the ligand does not protect the protein against chemical denaturation (by guanidinium hydrochloride) whereas it decreases the effect of pressure. The difference between these two effects comes from the fact that guanidinium hydrochloride, by competing with protein in the hydrogen bond network involved secondary and tertiary structures modifications and unfold the molecule from the surface of the protein. The pressure induces the penetration of water molecules into the hydrophobic core of the protein and thus unfolds the biomolecule from inside. Both unfolding processes lead to an increase of the radius of gyration by ∼50% in the case of the ligand-free beta-lactoglobulin. Former SANS measurements under pressure, performed by Loupiac et al [2], have shown an increase of the radius of gyration by about 7%. Indeed, the pressure released after pressurization at 1,5 kbar has an effect on the structure of the beta-lactoglobulin.

[1] V. Receveur et al, FEBS Letters, **426**, 57-61 (1998)

[2] C. Loupiac, M. Bonetti, S. Pin, P. Calmettes, BBA, **1764,** 211 (2006).

[3] V. Lacroix, M. S. Appavou, C. Loupiac, P. Cayot, D. Richter (in preparation)

Critical scaling and aging near the jamming transition

D. A. Head[1,2]

[1] IFF-2: Theoretical Soft Matter and Biophysics
[2] Institute of Industrial Science, University of Tokyo, Meguro-Ku, Tokyo 153-8505, Japan

Despite being an everyday phenomenon, the kinetic arrest or 'jamming' of *e.g.* sand, pills or coffee granules remains poorly understood. Recent simulations of model jamming systems have begun to elucidate the nature of this transition, but only measured static quantities. Here, we employed dissipative molecular dynamics to investigate the temporal aspects of jamming by tracking the relaxation from a random initial state. Particle motion was found to become correlated on a growing length that scales with distance from the jamming transition, in a similar manner to critical point phenomenology. This length can also be associated with the range over which local force balance is obeyed. The global dynamics were found to decay with time in a systematic manner, evoking the phenomenon of *aging* that also exists in glasses and critical fluids.

Many branches in physics are tasked with explaining the properties of materials in terms of their constituent components, be they atoms, molecules or larger sub–units such as bubbles in foam, or grains of sand in a sandpile. If the material exists in a state of thermodynamic equilibrium, for which a rigourous descriptive framework has been in place for over a hundred years, the problem is in principle solved. However, many materials do not reach equilibrium for a number of possible reasons. Of interest here are systems often referred to as *granular media*, consisting of solid objects that dissipate energy upon collision and are large enough that their thermally–induced (*i.e.* Brownian) motion can be ignored. Such systems undergo collective arrest, or 'jam', at sufficiently high densities, a strongly out–of–equilibrium effect.

To better understand the nature of this 'jamming transition', some have turned to computer simulations of model systems in which real–world complications such as friction and gravity can be removed from consideration. Studies of static packings generated *via* an optimization procedure have revealed that the jamming transition occurs at a well–defined density (more precisely, volume fraction) ϕ_J, and uncovered power–law scalings of various quantities with distance from the transition $|\phi - \phi_J|$ [1]. However, the numerical efficiency of this algorithm comes at the expense of removing all temporal behaviour from consideration. Restoring the time axis incurs a considerable computational cost, but is essential to fully understand the nature of the transition.

The aim of this project was to numerically simulate model granular packings using a dissipative molecular dynamics algorithm with a well–defined time scale, thus allowing the temporal aspects of jamming to be investigated. Rather than drive the system to a steady flowing state, it was allowed to freely relax from a random initial configuration, 'cooling' as energy is dissipated through inelastic collisions. Details of the simulation method are given in [2], but essentially consists of frictionless soft spheres iterated *via* a standard molecular dynamics algorithm with an additional velocity–dependent damping term that extracts kinetic energy from contacting particles. A snapshot of a system with volume fraction ϕ below the jamming transition $\phi_J \approx 0.843$ at late times is given in Fig. 1. For $\phi > \phi_J$ the system relaxes to a static amorphous solid with no long–range structure.

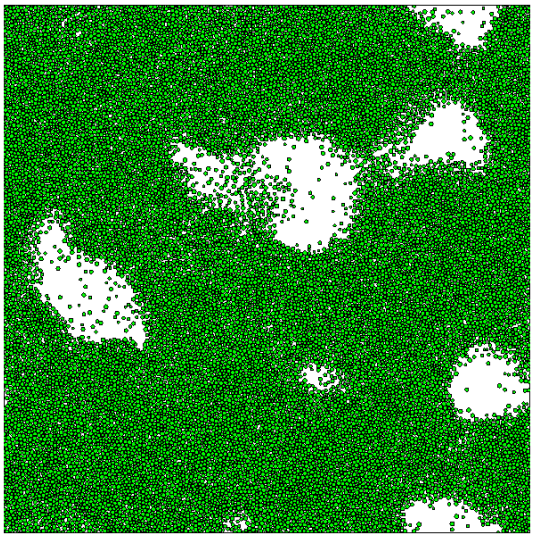

FIG. 1: Example of a low density system with a volume fraction $\phi = 0.7 < \phi_J$ which unjams and subsequently separates into high and low–density regions.

As the system relaxes from its random initial state, nearby grains are observed to move with similar velocities, and the range of this correlated motion expands with time. To quantify these correlations, we follow the procedure employed by Olsson and Teitel for their simulations of continuously sheared sys-

tems [3]: First the velocity autocorrelation function $C_{vv}(r,t) = \langle \mathbf{v}(\mathbf{r},t) \cdot \mathbf{v}(\mathbf{0},t) \rangle$ is measured as a function of interparticle separation r and time t, and then a characteristic correlation length $\xi_v(t)$ is extracted from some indentifiable feature of the curve (we used the global minimum of $C_{vv}(r,t)$ over r). In analogy with critical phenomena, it is possible to collapse $\xi_v(t)$ for different ϕ onto two master curves, one for $\phi > \phi_J$ and one for $\phi < \phi_J$, by scaling both t and ξ_v by suitable powers of $|\phi - \phi_J|$ as demonstrated in Fig. 2. Olsson and Teitel also observed collapse after scaling ξ_v and the shear stress in steady flow, and whereas our length scaling exponent $\nu = 0.57 \pm 0.05$ agrees with theirs, the time exponent $\varepsilon = 0.6 \pm 0.05$ is only measurable using our freely–cooling protocol.

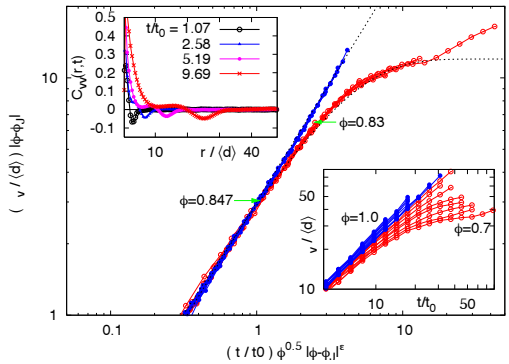

FIG. 2: Collapse of the velocity correlation length ξ_v versus time t after scaling ξ_v and t by powers of $|\phi - \phi_J|$. Densities above (below) ϕ_J are shown in blue (red). (Inset, upper left) *Example of $C_{vv}(r,t)$ for $\phi = 0.92$.* (Inset, lower right) *Pre–collapsed data. The additional time scaling of $\phi^{0.5}$ is a non-critical correction to scaling, $\langle d \rangle$ is the mean particle diameter and t_0 a base time unit.*

It should be noted that the plots of length *versus* time in Fig. 2 are initially straight lines, which, since the particles do not move along straight trajectories *(see below)*, suggests some *convected* quantity is driving the growing correlations. The most plausible candidate is wave–like propagation of contact forces through extended particle clusters. Intuitively, strongly correlated motion between touching particles should only be possible when there is no net resultant force acting between them, *i.e.* correlated motion should be coupled with local force balance. In [2] we defined a local measure of force balance $\psi(\mathbf{x})$, from which a characteristic length $\xi_\psi(t)$ could also be extracted, and showed that it obeyed similar collapse to that of ξ_v, confirming these two aspects of temporal relaxation are indeed coupled.

The scenario suggested by these findings is that for densities above ϕ_J, and for sufficiently short times below ϕ_J, the system obeys force balance *locally*, on a length scale that grows with time. This picture resembles the approach to *thermodynamic* equilibrium in models of glasses and critical fluids, with the key difference that thermodynamic equilibrium is here replaced by *mechanical* equilibrium, *i.e.* force balance. To push this analogy, we checked to see if the system's dynamics monotonically decays with the time t_w since the start of the simulation, a phenomenon known as *aging* and commonly associated with glasses, although also present in critical systems. As demonstrated in Fig. 3, the two–time mean squared displacement of particle positions $\mathbf{x}(t)$, $\Delta r^2(t_w + t, t_w) = |\mathbf{x}(t_w + t) - \mathbf{x}(t_w)|^2$, does indeed scale with t_w; particle motion slows down in a systematic fashion as the system ages. Fitting the data to suitable functions as indicated in the figure showed that the amplitude of Δr^2 decays with t_w as $\sim t_w^{-0.84 \pm 0.05}$, independent of density [2]. This lends weight to postulated analogies with both glassy and critical systems, although the scaling with $|\phi - \phi_J|$ observed in Fig. 2 indicates the critical–point analogy may be more appropriate.

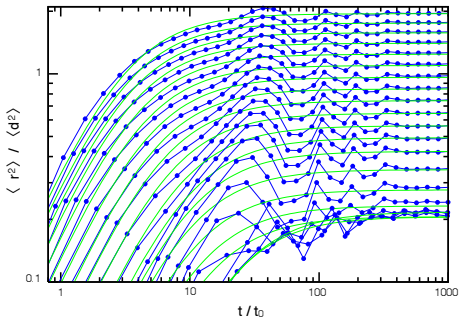

FIG. 3: Mean squared displacement $\Delta r^2(t_w + t, t_w)$ for a volume fraction above the jamming transition, $\phi = 0.88 > \phi_J$, with lines from top to bottom corresponding to increasing t_w. The green lines are fits to $M(t_w)/\{1+[t/\tau(t_w)]^{-a}\}$.

Finally, at late times our freely cooling system should crossover into regimes already studied from alternative perspectives, so to place our findings in a broader context we also checked for the expected convergence to known behaviour as $t \to \infty$. For $\phi > \phi_J$ the system relaxes to a static, amorphous solid with mechanical properties that scale with powers of $|\phi - \phi_J|$. The relevant exponents extracted from our cooling simulations matches those already determined from optimization algorithms, confirming the robustness of the final state to the preparation procedure. For $\phi < \phi_J$ structure emerges at large length scales as the system separates into high and low–density regions as in Fig. 1. The characteristic cluster size ℓ (extracted from the structure factor) was found to grow with time t as $\ell \sim t^{0.26 \pm 0.03}$, consistent with known values for hard sphere granular gases [4] and indicating that subsequent system evolution will follow known results from that field.

[1] C. S. O'Hern, L. E. Silbert and S. R. Nagel, Phys. Rev. E **68**, 011306 (2003).

[2] D. A. Head, Phys. Rev. Lett. **102**, 138001 (2009).

[3] P. Olsson and S. Teitel, Phys. Rev. Lett. **99**, 178001 (2007).

[4] S. Luding and H. Herrmann, Chaos **9**, 673 (1999).

Molecular adsorption transitions at attractive interfaces

M. Möddel[1,2,3], T. Vogel[1,2,3], S. Karalus[1,2,3], J. Adler[4], W. Janke[3], M. Bachmann[1,2]

[1] IFF-2: Theoretical Soft Matter and Biophysics
[2] IAS: Institute for Advanced Simulation
[3] Institut für Theoretische Physik, Universität Leipzig
[4] Department of Physics, Technion Haifa, Israel

Depending on environmental properties, such as the solvent quality or the temperature, and material parameters like binding affinity and intrinsic interface geometry, proteins and flexible polymers form in adhesion processes structures that can be associated to different conformational phases. We investigate mesoscopic, coarse-grained hybrid models for the adsorption of flexible polymers and proteins to solid or fluctuating surfaces to elucidate the general structural behavior of polymers under competing influences of energetic ordering and entropic disordering effects. Sophisticated Monte Carlo computer simulation methods enable a systematic analysis of all conformational transitions a polymer can experience when adsorbing to a substrate.

The interest in hybrid systems of single molecules attached or adsorbed to substrates has strongly increased in recent years since there are many potential applications including molecular nanoelectronic circuits and biosensors. This also regards the development of advanced technological methodologies allowing for a precise manipulation of molecules at surfaces. There is also a strong interest in structural biology as it has been realized that understanding the function of biomolecules, in particular proteins that mediate signal and substance exchange near membranes, is inevitably connected to their geometrical structure. Since many molecules are sufficiently flexible to modify their conformation if environmental parameters change, the understanding of conformational phase transitions of hybrid systems is crucial.

There are two theoretical approaches to studying molecular binding properties which differ in the detail and in the generality of gained informations. The understanding of the *specific* binding of a peptide to a substrate requires the detailed modeling of all inter-atomic interactions and the consideration of a large set of parameters. This includes a suitable parametrization for the intramolecular interactions as well as for the interactions with the substrate and the solvent. Also, geometric properties of the substrate, i.e., the atomic composition, crystalline or amorphous structure, local crystal orientation at the surface, roughness effects, defects, etc. need to be considered. The systems are typically too large for an analytic treatment and the semiclassical models on nanoscopic scales are so complex that even high-performance computer simulations can give only limited insights that typically cannot be generalized (see Fig. 1).

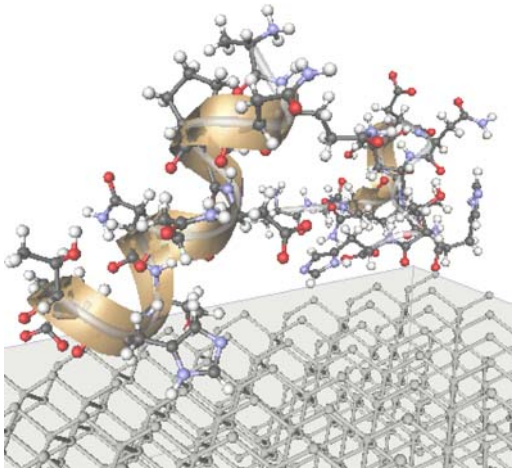

FIG. 1: The binding properties of a peptide adsorbing at a substrate are influenced by the strongly geometry-dependent, heterogeneous electronic properties of molecule, substrate, and environment. The resulting high specificity of adsorption requires a careful force-field parametrization in semiclassical models. The image shows a snapshot from a simulation of two synthetic helical peptides interacting with a de-oxidized silicon (100) surface.

On the other hand, if one is rather interested in the *generic* behavior of large classes of hybrid systems, it is neither possible nor desirable to employ models of high complexity. For a system that possesses microstates which allow for the formation of thermodynamically stable conformational phases, it must be possible to introduce a strongly simplified model on coarse-grained, i.e., mesoscopic, scales. In this case, the overall thermodynamic behavior is governed by only a few effective parameters. It is obvious that such models cannot unravel atomistic details of binding, which, however, are not relevant in a cooperative macroscopic effect like a thermodynamic phase transition. We follow both the microscopic and the mesoscopic approaches, but we will here concentrate on generic features of binding on a coarse-grained scale.

From recent intense studies of simple lattice mod-

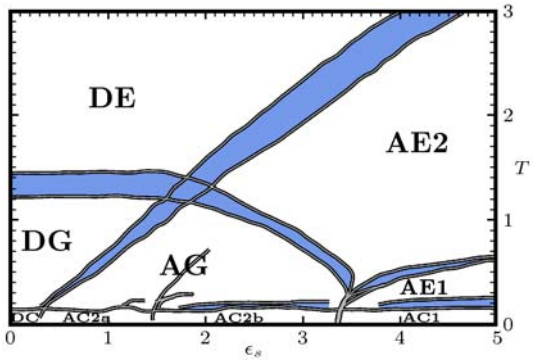

FIG. 2: Pseudophase diagram of adsorption for a flexible homopolymer with 20 monomers [4]. The bands separate the individual conformational phases, the band width indicates the statistical uncertainty.

els in contact-density chain-growth computer simulations [1], we have already gained a general picture of polymer adsorption and hydrophobic-polar peptide adsorption transitions at different types of planar, solid substrates [2, 3]. In dependence of a parameter that we associated with the solvent quality (more precisely, it is defined as the ratio of energy scales of the monomer-monomer and the monomer-substrate interaction) and the temperature, we identified a rich phase structure, comprising compact globular and crystalline mono- and multilayer adsorption phases, as well as the phase of extended coil-like adsorbed polymer structures [2].

In order to get rid of undesired lattice effects, we have investigated an off-lattice model for a polymer, where nonbonded monomers interact via a standard Lennard-Jones potential, whereas the interaction between the monomers and a planar, homogeneous solid substrate is modeled by an integrated Lennard-Jones potential [4]. The main result of this study is the (pseudo)phase diagram of adsorption as shown in Fig. 2. It is parametrized by the temperature T and the surface attraction strength ϵ_s, a model parameter that weighs the energy scales of surface attraction and intrinsic monomer-monomer interaction. In extensive simulations, different statistical mean values for geometric quantities such as the components of gyration tensor parallel and perpendicular to the substrate, for the relative numbers of short-distance contacts between nonbonded monomers and between monomers and the surface were estimated in addition to the mean energy.

From the peak structures of the fluctuations of these quantities as functions of T or ϵ_s, we identified the different conformational transitions and constructed the entire conformational phase diagram. Since this can to this extent only be done for rather short chains (the plot in Fig. 2 was obtained for a 20mer), the transitions are still influenced by finite-size effects (the width of the transition bands indicates the uncertainty) such that we call the regions, separated by the transition lines, “pseudophases”. However, simulations of larger systems strengthen this picture and therefore we have good reasons to assume that our simulations already revealed the correct general phase structure [4].

The bands in Fig. 2 separate the individual conformational phases: There are the bulk phases of desorbed conformations DE, DG, and DC which are associated to expanded coils, globular, and crystalline structures, respectively. The transition line between DE and DG signals the celebrated Θ transition, where by decreasing the temperature extended coil structures collapse to globular conformations. The freezing of these rather “liquid” globules into crystalline or amorphous compact structures is indicated by the transition line between DG and DC. In the adsorption region, AE1 is dominated by adsorbed single-layer expanded structures and AE2 by adsorbed conformations extending into the bulk. AG denotes the adsorbed globular regime. The crystalline phases differ in their topology. AC1 is the phase of two-dimensional compact film-like surface-layer conformations, whereas in AC2a compact, spherically or semi-spherically shaped droplets dominate. In AC2b, structures possess an ordered double-layer structure. The famous wetting transition corresponds to passing the transition lines DG $\rightarrow$ AG $\rightarrow$ AC2b $\rightarrow$ AC1 for fluid droplets, while compact polymers wet the surface in the direction DC $\rightarrow$ AC2a $\rightarrow$ AC2b $\rightarrow$ AC1. The latter process is simply induced by an increase of the surface attraction strength.

We also investigate the adsorption of polymers to nonplanar substrates such as ultrathin nanowires. The polymer is attracted by the string which possesses an effective thickness caused by volume exclusion. Attraction strength and thickness govern the competition between energetically favorable monomer arrangements and their distortion by steric constraints. A first interesting result is the formation of a conformational phase, in which cylindrical monolayers with strong similarities to single-walled carbon nanotubes (including, e.g., chiral symmetries) form spontaneously. We are going to extend this study to polymers wrapping around “real” carbon nanotubes.

Furthermore, we investigate the shape transitions of a polymer interacting with a membrane-like polymer network in dependence of attraction strength and volume exclusion. Since this is to be compared with the phase diagram shown in Fig. 2 for the adsorption at a planar, solid substrate, we quantitatively study the influence of the network (or membrane) fluctuations upon the general adsorption behavior.

[1] M. Bachmann and W. Janke, Phys. Rev. Lett. **91**, 208105 (2003); Lect. Notes Phys. **736**, 203 (2008).

[2] M. Bachmann and W. Janke, Phys. Rev. Lett. **95**, 058102 (2005); Phys. Rev. E **73**, 041802 (2006).

[3] M. Bachmann and W. Janke, Phys. Rev. E **73**, 020901(R) (2006).

[4] M. Möddel, M. Bachmann, and W. Janke, J. Phys. Chem. B **113**, 3314 (2009).

Dominance of finite-size effects in nucleation processes

T. Vogel[1,2,3], S. Schnabel[3], C. Junghans[4], M. Möddel[1,2,3], T. Bereau[5], J. Groß[1,2,3], W. Janke[3], M. Bachmann[1,2]

[1] IFF-2: Theoretical Soft Matter and Biophysics
[2] IAS: Institute for Advanced Simulation
[3] Institut für Theoretische Physik, Universität Leipzig
[4] Max Planck Institute for Polymer Research, Mainz
[5] Carnegie Mellon University, Pittsburgh, USA

Thermodynamic phase transitions are typically analyzed in the thermodynamic limit, i.e., for an idealized infinite system size. This approach is reasonable for inherently large systems, where finite-size effects vanish with increasing system size. Based on finite-size scaling for second-order phase transitions, this motivates the assumption of scale invariance at the phase transition point – the basis on which universality is founded. However, there are systems and transitions, where the thermodynamic limit is a nonsensical idealization. A typical scenario is the nucleation of a system and prominent examples for such processes are atomic cluster formation, the freezing of polymers, the aggregation of peptides, and the folding of proteins. Here, we will discuss properties of such first-order-like "liquid-solid" transitions from a general perspective and motivate their microcanonical analysis.

The coil-globule collapse transition of polymers is an example for a second-order phase transition. For increasing chain length, a comparatively clear finite-size scaling behavior is known. This transition is not accompanied by specific structure formation as dominant conformations in both phases are not (coils) or only locally (globules) ordered. The microcanonical entropy $S(E)$, i.e., the entropy as a function of energy E, does not change much at the transition point and thus the collapse (or Θ) transition occurs at a relatively high temperature $T_\Theta = (\partial S/\partial E)_\Theta^{-1}$. Except for field-theoretically predicted but numerically and experimentally not yet confirmed logarithmic corrections to scaling, the Θ transition is rather well understood.

This is completely different for the freezing or crystallization transition at low temperatures. In this case, we could recently show in lattice polymer studies that quantities indicating the transition, such as peak temperatures of energetic and geometric fluctuations, do not show any characteristic scaling behavior with increasing system size [1]. In fact, the thermodynamic behavior of the "liquid-solid" transition is governed by finite-size effects. Symmetries (or monomer arrangements) of the frozen, low-entropy conformations depend strongly on the precise chain length and model details such as the ratio of length scales of bonds and nonbonded interactions.

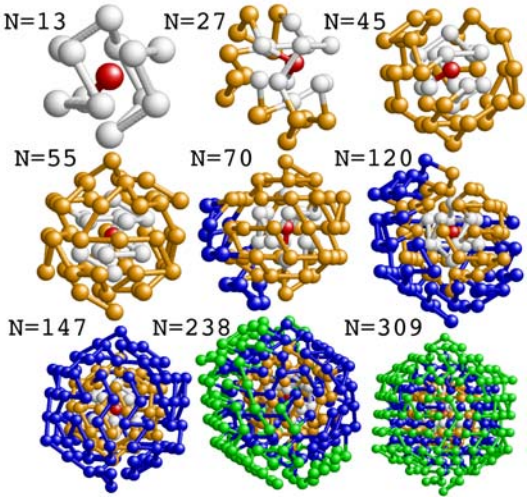

FIG. 1: Icosahedral or icosahedral-like ground-state state conformations of elastic polymers for different system sizes [3]. Equally colored monomers belong to the same shell.

In our latest studies of such systems, we investigated the crystallization transition of polymers with elastic bonds [2, 3]. The bond length is adaptive in a way that highly symmetric conformations can form in the crystalline phase. In high-performance Monte Carlo simulations we found for all different chain lengths low-energy conformations with basic icosahedral symmetries. The formation of such "discretized spherical" shapes is not surprising. Small systems that have to reduce surface contact with its environment and require stable structures prefer icosahedral shapes. A prominent example is a spherical-virus capsid enclosing the viral genetic material.

We also find the confirmation for our expectation that the thermodynamic crystallization behavior is different for all system sizes. We identified a nontrivial systematic chain length dependence that is associated with the type of growth of the nucleus [2, 3]. However, a conventional scaling behavior could not be identified – it simply does not exist. This is also known from atomic clusters. A particularly sharp transition signal from fluctuating quantities, such as the specific heat, is obtained for "magic" chain lengths $N = 13, 55, 147, 309, \ldots$, in which cases almost perfect icosahedra can form (see Fig. 1). These shapes

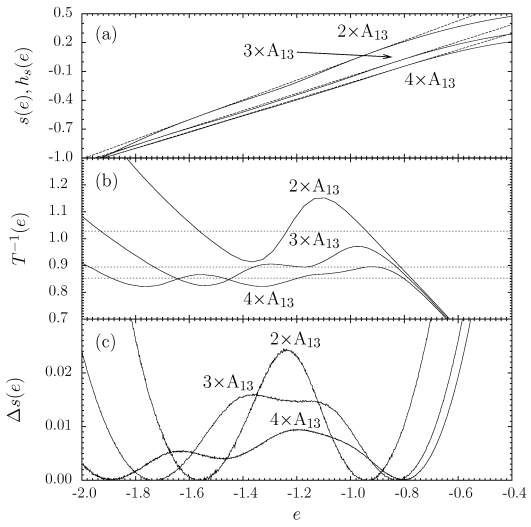

FIG. 2: (a) Microcanonical entropy per monomer $s(e)$ and the Gibbs constructions $h_s(e)$ (dashed lines) as functions of the energy per monomer $e = E/N$, (b) reciprocal caloric temperatures $T^{-1}(e)$ and Maxwell constructions, and (c) relative surface entropies per monomer Δs_{surf}.

are particularly stable and typically represent the core cells in the structure formation of longer chains.

The formation of optimally discretized spherical shapes is required for systems that have to optimize the contact surface to a less attractive environment (for example, a "poor" solvent). The residence of a monomer at this interface is energetically disfavored compared to a position in the interior. In small systems, however, all possible structures, including the most compact ones, have an insufficient surface-to-volume ratio, i.e., a large fraction of particles or monomers resides in the surface layer. Yet for the "magic" 309mer, more monomers are located on the surface (162) than in the bulk (147). Thus, all nucleation processes, even for much larger systems, are still influenced by surface effects. For this reason, quantitative analyses of "first-order-like" nucleation transitions require a treatment different from standard scaling approaches.

A possible approach based on microcanonical statistics shall be discussed for the aggregation of molecules which can also be considered as a nucleation transition [4, 5]. In biosystems, the formation of peptide plaque can have disastrous consequences. An example is the aggregation of Aβ peptides in the human brain which is associated to the neurodegenerative Alzheimer's disease. The central quantity in the microcanonical approach is the density of states $g(E)$ which can intuitively be understood as the degeneracy of the energetic states of the system. Then, the microcanonical entropy can be introduced by $S(E) = k_B \ln\, g(E)$. In Fig. 2(a), it is plotted for systems of two (2×A_{13}), three (3×A_{13}), and four polymer chains with 13 monomers (4×A_{13}). All these entropy curves exhibit a particularly interesting feature: In a certain energy region, they possess *convex* monotony [5]. Consequently, at a certain temperature, the canonical probability density distribution $p(E) \sim g(E)\exp(-E/k_B T_{\text{agg}})$ is bimodal with two peaks of equal height at two energies E_{agg} and E_{frag} that can be associated to phases, where aggregates or fragments dominate, respectively. A minimum at the energy E_{sep} separates the two coexisting phases at the transition temperature T_{agg}. Hence, we conclude that the convex region of the entropy corresponds to the phase separation of the first-order-like aggregation transition. This behavior is common to all nucleation processes. However, it is a finite-size effect and will vanish in the thermodynamic limit (provided, its definition makes sense at all).

It is useful to construct the concave Gibbs hull of the entropy curves in the transition region by connecting the two points $S(E_{\text{agg}})$ and $S(E_{\text{frag}})$. Since the temperature is defined via $T^{-1}(E) = \partial S(E)/\partial E$, the slope of the Gibbs tangent $H_S(E)$ is identical with the reciprocal aggregation transition temperature T_{agg}^{-1}. Figure 2(b) reveals the characteristic nonmonotonicity of the caloric temperature curves $T^{-1}(E)$. They bend back in the transition region, i.e., additional energy pumped into the system during the fragmentation process leads to a decrease of the temperature: the melting aggregate becomes first *colder* during the fragmentation transition. This is due to the entropic deviation $\Delta S(E)$ from the "expected" Gibbs hull [Fig. 2(c)]. The maximum at the separation energy is called "surface entropy" and corresponds to the entropic reduction due to monomer rearrangements at the surface of the aggregate during the melting process. Entropy reduction costs energy. This is why the caloric temperature decreases with increasing energy. In Fig. 2(b), we also see that the backbending region becomes flatter with increasing system size (number of chains) and converges to the Maxwell lines, i.e., to the slopes of the Gibbs hulls.

By closer inspection of Fig. 2(b), we find for the systems a *hierarchical substructure* caused by the surface effects. The increasing frequency of oscillations of the curves for the larger systems reveals that the aggregation transition is actually a composition of different subprocesses, each of which being an individual phase-separation process. The amplitude of these oscillations decreases with system size showing that these subprocesses have a smaller surface-entropic barrier [5].

[1] T. Vogel, M. Bachmann, and W. Janke, Phys. Rev. E **76**, 061803 (2007).

[2] S. Schnabel, T. Vogel, M. Bachmann, and W. Janke, Chem. Phys. Lett. **476**, 201 (2009).

[3] S. Schnabel, M. Bachmann, and W. Janke, J. Chem. Phys. **131**, 124904 (2009).

[4] C. Junghans, M. Bachmann, and W. Janke, Phys. Rev. Lett. **97**, 218103 (2006); J. Chem. Phys. **128**, 085103 (2008).

[5] C. Junghans, M. Bachmann, and W. Janke, Europhys. Lett. **87**, 40002 (2009).

Branch point confinement in star polymer melts

M. Zamponi[1], W. Pyckhout-Hintzen[1], M. Monkenbusch[1], A. Wischnewski[1], L. Willner[1], G. Kali[2], D. Richter[1]

[1] IFF-5: Neutron Scattering
[2] Institut Laue-Langevin, Grenoble, France

The combination of Neutron Spin Echo spectroscopy and a labeling scheme unique for neutron scattering allowed for the first time the molecular observation of branch point motion in star polymer melts. The measured dynamic structure factor of a branch point labeled symmetric three arm star shows a clear transition into a plateau, signifying the stronger confinement of the star center in comparison to a center labeled linear chain as expected. Keeping the label as before but shortening of one star arm to only one entanglement length surprisingly leads to the same topological confinement as for the symmetric star. This reflects a much stronger effect of such a small branch on the chain dynamics than expected.

The dynamics of polymers in the melt depends strongly on their architecture. By introducing a branch point the chain dynamics in branched systems like star polymers is considerably slowed down in comparison to linear chains. This can be explained within the tube model by the conjecture of hierarchical relaxation. Similar as in the linear case each star arm is confined inside a tube. But unlike entangled linear chains the whole star can not reptate, it is localized in space due to the branching point. In order for the whole polymer to move, the star arms have to fully retract to the branch point. These deep arm retractions are entropically unfavorable, so that the arm retractions become exponentially unlikely. For asymmetric stars the longer arms are still well entangled when the short arm already has fully retracted. The short arm is then expected to be dragged inside the tube of the yet unrelaxed longer arms so that the branch point can then perform a diffusive hopping motion along the tube.

In order to study the influence of the branching on the polymer dynamics three different polymer architectures have been synthesized: a symmetric three arm star with long well entangled star arms, an asymmetric three arm star with one arm shortened to only one entanglement length and a linear chain with a length corresponding to two long star arms [1]. In all cases only the segments around the branch points resp. the center of the linear chain have been protonated (labeled) in an otherwise deuterated melt and hence are visible in the neutron scattering experiment (see fig.1).

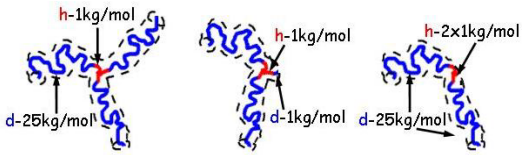

FIG. 1: Schematic drawing of the synthesized polymers with nominal molecular weights.

Neutron Spin Echo (NSE) spectroscopy has been performed on these polyethylene polymers in the melt at a temperature of 509K [1]. Using the large accesible time range available at the IN15 (ILL) the dynamics up to about 200ns over several momentum transfer values q has been explored. NSE measures directly the single chain dynamic structure factor $S(q,t)$ for protonated or partly labeled polymers in a deuterated environment. The results are displayed in fig.2 and fig.3.

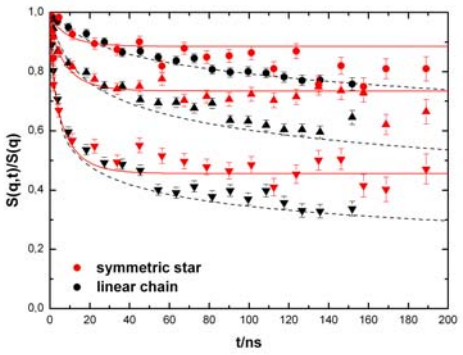

FIG. 2: Dynamic structure factor of the center labeled symmetric star (red symbols) in comparison to the center labeled linear chain (black symbols) for three different q values in the range of 0.05-0.115Å^{-1}. Lines are guides for the eye.

Comparing the dynamic structure factor for the branch point labeled symmetric star and the center labeled linear chain (fig.2) they initially show the same relaxation up to about 35ns, but then the branch point structure factor shows a clear transition into a plateau region, whereas the strucutre factor for the linear chain center continues to decay. The plateau region signifies the topological confinement

of the branch point. The additional relaxation in the linear case stems from the movement of the center segments along the tube which is not possible in the branched system.

In order for the branch point to move in the accessible time window, one star arm has been reduced to only one entanglement length. Then the short arm should not be entangled at all and should allow the motion of the branch point along the tube of the two long arm similar as in the linear case albeit with a larger friction. But surprisingly the dynamic structure factor for the branch point labeled asymmetric and symmetric star are within the accessible time range about the same (see fig.3). Apparently one short arm of only one entanglement length is already sufficient to dramatically slow down the branch point motion and localize the branch point as in the case of a much longer arm.

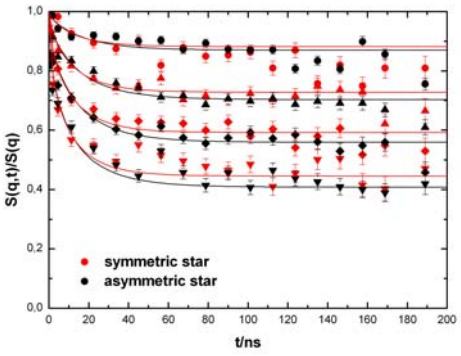

FIG. 3: Dynamic structure factors of the branch point labeled symmetric (red symbols) and asymmetric (black symbols) stars for four different q values in the range of 0.05-0.115Å^{-1}. Lines fit with the model of Vilgis and Boué [2].

To quantify the branch point confinement the theory from Vilgis and Boué [2] has been applied. They describe the dynamics of confined chain segments in a harmonic potential of a size defining the effective confinement. All parameters in the model are known from the linear chain and hence the confinement size can be determined. A fit of the dynamic structure factor yields as size of the branch point confinement in the symmetric case $d^* = 39$Å and for the asymmetric star $d^* = 40$Å which is somewhat smaller than the tube diameter for linear polyethylene $d = 47$Å. The friction at the branch point is expected to be increased by a factor of $f/2$, with $f = 3$ the functionality of the branch point. Leaving the friction as additional fit parameter an even larger value than expected in both cases is obtained.

These findings are also in agreement with rheological measurements on the same system [1]. Rheological measurements allow to observe the imprint of the molecular dynamics on the polymer flow behavior covering thereby the whole time range of interest. Up to intermediate times corresponding to the NSE time window no difference in the two branched system for the dynamic modulus is observed (see fig.4). Only at longer times the asymmetric star shows a flow behavior similar as for the linear chain. Applying the theory of Frischknecht et al.[3], which considers that in asymmetric stars the shorter arm relaxes faster and allows subsequently a diffusive motion of the branch point, gives an indication that the drag of the short arm is stronger than expected as was also found in [3]. The obtained arm retraction time for the short arm for the asymmetric star lies well within the NSE time range but the NSE data gives no indication of a relaxation. Hence, the time scale governing the short arm relaxation is much longer than expected.

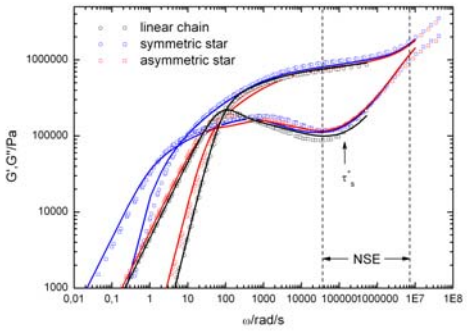

FIG. 4: Loss (squares) and storage (circles) modulus of the parent polybutadienes at roomtemperature. Solid lines fit with the model of Frischknecht et al. [3] for the branched systems and model of Likhtman and McLeish [4] for the linear chain. Dashed lines indicate the corresponding NSE time range and the arrow the arm relaxation time for the short arm in the asymmetric star.

Recent molecular dynamic simulation by Zhou and Larson [5] on similar branched polymer systems also showed that the effect of short side arms is stronger than expected. But they also demonstrated that once the short arm is retracted the branch point performs a distinctive hopping motion. Comparing the time scales with our system suggests that the diffusive hopping motion should be visible in the accessible NSE time range. But the short arm is apparently more confined than anticipated also from simulation. Reducing the length of the short arm should move the hopping motion into the NSE time frame. Probing the dependence of the branch point dynamics on the short arm length with NSE spectroscopy will also allow to shed more light on the arm retraction process.

[1] M.Zamponi et al., Macromolecules **2010**, *43*, 518.

[2] T.A. Vilgis, F.J. Boué, Polym. Sc.: Part B: Polym. Phys. **1988**, *26*, 2291.

[3] A. Frischknecht et al., Macromolecules **2002**, *35*, 4801.

[4] A.E. Likhtman, T.C.B. McLeish, Macromolecules **2002**, *35*, 6332.

[5] Q. Zhou, R. Larson, Macromolecules **2007**, *40*, 3443.

Polymer dynamics under cylindrical confinement

M. Krutyeva[1], J. Martín[2], A. Arbe[3], J. Colmenero[3,4], C. Mijangos[2], D. Richter[1]

[1] IFF-5: Neutron Scattering
[2] Institute of Polymer Science & Technology, CSIC, Madrid, Spain
[3] Center of Materials Physics (CSIC–UPV/EHU), San Sebastían, Spain
[4] Materials Physics Center (MPC) and Donostia International Physics Center, San Sebastían, Spain

Dynamics of poly(ethylene oxide) confined in cylindrical, parallel and hexagonally ordered pores of anodic aluminium oxide has been investigated by neutron scattering in the momentum transfer range $0.2 \leq \left|\vec{Q}\right| \leq 1.9$ Å^{-1} [1]. Rouse-like dynamics indistinguishable from that in the bulk, within the uncertainties, has been revealed in low-Q limit. In high-Q limit a slowing down of the dynamics with respect to the bulk behaviour evidences an effect of confinement. This effect is more pronounced for molecular displacements perpendicular to the pore axis than for parallel displacements. Our results clearly rule out the strong *corset effect* proposed for this polymer from NMR studies, and can be rationalized by assuming that the interactions with the pore walls affect one to two adjacent monomer monolayers.

Producing polymer nanocomposites with given properties requires deep knowledge of the dynamical properties of the polymer component in confinement. According to recent NMR experiments confinement should have a drastic effect on the dynamics of polymer chains in the melt. The NMR data were described in terms of the so called *corset effect* which is predicted to change the mesoscopically sized tube confinement in polymer meltsto a lateral confinement on the level of the chain diameter (∼0.5 nm) [2]. This phenomenon was argued to arise from the strong collectivity of the chain motion in the melt. In this paper we report results of time-of-flight (ToF) and backscattering (BS) measurements of dynamics of linear polymer melt confined in cylindrical nanopores. We aimed to explore the influence of the confinement on polymer dynamics and to check whether any interaction between the polymer and pore walls is visible in the dynamics.

Well ordered nanoporous anodic aluminium oxide (AAO) templates have been used as a confining matrix (Fig.1). The distance between pores was of order of 100 nm with a pore diameter d_{pore}=40 nm providing the porosity of the templates of order of 9%. The average end-to-end distance R_e of poly(ethylene oxide) (PEO) polymer chains with M_w= 43 kg/mol can be calculated to be 19 nm.

Two different orientations of the sample with respect to the incident beam (45° and 135°, see inserts in Fig.2) allow to separate the momentum transfer direction parallel and perpendicular to the pore axis. All experiments were performed at the temperatures above PEO glass transition temperature $T > T_g$. Previous experiments on PEO in bulk were taken as reference for comparison (e.g. [3]).

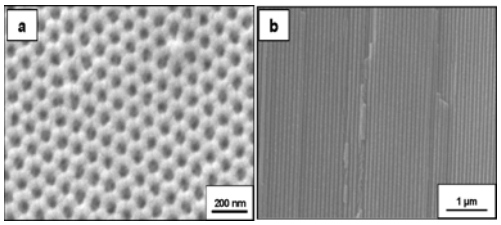

FIG. 1: Scanning electron microscope (SEM) micrographs of the surface (a) and cross section (b) of the anodic aluminium oxide (AAO) templates.

BS spectra obtained on SPHERES spectrometer of JCNS at the FRM II do not reveal any influence of the confinement on PEO dynamics. The intermediate scattering function was analysed based on Kohlrausch-Williams-Watts (KWW) function [4] typical for polymer melts. We observed the spectra were indistinguishable from those for the bulk PEO for the momentum transfer varying in the interval 0.3 Å$^{-1} < \left|\vec{Q}\right| < 1$ Å^{-1} limited by resolution of the small-angle detectors from the bottom and by completely flat spectra from above [1]. Q-dependence of relaxation time τ_{KWW} is well described by Rouse prediction [5].

ToF spectrometer TOFTOF at FRM II allows to measure intermediate scattering function in the range of the momentum transfer 0.2 Å$^{-1} < \left|\vec{Q}\right| < 1.9$ Å^{-1}. In low- Q limit $\left|\vec{Q}\right| < 1$ Å^{-1} we found the bulk and confined PEO results are indiscernible within the uncertainties that is in agreement with BS results. In high-Q limit $\left|\vec{Q}\right| > 1$ Å^{-1} the slowing down of the dynamics for the sample orientation corresponding to the perpendicular molecular displacement was observed (Fig.2).

Figure 2 shows the direct comparison between the intermediate scattering function of confined PEO at $\vec{Q}$ corresponding to the scattering angle 2θ=90° (see insert) and two sample orientations, and bulk PEO. The confinement effect shows up as stretching of the

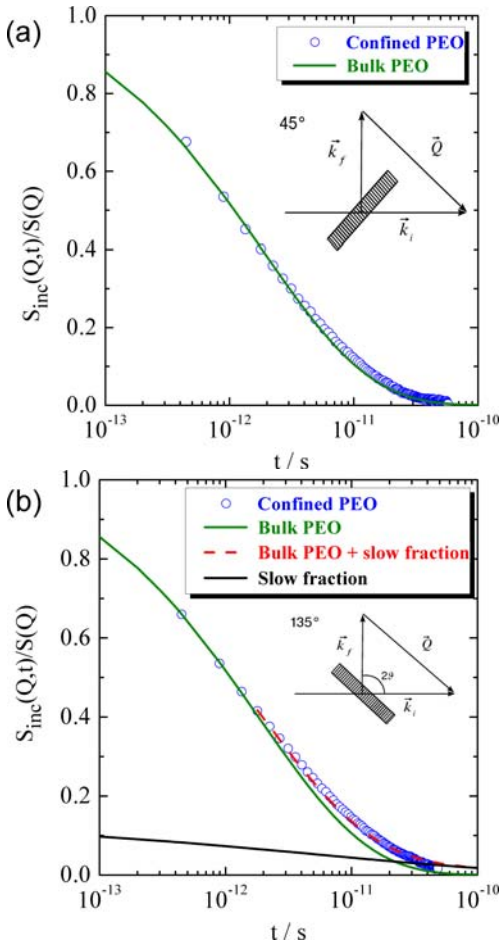

FIG. 2: Intermediate scattering function of PEO (circles) in the AAO templates oriented at 45° (a) and 135° (b) and for bulk PEO (solid line) at 375 K and $\left|\vec{Q}\right| = 1.4\,\text{Å}^{-1}$. The dashed line presents a fit by a sum of 87% of the fast component (τ_{KWW}=3.2 ps) with β = 0.5 like in a bulk and 13% slow component (τ_{KWW}=9.6 ps) with β = 0.25 (see Eq.(3) in Ref. [1]). The slower component is shown by dotted line.

decay in the long time regime for the scattering perpendicular to the pores. We describe these data by considering a fraction of 13% of polymer segments with slower response. Attributing this slow fraction to the amount of polymer close to the surface, this value corresponds to a polymer layer of 0.7 nm thickness.

It has been reported that the *corset effect* is seen already at $R_F \ll a$, where R_F is a Flory radii and a is the confinement size. Providing this relation to be true for our system ($R_e \ll d_{pore}$), we analysed the intermediate scattering function in terms of the mean-squared displacement in curvilinear coordinates along the tube axis.

Figure 3 presents the theoretical prediction for various values of the tube diameter together with the experimental data for both confined and bulk PEO. It is worth to mention that prediction of the theory is valid in the time limit $t > \tau_e$(dash lines in the Fig.3), where τ_e is the entanglement time. Obviously, the experimental results presented here are not compatible with *corset effect* of associated characteristic length scales of either 0.5 or 1 nm.

In conclusion, the incoherent scattering function is well described by the Rouse theory in low-Q limit showing no indication of confined segmental dynamics due to the *corset effect*. Around $\left|\vec{Q}\right| \approx 1.4$ Å^{-1} an anisotropic slowing down of the dynamics under confinement in the direction perpendicular to the pore axis is observed. This effect could be attributed to the interactions between the pore walls and polymer segments within an $\sim$1 nm layer. Based on these results we can exclude the existence of a *corset effect* on the length scale where it was proposed from NMR studies.

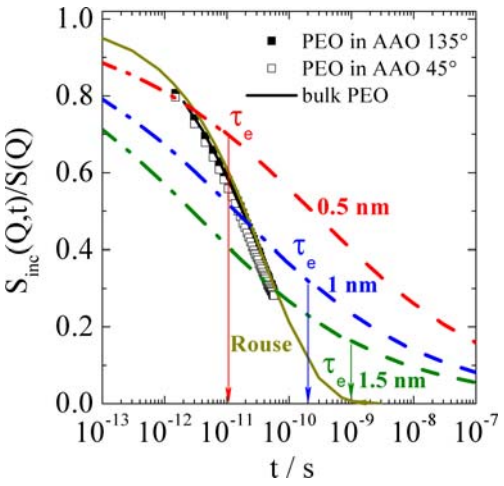

FIG. 3: Comparison of time-of-flight data for PEO in AAO pores (both sample orientations) and bulk PEO for $\left|\vec{Q}\right| = 0.6\text{Å}^{-1}$ at 375K with theoretical predictions calculated for tube diameter of 0.5, 1 and 1.5 nm relating to entanglement time τ_e of 0.012, 0.19 and 0.98 ns, respectively. Rouse self-correlation function is presented by the solid line.

The authors thank G. J. Schneider (Jülich Centre for Neutron Research - JCNS) and T.Unruh (Forschungsneutronenquelle Heinz Maier-Leibnitz - FRM-II) for scientific and technical support of the experiments.

Financial support from NoE SoftComp, Donostia International Physics Center and Spainish Ministerio de Educación y Ciencia is gratefully acknowledged.

[1] M. Krutyeva, J. Martin, A. Arbe, J. Colmenero, C. Mijangos, G. J. Schneier, T. Unruh, Y. Su, D. Richter, J. Chem. Phys. **131**, 174901 2009.

[2] N. Fatkullin et al., N. J. Phys. **6**, 46, 2004.

[3] A.-C. Genix, A. Arbe, F. Alvarez, J. Colmenero, L. Willner, and D. Richter, Phys. Rev. E 72, 031808 2005.

[4] F. Kohlrausch, Pogg. Ann. Phys. **119**, 352, 1863; G. Williams and D. C. Watts, Trans. Faraday Soc. **66**, 80, 1970.

[5] D. Richter, M. Monkenbusch, A. Arbe, J. Colmenero, Adv. Polym. Sci. 174, 1, 2005.

Polymer/silica hybrid nanoparticles via anionic polymerization

E. Hübner, J. Allgaier, M. Meyer, J. Stellbrink, W. Pyckhout-Hintzen, D. Richter

IFF-5: Neutron Scattering

We report on a new "grafting to" technique for the functionalization of silica particles with anionically produced polymers [1]. In the first step the silica nanoparticles were modified with multifunctional chlorosilanes. In the second step the anionically synthesized polymers were linked to the Si-Cl functionalized nanoparticle surface. Both the chlorosilane functionalization of the nanoparticles and the subsequent reaction with living polymer can be carried out without irreversible particle aggregation. The raw products were purified by a simple fractionation procedure. The new anionic based method offers the possibility for grafting densities up to 1 chain per nm^2 of particle surface which is significantly higher than reported in the past for other "grafting to" approaches. Our approach offers the possibility to obtain hybrid materials containing polymers which are not accessible via controlled radical techniques like polydienes. In addition the new technique allows grafting polymers of molecular weights up to 500,000 g/mol and still narrow molecular weight distributions.

Core-shell hybrid nanoparticles usually consist of an inner solid and inorganic core surrounded by a soft polymer shell. Typical examples for the inner part are SiO_2 or Fe_2O_3 while the shell is based on polymers such as polystyrene [2]. Frequently, the interest of such materials is focused on the properties of the core material, in terms of optical or magnetic properties whereas the polymer shell acts as a compatibilizer to render the inorganic substrate dispersible in a matrix polymer. Interactions of the polymer shell with the matrix become more important with increasing shell thickness.

To access such hybrid nanoparticles, two synthetic pathways are known: "grafting from" and "grafting to". The "grafting from" approach starts with the covalent attachment of a polymerization initiator onto the particle surface and subsequent addition of monomers. The following polymerization is mainly based on controlled radical polymerization techniques. Limitations are interparticle cross-linking, higher polydispersities especially for higher molecular weights and reactive chain-ends. The second synthetic pathway uses the "grafting to" approach. In this technique, the polymer is synthesized first. After functionalization, the chain ends are covalently attached to the particle surface. Due to the slow reaction of the linking groups the measured grafting densities are low.

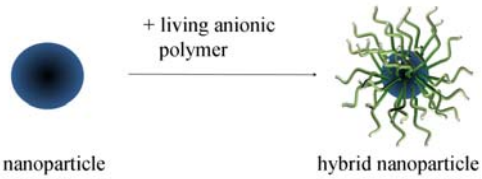

FIG. 1: New approach towards hybrid nanoparticles.

Here, we report a new "grafting to" technique for the functionalization of silica particles using anionic polymerization. It is based on a two-step procedure. In the first step the silica particles were modified with chlorosilanes. In the second step anionically synthesized polymers were linked to the nanoparticles (Fig. 2). The reaction of the highly re-active carbon-lithium head-groups with the chloro-silane surface groups was studied as a function of the chlorosilane functionalization, the polymer molecular weight and the nature of the head group.

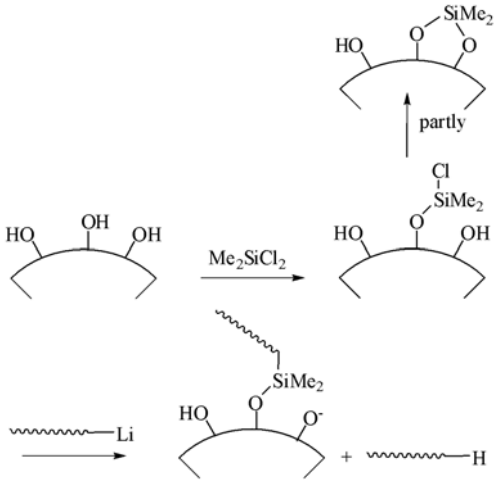

FIG. 2: Concept for the synthesis of polymer/silica hybrid nanoparticles using Me_2SiCl_2 as chlorosilane.

The core material used in this work is based on commercial silica with a mean radius of 10 nm. The nanoparticles are stabilized with organic groups (O-$SiMe_3$) on the surface to achieve solubility in the

organic solvent like n-butylacetate. This modification leads to roughly 4-5 remaining Si-OH groups on the particle surface. The surface Si-OH groups where functionalized with different chloro-silanes: Me_2SiCl_2, a mixture of Me_2SiCl_2 and Me_3SiCl in the molar ratio of 1:3, $SiCl_4$, and $SiMe(CH_2CH_2CN)Cl_2$. In case of Me_2SiCl_2 this leads to a surface providing O-$SiMe_2Cl$ end-groups, which are reactive towards living anionic polymers. The surface density was determined by analysis of the chlorine content to be 1.12 Si-Cl bonds per nm^2. The substitution of 3/4 of the Me_2SiCl_2 by Me_3SiCl leads to lower (0.36 Si-Cl/nm^2) and the usage of $SiCl_4$ to higher (5.06 Si-Cl/nm^2) Si-Cl densities. As a side reaction, the bridging of two adjacent Si-OH groups on the particle surface by the at least bifunctional chlorosilane was noticed (Fig. 2) and further analyzed using $SiMe(CH_2CH_2CN)Cl_2$.This compound allows distinguishing between silane molecules having reacted with one or two Si-OH groups. The fractions could be calculated to be 61% single bound and 39% double bound. The absence of irreversible particle aggregation or cross-linking of particles via the chlorosilanes was investigated by dynamic light scattering (DLS). The results revealed the particle size to be unchanged during the reaction although in case of the functionalization with Me_3SiCl/Me_2SiCl_2 the reaction product precipitated during the functionalization, but was resolubilized during the following synthetic steps.

The chlorosilane functionalized nanoparticles were reacted with an excess of a solution of living anionic 1,4-polybutadienyllithium (PB-Li) in benzene with molecular weights between 13 000 and 589 000 g/mol (Fig. 2).

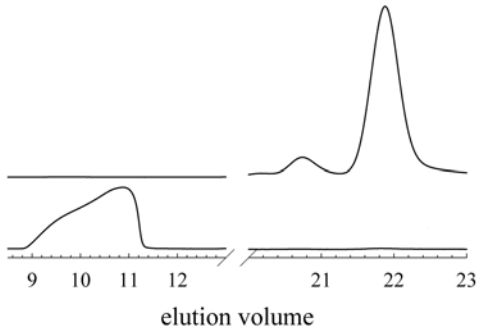

FIG. 3: SEC chromatograms of the reaction product after fractionation. Upper trace: soluble free polymer; lower trace: precipitated functionalized nanoparticle product.

By monitoring the reaction with size exclusion chromatography (SEC) a decrease of the amount of free polymer was noticed with ongoing reaction. In a first experiment a molecular weight of 15 300 g/mol was used in a 1.5 fold excess. According to the SEC 43% of the PB-Li was linked to the particle surface. This corresponds to a degree of functionalization of the Si-Cl binding groups of 65%. The unreacted polybutadiene was found to be terminated, possibly by the reaction with remaining Si-OH groups which were still present on the nanoparticle surface (Fig. 2). A fractionation with a mixture of toluene and methanol allowed separating the polymer functionalized particles from the free polymer to achieve the pure hybrid nanoparticles (Fig. 3). The pure material was further characterized by elemental analysis to determine the exact amount of bound polymer. This allowed calculating functionalization degree to be 54%, which is in good agreement with the SEC results. This translates to 0.6 polymer chains per nm^2 or 760 polymer chains per particle. Compared to other "grafting to" approaches, this is a high grafting density and can be compared to the grafting densities reached by "grafting from" techniques. Further experiments allowed modifying the grafting density by varying the molar ratio of Si-Cl to PB-Li and using chlorosilane functionalized nanoparticles with higher and lower Si-Cl surface densities. Both measures allowed varying the polymer density between 0.5 and 1.0 chains/nm^2. Furthermore, the molecular weight of the polybutadiene was increased to 105 000 g/mol without any decrease of the grafting density (0.7 chains/nm^2), which again is in contrast to other "grafting to" methods. Polybutadiene with a molecular weight of 589 000 g/mol was still found to react with the nanoparticle surface, although leading to a lower grafting density of 0.2 chains/nm^2. DLS as well as small angle X-ray scattering revealed the absence of particle aggregation and demonstrated the size of the particles to grow with increasing molecular weight with a shell thickness significantly larger then the diameter of the corresponding free chain in solution. The shell thickness in a good solvent for particles with the same grafting density was found to scale with $N^{0.6}$ (N = number of monomers) which is equal to the scaling of free polymer chains in a good solvent. Therefore, the stretching of the chains on the particle surface is independent of the molecular weight but depends on the grafting density. As a comparison to known hybrid particles, polystyryl-lithium with a molecular weight of 10 100 g/mol was grafted as well, leading to a grafting density of 0.5 chains/nm^2which could be enhanced to 0.7 chains/nm^2 by end-capping of the polystyrene chains with four units of butadiene.

Current work focuses on the synthesis of hybrid particles with a partially deuterated shell, which are hardly accessible by other synthetic methods and subsequent analysis by neutron scattering.

[1] E. Hübner, J. Allgaier, M. Meyer, J. Stellbrink, W. Pyckhout-Hintzen, D. Richter, *Macromolecules* **2010**, *43*, 856-867.

[2] S. M. Gravano, T. E. Patten In *Macromolecular Engineering: Precise Synthesis, Materials Properties, Applications*; K. Matyjaszewski, Y. Gnanou, L. Leibler, Wiley-VCH: Weinheim, **2007**; Vol. 2, Chapter 12, 1179-1207.

Kinetics of micelle formation

L. Willner[1], R. Lund[2], M. Monkenbusch[1], P. Panine[3], T. Narayanan[3], J. Colmenero[2], D. Richter[1]

[1] IFF-5: Neutron Scattering
[2] Donostia International Physics Center (DIPC), Donostia - San Sebastian, Spain
[3] European Synchrotron Radiation Facility, Grenoble, France

The route by which amphiphilic molecules self-assemble into nano-scale objects such as micelles is still not fully understood. The formation of block copolymer micelles in selective solvents occurs spontaneously usually in the subsecond range. By means of synchrotron x-ray scattering with millisecond time resolution we got direct structural information *in-situ* on the birth and growth of block copolymer micelles. Using a quantitative model we showed that the self-assembly process can be viewed as a primary micellization and growth process where the elementary growth mechanism is the exchange of single unimers.

A classical example and a model system for self-assembly are amphiphilic diblock copolymers that undergo micellization in aqueous solution [1]. The morphology of such systems has been widely studied during the past, a detailed understanding of the mechanism and kinetic pathways of the self-assembly process has not been reached to date. This is primarily due to the lack of experimental techniques having the correct spatial and temporal resolution with the combination of a suitable well-defined model system. In addition there is a prominent lack of detailed physical modelling of the data. Thus so far, results remain largely inconclusive.

In this work [2] we show that the required nano-scale spatial resolution and millisecond temporal resolution could be achieved for an *in situ* investigation by using synchrotron x-ray scattering. The self assembly process of a model amphiphilic block copolymer system was triggered by an interfacial tension jump experiment by rapidly changing the solvent quality for one of the blocks. Using a detailed quantitative model we further demonstrate that the kinetic pathway proceeds by unimer exchange where only single chains are added or removed at a time.

As a model system we employed a well-defined poly(ethylene-*alt*-propylene -poly(ethylene oxide) (PEP1-PEO20, numbers indicate the approximate molecular weight in Kg/mole)block copolymer. This block copolymer forms starlike micelles in water and water/dimethylformamide(DMF)mixtures which are both selective solvents for PEO [3]. A large difference in interfacial tension, γ, with respect to PEPallows an effective tuning of the micellization properties by varying the solvent composition. In pure DMF only single chains (unimers) are present but as soon as some water is added the block copolymers spontaneously aggregate into micelles. This phenomenon was exploited by rapidly mixing a DMF solution with unimers with water/DMF pure solvent mixture by means of a stopped flow apparatus. The stopped flow set-up was coupled to the small angle x-ray scattering (SAXS) instrument at the high brilliance beamline, ID02, at the European Synchrotron Radiation Facility (ESRF) allowing a synchronization of extremely fast mixing (4.5ms) with rapid data acquisition. We chose an optimized acquisition time of 20 ms.

A typical example of the time evolution of the scattering curves is presented in Figure 1. The data were obtained from a solution containing a total volume fraction of 0.25% block copolymer in a solvent mixture with 90 mole% DMF.

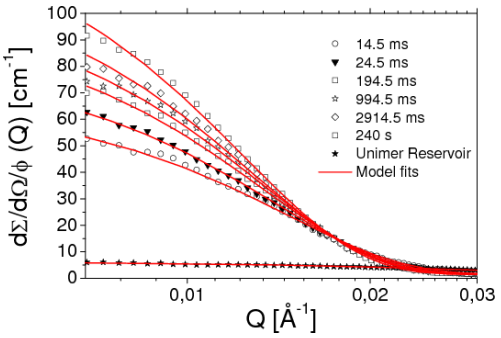

FIG. 1: Normalized absolute scattering cross sections at different times during the kinetics for the PEP-PEO system at a final polymer concentration of 0.25%. The solid lines display fit results from a standard core/shell model.

The induced self-assembly process causes a strong increase in intensity directly reflecting the growth of the micelles in real time. The scattering data were analysed using a standard core shell model describing the detailed structural features of both the inner PEP core and the outer PEO corona of starlike micelles. The solid lines in Figure 1 represent fit results of the core/shell model. The excellent agreement indicates that at all times a starlike structure is adopted. An important parameter which can be extracted by the model fit is the mean aggregation number, P_{mean}. The growth of the micelles in terms of an increasing

P_{mean} is shown in Figure 2 on logarithmic time scale for three different concentrations.

Qualitatively the evolution of P_{mean} can be summarized as follows: At shortest times the data suggest the existence of a fast initial aggregation ($t<\approx 5ms$) that cannot be entirely resolved experimentally. This process becomes exhausted at intermediate times leading to a "shoulder" of P_{mean}that changes with concentration.

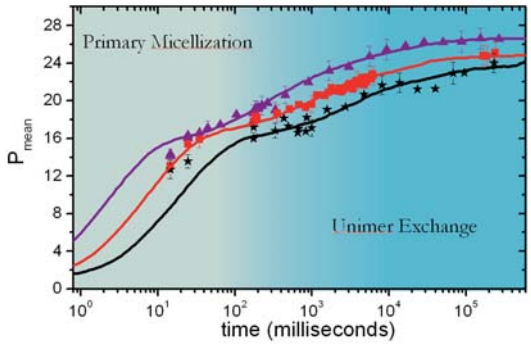

FIG. 2: Time dependence of the aggregation number, P_{mean}, extracted from the fits for three polymer volume fractionson a logarithmical time scale: 0.125% (stars), 0.25% (squares), and 0.5% (triangles). Solid lines represent a fit using the kinetical model described in the text.

The terminal relaxation towards a common equilibrium slows down with time. The overall rate increases with concentration.

In order to quantitatively discuss the experimental data we have derived a kinetic model that involves simple unimer exchange as the single elementary growth step:

$$M_P + U \underset{k_-}{\overset{k_+}{\rightleftharpoons}} M_{P+1}$$

with M_P as the number of micelles of size P and $U$the number of unimers. k_+/k_- denote the insertion and expulsion rate constants which both depend on P. Within the context of classical nucleation and growth theories [4, 5] the formation and growth of the polymeric micelles is governed by the micellization potential, $G(P,\phi_1)$ (ϕ_1=unimer volume fraction),which in our case was taken as the difference of the free energy of a starlike micelle and an equivalent amount of unimers taking properly into account the translational entropy. Following Neu et al. [5] we assume the validity of the "detailed balance" or "microscopic reversibility" principle, which gives a net creation rate in terms of the concentration, ϕ_{P+1}, and flux, j_{P+1}:

$$j_{P+1} = k_+(P)\phi_1\left[\phi_P - \phi_{P+1}\exp\left(G(P+1,\phi_1) - G(P,\phi_1)\right)\right]$$

which is only determined by the insertion rate constant k_+ and the potential $G(P,\phi_1)$. The whole micellar evolution can then be calculated by solving a system of differential equations which was done numerically by using standard routines and by fitting to the experimental data. Fit results are shown as solid lines in Figure 2. All concentrations could almost perfectly be described by a consistent set of parameters. The parameters nicely compare with macroscopically determined quantities, e.g. the interfacial tension, γ, between PEP and water/DMF was found to be 19mNm compared to 12mNm obtained by pendant drop tensiometry.

The kinetic pathway from unimers to the final micelle is schematically depicted in Figure 3. The initial free unimers are rapidly consumed in a primary micellization event as shown in region leading to classical overnucleation. Consequently, metastable micelles with a broader size distribution are obtained in region II corresponding to the shoulder in P_{mean} at intermediate times in Figure 2. A further growth of the micelles requires that some of them, particularly the smaller ones, disassemble to provide unimers. At later times in region III the equilibrium is approached with a narrow size distribution of the final micellar entity.

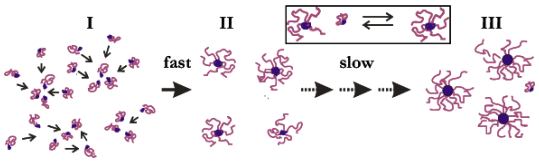

FIG. 3: Schematic view of the kinetic pathway in the formation of polymeric micelles.

In summary, the kinetics of formation of block copolymer micelles have been directly observed *in situ* by synchrotron small angle X-ray scattering with millisecond time resolution. Applying a quantitative model, we see that the formation and growth of micelles can accurately be described by a primary micellization and growth process governed by single unimer exchange mechanism. The contribution of other more complicated mechanisms, like fusion and fission, cannot entirely be excluded, however, the experimental data are sufficiently explained by insertion/expulsion of a single chain at a time.

[1] Hamley , I. W. The Physics of Block Copolymers, Oxford University Press, Oxford , UK (1998).

[2] Lund, R. et al. Phys. Rev. Lett., **102**, 188301 (2009).

[3] Lund, R. et al. Macromolecules, **39**,4566 (2006).

[4] "Nucleation Theory and Applications" (J.W.P. Schmelzer ed.), Wiley-VCH Verlag GmbH & Co., KGaA, Weinheim (2005).

[5] Neu, J.C. et al. Phys. Rev. E, **66**, 061406 (2002).

Internal dynamics in self-assembled PI-PDMS block copolymers

L. Willner[1], R. Lund[3], M. Monkenbusch[1], O. Holderer[2], J. Colmenero[3], D. Richter[1]

[1] IFF-5: Neutron Scattering
[2] JCNS: Jülich Centre for Neutron Science
[3] Donostia International Physics Center, Paseo Manuel de Lardizabal 4, 20018 Donostia - San Sebastian, Spain

We investigated the internal dynamics of a nano-structured block copolymer melt obtained by self-assembly of polyisoprene-*block*-polydimethylsiloxane, PI6-PDMS30 (numbers denote molecular weight in kD)[1]. Due to the asymmetric composition of the immiscible components this diblock copolymer forms hexagonally ordered cylinders of PI in a continuous matrix of PDMS polymer. By neutron spin echo (NSE) spectroscopy and using two different contrasts we were able to highlight the PI single chain dynamics and the dynamics of the interface between PI and PDMS polymer individually. Combining the results the dynamics can be consistently described in terms of Rouse motion modified by surface fluctuation and laterally restricted 2D surface diffusion.

For AB Diblock Copolymers with thermodynamically incompatible blocks microphase separation is observed when $\chi \cdot N \gg 10.5$, with χ the Flory-Huggins interaction parameter and N the overall degree of polymerization. Segregated AB diblocks generally show a variety of equilibrium morphologies which can be either spherical, cylindrical, lamellar or bicontinuous depending on the block composition[2]. While the structure has been extensively investigated in the past[3], only a few studies have been devoted to the dynamics in particular to the polymer dynamics in these systems[4]. One of the open questions is how the Rouse or Reptation type dynamics of homo polymer melts is affected by the presence of the interface and the junction zone in such self-assembled morphologies. In particular the geometrical confinement may play a role. To get access to the internal dynamics we have applied neutron spin echo spectroscopy combined with sophisticated H/D contrast variation schemes. In contrast to other techniques, e.g. NMR or forced Rayleigh scattering, NSE directly probes the relevant time (∼ps - 500ns) and length scales (∼nm)[5]. AB diblocks of the PI-PDMS type were chosen as model system for this study. Two differently labeled block copolymers were prepared by sequential application of living anionic polymerization, h-PI6-d-PDMS30 and d-PI6-d-PDMS30, with almost identical polymer characteristics. SANS-measurements of the h-PI6-d-PDMS30 revealed a hexagonally packed cylindrical morphology. In order to extract detailed information about single chain and overall interfacial dynamics two contrast situations were applied for the NSE experiments. The first 'single chain' contrast highlights the scattering from individual PI chains without contributions arising from contrast between the bulk polymer domains. This was achieved by a blend of the two block copolymers containing 24% of the h-PI6-d-PDMS30. With this composition the scattering length density of d-PDMS is exactly matched by the average of h-PI6/d-PI6. The second is the 'bulk contrast' obtained with pure h-PI6-d-PDMS30 block copolymer. The main scattering from this sample stems from the cylinder arrangement observed at very low Q, below the NSE range. The scattering intensity seen in the NSE experiments in this case originates from local intermixing of h-PI and d-PDMS segments. The intermixed region is of the order of $\sim$ 1 nm. Therefore, at large Q where the NSE experiments were performed the intensity stems predominatly from the contrast fluctuations in the intermixing zone. The two different contrast conditions are illustrated in Figure 1.

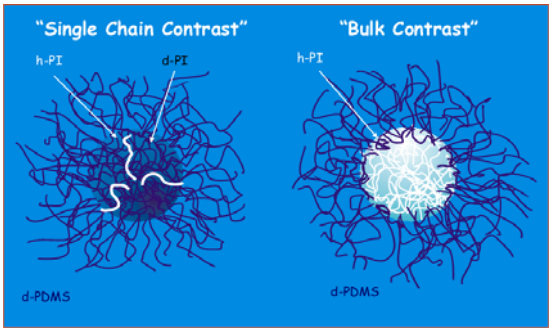

FIG. 1: Visualization of single chain and bulk contrast used for NSE experiments.

To take into account the salient features of polymer motion in the samples the NSE data were analyzed by model expressions involving Rouse dynamics, segmental diffusion and surface undulation. Figure 2 illustrates possible dynamical processes present in the cylindrical block copolymer system: 2c indicates local undulations of the interface (capillary waves) that causes fluctuations of the polymer linking point in z-direction and in addition a two dimensional diffusion along the interface in the xy-plane; 2b depicts the center of mass chain diffusion process affected by the movement of the linking point on the cylinder

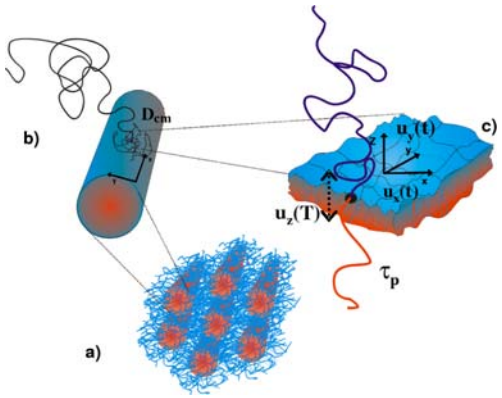

FIG. 2: Illustration of possible dynamical processes occuring in the cylindrical morphology of the PI6-PDMS30 block copolymer.

surface; 2a shows the hexagonally packed cylindrical morphology of the PI6-PDMS30 block copolymer. The center of mass diffusion of individual cylinders needs not to be taken into account because it is much slower than would be observable in the presently considered time scale.

Depending on contrast the above discussed dynamical processes contribute differently to the scattered intensity of the NSE experiments. In bulk contrast, which is sensitive to the interface, the surface undulations and the segmental diffusion within the interface plane are the important motions determining the relaxation of the NSE intensity. Therefore the employed model essentially accounts for these motions to sufficiently describe the data. The analysis allows to determine the interfacial tension and the local viscosity damping the indulations. The single chain contrast on the other hand is more sensitive to the motions of individual PI chains inside the cylindrical domains. In order to understand the corresponding dynamics the model is composed of three basic ingredients: i) the Rouse dynamics of the PI chain fixed on one end at the interface; ii) the movement of the linking section due to the undulations and the 2D diffusion along the interface directly influencing the PI chain dynamics; and iii) a residual center of mass diffusion of the whole PI-PDMS block copolymer. Bulk contrast and single chain contrast cannot be independently described. They were alternatingly fitted to get a complete description of the data with a consistent set of parameters. These parameters were essentially the Rouse parameter, $WI^4 = 5650\,Å^4$/ns, the interfacial tension, $\gamma = 4.5\,m$N/m and an effective interfacial viscosity, $\eta = 1.5 \cdot 10^{-2}$ Pas. The Rouse parameter is very similar to the value obtained from a PI homo polymer blend which was separately measured as a reference. The values for γ and η are close to values obtained from other experiments or to theoretical prediction indicating the validity of the model approach. The excellent fit quality can be seen from Figure 3 where scattering curves (symbols) and corresponding model fits (red lines) are shown for both contrast. It should be noted that model fits without contribution from the surface undulations and Rouse segmental diffusion considerably deviate from the measured

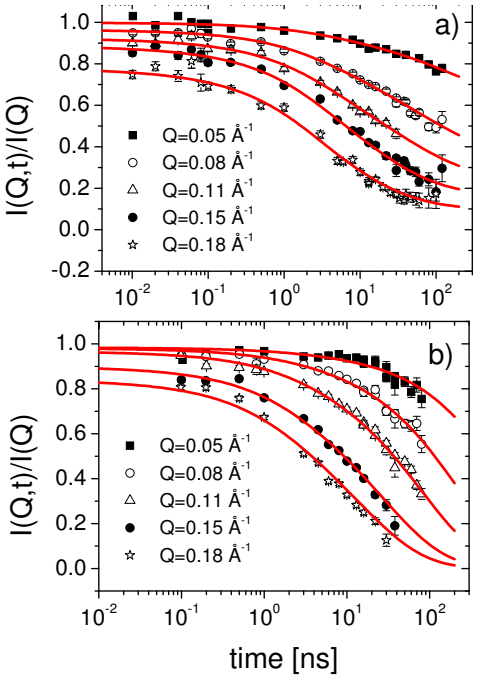

FIG. 3: Neutron spin echo data of PI6-PDMS30 in bulk a) and single chain contrast b) at different Q values. Red lines represent corresponding model fits.

data indicating the importance of these processes to the overall dynamics.
Concluding we may say that the observed dynamics for both contrasts could consistently be described by a combination of known capillary wave effects, Rouse dynamics, segmental and center of mass diffusion. No significant influence of the confinement (beyond anchoring of the junction to the interface) has been observed.

[1] L. Willner, R. Lund, M. Monkenbusch, O. Holderer, J. Colmenero and D. Richter *Soft Matter*, DOI:10.1039/B922649D

[2] F. S. Bates and G. Fredrickson *Phys. Today*, 1999, **52** 1999, 32.

[3] I. W. Hamley *The Physics of Block Copolymers*, Oxford University Press, Oxford, UK **1998**.

[4] H. Montes M. Monkenbusch, L. Willner, S. Rathgeber, D. Richter, L. J. Fetters and B. Farago *Europhys. Lett.*, 1998 **58**(3), 398.

[5] D. Richter, M. Monkenbusch, A. Arbe and J. Colmenero *Neutron Spin Echo in Polymer Systems*, *Adv. Polym. Sci.*, 2005, **174**, Springer, Berlin, Germany.

MD simulations and neutron scattering experiments on PEO/PMMA blends

M. Brodeck[1], R. Zorn[1], F. Alvarez[2,3], J. Colmenero[2,3,4], D. Richter[1]

[1] IFF-5: Neutron Scattering
[2] Centro de Física de Materiales, CSIC-UPV/EHU, San Sebastián
[3] Departamento de Física de Materiales, UPV/EHU, San Sebastián
[4] Donostia International Physics Center, San Sebastián

Polymer blends offer an excellent possibility to engineer materials with specific properties by mixing different components and using e.g. the mixing ratios as an adjustable parameter. One of the simplest forms is a binary blend consitsting of two different polymers. The study of these systems is highly interesting because only the detailed microscopic knowledge of the behavior of such a system allows the selective change of macroscopic parameters.

The polymer blend PEO/PMMA is a typical example for dynamically asymmetric polymer blends. Both components, polyethyleneoxide (PEO) and polymethylmethacrylate (PMMA), are characterized by significantly different glass transition temperatures T_g with ΔT in the order of 200 K. At the same time, both components are fully miscible forming a stable polymer blend within a wide range of temperatures. The behavior of the polymers at temperatures between the glass transition temperatures of the two components is of particular interest. The low T_g component (PEO) is found in a mobile situation while the other component (PMMA) forms a rather stiff matrix. The question addressed in this work concerns the dynamic behavior of PEO in this PMMA environment in comparison with the behavior of the pure PEO polymer. The temperature of the system offers a parameter to tune the stiffness of the PMMA matrix: as T is increased the glass transition of PMMA is approached and the chains become more flexible.

We have investigated the system by combining MD simulations and neutron scattering experiments. Both methods have access to similar length- and timescales which allows us to validate the simulated systems with a comparison to neutron scattering experiments. By chemically labeling the chains with deuterium instead of hydrogen atoms we can experimentally highlight different aspects of the polymer blend such as the self-motion of single hydrogen atoms or the general relaxation of the chains in their environment. After this verification we can directly study the motion of the chains by looking at the coordinates in real-space. In addition, the limits of different polymer models for these systems can be examined.

The simulated systems contains 5 PEO chains ($M_w = 2$ kg/mol) and 15 PMMA chains (the weight ratio of PEO is 20%). Temperatures of 300, 350, 400 and 500 K were investigated to cover temperatures below and above T_g of PMMA (400 K). The system was validated by comparing the single chain dynamic structure factor of the PEO chains calculated from these simulations with neutron spin echo (NSE) measurements. Therefore, the investigated sample had to highlight the correlation of single PEO chains within the surrounding environment. To achive this contrast we have mixed 10% protonated PEO chains with 10% deuterated PEO and 80% deuterated PMMA. The resulting relaxation function contains contributions from the motion of PEO in comparison to the other PEO chains as well as an almost constant contribution from the rather frozen PMMA matrix. The exact composition of the relaxation function can be calculated using the dynamic random phase approximation.

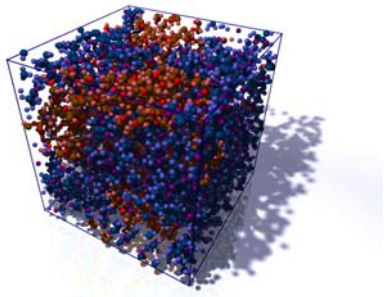

FIG. 1: The simulated system contains 5 PEO chains and 15 PMMA chains. Periodic boundary conditions are applied during the simulation, the size of the cell is fixed.

Figure 2 shows the comparison between simulation and experiment at $T = 400$ K and two different Q-values. The agreement is excellent, small deviations are only found at higher times where the statistical significance of the simulation is significantly reduced (the total simulation time is $t_{max} = 100$ ns). Due to the short chain length the exact chemical composition of the (always protonated) head-groups of the polymer chains has to be taken into account when calculating the relaxation functions using the MD simulations.

After the verification of the simulated system we can now proceed to a detailed analysis of the PEO motion in context of the Rouse model. This model starts

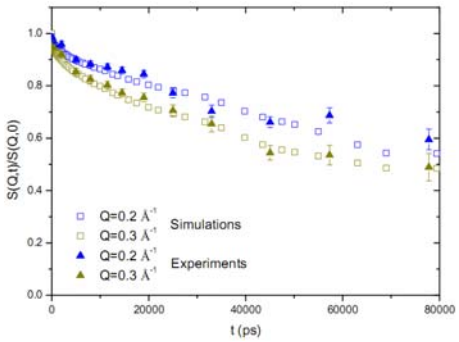

FIG. 2: Comparison of the single chain dynamic structure factor calculated using the MD simulations (hollow symbols) and measured by NSE (full symbols) at 400 K.

from a Gaussian chain representing a coarse grained polymer where springs stand for the entropic forces between hypothetic beads and a constant local friction coefficient is assigned to each bead [1]. The analytical solution of this problem is given by normal coordinates of the beads: higher modes express correlations between few beads while low modes express the overall motion of the chain. The Rouse model now predicts an exponential decay of these correlators with a characteristic time $\tau_p \propto p^{-2}$. We have recently shown that the pure PEO system nicely follows these predictions independent of the temperature [2]. Only small deviations are found for the higher modes where the simple model breaks down due to the complex local chemical composition of the chains.

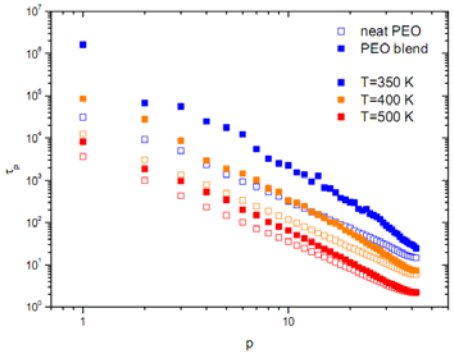

FIG. 3: Characteristic Rouse times for pure PEO (hollow symbols) and for PEO in PMMA (full symbols). The PEO chains in the PMMA environment are significantly slower compared to the pure system. This effect is increased as the temperature is decreased.

For PEO in PMMA, however, strong deviations are found. As the temperature of the system is decreased, the dynamic asymmetrie between the two polymers increases. Figure 3 shows a comparison of the the characteristic relaxation times τ_p in depence of the mode p for the two systems at different temperatures. For lower temperatures the motion of PEO in PMMA is slowed down significantly. This discrepancy is especially distinct for the lower modes. The higher modes, corresponding to the very local motion of the chain, are less affected. Similar results were also found in bead-spring simulations by A. Moreno who modeled the dynamical asymmetrie by introducing chains with two different monomer sizes corresponding to the fast and the slow component. The agreement between the atomic and these coarse grained simulations hints at a generic origin of this effect.

These results can be interpretated by assuming that the friction coefficient, which is connected to the local environment of each bead, depends on the concentration of PMMA molecules that surround the PEO monomers. In the past, the single chain dynamics structur factor of PEO in PMMA was measured by NSE at different temperatures and successfully fitted by the Rouse model assuming a random log-normal distribution of friction coefficients (random Rouse model) [3]. The idea is that some PEO beads inside the PMMA rich environment are slowed down by the frozen matrix. A high friction is assigned to these beads which slows down the relaxation of the whole chain. Calculations with these assumptions have shown that this model can qualitatively describe the immense increase of the relaxation times for the low modes while the higher modes are less affected. The limits of this model are reached if the PMMA matrix can not be assumed to be completely frozen. Once a low ammount of mobility is reached the local environment of a single PEO bead will change over time and the corresponding friction coefficient decreases. To allow for these effects a memory kernel has to be introduced.

In summary, the presented MD simulations of PEO/PMMA show an excellent agreement with NSE results establishing a quantitatively valid system for further analysis. The direct investigation of the motion in real space further allowed us to study the dynamic effect of the PMMA matrix and test the validity and limits of the random Rouse model.

Acknowledgments: This research project has been supported by the European Commission NoE SoftComp, Contract NMP3-CT-2004-502235, and the 'Donostia International Physics Center'. We thank Y. Su (JCNS), O. Holderer (JCNS) and N. de Souza (JCNS) for experimental help.

[1] P. E. Rouse, A theory of the linear viscoelastic properties of dilute solutions of coiling polymers, Journal of Chemical Physics **21(7)**, 1272-1280, (1953).

[2] M. Brodeck, F. Alvarez, A. Arbe, F. Juranyi, T. Unruh, O. Holderer, J. Colmenero, and D. Richter, Study of the dynamics of poly(ethylene oxide) by combining molecular dynamic simulations and neutron scattering experiments, J. Chem. Phys. **130**, 094908, (2009).

[3] K. Niedzwiedz, A. Wischnewski, M. Monkenbusch, D. Richter, A.-C. Genix, A. Arbe, J. Colmenero, M. Strauch, and E. Straube, Polymer Chain Dynamics in a Random Environment: Heterogeneous Mobilities, Phys. Rev. Lett. **98**, 168301, (2007).

[4] A. J. Moreno and J. Colmenero, Entangledlike Chain Dynamics in Nonentangled Polymer Blends with Large Dynamic Asymmetry, Phys. Rev. Lett. **100**, 126001, (2008).

Chemical denaturation of Myoglobin observed by SANS on KWS-2

M. S. Appavou[1], D. Richter[2]

[1] JCNS: Jülich Centre for Neutron Science
[2] IFF-5: Neutron Scattering

In the frame of understanding the folding of proteins, we have investigated the mainly helical structured myoglobin. Guanidinium hydrochloride was used as denaturing agent at several concentrations in order to trap some of the folding intermediates of this protein. Small Angle Neutron Scattering spectroscopy allows to characterize these intermediates by applying polymer physics theory: by the extrapolated radius of gyration in the Guinier regime, the intermolecular interactions using the Zimm approximation and using the Kratky representation of the scattered intensity.

Proteins can be assumed as heteropolymers composed by a sequence of amino acid residues which have different chemical properties. According to their position along the main backbone and involving hydrogen bonds, they induce a specific folding into secondary (alpha helix, beta sheet, turns ...) and tertiary structures related to the function of the protein [1]. Proteins acquire this three-dimensional native structure in few seconds probably because they do not explore all the space conformations. Indeed, some parts of the proteins fold more quickly than others and lead to folding intermediates. In a medical point of view, it was shown that degenerative diseases like Alzheimer originate from a misfolding of some proteins which aggregates around some brain receptors. This phenomenon leads to typical symptoms like lake of memory and even trouble in nerve-induced muscle motions. In the frame of understanding the folding of proteins, we have investigated the unfolding of a model protein: the horse heart myoglobin. It is mainly alpha-helix protein which store and make oxygen available in muscle. Guanidinium hydrochloride (GdmCl) was used as denaturing agent at several concentrations in order to get some of the folding intermediates of this protein. Its structure is similar to peptide bond and enters in competition with protein for hydrogen bonding. As a salt, GdmCl induces also electrostatic interactions leading to protein unfolding.

By using SANS techniques, we play with the contrast between the hydrogenated protein and the deuterated solvent. The SANS spectroscopy can allow to access these folding intermediate by applying polymer physics theory [2, 3]. These folding intermediates are characterized at low q values by the radius of gyration extrapolated at null concentration in the Guinier regime [4].

Small angle neutron scattering experiment using the JCNS-KWS-2 spectrometer were performed at room temperature and at atmospheric pressure using a 4,5 Å wavelength and two detector distances : 2 m and 8 m. Then, it is possible to investigate a q-range from 1.10^{-2} to 0,32 $Å^{-1}$. Myoglobin solution in deuterated phosphate buffer 100 mM pD 7.0 were prepared in dilute regime (2,5 to 7,5 mg/mL) in order to extrapolate radius of gyration at null concentration. We have added increasing concentration of deuterated guanidinium hydrochloride into these solutions in order to trap intermediate folding state of the protein. Radius of gyration Rg and forward intesities I(0) were extracted from fit of intensity curve in the Guinier regime using Guinier approximation for the native myoglobin and Debye approximation for the denatured myoglobin.

From Guinier regime investigation, we have observed an increase of the radius of gyration extrapolated at null concentration as far as chemical denaturing agent is added to the protein solution. We recover a radius of gyration of 13,5 $\pm$ 1,0 Å in the native state which values is in agreement with those found in the literature and by simulation. We have obtained a radius of gyration of 32,5 $\pm$ 2,0 Å in presence of 2 M GdmDCl corresponding to an unfolded myoglobin. From the forward intensities and using the Zimm approximation we were able to extract the second virial coefficient related to intermolecular interactions. Zimm plots for myoglobin in the native and fully denaturated state are shown in figure 1.

We have observed repulsive interactions in the native state and GdmDCl inducing the unfolding of the protein leads to attractive interactions by exposing some hydrophobic residues usually buried into the protein. Proteins tend to get together, leading to some aggregation phenomenon for higher protein concentrations.

Large q-range measurements allow us to get information about the shape of the protein as a function of denaturing agent concentration. Figure 2 shows the Kratky representation of the intensity signal for each GdmDCl concentration conditions. It is possible to assign protein intermediate folding state description to some typical polymer behavior. Thus from a bell-shape spectrum characteristic of a native globu-

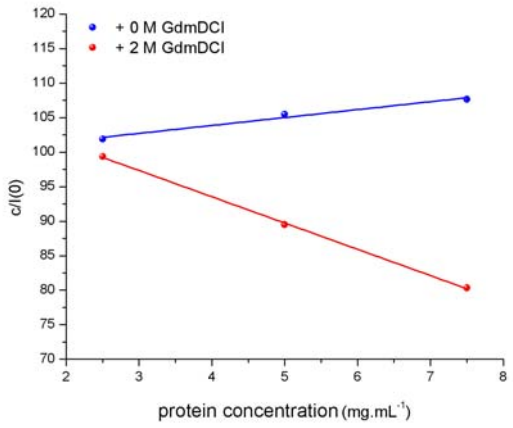

FIG. 1: Zimm representation (c/I(0) = f(c)) for myoglobin in the native (blue : + 0 M GdmDCl) and fully denaturated state (red:+ 2 M GdmDCl).

lar molecule, we can distinguish one kind of molten globule which starts to have a Gaussian like behavior (plateau) until a fully unfolded protein behaving like a polymer in good solvent (proportionality as a function of q).

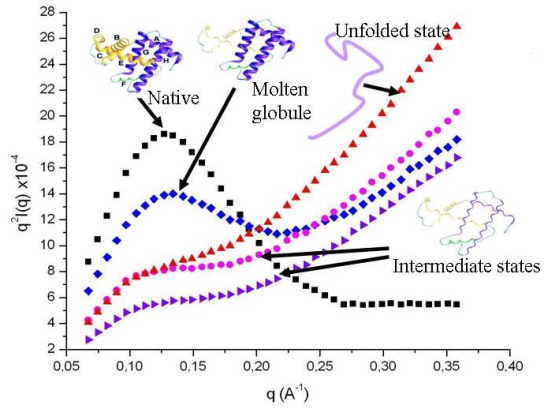

FIG. 2: Kratky representation of the intensity signal for myoglobin in solution at 10 mg/mL at several concentration of GdmDCl. black square : 0 M GdmDCl, blue diamonds : 1,2 M GdmDCl, violet triangle : 1,5 M GdmDCl, pink full circle : 1,8 M GdmDCl, red triangle : 2 M GdmDCl.

We were able to trap some intermediate folding states of a model protein, myoglobin, using a chemical denaturing agent. We have investigated these different states using small angle neutron scattering. As protein can be assumed as heteropolymer, polymer theory was used as a first tool to characterize the different folding states of myoglobin in presence of different concentration of denaturing agent. In the low q-range (Guinier Regime) we have recovered a value of radius of gyration in agreement with those from the literature. Then increasing the denaturing agent concentration, we observe an increase of the Rg from 13,5 $\pm$ 1,0 Å in the native state to 32,5 $\pm$ 2,0 Å for the fully denatured protein. From the forward intensities, one can get information related to intermolecular interactions. The native protein shows a change from repulsive to attractive intermolecular interactions as far as we add some GdmDCl. Indeed, some residues usually buried nearby the core of the protein are exposed and then tend to recover their initial environment by getting together with the other unfolded molecules. This leads to some aggregation phenomenon for high protein concentration. In the larger q-range, we have used a Kratky representation to describe the different folding states of myoglobin trapped by the different GdmCl concentration. From a compact globular molecule in the native state, we define a molten globule state with a larger radius of gyration and a behavior between the native compact globular molecule and a Gaussian chain. The intermediate folding state was found at the mid-point denaturation and looks like a Gaussian chain with an even larger radius of gyration and starts to behave like a polymer like molecule. The early stage folding state seems to have the same behavior as the intermediate folding state. The fully unfolded protein has a similar behavior as a polymer in good solvent. This is essentially due to electrostatic interactions between the GdmDCl and the protein.

[1] C. B. Anfisen, Science, **181**, 273 (1973)

[2] C. Tandford, Adv. Prot. Chem., **23**, 121-282 (1968)

[3] A. Guinier et G. Fournet, Small Angle Scattering of X-Rays (1955)

[4] M. S. Appavou et D. Richter (in preparation) (2010)

Elastic properties of the interfacial membrane in fluctuating supercritical CO_2-microemulsions

O. Holderer[1], M. Klostermann[2], M. Monkenbusch[3], R. Strey[2], D. Richter[1,3], T. Sottmann[2]

[1] JCNS: Jülich Centre for Neutron Science
[2] Institut of physical chemistry, University of Cologne, 50939 Cologne, Germany
[3] IFF-5: Neutron Scattering

Supercritical carbon dioxide ($scCO_2$) has attracted much attention as an environmentally friendly solvent. Recently, bicontinuous microemulsions, containing water, supercritical carbon dioxide and the surfactant, have been formed with certain perfluoro-surfactants. The membrane fluctuations of a surfactant monolayer in such a bicontinuous microemulsion has been measured with neutron spin-echo (NSE) spectroscopy and allowed to determine the membrane rigidity to be 0.4 k_BT in this novel type of bicontinuous microemulsions.

The waste of chemical solvents from chemical processing and related industries represent a huge environmental concern nowadays. During the last decades supercritical fluids have attracted much attention as potential replacements for conventional organic solvents in the field of green chemistry. Among all of these fluids supercritical CO_2 (Tc = 31.1°C, pc = 72.8 bar) is seen as the most promising candidate for a use in green chemistry since it is cheap, abundant, inflammable, non-toxic, bio- and food-compatible. To improve the solvent properties of sc CO_2 especially for polar and/or high molecular weight solutes microscopic dispersions of water and CO_2 in form of thermodynamically stable microemulsion have shifted into the focus of current researches [1]. So far studies on these novel microemulsion systems were concentrated on the phase behaviour and the microstructure of water- and CO_2-rich microemulsions, respectively [1-3]. Recently we were for the first time able to formulate balanced supercritical CO_2-microemulsions containg equal volumes of water and CO_2 using technical grade polyethyleneglycol-perfluoroalkylether surfactants [4]. The phase behaviour of such a microemulsion system H2O/NaCl-$scCO_2$-Zonyl FSH/Zonyl FSN 100 is shown in Figure 1 for various pressures in a range from p = 160 to 300 bar as a function of the overall surfactant mass fraction γ and the temperature T [4]. The mass fraction α of CO_2 has been adjusted to $\alpha = 0.4$.

One applicable method for a direct investigation of the dynamic properties of membrane patches in bicontinuous microemulsions is the use of Neutron spin-echo (NSE) spectroscopy. Furthermore the decay time τ for thermally activated fluctuations of surfactant membrane patches is in the regime of nanoseconds and therewith inside the time window of NSE spectroscopy. The neutron spin-echo experiments on $scCO_2$ microemulsions have been performed at the J-NSE instrument at the FRM II research reactor of the TU München with an in house built high pressure NSE-cell. It delivers the intermediate scattering function S(q,τ), the Fourier transform of the scattering function S(q,ω).

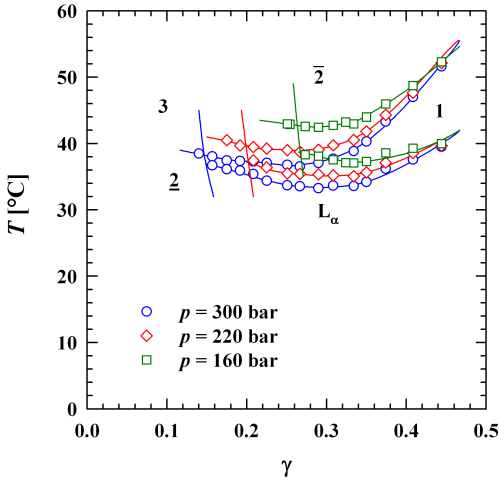

FIG. 1: Phase diagram of the described microemulsion with supercritical carbon dioxide. The pressure varies from 160 to 300 bar.

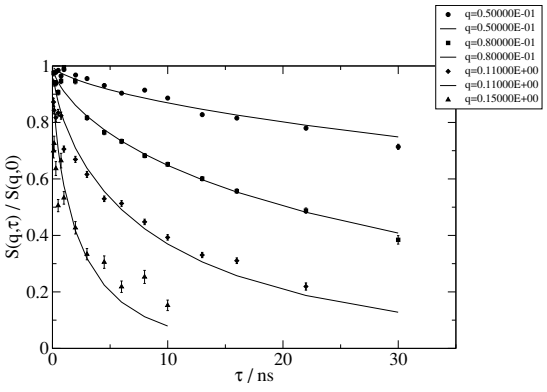

FIG. 2: Intermediate scattering function of a supercritical CO_2-microemulsion at 220 bar and 35 °C measured with the J-NSE.

The fluctuation of membrane patches in "classical" microemulsions at ambient pressure has been described by the theory of Zilman and Granek [5]. It relates the relaxation rate of the membrane to the bending rigidity κ. In an approximation, the intermediate scattering function is described by a stretched exponential function:

$$S(q,\tau) \simeq S(q) exp(-(\Gamma_q \tau)^{\beta}) \qquad (1)$$

with the relaxation rate

$$\Gamma_q = 0.025 \gamma_{ZG} (\frac{k_B T}{\kappa})^{1/2} \frac{k_B T}{\eta} q^3 \qquad (2)$$

whereas η is the viscosity of the solvent that surrounds the surfactant membrane (in this case the average viscosity of water and CO_2). In equation (2) $\gamma_{ZK} = 1 - 3(kBT/4\pi\kappa) ln(q\xi_{TS})$. According to the Zilman-Granek model the stretching exponent β is predicted to be β = 2/3. Fig. 2 shows the intermediate scattering function S(q,τ) of the D2O/NaCl-scCO_2-Zonyl FSH/Zonyl FSN 100 (α = 0.40, δ = 0.50) microemulsion near the optimum point at T = 35 °C, γ = 0.26 and a pressure of p = 220 bar for four different q-values between q = 0.05 and q = 0.15 $Å^{-1}$ (corresponding to length scales in real space of d = 2π/q = 125 - 42 Å). Thus, the dynamics of the surfactant membrane patches is studied on a local scale, smaller then the average membrane-membrane distance of about 150 Å. In this q-region only the single membrane patch dynamics is probed, influences of hydrodynamic interactions with neighbouring membranes are neglected. Fitting the experimental data with the expression of Equation 1 shows that the q^3-dependence of the relaxation rate, which is predicted for bicontinuous microemulsions according to Equation 2, is found also for supercritical CO_2-microemulsion, as well as the typical stretching exponent β= 2/3.

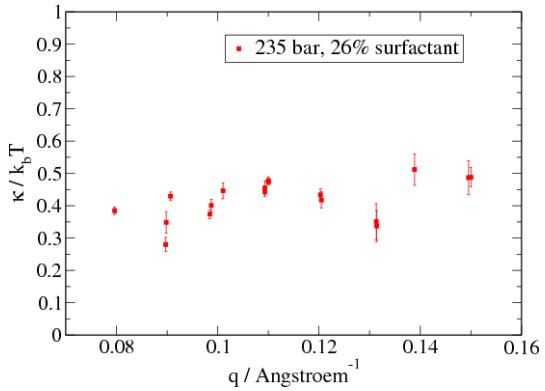

FIG. 3: Bending rigidity as a function of q of a supercritical CO_2-microemulsion at 220 bar obtained from the numerical evaluation of the Zilman-Granek theory.

A quantitative determination of the bending rigidity with the Zilman-Granek theory implies that not all the approximations leading to the Equation 1 are carried out, but numerical integrations of the expression of a fluctuating membrane patch are used instead. The intermediate scattering function S(q,τ) expressed in this framework contains the bending rigidity as only fitting parameter. By integrating explicitly over all undulation wave vectors of the membrane one gets κ without effects of renormalization. Figure 3 shows the bending rigidity obtained from the NSE experiment using the integral version of the Zilman-Granek model of fluctuating patches as a function of scattering vector q.

Comparing κ_{NSE} with the corresponding value from classical microemulsions which is typically 1 k_BT, it is observed that the bending rigidity is significantly smaller.

We demonstrated in this experiment that membrane fluctuations in bicontinuous supercritical CO_2 microemulsions can be measured using high pressure NSE. The obtained relaxation rate is about twice as high as in similar water-oil microemulsions. The bending rigidity has been determined by applying the Zilman-Granek theory with numerical integration over the undulation mode spectrum, yielding a value of 0.4 kBT, which is smaller than in water-oil microemulsions, where the "bare" bending rigidity κ_{bare} is typically about 1 k_BT. Future studies on supercritical CO_2 microemulsions will be directed towards the investigation of the pressure dependence of the membrane fluctuations. Since the viscosity of the supercritical CO_2 domains can be varied at otherwise unchanged conditions a deeper insight into the elastic properties of the membrane is expected. Internal frictions of the membrane or influences of the pressure dependent hydration of the surfactant headgroup will thus be studied in the future.

[1] Eastoe; S. Gold; D. C. Steytler, Langmuir, 2006, 22, 9832-9842.

[2] K. Harrison; J. Goveas; K. P. Johnston; E. A. Orear, Langmuir, 1994, 10, 3536-3541.

[3] M. Klostermann, L. Kramer, T. Sottmann, R. Strey, Langmiur, in preparation.

[4] L. Kramer, M. Klostermann, R. Strey, R. Schweins, P. Lindner, T. Sottmann, Langmuir, in preparation.

[5] A. Zilman, R. Granek, Phys. Rev. Lett., 1996, 77, 4788.

Depletion-induced aggregation and phase separation of colloid-polymer mixtures

C. Gögelein[1,2], G. Nägele[1], J. Buitenhuis[1], R. Tuinier[1,3], J. K. G. Dhont[1]

[1] IFF-7: Soft Condensed Matter
[2] MPI for Dynamics and Self-Organization, Göttingen
[3] DSM Research, ACES, Geleen, The Netherlands

We study polymer depletion-driven cluster aggregation and initial phase separation in aqueous dispersions of charge-stabilised silica spheres, where the ionic strength and polymer (dextran) concentration are systematically varied, using dynamic light scattering and visual observation. At low colloid concentration, we observe an exponential cluster growth rate for all polymer concentrations considered, indicating a reaction-limited aggregation mechanism. At sufficiently high polymer and colloid concentrations, and lower salt content, a gas-liquid-like demixing is observed initially. Later on, the system separates into a gel and fluid-like phase. The experimental time-dependent state diagram is compared with the theoretical equilibrium phase diagram obtained from a generalised free-volume theory and is discussed in terms of an initial reversible phase separation process in combination with irreversible aggregation at later times.

Mixtures of colloids and polymers show interesting equilibrium and non-equilibrium phase behaviour [1]. In thermal equilibrium, the system may macroscopically phase separate into a dilute fluid and a dense fluid or crystalline colloid phase. This is similar to coexisting gas and liquid or crystalline phases in molecular systems. However, in many situations, colloid-polymer mixtures form dynamically arrested colloidal structures out of equilibrium like clusters, gels or glasses. Gels and glasses are non-crystalline, solid-like and long-living macroscopic structures. Equilibrium and non-equilibrium processes have been studied in the past mainly as two well distinct phenomena. However, more recent experiments on colloid-polymer mixtures point to a connection between the spinodal line of the equilibrium phase diagram and the gelation boundary. In fact, strong evidence has been given that spinodal decomposition induces gelation in neutral colloid-polymer mixtures with small polymer-to-colloid size ratios q [2]. Whether the onset of gelation is governed by equilibrium phase separation also at larger q, and for charged colloids at low salinity, has not been explored to date.

In this work, we investigate the aggregation and demixing of mixtures of nanosized Ludox silica particles and dextran polymers in (salty) water [3, 4, 5]. The colloidal particles interact by a short-ranged van der Waals (vdW) attraction and a screened Coulomb repulsion. By varying the salt concentration, we have tuned the Coulomb repulsion and thus, the colloid cluster aggregation rate. The polymer chains add an additional effective attraction to the colloids by the well-known depletion mechanism. The range of the depletion-induced attraction can be tuned by the polymer molar mass. We focus here on the effect of longranged depletion-induced attractions, where $0.49 \leq q \leq 2.6$. For these q-values a (stable) gas-liquid phase coexistence appears in equilibrium. Thus, our system offers the opportunity to study systematically the interplay between phase separation and cluster aggregation of charged colloids by varying the salt and polymer concentrations, c_s and c, respectively, and the colloid volume fraction ϕ. In our system, the gas-liquid demixing is mainly caused by the polymer-induced depletion attraction, whereas the cluster aggregation is induced by the vdW forces.

Using dynamic light scattering (DLS), we study the initial aggregation of dimers as quantified by the collective diffusion coefficient from which the time-dependent cluster size and the cluster growth rate

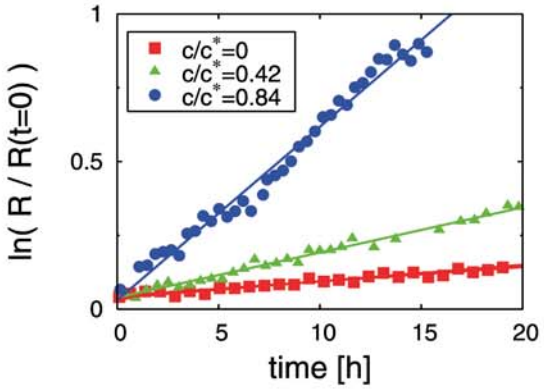

FIG. 1: Semi-logarithmic plot of the reduced effective hydrodynamic radius of colloid clusters as a function of elapsed time, for a mixture of silica spheres at ϕ = 0.01 and dextran at varying concentrations, with q = 1.4, and c_s = 0.3 mol/l, for the reduced polymer concentration c/c^*, with c^* the overlap concentration. The straight lines are fits to the form $R(t) = R(t=0)\exp(t/\tau_a)$, with the characteristic aggregation time τ_a.

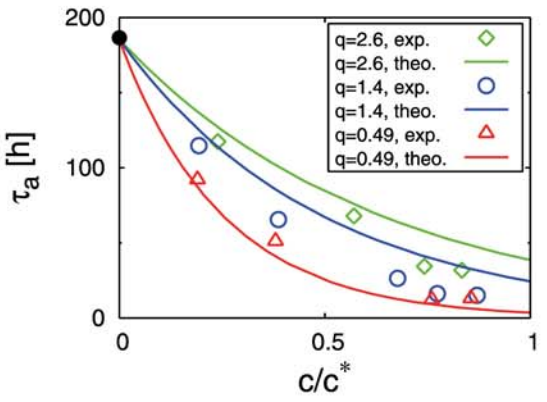

FIG. 2: The data points (symbols) give the experimentally determined aggregation time τ_a as a function of the reduced polymer concentration, in a mixture of dextran with varying range of attractions, q = 0.49, 1.4, and 2.6, at ϕ = 0.01 and c_s = 0.3 mol/l. The curves are the theoretically predicted τ_a based on the AOV potential and values of Z_{eff}.

are deduced. Plotting $R(t)$ versus the observation time on a logarithmic-linear scale, results in a linear relation (see Fig. 1), and the clusters grow faster with increasing c/c^*. From the exponential time behavior of $R(t)$, we conclude that the initial cluster growth is induced by a reaction-limited aggregation process (RLA). The values of τ_a depicted in Fig. 2 have been determined from the slopes to the curves in Fig. 1. Decreasing values of τ_a with increasing c correspond to an enhanced cluster growth rate. The onset of aggregation is quantified and analysed using a dimer formation theory of initial flocculation based on the Derjaguin, Landau, Verwey and Overbeek (DLVO) pair potential and the Asakura-Oosawa-Vrij (AOV) polymer-induced depletion potential. The effective colloid charge Z_{eff} entering the electrostatic part of the pair potential is the only unknown parameter, which we determine by matching the calculated aggregation rate to the experimental one, for systems without added polymers. The curves in Fig. 2 are our theoretical results for $\tau_a(c, q, c_s, \phi)$. This yields an overall good description of our experimental observations also in the case of added polymers.

The silica-dextran mixtures investigated so far were characterised by a low ϕ = 0.01 and low polymer concentrations $c \leq c^*$. These samples initially form a homogeneous and transparent mixture. With progressing time, the samples gradually turn turbid. The dispersions behave quite differently when ϕ and c are increased at low salt content (i.e., for $0.1 \leq c_s \leq 0.2$ mol/l). At high ϕ and c, and low c_s, the samples become turbid right after mixing. Several hours or days later, a turbid and highly viscous fluid-like phase can form at the container bottom. On top of this viscous bottom phase, a slightly turbid fluid-like phase is observed. With increasing observation time, the bottom phase ceases to flow, and forms a white gel-like phase after several days up to a few weeks.

Our observation that samples at high ϕ and c turn turbid immediately after mixing, could be an indication of a spinodal decomposition driven by the long-ranged polymer depletion effect. Furthermore, additional dilution experiments show that the silica particles do not irreversibly aggregate up to a few hours after sample preparation, showing that the initial demixing process, is reversible, and indeed might be due to spinodal decomposition or a nucleation and growth process.

Fig. 3 shows the binodal and spinodal lines calculated by GFVT for a stable colloidpolymer system at c_s = 0.15 mol/l without vdW attractions included. These lines are shown in search of possible relations between the experimental non-equilibrium state diagram two days and two weeks after sample preparation, which are also shown in the figure, and the GFVT phase behaviour prediction. As seen, all samples which phase separate two days after mixing, are located within the GFVT predicted spinodal region located to the right of the solid red spinodal line in Fig. 3. These observations indicate that the initial demixing process, causing the turbidity right after sample preparation, is reversible, and might be due to spinodal decomposition or a nucleation and growth process. However, whether gelation is related to the initial phase separation process remains to be an interesting open question.

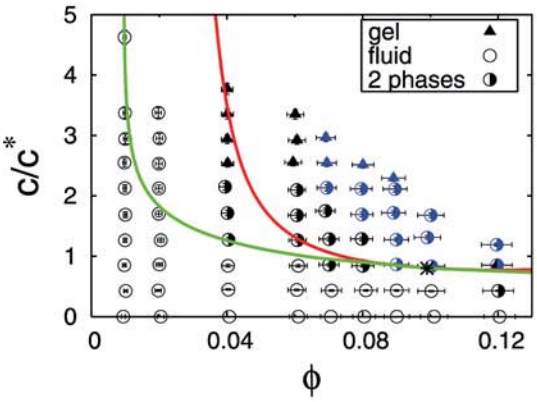

FIG. 3: Time evolution of the non-equilibrium state diagram for an aqueous mixture of silica particles and dextran, with $c_s = 0.15$ mol/l and $q = 1.4$ nm. The blue symbols give the state of the sample two days after sample preparation. The black symbols describe the state after two weeks. The theoretically predicted binodal (green dashed curve) and spinodal (red solid curve) are obtained form GFVT.

[1] W. C. K. Poon, J. Phys.: Condens. Matter **14**, R859 (2002).

[2] P. J. Lu, E. Zaccarelli, F. Ciulla, A. B. Schofield, F. Sciortino, and D. A. Weitz, Nature **453**, 499 (2008).

[3] C. Gögelein, *Phase behavior of proteins and colloid-polymer mixtures*, PhD-Thesis, Heinrich-Heine Universität Düsseldorf, November 2008.

[4] C. Gögelein and R. Tuinier, Eur. Phys. J. E **27**, 171 (2008).

[5] C. Gögelein, G. Nägele, J. Buitenhuis, R. Tuinier and J. K. G. Dhont, J. Chem. Phys. **130**, 204905 (2009).

Dynamics of charged and porous particles in dense suspensions

G. Nägele, P. Holmqvist, M. Heinen

IFF-7: Soft Condensed Matter

The dynamics in dense suspensions of charge-stabilized colloidal particles has been explored using advanced simulation methods, many-body theory, and dynamic light scattering (DLS) experiments on well-characterized systems. We have shown that a far-reaching scaling behavior of the dynamic scattering function of hard spheres relating short- to long-time dynamics, applies also to the wide class of charged colloids. Using a high-precision simulation method, a full survey on short-time transport properties in dense suspensions of porous particles has been achieved. Unexpected results have been obtained such as a scaling relation for the hydrodynamic function describing short-time diffusion. Our study provides new insights into the dynamic behavior of porous systems, e.g., hydrogels, protein solutions and colloids stabilized by polymer brushes.

The dynamics in suspension of charged colloidal particles undergoing correlated Brownian motion is of fundamental interest and the subject of ongoing experimental and theoretical research. Charge-stabilized colloids occur ubiquitously in biology, food and chemical industry. Suspensions of solvent-permeable colloidal particles are found in a great variety of synthesized materials. Examples are highly porous, cross-linked microgel particles of temperature-dependent size, and the extended class of core-shell particles with an impermeable core and a stabilizing, permeable layer of polymer chains.

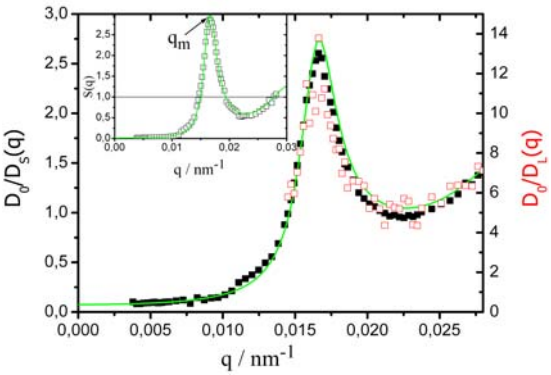

FIG. 1: DLS results for normalized inverse short-time diffusion function $D_0/D_S(q)$ (filled squares, scale on left axis) and inverse long-time diffusion function $D_0/D_L(q)$ (open squares, scale on right axis) of coated charged silica spheres at volume fraction $\phi = 0.14$. Inset: static structure factor $S(q)$. Lines: theoretical prediction for $D_0/D_S(q)$ and $S(q)$. From [1] and [2].

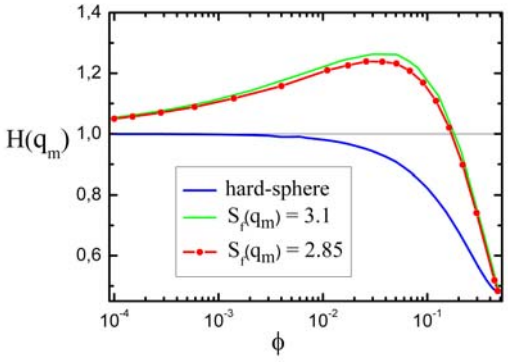

FIG. 2: Freezing line of the hydrodynamic function peak height of charged particles, for two indicated values of the structure factor peak height, $S_f(q_m)$, at freezing. The fluid phase region in between the upper freezing line, and the lower hard-sphere line (in blue), is insensitive to the Hansen-Verlet values for $S_f(q_m)$. From [3].

Despite the importance of charged and permeable particles both from a fundamental viewpoint and in terms of applications, comparatively little is known theoretically about transport properties in dense systems, such as the self- and collective diffusion coefficients, sedimentation velocity and rheological properties. The calculation of transport properties is challenging since one needs to cope with many-body hydrodynamic interactions (HIs), mediated through the solvent flowing outside and, for non-zero porosity, also inside the particles. A better control on diffusion and viscoelastic properties for industrial processing of concentrated colloids requires a deeper understanding of the influence of the HIs.

The diffusion of charged silica spheres in an organic solvent mixture was studied using DLS over the full colloidal time range. We have shown that a far-reaching dynamic scaling property of the dynamic structure factor for neutral hard spheres, relating the long-time to the short-time dynamics, and collective diffusion to self-diffusion, applies also to charged colloids [1]. The universality of the experimentally observed scaling behavior was analyzed

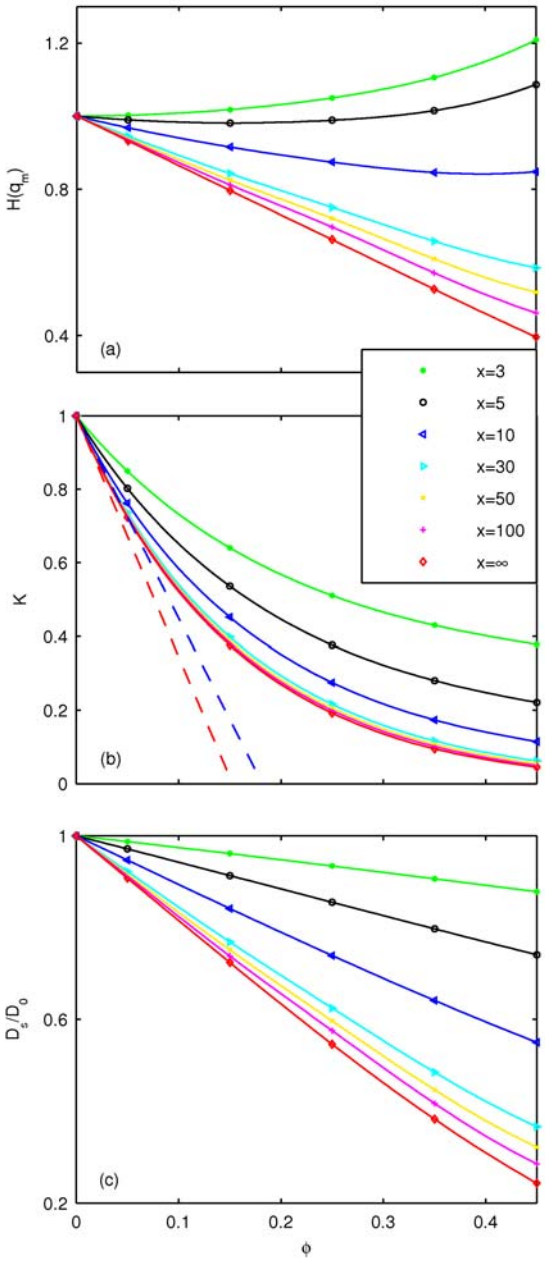

FIG. 3: Simulation results for permeable hard spheres of inverse porosity values x as indicated. (a) Principal peak value, $H(q_m)$, of hydrodynamic function $H(q)$. (b) Sedimentation coefficient $K = H(0)$. Dashed lines: first-order concentration results for non-permeable hard spheres ($x = \infty$), and highly permeable spheres ($x = 10$). (c) Normalized self-diffusion coefficient D_S. From [5].

theoretically by mode-coupling theory and Brownian dynamics simulations. According to our results, dynamic scaling is an approximate feature whose accuracy depends on the strength of particle interactions and the considered scattering wavenumber q. Fig. 1 shows DLS data for the inverse of the short-time and long-time diffusion functions, $D_S(q)$, and $D_L(q)$, respectively, of charged silica spheres, normalized by the single-particle diffusion coefficient D_0. As one notices from this figure, $D_L(q)$ is practically proportional to $D_s(q)$, independent of the wavenumber. This proportionality demonstrates a salient facet of the dynamic scaling relation between short-time and long-time diffusion properties. Our experimental data confirm additionally two dynamic freezing criteria proposed, respectively, for the long-time self- and cage diffusion coefficients, along with theoretical predictions for the concentration dependence of the sedimentation and self-diffusion coefficients [1].

Another useful result is our derivation of the limiting form of the hydrodynamic function peak height, $H(q_m)$, of charged particles at the liquid-crystal freezing transition [3]. The limiting freezing line gives a map of attainable peak values in the fluid phase state (see Fig. 2). Moreover, it has led us to a convenient, from the experimental viewpoint, short-time dynamic criterion characterizing the onset of freezing. The criterion has the virtue of being insensitive to the range of the particle pair potential. The hydrodynamic function, $H(q)$, which we studied in great detail both theoretically and experimentally [4], is the key quantity containing information on the influence of HIs on short-time diffusion. It is related to $D_S(q)$ by $D_S(q) = D_0\, H(q)/S(q)$, where $S(q)$ is the structure factor obtained in a static scattering experiment.

In collaboration with Prof. Cichocki and his team from the Warsaw University and Polish Academy of Sciences, we have extended a versatile simulation method with unsurpassed accuracy in the many-body HIs treatment, to dense suspensions of solvent-permeable, rigid colloidal particles with excluded volume interactions [5]. Properties calculated by this method have been the reduced suspension sedimentation velocity, $K = H(q \to 0)$, self- and collective diffusion coefficients, hydrodynamic function $H(q)$, and high-frequency limiting viscosity. All these properties have been studied as functions of the inverse reduced particle porosity x, by covering the complete fluid-phase regime. Our main focus has been on generic features of the permeable sphere model. According to Fig. 3, the transport properties K, D_S and $H(q_m)$ are distinctly sensitive to the particle porosity. The most important result of our study of porous particles is that the q-dependence of $H(q)$ can be shifted and scaled to that of impermeable hard spheres, using the coefficients depicted in Fig. 3, which by themselves are strongly permeability dependent.

[1] P. Holmqvist and G. Nägele, Phys. Rev. Lett. **104**, 058301 (2010).

[2] M. Heinen, A. J. Banchio and G. Nägele, submitted (2010).

[3] J. Gapinski, A. Patkowski and G. Nägele, J. Chem. Phys. **132**, in press (2010).

[4] J. Gapinski, A. Patkowski, A. J. Banchio, J. Buitenhuis, P. Holmqvist, M. P. Lettinga, G. Meier and G. Nägele, J. Chem. Phys. **130**, 084503 (2009).

[5] G. C. Abade, B. Cichocki, G. Nägele, M. L. Ekiel-Jezewska and E. Wajnryb, J. Chem. Phys. **132**, 014503 (2010); ibid., Phys. Rev. E, in press (2010).

Criticality of charged fibrous viruses (fd) in electric fields

K. Kang, J. K. G. Dhont

IFF-7: Soft Condensed Matter

Experiments on suspensions of charged fibrous viruses (fd) in external electric fields have been performed, which reveal a rich non-equilibrium phase/state behaviour. Several transition lines of field-induced phases and states meet at a single point that can be identified as a non-equilibrium critical point in the sense that a time- and length-scale diverges on approach of this point. Both power law and logarithmic divergences are found. The critical behaviour is investigated by means of image correlation spectroscopy.

One may ask whether critical points can be associated to field-induced, far-out-of equilibrium phase/state transitions, where length-scales and characteristic time constants diverge. We recently found that several phases and dynamical states in suspensions of charged colloidal rods (fd-virus particles) can be induced by AC electric fields [1, 2]. These phases and dynamical states result from rod-rod interactions which are due to field-induced polarization of double layers. The aim here is to show that a non-equilibrium critical point can indeed be identified in this driven system, with a divergent length- and time-scale. The experimental details can be found in Ref. [3], where the system and image correlation method are explained in more detail. The non-equilibrium electric phase/state diagram in the field-amplitude versus frequency plane is given in Fig.1, together with depolarized optical morphologies of the various phases and dynamical states. The phase/state diagram is corrected for the electrode polarization [2]. The solid lines indicate "sharp" transition, while the dotted lines are related to gradual changes in both morphology and dynamics. At low field amplitudes the state is in an isotropic-nematic phase coexistence. On increasing the field amplitude at low frequency, a chiral-nematic$N*$-phase is induced which melts on further increasing the amplitude. A dynamical state now exists, where nematic domains melt and form. The dynamics of melting and forming is slow near the transition line (in the *D_s* state) and fast further away from the transition line at relatively high field amplitudes (in the *D_f* state). At high frequencies, larger than a few kHz, a uniform depolarized image is observed. Electric birefringence measurements reveal that the rods are "homeotropically" aligned in this H-phase [2].

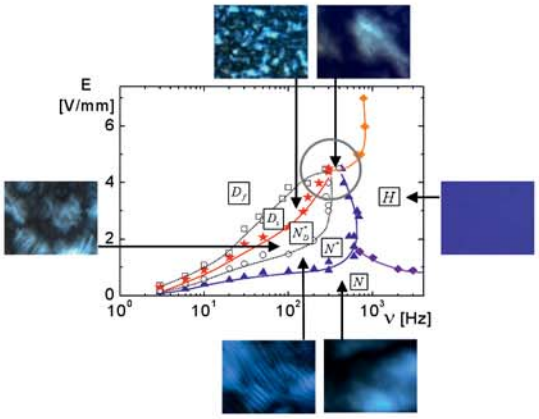

FIG. 1: Electric-field driven phase/state diagram of fd-virus suspensions with a concentration of 2.0 mg/ml. Several phases/states are induced at frequencies below a few kHz, while a uniform aligned phase is observed at higher frequencies. The critical point is indicated by the circle.

The size of nematic domains in the dynamical state is obtained from time-resolved series of depolarized microscopy images. The "apparent size of domains" is the measured domain size during its formation, just before melting sets in. Since most of the domains are not centred within the 2D field-of-view of the microscope, the largest of such apparent domain sizes identifies "the true domain size" as our length-scale [3].

Domain sizes are determined from the transmitted light intensity profiles in x-y pixel dimensions, as shown in Fig.2a. The average of the 2 linear dimensions measures the domain size. The variation of the domain size $d$on approaching the critical point at the fixed critical frequency of $335Hz$ on lowering field amplitude is shown in Fig.2b. Fig.2c shows the domain-size variation on approach of the critical point by variation of the frequency at the fixed critical field amplitude of *3.50 V/mm*. The domain size is corrected for the noncritical

background domain size d_b, which is the domain size far away from the critical point.

As can be seen in the Fig. 2b, a double-logarithmic plot shows a power-law divergence of the domain size,

$$d(E) - d_b \sim \left(\frac{E}{E_c} - 1\right)^{-\mu_d^E}$$

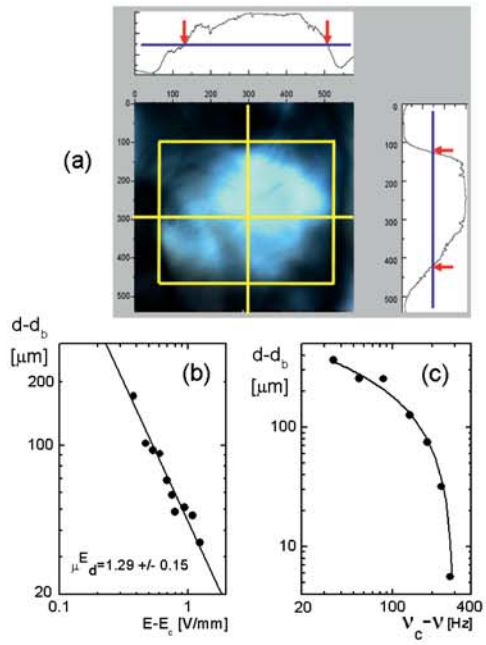

FIG. 2: Critical behavior of the domain size. (a) The determination of the domain size from the microcopy images. (b) The domain size as a function of the applied field amplitude, and (c) of the applied frequency, on approach of the critical point..

Where the critical exponent is equal to $\mu_d^E = 1.29 \pm 0.15$. A weaker divergence of the critical domain size is observed as a function of the applied frequency, as can be seen from Fig.2c. We now find a logarithmic divergence, where,

$$d(\nu) - d_b \sim \log_{10}\left\{1 - \frac{\nu}{\nu_c}\right\}.$$

The solid line in Fig.2c is a fit to such logarithmic domain-size dependence.

The time-scale is the time for melting and forming of the nematic domains [3]. For the determination of the time-scale, a time-series of images is recorded with a time resolution of 0.3 – 1 s, with typical measuring times of 1200-1800 s. From these images we then calculate the image correlation function,

$$C_V(t) = \frac{\langle [I(t) - < I(t) >]\,[I(0) - < I(0) >] \rangle}{\langle [I(0) - < I(0) >]^2 \rangle},$$

Where/is the transmitted intensity at a given pixel and the brackets $<\ldots>$ denote averaging over all pixels. This correlation function can be fitted accurately with a single, stretched exponential function of the time. The time constant in this fitting function defines the time-scale for melting and forming of the nematic domains. It turned out that the divergence of the time-scale, contrary to the domain size, follows a power-law for both approaches of the critical point.

For an off-critical approach of the transition line of the N* phase to the dynamical state, the domain size remains finite while the characteristic time for melting and forming of nematic domains diverges logarithmically. An overview of the critical behaviour of the

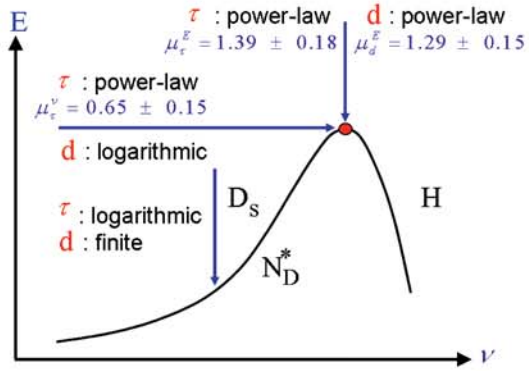

FIG. 3: A schematic overview of the critical and off-critical behavior of the domain size and the characteristic time for melting and forming of nematic domains.

domain size and melting-forming time of domains is given in Fig.3.

The mechanism that underlies the formation of the various phases and dynamical states is not yet understood. Also the behaviour on approach of the critical point from the H-phase, at high frequency, needs further investigation in terms of microscopic dynamics.

[1] K. Kang, J. K. G. Dhont, Eur. Phys. Lett. 84, 14005, 2008

[2] K. Kang, J. K. G. Dhont, Soft Matter. 6, 273, 2010

[3] K. Kang, J. K. G. Dhont, Eur. Phys. J. E. 30, 333, 2009

Dynamic response of wormlike micelles to step rate tests and oscillatory shear as probed by SANS(t)

M. P. Lettinga, E. Stiakakis

IFF-7: Soft Condensed Matter

We probe the dynamic response of surfactant wormlike micelles, cetylpyridinium chloride/sodium salicylate (CPyCl-NaSal) at 6 % wt to oscillatory shear flow and step rate tests, using time-resolved Small Angle Neutron Scattering facility SANS(t). These measurements give a unique insight in the response of the Kuhn segments of the wormlike micelle, i.e. about 50 nm, as well as the formation of structures at a μm length scale.

Surfactant wormlike micelles, as formed in a 6 % wt (CPyCl-NaSal) dispersion, are known for there extreme shear thinning behavior, which results in shear band formation, i.e. a flow profile that consists of a part with low viscosity and high shear rate and a part with high viscosity and low shear rate[1, 2]. The microscopic structure underlying this behavior is poorly understood, but can be probed by studying the linear and non-linear dynamic response to Large Amplitude Oscillatory Shear flow (LAOS) of surfactant wormlike micelles. To this end we exploited, in collaboration with Joachim Kohlbrecher from the PSI in Villigen, Switzerland, the time-resolved Small Angle Neutron Scattering facility SANS(t). This technique yields the dynamic structural data provided that the system under study is submitted to a periodic field. As compared to earlier experiments on block copolymer wormlike micelles[3] we observed three new features: high shear rates that large scale structures are formed; the appearance of an additional time response for high maximum shear rates and low frequencies; access the structural response of a step up experiment in shear rate. The interpretation of the results can be done on the basis of the well characterized flow behavior of this system.

SANS experiments have been performed at the SANS I instrument at the SINQ spallation. For the Rheo-SANS experiments a Anton Paar MCR 513 stress and strain controlled Rheometer with a Couette type shear cell was placed in the neutron beam in the so-called radial configuration was used. In order to probe the time dependent structural changes with SANS under oscillating shear, a stroboscopic data acquisition scheme, implemented on the SANS-1 instrument, has been used. In case of oscillatory flow the trigger is send when the maximum shear rate

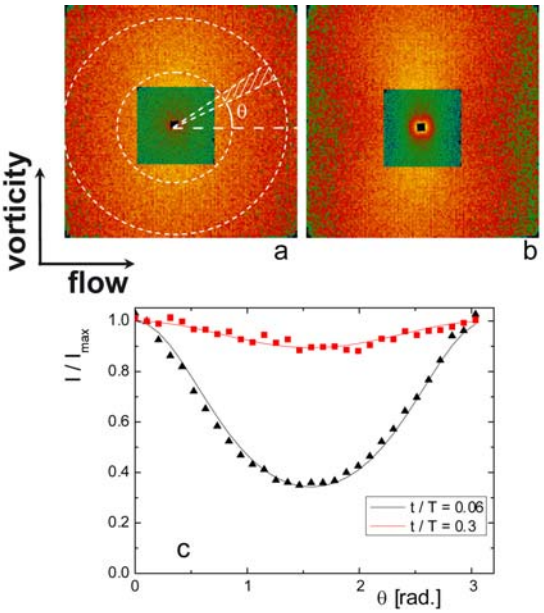

FIG. 1: Scattering pattern after $t/T = 0.06$ (a) and $t/T = 0.3$ (b) at a maximum shear rate of $\dot{\gamma}_{\max} = 18\ s^{-1}$ and frequency $f = 0.25\ s{-}1$ in the flow-velocity plane. The dashed lines indicate the q-range that is used to obtain the azimuthal intensity profile as plotted in (c). The plot contains data taken at a detector distance of 6 and 18 meters. Here θ is the angle with the shear flow, and the full line indicates a fit to $\langle P_2(\theta)\rangle = \frac{\int_0^\pi \exp\{\beta P_2(\theta)\}\ P_2(\theta)\sin(\theta)d\theta}{\int_0^\pi \exp\{\beta P_2(\theta)\}\ \sin(\theta)d\theta}$.

is reached, while for step rate experiments the trigger is send at the end of a cycle or oscillation. With this technique the temporal evolution of the structural alignment of the wormlike micelles during a whole shear cycle could be measured.

As compared to earlier measurements on Block copolymer wormlike micelles [3] there are three features that were not observed so far. *First*, we observe for high shear rates that large scale structures are formed, see the structures at small q values in Fig. 1a and b. The response of these structures is in phase with the response of the Kuhn segment. *Second*, we observe the appearance of an *additional time response* for high maximum shear rates and low frequencies, as it is manifested by the growth of a shoulder in the response. This additional process is probably connected with the formation of *shear bands*[1],

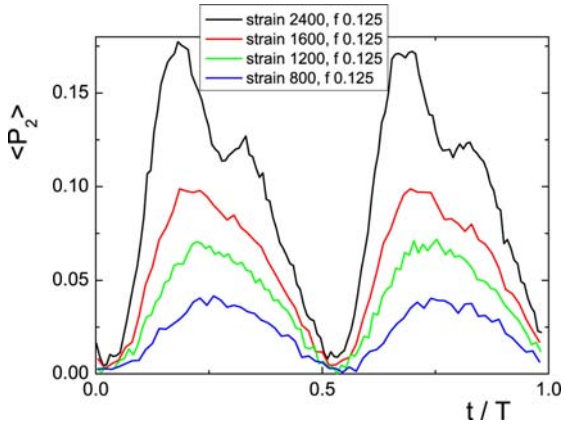

FIG. 2: Time-dependent response of the orientational order parameter $\langle P_2 \rangle_{max.}$ for shear rates up to $\dot{\gamma} = 10\ s^{-1}$ and a fixed frequency of $f = 0.125Hz$. (b) as in (a) after a shear rate quench from 0 to various shear rates as indicated.

as it occurs in the shear thinning regime of the flow curve. In Fig. 2 the response is plotted of the orientational order parameter to oscillatory shear flow, with a maximum shear rate of $\dot{\gamma}_{\max} = 18\ s^{-1}$ and with varying frequency. This shear rate is far into the plateau region, see Ref[1, 2]. When varying the frequency in the high frequency range we see an increasing phase shift and linearity with increasing frequency, while the amplitude of the response, maximum order parameter $\langle P_2 \rangle_{max.}$, is decreasing. The Fourier analysis of the response as well as the stress response will follow. When decreasing the frequency we observe an interesting behavior, in the sense that a frequency shifted response seems to come up. Probably this is connected to the formation of shear bands.

Third, in addition with dynamic experiments, we could also perform *step up experiments* in the shear rate and probe the response in stress as well as in the ordering of the system. This was feasible due to the new versatile rheometer which is now available at the PSI. To obtain the data from the time-resolved SANS we did cycles of 30 seconds at a high shear rate and 10 seconds at zero shear. This cycle was repeated typically 50 times. The response of the stress and orientational order parameter after a step in the shear rate from 0 to a few finite shear rates into the plateau region is plotted in Fig. 3. As can be seen, the responses in stress and order parameter are very similar, illustrating the connection between the two. The structure that are formed at small Q are also responding in the same way. The response is not anymore overdamped and shows several oscillations entering the shear thinning regime.

The response of the stress and orientational order parameter after a step in the shear rate from 0 to a few finite shear rates into the plateau region. To obtain the data from the time-resolved SANS we did cycles of 30 seconds at a high shear rate and 10 seconds at zero shear. This cycle was repeated typically 50 times. As can be seen, the responses are very similar, but there is some shift in time. in the future we plan to interpret the data on the basis of recently

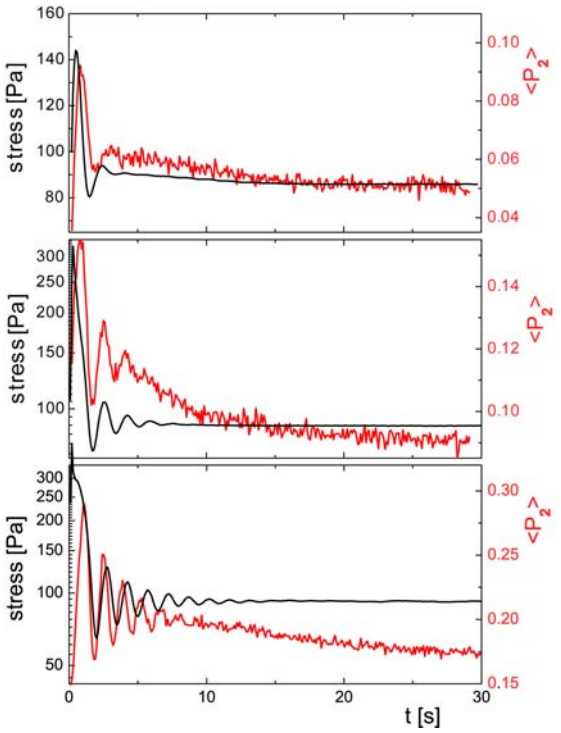

FIG. 3: The response of the order parameter $\langle P_2 \rangle_{max.}$ (red) and stress (black) for shear rate quenches from 0 to 8, 18, and $35\ s^{-1}$.

develloped theory[4].

[1] J.-B. Salmon et al, Phys. Rev. Lett. **90** 228303 (2003)

[2] M. P. Lettinga and S. Manneville, Phys. Rev. Lett. **103** 248302 (2009)

[3] Lonetti et al, J. Phys.: Condens. Matter **20** 404207 (2008)

[4] Ewoldt et al.,J. Rheol. textbf52 (6), 1427-1458 (2008)

Accumulation of biological and soft matter in a temperature gradient

S. Wiegand[1], B. Arlt[1], S. Datta[2], T. Sottmann[2]

[1] IFF-7: Soft Condensed Matter
[2] Physikalische Chemie, Universität zu Köln, Luxemburgerstr. 116, D-50939 Köln, Germany

A simple nonequilibrium environment can be created by using a temperature gradient. On these conditions DNA can be replicated by polymerase chain reaction. Here convection drives the replication and thermal diffusion acts as a molecular trap. Recently, we could show that the accumulation behavior of sugar surfactants changes significantly at the critical micelle concentration and shows an asymptotic decay at higher concentrations. This observations need to be considered when the micelles of the biocompatible sugar surfactants are used as pharmaceutical containers for drug delivery. Depending on the temperature gradients in the body, an enrichment of the drug will occur in certain areas of the body.

For pratical applications in polymer characterization, crude oil exploration, combustion and alternative energies an understanding of diffusion in a temperature gradient is essential. Additionally, the effect contributes to the comprehension of some fundamental aspects related to the origin of life. Recently, it could be shown that a simple nonequilibrium environment using a temperature gradient makes the replication of DNA by polymerase chain reaction possible. The underlying mechanism is a combination of convection and thermal diffusion, which acts as a molecular trap. This scenario of thermal gradients between warm volcanic rocks and colder ocean water is a very likely scenario on the early earth. A deeper understanding of the effect of temperature gradients is also important, if one wants to understand how sperm cells navigate towards the egg [1].

In a multicomponent mixture thermal gradients lead to thermal diffusion. In the stationary state, the mass fluxes induced by the temperature gradient and the induced concentration gradient cancel each other. The ratio of the concentration gradient ∇c and temperature gradient ∇T that comply with such a stationary state is characterized by the Soret coefficient S_{T}, which is defined as, $S_{\mathrm{T}} = D_{\mathrm{T}}/D$, where D_{T} is the thermal diffusion coefficient and D is the mass diffusion coefficient.

One of the major challenges to study this phenomenon experimentally is the inset of convection if the temperature gradients become to large. An outstanding method, especially for aqueous mixtures, is the so called infrared-thermal diffusion forced Rayleigh scattering (IR-TDFRS) method [2].

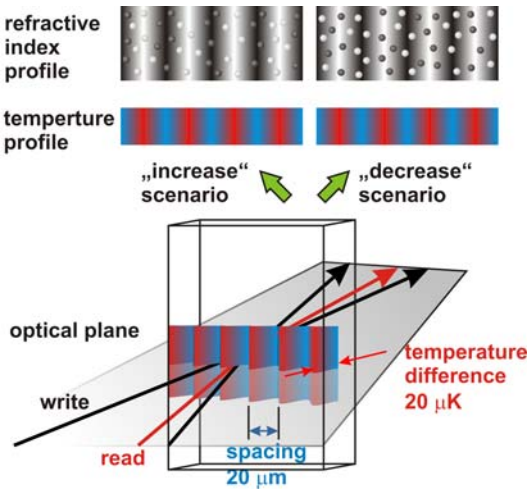

FIG. 1: Schematic drawing of the holographic grating experiment. The two IR-beams (black) writing beams intersect in the sample cell and create a sinusoidal interference grating with a fringe spacing on the order of 20 μm and a temperature amplitude of approximately 20 μK due to absorption of the laser light in the sample. The temperature grating causes a refractive index grating. After equilibration of the temperature the diffusion process starts. This leads depending on the movement of the components to an increase or decrease of the refractive index contrast of the grating. The build up and contrast variation of the refractive index grating is probed by a read-out laser beam (red).

The basic principle of the method is sketched in figure 1. By intersection of two infrared writing beams an interference grating is created in the sample. Due to absorption of the laser light by aqueous samples the intensity grating is converted into a thermal grating, which leads to a periodic modulation of the refractive index in the sample. The strength of this refractive index grating can be probed by a red readout laser beam, whereas the intensity of the diffracted beam depends on the amplitude of the grating. While the equilibration time of the temperature grating is only on the order of 100 μs, the mass diffusion process can take seconds or minutes. The advantages of this unique set-up are manifold. Due to the small distance between the cold and the warm region of 20 μm the equilibration times are much shorter than for

other methods. Another crucial point of our method is the use of an IR-laser, which is naturally absorbed by the biological relevant aqueous samples and does not need the addition of dye as often used by other methods. Additionally, the temperature difference is only on the order of 20-100 μK, which keeps the system close to equilibrium so that the responses of the system are still linear. Another relevant advantage is the detection of the thermal plateau, which gives an internal temperature reference point, so that no absolute temperature measurement is required.

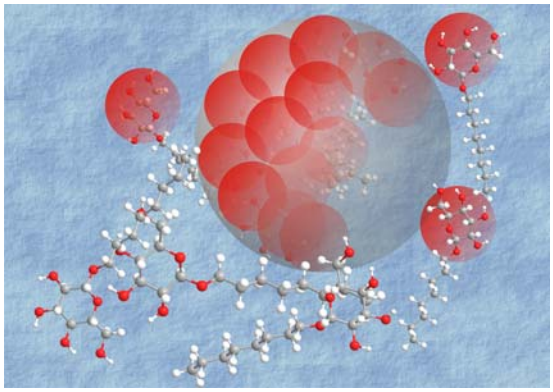

FIG. 2: Schematic picture of the self organisation of n–Octyl β–D–glucopyranoside to spherical micelles.

Sugar surfactants have frequently been used to study the dissolution and formation of biological membranes and the stabilization of proteins [3]. Among the nonionic sugar surfactants *n*–Octyl β–D–glucopyranoside has a fairly high critical micelle concentration (*cmc*). This makes measurements below the *cmc* possible. As schematically illustrated in figure 2, the sugar surfactant molecules form spherical micelles above the *cmc*, while below the *cmc*, the surfactant molecules in solution are in equilibrium with those adsorbed at the water/air interface. Therefore, below the *cmc* we will observe the thermal diffusion behavior of individual surfactant molecules, and above the *cmc* we additionally have a thermophoretic motion of the micelles. This might lead to a pronounced change of the thermal diffusion or Soret coefficient, because above the *cmc* the interface between micelles and solvent is mainly determined by the polar headgroups of the sugar surfactant molecules.

Figure 3 shows the measured Soret coefficient as function of the concentration in the vicinity of the *cmc* at 40 °C [3]. The slope of the concentration dependence of the Soret coefficient becomes much steeper for concentrations above the *cmc*. Two physical reasons are responsible for the observed behavior. The micelles are larger than the single sugar surfactant molecules, which leads to a slower diffusion and therefore to an increase of the Soret coefficient. Additionally, the interface interactions between the solvent molecules and the micelles are mainly determined by the hydrophilic glucopyranoside headgroups and not anymore by the alkyl chains as below the *cmc*. The obtained *cmc* values are in good agreement with the results from surface tension measurements.

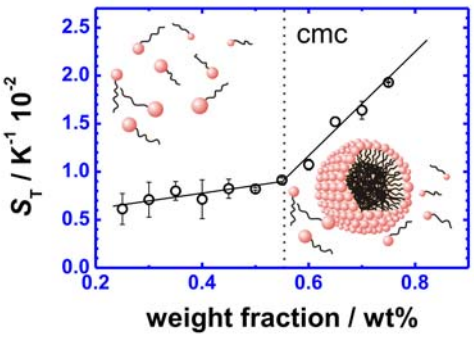

FIG. 3: The Soret coefficient S_{T} at at 40 °C versus concentration. All measurements have been performed with the IR–TDFRS without dye. The vertical line marks the cmc*. The solid lines are guides to the eye.*

We also investigated the thermal diffusion behavior for higher surfactant concentrations [3]. For high concentrations above $w = 1.0$ wt% the Soret coefficient decays almost linearly. By decreasing the temperature this decay becomes steeper and the Soret coefficient becomes negative indicating that the micelles enrich at the warm side. For the two highest temperatures of 30 °C and 40 °C we did not observe a sign change in the investigated concentration range, but it is expected that it will occur at higher concentrations.

The decay of the Soret coefficient at high concentrations seems to be a typical phenomenon and has also been found for polymer solutions [4] and colloidal dispersions [5]. For high concentrations the Soret coefficient of the polymeric system shows an asymptotic scaling law with concentration $S_{\mathrm{T}} = C_0 \cdot C^{-0.65}$, whereas the exponent changes from -0.65 to -1 approaching the concentrated regime. For the colloidal system an asymptotic power law for the Soret coefficient S_{T} in dependence of the volume fraction ϕ of the form $S_{\mathrm{T}} = \phi_0 \cdot \phi^{-0.0095}$ has been found. For the investigated sugar surfactant system the exponent is not temperature independent but decreases from -0.42 to -1.44 with decreasing temperature.

With this contact free method we are able to study the transport of biocompatibel materials in a nonequilibrium environment caused by a temperature gradient.

[1] A. Bahat, I. Tur-Kaspa, A. Gakamsky, L. C. Giojalas, H. Breitbart, and M. Eisenbach. *Nat. Med.* **9**, 149–150 (2003).

[2] Wiegand, S., Ning, H., Kriegs, H. *J. Phys. Chem. B* **111**, 14169–14174 (2007).

[3] Arlt, B., Datta, S., Sottmann, T. and Wiegand, S. *J. Phys. Chem. B*, 10.1021/jp907988r (2010).

[4] Rauch, J., Köhler, W. *J. Chem. Phys.* **119**, 11977-11988 (2003).

[5] Ning, H., Buitenhuis, J., Dhont, J. K. G. and Wiegand, S. *J. Chem. Phys.* **125**, 204911 (2006).

New velocimetry technique to measure particle near wall velocities

P. R. Lang[1], J. K. G. Dhont[1], B. Loppinet[2]

[1] IFF-7: Soft Condensed Matter
[2] ESL Foundation for Research and Technology Hellas, Heraklion, Greece

A new near wall velocimetry technique, based on evanescent wave dynamic light scattering, was developed, which provides a robust and simple method to obtain precise measurement of the near wall velocity of colloidal particles. The technique is demonstrated for latex spheres dispersed in water-glycerol mixtures.

Fluid flow near hard surfaces attracts an ever increasing attention because of its relevance in various fields, like tribology, micro-fluidics or rheology reflecting the general need to control and understand flow close to surfaces. A broad range of experimental techniques with various resolutions have been applied to measure fluid velocities and velocity profiles close to surfaces from macroscopic rheology to near field force microscopy [1]. More recently a number of optical techniques have been introduced mainly using fluorescence, some of them taking advantage of the evanescent near field produced at total internal reflection.

We developed a new optical technique, namely Near Field Laser Doppler Velocimetry (NFLDV) that provides a simple measurement of near wall velocity with resolution of tens of nanometers. It is an extension to flowing samples of evanescent wave dynamic light scattering [2, 3] that has been used to evaluate diffusion near walls [4, 5]. The principle is as follows : At total internal reflection, an evanescent electric field penetrates the medium of higher refraction index, $E(z) = E_0 \exp(-\frac{1}{2}\kappa z)$ where the intensity penetration depth $1/\kappa$ is given as $\kappa = 2k_0\sqrt{\sin^2\varphi - (n/n_s)^2}$ where k_0 is the incident light wave vector in vacuum, φ the incidence angle, n and n_s the refractive index of the fluid and the solid substrate respectively. This evanescent near field can be scattered into a far field intensity that can easily be detected. The experimental set–up is sketched in Figure 1. It consists of a microscope slide as the bottom part and a plexiglass piece fitted with flow input and output, separated by a spacer of approximately 100 μm height, which has a 10 mm wide channel. This cell is coupled to the flat surface of a semi–cylindrical lens. The flow is imposed by a syringe pump with adjustable speed. In the case of flowing scatterers, the collected scattered intensity in the far field carries a signature of the velocity distribution within the exponentially decaying evanescent field, in a way similar to standard

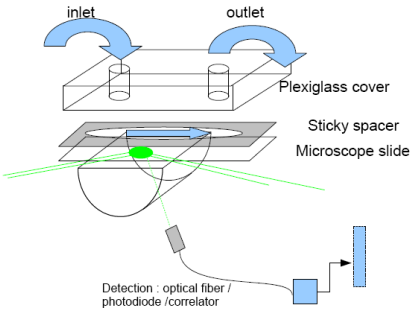

FIG. 1: Schematic sketch of the sample cell and data aquisition set–up

bulk Laser Doppler Velocimetry (LDV), which provides a way to determine the velocity profile. The incident laser light is totaly reflected from the interface between the bottom microscope slide and the flowing liquid. Light which is scattered off the resulting evanescent field is detected and auto–correlated in time using standard components. In the simple case of ballistic like flow motion, i.e. when Brownian motion can be neglected (corresponding to high Peclet numbers), the correlation function of interest can be written as:

$$g(t) = \frac{\int_0^\infty c(z)\exp(-\kappa z)\exp(i\vec{q}.\vec{v}(z)t)dz}{\int_0^\infty c(z)\exp(-\kappa z)dz} \qquad (1)$$

where $c(z)$ is the z-dependent concentration of the non interacting scatterers and $\vec{v}(z)$ is the velocity of a scatterer situated at a distance z from the wall, $\vec{q}$ is the scattering wave vector of the specific experiments. In purely heterodyne detection conditions, when a large part of the detected intensity does not fluctuate in time, the real part of $g(t)$ will be measured. In purely homodyne detection the square modulus of $g(t)$ is detected. In the most general case of partial heterodyne conditions, where most EWDLS–data are obtained, the measured intensity autocorrelation function $g_m(t)$ is given by the generalized Siegert relation

$$g_m(t) = (1-B)^2|g(t)|^2 + 2B(1-B)Re(g(t)) \qquad (2)$$

where B relates to the maximum amplitude of the computed correlation function $A = g(0) - g(t \to \infty)$ as $B = \sqrt{1-A}$. Assuming an homogeneous distribution of the particles, $c(z) = 0 \; for \; z < H$ and $c(z) = c_0 \; for \; z \geq H$ (H being the height of an interfacial layer that is depleted from particles due to repulsive interaction with the wall) and a simple linear profile of the near wall velocity of the scatterers, $(v(z) = \dot{\gamma} z + v_0)$ the real part of $g(t)$ is

$$Re(g(t)) = \frac{\cos(\Gamma_1 t) - \Gamma_2 t \sin(\Gamma_1 t)}{1 + (\Gamma_2 t)^2} \qquad (3)$$

and

$$\mid g(t) \mid^2 = \frac{1}{1 + (\Gamma_2 t)^2}. \qquad (4)$$

Here the rate Γ_1 is given by $\Gamma_1 = v_{min} q_{||}$ where v_{min} is the velocity of the slowest particles nearest to the wall $v_{min} = v_0 + \dot{\gamma} H$, and the rate and Γ_2 is $\Gamma_2 = \dot{\gamma} \frac{q_{||}}{\kappa}$. Homodyne measurements should result in a Lorentzian decay of the correlation function where the width Γ_2 relates to an average shear rate within the illuminated volume.

Heterodyne and partial heterodyne measurements will also provide the rate Γ_1. This rate relates to the velocity of the particles nearest to the wall. It will appear as the frequency of an oscillating part in the correlation function, in a similar way than velocity appears in standard LDV.

Experimental correlation functions obtained for 170 nm diameter latex spheres in a water/glycerol mixture at a flow rate of 2 ml/hour are shown in Figure 2. The different curves correspond to correlations measured at different laser incidence angles above the critical angles $\varphi_c \approx 74^o$ corresponding to various field penetration depth from 200 to 1000 nm . An oscillating part in the correlation function is clearly visible, that becomes more apparent at reduced penetration depth and the frequency of which does not depend on the penetration depth. This qualitative behavior is expected from the derived theoretical $g(t)$ and this frequency should be Γ_1. The solid lines in Figure 2 are fits with the theoretical expressions of eqns. 2-4 with B, Γ_1 and Γ_2 as fitting parameters. The extracted rates Γ_1 and Γ_2 are shown in Figure 2 (bottom) as a function of evanescent field penetration depth. Both rates qualitatively present the expected variation, as Γ_2 shows a linear dependence with the penetration depth and Γ_1 is independent of it. The value of $\Gamma_1 = 58 s^{-1}$ leads to a velocity $v_{min} = \Gamma_1 / q_{||} = 3600$ nm s^{-1} . The slope of Γ_2 versus $1/\kappa$ leads to a near wall apparent shear rate $\dot{\gamma} = 15$ s^{-1}. The obtained values can be compared to the theoretical shear rate at the plate, which can be estimated from the channel geometry and the imposed flow rate as$\dot{\gamma} = 6Q/h^2 w$. We obtain good agreement within experimental error between these values. However, it has to be emphasized that our new method allows the determination of the particles' near wall velocity without any knowledge about the channel geometry. The non–zero near wall velocity may appear at odd with sticks boundary conditions, for which the particle velocity should approach zero

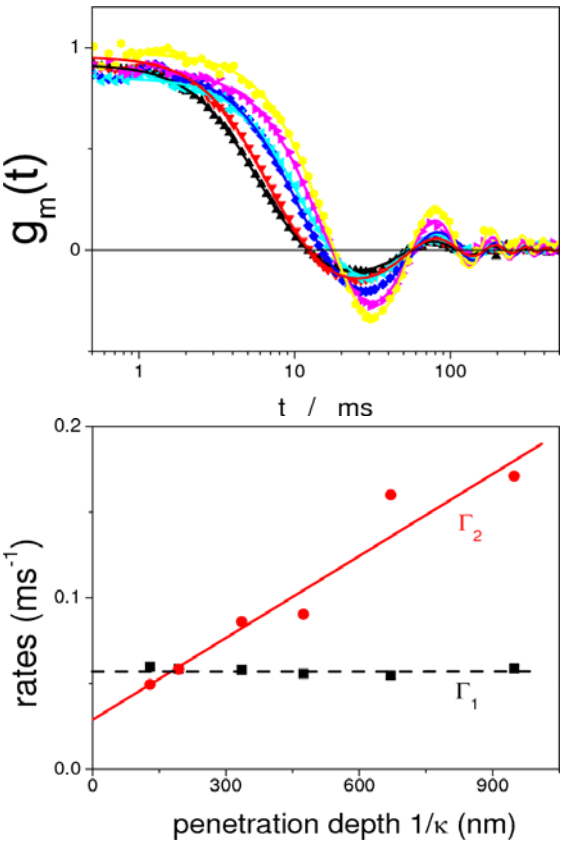

FIG. 2: top: measured time intensity autocorrelation functions $g_m(t)$ at different penetration depthes of the evanescent field (points) and best fits with the theoretical expression of eqns. 2-4 (lines). bottom: rates Γ_1 and Γ_2 as a function of the penetration depth

at contact with the wall. However, due to repulsive electrostatic interaction between the wall and the particles the are not in contact. In the present case, the particles are effectively expelled from a layer of the order of 50 nm. Therefore, the velocity of the particles which are closest to the wall can be relatively large.

In conclusions, we have here a powerful and simple method to obtain precise measurements of near wall velocity which could potentially find use in a number of applications. Because of its relative simplicity, the technique could easily be implemented in a number of different environments and geometries, like microscopes, rheometers, or micro–fluidic devices.

[1] L. Bocquet, J.–L. Barrat Soft Matter **3**, 685 (2007).

[2] K. H. Lan, N. Ostrowsky, and D. Sornette, Phys. Rev.Lett. **57**, 17 (1986).

[3] for an actual overview see R. Sigel Current Opinion in Colloid and Interface Science **14**, 426 (2009).

[4] P. Holmqvist, J. K. G. Dhont, and P. R. Lang, Phys. Rev.E **74**, 021402 (2006).

[5] P. Holmqvist, J. K. G. Dhont, and P. R. Lang, J. Phys. Chem. **126** 044707 (2007).

Adhesive colloidal dispersions under high pressure

G. Meier[1], M. P. Lettinga[1], J. Buitenhuis[1], R. Vavrin[2], J. Kohlbrecher[2], A. Wilk[2], M. Ratajczyk[1], K. Tomczyk[1]

[1] IFF-7: Soft Condensed Matter
[2] Laboratory for Neutron Scattering, ETH Zürich and PSI, 5232 Villigen Switzerland

We have applied small angle neutron scattering (SANS), diffusing wave spectroscopy (DWS) and static and dynamic light scattering (SLS and DLS) to investigate the phase diagram of a sterically stabilized colloidal system under pressure. We have determined by DLS the pressure dependence of the coexistence temperature, the gel line or percolation limit was measured by DWS, and from SANS measurements we determined the stickiness parameter of the Baxter model. On the basis of our results we constructed an experimental phase diagram for this poly-disperse sticky hard sphere model system. A comparison with theory shows good agreement especially concerning the predictions for the percolation threshold.

The system of sticky hard colloidal spheres belongs to a class of systems where phase separation competes with arrested states like gels or glasses. Systems where these kinds of effects are at hand vary between model colloidal systems like highly concentrated hard spheres with added depletion interaction, to biological systems to networks of rods. Thus, identifying the structural features underlying such a complex phase behavior for a system of sticky hard spheres would not only be of interest for the colloid field, but would also shed light on general physical aspects which combine glasses with colloidal physics and gel phases and demixing phenomena. Thus, knowledge of the connection between gelation and phase separation for sticky hard spheres would greatly help also the understanding of other arrested systems.

The model system we used consists of silica spheres of 65nm diameter grafted with octadecyl chains in toluene at various volume fractions [1]. Adhesive polydisperse core-shell particles are assumed to interact on the pair level through an interaction potential given by the Baxter-model.

This pair interaction is a square well of infinitesimal width and infinite depth which is superimposed on a hard core repulsion. In Fig.1 the theoretical phase diagram is depicted. The two recent approaches taking polydispersity into account agree well with each other and substitute the old model C1, which was based on the approximate character of the Perkus-Yevick approach for a polydisperse sticky hard sphere system.

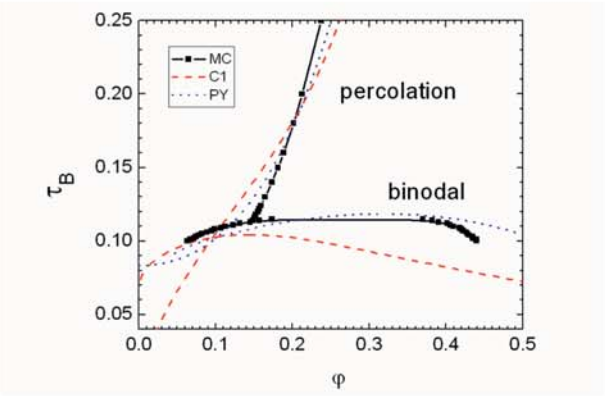

FIG. 1: The Baxter stickiness parameter τ_B vs. the volume fraction for the theoretical phase diagram of an adhesive hard sphere model taken from Fantoni et al [2]. Their data (dotted lines) is denoted as PY and is in this plot compared with MC simulations, which are shown as full lines and filled squares. Dashed lines denote a simplified model, which predicts a different critical point.

We determined [3] first of all the phase coexistence line using dynamic light scattering under high pressures. On passing the phase coexistence we notice a substantial broadening of the intensity autocorrelation function. The percolation threshold was determined by diffusive wave spectroscopy DWS using the fact that the transition between ergodic to non-ergodic is identified with passing the percolation line. DWS uses a proper ensemble averaging procedure by applying the so-called two cell technique, which gives the physically correct baseline. Another access to the percolation threshold is provided by SANS, where we have used a so-called global fitting routine which has taken all measured scattering curves into account simultaneously. We correlated the stickiness parameter τ_B(P,T) at a given volume fraction with quantities related to the square well potential: the hard core diameter 2R; the width of the potential Δ; the overlap volume between spheres L; the Θ temperature, which describes the enthalpic and entropic interactions between solvent and solute. We have assumed that the Θ temperature depends linear on pressure.

Percolation in this scheme is seen, when above a certain percolation threshold the stickiness does not change any further with changing P or T. In Fig.2 we

show our experimental phase diagram together with the theoretical predictions as already given in Fig.1.

$$\tau_B(P,T) = \begin{cases} \tau_B(P,T) & \text{for } \tau_B(P,T) > \tau_{B,perc}(\text{vol}\%) \\ \tau_{B,perc}(\text{vol}\%) & \text{otherwise} \end{cases}$$

with

$$\tau_B(P,T) = \frac{2R+\Delta}{12\Delta} exp\left[-L\left(\frac{\Theta(P)}{T}-1\right)\right]$$

As one can see from Fig.2, the agreement between different methods and simulation with regard to percolation is good, however, the determination of the coexistence line, the binodal, and likewise the spinodal line is experimentally difficult as it is not clear how the system interferes with the percolation for volume fractions above about 10%.

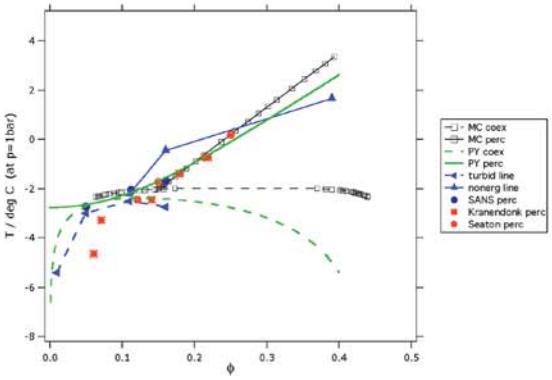

FIG. 2: Comparison between the theoretical phase diagram (black symbols) and our data (triangles, for percolation upright, for binodal left pointing). Simplified model as in Fig.1 in green. In red other experimental data for percolation. Our data are converted into temperature using parameters from the SANS global fit.

We have performed time dependent measurements of samples with volume fractions around the intersection point between percolation and binodal line. However, the exact locus of that point is still under debate and hence decisive conclusions can not be drawn up to now. For this purpose the critical scaling behaviour could be used, which by definition locates the spinodal line and can give access to this thermodynamically determined quantity even in the presence of percolation if one waits long enough. Typical time dependence is shown in Fig.3.

As shown in the Fig.3, between 500-700bar a time dependence sets in, which is indicative for passing the percolation. Intensity values at long times are in agreement with critical scaling predictions. Further research is in progress.

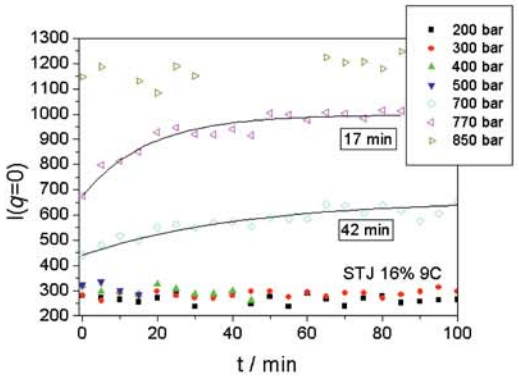

FIG. 3: Time dependence of SANS forward scattering for a 16% sample at various pressures at 9° C.

[1] J. Kohlbrecher, J. Buitenhuis, G. Meier, and M. P. Lettinga, J. Chem. Phys. **125**, 044715 (2006)

[2] R. Fantoni, D. Gazzillo, and A. Giacometti, J. Chem. Phys. **122**, 034901 (2005)

[3] R. Vavrin, J. Kohlbrecher, A. Wilk, M. Ratajczyk, M. P. Lettinga, J. Buitenhuis, and G. Meier, J. Chem. Phys. **130**, 154903 (2009)

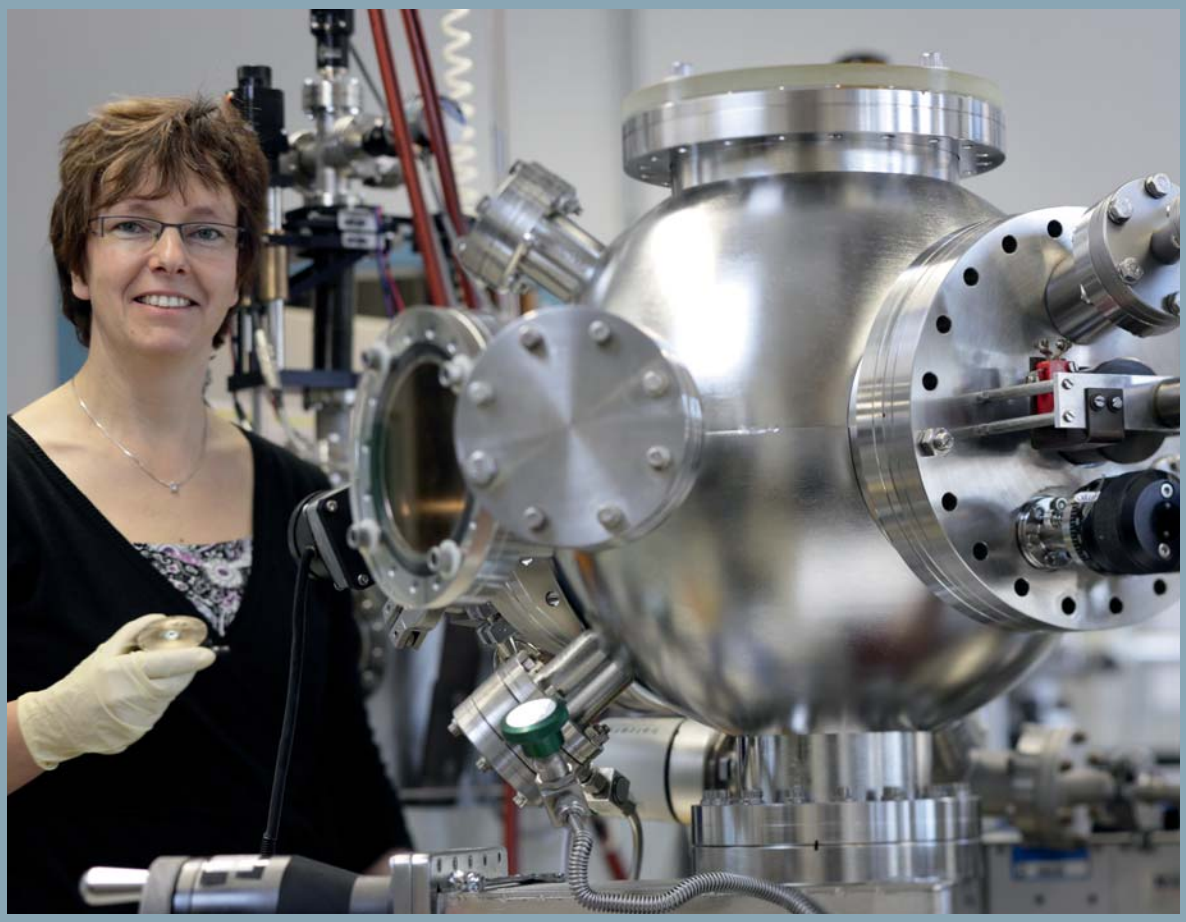

IFF researchers conduct research on the basic physicochemical principles of resistance channels, which may be used as tiny basic elements in memories.

Information technology with nanoelectronic systems

This research programme focuses on medium-term and long-term tasks in nanoelectronics, on emerging far-reaching concepts, and on issues of physics and technology well ahead of the mainstream development. On the eve of the transition from microelectronics to nanoelectronics, the traditional routes of down-scaling along the roadmap will no longer guarantee a long-term success. Exploratory research in the field of information technology is entering a new era and is unfolding into new degrees of freedom. This applies to all three major fields, information processing, information storage, and information transmission. The major routes of exploratory research in nanoelectronic systems to be followed are:

- scalability of device concepts,
- exploration of new material classes and phenomena,
- new concepts beyond conventional CMOS technology, and
- alternative architectures.

Our research towards these general goals utilizes three approaches, irrespective of the specific programme topics. One approach is dedicated to new electronic materials such as ferromagnetic and ferroelectric layer structures, group III nitrides, and electronically active organic molecules. These material classes are studied because of their potential for introducing improved or completely new functions onto Si chips and new emerging substrates. Another approach is devoted to process technologies for minimum feature sizes well below 100 nm. Apart from using conventional top-down approaches, which are limited to lithographically defined resolutions, we are investigating cost-effective bottom-up approaches, which aim at the generation and assembly of functions from self-organized inorganic nanostructures as well as tailored organic molecules at surfaces. Yet another approach explores novel electronic functions as the basis for new device concepts. These may aim at, for instance, bioelectronic applications, ultra-dense and non-volatile resistive memories, spin-controlled devices, Terahertz imaging systems, and self-organized semiconductor nanostructures.

Impact of defect distribution on resistive switching characteristics of Sr_2TiO_4 thin films

K. Shibuya, R. Dittmann, S. Mi, R. Waser

IFF-6: Electronic Materials

In this study, we will compare thin film samples with significant different defect structure and will thereby provide the experimental evidence of the correlation between defect density and switching properties. We will furthermore demonstrate the coexistence of two different switching characteristics with opposite polarity which can be reversible and controllable selected by the current load. We will clearly show that the two switching mechanisms are differently pronounced in different defect density and thickness regimes.

In order to develop resistive materials to applicable memory cells and to advance to the ultimate scaling limits for future ReRAM, deep understanding of switching mechanisms is indispensable. There exists a general agreement that the migration of oxygen vacancies under applied electric field plays an important role for resistive switching phenomena in oxides. Extended defects within the active thin film matrix have been claimed to play a crucial role, associated with the fact that oxygen-vacancy migration is significantly enhanced along extended defects. [1, 2] However, direct experimental demonstration of a correlation between defect distribution and switching properties has not been reported up to now. One of the reasons is the lack of materials with a well defined distribution of defects.

One advantage of using Sr_2TiO_4 thin films is the opportunity to control the defect density in the layer by the growth temperature. [3] Transmission electron microscopy (TEM) images of the films grown on nondoped $SrTiO_3$ surfaces at 700 and 900 ^oC are presented in Figures 1 (a) and (b), respectively. The reduction of the thermal energy during the deposition resulted in a local cation nonstoichiometry and thereby in a high density of defects in the Sr_2TiO_4 layer. On the other hand, well-ordered layered sequences of Sr_2TiO_4 were formed at a higher growth temperature.

The as-grown insulating Sr_2TiO_4 films were transformed into a switchable state by performing an electroforming process. [2, 4] Typical I-V characteristics of junctions with defective and nearly perfect Sr_2TiO_4 layers are shown in Figures 1 (c) and (d), respectively. In the case of the defective layer, large hysteresis windows especially in the reverse bias were observed in I-V cures, as shown in Figure 2 (c). On the other hand, little currents were seen in the reverse bias in the case of the less defective layer, as shown in Figure 2 (d). This was because the electroforming procedures could not be completed in the less defective films according to the less effective oxygen diffusion. Although the amount of oxygen vacancies was enough to obtain conductivity in the thin film, it was insufficient to overcome the Schottky-like barrier. Therefore a strong rectifying behavior was seen in Figure 2 (d). A high density of lattice defects was required for the completion of the conducting filaments.

Another intriguing feature was that the conductance in the incompletely formed interfaces as shown in Figure 2 (d) scales with the pad size of the top electrodes, denoting a homogeneous conduction.

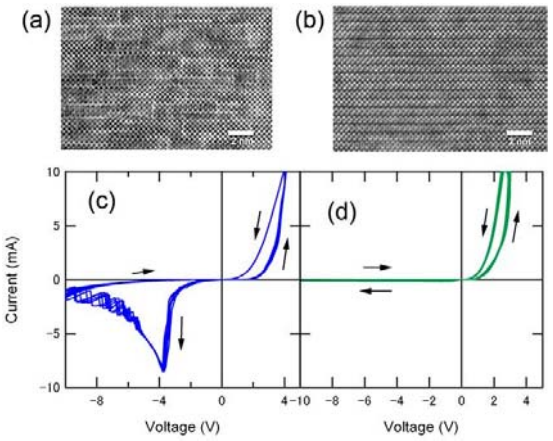

FIG. 1: TEM images of Sr_2TiO_4 films grown on nondoped $SrTiO_3$ substrates at (a) 700 ^oC and (b) 900 ^oC. I-V characteristics of the films grown on Nb-doped $SrTiO_3$ surfaces at (c) 700 ^oC and (d) 900 ^oC, respectively. The thickness of the Sr_2TiO_4 layer was about 10 nm in both cases

A typical feature of the Au/Sr_2TiO_4/Nb:$SrTiO_3$ junctions with well pronounced hysteresis curves is that one can see two types of switching properties represented by the red and the blue curves in Fig. 2. The red curves were observed in the smaller voltage range of $\pm$4 V. When a negative bias exceeded -4 V, negative differential resistance shows up and afterwards the switching polarity converts into the other direction (blue curve). The polarity of the red curve can be explained by oxygen-vacancy migration [1, 2], judging from the resistance changes from LRS to

HRS in the positive or the forward bias. The conductance of these switching curves was independent of the pad area, indicating a filamentary conduction.

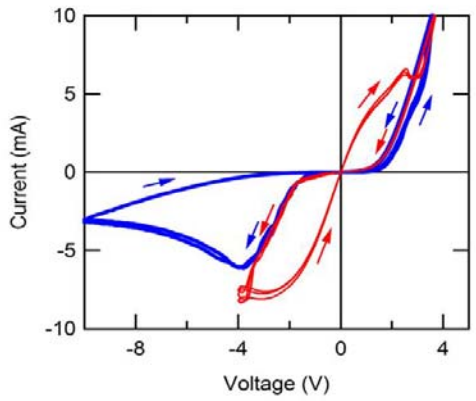

FIG. 2: I-V curves of the junction with a 10-nm thick Sr_2TiO_4 layer grown at 700 °C

The other switching type (blue curve) showed a rectification behavior as the I-V curves of the pristine junction. The Schottky-like barrier seemed to be slightly modified during a voltage sweeping. This switching type is more stable than the other one and can exhibit area scaling depending on the used forming procedure. This behavior is similar to the interface-type switching reported by Sawa in metal/Nb-doped $SrTiO_3$ single crystal structures without active layer. [5] Trapping and detrapping of electrons at oxygen vacancies in the interface has been suggested as possible switching mechanisms [4], but the exact origin will have to be investigated in future work.

The polarity conversion of these two switching types can be reversibly adjusted by the sweeping voltage range as shown in Fig. 2. The HRS of the red curve polarity corresponds to the LRS of the blue curve. The switching polarity conversion and the coexistence of the two switching types were exhibited above a film thickness of around 5 nm. Below the thickness only the "red-curve type" switching was observed. Figure 3 (a) is a schematic drawing of the switching polarities as functions of Sr_2TiO_4 layer thickness and growth temperature. It shows that both types of switching coexist in a broad range of conditions. Figure 3 (b) corresponds to Figure2 which shows I-V curves of the junction with a 10-nm thick Sr_2TiO_4 layer where both switching polarities were observed.

When the layer is less defective, only the "blue-type curve" switching was seen, independent of the layer thickness. At ultrathin layers below 5 nm, the same polarity merely appeared even though the layers were defective, grown at lower temperatures. Typical I-V curves are presented in Figure 3 (c). Similar to Figure 1 (d), a rectification appeared but a relatively large reverse conductance showed up due to large tunneling currents through a very thin barrier. These results indicate that the "blue-curve type" switching emerges exactly at the interface while the switching process of the "red-curve type" polarity is more bulk-

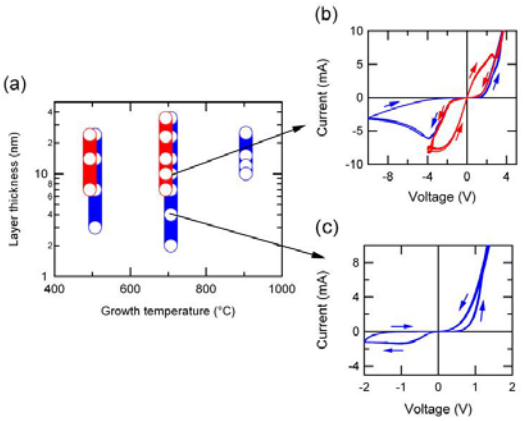

FIG. 3: (a) A schematic drawing of switching polarities as functions of Sr_2TiO_4 layer thickness and growth temperature. I-V curves of the junction with (b) a 10-nm thick and (c) a 3.6-nm thick Sr_2TiO_4 layers grown at 700 °C.

like due to the oxygen-vacancy migration along the extended defects.

In conclusions, we have demonstrated in $Au/Sr_2TiO_4/Nb$-doped $SrTiO_3$ junctions the clear correlation between resistive switching properties and the density of defects which work as fast migration paths for oxygen vacancies. Therefore, the control of the distribution and the density of defects is a major task in terms of the fabrication of reproducible and scalable resistive switching devices. Furthermore, we observed the coexistence of two switching polarities which could be reversibly adjusted by the applied voltage range.

[1] K. Szot et al., Nature Materials 5, 312 (2006)

[2] R. Waser, R. Dittmann, G. Staikov, K. Szot, Advanced Materials 21, 1-32 (2009)

[3] K. Shibuya, S. Mi, C.-L. Jia, P. Meuffels, R. Dittmann, *Appl. Phys. Lett.*, **92**, 241918 (2008)R. Waser, R. Dittmann, G. Staikov, K. Szot, Advanced Materials 21, 1-32 (2009)

[4] K. Shibuya, R. Dittmann, S. Mi, R. Waser, Advanced Materials **22** , 411 (2010)

[5] A. Sawa, *Mater. Today* **11**, 28 (2008).

Intermixing at $DyScO_3/SrTiO_3$ interfaces

M. Luysberg[1], J. Schubert[2]

[1] IFF-8: Microstructure Research
[2] IBN-1: Semiconductor Nanoelectronics

Recently, highly conducting layers were reported at the interfaces between complex, insulating oxides of different polarity [1]. The polar discontinuity delivers the driving force for a charge accumulation in the interfacial region which has been demonstrated for $LaAlO_3$ interfaces with $SrTiO_3$. Here it is shown that the polar discontinuity can be accommodated by variations in composition of cat ion lattice planes at the polar oxide interface between $DyScO_3$ and $SrTiO_3$, where $DyScO_3$ holds the same polarity as $LaAlO_3$. An intermixing extending over two monolayers at the interfaces for both the Dy-Sr sublattice and the Sc-Ti sublattice is quantified.

In order to measure the composition across $DyScO_3/SrTiO_3$ interfaces high angle annular dark field (HAADF) images and electron energy loss (EEL) spectra have been recorded. The atomic structure of the $DyScO_3$ layer embedded into $SrTiO_3$ is revealed in the HAADF image shown in figure 1. The image has been recorded with an aberration corrected STEM, which produces a probe size of 0.08 nm. The HAADF signal intensity of each atom column position reflects the difference in atomic number of the various species within the columns. The positions of different types of atoms can be identified by inspection of the structure models displaying one orthorhombic unit cell of $DyScO_3$ and four cubic unit cells of $SrTiO_3$, respectively. Here $DyScO_3$ is imaged along the [101] direction of the orthorhombic unit cell resulting in zigzag arrangement of the Dy columns parallel to the interface [2]. Scandium and titanium atoms located at the centre of the oxygen octahedra (displayed in orange within the structure models) result in a considerably weaker contrast compared to the heavier elements strontium and dysprosium, where the latter shows highest intensity. The oxygen atoms cannot be resolved due to their low scattering cross section.

The layers shown here are part of a multilayer system, grown by pulsed laser deposition on Si substrate [3]. All layers are characterized by a high crystalline quality and exhibit the same layer thickness. Along the interfaces, i.e. in atom rows 4 and 14, the contrast at the Dy/Sr positions can be clearly observed to alternate between neighbouring atom columns. This is seen in the image as well as in the concentration profile shown at the bottom. Hence an ordered interface structure is unambiguously detected.

The concentration values shown at the bottom of figure 1 were evaluated by quantification of the intensities through two-dimensional Gaussian fits to each atom position in the HAADF image. Here, only the Sr and Dy atoms were considered, since the weak contribution of the lighter elements is partly covered by the tails of the heavy elements. In each atom row the intensities of five equivalent positions, i.e. positions A and B, respectively, are averaged. Error bars denote the standard deviation obtained from concentration values in regions of constant composition. The Dy concentration was obtained by calculating the integrated intensity to the power of 1/2 and subsequently normalizing to 100% within the $DyScO_3$ layer and 0% within the $SrTiO_3$ layer.

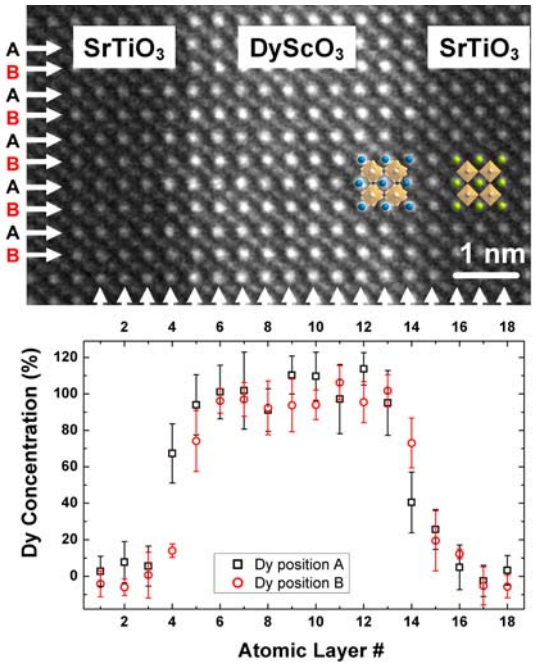

FIG. 1: HAADF image of $SrTiO_3/DyScO_3$ multilayers (top). For each Dy layer the concentrations of positions A and B are deduced (bottom). The interface layers, rows 4 and 14, show a distinct difference in contrast between the neighbouring positions A and B. Hence, an ordered interface structure is formed.

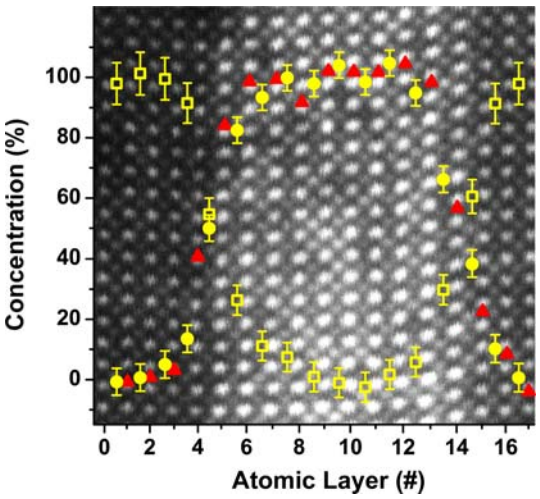

FIG. 2: HAADF image of $SrTiO_3/DyScO_3$. The fast scan direction runs from bottom to top. Superimposed are the average Dy concentrations as red triangles (average of positions A and B in Fig. 1) as well as the Sc (yellow circles) and Ti (yellow open squares) concentrations for each atom row.

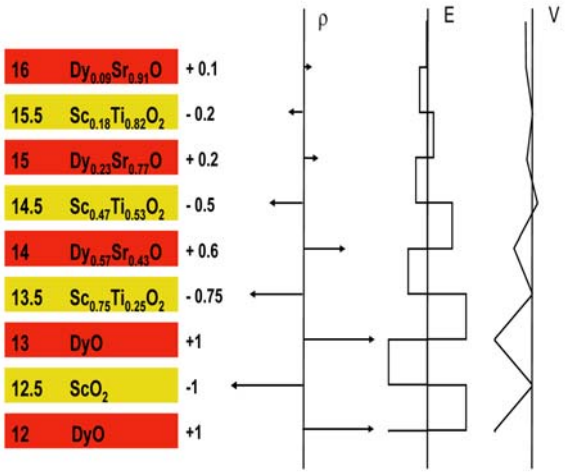

FIG. 3: Summary of composition and charges according to the composition for layers 12 through 16 shown in figures 1-2. The electric field E deduced from the charges ρ is displayed schematically. The corresponding variations of the electric potential V are seen to decrease as the $(Dy_{0.1}Sr_{0.9}O)$ layer 16 is approached.

The Sc and Ti composition of each atomic layer were determined by the StripeSTEM method developed by Heidelmann et al., which is based on the isochronous acquisition of EELS data and HAADF signals [4]. In order to obtain a sufficient signal to noise ratio within the EEL spectra, larger probe sizes about 0.2 nm in diameter and long acquisition times of 1 s per spectrum have to be chosen. The Sc and Ti spectra (not shown here) consist of the four characteristic lines, which implement a splitting into e_g and t_{2g} levels of the L_2 and L_3 edges due to the octahedral crystal field imposed by the oxygen atoms [5]. Furthermore, the valence of Ti is for all atomic layers close to 4+, which can be concluded form the fact that the shape of the Ti L-lines, does not change.

In figure 2 a high-resolution HAADF image of a $SrTiO_3/DyScO_3/SrTiO_3$ is displayed, which has been recorded within 100 s in parallel with EEL spectra. Despite the large acquisition time and the broader probe the individual atomic columns of Dy, Sr, Ti and Sc can be resolved. Sc and Ti concentrations, which have been determined from the EEL spectra recorded for individual atomic planes, are superimposed in the HAADF image in Figure 2 (for details see [5]). In addition, the average Dy concentration is displayed, i.e. the average of positions A and B shown in figure 1. An intermixing extending over two monolayers at the interfaces is observed for both the Dy-Sr sublattice and the Sc-Ti sublattice. [5].

The compositions of the atomic layers 12 through 16 are summarized in figure 3. Following the ionic model [1], the unit cells have been divided into (AO) layers and (BO_2) of the ABO_3 compounds involved. According to the valences of +3 for Dy and -2 for O, the (DyO) layers 12 and 13 carry a charge of +1. For the same reason the (ScO_2) layers are negatively charged. As the interface is approached, mixed layers occur, which contain ions of different valences. Accordingly the charges per unit cell change, e.g. for layer 13.5, which contains 25% Ti^{4+} and 75% Sc^{3+}, the charge adds to -0.75. In a similar way the charges of the mixed Dy/Sr layers can be determined. In consequence of the charge distribution ρ the electric potential V oscillates around zero and finally vanishes. Hence, the interface dipoles arising from the polar discontinuity are compensated by adjusting the concentration of ions with different valences within individual atomic layers.

In consequence, the interface between $DyScO_3$ and $SrTiO_3$ does not contain free carriers and is expected to be neutral. Indeed, electrical measurements reveal insulating behaviour [5]. This result is surprising in view of the fact that a conducting interface was reported for $LaAlO_3/SrTiO_3$, which is similar to the system investigated here regarding the polarity and bandgap of the materials involved. Hence it has to be concluded, that aside form a charge transfer mechanism the composition of the cat ion layers is crucial for the macroscopic electrical properties of polar oxide interfaces.

[1] N. Nakagawa, H. Y. Hwang, and D. A. Muller, Nature Materials **5** (2006) 204

[2] M. Boese, T. Heeg, J. Schubert, and M. Luysberg, Journal of Materials Science **41** (2006) 4434

[3] T. Heeg, M. Wagner, J. Schubert, Ch. Buchal, M. Boese, M. Luysberg, E. Cicerrella, J. L. Freeouf Microelectronic Engineering **80**, 150 (2005)

[4] M. Heidelmann, J. Barthel, and L. Houben, Ultramicroscopy **109** (2009) 1447

[5] M. Luysberg, M. Heidelmann, L. Houben, M. Boese, T. Heeg, J. Schubert, and M. Roeckerath, Acta Materialia **57** (2009) 3192

Exchange splitting and bias-dependent transport in EuO tunnel barriers

M. Müller[1,2], G.-X-Miao[2], J. S. Moodera[2]

[1] IFF-9: Electronic Properties
[2] Francis Bitter Magnet Laboratory, Massachusetts Institute of Technology, Cambridge MA, USA

We study characteristic features of spin filter tunneling in EuO-based magnetic tunnel barriers. Transport measurements show a unique voltage dependence, which give direct evidence for a spin filtering effect without relying on the use of external magnetic fields for spin detection. The variation of the effective tunnel barrier height systematically correlates with the spontaneous magnetization of EuO and allows the evaluation of spin filter efficiency of magnetic tunnel barriers by fully electrical means.

Realizing highly spin-dependent electron transport is an important challenge in spintronics, either for obtaining large magnetoresistive effects or for establishing spin injection into semiconductors. Magnetic tunnel junctions (MTJs) are main building blocks of spintronic devices and their figure of merit, i.e. the tunnel magnetoresistance (TMR) ratio, has steadily increased over the last two decades. An emerging route to realize spin-polarized tunneling is using a magnetic tunnel barrier as the spin-selective element. This approach does not require FM electrodes as the source of spin-polarized carriers, but takes advantage of the spin-dependent tunnel probabilities in a magnetic tunnel barrier: In contrast to its nonmagnetic counterpart, *two* spin-split barrier heights ($\Phi_\uparrow$, $\Phi_\downarrow$) are in effect and a highly spin-polarized tunnel current is created due to the exponential dependence of the tunneling probabilities on barrier heights.

Spin filter (SF) tunneling has been observed up to now only in few materials, such as selected Europium chalcogenides, spinel ferrites and perovskites [2, 3]. The effectiveness of spin filtering is intimately connected with the magnetic ordering of the magnetic insulator, in particular with the magnitude of exchange splitting E_{xc} of the conduction band. We studied electronic transport and its dependence on magnetic ordering in Europiumoxide (EuO) spin filter tunnel barriers, with EuO being a prototype Heisenberg ferromagnet with a bulk Curie temperature T_C of 69 K and a bandgap of 1.12 eV, with an exchange splitting of the conduction band of up to 0.6 eV below T_C [4].

Current-voltage (I-V) characteristics across EuO spin filter tunnel barriers typically reveal a highly nonlinear shape, which is indicative of tunnel transport. Basically, two different tunneling mechanisms must be expected in a magnetic tunnel barrier at different bias voltages, i.e. direct tunneling (DT) and Fowler-Nordheim (FN) tunneling. DT occurs when the applied bias voltage is less than the average barrier height, whereas FN tunneling is observed if the bias voltage exceeds it. Due to the reduced effective barrier width, the probability for FN tunneling is much larger compared to that of DT.

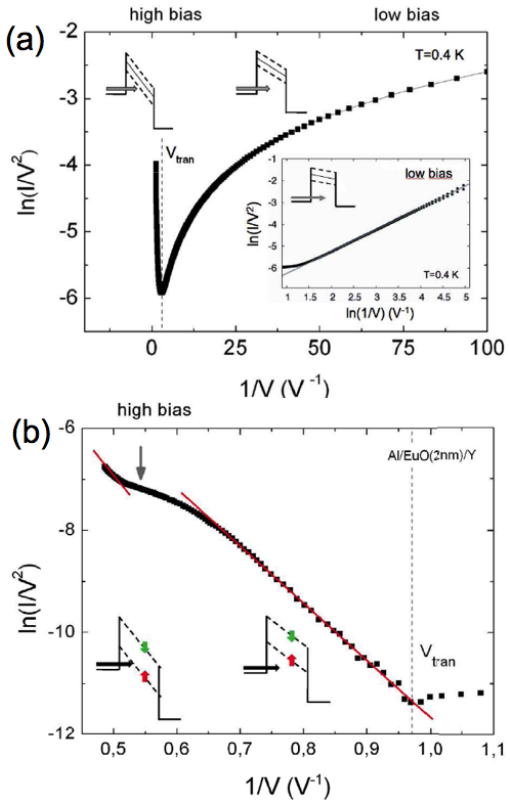

FIG. 1: (a) $\ln(I/V^2)$-$1/V$ plot of an Al/EuO(4 nm)/Y junction at T=0.4 K. The dotted line denotes the transition voltage at which the transport mechanism changes from DT to FN tunneling. (b) $\ln(I/V^2)$-$1/V$ plot for the high bias region of an Al/EuO(2 nm)/Y junction. Two onsets of linear decaying slopes are observable, separated by a crossover region.

Within a two-current model and applying the WKB approximation, we show in Ref. [1] that both tunnel transport mechanisms can be directly compared by rearranging I-V curves in terms of the variables $\ln(I/V^2)$ and $1/V$. We derived, that in the high bias

voltage regime a plot of $\ln(I/V^2)$ versus $1/V$ will yield a linear curve, the slope of which depends on the barrier height. In the low bias regime, however, a plot of $\ln(I/V^2)$ against $1/V$ will exhibit a logarithmic growth, which describes transport in terms of direct tunneling. Using those criteria, one can distinguish different tunneling mechanisms.

In Fig. 1(a), the tunneling characteristics across a 4 nm thick EuO tunnel barrier at 0.4 K is shown at positive bias. Two distinct voltage regimes are evident from this plot: At low bias, the curve follows a logarithmic growth, with transport being interpreted as direct tunneling. The dotted line denotes the transition voltage V_{tran}, above which a linear behavior appears. In this high bias region, transport is carried by FN tunneling. Fig. 1(b) shows the high bias transport region for a 2 nm thick EuO barrier on a larger scale, with *two* linear decaying slopes joined by a crossover region. This particular shape is attributed to the spin-selective onsets of FN tunneling. Raising the bias above V_{tran} for the lower barrier height ($V \geq \Phi_{\uparrow}$) leads to a sharp increase of tunnel current ($\Phi_{\uparrow} \leq V < \Phi_{\downarrow}$). If the bias exceeds the upper conduction band $\Phi_{\downarrow}$, FN tunneling for the second spin type sets in and leads to a further significant increase of the tunnel current. The data thus provides direct evidence for spin filtering, as it clearly visualizes the stepwise onset of two FN tunneling regimes.

In general, our findings show that the tunneling spin polarization resulting from the specific transport mechanism in magnetic tunnel barriers is highly bias voltage-dependent. In particular, the highest spin polarization is to be expected for bias voltages, for which FN tunneling is active for one spin type only, whereas transport for the second spin type is by direct tunneling. Moreover, it becomes clear that by choosing the appropriate bias voltage, the spin polarization P provided by spin filter tunneling in principle can be tuned to any value between $0 \leq P \leq 100\%$.

In order to quantify the exchange splitting E_{xc} of EuO spin filter tunnel barriers, a systematic study of the temperature-dependent I-V behavior was performed. In Fig. 2(a), we compile the I-V characteristics of an Al/EuO(4 nm)/Y system over a wide temperature range. The current increases rapidly with bias voltage, and we note a pronounced shift of the I-$V(T)$ curves towards higher bias voltages with increasing temperature. Above 80 K, the temperature-dependent voltage shift disappears. We conclude, that the temperature-dependent shift of the I-V curves is mainly due to a change in barrier height, $\Delta\Phi(T) = \Phi_0 - \Phi_{\uparrow(\downarrow)}(T)$, brought about by the spontaneous conduction band splitting in EuO for $T < T_C$.

Within the Weiss molecular field model, the exchange splitting E_{xc} may be approximated as $E_{xc}(T) \propto J_{df} S \sigma(T)$, where J_{df} is the d-f exchange constant, $S = 7/2$ is the spin quantum number of an Eu^{2+} ion and $\sigma(T)$ the reduced magnetization $M(T)/M(T = 0)$ of EuO. Hence, the change of the effective barrier height $\Delta\Phi(T)$ corresponds to half of the exchange splitting as $\Delta\Phi(T) = 1/2\, E_{xc}(T)$. We determined the relative change of the EuO barrier height with the

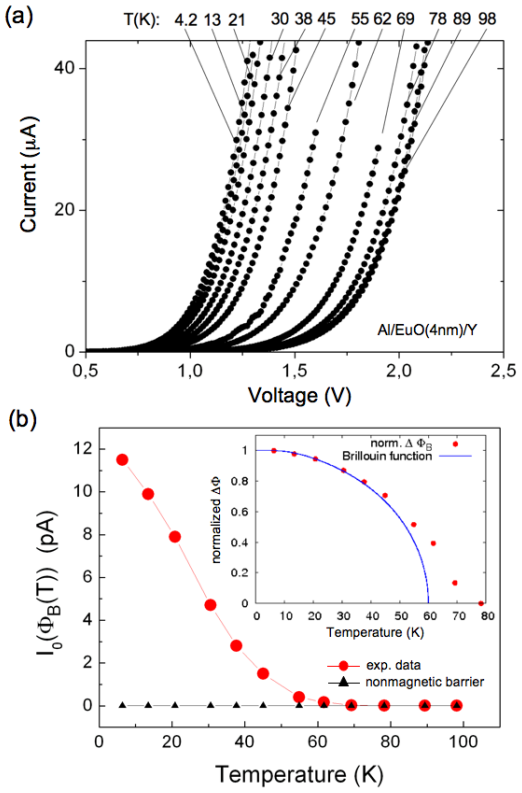

FIG. 2: (a) I-$V(T)$ plot of an Al/EuO(4 nm)/Y spin filter tunnel junction at positive bias. (b) Saturation current $I_0(\Phi_{\uparrow(\downarrow)}(T))$ as a function of T, shown together with the result for a nonmagnetic barrier. The inset shows the normalized change in effective barrier height $\Delta\Phi(T)$ fitted to a Brillouin function with $S = 7/2$.

result shown in the inset of Fig. 2(b). By fitting $\Delta\Phi(T)$ to a Brillouin function ($S = 7/2$), the correlation between the spontaneous magnetization originating from the Eu^{2+} magnetic moment and the lowering in barrier height is visualized. An exchange splitting of $E_{xc} = (0.49 \pm 0.04)$ eV was deduced and the resulting SF efficiency was determined as $P \approx 80\%$.

In summary, we were able to assign characteristic transport mechanisms in Eu-based spin filter tunnel barriers, revealing direct evidence for spin filtering without relying on external magnetic fields for spin detection. Moreover, we determined the exchange splitting E_{xc} by fully electrical means. The deduced spin filter efficiency implies that electron transport through EuO barriers is highly spin selective and thus of great interest for the use as spin polarizers or -detectors in spintronic devices.

[1] M. Müller, G.-X. Miao, and J. S. Moodera, Europhys. Lett. 88, 47006 (2009)

[2] M. Gajek *et al.*, Nature Mat. 6, 296 (2007)

[3] G.-X. Miao, M. Müller, and J. S. Moodera, Phys. Rev. Lett. 102, 076601 (2009)

[4] A. Schmehl *et al.*, Nature Mat. 6, 882 (2007)

Linear and quadratic magneto-optical Kerr effect in ultrathin Fe(001) films

M. Buchmeier[1], R. Schreiber[1], D. E. Bürgler[1], C. M. Schneider[1]

[1] IFF-9: Electronic Properties

The magneto-optical Kerr effect (MOKE) is a widely employed technique for the characterization of ferromagnetic thin films. However, a quantitative analysis is usually hampered by the lacking knowledge of precise magneto-optical parameters. We report the thickness dependence (0–60 nm) of the linear and quadratic MOKE in epitaxial bcc-Fe(001) samples and extract a complete set of parameters for the quantitative description of the MOKE response of bcc-Fe(001).

The magneto-optical Kerr effect (MOKE) is probably the most important tool for the magnetometric characterization of thin-film samples relevant for spintronics. Among its most common applications are the quantitative determination of the coercivity, magnetic anisotropy, and interlayer exchange coupling from the analysis of hysteresis loops recorded with the MOKE signal. Other prominent applications are the investigation of spin dynamics in the time-domain and magnetic domain imaging. The main advantages of the MOKE over other techniques are its compatibility with high magnetic fields, surface sensitivity with a typical information depth of some 10 nm, a time resolution down to the sub-picosecond regime, and a reasonable spatial resolution of the order of about 0.5 μm. However, many applications of the MOKE neglect the absolute magnitude of the Kerr effect, which is given by the magnitude and phase of the complex Kerr angle. The reason is that the full quantitative MOKE information is generally not linked by simple analytic formulae to the material properties, i.e. indices of refraction n and linear and quadratic magneto-optical (MO) coupling parameters K and G of all involved layers.

Here we report on a magnetometric study of the MO response of bcc-Fe(001) wedge-type samples with thicknesses ranging from 0 to 60 nm. We have determined both components of the complex Kerr angle, the Kerr rotation θ and the Kerr ellipticity ϵ. Effects linear and quadratic in the magnetization, LMOKE and QMOKE respectively, are separated by fitting the hysteresis loops to a single domain model. The QMOKE, which is known to be anisotropic, i.e. dependent on the sample orientation, has been determined for both Fe(001)[110] and Fe(001)[100] directions parallel to the plane of incidence. By fitting the thickness dependence of LMOKE and QMOKE we are for the first time able to extract a full set of Fe material parameters n, K, $(G_{11} - G_{12})$, and G_{44} at a light wavelength of 670 nm [1].

Epitaxial bcc-Fe(001)(wedge)/Ag(1 nm)/Au(2 nm) films have been prepared by molecular beam epitaxy on a GaAs/Ag(001) buffer system. The Au capping layer has been chosen thick enough to prevent oxidation and thin enough to be able to determine large Kerr angles. The Ag interface layer prevents a possible alloying of Fe and Au. The Fe thickness has been varied continuously between 0 and 8 nm for sample A and stepwise in sample B with discrete Fe thicknesses of 5, 8, 12, 18, 24, 32, 44, and 60 nm. MOKE measurements were performed using light from a diode with a wavelength of 670 nm and a spectral half-width of less than 2 nm. The incident light is polarized in $\hat{p}$ direction (electric field component in the plane of incidence), and the angle of incidence is 15° with respect to the sample normal. A photo-elastic modulator (PEM) with diagonal modulation axis operating at $f = 50$ kHz, a polarizer oriented in $\hat{s}$ direction, and a homemade diode detector are used to convert the light intensity into an electrical voltage. With this setup the small f (50 kHz) component determined with a lock-in amplifier is to first order proportional to the $\hat{p}$-ellipticity ϵ times the reflected intensity, while the much larger $2f$ (100 kHz) is to first order proportional to the reflected intensity alone. By introducing a quarter wave plate between sample and PEM we are able to measure the $\hat{p}$-rotation θ instead of the ellipticity ϵ. The two Kerr angle components (θ and ϵ) are calculated by dividing the measured f component with and without quarter wave plate by the $2f$ component.

It is convenient to expand the complex Kerr angle $\Phi = \theta + i\epsilon$ as a function of the directional cosines of the magnetization [2], e.g. in longitudinal and transversal cosines $m_{l,t}$ for in-plane magnetization:

$$\Phi = \sum_{layers\ i} \left[l_i m_{l,i} + q_{1,i} m_{l,i} m_{t,i} + q_{2,i} m_{t,i}^2 + O(m^3) \right], \quad (1)$$

where l_i are the longitudinal, and $q_{1,i}$ and $q_{2,i}$ the quadratic response coefficients. The longitudinal coefficients l_i stem from the linear MO coupling parameter K alone and are isotropic as long as the FM layers have cubic symmetry. The quadratic coefficients are due to a combined effect of the linear and

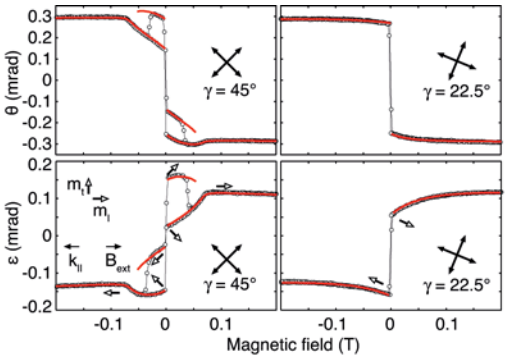

FIG. 1: Field dependence of measured (black) and calculated (red) Kerr ellipticity ϵ and Kerr rotation θ for a 60 nm Fe film. The direction of the magnetization is with short arrows, the easy axis directions of the magnetocrystalline anisotropy with crossed long arrows.

quadratic MO couplings and are anisotropic. For cubic systems the q coefficients have the form [2]:

$$q_1 = q_{001} + (q_{011} - q_{001}) \sin^2(2\gamma) \quad (2)$$

$$q_2 = \frac{1}{2}(q_{011} - q_{001}) \sin(4\gamma), \quad (3)$$

where γ is the angle between the in-plane component of the light wavevector and an in-plane Fe[001] direction. q_{001} and q_{011} are QMOKE constants for the plane of incidence parallel to the [001] and [011] directions, respectively. We determine l, q_{001}, and q_{011} by analyzing remagnetization loops recorded with different sample orientations γ. The explicit relations between l, q_{001}, and q_{011} and the MO coupling parameters K, $(G_{11} - G_{12})$, and G_{44} are given in [2].

Typical MOKE loops for a 60 nm Fe film are shown in Fig. 1. The experimental θ and ϵ curves are plotted in black. The red lines are fits to a single domain model taking into account the sample orientation γ, the cubic anisotropy parameter, and describing the Kerr angle via Eqs. (1–3). While the left loops recorded at $\gamma \approx 45°$, i.e. with field parallel to a hard [011] direction, depend on l and q_{011}, the right loops are recorded at $\gamma \approx 22.5°$ and, therefore, depend on l and both q_{011} and q_{001}. The simultaneous fitting of the loops for both orientations γ yields a full set of MOKE response coefficients l, q_{001}, and q_{011}.

The thickness dependence of the experimental LMOKE and QMOKE measured in [011] direction are shown in Fig. 2 by red circles and blue triangles for sample A and B, respectively. QMOKE is also measured in [001] direction, but not shown here, see [1]. The slope of all curves begins to asymptotically flatten at about 40 nm, which determines the MOKE information depth. The non-monotonic thickness dependence indicates that the additivity law [3] is generally not valid. Black, dotted lines show the thickness dependences of LMOKE calculated using literature values for the indices of refraction and the linear MO coupling. Obviously, these calculations fail to describe θ properly. The red and blue lines are the result of our fits based on the full 4×4 matrix formalism [4] using fixed indices of refraction for Ag and Au

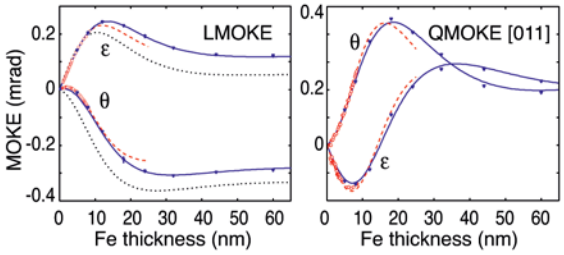

FIG. 2: Thickness dependence of the measured (red circles and blue triangles for sample A and B, respectively) and calculated (lines) LMOKE (left) and QMOKE for the Fe[011] direction (right) parallel to the plane of incidence. The black, dotted line is calculated from literature parameters.

from literature as specified above, and treating the index of refraction and the MO couplings of Fe as free parameters. The red and blue curves correspond to the data of samples A and B, respectively. The fit results and a comparison to literature values are given in [1]. It turns out that a satisfactory fit over the whole thickness range with only one thickness-independent set of material parameters is impossible. The fit to the data of sample A with smaller thicknesses results in a significantly (10%) larger index of refraction with different phase as compared to the thicker sample B. On the other hand, the MO coupling parameter K mainly differs in phase by about 10°, while the absolute values are in rather good agreement (<3%). Thus, it seems that the difference between thin and thick Fe layers is mainly of optic rather than of magneto-optical origin. Possible explanations for the thickness dependence are: (i) The tensile strain of the Fe due to the small lattice mismatch of 0.7% between Fe and the Ag substrate (ii) a relaxation of the lattice constant of Fe for larger thicknesses resulting in a thickness dependence of the optic properties of the Fe layer, (iii) altered electronic properties of the thin Fe layer due to the proximity to the noble metal substrate and the capping layers, and (iv) interfacial MOKE contributions, which have been neglected in the theoretical description.

To our knowledge this is the first report of the second-order MO coupling constants of Fe. They are comparable to the first-order constants and thus, of general significance for the theoretical and quantitative description of the MOKE.

[1] M. Buchmeier, R. Schreiber, D. E. Bürgler, and C. M. Schneider Phys. Rev. B **79**, 064402 (2009).

[2] K. Postava, D. Hrabovsky, J. Pistora, A. R. Fert, S. Visnovsky, and T. Yamaguchi, J. Appl. Phys. **91**, 7293 (2002).

[3] Z. Q. Qiu, J. Pearson, and S. D. Bader, Phys. Rev. B **45**, 7211 (1992).

[4] P. Yeh, Surf. Sci. **96**, 41 (1980).

Dynamics of spin-torque oscillators in vortex and uniform magnetization state

R. Lehndorff[1], D. E. Bürgler[1], S. Gliga[1], R. Hertel[1], P. Grünberg[1], C. M. Schneider[1], Z. Celinski[2]

[1] IFF-9: Electronic Properties
[2] Center for Magnetism and Magnetic Nanostructures, University of Colorado at Colorado Springs, USA

Current-driven magnetization dynamics in spin-torque oscillators (STO) has a high potential for high-frequency (HF) applications. We experimentally study current-driven HF excitations of STOs in the vortex and uniform in-plane magnetized state. Our ability to switch between these two states in a given STO enables a direct comparison of the STO characteristics. We find that the vortex state maximizes the emitted HF power and shows a wider frequency tuning range.

Spin-torque oscillators (STO) based on ferromagnet/non-magnet/ferromagnet (FM_{fixed}/NM/FM_{free}) layered structures are an application of current-induced magnetization dynamics. They show a steady precession of the magnetization of FM_{free} under the action of a spin-polarized DC current. This precession generates via the giant or tunnel magnetoresistance (GMR, TMR) effect a HF voltage oscillation with frequencies in the GHz range, which can be tuned by the DC current amplitude and the external magnetic field strength. Still, one drawback of STOs is their low output power. Several groups work on the synchronization of arrays of STOs in order to achieve useful power levels. While this is a very promising approach, maximizing the output power of every single STO is undeniably the first step to do.

There are several possible arrangements for STOs, e.g. with in-plane, out-of-plane, or vortex-type magnetized FM_{fixed} and/or FM_{free}. Comparing the characteristics of HF excitations – especially output power – from different experiments is not conclusive, because impedance and absolute resistance variations of the samples strongly influence the detected power. Here, we study HF excitations in two mentioned arrangements that we are able to realize in the same STO. While FM_{fixed} is uniformly in-plane magnetized, FM_{free} is either uniformly in-plane magnetized or in a vortex state. The direct comparison shows some advantages of the vortex state for the application of STOs [1].

Samples are fabricated by depositing 150 nm Ag/ 2 nm Fe/ 6 nm Ag/ 20 nm Fe/ 50 nm Au by molecular beam epitaxy on GaAs(100). The nanopillars are defined by electron beam lithography and ion beam etching and have a circular cross section with a diameter of 230 nm. Only the top magnetic layer (FM_{free}) is laterally confined, while the bottom layer (FM_{fixed}) is extended with a typical width of 15 μm (see inset in Fig. 1). The dimensions of FM_{free} are in a regime where a magnetic vortex and a uniform in-plane magnetization are both stable states [2]. The 2 nm-thick FM_{fixed} is uniformly magnetized on length scales much larger than the pillar diameter as long as a small magnetic field suppresses domain formation.

Figure 1 shows current-perpendicular-plane (CPP) GMR curves at 10 K with the magnetic field applied in the sample plane. Starting from saturation at 150 mT (blue curve) FM_{free} and FM_{fixed} undergo a gradual change from parallel to antiparallel alignment due to stray field interaction. The completely antiparallel alignment is reached at 0 mT and results in a high resistance. FM_{free} shows a uniform in-plane magnetization in this field range. After field reversal at about -20 mT in the formation of a vortex in FM_{free} results in a drop of the resistance. Upon further sweeping the field, the vortex core is moved from the center of the disk to the rim until it is expelled at about -100 mT. Micromagnetic simulations qualitatively reproduce this behavior as shown by the magnetization patterns in Fig. 1 (for more details see [1]).

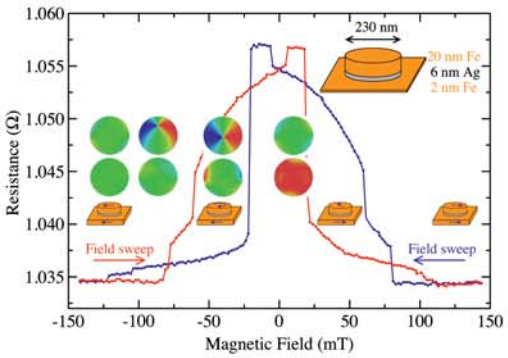

FIG. 1: CPP-GMR curves for increasing and decreasing field. Symbols and simulated micromagnetic magnetization patterns for FM_{fixed} (bottom) and FM_{free} (top) correspond to the decreasing (blue) sweep direction.

Figure 2 shows current-induced CPP resistance changes at 10 K and various field strengths. The initial states were prepared by magnetic field sweeps according to Fig. 1. We observe hysteretic switching of FM_{free} (e.g. green and red curves). The high-resistive state at positive currents corresponds to uniformly and antiparallelly aligned magnetizations in

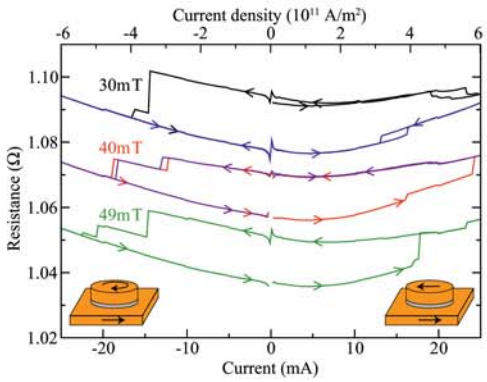

FIG. 2: Current-induced switching between the low-resistive vortex and high-resistive uniform state. The black and purple curves start in the uniform state, all others in the vortex state. For clarity the graphs measured at 40 and 30 mT are offset by +20 and +40 mΩ, respectively.

FM_{free} and FM_{frixed}, whereas the low-resistive state at negative currents is due to the vortex state in FM_{free}. This is in agreement with previous experiments on Fe/Ag/Fe nanopillars [3], which have established that the spin-transfer torque due to a positive current acts towards an antiparallel alignment. The fact that we do not observe a switching to the vortex state at positive currents in Fig. 2 proves that the prevalent torque in the switching processes does not originate from Oersted fields. These circumferential fields tend to switch the magnetization of FM_{free} into a vortex state also at positive currents, just with the opposite vorticity compared to negative currents.

We measure DC current-induced HF excitations of the magnetization at room temperature by amplification and detection of voltage oscillations across the nanopillar using a microwave probe station. The voltage variation arises from the GMR of the Fe/Ag/Fe stack, which reaches 2% or 22 mΩ in Fig. 1. The impedance of our sample was 11 Ω at 1.5 GHz. Figure 3(a) shows the HF response of a STO in the uniform state measured in an in-plane field of 82 mT. The low frequencies of the excitations are the result of the cancellation of the dipolar coupling field of about 80 mT by the external field and the rather large size of the element, for which the standing-wave mode has a low frequency. The observed blue-shift behavior at low currents can be interpreted in terms of standing-wave modes, which are deformed by the Oersted field. At higher currents the red-shift sets in that is explained by a predominantly homogeneous in-plane precession of the magnetization. Figure 3(b) shows representative HF excitations of a STO in the vortex state. Here, the gyrotropic mode [4] of the vortex is excited as previously reported by Pribiag *et al.* [5]. The gyrotropic mode is the lowest excitation mode of a magnetic vortex and consists of a circular motion of the vortex core around the equilibrium position. The radius of the trajectory is proportional to the excitation amplitude. When for increasing current the trajectory approaches the rim of the disk, the vortex experiences a stronger restoring force, increasing its precessional frequency. This results in a linear

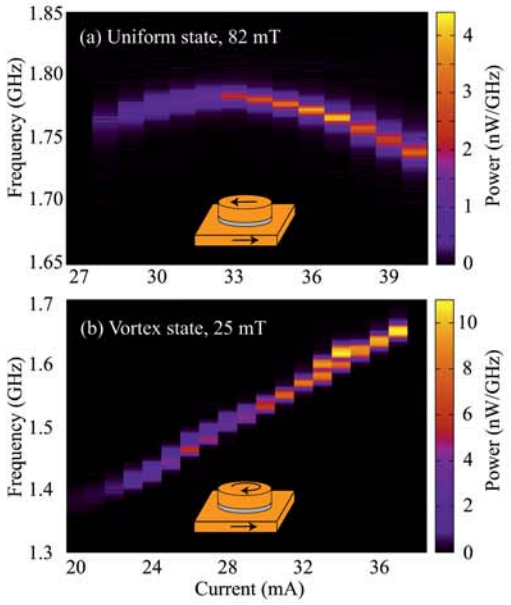

FIG. 3: Spin-transfer torque induced excitation of qualitatively different oscillatory modes in a STO: (a) Standing-wave mode in the uniform state and (b) gyrotropic mode of the vortex state. The microwave power generated by the gyrating vortex for a given DC current in (b) is much higher than for the standing-wave mode in (a).

increase of the frequency yielding a mode agility of +17 MHz/mA [Fig. 3(b)]. At each spot within the trajectory of the vortex core, the magnetization rotates during one period of the gyrotropic cycle by full 2π about the sample normal. Thus, for a vortex core moving on a trajectory close to the rim of the sample the product of oscillation amplitude times area, where oscillations take place, is maximized. As a consequence, the emitted power of the STO in the vortex state is nearly three times the power emitted in the uniform state (Fig. 3).

In conclusion, we directly compared the characteristics of a STO in either the uniform state or the vortex state. Higher agility, wider tuning range, and higher output power are all advantageous for the application of the vortex state in STOs. Although this conclusion is derived from metallic, GMR-type STOs, our generic, micromagnetic arguments are also valid for the technologically more relevant TMR-based STOs.

[1] R. Lehndorff, D. E. Bürgler, S. Gliga, R. Hertel, P. Grünberg, C. M. Schneider, and Z. Celinski, Phys. Rev. B **780**, 054412 (2009).

[2] R. P. Cowburn, J. Phys. D: Appl. Phys. **33**, R1 (2000).

[3] R. Lehndorff, M. Buchmeier, D. E. Bürgler, A. Kakay, R. Hertel, and C. M. Schneider, Phys. Rev. B **76**, 214420 (2007).

[4] K. Y. Guslienko, B. A. Ivanov, V. Novosad, Y. Otani, H. Shima, and K. Fukamichi, J. Appl. Phys. **91**, 8037 (2002).

[5] V. S. Pribiag, I. N. Krivorotov, G. D. Fuchs, P. M. Braganca, O. Ozatay, J. C. Sankey, D. C. Ralph, and R. A. Buhrman, Nature Physics **3**, 498 (2007).

Magnetism-hindered chain formation in transition-metal break junctions

A. Thiess[1,3], Y. Mokrousov[1,3], S. Heinze[2], S. Blügel[1,3]

[1] IFF-1: Quantum Theory of Materials
[2] Institut für Theoretische Physik und Astrophysik, Christian-Albrechts-Universität zu Kiel
[3] IAS: Institute for Advanced Simulation

Based on first-principles calculations, we demonstrate that magnetism hinders the formation of long chains in break junctions. We find a distinct softening of the binding energy curve of atomic chains due to the creation of magnetic moments that crucially reduces the probability of successful chain formation. Thereby, we are able to explain the long standing puzzle why most of the transition-metals do not form long chains in break junctions and provide an indirect proof that in general suspended atomic chains in transition-metal break junctions are spin-polarized.

One of the most exciting challenges in break junction (BJ) experiments is the search for evidence of magnetism in suspended monoatomic transition-metal (TM) chains. From the theoretical point of view everything is clear: recent first-principles studies show that $3d$, $4d$ and $5d$ freestanding and short suspended monowires are magnetic and possess giant values of magnetocrystalline anisotropy energies [1]. However, experimentally still no unambiguous evidence for magnetism in BJs exists. Our strategy to tackle this open question is a theoretical analysis of the most fundamental and experimentally easily accessible property of these systems: the probability for successful chain creation itself [2]. The trend arising from numerous BJ experiments is that monoatomic chain formation is most probable for late $5d$ TMs as well as Ag and Au.

To analyze the influence of magneism on chain creation probability we apply our recently developed model which describes the chain formation in BJs and which is able to provide a detailed insight into the complicated process of chain elongation and breaking based on energy arguments [3]. Being computationally easily accessible, this model relies only on a few system-specific parameters with transparent physical meaning which chracterize the thermodynamics of chains in break junctions. In our model chain formation succeeds if the *criterion for stability* and *producibility* are met. The *criterion for stability* quantifies the breaking of the bonds between the nearest neighbor atoms within the suspendend monowire, while the *criterion for producibility* formulates the condition for a successfull transfer of a lead atom into the chain. The validity of this model for predicting trends in BJ formation of pure chains and even chains with adatoms and impurities for transition and noble metals has been demonstrated [3].

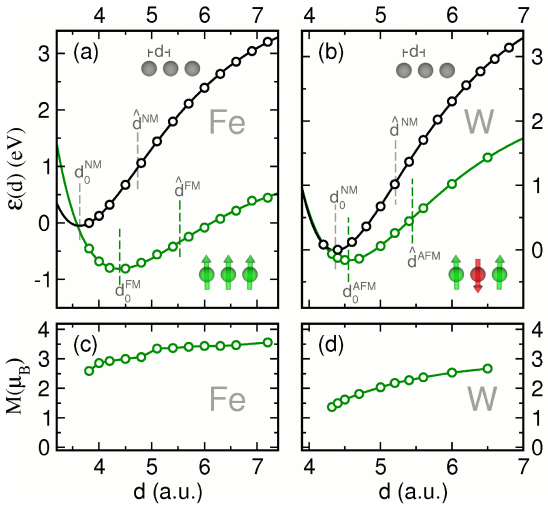

FIG. 1: Calculated chain energy $\mathcal{E}(d)$ (circles) as a function of interatomic distance d for both nonmagnetic (black) and magnetic state (green) are shown for (a) Fe and (b) W. The Morse-fit is shown with solid lines. The binding energy curves and the magnetic moments M in (c) and (d) correspond to the ferromagnetic and antiferromagnetic ground state for Fe and W, respectively.

We obtained the material-specific parameters needed for analyzing the elongation criteria for magnetic and nonmagnetic chains by performing density-functional theory calculations with the one-dimensional version of the Jülich FLAPW code FLEUR [4]. In all cases we included spin-polarization and spin-orbit coupling. In order to operate with continuous quantities we fit the calculated binding energy $\mathcal{E}(d)$ as a function of interatomic distance in the chain d by the so-called Morse-potential, which provides the analysis on the basis of a couple of physically meaningful parameters.

By comparing the tendency for successful chain creation with and without magnetism, we find that the presence of magnetism crucially softens the total energy profile $\mathcal{E}(d)$ – an effect mainly attributed to the intra-atomic exchange, Fig. 1. This bond softening has a crucial impact on the chain formation probability: the softer the bonds the harder chain elongation gets. Thus, we come to a conclusion that magnetism significantly suppresses chain formation. While nonmagnetic chains successfully form for almost all TM elements, the formation of chains with magnetism in-

cluded is, in agreement with experiments, predicted to take place only for Ir, Pt, Au and Ag [2].

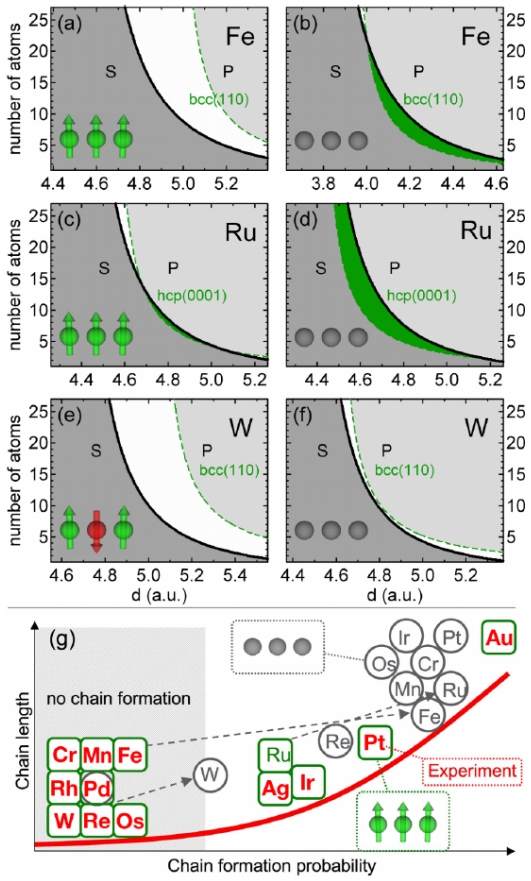

FIG. 2: Phase diagrams for Fe, Ru, and W-BJs with (a),(c),(e) and without (b),(d),(f) spin-polarization of the chain atoms. Plots indicate regions of stability (S, dark gray), producibility (P, light gray), separated by a white region or overlapping in the SP region (in green). The starting point along the x-axis is the chains' equilibrium interatomic distance, while the assumed surface orientations of the leads are indicated explicitly. The input parameters for W, Fe and Ru are given in [2]. (g) provides a schematic summary of our results. Shown is the chain formation probability, proportional to the size of SP-regions, versus chain length, proportional to the highest N for which an SP-region exists, with (green) and without spin-polarization (gray) in relation to the experimental findings (red) in all cases in arbitrary units relative to Au. Arrows indicate (exemplified for Fe, Ru and W) the consequence on the chain formation caused by switching off the finite magnetization in the chain.

With the knowledge of all key quantities entering the *criteria for stability* and *producibility* we can further analyze both criteria in the phase space of the number of atoms (N) and interatomic distance (d) (see Fig. 2). Each of the criteria leads to a distinct region where it is fulfilled and accordingly the chain is stable (S) or producible (P). Ideally for a successful chain elongation event to happen, both regions (S) and (P) have to overlap (SP). Analysis in terms of S and P diagrams provides a simple and insightful way to analyze the complicated process of chain formation [3].

Comparison of the phase diagrams for different TMs, shown for Fe, Ru, and W in Fig. 2, underlines, that the formation of local magnetic moments strongly suppresses the probability of chain formation for $3d$, $4d$, and $5d$ elements. If we ignore the formation of magnetism among the $3d$-, $4d$-, and $5d$-TM series Cr, Mn, Fe, Ru, Rh, Ag, Re, Os, Ir, Pt and Au exhibit extensive SP regions (Fig. 2(b),(d)) indicating successful chain formation for these elements. Even for W (Fig. 2(f)) with bcc(110) electrodes neglecting magnetism results in touching S and P regions, indicating chain formation for more open lead structures. Allowing for the formation of local spin moments the picture changes completely: SP regions emerge exclusively for Ru (Fig. 2(c)), Ag, Ir, Pt, and Au while for all other elements the S and P regions are clearly separated and no chain formation occurs (Fig. 2(a),(e) and in [3]). While for Pd and Pt chains the influence of magnetism is small due to relatively small spin moments, the SP-regions of Ru (Fig. 2(c)) and Ir are considerably less extended for magnetic chains than for non-magnetic ones, underlining the suppression of chain formation by magnetism.

While our predictions based on the assumption that chains in BJs are magnetic match and explain the experimental findings for successful Ag, Ir, Pt and Au chain formation, the results of the model for non-magnetic suspended chains contradict the experimental observations at several crucial points (Fig. 2(g)). Firstly, nanocontacts of $3d$-TMs such as Fe are reported to form only point-contacts with no tendency to form longer chains. Secondly, also BJ-experiments using W as tip-material result only in point-contacts, moreover, W tips are widely used in STM- and AFM-experiments due to their structural rigidity preventing substrate-induced reformations. Thirdly, non-magnetic Ir chains would become as long as those of Pt, and almost as long as those of Au, in direct disagreement with experiments which report significant decrease of chain formation probability and length when going from Au to Ir. These clear contradictions to existing experimental evidence lead us to the conclusion that only when chains in BJs are magnetic, the experimentally observed trends can be reproduced and explained throughout the $3d$, $4d$, and $5d$ transition- and noble-metal series. Therefore, by *reductio ad contradictum*, comparing theoretical predictions with experimental findings, we provide a convincing evidence that TM chains in BJs are magnetic [2].

Financial support of the Stifterverband für die Deutsche Wissenschaft is gratefully acknowledged.

[1] Y. Mokrousov, G. Bihlmayer, S. Heinze, and S. Blügel, Phys. Rev. Lett. **96**, 147201 (2006).

[2] A. Thiess, Y. Mokrousov, S. Heinze, and S. Blügel, Phys. Rev. Lett. **103**, 217201 (2009).

[3] A. Thiess, Y. Mokrousov, S. Blügel, and S. Heinze, Nano Lett. **8**, 2144 (2008).

[4] Y. Mokrousov, G. Bihlmayer, and S. Blügel, Phys. Rev. B **72**, 045402 (2005).

Tunneling through ferroelectric $BaTiO_3$: breakdown of the effective mass model

D. Wortmann[1,2]

[1] IFF-1: Quantum Theory of Materials
[2] IAS: Institute for Advanced Simulation

Some of the proposed novel functionalities of future oxide-based electronics will have their physical origin in the use of transition-metal oxide barrier materials, in particular of ferroelectric oxides. The different directions of the ferroelectric polarization will modify the tunneling conductance and thereby allow to utilize the polarization state for data storage. We show that tunneling through $BaTiO_3$ in its ferroelectric phase cannot be described with the effective-mass model and hence simple assumptions of the barrier shape turn out to be inappropriate.

The possibility to use ferroelectric materials in magnetic tunnel junctions has recently attracted much attention [1]. The polarization state of the barrier represents an additional degree of freedom opening the perspective for 4-bit memory cells. We studied barium titanate as a prototype ferroelectric barrier material.

Disregarding any effects due to possible disorder, defects or dislocations, different physical effects can be imagined that will lead to a modification of the tunneling through a perfect ferroelectric barrier when switching its polarization: (i) The probably most undesirable effect for application is a change of the geometry, especially of the thickness, of the tunneling barrier. As all ferroelectrics are also piezoelectrics, the change in the polarization can lead to a structural modification that influences the tunneling. (ii) The modification of the interface between the ferroelectric barrier and the metallic leads. The change of the polarization will strongly affect these interfaces, inducing the formation of large screening charges and the modification of the chemical binding. These modifications change the matching conditions of the electronic wavefunctions at the interface and hence will modify the tunneling probability of electrons. In general, this purely electronic effect can be expected to be quite substantial as the tunneling current is typically carried by only a few states at energies around the Fermi level. (iii) As a third effect the switching of the polarization can change the electronic properties of the tunneling barrier itself. In particular, the differences in band alignment at the interfaces will manifest itself in a change of the local potential within the tunnelbarrier, which will influence the decay of the wavefunction and thus the tunneling probability.

It is this third case in which the potential profile of the barrier will change upon switching that we will further discuss. This effect is most frequently discussed in terms of the effective mass model. In this simple approximation the decay constant is linked to the height of the potential barrier V_0 relative to the energy of the tunneling electron and to the effective mass m^* as

$$\kappa = \sqrt{\frac{2m^*}{\hbar^2}V_0}.$$

Obviously, the effective mass model assumes a parabolic dispersion of the bands – an assumption not appropriate in most transition-metal oxides. To check the validity of this simple assumption, we calculate the decay constant κ of electrons tunneling through an insulating barrier from the realistic electronic band structure of $BaTiO_3$.

Our investigation is founded on calculations of the electronic structure with the FLEUR [2] code, which is based on density-functional theory (DFT) and the all-electron FLAPW method. Based on the results for the self-consistent density we calculate the complex band structure using our embedded Green-function method and the transfer-matrix approach [3]. These methods yield for – any energy ϵ and any two-dimensional $\vec{k}_\parallel$ point – the set of real and complex $k_\perp$ values. The real $k_\perp$ solutions correspond to the usual propagating Bloch states with $\vec{k} = (\vec{k}_\parallel, k_\perp)$, while complex $k_\perp = q + i\kappa$ values correspond to wave functions which decay exponentially with the decay constant κ

$$\phi_{\vec{k}}(\vec{r}) = e^{ik_\perp r_\perp} e^{i\vec{k}_\parallel \vec{r}_\parallel} u_k(\vec{r}) = e^{-\kappa r_\perp} e^{iqr_\perp} e^{i\vec{k}_\parallel \vec{r}_\parallel} u_{\vec{k}}(\vec{r})$$

where $u_{\vec{k}}(\vec{r})$ is a lattice-periodic function. These decaying or evanescent states are those solutions which are responsible for the tunneling of electrons through the tunnelbarrier. We assumed the barrier to be grown along (001) direction and consequently we consider $k_\perp$ as those states decaying in (001) direction and choose $\vec{k}_\parallel$ from the two-dimensional Brillouin zone (2D-BZ) perpendicular to $k_\perp$.

$BaTiO_3$ is one of the simplest and best known ferroelectric perovskites. It exhibits a large electric polarization even at room temperatures and hence might

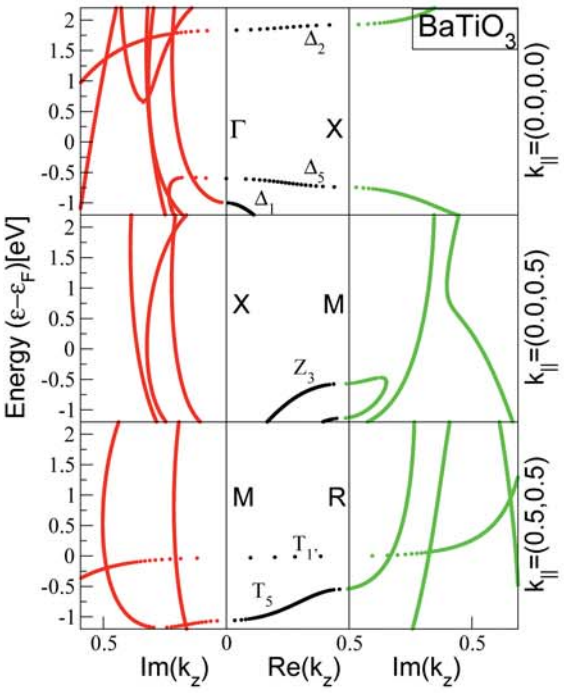

FIG. 1: Complex band structure of $BaTiO_3$. The energies of the states are plotted in eV with respect to the Fermi energy ϵ_F defined as the highest occupied state. The horizontal axis gives k_z in internal units ($2\pi/3.95\text{Å}^{-1}$). The three panels show the bands for different $k_\parallel$ points corresponding to the $\overline{\Gamma}$, $\overline{X}$, and $\overline{M}$ point of the 2D-BZ. Bloch states with $Im(k_z) = 0$ are represented in black, evanescent states with $Re(k_z) = 0$ in red and evanescent states with $Re(k_z) = 0.5$ in green.

be an ideal candidate for a ferroelectric tunnelbarrier material which is expected to show different resistance states depending on its polarization state. The ferroelectric phase is obtained starting from the cubic structure by a tetragonal distortion of the unit cell and a buckling in the BaO and TiO_2 layers. We fixed the in-plane lattice constant to that of a $SrTiO_3$ substrate (3.95 Å) and relaxed the structure in the out-of-plane direction, which resulted in a unit-cell height of 4.13 Å. The Ti atoms are displaced by -0.05 Å from the center of the tetragonal cell spanned by the Ba atoms at the corners of the unit cell, while the O atoms in the Ba layer are shifted by 0.24 Å and the O atoms of the Ti layer by 0.15 Å. The very same structure has been presented in Ref. [4] and its ferroelectric polarization has been calculated to be $49\ \mu C/cm^2$.

The tetragonal distortion in the ferroelectric phase modifies the band structure around the gap significantly. As shown in Fig. 1 the loss of cubic symmetry results in a splitting of the bands at the high-symmetry points of the BZ. This leads to an important modification of the character of the band edges. The band edges are now formed by states with high effective mass only. The bottom of the conduction band is formed by the very flat band at the Γ point which can be seen in the top panel of Fig. 1, and the valence band maximum is at the R point. As all these bands are very flat the corresponding evanescent states very quickly acquire a large imaginary $k_\perp$ value so that these states will not be relevant for tunneling except very close to the band edges. For $\vec{k}_\parallel = 0$, the most slowly decaying state over (nearly) the whole band gap is given by the evanescent band starting at ~ -1 eV. Similar bands can also be identified at the other $\vec{k}_\parallel$ values shown in Fig. 1. Over the energy range of the band gap these bands show little variation of $\kappa = Im(k_\perp)$, i.e. they form roughly vertical lines. The surprising consequence is that tunneling electrons with different energies will all decay similarly fast. In the effective-mass model this would correspond to potential barriers of equal height.

An interesting aspect of the electronic structure of $BaTiO_3$ could be expected considering the effect of an applied bias on a tunnel junction with a $BaTiO_3$ barrier. The voltage drop across the insulating barrier translates into a slope of the potential and therefore into a modification of the energy difference between the tunneling electrons and the band edges. The same effect might be induced by the ferroelectric polarization leading to different band alignments at the interfaces. This leads to a trapezoidal potential shape of the tunneling barrier. However, results demonstrate that the linear variation of the potential does not lead to a substantial variation of the decay constant.

Summarizing, we found that in tetragonally distorted ferroelectric $BaTiO_3$, electrons and holes at the conduction and valence band edges have very high effective masses. Evanescent states deriving from these bands will therefore quickly acquire large decay constants and will not contribute to the tunneling current except for energies very close to the band edges. Other valence and conduction bands with smaller effective mass still form evanescent states with significant tunneling probability. However, these appear as roughly "vertical" lines in the complex band structure with only little variation of the decay constant, such that all tunneling electrons will exhibit similar decay lengths independent of their energy. Thus, models arguing with differences in the barrier height to predict changes in the tunneling current will not be valid in junctions with $BaTiO_3$ barriers.

[1] E. Y. Tsymbal and H. Kohlstedt, Science **313**, 181 (2006)

[2] http://www.flapw.de

[3] D. Wortmann, H. Ishida, and S. Blügel, Phys. Rev. B **65**, 165103 (2002); ibid. **66**, 075113 (2002)

[4] F. Freimuth, Y. Mokrousov, D. Wortmann, S. Heinze, and S. Blügel, Phys. Rev. B **78**, 035120 (2008)

Hilbert spectrometer for identification of liquids

Y. Divin, M. Lyatti, U. Poppe, K. Urban

IFF-8: Microstructure Research

One of future public security techniques will be related with non-invasive, fast and reliable detection of liquids. To distinguish between benign and threat liquids, we have suggested using Hilbert spectroscopy, which is the only technique for a frequency range of the main dispersions of liquids. Two demonstration setups, consisting of Hilbert spectrometers integrated in Stirling coolers and synthesized polychromatic radiation sources, have been developed and characterized. Reflection polychromatic spectra of various bottled liquids have been measured at the spectral range of 15 – 400 GHz with total scanning time down to 0.2 second and possibility of reliable identification of liquids has been demonstrated.

In addition to conventional X-ray and metal detectors at airport gates, a specific screening of passenger's luggage is required to find and identify the liquids, which might be dangerous themselves or could be used as components for fabrication of explosives. We have recently presented our results in developing of Hilbert spectroscopy, based on high-T_c Josephson detectors, and attracted attention to a great potential of our Josephson technology in security applications [1]. Here, we discuss our concept of liquid identification, present the results of development of corresponding Hilbert spectrometers, demonstrate the results of spectral measurements of reflectance from liquids.

Reliable identification of liquids with low false alarms, in principle, could be made by electromagnetic measurements of their dielectric functions at the frequency range of their main dispersions [1]. Specific dispersion in the dielectric functions of liquids is reproduced in their reflection spectra, which might be measured by some spectroscopic technique (see Fig.1). The differences in reflectance are relatively high for practically all pure liquids, but for water and hydrogen peroxide this difference is only a few percent. To resolve this difference in reflectance measurements a signal/noise ratio of better than 10^2 is required.

The spectral range of dispersion for presented liquids is rather broad, from a few GHz to a few THz, and not covered by any single conventional spectroscopic technique. Only our Hilbert spectroscopy, based on high-T_c Josephson junctions, has demonstrated applicability at this intermediate frequency range [1].

Based on our previous experience in Hilbert spectroscopy, the conceptual scheme of a liquid identifier was suggested and previously presented [2]. It consists from the following components: a Hilbert spectrometer with a high-T_c Josephson detector and analogue electronics in a Stirling cooler, a radiation source, a radiation coupling unit between the source, the Hilbert spectrometer and a bottle with liquid, as well as a data acquisition system and a computer with application-oriented software.

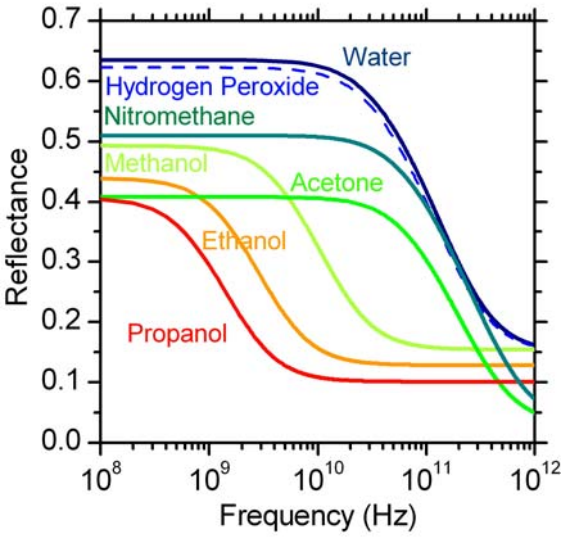

FIG. 1: Reflection spectra for various liquids, calculated in Debye approximation at normal incidence [2].

We have tested two types of Stirling coolers: a model SL200 from AIM Infrarot Module GmbH and a model LSF9589 from Thales Cryogenics B.V. With the first one we got more than 10 years experience in applications of high-T_c Josephson detectors, while the second, new one has twice less weight, is more compact and less noisy.

The fabricated $YBa_2Cu_3O_{7-x}$ bicrystal junctions with log-periodical$YBa_2Cu_3O_{7-x}$ antennas were mounted on coldfingers of cryocoolers together with self-made voltage bias electronics. The electronics integrated with the SL200 cryocooler had a spectral bandwidth of 6 MHz and a maximum current of 25 mA, and

the one integrated with the LSF9589 cryocooler - the bandwidth of around 1 MHz and the higher maximum current of 60 mA.

Various combinations of conventional frequency multipliers and their microwave pump oscillators were used to synthesize a radiation source which covers the dispersion range of liquids. By this technique and using a combination of two multipliers, we succeeded in developing a source, which has 4 spectral lines at frequencies 15.3, 30.6, 91.8, and 282 GHz in the output spectrum.

A photo of one of the set-ups, used in the reflectance measurements of bottled liquids, is shown in Fig.2. The synthesized radiation source can be recognized on the left side of Fig.2. Polychromatic radiation from the source was focused by an elliptical mirror on the bottle with some liquid, and the radiation, reflected from the bottle, was focused on the Josephson detector with the help of a second elliptical mirror. The voltage dependences of the detector response $\Delta I(V)$ were recorded by a lock-in amplifier, displayed on the oscilloscope (see two insets in Fig.2) and processed into the spectrum by Hilbert transformation with a PC notebook. Measurement time for each spectra was as low as 0.2 s for a lock-in time constant τ = 10 μs with reasonable signal/noise ratios and dynamic errors.

The calibration of the reflectance in the set-up was carried out with a metal foil, installed inside a bottle just behind the wall. A corresponding polychromatic spectrum is shown in Fig.3 by a black line. When the metal foil in the bottle was replaced by water, the intensities of all four peaks in the spectrum slightly went down. When the container was filled with acetone, methanol, ethanol or propanol, the modification of reflection spectrum was even more pronounced as it is shown in Fig.3 [3].

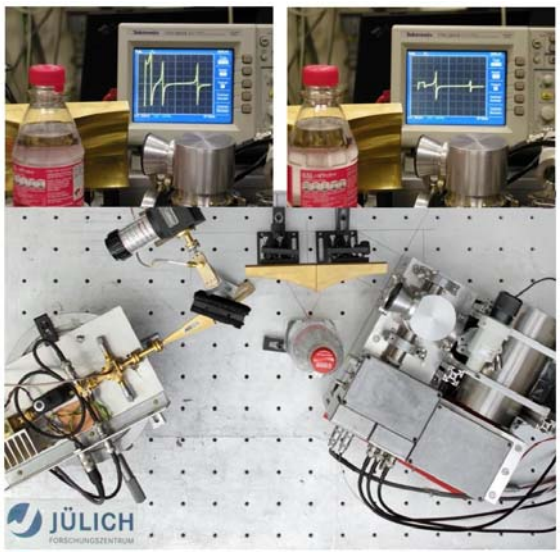

FIG. 2: Experimental set-up with synthesized polychromatic source (left), Hilbert spectrometer in Stirling cooler (right) and quasioptical coupling unit between source, spectrometer and bottle with liquid (center). Insets: two examples of spectrometer response $\Delta I(V)$ for water (left) and propanol (right).

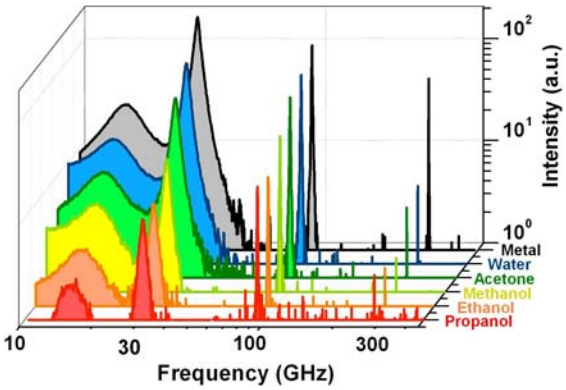

FIG. 3: Spectra of radiation of polychromatic source, reflected from a bottle with metal plate, water, acetone, methanol, ethanol or propanol inside. Spectra were measured by Hilbert spectrometer.

The measured spectra in Fig.3 are in a qualitative agreement with the reflection spectra, calculated in oversimplified approximation (see Fig.1). To make identification reliable, experimental data base for liquids should be developed at this intermediate frequency range from a few GHz to a few THz.

Our first experiments showed that with simple measurements at four frequencies, covering the dispersion range of liquids, we are able to detect various liquids, such as water, methanol, ethanol, propanol and acetone, in a plastic container. Our experiments show that spectral measurements are more reliable for liquid identification than conventional approaches involving measurements at a single low frequency only. The signal/ noise ratio in our reflection measurements was higher than 10^2 (Fig.3), which is sufficient to resolve the difference between water and hydrogen peroxide.

We plan to optimize the high-T_c Josephson detector, improve dynamics of data acquisition and enhance the spectral range of the radiation source. These developments will help us to make a significant step towards a practical device.

[1] Y. Divin, U. Poppe, V. Gubankov, K. Urban. IEEE Sensors J.,v.8, pp.750-757 (2008).

[2] Y. Divin, U. Poppe, K. Urban. *Detection of Liquid Explosives and Flammable Agents in Connection with Terrorism.* (NATO Science for Peace and Security Series) eds H Schubert, A Kuznetsov (Dordrecht: Springer) pp. 189 – 204 (2008).

[3] M. Lyatti, Y. Divin, U. Poppe, K. Urban. Supercond. Sci. Technol., v.22, 114005 (2009).

Noise analysis of DC SQUIDs with damped flux transformers

M. I. Faley[1], U. Poppe[1], K. Urban[1], R. L. Fagaly[2]

[1] IFF-8: Microstructure Research
[2] Quasar Federal Systems, San Diego, CA 92121 USA

We have analysed noise properties of high-T_c flip-chip direct-current superconducting quantum interference devices (DC SQUID) magnetometers intended for sensitive measurements with no magnetic shielding in the Earth's magnetic field. These include low-inductance DC SQUIDs with large voltage swings and DC SQUID sensors with a high-pass filter integrated in the thin-film multilayer flux transformer [1, 2].

The high-T_c direct-current superconducting quantum interference devices (DC SQUIDs) demonstrate superior sensitivity for measuring the vector components and spatial gradients of magnetic fields, as well as an ability to resolve tiny changes in large signals. These features are particularly useful and have already been implemented in many applications such as low-noise amplifiers, biomagnetic research (for example, for magnetocardiography and magnetoencephalography), geomagnetic survey, nondestructive evaluations, and materials science. In the case of high-T_c SQUIDs with a 16-mm multilayer flux transformer (FT), a field resolution greater than 4 fT/$\sqrt{}$Hz at 77.4 K in magnetic shielding has been demonstrated [3].

The high-oxygen-pressure sputtering technique in pure (99.999 %) oxygen at a pressure of about 4 mbar was used to deposit $BaZrO_3$ (BZO), $SrTiO_3$ (STO), $YBa_2Cu_3O_{7-x}$ (YBCO), and $PrBa_2Cu_3O_{7-x}$ (PBCO) films of the SQUID magnetometers from dc- or rf-magnetron targets with diameters of 50 mm. The deposition from larger targets and the optimized arrangement of the Sm_2Co_{17} magnets in the magnetron target holders improved the thickness homogeneity of the films.

We used a PBCO/STO heteroepitaxial layer to construct an insulator between the superconducting films of the FT. This allowed us to provide the required epitaxial growth and insulation properties of the insulator. Thanks to its conductivity along the substrate surface, the PBCO/STO heteroepitaxial layer also served as an integrated resonance-damping resistor. As a result, the V(Φ) characteristics of the magnetometers were sinusoidal and the estimated Nyquist noise of the resistor was below 2 $\mu\Phi_0/\sqrt{}$Hz at 77 K.

Two types of high-T_c flip-chip DC SQUID magnetometers were prepared and investigated in this study: (type A) with the superconducting multilayer FT containing only pickup and input coils (see Figure 1) and (type B) where the superconducting multilayer FT contained an integrated passive high-pass filter (HPF) as an ultra-low-ohmic resistor R placed in series with the coils of the FT (see Figure 2).

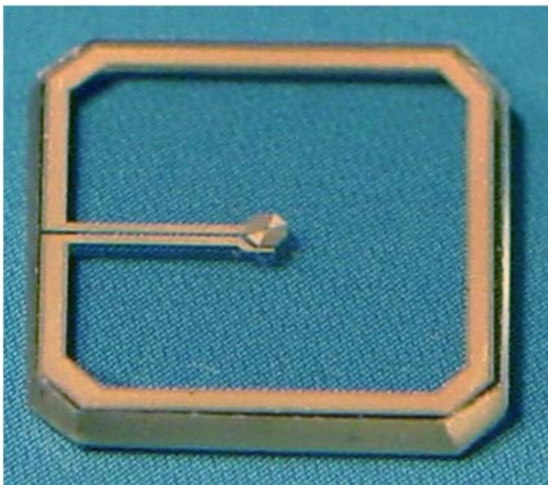

FIG. 1: Photo of the 8 mm x 8 mm multilayer FT intended for type A magnetometers.

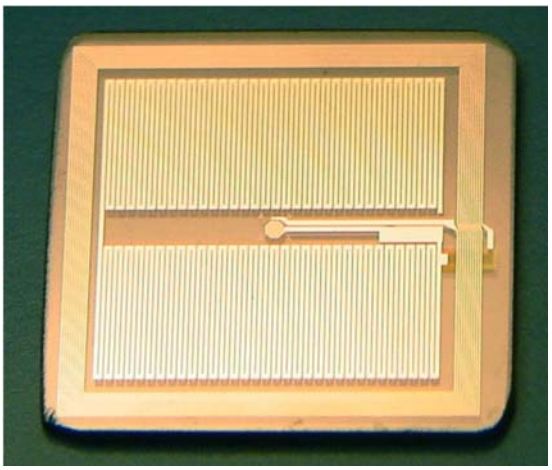

FIG. 2: Photo of the 16 mm x 16 mm multilayer FT with integrated HPF intended for type B magnetometers.

An analysis was performed of intrinsic noise for high-T_c DC SQUID with FT containing resistive elements.

The main sources of white flux noise of the standard SQUID were found to be the Nyquist noise in the Josephson junctions and the FT, as well as the suppression of the DC SQUID voltage swings caused by parasitic capacitance between the FT and the SQUID. An ultra-low-ohmic resistor with resistance value between the flux-creep-induced resistances of superconductors (below $\sim$ 0.1 nΩ) and resistances of conventional resistors (above $\sim$ 0.1 mΩ) was developed. An RL-circuit-based HPF with time constant $\sim$ 7 sec was realized and integrated in the superconducting FT. The contribution of the HPF to the noise of the sensors was measured and compared with calculated values.

For the best 40-pH DC SQUID intended for type A magnetometers, the maximal voltage swing (peak to peak) measured was up to about 55 μV and the best flux resolution of was as low as $\sim$ 4 $\mu\Phi_0/\sqrt{\text{Hz}}$ at 77 K (see Figure 3).

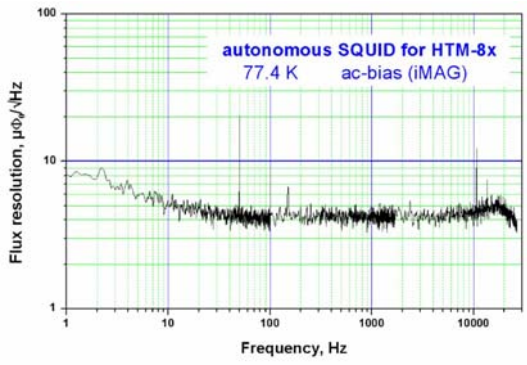

FIG. 3: Noise spectrum of an autonomous DC SQUID with $L_S \sim$ 40 pH.

A non-monotonous dependence of the voltage swing was observed on the coupling between the input coil of the FT and the washer of the DC SQUID. The reduction in insulation thickness first increased the voltage swing due to effective reduction of the SQUID inductance L down to $L_{Seff} \approx$ 25 pH. However, thicknesses of less than $\sim$1.5 μm led to a reduction in voltage swing, the appearance of two maxima in the dependence of voltage swing on the bias current, and an increase in the flux noise. Our experience shows that reducing SQUID inductance L down to at least 40 pH does not degrade the field resolution, but rather significantly improves the voltage swing and operational stability of the DC SQUID magnetometers in the magnetically unshielded environment. For the best type A magnetometer, the field resolution achieved was $\sim$18 fT/$\sqrt{\text{Hz}}$ at 77 K.

For the type B magnetometers we realized a low-noise ultra-low-ohmic resistor with resistance values between the flux-creep-induced resistances of the superconductors (below 0.1 nΩ) and resistances of conventional resistors (above 0.1 mΩ). For the type B magnetometers we constructed a special FT with 10 turns in a pickup coil measuring 16 mm x 16 mm with a serially connected meander-formed 1-$\mu\Omega$ thin-film silver resistor. The FT had two epitaxial YBCO layers for the coils and their return lines. An epitaxial PBCO/STO multilayer film was used for the insulation between the superconducting layers.

First tests were performed on the flux transformers simply by turning them in the Earth's magnetic field under a high-T_c DC SQUID gradiometer system [4]. While for the FT in the type A magnetometers, the gradiometer signal changed from one constant level to another, in the case of the FT in the type B magnetometers, it always relaxed to a value of zero in a few seconds. This simple experiment demonstrated the achievement of a dissipation time constant of τ = L_{pu}/R $\approx$ 7 sec for the integrated HPF due to a resistance R $\approx$ 1 $\mu\Omega$ of the silver resistor and inductance of the multiturn pickup coil $L_{pu} \approx 7\ \mu\text{H}$.

A low frequency noise contribution to the intrinsic noise of the magnetometer is limiting the magnetic field resolution of the magnetometer B at low frequencies f:

$$B_N = \frac{L}{\sigma m}\sqrt{\frac{4k_BTR\Delta f}{R^2+(2\pi Lf)^2}} \quad ,$$

where m =10 is the number of turns in the pickup coil and σ = 2.56 cm^2 is the area of one loop of the pickup coil of the FT.

Two main disadvantages of the present type B magnetometers were observed: high low frequency noise and weak coupling of the feedback coil. To reduce the low frequency noise of the type B magnetometers down to the level of the type A magnetometers of about 100 fT/$\sqrt{\text{Hz}}$ at 77 K, an increase in the dissipation time constant to more than about 2.5 hours is required. This would be possible if the resistance of the integrated resistor was reduced and the inductance increased both about thirtyfold. The increase in the size of the pickup loop and/or use of low-T_c SQUID magnetometers with the coils wound from a superconducting wire would make it easier to increase the dissipation time constant. Improving the quality of the high-T_c films, conducting the measurements in a smaller residual magnetic field of the magnetic shield, and improved pinning of the Abrikosov vortices (as done, for example, in [5]) can further reduce the noise of the sensors.

[1] M. I. Faley et al., German Patent Application Nr.102009025716.0 (2009)

[2] M. I. Faley et al., J. Physics: Conf. Ser. (2010)

[3] M. I. Faley et al., Supercond. Sci. Technol. **19** S195 (2006)

[4] M. I. Faley et al., Supercond. Sci. Technol. **17** S301 (2004)

[5] B. Maiorov et al., Nature Materials **8** 398 (2009)

Resistive switching in 8 nm thin TiO_2 films grown by ALD

S. K. Kim[1,3], J. Zhang[1,3], C. Nauenheim[1,3], S. Mi[2,3], C. Kügeler[1,3], S. Hoffmann-Eifert[1,3], R. Waser[1,3]

[1] IFF-6: Electronic Materials
[2] IFF-8: Microstructure Research
[3] JARA-FIT: Jülich Aachen Research Alliance - Fundamentals of Future Information Technology

We report on the development of a special atomic layer deposition (ALD) process for the growth of homogeneous and dense TiO_2 thin films from a stabilized titanium-isopropoxide precursor ($Ti(O\text{-}i\text{-}Pr)_2(tmhd)_2$) and water. Films deposited at 365°C showed a nano crystalline structure and a surface roughness of about 1 nm. We integrated the films into cross point structures which represent the building blocks of future RRAM devices. Binary resistive switching was demonstrated on 100 x 100 nm^2 crosspoint structures containing ALD grown anatase type TiO_2 films with thicknesses as low as 8 nm.

Titanium oxide (TiO_2) films may act as functional layers in non-volatile resistive random access memories (RRAM). Titanium oxide shows binary stable electric resistance states, which can be switched from high to low resistance and vice versa by applying a certain voltage. This concept provides the benefit of a two-terminal device that permits the integration of electronic functions into crossbar structures with the ease of a moderate integration effort as compared to CMOS technology. Atomic layer deposition (ALD) is a surface-reaction controlled process and thereby allows homogeneity and excellent film thickness controllability to be achieved on complex structures. ALD is one of the most important technologies in today's DRAM and FLASH memory production.

In our study we applied the ALD technique to integration of dense TiO_2 films with thickness below 10 nm into sub-micron crosspoints as a pre-study for future integration into crossbar structures.

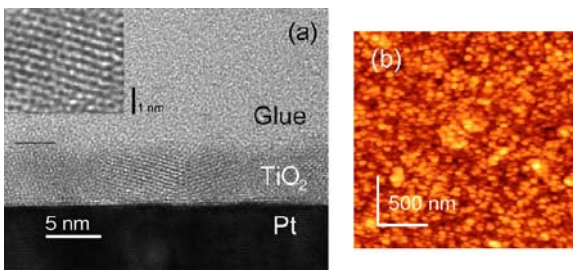

FIG. 1: a) Cross-sectional HRTEM image of a 5 nm thin TiO_2 film grown by ALD at 365 °C using $Ti(O\text{-}i\text{-}Pr)_2(tmhd)_2$ and H_2O as precursors. b) AFM image of a corresponding 25 nm TiO_2 film showing the homogeneous nano crystalline structure (taken from [1]).

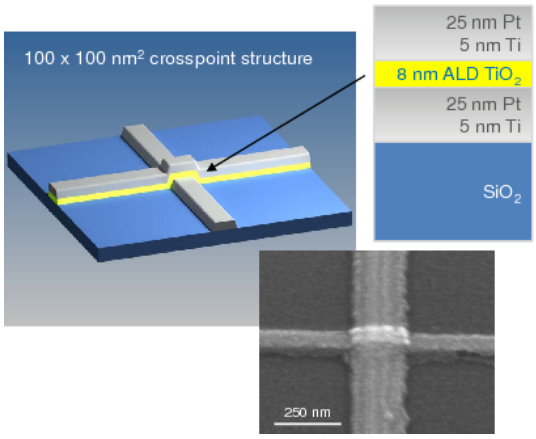

FIG. 2: Schematic and layer structure of a single crosspoint test structure. On one wafer thousand of crosspoints are fabricated for statistical characterisation. Each test device consists of an oxidized silicon substrate with a 5 nm Ti / 25 nm Pt bottom electrode, a 8 nm thin TiO_2 film grown by ALD and a Ti/Pt top electrode. The SEM picture shows the top view of a single 100 x 100 nm^2 crosspoint device.

For the ALD process we chose a liquid delivery injection technique which enables the use of a Ti-precursor with high thermal stability, $Ti(O\text{-}iPr)_2(tmhd)_2$ dissolved in ethylcyclohexane. The relatively high growth temperature during ALD of about 365°C resulted in TiO_2 films which were crystallized in an anatase-type phase as deposited.[1] The obtained nano crystalline structure shows a dense morphology combined with a smooth surface structure for film thicknesses between 5 to 30 nm (see Figure 1). The residual carbon content in the films was below 3 at% as determined by XPS analysis.[1] The optimized ALD process was then integrated into the process line of crosspoint structures without any further modification. A schematic of the crosspoint structures is shown in Figure 2.

Nano crosspoint devices were fabricated for the electrical characterization of the resistive switching properties. For this a combination of nanoimprint lithography (NIL), electron beam lithography, sputter deposition, e-beam evaporation, ALD and dry etching techniques was used. First, an oxidized silicon wafer was covered with an adhesion layer and a 30 nm Pt layer by sputter deposition. A subsequent structuring with UV-NIL and Ar plasma etching then defines the 100 nm wide bottom electrode together

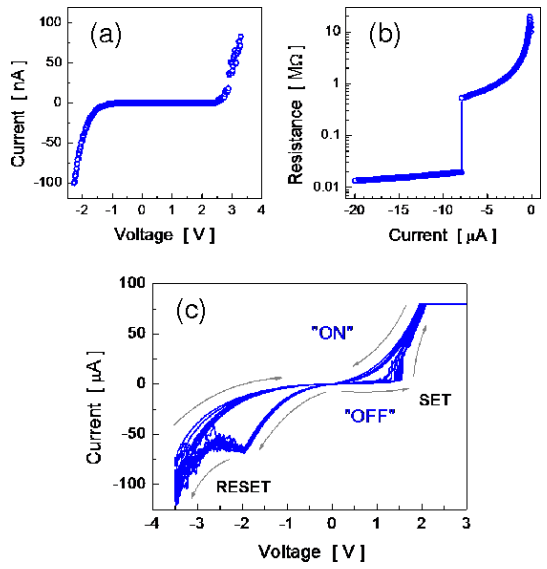

FIG. 3: Sequence of electrical measurements on a representative Pt/TiO_2/Ti/Pt crosspoint structure with an 8 nm ALD TiO_2 film. a) I-V characteristic of the test device in as deposited state; b) negative current driven electroforming characteristic; c) reproducible resistive switching behavior with currents in the μA regime.

with the attached contact pad of 100 x 100 μm^2.[2] Next, the TiO_2 functional layer was deposited by the above described ALD process. Only the excellent step coverage of ALD in comparison to physical deposition techniques like sputtering enabled us to reduce the film thickness of the functional TiO_2 layer below 10 nm. The homogeneity of the ultra thin ALD TiO_2 layer was obvious from the high yield of switching devices on the wafer of about 80 % which is a reasonable value for this type of laboratory devices. The 100 nm wide top electrode was made by e-beam lithography with a two layer resist system, which ensures an undercut so that after the evaporation of 5 nm Ti and 25 nm Pt a lift-off releases the metal electrode. A final dry etching step through the TiO_2 uncovers the bottom electrode contact pad to make contact for the electrical measurement set up. The scanning electron microscopic (SEM) picture in Figure 2 shows a slightly tilted top view onto a representative 100 x 100 nm^2 test structure where both electrodes crosses each other with the 8 nm ALD TiO_2 layer in between.

The electrical characterization was performed with an Agilent 1500B semiconductor analyzer and a Suss probe station. A representative initial I-V characteristic measured at room temperature on a virgin Pt / 8 nm ALD TiO_2 / Ti / Pt crosspoint structure is shown in Figure 3a. Despite the film thickness of below 10 nm the TiO_2 films show a very good insulation behavior with values of the leakage current density in the range of 10^{-6} A/cm^2 at 1 V. This indicates the good quality of the functional layer with respect to coverage of the bottom electrode, homogeneity and absence of pinholes or voids. The asymmetric diode like behavior of the I-V characteristic is attributed to the difference of bottom and top contact, one Pt and one Ti, respectively. From previous work it is known that an electroforming process is mandatory to achieve resistive switching. A current driven process with negative polarity has been proofed to be the most reliable one.[3] The corresponding forming characteristic of the ALD TiO_2 film is shown in Figure 3b. Thereby, the current was increased in small steps and the voltage was measured. When the electrical breakdown field was exceeded the device resistance decreased dramatically, here from an initial value of > 1 MΩ down to about 10 kΩ. The lower resistance level (LRS) was then defined as the 'ON' state. After the electroforming process the devices show stable resistive switching. Figure 3c presents five subsequent bipolar switching cycles with small currents and suitable switching voltages. The limiting current compliance was only 80 μA and the RESET performed without any current limitation at less than 100 μA.

Summarizing we produced Pt / TiO_2 / Ti / Pt nano crosspoint structures with functional ALD grown TiO_2 films as thin as 8 nm which exhibited reproducible bipolar resistive switching behavior with currents in the μA-regime.

Acknowledgments: The authors thank A. Besmehn (ZCH) for XPS analysis, R. Borowski and H. John (IFF-6) for technical support and M. Reiners (IFF-6) for fruitful discussions. S.K. Kim acknowledges the financial support from the Alexander von Humboldt foundation.

[1] S. K. Kim, S. Hoffmann-Eifert, S. Mi, R. Waser, J.Electrochem. Soc. **156**, D296 (2009).

[2] C. Kügeler, M. Meier, R. Rosezin, S. Gilles, R. Waser, Solid-State Electronics **53**, 1287 (2009).

[3] C. Nauenheim, C. Kügeler, A. Rüdiger, R. Waser, A. Flocke and T. G. Noll, Nanotechnology (2008) NANO 08, Arlington, Texas, USA (2008).

Voltage - time dilemma in ReRAMs with trapped charge

H. Schroeder

IFF-6: Electronic Materials

Metal/insulator/metal (MIM) thin film stacks showing stable resistive switching (RS) are promising candidates for future application as a non-volatile resistive random access memory (ReRAM), competitive to FLASH and DRAM. Many theories and models try to describe the switching effects. One of them postulates the trapping and de-trapping of electronic charge in immobile traps as the reason for the resistance changes. It is shown [1] that this "pure electronic" switching mechanism will face a voltage-time dilemma - general to all switching insulators - at conditions competitive to the state-of-the-art FLASH. This is exemplified in two detailed scenarios with different electronic band and defect properties.

To be competitive to the state-of-the-art FLASH memories certain benchmark data for a future ReRAM are postulated: The stack area is 10^{-10} cm^2 (100 nm x 100 nm) making the necessary READ current of 1 μA a high current density of 10^4 A/cm^2. The READ and WRITE / ERASE times are 100 ns, while the retention time for the different RS states is 3×10^8 s (10 years) at 85˚C for a non-volatile memory. For easy detection of the different states (ON vs. OFF) their resistances ratio should be about a factor of 10. The READ voltage is $V_{READ} \leq 1$ V, whereas the one for WRITE, $V_{WRITE} \leq 10\times V_{READ}$. These benchmarks are used for the order of magnitude estimations of the performance of a ReRAM with trapped charge.

One of the earliest reports on a model assuming trapping and de-trapping of electronic charge in *immobile* defects as the reason for the RS is the paper by Simmons and Verderber [2] for explaining their data on Au/SiO/Al stacks. The main condition for applying this "Simmons-Verderber" model is that the traps keep their respective state (charged or uncharged) for 10 years, but that the charge state can be exchanged by 100 ns short voltage / current pulses. The different space charge in the traps is the reason for the different resistance states.

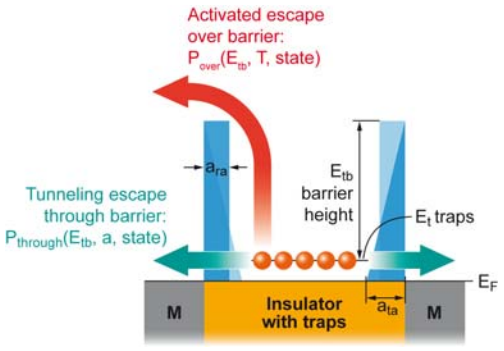

FIG. 1: Scheme of trapped charge inside potential wells (rectangular, triangular) and possible escape paths.

In the schematic Fig. 1 some trapped charge is shown in a MIM stack with possible escape routes over or through the limiting energy barriers. Using a probability of 0.5 for escape, for thermally activated processes over the barrier a minimum height is required, about 1.5 eV at 85°C. For tunnelling through barriers with the same height a minimum thickness is required, depending on the geometry, e.g. about 4 nm for rectangular and 6 nm for triangular ones, respectively [1]. In addition the barriers have to be manipulated by the applied voltage to assure the charge exchange with short high-current pulses. Such barriers (for electrons) are created by 2 different scenarios (SC):

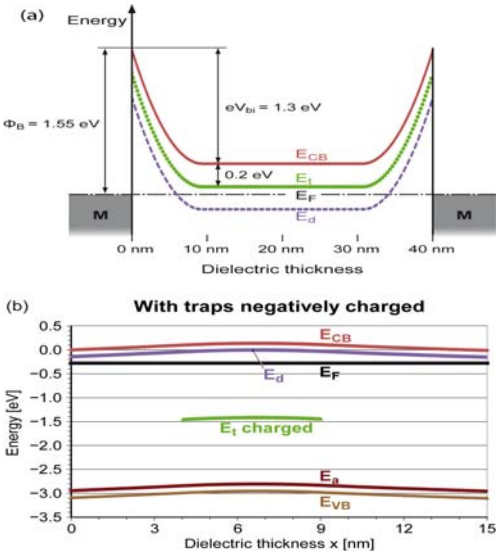

FIG. 2: Possible band diagrams with trapped charge (green).
(a) Scenario #1: "Simmons-like" case, i.e. charge trapped in shallow and homogeneously distributed acceptor-like traps.
(b) Scenario #2: Charge trapped in deep and inhomogeneously distributed acceptors-like traps.

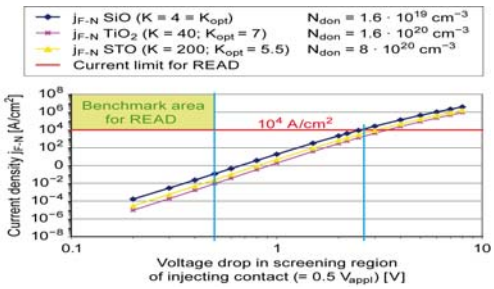

FIG. 3: READ operation for SC#1: Tunnelling injection current density (from cathode) into traps (0.2 eV below CB) for three different dielectrics with different dielectric constant K vs. voltage drop in the interface screening region.

#1) High offset between metal Fermi level (E_f^M) and conduction band (CB) of insulator and large built-in voltage due to high donor densities. Under these conditions, which are sketched in Fig. 2a, the trap level can be close to the CB, in the example 0.2 eV.

#2) If the mentioned offset and the built-in voltage are small, i.e. the bands are nearly flat without a large barrier, the traps have to be deep in the gap (thermal activation) and away from the interfaces (tunnelling) as it is sketched in Fig. 2b.

The first tests of the assumed model under the conditions of the postulated scenarios is the READ current under small applied voltage. The current has to be supplied by the electrode by injection over the barrier or tunnelling through it. For SC#1 the current over the barriers is many orders of magnitude to small. The current density for Fowler-Nordheim (F-N) tunnelling through the triangular barrier is shown in Fig. 3: At the highest acceptable applied voltage of 1 V (corresponds to 0.5 V at the injecting interface!) it is several orders of magnitude too small and the postulated number is reached at unacceptable applied voltage of about 5 V. As this result is independent of the switching materials [1], the SC#1 completely fails already at this point!

In contrast, the SC#2 satisfies the condition for the read current density as it is demonstrated in Fig. 4 for both assumed charge states: The leakage current density calculated by a model combining thermal injection at the interface with band conduction in the insulator [3] is large enough and shows the postulated difference between ON and OFF states at low read voltage for an assumed trapped charge of –10 μC/cm^2 (i.e. 1.2$\times$10^{20} cm^{-3} in the range 4 to 9 nm in the 15 nm thick sample [1]).

As the equilibrium state of the acceptor-like traps is the charged one (Fig. 2b) first the release of the trapped charge by applying voltage is tested corresponding to a WRITE from OFF to ON. In order to exchange the complete charge in 100 ns a current density of 100 A/cm^2 is needed. As the thermal escape to the CB is prohibited by the design rules only the escape by tunnelling into the CB (and then transported away) is possible in the band structure tilted by the applied voltage [1]. This tunnelling current density is plotted in Fig. 5: The requested density is reached at about 13 V, while at about 10 V (the max. allowed voltage!) the density is more than 100x lower.

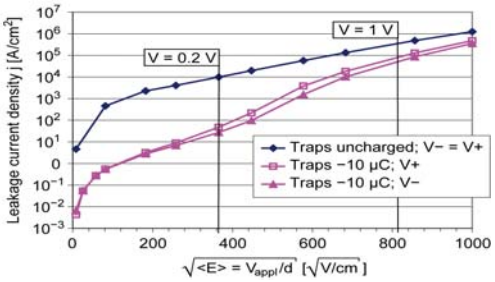

FIG. 4: READ operation for scenario #2: Steady state leakage current densities vs. square root of mean applied field, $< E >^{1/2}$, ("Schottky-plot") for a M / STO (15 nm) / M thin film stack, i.e. charge trapped in deep and inhomogeneously distributed acceptors-like traps for electrons: Blue: traps neutral; Pink: traps (negatively) charged for $\pm < E >$. Below $V_{appl} < 1$ V the ratio is a factor of $\geq$10x.

The larger voltage needed may be acceptable, but there is a severe drawback. At these large applied voltages the CB leakage current density, also plotted in Fig. 5, is more than 6 orders of magnitude higher. That means for any released electron one of more than 10^6 electrons in the CB can refill the trap and this probability is practically 1! Therefore, in the SC#2 the WRITE operation will fail due to the postulated conditions.

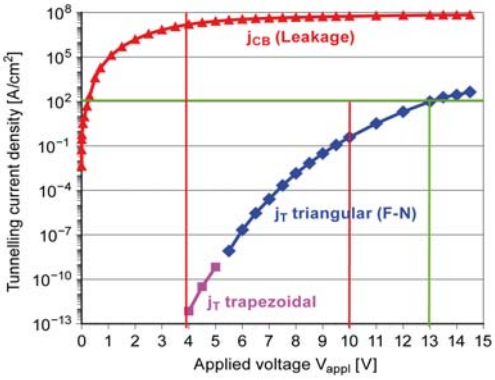

FIG. 5: WRITE operation for scenario #2: Tunnelling current densities for WRITE, (i.e. the release of the trapped charge in acceptor-like defects at E_t) vs. applied voltage, V_{appl}. $V_{appl} < 4V$: no significant tunnelling due to $E_t(x = 4nm) < E_f^M$; 4 $V \leq V_{appl} < 5.5V$: tunnelling through trapezoidal barrier (pink); $5.5V \leq V_{appl}$: tunnelling through triangular barrier (blue). For comparison, the leakage current density in the conduction band is also shown (red)

In conclusion it has been shown that a fast resistive switching at reasonable voltages and low voltage read-out are not consistent with non-volatile large retention times within a model postulating the different RS states as different occupation of charged traps which are immobile defects.

[1] H. Schroeder, V. Zhirnov, R. K. Cavin, R. Waser, J. Appl. Phys. **107**, in press (2010).

[2] J. G. Simmons and R. R. Verderber, Proc. Roy. Soc. **A301**, 77 (1967).

[3] H. Schroeder, S. Schmitz, and P. Meuffels, Appl. Phys. Lett. **82**, 781 (2003).

Self-neutralization in photoemission from $SrTiO_3$ single crystals

J. Szade[1,2], B. Psiuk[2,3], M. Pilch[2], R. Waser[1], K. Szot[1,2]

[1] IFF-6: Electronic Materials
[2] A. Chelkowski Institute of Physics, University of Silesia, Universytecka 4, 40-007 Katowice, Poland
[3] Institute of Glass, Ceramics, Refractory and Construction Materials, Department of Refractory Materials, Toszecka 99, 44-101 Gliwice, Poland

The effect of bulk mediated neutralization in photoemission from insulating monocrystalline $SrTiO_3$ was studied. Long term measurements of the photoemission line shift and emission current allowed us to relate the observed systematic reduction of the surface charging to increasing conductivity of the samples. The bulk resistance of the $SrTiO_3$ samples was found to scale with their thickness. We present a model of the observed behaviour based on well-conducting filaments connecting the surface with the grounded sample holder, similar to the hypothesis explaining resistive switching in single crystals and thin films of $SrTiO_3$. In our model the changes of the local oxygen stoichiometry are driven by surface potential and consequently electric field and chemical gradients which cause electroreduction and electromigration along extended defects in the crystals [1].

The studied samples were epi-polished single crystals from CrystTec with a defined orientation (100) or (110) and a thickness of 0.5 mm or 3 mm, and for the (111) orientation of a thickness of 0.4 mm. The bulk through resistance of the samples measured by covering the surfaces with metal electrodes was of the order 10^{13}-10^{14} ohm. The photoelectron spectra were acquired with the use of two different spectrometers from Physical Electronics - the PHI 5700 and PHI 5600. We applied the monochromatized Al Kα radiation focused on the small spot. The measurements were performed in a vacuum of about 5 10^{-10} torr. No neutralization with a flood gun was used. The sample holder was grounded and the emission current was registered.

To study the process of time-resolved charging we chose the O 1s line, for selected sets of measurements we also registered Ti 2p, Sr 3d and C 1s lines. The x-ray was on all the time during the measurements which were performed in the profile mode, so that every spectrum was registered separately. Immediately after switching on the x-rays we observed some instabilities of line position and the starting values of the shift with respect to the neutral line position reached a value between 50 and 150 eV. In any case, after about 5 – 15 min of exposure to x-rays, regular and smooth changes were observed with tendency to reach values close to equilibrium after several hours as it is shown in Fig. 1 for the Ti 2p line. Fig. 2 shows the O 1s line position as a function of exposure time to x-rays in the range limited to 120 min. The curves were obtained for three orientations of the crystal surface. Additionally, Fig. 2 includes the O 1s line position for the $Sr_{0.95}La_{0.05}TiO_3$, $SrTi_{0.99}Nb_{0.01}O_3$ crystals and for the thermally reduced crystal. For the sample isolated electrically from the ground we found a very large and unstable line shift.

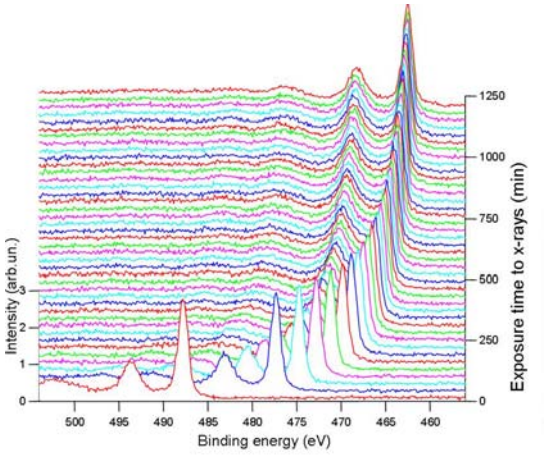

FIG. 1: Photoelectron spectra of the Ti 2p multiplet for the $SrTiO_3$ (111) crystal as a function of exposure time to x-rays

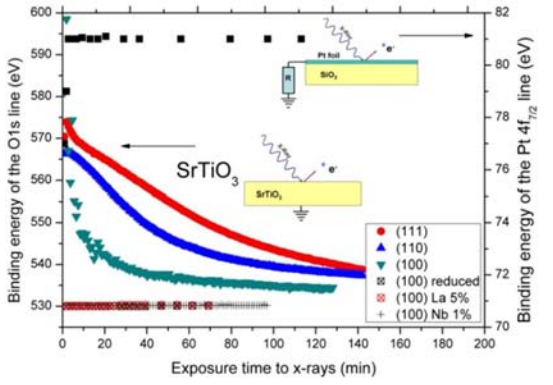

FIG. 2: Binding energy of the photoelectron O 1s line from $SrTiO_3$ crystals of various orientations and compositions as a function of exposure time to x-rays – left axis. The right axis shows the position of the photoemission Pt $4f_{7/2}$ line for the Pt/SiO_2 with the resistor R of resistance 100 GΩ between the foil and ground. The standard position of this line for Pt metal is 71.2 eV.

The final positions of the O 1s line in the undoped crystals, observed after 12 hours of exposure to x-rays, reached values close to the neutral value established in our studies as 530.0 eV. To obtain the starting situation of a shift of 30 eV or more a sample had to be removed from the UHV chamber to air for a few minutes. La doped STO, Nb doped STO and thermally reduced crystal showed binding energy values equal, within the range of 0.3 eV, to the value of 530.0 eV and exhibited no influence of the x-ray dose (see Fig. 2).

The photoemission current as a function of the x-ray dose showed roughly an inverse characteristic to the surface potential – it decreased during the first few minutes and then gradually increased. This indicates the direct relation between the electrical resistance through the sample and the observed surface potential changes.

For the Pt/SiO_2 system - a fully insulating substrate, we showed that the photoemission line position is strictly determined by the balance between the photoelectron flux proportional to the x-ray intensity and the current neutralizing surface charge. This allows us to modify the standard equation used to determine binding energies of electronic states from the photoelectric effect by adding a term describing self-neutralization through the sample:

$$E_B = h\nu - E_k - W_e - (I_{ph}R_{in})e$$

where the last term is equivalent to the potential at the surface as I_{ph} is photoelectric current from the sample, equal for the equilibrium state to the neutralizing current through the sample and R_{in} – resistance of the sample, between the surface exposed to x-rays and the grounded holder.

This clear attempt to describe photoemission from a poor conductor should be useful in estimating of the sample resistivity.

The model of the observed behaviour should, in our opinion, be based on the recent findings of resistive switching in STO [2, 3] and observed STO conductivity as a consequence of heat treatment in reducing atmosphere or doping in place of A (La) or B (Nb) sublattices. As was shown in earlier work [2] a metallic conductivity through the bulk STO crystals could be detected when a local electric field was applied by the AFM tip. This conductivity was related to nanometre-sized filaments formed by the extended defects. Such defects are the paths of easy oxygen diffusion.

During the long lasting photoemission experiment the process leading to the surface potential changes is related, in our opinion, to the activation of oxygen transport along existing extended defects and creation of reduced Ti electronic states.

Fig. 3 presents a model of the self-neutralization process. Photoionization of the oxygen atom taking place in the skin region close to the surface can lead to breaking bonds and leads to emission of an oxygen atom to vacuum. As a consequence, a reduced valence of Ti appears in the region of the oxygen deficit.

The extended defect shown in Fig. 3 forms a kind of additional crystal - vacuum interface. The presence of oxygen vacancies in the skin region is not sufficient to reach the percolation of conductive regions. The factor which is responsible for the oxygen transport and consequently charge transfer towards the surface is the potential caused by photoionization. The oxygen defects created along the channel travel due to the electric field.

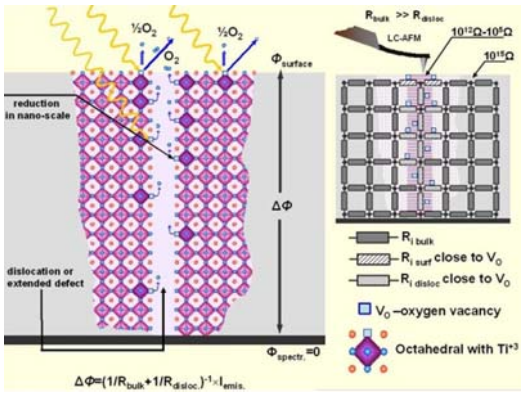

FIG. 3: Model of photoemission process and mechanism of electroreduction leading to good conductivity of filaments, in presence of surface potential due to charging. The right panel presents the equivalent resistor network for STO crystal with a dislocation or extended defect.

Electroreduction takes place through the sample along the limited regions where oxygen diffusion and electromigration take place after exposure of the surface to x-rays.

Fig. 3 shows how the extended defect crossing the sample plus the surface potential acting as an oxygen pump can form a line of surface neutralization. At a high enough temperature in vacuum the process is so efficient that the STO sample has a conductivity which allows photoemission measurements without neutralization.

Oxygen deficit is a result of thermal treatment or exposition to x-rays and photoelectron emission in UHV and it can decrease only when a sample is exposed to high partial oxygen pressure.

The observed differences between the results obtained for various orientations of the crystal surface can be related to various densities of extended defects – filaments which are oriented along the main crystallographic directions and to various diffusion rates along these directions.

[1] J. Szade, B. Psiuk, M. Pilch, R. Waser, K. Szot, Applied Physics A-Materials Science & Processing 97, 449 (2009)

[2] K. Szot, W. Speier, G. Bihlmayer, R. Waser: Nature Materials 5, 312 (2006)

[3] K. Szot, R. Dittmann, W. Speier, R. Waser: Phys Status Solidi (RRL) 1, 86 (2007)S

Oxygen octahedron reconstruction in the $SrTiO_3/LaAlO_3$ heterointerfaces

C. L. Jia[1,2], S. B. Mi[1,2], M. Faley[1], U. Poppe[1], J. Schubert[3], K. Urban[1,2]

[1] IFF-8: Microstructure Research
[2] ER-C: Ernst Ruska-Centre for Microscopy and Spectroscopy with Electrons
[3] IBN-1: Semiconductor Nanoelectronics

We investigate the $LaAlO_3/SrTiO_3$ interface by means of aberration-corrected transmission electron microscopy allowing us to measure the individual atomic shifts in the interface at a precision of a few picometres. We find that the oxygen octahedron rotation typical for rhombohedral $LaAlO_3$ is across the interface also induced in the originally cubic $SrTiO_3$ layer. Octahedra distortion leads to ferroelectricity-like dipole formation at the interface. [1]

The report [2] of a high-mobility electron gas at the heterointerface between the two nominally insulating perovskites $LaAlO_3$ (LAO) and $SrTiO_3$ (STO) has stimulated intensive research efforts concerning the physical origin of this intriguing effect and the possibility to derive from it new electronic device applications. [3] The effervescent magic source of a seemingly inexhaustible flux of new and surprising properties is provided by the manifold of ways the cation-oxygen octahedra representing the prominent structural element of perovskites can be modified by, e.g., distortions, rotations or particular atomic shifts. Even small atomic rearrangements as they are expected to occur in interfaces between perovskites of different structure can change dramatically the electronic system. High-resolution structural investigations are therefore highly desirable to elucidate the mechanisms behind the observed interface-related properties. In the light of the versatility of physical properties of perovskites and the complex response to even very small atomic rearrangements progress in the atomic characterization will help to advance the theoretical modelling of the interfaces.

In the present work we reveal rearrangements of the oxygen octahedra in the LaO-TiO_2–type interfaces in epitactic LAO/STO heterostructures employing the negative-spherical aberration imaging (NCSI) technique. [4] The LAO/STO multiplayer systems used for our study were prepared on STO substrates by high oxygen pressure rf-sputtering at about 800 °C as well as pulsed laser deposition (PLD) techniques at an oxygen pressure of 1.5 and 2x10^{-3} mbar.

Figure 1 shows a [110] image of a sputter-prepared sample with a 2.5 nm thick LAO layer sandwiched between two STO layers. Under the conditions for NCSI technique the atoms appear bright on a dark background. The individual atoms can be clearly recognized; in particular this refers to the projection of the oxygen octahedra (arrows) and their central Al-position (between arrows). Regarding the horizontal -Al-O-Al-O- atom sequence an alternating shift of the oxygen-atom positions upward and downward, respectively, is clearly visible in LAO due to the oxygen octahedron rotation. For measurement of the shifts and the lattice parameters of the film layers we derive from the image intensity distribution the real atomic positions. This is achieved by comparison of the experimental image with calculated images.

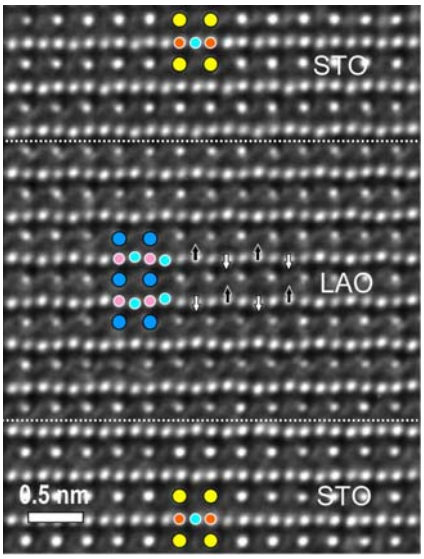

FIG. 1: Image of a 2.5 nm LAO layer sandwiched between two STO layers taken under NCSI conditions along the [110] direction. The two dotted lines indicate the (001) interfaces. Color circles give the atomic structures of STO and LAO. In the LAO layer the projected shift of the oxygen atoms out of the respective Al-atom rows as a result of oxygen octahedron rotation is clearly visible (arrows).

Figure 2(a) displays the value of the c-axis [001] lattice parameter in STO and in LAO as a function of vertical distance (in units of c) from bottom to top of Fig. 1. Close to the interfaces (shade lines) the lattice parameter of LAO does not abruptly adopt its central value of 0.375 nm. This, in turn, is by 1 % smaller than the bulk value. Fig. 2(b) displays the shift parameter of the oxygen atoms relative to the neighbouring Al and Ti-atom positions, respectively,

as a function of vertical distance. In LAO the values are given by squares for oxygen shifted upward and by circles for oxygen shifted downward. In the centre of the LAO layer the moduli, about 10 pm, of the two types of shifts are essentially equal as expected for the ideal structure. Moving downward into the lower STO layer (left-hand side in Fig. 2(b)) the upward (squares) and downward (circles) shifts of corresponding oxygen positions persist over a distance of about $3c$ into the STO layer. Moving upward into the upper STO layer (right-hand side of Fig. 2(b)) a corresponding behaviour is seen. On the right-hand side of Fig. 2(b) negative values for both squares and circles mean that all the oxygen atoms have shifted towards the interface and away from the appertaining Ti plane. As a result the centre of the octahedron shifts in the direction of the interface. Fig. 2(c) displays the measured values of the shifts of the centres of the oxygen octahedra out of the Al-plane in LAO (centre) and out of the Ti-plane in the lower (left-hand side) and upper (right-hand side) STO layer. No shift is, as expected, observed in the LAO. In contrast, an upward shift of 3.5 pm is observed in the lower and a downward shift by about 5 pm in the upper STO layer, i.e. always towards the LAO layer, over a distance of about $5c$. This indicates polarization-dipole formation with the polarization vector pointing away from the LAO layer.

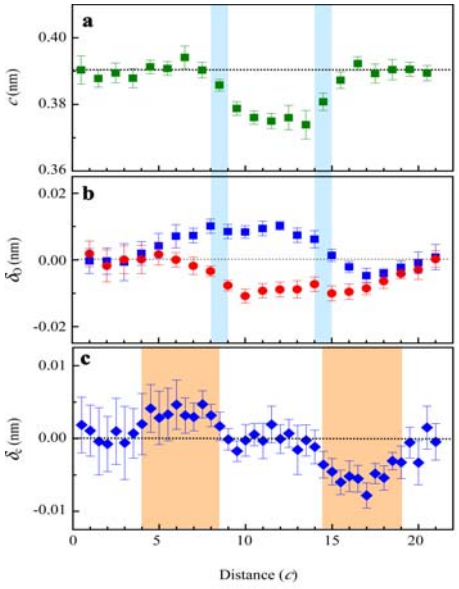

FIG. 2: (a) c-lattice parameter in STO and in LAO as a function of distance (in units of c) from a reference plane in the lower STO layer. The vertical shade lines mark the interfaces. (b) The value of the shift parameter δ_o of the oxygen atoms as a function of distance from the reference plane. Squares denote upward shifts and circles downward-shifts. (c) The value of the shift parameter δ_c of the centre of the oxygen octahedra with respect to the appertaining cations.

Figure 3 shows schematics of the LAO/STO interface where a LaO plane faces a TiO_2 plane (orange band). Fig. 3(a) refers to "rigid" octahedron rotations neglecting for the moment charge effects. At the interface this rotation correlation has to be harmonized with the octahedron arrangement in the STO lattice in which ideally the octahedra are in unrotated form. The rotation mismatch forces the interfacial octahedra to distort also in the STO (small green arrows). Fig. 3(b) illustrates the effects induced by electric plane charges. At the interface, a positively charged $[La^{3+}O^{2-}]$ plane faces a neutral $[Ti^{4+}(O^{-2})_2]$ plane. It can be expected that the negatively charged oxygen atoms relax in the electric field upward towards the $[La^{3+}O^{2-}]$ plane (red arrows). This is indeed predicted by theory. This leads to ferroelectricity-like distortions of the TiO_6 octahedra with the polarization vector pointing away from the interface as evidenced by our atomic displacement measurements. Fig. 3(c) displays the combined effect of "rigid" octahedron rotation and electric-field induced atom relaxation.

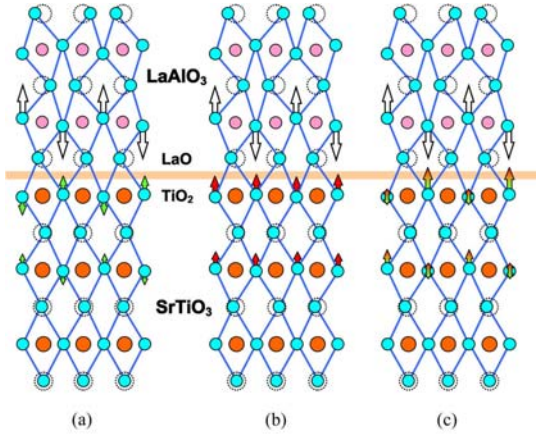

FIG. 3: Schematic of octahedron reconstruction at the interface of LAO/STO. (a) Rotation (green arrows) of "rigid" octahedra in STO as a result of elastic constraints resulting from the rotation of the oxygen octahedra in LAO. (b) Shift of the oxygen atoms in the TiO₂ planes of STO in the interface area towards the first LaO layer in LAO. (c) When the action due to the forces indicated in (a) and (b) are added the shift is enhanced for every second vertical oxygen position while it is diminished in every other.

Our study reveals the real atomic structure of the LAO/STO interface. The prominent result is the oxygen octahedron rotation and the TiO_6 octahedra distortion induced by LAO in STO at the interface. We consider the LAO/STO system just a particularly useful example for the demonstration of complicated structural reconstructions occurring in the interface region of structurally mismatched oxides. These introduce additional variables into the theoretical efforts to understand the electronic reconstruction intrinsically interrelated with the structural one.

[1] C. L. Jia, *et al.* Phys. Rev. B **79**, 081405(R) (2009).

[2] A. Ohtomo, H. Y. Hwang, Nature **427**, 423, (2004).

[3] S. Thiel *et al.*, Science **313**, 1942 (2006).

[4] C. L. Jia, M. Lentzen and K. Urban, *Science* **299**, 870 (2003).

Cu-adatom mediated bonding in close-packed benzoate/Cu(110)-systems

M. C. Lennartz[1], N. Atodiresei[2,3], S. Karthäuser[1], R. Waser[1], S. Blügel[2,3]

[1] IFF-6: Electronic Materials
[2] IAS: Institute for Advanced Simulation
[3] IFF-1: Quantum Theory of Materials

Using UHV-STM investigations and density functional theory (DFT) calculations we prove the contribution of Cu-adatoms to the stabilization of a new high-density phase of benzoate molecules on a Cu(110) substrate. We show that two different chemical species, benzoate and benzoate Cu-adatoms molecules, build the new close-packed structure. Although both species bind strongly to the copper surface, we identify the benzoate Cu-adatoms molecules as the more mobile species on the surface due to their reduced dipole moment and their lower binding energy compared to benzoate molecules. Therefore, the self-assembly process is supposed to be mediated by benzoate Cu-adatom species, which is analogous to the gold-thiolate species on Au(111) surfaces.

In future technological applications, metals should act as electrodes or interconnectors to the CMOS world, whereas molecules with their functional groups and their effort to self-assemble in ordered layers are envisaged as the functional elements. Irrespective of the final circuit design, it is necessary to find suitable molecule/metal combinations that provide the desired functionality reliably. Because of its low resistance and its high heat capacity, copper combined with molecular materials is supposed to provide the prerequisites for developing integrated circuits with decreasing switching times, reduced heat dissipation, and higher reliability. Therefore, the carboxylate/copper system is a promising alternative to the intensively studied thiol/gold system.

First characterizations of benzoic acid (C_6H_5COOH) on Cu(110), done by Richardson et al. [1], showed that benzoic acid forms large domains of several well-ordered structures, depending on temperature and coverage. In this article, we present a UHV-STM experimental study and DFT calculations on the adsorption of benzoic acid on a Cu(110) surface [2]. We demonstrate the role of the copper adatoms in modifying the carboxylate/copper interface.

Straight forward vapor-deposition (T_{Sub}=293 K, t=5 min, p=4.7·10^{-4} mbar) with an additional annealing step at around 590 K results in a surface covered by a close-packed c(8x2) surface structure of standing molecules. Beside this, we found regions with a new high-coverage structure [2]. The latter has a smaller feature size of the spots displaying a row direction rotated by an angle of 35˚ with respect to the known c(8x2) structure. Assuming commensurability and a standing-up configuration, high-resolution STM images and linescans along and between the molecular rows allow us to identify the unit cell of the new high-coverage phase as a (1 1; -4 2) structure with two molecules in the unit cell (Fig. 1).

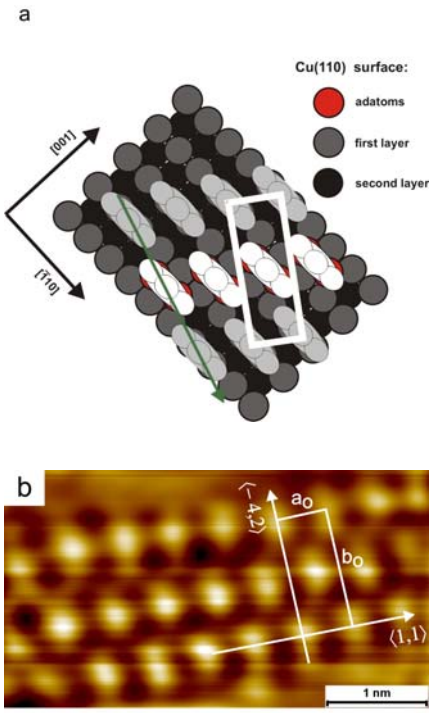

FIG. 1: a) Schematic of the new adatom-stabilized (1 1; -4 2) structure of the benzoates on the Cu(110) surface. b) High-resolution STM image (U_T=0.78 V, I_T=0.36 nA) of the new close-packed structure with unit cell and substrate vectors.

Both the benzoates at the corners and the benzoates in the centers of the unit cell build rows in the [112] direction. The molecules at the corner can be identified as chemisorbed on top of the copper atom rows of the outermost substrate layer, whereas this is not the case for the benzoate molecule in the center of the unit cell. A short bridge site at the center of the unit cell can only be provided by the incorporation of copper adatoms. This assumption is supported by the heights of our linescans from STM measurements and studies on flat-lying benzoate monolay-

ers which can be interpreted by the incorporation of copper adatoms. Therefore, the new structure is described with a row of adatoms between the central benzoate molecule and the outermost copper layer so that all benzoate molecules of the unit cell bind on top of copper atoms and bridge the short lattice site (Fig. 1).

For details our theoretical calculations (for details of our ab initio total energy calculation see [2] and references therein) prove that the strong covalent interaction between the oxygen atoms of the carboxylate moiety and copper surface atoms favors the adsorption of molecules in the so-called bridge position. Neglecting the copper adatoms, we calculate a first structure where one benzoate is placed on two copper first-layer atoms and another benzoate molecule is placed on top of two copper second-layer atoms. During the geometry optimization, the second molecule relaxes to a configuration where it binds directly to copper atoms of the first layer due to a stronger covalent interaction, which can not be established with copper atoms of the second layer. This relaxed structure does not agree with the one observed in the experiment. In a second configuration, one benzoate molecule is placed on top of copper first-layer atoms as before, but the second benzoate is substituted by a benzoate copper-adatom molecule placed on top of two copper second layer atoms. This configuration relaxes toward the experimentally observed (1 1; -4 2) structure with all benzoate molecules in bridge positions.

Adsorption energy and enthalpy calculations demonstrate that two different chemical species, namely the benzoate and benzoate Cu-adatoms molecule, are strongly binding to the Cu(110) surface. The absolute value of the adsorption energy of the benzoate copper-adatoms molecule adsorbed on Cu(110) is 0.9 eV smaller than the one of the benzoate adsorbed directly on Cu(110) [2]. Therefore, the adsorption of the benzoate copper-adatoms molecule is weaker, the bonds formed between the copper-adatoms and the Cu(110) surface are easier to break and this suggests that the benzoate copper-adatoms molecules may have a higher surface mobility than the benzoate molecules.

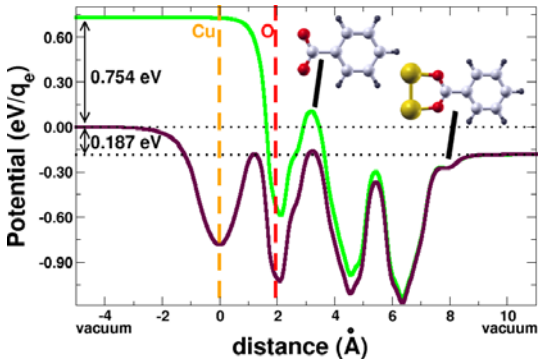

FIG. 2: Plane averaged electrostatic potential of the benzoate and the benzoate copper-adatoms molecules. The vertical dashed lines represent the positions of the copper and oxygen atoms.

In FIG. 2 we present the plane averaged electrostatic potential of the benzoate and the benzoate copper-adatoms molecule. The difference between the right and the left vacuum level shows the magnitude of the dipole moment and represents the change in the electrostatic potential along the molecule, when going from the right to the left. Based on frontier molecular orbital interaction theory arguments, due to the huge decrease of the dipole moment together with the smaller adsorption energy of the benzoate copper-adatoms molecule as compared to benzoate, we conclude that the bonds between benzoate copper-adatoms molecules and the Cu(110) are much easier to break than those between benzoate molecules and the copper surface. The feature indicates that the chemical species with higher surface mobility are the benzoate copper-adatom molecules. This is not surprising, since for the well studied thiol/gold systems it has also been shown that gold-thiol complexes are more mobile on the metal surface than thiol molecules.

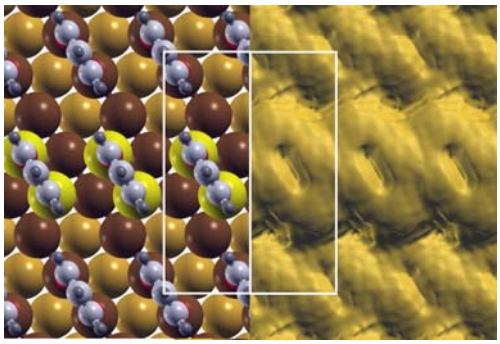

FIG. 3: Simulated constant-current STM image of the (1 1; -4 2) monolayer chemisorbed on Cu(110) for an applied bias voltage of U_T=-0.78 eV.

Finally we analyzed the real space topography of the (1 1;-4 2) structure by simulating STM images for an applied voltage of U_T=-0.78 eV (Fig. 3). Comparing the experimentally measured data, the surface schema and the simulated STM images, we conclude that the bright spots seen in experiment correspond to the spacing between the molecules. These spots represent the tail of the σ and π bonding wave functions, which have a maxima located at the anchoring carboxylate moiety. Although less obvious in the experimental STM image, the different highs of the molecular rows seen in the measured linescans are clearly visible in the simulated STM image.

Acknowledgments: This work was supported by the DFG Priority Program SPP1243. The theoretical calculations have been performed on the IBM Regatta and Blue Gene/L supercomputers in Jülich Supercomputing Centre (JSC).

[1] B. G. Frederick, F. M. Leibsle, S. Haq, and N. V. Richardson, Surf. Rev. Lett. **3**, 1523–1546 (1996).

[2] M. C. Lennartz, N. Atodiresei, L. Müller-Meskamp, S. Karthäuser, R. Waser, and S. Blügel, Langmuir **25**, 856 (2009).

High density 3D memory architecture based on the resistive switching effect

C. Kügeler, M. Meier, R. Rosezin, S. Gilles, R. Waser

IFF-6: Electronic Materials

We demonstrate the fabrication of a 3D memory architecture based on the resistive switching effect. Resistive memory (RRAM) is under wide investigation since it is non-volatile, promises fast operation and can be integrated into high density architectures like crossbar arrays. Here, silver-doped methyl-silsesquioxane (MSQ) is integrated in crossbar array structures providing good planarization properties so that emerging lithography techniques like nanoimprint lithography (NIL) are applicable. Futhermore, we could prove that silver-doped MSQ can be used as resistive switching material on the nano scale. Using this technique, crossbar arrays with a minimum feature size of only 100 nm are stacked on each other, which comprises the doubling of the memory density. Furthermore even higher integration is in principle not limited by this technique, while the CMOS overhead increases only slightly.

The resistive switching effect belongs to a new storage concept, which recently became very attractive, since it combines fast operation with non-volatile data storage [1]. A resistive switching memory is in principle comprised of two metal electrodes separated by a functional isolator (MIM structure). This device can exhibit two or more different ohmic resistances referred to in the simplest case as high resistance state (HRS) and low resistance state (LRS). The resistance states are non-volatile and can be toggled by simply exceeding threshold voltages $V_{th,SET}$ or $V_{th,RESET}$. Digital information like “0” can be defined by LRS and “1” by HRS. Stored information is retrieved by measuring the electrical current, when a small read voltage V_{read} is applied.

One benefit from resistive switching cells is that the concept deals with two terminal devices instead of three terminal devices like DRAM where always one access transistor is used. This offers the opportunity to invent novel and advanced architectures. Passive nano crossbar arrays on top of a conventional active CMOS infrastructure are one alternative approach [2]. In this architecture, a highly regular grid of parallel bottom electrodes and perpendicular top electrodes sandwiches the functional material in between and each crosspoint is equal to one memory cell with a size of $4F^2$. Recently we demonstrated the fabrication of nanocrossbar arrays with nanoimprint technology and the use of amorphous methyl-silsesquioxane (MSQ) in combination with silver electrodes [3]. However, purely passive crossbar structures suffer from the drawback that sneak paths will occur during the read/write process, if no non-linear elements like diodes are integrated with each resistive cell. Theoretical considerations show that dependent on the R_{OFF}/R_{ON} ratio passive crossbar arrays without rectifying elements will work, but the number of rows and columns is strongly limited, because error free operation, meaning a sufficient voltage swing for the CMOS periphery, is required even if a worst case pattern is stored in the memory. Using a three dimensional structure, where several crossbar arrays are stacked on top of each other, can circumvent the loss of lateral crossbar size.

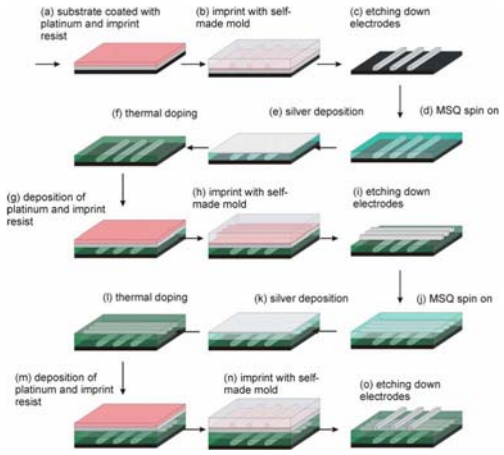

FIG. 1: Process flow of the fabrication procedure for silver-doped MSQ. The process starts with a platinized SiO2 substrate and imprint resist on top (a), which is then indented by a homemade mold (b). The patterns are transferred by etching (c). Afterwards, MSQ is spun on (d), covered by a thin silver layer (e), which is thermally doped into the material (f). By another imprint process, the top electrodes are created (g)–(i). The process is repeatable, creating multiple functional layers (j)–(o).

The fabrication of 3D crossbar arrays is shown in Fig. 1 and starts from a 30 nm thin platinized Si/SiO_2 substrate with the structuring of the bottom electrode set (Fig. 1a). First, a resist is structured by nanoimprint lithography using a self-made quartz mold, which was made by electron beam lithography and dry etching (Fig. 1b). Next, the resist pattern is used to trans-

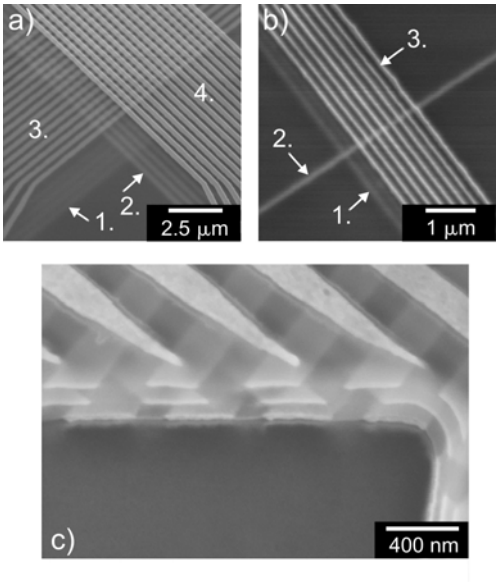

FIG. 2: (a) SEM images of multilayer crossbar memory structures with a half pitch of 200 nm. (b) Multilayer word structure with a half pitch of 100 nm. (c) FIB cross section of a four metal layer crossbar structure.

fer the structures into the Pt layer by ion beam dry etching (Fig. 1c). This first bottom electrode set is covered by MSQ (Fig. 1d), which in this case fulfills two functions. First it provides good planarization properties and secondly it can be used as resistance switching matrix material [4]. After thinning the MSQ down to around 40 nm by Ar dry etching, the top electrodes can be applied.

Silver, as used in our previous work, cannot be chosen as electrode material, since our experiments have shown that during the curing of the MSQ film (1h, 425˚C, nitrogen atmosphere) silver would diffuse uncontrolled into the film, leading to numerous defects in the electrode and thus destroying the memory array. So, for 3D crossbar arrays, temperature stable electrodes have to be used. To achieve the resistance switching property, silver has to be incorporated into the film, which is done thermally. A 15 nm thick silver film is evaporated on top of the sample (Fig. 1e), which is then treated at 450˚C in N_2 for 5 min. A part of the silver diffuses into the MSQ and the remaining silver on top is removed by ion beam etching (Fig. 1f). Now, a Ti(5 nm)/Pt(25 nm)/Ti(5 nm) metal stack is sputtered on top for the second electrode layer (Fig. 1g). The process of imprint and dry etching is now repeated with a rotated mold (Fig. 1h) to form the top electrodes of the first crossbar array (Fig. 1i). One can repeat the procedure very often and fabricate a stack of many memory layers (Fig. 1j–o). Fig. 2 shows SEM images of some resulting nano crossbar and word structures. In Fig. 2a four metal layers with 16 parallel electrodes each (200 nm wide) are stacked on each other. The subsequent layers are rotated by 90˚. In Fig. 2b two vertical word structures with a common single intermediate electrode are shown. This single electrode is 100 nm wide. A Focused Ion Beam (FIB) was used for cross

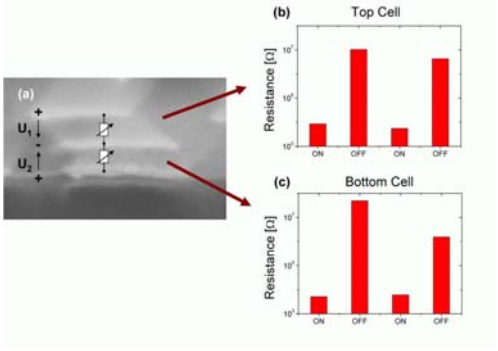

FIG. 3: (a) Two Pt/Ag doped MSQ/Pt memory cells on top of each other with applied voltages (magnification from Fig. 2c). (b) Resistances measured at the top cell during a SET and RESET sequence. (c) Resistances measured at the bottom cell during a SET and RESET sequence.

section images (Fig. 2c). This cross section reveals the memory cell arrangement with four metal layers in the vertical direction whereby in this example every MSQ interlayer is Ag-doped and consequently defined as a functional layer. The presented solution to sandwich silver-doped MSQ between two inert Pt electrodes circumvents electrode degradation during the temperature treatment processes.

To prove that Ag doped MSQ will work the functionality in 3D nanocrossbar arrangements needs to be tested. The experiments are performed on a cell in the corner of a crossbar array with an electrode width of only 200 nm, similar to that in Fig. 2c. Two superposed cells with one shared middle electrode (Fig. 3a) are contacted and then switching pulses are applied. The result for the top cell is presented in Fig. 3b. The cell is switched to the LRS by a voltage sweep and the resistance decreases to 10 kΩ followed by a RESET sweep, which turns the cell OFF to a resistance of 10 MΩ. Those switching characteristics are repeatable. The bottom cell exhibits similar properties and can be toggled between LRS and HRS achieving a good R_{OFF}/R_{ON} ratio > 100 (Fig. 3c).

We present a new three dimensional multilayer stack architecture for future non-volatile high density memory applications. As core structures, passive crossbar arrays were fabricated with nano imprint lithography, offering immense scaling potential. The memory functionality is based on the resistive switching effect in silver-doped MSQ with inert Pt electrodes. The results suggest a method to fabricate a non-volatile memory with a dramatically increased memory density.

[1] R. Waser and M. Aono, Nat Mater **6,** 833 (2007).

[2] D. Strukov and K. Likharev, Nanotechnology **16**, 888 (2005).

[3] M. Meier, S. Gilles, R. Rosezin, C. Schindler, S. Trellenkamp, A. Ruediger, D.Mayer, C. Kuegeler, and R. Waser, Microelectronic Engineering **86**, 1060 (2009).

[4] M. Meier, C. Schindler, S. Gilles, R. Rosezin, A. Ruediger, C. Kuegeler, and R. Waser, IEEE Electron Dev Lett 30, 8 2009.

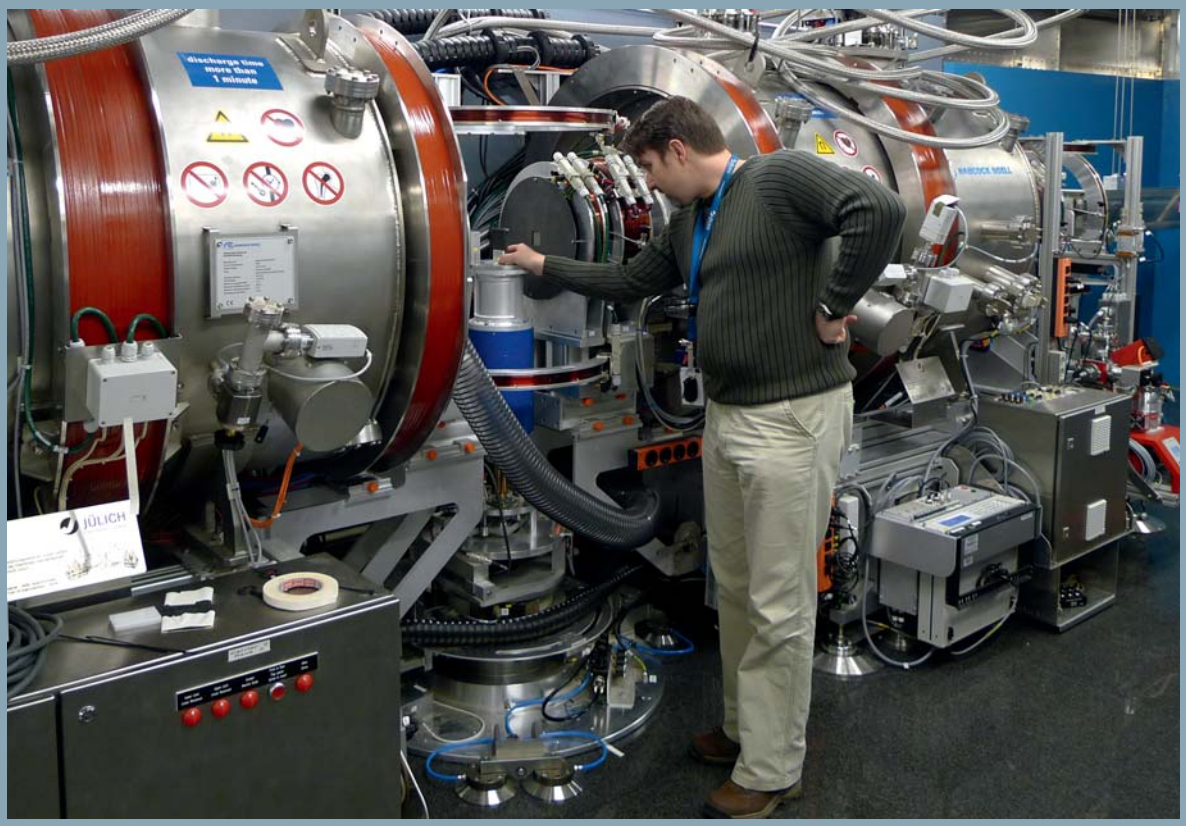

With the Jülich neutron spin echo spectrometer at the Spallation Neutron Source in Oak Ridge, USA, it is possible to measure minimal velocity changes of neutrons hitting the sample.

Photo: Oak Ridge National Laboretory

Large-scale facilities for research with photons, neutrons and ions

This research programme coordinates the activities taking place at the large scale facilities involved in the HGF research field Structure of Matter. These facilities offer unique research opportunities with photons, neutrons and ions for a multitude of science disciplines, ranging from physics, chemistry, biology and geology to material science, engineering science, and environmental research. A particular feature of this programme is the support of external user groups, which utilize the major part of the available access time. These user groups come mainly from universities, but also from non-university research institutions and industry.

With its excellence in neutron research – manifested in the Jülich Centre for Neutron Science (JCNS) – the IFF supplies a key contribution to this research programme. The strong reputation of the IFF in the German and international neutron landscape is closely related to:

- a powerful in-house research in the area of condensed matter focusing particularly on soft matter and magnetism,
- a large user operation in these research areas being extensively supported by IFF experts and facilities,
- a science-driven programme for the development of new methods and instruments, and
- exploitation of the novel neutron research opportunities provided by pulsed MW spallation sources.

The IFF neutron research is carried out to a large extent at the new state-of-the-art research reactor FRM II in Munich and at the ILL in Grenoble (France), with new opportunities being created at the SNS spallation source in Oak Ridge (USA). These activities are a cornerstone of the HGF programme "Condensed Matter Physics" and provide important contributions also to other HGF programmes, such as "Information Technology with Nanoelectronic Systems".

JCNS user office

T. Gutberlet[1]

[1] JCNS: Jülich Centre for Neutron Science

In 2009 the Jülich Centre for Neutron Sciences (JCNS) operated state-of-the art neutron instruments under a common scientific objective at the national and international leading sources FRM II, ILL and SNS. The instruments of JCNS are open to scientists from Germany, Europe and across the globe for the benefit of their scientific research goal. Access is organized by the JCNS User Office. 140 proposal for beam time were received in 2009 which received 489 beam days at the JCNS instruments.

Being an inter-departmental institution run by the division Scattering Methods (IFF-4) and Neutron Scattering (IFF-5) of the Institute of Solid State Research (IFF) at Forschungszentrum Jülich GmbH the JCNS, founded in 2006, focuses the research activities with neutrons in Jülich and at national and international neutron sources. For this purpose JCNS operates various state-of-the art neutron instruments at the leading neutron sources FRM II, ILL and SNS.

At the FRM II JCNS offered full access in 2009 to the high-flux small angle neutron scattering spectrometer KWS-2, the Jülich neutron spin echo spectrometer J-NSE, the diffuse polarized neutron spectrometer DNS and the backscattering spectrometer SPHERES. In this year also the second small angle neutron scattering spectrometer KWS-1 became operational serving users fully in 2010. The novel focussing VSANS machine KWS-3 received a major upgrade and refurbishment with a new coating of the focussing mirror. The instrument is back in operation with internal and external users in 2010. The high intensity magnetism reflectometer MARIA received first neutrons in 2009 and will become full operational within 2010. In collaboration with TU München construction of the diffractometer for protein crystallography BIODIFF has started in the neutron guide hall and will be finished in 2010. Furthermore the reflectometer TREFF was running in 2009 for in-house research projects and testing of detectors and neutron optical devices.

At the American megawatt spallation neutron source SNS in Oak Ridge the construction of the next generation neutron spin echo spectrometer NSE@SNS aiming for Fourier times of 1 μsec was completed

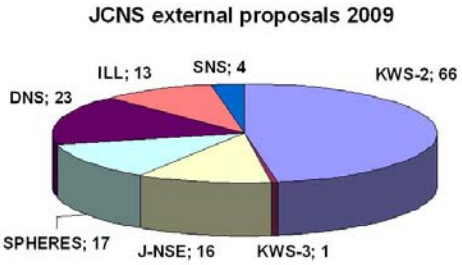

FIG. 1: Number of proposals submitted in the year 200 on the neutron scattering instruments of JCNS.

in 2009 and commissioning of the instrument has started. The engagement of JCNS provides access for German users to the backscattering spectrometer BASIS and the time-of-flight powder diffractometer POWGEN3 at this unique source.

At the hight flux neutron source ILL in Grenoble JCNS operates the Collaborative Research Group instrument IN12 and offers access for German users to the triple axis spectrometer IN22 and the 2-axis diffractomter D23 through a collaboration with the French CEA.

JCNS also offered the users specialized and unique sample environment and laboratory facilities on-side. A particular strong activity of JCNS is to use and provide polarized neutrons for experiments by in house development of devices to polarize and/or analyze neutron beams. Here the construction of SEOP based ^{3}He polarization device with a constant high polarization of about 80% was achieved recently.

User Operation: JCNS instruments are open to scientists from Germany, Europe and across the globe for the benefit of their scientific research goals. 2/3 of the available beam time at JCNS instruments is distributed to external users by application for beam time reviewed by an international Scientific Review Committee twice a year. Proposals for beam time are submitted via a web based process through the JCNS online user office system. The organizational work for this activity is provided by a User Office established on site of JCNS at FRM II in Garching. Funding support from the EU for European JCNS users within the 7th Framework Programme through

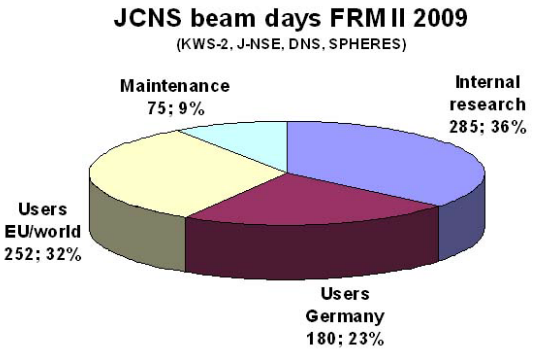

FIG. 2: Used beam days at JCNS instruments operated at FRM II in 2009.

the Research Infrastructures action of the Capacities Programme for the Integrated Infrastructure Initiative for Neutron Scattering and Muon Spectroscopy (NMI3) is gratefully acknowledged.

In 2009 users submitted 140 proposals for external beam time on the instruments of JCNS with a request for 854 beam days. 99 proposals by users were selected and received 489 beam days at JCNS spectrometers at FRM II, SNS and ILL. Figure 1 shows the distribution of external proposals received in the two proposal rounds in 2009 for the instruments of JCNS. Concerning the number of proposals the small-angle scattering machine KWS-2 clearly stands out, which is mostly due to the fact that SANS experiments can be done in short time.

In addition 104 proposals on internal beam time by researchers within JCNS were received, requesting a total amount of 436 beam days. 304 beam days were allocated to these proposals. On the in-house instrument TREFF 26 proposals were submitted which received 113 days of beam time. The distribution of the used beam days at JCNS instruments at FRM II by the different user groups is shown in Figure 2.

The largest share of the experiments was on soft matter systems. This is due to the high throughput instruments KWS-2 and J-NSE, which have both a well established soft matter user community.

Based on the affiliation of the main proposer the number of German research groups is the largest. Also not given by numbers the vast majority of experimental groups is from universities, followed by research centers. This stresses the importance of JCNS in the academic community and across the European landscape of neutron sources.

Since February 1, 2009 European users could receive financial support to access JCNS instruments by NMI3 within the 7th Framework Programme of the EU. Proposals accepted under the programme benefit from funding for travel expenses and local costs of the user. Within eleven months a total of 90 beam days were allocated and 29 European users were supported. In addition to the EU programme, support for users from German university was given by own resources.

JCNS LabCourse and Workshops: The 14th JCNS Laboratory Course - Neutron Scattering was held in 2009 on Sept. 7-18th. First part took place at the Forschungszentrum Jülich GmbH with lectures on neutron scattering theory and methods while the second part took place in Garching with hands on experiments at instruments of JCNS and various university groups operating instruments at FRM II. The courses for students were partly supported by NMI3. The number of students was limited to 55 participants, with more than double as many applications so that there had to be a strict selection. About one half of the accepted students came from foreign countries.

Instruments of JCNS at FRM II also participated active in the student courses offered by the Physics Department of TU München at FRM II.

Two successful scientific workshops were organized by JCNS in 2009. On Sept. 27-28th the workshop Off-Spec 2009 on "Modelling and Data Analysis for Grazing Incidence and Off-Specular Scattering" took part in Feldafing with more than 40 participants from Europe and abroad. More than 65 scientists attended the annual JCNS Workshop on Oct. 5-8th in Tutzing on "Trends and Perspectives in Neutron Scattering on Soft Matter".

Future development: Since start of operation of the instruments of JCNS at FRM II a very successful use by internal and external users of JCNS has been established which increased further in 2009. Despite this successful establishment of the user operation at JCNS two major obstacles for users are recognized: i) the availability of more dedicated sample environment devices at JCNS instruments and ii) a unified graphical user interface to run the instruments and to reduce the raw data for further treatment. On both subjects JCNS has started actions to offer solutions. Dedicated sample environment will be a constant challenge in close collaboration with the various and changing demands of the user experiments. The development and setup of a graphical user interface for instrument control and data handling has been started and is planned to be implemented at first instruments of JCNS within 2010.

Further information on the instruments of JCNS and Call for proposals for beam time can be found on the JCNS web pages at www.jcns.info.

BIODIFF: first installations and detector concepts

T. E. Schrader[1], A. Ostermann[2], B. Laatsch[3], P. Jüttner[2], M. Monkenbusch[4], W. Petry[2], D. Richter[1,4]

[1] JCNS: Jülich Centre for Neutron Science
[2] FRM II: Research Reactor Heinz Maier-Leibnitz
[3] ZAT: Central Technology Division
[4] IFF-5: Neutron Scattering

In collaboration between the Forschungszentrum Jülich (FZJ) and the Forschungsneutronenquelle Heinz Maier-Leibnitz (FRM II) a single crystal diffractometer optimised for crystals with large unit cells is being built. Its scientific focus will be the determination of the exact location and bonding properties of hydrogen atoms in protein or DNA crystals. With this information the hydration pattern of proteins can be studied, the protonation state of critical amino acid side chains can be determined and even dynamical information can be obtained by determining the hydrogen-deuterium exchange of the protein backbone. In order to achieve these results two detector concepts are foreseen: a) an image plate detector covering a large solid angle and b) a neutron scintillator imaged onto a CCD-camera providing a fast read out for a timely alignment of the crystals and additional detection abilities.

Crystallography is a powerful tool to determine the structure of biopolymers like DNA or proteins. Knowing the structure of proteins for example is a prerequisite for understanding their function. Often hydrogen atoms play a crucial role in the functioning of proteins, be it as liable protons in acidic side chains near the active core or as part of a water molecule involved in the catalytic reaction of the protein. Unfortunately, x-ray crystallography can only resolve the exact position of hydrogen atoms at very high resolutions which are not readily reached with protein crystals. Here, neutrons as probes for crystallography offer the advantage to make the hydrogen positions in a protein crystal accessible even at moderate resolutions. In particular neutrons allow distinguishing between hydrogen and deuterium. Thereby acidity and exposure of hydrogens in a protein may be classified. Figure 1 shows an example where neutron scattering gave important insights into the H/D exchange pattern in the protein myoglobin. The corresponding data set was recorded at the monochromatic BIX-3 beam line at the JRR-3M reactor at the JAEA - a beam line similar in design with the BioDiff instrument. The degree of hydrogen exchange of the protein backbone was determined for the 8 α-helices of myoglobin using a special refinement method. Obviously, the hydrogen bond between amino acid 67 and 71 is more susceptible to hydrogen/deuterium exchange than the H-bond between amino acid 72 and 76. This means that the packing of the protein is tighter or less flexible at the latter position.

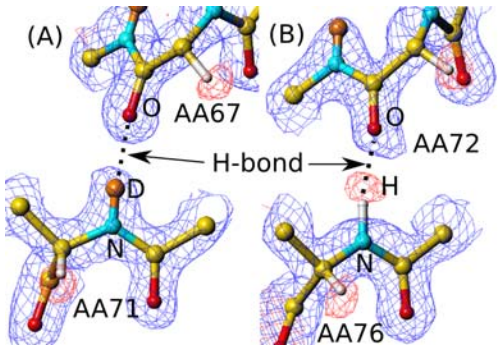

FIG. 1: Monitoring hydrogen/deuterium in the E-Helix of myoglobin. (A) Here, complete exchange of hydrogen atoms with deuterium is observed. This indicates a dynamical opening and reformation of the H-bond between amino acid 67 and amino acid 71.(B) Only very little exchange is seen in the H-bond between amino acid number 72 and 76 showing that this H-bond is not so much accessible to solvent molecules. From Ostermann, A. and Parak, F. G. in "Hydration- and Hydration-Sensitive Structural Biology", Niimura, N. et al. (Eds.) Tokyo, Japan (2005) pp. 111-122.

The BioDiff instrument (see Fig. 2) being built at the neutron guide NL1 in the neutron guide hall west of the FRM II is designed to perform neutron crystallographic experiments on protein crystals with large unit cells. The wavelengths of the monochromatic neutron beam can be adjusted to the size of the unit cell between 2.4 Å and 5.6 Å. A pyrolytic graphite crystal will be used to deflect the neutrons out of the neutron guide NL1. Higher order contaminations will be removed by a velocity selector.

Whereas the monochromator shielding has been already installed in the neutron guide hall (see Fig. 3 for a recent picture), the detector housing is still in its design phase. The requirements on this housing are fourfold:

- Proper shielding should be provided to the γ-radiation background from outside.
- One should be able to position both detectors accurately and reproducibly relative to the sample position.

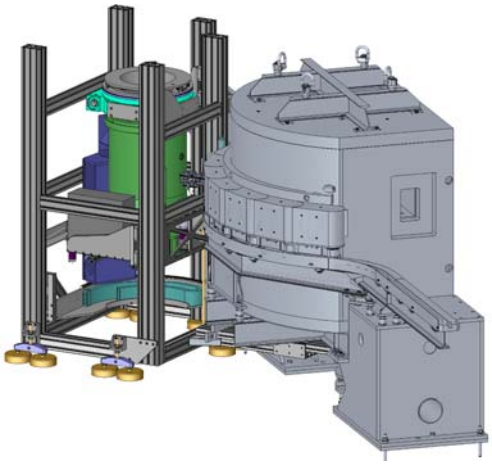

FIG. 2: Overview over the complete BioDiff instrument: monochromator shielding on the neutron guide NL1 at the FRM II (grey), image plate detector (green) and CCD-detector assembly (blue).

- The whole detector housing has to move when another neutron wavelength is desired.
- Enough space should be provided to accommodate the sample environment for the crystals under investigation.

FIG. 3: The monochromator shielding as it was installed on the neutron guide NL1 in the neutron guide hall west of the FRM II in 2009. As the desired wavelength changes the monochromator crystal will be turned and with it the neutron beam and the whole detector unit moves. This requires the lead "curtain" γ-ray shielding to move with it.

The γ-radiation shielding is provided by 5 cm thick lead walls surrounding the detector housing (not shown in Fig. 2). The sample environment will enter the detector housing from the top, here only the goniometer for the sample environment is indicated in Fig. 2 (light blue). When changing to another neutron wavelength the whole detector housing will be lifted by pressurizing the air cushions. A friction wheel will drive it to the new position where the air pressure is then released again.

A sophisticated mechanical design has been developed to be able to switch between both detectors (see Fig. 4). The neutron image plate detector (depicted in green in Fig. 4) can be moved downwards to give way for the neutron scintillator. The converted light of the scintillator is bent by an aluminium mirror and imaged with a commercial objective onto the CCD-chip (blue assembly in Fig. 4). Special attention is paid to avoid any possibility for stray light to enter the CCD assembly.

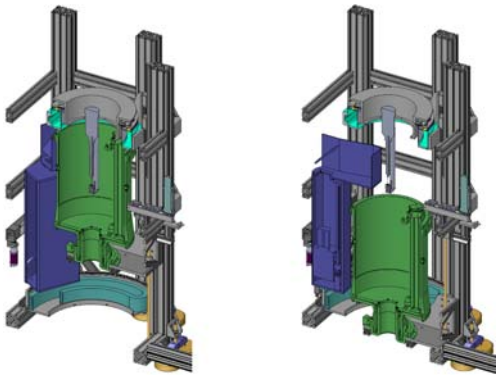

FIG. 4: Cut through the middle plane of the detector housing of the BioDiff instrument: (left) The image plate detector is positioned for recording data. (right) When the image plate detector is moved to the bottom, the CCD-detector assembly can be used to take data.

The scintillator of the CCD-assembly (dimensions: 20 cm by 20 cm) is closer to the sample location (10 cm distance) as the neutron image plate (20 cm radius). Additionally it can be dislocated in height by 10 cm upwards and downwards relative to the neutron beam. Furthermore, it can be swung around up to an angle of 113° with respect to the neutron beam.

The neutron image plate detector provided by Maatel (Voreppe, France) will have a software selectable spatial resolution between 125 μm and 500 μm. It covers a solid angle of approximately 2π. The spatial resolution of the CCD-assembly is limited by the thickness of the scintillator which smears out the recorded Bragg reflexes to about 300 μm. A solid angle of ca. 0.7π can be covered at once by the CCD-assembly and 2π is accessible in total.

DNS – polarized neutrons shine

Y. Su[1], W. Schweika[2], W. Boghols[1], R. Mittal[1], P. Harbott[2], K. Bussmann[2], H. Schneider[1], A. Gussen[3], H. Kleines[4], M. Wagner[4], R. Möller[4], A. Ioffe[1], Th. Brückel[1,2]

[1] JCNS: Jülich Centre for Neutron Science
[2] IFF-4: Scattering Methods
[3] ZAT: Central Technology Division
[4] ZEL: Central Institute for Electronics

DNS is a versatile diffuse scattering spectrometer with polarization analysis at FRM II. With its compact design, DNS is optimized as a high intensity instrument with medium resolution. In 2009, DNS has experienced another year of successful user operation on the studies of magnetism, soft condensed matter and novel materials via intense polarized neutrons.

DNS is a new cold neutron multi-detector time-of-flight spectrometer with both longitudinal and vector polarization analysis at FRM II. This allows the unambiguous separation of nuclear coherent, spin incoherent and magnetic scattering contributions simultaneously over a large range of scattering vector Q and energy transfer E, which attracts a broad user community from soft matter physics to magnetism. With its compact size DNS is optimized as a high intensity instrument with medium Q- and E- resolution. DNS is therefore ideal for the investigations of magnetic, lattice and polaronic correlations in frustrated magnets and highly correlated electron systems. With its unique combination of single-crystal time-of-flight spectroscopy and polarization analysis, DNS is also complimentary to many modern polarized cold neutron triple-axis spectrometers.

The DNS instrument has experienced a major reconstruction within the process of relocation from the Jülich reactor FRJ-2 to the FRM II at Garching. This process and the construction of the new DNS at FRM II have started in 2006. A new double focussing graphite monochromator has been built and set up at the neutron guide NL6. With its fine, almost transparent Mg-support structure, the transmitted beam can be used without significant losses at the down stream backscattering instrument SPHERES. The first neutrons and intense polarized neutron beam were delivered to DNS in September of 2007. Newly constructed polarizer and polarization analyzers, both using m = 3 Schärpf bender-type focusing supermirrors, perform extremely well. A polarized neutron flux as high as 5×10^6 n/s/cm^2 has been achieved at the neutron wavelength with 4.74 Å. The polarization rate of the incident neutron beams is nearly 96%. The expanded polarization detector bank has largely improved the measurement efficiency.

Since early 2008, DNS has been in routine operation for both internal and external user groups using polarized neutrons and polarization analysis in diffraction mode. Attractive sample environment, such as He^3/He^4 dilution refrigerator for cooling down to 20 mK, has been provided to the users in routine operation. In 2009, significant progress has been made on the construction of the new chopper system for time-of-flight spectroscopy and a new position sensitive detector system. The implementation of both new components for DNS is expected in the Spring of 2010. The DNS will greatly improve possibilities for single crystal TOF spectroscopy with efficient measurements in all 4 dimensions of S(Q,E). Another major progress achieved in 2009 is the successful delivery of intense polarized neutrons at the wavelength with 2.36 Å, the shortest possible wavelenghth available at DNS.

FIG. 1: Current look of DNS at FRM-II.

With the increased flux and efficiency at FRM-II, DNS has been very attractive for the studies of complex spin correlations in highly frustrated magnets [1], strongly correlated electrons [2, 3] and soft condensed matter, such as nanoscale confined polymers

[4] and proteins [5]. The exploration of unusual magnetic properties can also be efficiently undertaken on single-crystal samples by involving hundreds of sample positions each measured for a few minutes. In addition to the separation of magnetic cross section from nuclear and spin-incoherent ones, polarization analysis also allows to distinguish in detail the anisotropy of spin correlations. Fig. 2 shows the reciprocal space maps obtained on a prototypical iron pnictide parent compound $EuFe_2As_2$ via polarized neutron scattering at DNS [2]. These observations allowed us for the first time to identify two different magnetic modulation wavevectors, respectively represented by the Eu and Fe magnetic sublattices. The interplay between these two sublattices is believed to be among key ingredients for superconductivity in iron pnictides.

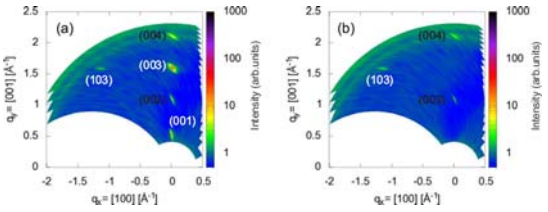

FIG. 2: Contour maps in the reciprocal space at (a) T=10 K and (b) T=40 K obtained by polarized neutron scattering on $EuFe_2As_2$, Miller indexes of nuclear (crystallographic) and magnetic reflections are labeled in black and white, respectively [2].

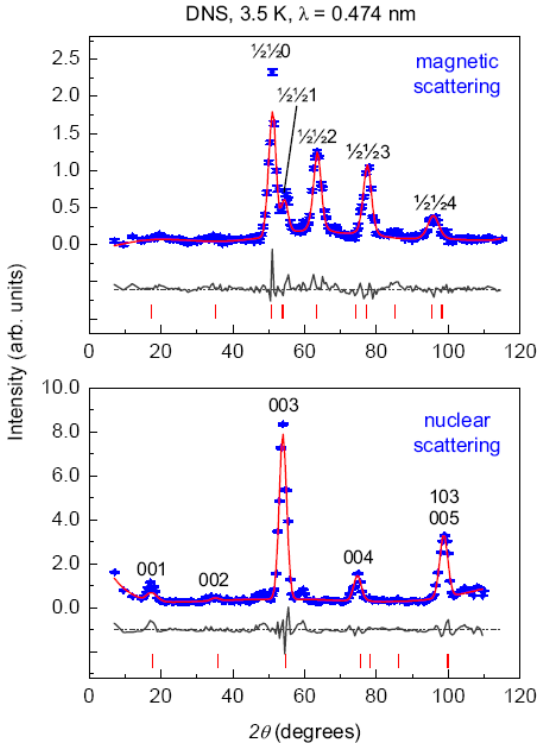

FIG. 3: Magnetic and nuclear reflections of Sr_2CrO_3FeAs (blue) and Rietveld fit (red) at 3.5 K measured at DNS [3].

Recently, it has also been realized that polarized diffraction on DNS is complementary to standard neutron powder diffraction and may be extremely useful for magnetic structure refinements, particularly in case of small moments by improving the signal to background ratio. Fig. 3 shows the magnetic and nuclear scattering as well as the Rietveld refinement of a newly discovered pnictide compound Sr_2CrO_3FeAs as obtained by polarization analysis [5].

DNS also represents a powerful instrument for the soft condensed matter community for the separation of nuclear coherent scattering from often dominating spin incoherent scattering background. Fig. 4 shows a recent example of such an application on the studies of some protein samples [5].

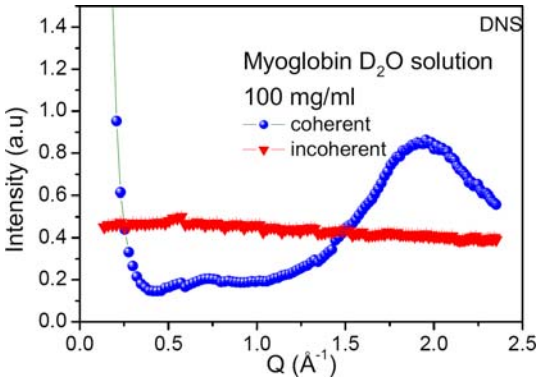

FIG. 4: Coherent and incoherent scattering intensities obtained for some solutions of protonated proteins in D2O [5].

[1] Krott M., etc., Phys. Rev. B **80** (2009) 024117.

[2] Herrero-Martin J., etc., Phys. Rev. B **80** (2009) 134411.

[3] Tegel M., etc., arXiv:0911.0450 (2009)

[4] Krutyeva, M., etc., J. Chem. Phys. **131** (2009) 174901.

[5] Gaspar, A.M., etc., Biochimica et Biophysica Acta **1804** (2010) 76.

Slow motion on the nanoscale: the neutron spin-echo spectrometer J-NSE

O. Holderer[1], N. R. de Souza[1], M. Monkenbusch[2], D. Richter[1,2]

[1] JCNS: Jülich Centre for Neutron Science
[2] IFF-5: Neutron Scattering

The neutron spin-echo spectrometer J-NSE was in user operation in 2008. Its performance has been improved continuously by the ongoing development of new correction coils and the installation of a new detector. The highest Fourier time actually used in experiments has been extended to 200 ns. Experiments have been carried out on a variety of topics, including microemulsions, polymers in confinement, supercritical CO_2-microemulsions, microgels, confined water. As a new topic for the J-NSE, experiments addressing the dynamics close to an interface with a grazing incident beam have performed.

Instrument development: The major advance in resolution (i.e. maximum achievable Fourier time) during this year has been acieved by the successive change to the new design of ”Pythagoras” type correction coils. Figure 1 shows a photograph of a pythagoras coil, which consists of two rectangular parts, each part applying a quadratic correction to the magnetic field in x- and y-direction. The sum of the two coils leads then to a radial quadratic correction.

So far, five of the six correction coils are now of the new design, which improved siginficantly the resolution function of the spectrometer and made experiments up to 200 ns feasable.

The largest correction coil, located at the end of the second main precession coil where the scattered beam has the largest cross section, is still a spiral Fresnel coil made from copper. It is the position with the highest requirements concerning the correction and higher terms than the quadratic one play a significant role. There, a coil with the ”Pythagoras” design can only do a part of the correction. It is forseen that during the next year, this coil will be replaced either by also a ”Pythagoras” coil, resulting in a significantly higher transmission but neglecting higher order corrections, or a combination of a ”Pythagoras” coil and a second coil for higher order corrections.

Experiments at the J-NSE. Soft Matter Experiments in general: The influence of confinement on the polymer dynamics has been studied with different confining systems, as e.g. tubes in silicon wafers or soft confinement in rodlike micelles (M. Krutyeva, A. Kusmin, R. Lund, L. Willner). Also related to the subject is the dynamics of polymer systems in the presence of filler nanoparticles (K. Nusser, S. Neueder, G.J. Schneider). First experiments on the dynamics of proteins have been conducted (M.S. Appavou).

FIG. 1: Pythagoras correction coil.

Supercritical CO_2-microemulsions: Microemulsions containing supercritical CO_2 as the “oil”-component have been investigated in an amagnetic pressure cell in the pressure range from 160 bar to 300 bar (collaboration with M.Klostermann, T. Sottmann, R. Strey, Univ. Köln). As a new component to the high pressure setup, an automated ISCO syringe pump has been used to apply and regulate the pressure. A much higher precision in pressure stability has thus been achieved.

Microgels: Stimuli-responsive polymeric hydrogels react strongly even to weak changes of their environment and are therefore of interest for a number of applications At J-NSE, a solutions of a symmetrical triblock copolymer with a thermo- responsive poly(N-isopropylacrylamide), PNIPAM, middle block and two short, fully deuterated polystyrene, P(S-d8), end blocks has been investigated. Solutions of 5 and 17 wt.-% in D2O were investigated (J. Adelsberger, C. Papadakis et al., TU München, see Ref. [1]). Whereas the 5 wt.-% solution consists of single core-shell micelles with a P(S-d8) core and a thermo-responsive PNIPAM shell, the micellar shells overlap in the 17 wt.-% solution, as evidenced by small-angle neutron scattering (SANS). PNIPAM shows lower critical solution temperature (LCST) behavior with an LCST of 32°C. The micellar shell is swollen

below this temperature and collapsed above. Using neutron spin echo spectroscopy (NSE) at J-NSE, the segmental dynamics of the PNIPAM shell as a function of polymer concentration and temperature has been studied. Figure 2 shows the intermediate scattering function at 24.4 and 32.1ĄřC, below and above the LCST. For the 17 wt.-% solution below the LCST, the diffusion coefficient does not depend on temperature, in agreement with the absence of structural changes, as evidenced using SANS. It changes discontinuously at the LCST. Above the LCST, the observed segmental diffusion coefficient is for both concentrations faster than below. This has been attributed to a freezing-in of the dynamics of most of the shell dynamics when the shell is collapsed and thus in a melt state.

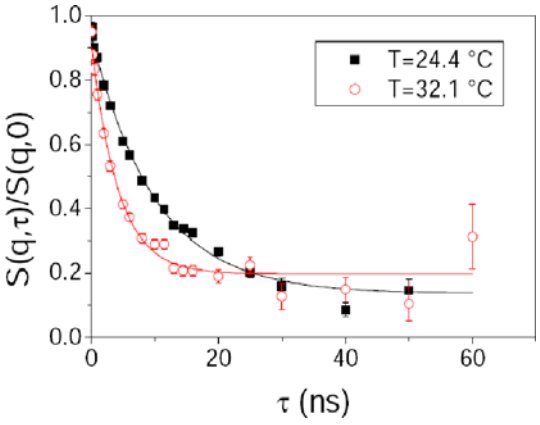

FIG. 2: Intermediate scattering function of a microgel below and above the LCST for q=0.15Å.

GINSENG (Grazing Incidence NSE Near Garching): Recently, grazing incidence neutron spin-echo spectroscopy has emerged as a possibility of resolving the dynamics of soft matter near an interface.

The first GI-NSE experiments at the J-NSE spectrometer at the FRM II investigated SDS micelles in water, which proved the principle feasibility in terms of resolution, background correction and scattered intensity in an inverted geometry (M. Walz, P. Falus, A. Magerl).

Normal geometry, i.e. gracing incident beam, scattered beam at finite q, has been used for measurements on a water/oil/surfactant microemulsion with a lamellar phase close to the interface and a bicontinuous phase in the bulk (M. Kerscher, H. Frielinghaus). By varying the incident angle the penetration depth of the evanescent wave can be changed and thus a depth profile of the dynamics at a certain q value is measured. Fist results of the surfactant layer dynamics near the interface are presented which indicate a significant increase of the relaxation rate in the region where the transition from a lamellar to a bicontinuous phase takes place.

Magnetic form factors: First experiments on magnetic nanoparticles have been done, with the aim to measure the magnetic form factor of the nanoparticles (S. Disch, R. Hermann). Nuclear and magnetic scattering has been separated by turning the polarization in x, y and z direction at the sample position. It has been possible to extend the q-range of the SANS experiments to larger q-values, and separate coherent and incoherent scattering. As a preliminary result, a significant magnetic scattering contribution has been detected in the small angle range for iron oxide nanoparticles of 9 nm diameter.

Nuclear spin excitations: A first test has been performed with the aim measuring nuclear spin excitations in Nd2CuO4 on the J-NSE spectrometer of Juelich Centre for Neutron Science at FRMII (T. Chatterji). Below a temperature of 400 mK, nuclear spin waves are expected to occur in this crystal. We performed neutron spin echo experiments at 50 mK at a Q vector close to the nuclear magnetic Bragg peak at Q = (1/2,1/2,0). The experiment has been carried out at a central wavelength of 5 Å. A velocity selector provided a beam with a wavelength spread $\delta\lambda/\lambda$ = 10 %. At a fixed angle of the second spectrometer arm of 53.6°, corresponding to |Q|=1.128 $Å^{-1}$, the scattering of the sample has been measured at two different angles: in the (1/2 1/2 0) orientation such that the nuclear magnetic Bragg peak was visible and then at position with the sample rotated by 7°. First hints of the presence of inelastic scattering of nuclear spin waves have been found.

[1] C. M. Papadakis, J. Adelsberger,et. al., Exp. Report for Proposal No. 2084

Small angle neutron scattering instrument in operation for users

H. Frielinghaus[1], P. Busch[1], V. Pipich[1], A. Radulescu[1], V. Ossovyi[1], M. Heiderich[2], G. Kemmerling[3], R. Engels[3], M. Wagener[3], L. Fuß-Fleischhauer[3], M. Drochner[3], H. Kleines[3], R. Hanslik[4], K. Dahlhoff[4], D. Schwahn[2], D. Richter[1,2]

[1] JCNS: Jülich Centre for Neutron Science
[2] IFF-5: Neutron Scattering
[3] ZEL: Central Institute for Electronics
[4] ZAT: Central Technology Division

KWS-1 came to user operation at the turn of the year 2009/2010. The machine is equipped with the full detector tube such that detector distances of 20m are routine and smallest scattering vectors of 10^{-3}Å^{-1} and below become accessible. Furthermore, the fast detector electronics – similar to KWS-2 – have been installed. Neutron lenses, a high resolution detector, the chopper, the hexapod sample stage, and polarization analysis will be installed in the last months of 2010.

KWS-1 started user operation at the turn of the year 2009/2010. The machine is equipped with the full detector tube such that detector distances of 20 m are routine and smallest scattering vectors of 10^{-3}Å^{-1} and below become accessible. Furthermore the fast detector electronics – similar to KWS-2 – have been installed.

FIG. 1: View on KWS-1 (left) and KWS-2 (right) from the rear – close to the control computers.

The maximum flux at the sample was determined to be 10^8 neutrons/cm^{2}s. This result is a factor of 2 lower compared to KWS-2, and arises from the better defined wavelength spread (10% vs. 20%). This high value is obtained from a wavelength of 4.7Å and a 2m collimation. This flux is comparable to the world leading instruments, and therefore high resolution experiments and investigations of thin films become possible.

The new collimation apertures are made from boron containing ceramics, and allow a smaller beam stop area of 5x5cm in front of the detector for typical entrance apertures of 3x3cm. This in turn reduces the minimal Q of a typical measurement with a wavelength of 7Å to 1.3x10^{-3}Å^{-1}, which is roughly 2 times better than formerly achieved in Jülich.

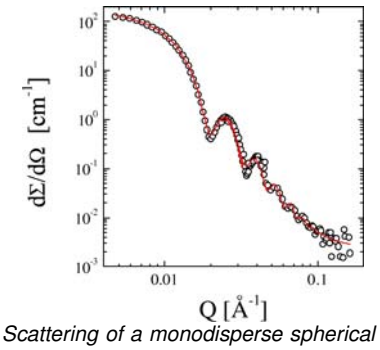

FIG. 2: Scattering of a monodisperse spherical silica colloid. The open circles represent the experimental macroscopic cross section, while the solid red line arises from a model description including the experimental resolution. The experimental radius of the colloid is 236Å. Interestingly, 5 maxima are clearly indicated by the scattering fringes.

The very good performance of KWS-1 is demonstrated by studies of highly monodisperse spherical colloid (Fig. 2). A large number of fringes is clearly visible (5 maxima) in the Q-range between 0.02 and 0.1Å^{-1}. Such observation is only possible due to the low polydispersity of the colloids *and* the high resolution of the instrument. The resolution arises from the wavelength spread (10%) given by the velocity selector and a well collimated beam. The new boron containing ceramics improved the collimation tremendously. These model systems serve for benchmarking the resolution – as shown here – and for absolute calibrations as a reference system. If the concentration and the particle size are known, the scattering at small scattering angles can be calculated theoretically, and any sample scattering will be referred to the theoretical forward scattering. This method is highly needed for the focussing instrument KWS-3, where incoherent references are of no use, since the detector is fixed at large distances. The theoretical forward scattering can always be cross-checked by KWS-1 measurements.

First grazing incidence small angle neutron scattering (GISANS) experiments have been performed at KWS-1. A bicontinuous microemulsion was studied in the vicinity of a hydrophilic surface. In former static experiments it was found that the microemulsion forms a lamellar ordered structure near the surface. This region is 400Å thick, and corresponds to two bilayers of oil and water. The thickness was consistently determined by GISANS and reflectometry. The latest experiments focused on the influence of

flow on the surface near ordered structure. The example figure (Fig. 4) shows the bicontinuous structure at large penetration depths. At smaller penetration depths a lamellar peak superimposes, and indicates the fraction of the lamellar region with respect to the penetration depth. For our flow experiments we find that the thickness of the lamellar region is decreased with increasing flow speed. This finding is counterintuitive, since the lamellar structure facilitates the flow and so its thickness should increase. Only very high shear rates might act destructive on the ordered region. Future experiments on slower flow rates are in preparation.

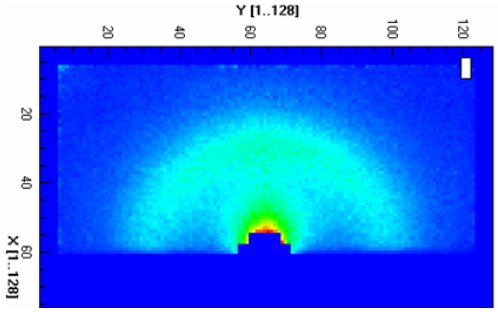

FIG. 3: Grazing incidence neutron scattering pattern of a bicontinuous microemulsion near a hydrophilic planar surface. The incident angle was above the critical angle, and so the bicontinuous scattering pattern dominates, i.e. a Debye-Scherrer ring is seen. The scattering gets weaker around the horizon, since then the outgoing wave is also evanescent. The strong scattering in the centre arises from surface roughness.

The neutron lenses support increased intensities with larger samples at constant resolution, or increased resolution to lowest Q in the range of 10^{-4}Å^{-1}. For these low Q a high resolution detector will be installed. The chopper supports the high resolution mode by reducing the wavelength spread using the time-of-flight analysis. The hexapod sample stage allows to precisely position thin film samples placed in a heavy sample environment (including strong magnets) to perform grazing incidence measurements. The polarization analysis will support the characterization of magnetic samples, particularly thin magnetic films. So finally KWS-1 will be dedicated to high resolution experiments and the characterization of thin magnetic films.

Neutron lenses have been tested experimentally in the latest years [1]. The cooled lens holder is in preparation. This cooling suppresses the phonon scattering. In parallel resolution calculations – analytically and computer simulated – are in preparation, in order to do the resolution corrections of the measurements.

The transmission polarizer to be placed in front of the collimation base was designed upon thorough computer simulations as three cavities with two polarizing mirrors in a V-shape, and finally manufactured by Swiss Neutronics. The first polarizer characterization at a wavelength of 5Å showed the average polarization of 93% (max. polarisation is 95%) (Fig. 3). An even higher polarization is expected for larger wavelengths as supported by computer simulations on single sided polarizing mirrors. Measurements for an incident neutron beam with realistic divergence and for lager wavelengths are in preparation to confirm the overall performance.

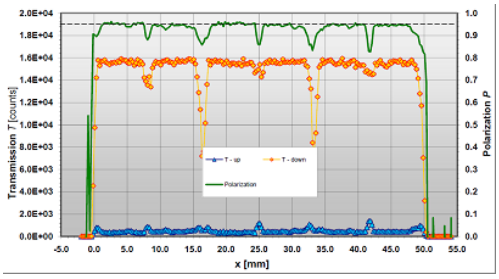

FIG. 4: Characterization of the polarizer for KWS-1.The used wavelength was 5Å. A spatial scan was done horizontally. The vertical edges of the mirrors (weak dips) and the separating walls (strong dips) are indicated clearly. The maximum polarization is ca. 95%, while the average polarization is 93%.

The installation of this polarizer at KWS-1 is planned for 2011. Therefore for preliminary experiments a single mirror transmission polarizer providing however smaller beam cross-section will be installed in front of the sample. This assumes a weak diffuse magnetic scattering at the polarizing mirror that thus will be put in a strong magnetic field ($>$0.2T). Our feasibility studies proved the applicability of such approach so that already in 2010 experiments with polarized neutrons are possible on KWS-1.

A stopped flow apparatus was successfully installed on KWS-1 for first test measurements. It was shown by transmission measurements that H_2O and D_2O are well mixed in the ms time scale. This new apparatus will allow for study of kinetics which are initiated by mixing of two or more fluids. A good example is the exchange of polymers between micelles formed of amphiphilic diblock copolymers [2]. Within the time window of SANS a logarithmic time dependence was found indicating a complex relaxation picture where the chains are slowed down due to mutual topological and geometrical interactions.

In the near future rheometers will be available for complex fluids and polymers. The geometries will allow to study the influence of shear on the volume of the sample and on the surface near structure. The latter will be studied by the grazing incidence geometry. So the deformation of soft colloids and the induced or reduced order of microemulsions by the shear field will be accessible.

The latest experiments were all successful, and support the heavy duty use of KWS-1 by external users. In this sense we are looking forward on a successful 2010.

[1] H. Frielinghaus, V. Pipich, A. Radulescu, M. Heiderich, R. Hanslik, K. Dahlhoff, H. Iwase, S. Koizumi, D. Schwahn, J. Appl. Cryst. **42**, 681 (2009)

[2] R. Lund, L. Willner, D. Richter, E. E. Dormidontova, Macromolecules 39, 4566 (2006)

KWS-2 SANS diffractometer for soft-matter and biological systems

A. Radulescu[1], V. Pipich[1], H. Frielinghaus[1], P. Busch[1], M. S. Appavou[1], A. Ioffe[1], D. Schwahn[2], M. Vaccaro[3], G. Mangiapia[3], L. Paduano[3], M. Heiderich[2], V. Ossovyi[1], G. Kemmerling[4], R. Engels[4], M. Wagener[4], L. Fuß-Fleischhauer[4], M. Drochner[4], H. Kleines[4], D. Richter[1,2]

[1] JCNS: Jülich Centre for Neutron Science
[2] IFF-5: Neutron Scattering
[3] Universita degli Studi di Napoli "Federico II" 80126, Naples, Italy
[4] ZEL: Central Institute for Electronics

The KWS-2 classical pinhole small-angle scattering instrument is a dedicated facility for structural studies in the fields of soft-condensed matter, chemistry and biology. Recent upgrades of the detection system aimed for optimization of the instrument towards high intensity structural studies and investigations of fast structural changes due to rapid kinetic processes.

The KWS-2 small-angle neutron diffractometer is dedicated to high intensity / wide-Q investigations of structures and morphologies on a wide length scale (from nm up to μm) and of fast structural changes in the fields of soft condensed matter, chemistry and biological systems. The combination of high neutron flux supplied by the cold neutron source of FRM II reactor, newly designed neutron guide system [1], 20% wavelength selector, and a new, "fast" detection electronics supports the high intensity operation mode.

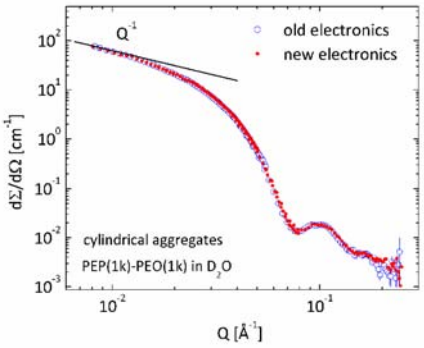

FIG. 1: SANS patterns from cylindrical aggregates formed by a diblock copolymer in D_2O measured with the old (20 kHz) and new (150 kHz) detector electronics for 10% dead-time; the incoming neutron intensity on the sample varied by choosing different collimation lengths and apertures sizes.

The neutron flux is comparable with the world leading SANS instruments with the potential for a further increase of intensity by one order of magnitude that will be achieved by the cooled (70K) aspherical neutron lenses [2] allowing for a larger sample aperture at the same resolution. An upgraded electronics for the Anger-type detection system (1mm ^{6}Li glass scintillator with an active area of 60x60 cm^2 and 95% detection probability for 7Å) was commissioned in 2009 (Fig.1). The new "fast" electronics with a dead-time of 0.64 μs allows a counting rate of 1.5x10^5 n/s with 10% dead-time (with a maximum counting rate of 6x10^5 n/s).

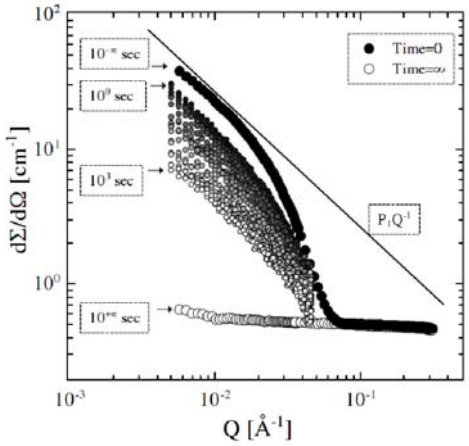

FIG. 2: Time-resolved SANS (1s resolution) of fast chain exchange under equilibrium between PEP(1k)-PEO(1k) cylindrical micelles in water solution using a stopped flow apparatus and real-time detection mode at KWS-2.

This opens opportunities to study structural and morphological changes due to rapid kinetic processes within the ms range. For this purpose the new detection electronics was optimized for two working modes: (a) the "normal" mode that permits a minimal time resolution of 1min with a 6s time loss between two consecutive measurements and (b) the "real time" mode that enables the external start of the detection process (e.g. by the command of the stopped-flow device) and a continuous data acquisition for variable time slots (technically optimized for time resolutions as low as 1μs). Both detection modes were successfully tested in 2009. Fig.2 presents a set of results obtained during the test of the "real time" detection mode: the fast kinetics of chain exchange between polymeric micelles in solution [3] was investigated with a time resolution of 1s. The process can be understood by following the time evolution of the scattered intensity when differently labelled polymers (fully deuterated and fully protonated) are mixed (t=0s) in an isotropic solvent mixture with the scattering length density exactly matching the average of the two polymers.

KWS-2 contributes both to the in-house research activity in the traditional field of soft-matter and to the user program. Polymer effects on microemulsions, on diesel fuels and mineralization of inorganic compounds, thermal composition fluctuations in polymer blends and diblock copolymers, polymer aggregation behaviour and their response on shear, the rubberelasticity and "living anionic" polymerization, the denaturation of proteins by chemical agents or by the change of temperature and pressure are usually studied topics.

As a research highlight at KWS-2, the structural study of supramolecular aggregates able to transport contrast agents and metal complexes used for the detection and for the therapy of tumours is further shortly presented (experimental proposals from the University of Naples). The design of highly contrast agents and new anti-cancer drugs presenting selective effects toward solid tumors and a lower toxicity can be achieved considering the relationship between their structure and dynamics and the relevant parameters determining their effects on the cancer tissues.

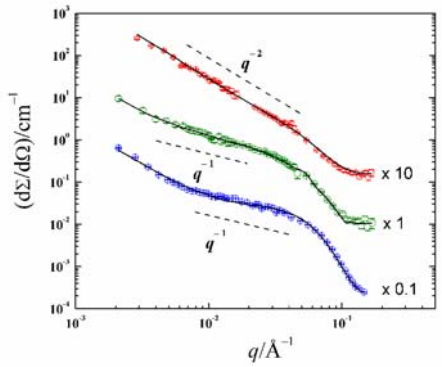

FIG. 3: Scattering profiles measured on $(C18)_2$DTPAGlu(Gd) - D_2O system at pH=7.4; 4.5 and 3 (from bottom to top) and fitted with structural models for thread-like micelles (q^{-1} behavior of the scattered intensity) and unilamellar vesicles (q^{-2} behavior).

Specific supramolecular aggregates formed by novel amphiphilic molecules that contain gadolinium complexes (detectable through magnetic resonance imaging) and surface exposed bioactive peptides for selective delivery have been synthesized and characterized. SANS measurements performed at KWS-2 have allowed detecting a rich variety of aggregates (Fig.3) formed by these molecules in dependence of the parameters such as pH and ionic strength [4]. Metastases rather than primary tumours are the leading cause for cancer death, and yet metastases are almost never the target in chemotherapy. New amphiphilic unimers able to coordinate ruthenium complexes and to form supramolecular aggregates both in the presence and in the absence of DOPC:DOPE phospholipids in equimolecular amount have been recently synthesized [5]. Preliminary SANS, cryo-TEM (Fig.4) and DLS investigations [5] have confirmed the presence of unilamellar and oligolamellar liposomes, as well as the existence of more complex structures like bicontinuous cubic phases.

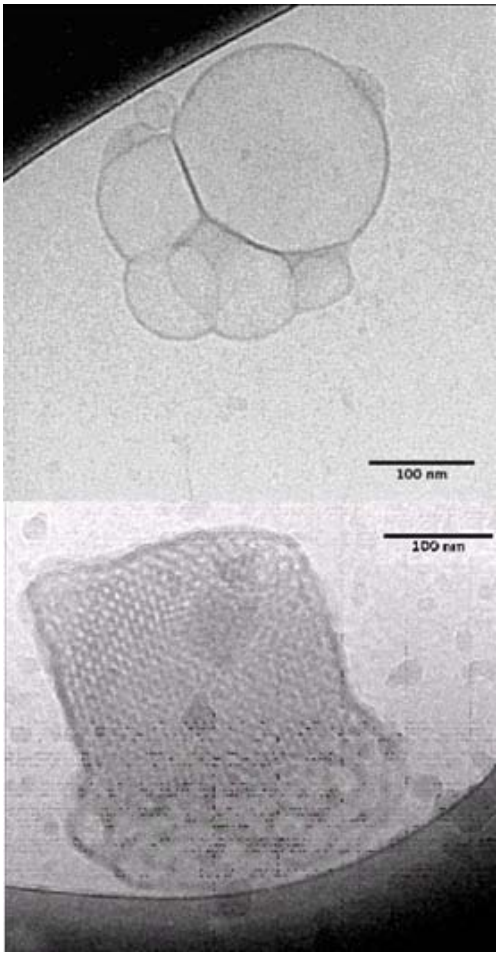

FIG. 4: Cryo-TEM images showing the rich variety of aggregates formed in the aqueous dispersions of (DOPC/DOPE)/DOPURu, such as unilamellar vesicles and cubic phases.

The findings in the present study open new vistas for the application of lipid-based supramolecular systems in Ru anti-cancer therapy. The lodgement of Ru complexes in amphiphilic nanovectors allows a higher amount of drug in the bloodstream compared to the case when it is administrated as a free complex.

[1] A. Radulescu and A. Ioffe, *Nuclear Instruments and Methods* A 586, 55, 2008; A. Radulescu, V. Pipich and A. Ioffe, *in preparation*.

[2] H. Frielinghaus, V. Pipich, A. Radulescu, M. Heiderich, R. Hanslik, K. Dahlhoff, H. Iwase, S. Koizumi, D. Schwahn, *J.Appl.Cryst.* 42, 681, 2009.

[3] L. Willner, A. Poppe, J. Allgaier, M. Monkenbusch, P. Lindner, D. Richter, *Europhys.Lett.* 55, 667, 2001.

[4] M. Vaccaro, G. Mangiapia, A. Radulescu, K. Schillen, G. d'Errico, G. Morelli, L. Paduano, *Soft Matter* 5, 2504, 2009.

[5] M. Vacarro, R. del Litto, G. Mangiapia, A. M.Carnerup, G.d'Errico, F.Ruffo, L.Paduano, *Chem.Comm.* 11, 1404, 2009; L.Paduano et al., *in preparation.*

JCNS-instrument KWS-3 for high resolution SANS started at FRM II

G. Goerigk[1,2]

[1] IFF-4: Scattering Methods
[2] JCNS: Jülich Centre for Neutron Science

Small-Angle Scattering (SAS) is used for the analysis of structures with sizes just above the atomic scale between 1 and about 100 nanometers (nm), which cannot be assessed or sufficiently characterized by microscopic techniques. KWS-3 is an important supplementary instrument, which extends the accessible range to very small scattering angles with a superior neutron flux when comparing to a conventional instrumental setup with pinhole geometry. Thus the length scale, which can be analyzed, is extended beyond 1 micrometer for numerous materials from physics, chemistry, materials science and life science, like alloys, diluted chemical solutions and membrane systems.

FIG. 1: Photo of the toroidal mirror installed inside its vacuum chamber after refurbishment. With the double focusing mirror the KWS-3 gains superior flux in the Q-range below 10^{-2} Å when comparing to instruments with pinhole geometry [1].

After moving from Jülich to Munich the instrument underwent a fundamental evaluation with the final result, that a major upgrade for the whole instrument became necessary. The main topic of the upgrade project was a general mirror refurbishment i.e. a new polishing and subsequently a new coating of the mirror surface with the isotope ^{65}Cu with the aim to improve the resolution properties of the whole instrument. The mirror refurbishment was successfully performed by Carl Zeiss Laser Optics GmbH. Due to the minimization of the mirror's micro roughness the parasitic scattering contributions have been reduced by about a factor of 3, when comparing to the old mirror coating [2].

In parallel to the mirror refurbishment comprehensive upgrade activities in the vacuum system, electronics and programming have been performed with the aims of protecting the new mirror coating from aging (degradation of the mirror's surface properties), transforming the instrument into a user-friendly state and introducing conceptual improvements.

Since the reactor cycle 21 (August 2009) the KWS-3 entered commissioning. The success of the mirror refurbishment and the upgrade activities was confirmed by different test measurements. Numerous calibration measurements have been performed and it is planned to finally implement KWS-3 into the regular scheduling system within the running reactor cycle 22 (November 2009 until February 2010). With KWS-3 an additional instrument of 'Jülich Centre for Neutron Science' (JCNS) becomes operative and a joint project of JCNS, ZEL, ZAT, B und IFF approaches completion.

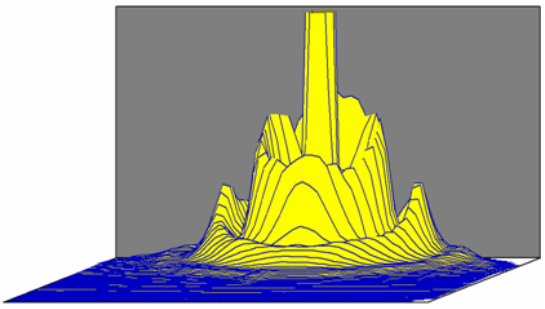

FIG. 2: Three-dimensional plot of the neutron intensity scattered by ordered PMMA-colloids with a diameter of 1.5 micrometer. The very high intensity contributions in the centre are caused by the primary beam.

In Figure 2 the V-SANS (Very Small-Angle Neutron Scattering) measurement of an ordered polymer (PMMA) with a radius of 776 nm is depicted. The spherically shaped polymer particles with a diameter of about 1.5 micro meter causes rings of scattered neutron intensity around the beam centre. The very high scattering intensities caused by the primary beam in the centre of the rings are not depicted on the full scale.

Future scientific topics to be addressed by KWS-3 (in combination with Anomalous Small-Angle X-ray Scattering) are among others bio-membranes serving as nano-reactors for the synthesis of semiconductor colloides [3], unilamellar vesicles (ULV) for drug delivery, proton-conducting membranes from fuel cell technologies [4], the conformational changes of polyelectrolytes depending on counter ion distributions [5] and Metal Organic Frameworks within the DFG priority program PP-1362.

---

[1] Alefeld, B., Schwahn, D., and Springer, T., Nucl. Instrum. Methods A 274 (1989) 210

[2] Kentzinger, E., Dohmen, L., Alefeld, B., Rücker, U., Stellbrink, J., Ioffe, A., Richter, D., and Brückel, T., Physica B 350 (2004), 779-781

[3] Bota, A.; Varga, Z.; Goerigk, G. Journal of Physical Chemistry B (2007), 111(8), 1911-1915

[4] Prado, L. A. S. de A.; Ponce, M. L.; Goerigk, G.; Funari, S. S.; Garamus, V. M.; Willumeit, R.; Schulte, K.; Nunes, S. P. Journal of Non-Crystalline Solids (2009), 355(1), 6-11

[5] Goerigk, G. ; Huber, K. ; Schweins, R. J. Chem.Phys. (2007) 127, 154908

First neutrons for MARIA

S. Mattauch[1], U. Rücker[2], D. Korolkov[1], K. Bussmann[2], V. Fracassi[3], R. Schmitz[3], J. Daemen[3], A. Budwig[3], P. Kämmerling[4], F. Suxdorf[4], H. Kleines[4], M. Bednarek[5], E. Babcock[1], A. Ioffe[1], Th. Brückel[1,2]

[1] JCNS: Jülich Centre for Neutron Science
[2] IFF-4: Scattering Methods
[3] ZAT: Central Technology Division
[4] ZEL: Central Institute for Electronics
[5] G-TG: Technical Management, Process Technology/Switch Cabinet Construction

The new reflectometer MARIA at the outstation of the Jülich Center for Neutron Science JCNS at FRM II has been build up to the sample position and has seen first Neutrons. This instrument is optimised for the study of magnetic nanostructures, serving the rapidly growing field of Spintronics or Magnetoelectronics, i.e. information storage, transport and processing using the spin of the electrons. The instrument will have unique features, such as polarisation analysis for large angular range, extreme focusing to small sample sizes, high flux, largely variable wavelength band selection, GISANS option, provision for kinematic studies down to the μs range, in-situ sample preparation etc. Its neutronic performance was optimised by Monte Carlo simulations and specially developed codes for various neutron optical devices.

The new neutron reflectometer MARIA (MAgnetism Reflectometer with high Incident Angle) of the JCNS (Jülich Center of Neutron Science) is designed for investigations of thin magnetic layered structures down to the monolayer scale (optimised for layer thicknesses between 3-300Å) and lateral structures of nm to μm sizes. Consequently the instrument is optimised for small focused beam and sample sizes of 1cm^2 and has polarisation analysis as standard. Beside the reflectometer mode with good resolution in the horizontal scattering plane, MARIA will be able to measure in the GISANS mode with additional resolution in the vertical direction. The latter mode allows one to measure lateral structures down to the nm scale.

Scattering plane	horizontal
Monochromator	velocity selector
Wavelength	4.5-10Å
Wavelength spread	1%, 3%, 10%
Expected pol. flux	7x10^7 n/(s*cm^2) (3mrad coll.)
Detector size	400 x 400 mm^2
Detector resolution	2mm
Sample detector dist.	2m
Max. detector angle	120°
Q_z-range	0.002 - 3.2Å^{-1}
Q_x-range	6·10^{-5} - 0.001Å^{-1}
α_f	-10 - 90°
Polarisation	double reflection polariser
Polarisation analysis	Radial solid state polariser / ^{3}He
Collim. (scat. plane)	4m long, Slits: 0 - 40 mm
Focussing	vertically focussing elliptic guide
GISANS option	4m long collimation
Q_y-range	0.002 -0.2 Å^{-1}

TABLE 1: Characteristic data of MARIA.

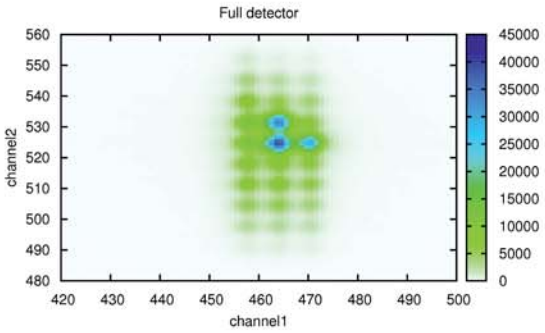

FIG. 1: Image of the detector image of a 4mm by 4mm array with 1mm wholes

The neutronic performance of the complete instrument was optimised with the Monte Carlo simulation package VITESS and specially developed codes for various neutron optical devices like Fermi chopper and selector. Compared to the former HADAS reflectometer at the Jülich research reactor DIDO, we expect a gain in flux of at least two orders of magnitude.

The rising interest in thin magnetic layers with lateral structures in the nanometer scale started with the discovery of the Interlayer Coupling in 1986 and the GMR-Effect in 1989 by P. Grünberg (IFF) and A. Fert (Paris). These effects allow one to store, transport and process information related to the spin of the electron. In combination with lateral structures approaching the nanometer size in thin film materials, new effects are expected. For the investigation of effects like the behaviour of magnetic domains inside nanostructures buried under nonmagnetic layers, magnetic effects in the vicinity of interfaces of different materials or dipolar interactions of nanostructures, polarised neutrons are a powerful and unique tool. All these phenomena can be studied with a polarised neutron reflectometer designed to have a high signal to noise ratio (8-9 orders of magnitude) with standard polarisation analysis on an area detector.

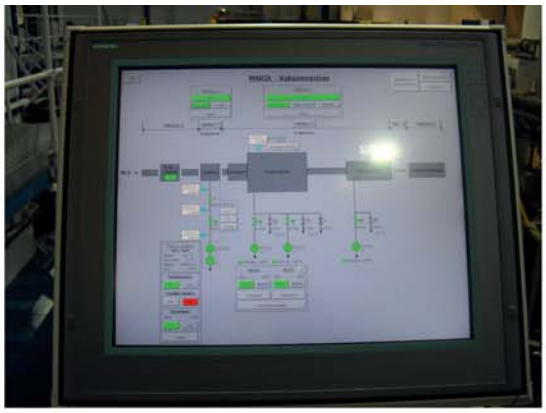

FIG. 2: Information Panel of MARIA in operation. The picture shows the vacuum overview of three sections of the instrument. The panel will serve the user, technicians and the instrument responsible world wide with the status of the machine.

FIG. 3: First Neutrons of MARIA at the 18.12.2009. Right from the start the radiation shielding withstands the high flux.

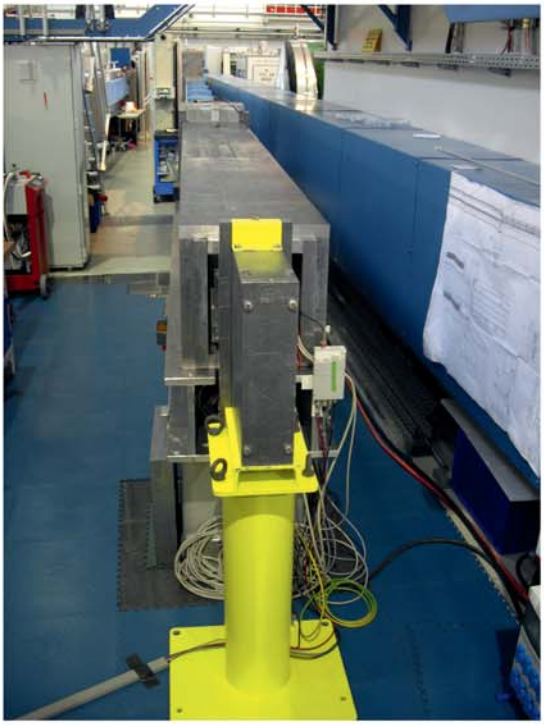

FIG. 4: The status of the instrument in December 2009. All components (beside the Fermi chopper) up to the sample position are installed and fully functional.

The main task in the last year was to assemble the different parts of the reflectometer, as the polarisation chamber, the flipper, the neutron guides, the collimation, the Hexapod, the detector and the electrical racks. The Fermi chopper will follow at a later stage. All the moving parts had been tested in Juelich and were available right after the installation, justifying the extensive testing. The same is valid for the vacuum system and the automatic control of it by the software running in the information panel. The neutron guides were installed by the Neutron Optic Group of the FRM II. Beside the hardware the software had to be written and tested. In the future JCNS will develop a GUI-system to help the users controlling and managing the different instruments. Therefor a standardised command line language with a small set of basic commands had been developed and for the first time implemented at MARIA. This will allow the different types of instrument of the JCNS to migrate easily to the new GUI-system without loosing the power full and existing software.

Before opening the beam for the first time the vacuum system immediately went to the expected average value of 0.02 mbar. With the three available Edwards scroll pumps for the vacuum unit from the selector down to the end of the collimation (20m) allows an up time of 7 to 8 years without an exchange of pumps. In December, shortly before the end of the last cycle of the year 2009 of the FRM II, we achieved to get the first neutrons of MARIA. Right from the start the shielding proofed to be strong enough to withstand the high flux of the machine. First intensity measurements manifest the flux values given in table 1. The tasks of the year 2010 are to characterise the reflectometer fully, starting from the beam profile at different wavelengths, different slit alignments and ending with the measurement and characterisation of reference samples in the reflectometer and GISANS mode unpolarised as well as polarised. This will be hopefully finished in the middle up to end of the year 2010, so that we can start afterwards with the general user operation.

POWTEX – updated design of the high-intensity TOF diffractometer

A. Houben[1], W. Schweika[2], P. Harbott[2], J. Walter[3], B. T. Hansen[3], R. Dronskowski[1], Th. Brückel[2]

[1] Institute of Inorganic Chemistry, Chair of Solid-State and Quantum Chemistry, RWTH Aachen
[2] IFF-4: Scattering Methods
[3] Geoscience Centre Göttingen, University of Göttingen

During the BMBF funding period since 2007, POWTEX has undergone many changes and improvements. The optimized chopper system and the increase of solid angle detector coverage were reported last year. This year, we want to address the dramatic changes to the detector system, unavoidably caused by the ^{3}He shortfall, as well as our improvements to the neutron guide design and our contribution to the open source Monte Carlo instrument simulation program VITESS. The proposal for the follow-up funding of POWTEX by the BMBF from 2010−2013 has been recently submitted.

^{3}He: At present, the so called ^{3}He crisis is becoming aware to a broader public, and it is not mere coincidence that this crisis is the central theme in Schätzing's last novel called "Limit". While maybe interesting to read in a novel, for POWTEX and many other parts of science the shortage of ^{3}He is a sad reality that came true long before attracting public attention.

Because the reasons have been elaborately discussed already in all kinds of literature [1, 2], we want to address herein how the POWTEX project plans to deal with this shortage. It is obviously not possible to buy the demanded 3700 l $\times$ bar ^{3}He within the next years. Currently, many alternative neutron detector concepts are under investigation by different groups world wide. For POWTEX, because using thermal neutrons with a wavelength down to $\lambda = 1.0$ Å and the huge coverage in detector solid angle (large detector surface) of 10 sr the ^{3}He-PSD tubes were an ideal choice because of their high detection efficiency for such wavelengths and the formerly low price/area. Thus, the search for alternative concepts will meet the same conditions. Gas based detectors using BF_3 suffer from a low detection efficiency and there is no prospect of an improvement to this. Semiconducting detectors are in very early design states and do not match POWTEX's short time scale for finding a proper solution. The remaining methods are scintillation detectors using ^{6}Li or ^{10}B. While the concept of the CASCADE detector is far too expensive for our huge detector coverage, two promising concepts can be found, namely the Wavelength-Shifting-Fibre (WSF) concept and the Blade concept. In order to investigate and proof the applicability of both concepts to the POWTEX requirements a prototype will be build of each method. Only by this, a decision for the future POWTEX detector concept can be made. The WSF-concept uses ^{6}Li/ZnS to convert neutrons to photons which can be captured by a wavelength shifting fibre and transported to a photo-multiplier. This type of detectors is currently installed at two instruments, namely POWGEN, which has similar requirements to POWTEX, and VULCAN, both located at the SNS. The Blade concept uses a ^{10}B converter under grazing incidence in order to yield a higher neutron detection efficiency.

Neutron guide: A detailed description of the initial instrument design, including the neutron guide system, has been published in [3]. In general, the highest neutron flux can be achieved using a double elliptic neutron guide geometry. In the case of POWTEX, the neutron guide system will be intersected by the pulse chopper (opening of 1x1 cm^2), such that it is a needles eye between two separate elliptic guides.

Next to the choice of the best geometry the super-mirror reflectivity is of crucial importance while optimizing the neutron beam properties. These are namely, a high and equally distributed flux and in contradiction to this, a homogeneous and gaussian-like divergency distribution at the sample position of 1x1 cm^2. The neutron guide geometry, as shown in FIG. 1 (left), has been chosen to have a maximal transported divergency (FWHM) of 0.5° for neutrons with a wavelength of λ = 1.0 Å. By this, the ratio of both elliptic half-axes is already fixed.

The super-mirror reflectivity can be characterized by its total reflection properties up to a critical momentum transfer perpendicular to the surface ($Q_c = 4\pi\lambda^{-1}\sin(\theta)$). This is usually expressed by the index m = $Q_c/Q_c(^{58}\mathrm{Ni})$ that is relative to ^{58}Ni. In FIG. 1 (left) this index is represented by the color and along the flight path x it changes symmetrically to the pulse chopper. The higher the index, the higher is the super-mirror's maximal angle of total reflection for a given wavelength. Due to the symmetric arrangement of the two ellipses (the second one is shrunk by a constant factor in all dimensions, leaving the optical properties unaltered), the focal points are coinciding in the center of the pulse chopper. The following considerations are characteristic for such coupled elliptic systems with an even number of guides and a needles eye (pulse chopper) in between. Assuming an

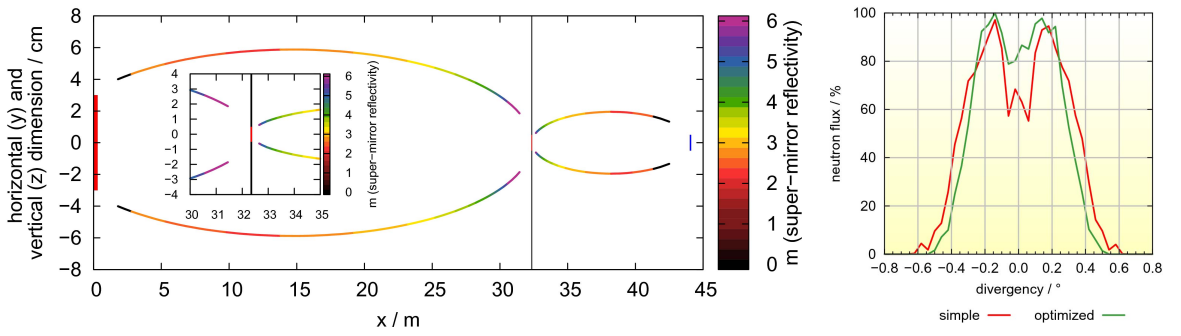

FIG. 1: Left: Elliptic neutron guide system with varying super-mirror reflectivity, i.e. color. Right: Two divergency profiles with similar neutron flux (1×1 cm² sample; λ = 1.0−2.4 Å). The optimized one is more homogeneous and has a smaller FWHM.

ideal point source, neutrons with a small divergency are reflected for the first time in the half-ellipse near the chopper. Hereby, owing to the elliptic shape, the divergency is increased. After passing the chopper, the neutron is scattered gain in the half-ellipse near the chopper, but this time the divergency is (almost) reduced to the initial value. Such neutrons reach the sample position with the maximal divergency as defined by the geometry of the ellipses for the lowest wavelength (1.0 Å). In accordance to this, neutrons starting with a high divergency are always reflected on the half-ellipse far away to the chopper. In order to avoid such neutrons with a high divergency the areas far away from the chopper are absorbers while neutrons with a small initial divergency are transported using high m-values near the chopper.

Owing to this, a minimum divergency can be achieved by applying the super-mirror coating only to both half-ellipses near the chopper. Of course, this leads to a dramatic loss in neutron flux. Therefore, and also due to the fact, that the FRM II is not a point source, one needs to apply further corrections, e.g. the choice of the other two focal points. While the second ellipse will be focused on the sample position, the focus of the first ellipse will lie behind the area with the highest neutron flux inside the reactor in order to transport neutrons coming from any position of the source. Furthermore, the super-mirror m-values have to be adjusted with regard to this. In order to simulate and optimize the neutron guide system, the open source software VITESS (Virtual Instrumentation Tool for Neutron Scattering at Pulsed and Continuous Sources) working with the Monte Carlo technique is used. FIG. 1 (right) compares two simulations with similar neutron flux (1×1 cm² sample; λ = 1.0−2.4 Å). The optimized profile is more homogeneous and has a smaller FWHM.

VITESS Instrument Simulations: In last year's report we presented a diffractogram simulation based on the analytical description of the instrument parameters of POWTEX. By this, we gained experience on simulating such diffractograms which will also help to do the data analysis of the experimental diffraction data once POWTEX is in operation. In early summer 2009 we started to focus our work on numerical simulations of such diffractograms. Of course, an excellent choice for this is the open source project VITESS that is already used for the simulation of the neutron guide system and that also has support for the simulation of a diffraction process. Thus, the final goal is to simulate the complete instrument. In contrast to conventional neutron diffractometers at research reactors being monochromatic instruments, POWTEX will be the first pulsed instrument located at a continuous source and used for diffraction experiments by using a wide wavelength spectrum combined with time-of-flight analysis and a huge detector coverage. For this reason, one of our contributions was to implemented the evaluation of the diffraction process as a function of the two parameters scattering angle and wavelength in [4] (module eval_elast2). The preliminary results can be seen in FIG. 2.

Funding: The RWTH Aachen and the Forschungszentrum Jülich submitted a proposal for a BMBF funding from 2010 to 2013 in order to build the POWTEX instrument, while our colleagues at the University of Göttingen proposed to build the sample environments for the geo-sciences.

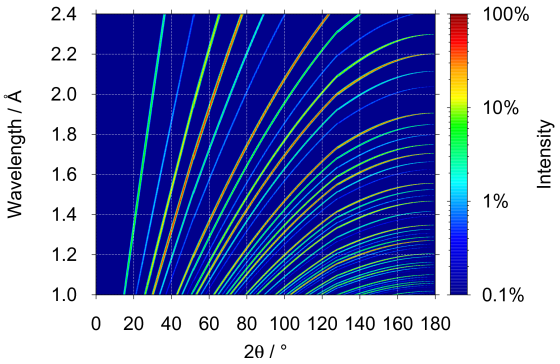

FIG. 2: Simulation of a POWTEX diffractogram using VITESS ($RhFe_3N$, perovskite-like, space-group $Pm\bar{3}m$).

[1] T. Feder *Phys. Today* **2009**, *October*, 21–23.

[2] M. L. Wald *The New York Times* **2009**, *November*, 22.

[3] H. Conrad, Th. Brückel, W. Schäfer, J. Voigt *J. Appl. Cryst.* **2008**, *41*, 836–845.

[4] VITESS 2.9, G. Zsigmond, K. Lieutenant, S. Manoshin, M. Fromme, P. Bentley, A. Houben, D. Champion, **2009**, *October*.

Stable operation of the backscattering spectrometer SPHERES

J. Wuttke[1], G. J. Schneider[1], A. Budwig[2], A. Ioffe[1], H. Kämmerling[2], V. Ossovyi[1], H. Schneider[1], S. Staringer[1], D. Richter[5]

[1] JCNS: Jülich Centre for Neutron Science
[2] ZAT: Central Technology Division
[5] IFF-5: Neutron Scattering

Our backscattering spectrometer SPHERES has been successfully operated throughout 2009. Depending on sample thickness, the signal-to-noise ratio reaches up to 1200:1. Fourteen external experiments were performed.

Instrument development: After the highly successful chopper refurbishment in the end of 2008, SPHERES ran very stable throughout 2009. Depending on sample geometry, the signal-to-noise ratio reaches up to 1200:1.

A further improvement is now in sight: in future, we intend to operate the instrument with an argon filling that will reduce background from and losses due to air scattering. In close cooperation with FRM II, a concept for filling, holding, and discharging the gas was worked out that meets the complex safety requirements. Installation of the pneumatic components has started.

Inside the spectrometer, horizontal position-sensitive detectors were installed in order to allow for real-time diffractogram monitoring. The driver software is currently under commissioning.

Guided by simulations, parts of the annular small-angle analyzers were eclipsed by Cd shields in order to exclude neutron paths that were too far out of backscattering. The improvement of the resolution function is quite spectacular (Fig. 1).

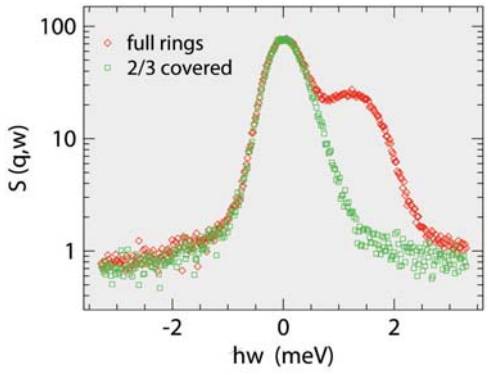

FIG. 1: Instrumental resolution at $2\theta = 27 \pm 3°$ with full annular analyzer (red), and after eclipsing 1/3 of the circumference (green). Excluding off-backscattering trajectories greatly improves the resolution at no cost in useful flux.

Software development: Commands needed for regular user operation can now be scripted. The script engine is integrated in a novel way with the graphical user interface so that the user is at any moment informed about the status of script execution.

New data reduction software was designed, specified, and implemented in prototype version [1]. In the future, the front-end shall be extended to provide similar ease of operation for other inelastic spectrometers.

For fitting relaxation in complex systems, a new algorithm was developed that calculates the Fourier transform of Kohlrausch's stretched exponential function with unprecedented speed and accuracy [2].

Nuclear magnetism: As in the last year, several experiments addressed nulcear spin excitations. The systematic investigation of Nd compounds was continued with the antiferromagnet $NdMnO_3$ [3] and the ferromagnet $NdAl_2$ [4]. In both cases, the linear relationship between hyperfine splitting and local electronic moment could be confirmed. The same relation holds in the small number of Co compounds investigated so far [5], with the notable exception (Fig. 2) of the antiferromagnet CoF_2 [6]. At our present understanding, the most likely cause is a significant unquenched orbital momentum in CoF_2.

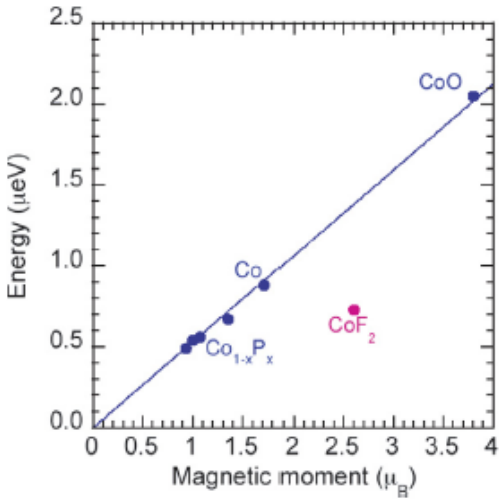

FIG. 2: Hyperfine splitting versus electronic moment of Co-based materials. CoO and CoF_2 measured at SPHERES [5, 6].

Molecular rotations: Again, SPHERES was used in several experiments to investigate the slow rotations of methyl groups.

A comprehensive study of the molecular crystal diaminodurene, involving structure determination, vibrational spectroscopy, and backscattering, was completed [7]. Methyl group rotation was originally measured on IN16 of the ILL. It then turned out that the larger energy range of SPHERES was needed to resolve a second tunneling line (Fig. 3). From the fits, rotational potentials could be determined. These potentials were then used as input to the analysis of time-of-flight spectra. As result, a consistent description of structure and dynamics was obtained, with packing effects and ring torsions having strong impact upon the mobility of methyl groups.

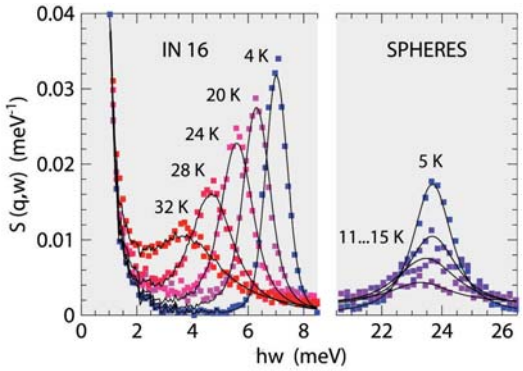

FIG. 3: Tunneling spectra of diaminodurene measured with the neutron backscattering spectrometers IN16 (left frame, energy range of ±10 μeV, and concentrating on tunneling peak 1) and SPHERES (right frame, energy range of ±31 μeV, and concentrating on low temperatures where tunneling peak 2 shows a rapid softening). Wavelength of 6.27 Å; averaged over all large-angle detectors (Q = 0.61.9 Å^{-1}). Solid lines are fits [7].

[1] J. Wuttke, SLAW: a neutron histogram to scattering law converter. `http://iffwww.iff.kfa-juelich.de/~wuttke/slaw/`.

[2] J. Wuttke, KWW: Kohlrausch-Williams-Watts function. `http://www.messen-und-deuten.de/kww/kww.html`; `http://arxiv.org/abs/0911.4796`.

[3] T. Chatterji, G. J. Schneider, L. van Eijck, B. Frick, D. Bhattacharya: Direct evidence for the Nd magnetic ordering in NdMnO3 from the hyperfine field splitting of Nd nuclear levels. J. Phys.: Condens. Matter 21, 126003 (2009).

[4] Tapan Chatterji, G. J. Schneider, and J. Persson: Low-energy nuclear spin excitations in NdAl2. Phys. Rev. B 79, 132408 (2009).

[5] T. Chatterji and G. J. Schneider: Low-energy nuclear spin excitations in CoO. Phys. Rev. B 79, 212409 (2009).

[6] T. Chatterji and G. J. Schneider: Anomalous hyperfine interaction in CoF2 investigated by high resolution neutron spectroscopy. J. Phys.: Condens. Matter 21, 436008 (2009).

[7] L. Sobczyk, M. Prager, W. Sawka-Dobrowolska, G. Bator, A. Pawlukojc, E. Grech, L. van Eijck, A. Ivanov, S. Rols, J. Wuttke, and T. Unruh: The structure of diaminodurene and the dynamics of the methyl groups. J. Chem. Phys. 130, 164519 (2009).

Progress on TOPAS

J. Voigt[1], K. Bussmann[2], P. Harbott[2], E. Babcock[1], H. Kämmerling[3], Th. Brückel[2]

[1] JCNS: Jülich Centre for Neutron Science
[2] IFF-4: Scattering Methods
[3] ZAT: Central Technology Division

TOPAS is the future thermal time-of-flight spectrometer at the research reactor FRM II. The scientific scope of the instrument includes the determination of coherent and localized excitations in novel materials. Equipped with a position sensitive detector system, it will allow the mapping of 4D dispersion relations over an energy range from 20 to 150 meV. The high neutron flux over the wide energy range with a modest divergence is realized by the combination of a focusing neutron guide system and a high resolution energy selection, consisting of a set of Fermi choppers. The application of polarization analysis will make TOPAS a unique instrument for the investigation of the dynamics in magnetic and hydrogen containing materials.

Inelastic neutron scattering has proven to be one of the most powerful techniques for the study of dynamics in novel materials. Our understanding of phonons, magnetic excitations, hydrogen bonding in materials, and soft-modes at phase transitions has come primarily from the results of inelastic neutron scattering studies. In recent years, this technique has been used to examine an ever-widening range of subjects and phenomena such as the dynamics of polymers, the nature of disordered and amorphous materials, phase transitions in geological materials and subtle electron-lattice interactions. By the use of thermal neutrons, a large range in energy and momentum transfer can be probed. In the direct time-of-flight geometry, the measurement of the momentum transfer is decoupled from the measurement of the energy transfer. Time-of-flight spectroscopy from single crystals explores simultaneously the $(\vec{Q}, \omega)$ space and maps a variety of excitations by covering a large solid angle with detectors. Accordingly, TOPAS can be used for a wide range of applications, particularly for novel materials:

The physics of correlated electrons is one of the most active and challenging fields today in hard condensed matter. High temperature superconductivity, colossal magneto resistance and many more phenomena have attracted interest because of their high relevance to both, the basic understanding of condensed matter and the potential for new technical applications. Electronic, spin, lattice and orbital degrees of freedom determine the ground state and dynamics by a subtle interplay. The dynamics of these degrees of freedom can be studied by inelastic neutron scattering, some of them exclusively. Frustration in such systems leads to a loss of long range order, but the dynamic correlations on a mesoscopic length scale, that will be visualized by TOPAS, reflect the atomic interactions. For the study of magnetic systems, the full information about the vector properties can be extracted by polarization analysis.

The interaction potentials within a single molecule and between molecules determine the molecular and crystal structure and therewith for example the structure-activity relation of biological systems. The experimental vibrational phonon density of states is the benchmark to test new concepts in molecular dynamics and the corresponding software systems. A special case remains water with its 12 known phases. Polarization analysis will allow to suppress the incoherent scattering to study the dynamics also in non-deuterated samples.

It is well known that the properties of a solid can change dramatically with the reduction of the size of crystallites. Since band formation may be suppressed a conducting microcrystal may transform into an isolating nanocrystal etc. The change of macroscopic properties is based on changes on the atomic level which can be characterized by the vibrational density of phonon states or a broadening of excitations due to the finite size of nanoparticles.

A sufficiently fast proton dynamic is needed to use metal hydrides as hydrogen storage systems or batteries. The extreme sensitivity of neutrons for hydrogen makes inelastic incoherent neutron scattering an exceptionally suited tool to study the hydrogen potentials via the microscopic jump diffusion step.

During this year, we had to realize that the detector concept of TOPAS has most likely to be fully revisited. The suppliers for the ^{3}He detector have redrawn their offers due to a world wide shortage of ^{3}He. While the design of the detector banks was near completion, we are now faced with the situation, that the final neutron detection concept is unclear. Possible solutions to be investigated include wave length shifting fibers, the so called "Blade" concept and the use of BF_3 detector tubes. At the moment, we keep the design of the secondary spectrometer vessel as flexibel as possible to account for different detector designs

in the future. As a temporary solution we plan to revive the detection system of SV29.

While the neutron guide design has reached a final stage, the installation of the instrument is linked to the change of the beamport SR5, which is not yet scheduled. Therefore the development of the secondary spectrometer has been focused during this year. Two key requirements have to be fulfilled by the design: (i) The vessel has to be vacuum tight to hold the cryogenic vacuum around the sample position. (ii) The materials have to be chosen not to disturb the neutron polarization. Consequently all parts close to the neutron path will be of non-magnetic materials. The sample space inside the vessel can be separated from the rest of the volume. Accordingly only a small volume has to be vented for the change of the sample environment, while the major fraction of the flight path is kept under vacuum. A novel mechanic has been designed to close the large neutron window and will be tested in the near future. The sample environment will be accommodated in a rotating stage that allows the sample to be rotated around a vertical rotation axis. This motion combined with a position sensitive detector is necessary to explore fully the dispersion landscape of single crystalline materials

The final design of the neutron guide freezes also the parameters for the Fermi chopper windows. The sample to detector distance determines the maximum repetition rate. For a distance of 2.5 m one may run repetition rates up to 900 Hz without frame overlap, i.e. one can record the complete spectrum before the fastest neutrons from the next pulse arrive. Since we want to use a Fermi chopper with straight channels, the repetition rate is twice the frequency of the chopper. The revolution speed of up to 36000 revolutions per minute is at the edge of the existing technology for the window size given by the neutron guide. In particular the use of single crystalline chopper channels requires a new system to fix the Fermi package, when it spins at high speed. The main reason to opt for single crystal Si chopper blades is the operation of the instrument with polarized neutrons. The eddy currents induced in a metallic material such as Al can depolarize the neutron beam. A semi-conducting or insulating material avoids these complications. Furthermore the transmitted intensity can be slightly higher due to the reduced scattering of a good single crystal. The chopper system is completed by the higher order removal disc chopper. The positioning and the opening times of this chopper have been investigated numerically. It has become clear, that the simple solution as indicated in Fig. 1 is not suitable for the complete suppression of higher order neutrons. Instead two alternatives have been identified: (i) the single chopper is replaced by two counter rotating choppers at a position close to FC2. This enables a short enough opening time to suppress the unwanted neutrons. (ii) A system of two disc choppers, which are placed at the right distance to avoid the same higher harmonics, which pass through the Fermi chopper system. The disc choppers have 4 windows, hence the ratio

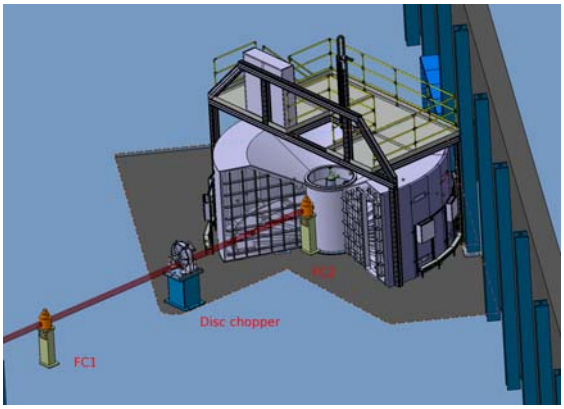

FIG. 1: 3d model of the primary and secondary spectrometer. The neutron energy is selected by the phase between the Fermichoppers FC1 and FC2. The disc chopper suppresses neutron velocities that could also pass through the Fermi choppers

between Fermi chopper frequency and disc chopper frequency is 1/2.

Finally the polarization system of the new reflectometer MARIA has become operational. Since TOPAS will use a down-scaled version of the continuously pumped SEOP device this development is the first step towards the polarization for TOPAS. The requirements of the polarization are a permanent guide during the design of the instrument. For any component behind the polarizing unit, the feedback onto the neutron polarization is considered. Examples are the magnetic bearing of the Fermi choppers and materials used for the vacuum vessel of the secondary spectrometer.

All components of TOPAS are now in the stage of technical realisation. During this year the first hardware will be installed in Jülich. Comprehensive tests will be performed before the components are transferred to their final site in Munich.

On-line polarization of ^{3}He using SEOP at the JCNS

E. Babcock[1], A. Ioffe[1], S. Mattauch[1], A. Radulescu[1], V. Pipich[1], S. Staringer[1], M. Gödel[1], H. Kusche[1], V. Ossovij[1], A. Nebel[1], G. D'Orsaneo[2], P. Pistal[2], A. Schwaitzer[2], Th. Brückel[3]

[1] JCNS: Jülich Centre for Neutron Science
[2] ZAT: Central Technology Division
[3] IFF-4: Scattering Methods

Only ten years ago, world leading polarized neutron scattering experiments using neutron spin filters (NSF) were being conducted using starting ^{3}He polarizations of 55%. This polarization typically decayed with T_1 time constants of about 100 hours. Immense progress in the last 10 years has resulted in ^{3}He polarizations of up to 80% being reported in NSF's by the world's leading labs. We have constructed in-situ ^{3}He polarizer which obtained a saturation polarization of 80% and maintained it constant with high stability via the on-beam optical pumping. This is part of the ongoing work to provide polarized ^{3}He neutron polarization and analysis techniques to the JCNS. This particular polarizer will be installed on the new magnetic reflectometer, MARIA, when complete. Future work will extend the methods to use on SANS (KWS) where work has be done to explore appropriate ^{3}He cell materials, and eventually a large scale device will be developed for the TOPAS spectrometer which is in the design phase.

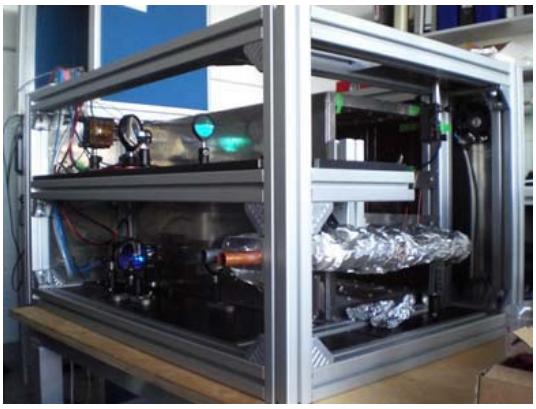

FIG. 1: SEOP based in-situ polarizer designed for MARIA.

The in-situ ^{3}He polarizer, based on the spin-exchange optical pumping method (SEOP), reached this high level of ^{3}He polarization in a recent test performed on the TREFF reflectometer. The major components are similar to one utilized in prior work with an in-situ SEOP polarizer developed during the sixth European framework program, or FP6 [1, 2]. The system shown in FIG.1 has been redesigned and re-optimized for use as a wide angle analyzer for a new magnetic reflectometer MARIA at the JCNS. Eventually the system is designed to accept a cell of up to 15 cm in diameter. It incorporates two frequency narrowed diode array bar lasers [3], a "SEOP magic box" style magnetic cavity [1], and an integrated AFP ^{3}He flipper [4] driven by an amplified RF pulse provided by a high speed DAQ card on a PC.

For this early test we have polarized a ^{3}He cell, called J1, which was prepared in collaboration with the ISIS ^{3}He team. This cell was previously tested and known to achieve a high level of ^{3}He polarization when polarized in the laboratory [5]. The cell has an inside diameter of 5.6 cm and contains 5.2 bar cm of ^{3}He. We monitored the ^{3}He polarization over time with an NMR free induction decay system and unpolarized neutron transmission. The transmission of unpolarized neutrons then gives us the absolute ^{3}He polarization, knowing the ^{3}He pressure length product of the cell and the neutron wavelength.

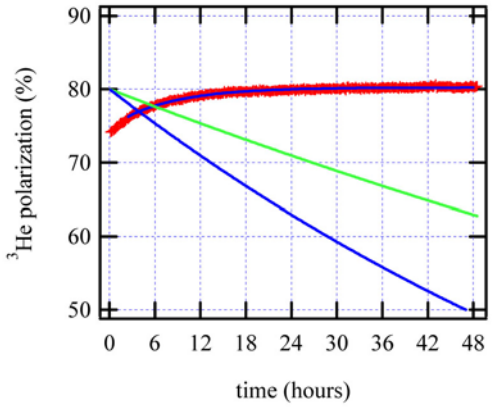

FIG. 2: Polarization vs. time of cell J1 polarized in-situ on TREFF. The green/blue line, for comparison, indicates the performance if the same cell polarized to the same level were allowed to undergo normal T_1 decay of the polarization with a 200/100 hour time constant.

As can be seen in FIG. 2, after final optimization, the ^{3}He polarization of cell J1 climbed to a high level of 80%. Very good stability was also observed over the course of the two day measurement with the polarization exceeding 75% for the whole period. During this time the system was allowed to run without any

adjustments to the lasers or optical pumping parameters. As a reference, the green and blue lines are added to demonstrate the polarization over time if the same ^{3}He cell were polarized offline and allowed to undergo T_1 decay of polarization, assuming a 200 hour and 100 hour on-instrument T_1 respectively.

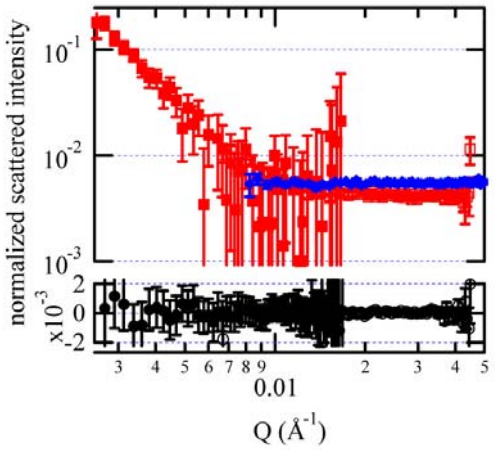

FIG. 3: SANS data from GE180 glass (red squares) and polished single crystal silicon (black circles) with 1 mm of D2O (blue diamonds) as a reference. The polished silicon showed statistically 0 scattering while GE180 was a strong scatterer for Q > 0.01 Å^{-1}.

A similar in-situ polarizer could also be utilized for polarized SANS measurements. Therefore we have conducted testing of possible cell window materials, GE180 glass and polished silicon crystal, on the SANS diffractometer KWS2. GE180 glass is the typical material used to construct ^{3}He SEOP cells and single crystal silicon has been used as a material for ^{3}He cells where the gas is polarized in a different volume. The materials were measured in the vacuum chamber on KWS2 so that there was no background contribution from other windows or air. FIG. 3 shows strong small angle scattering from the GE180 cell was found for Q<0.01 Å^{-1}, however the polished silicon single crystal showed no statistically significant small angle scattering.

Consequently we are developing two chamber cells that could be used for the SANS applications. A large chamber made of GE180 will be optimized for low resolution, i.e. Q>0.01 Å^{-1}, which typically uses

shorter sample-detector distances and neutron wavelengths <10 Å. To this large all glass chamber a small silicon crystal windowed chamber, optimized for high resolution which requires the use of long sample-detector distance and neutron wavelengths >10 Å, will be attached via a thin transport tube for the polarized ^{3}He gas. In this way both cells can be polarized simultaneously by optically pumping the GE180 volume thus allowing one to easily choose between optimized ^{3}He analyzing efficiencies for either high resolution or low resolution by a simple translation of the polarizer (and cell). A picture of the constructed cell ready for filling with alkali-metal and ^{3}He is shown in FIG. 4.

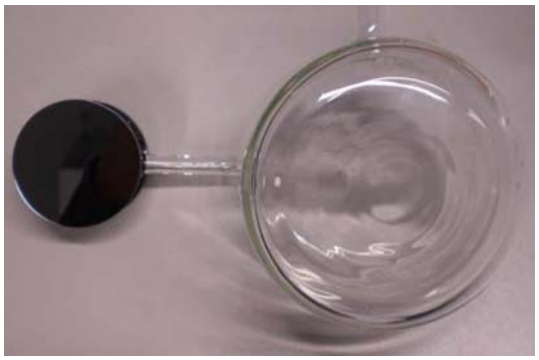

FIG. 4: Photo of double cell for KWS1. The silicon windowed chamber Ø=5cm (left) is for high resolution measurements while the all glass chamber Ø=9cm (right) is for optical pumping and low resolution measurements. Two copies of this cell are ready to be prepared and tested.

Continuing developments will focus on refinement of the in-situ polarizer device and components, polarizing larger diameter cells, interfacing the system with the MARIA instrumentation, and obtaining practical experience to best apply the system and techniques for routine daily use. We expect the system to be able to provide polarization analysis concurrent with the commissioning of MARIA in 2010. Experience gained for this system will then be applied to other applications of polarized ^{3}He in either neutron polarization or polarization analysis at the JCNS. Further work will also be conducted on cell manufacturing techniques and testing.

[1] E. Babcock et al. PRA **80**, p. 033414, (2009)

[2] S. Boag et al. Physica B **404**, p. 2659, (2009)

[3] E. Babcock et. al. App. Optics **44**, p. 3098 (2005)

[4] E. Babcock et al. Physica B **397**, p. 172, (2007)

[5] S. R. Parnell et al. NIM-A **598**, p. 744, (2009)

IN12: the cold neutron three-axis spectrometer at the ILL

K. Schmalzl[1], W. Schmidt[1], S. Raymond[2], P. Harbott[3], H. Feilbach[4], K. Bussmann[3], T. Brückel[1,3]

[1] JCNS at ILL, 38042 Grenoble, France
[2] CEA-Grenoble, INAC SPSMS MDN, 38054 Grenoble, France
[3] IFF-4: Scattering Methods
[4] IFF Technical Services and Administration

The cold neutron three-axis spectrometer IN12 is operated by JCNS in collaboration with the CEA Grenoble as a CRG-B instrument at the Institut Laue-Langevin (ILL) in Grenoble, France. IN12 is dedicated for elastic and inelastic studies of low energy structural and magnetic excitations. The upgrade with a multi analyzer - multi detector option is still active, likewise are studies concerning the move of IN12 and upgrade of the primary spectrometer, the design of the guide layout and the monochromator shielding. The relocation to a new guide with end position will be a unique chance for improvements and ensure also in future a powerful instrument.

As a CRG-B instrument the scheduled beam time is shared amongst the collaborating partners: 30% of the beam time is made available for the ILL, whereas the remaining time is assigned to CEA and FZ Jülich with 35% share each. Two thirds of the available time for German users is distributed through the JCNS proposal process by an international review committee, while one third is reserved for in-house research.

In 2009 IN12 showed very reliable user operation. Out of 197 available reactor days only 3 days were lost (1.5%), due to instrument, sample environment or software failure. 14 test days (7.1%) were given. Besides instrument alignment and maintenance as well as set-up for complicated sample environment the test days were also used for the new multi-analyzer-multi-detector option UFO (Universal Focusing Option).

IN12 holds a wide variety of different scientific questions. Users have access to the whole ILL sample environment suite. Some recent experiments with JCNS contribution on IN12 included, e.g., the study of frustrated quasi one dimensional spin chain compounds or multiferroic systems, where a strong magnetoelectric effect occurs. The switching of the magnetism by an external electric field suggests its high potential for future application. With spherical polarization analysis and the simultaneous application of an electric field details of chiral hysteresis curves could be observed.

Besides bulk systems also thin films and multilayers are investigated. One interest lies in, e.g., the difference in structure or in phase transition with change of external parameters compared to bulk systems. Experiments were done in multiferroic thin films or in thin FePtRh films, which are candidates for soft magnetic underlayers in perpendicular recording media, where the (anti)-ferromagnetic phase transition in dependence of Rh-concentration has been studied.

But also the measurement of the magnetic form factor in magnetic nanoparticles dispersed in toluene by small angle scattering with polarization analysis has been successfully run. For this, a vacuum box together with costum-made Helmholtz-coils [1] have been installed for the first time. In future this set-up will be available as standard sample environment for all users.

Presently IN12 is being upgraded with a multi analyzer - multi detector option. IN12-UFO (Universal Focusing Option) is a new secondary spectrometer interchangeable with the present set-up. 15 analyzers, which can be rotated and positioned individually, and a two-dimensional position sensitive detector will allow to program simultaneous scans in Q-ω-space [2, 3]. The user will be able to define scans, e.g., with a constant energy transfer or scans that map a path along a certain Q-direction. The analyzers will be positioned so as to avoid gaps or overlaps as seen from the sample (optimum coverage) while all reflected beams meet at one single focus point on their way to the detector. The mechanics of the analyzer array can be seen in Fig. 1.

FIG. 1: Mechanics and cabling of the UFO analyzer. On the top the mountings for the analyzer crystals can be seen.

The testing and programming of the control electronics is currently done by the ZEL institute.

Another major project concerns the move of the IN12 spectrometer to a new position. This project is handled in collaboration with engineers from the Projects and Techniques Division (DPT) at ILL as well as from IFF, Jülich. In the framework of the ILL Millennium Programme IN12 will be relocated within the guide hall ILL7 and will get its own new guide with an end position. This allows further improvements and new key components will be implemented:

- A new guide and the upgrade from an m=1 (present) to m=2 coating,
- a focusing end part of the guide (8 m, virtual source concept) together with a double focusing monochromator.

This new concept will provide IN12 with an extended wavelength range of 1.5 - 6.3 Å (now 2.4 - 6 Å) and promises an increase of the overall count rate of about an order of magnitude.

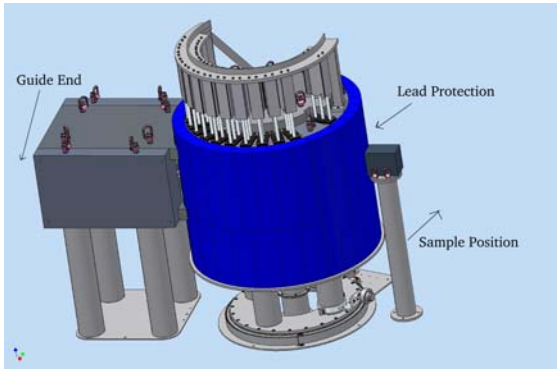

FIG. 2: Schematic drawing of the new monochromator shielding. Between the end of guide and the monochromator an optical bench with diaphragms and possible collimation will be installed (lead channel on the left).

Additional components will further improve the performance and efficiency of the spectrometer:

- A velocity selector will eliminate higher order contributions and guarantee a low background,
- a new monochromator shielding adapted to the requirements of the end position, the higher flux, and the larger energy range of the extended wavelength band, see Fig. 2.
- Foreseen is also a guide changer and transmission polarizer cavities for an efficient and easy-to-use polarization of the incident beam,
- a guide changer for the focusing nose at the guide end to permit also the use of a collimated option (high and tunable Q-resolution) instead of the focusing (high divergence) option.

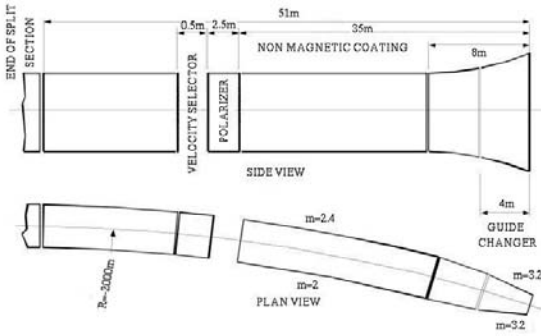

FIG. 3: Schematic drawing of the new guide for IN12 in side and plan view. (Orig. drawing: L. Perrott).

- Optionally a perfectly bent silicon monochromator to focus the beam on small sample volumes is planned.

The new position of IN12 will be 7 m further downstream compared to the present one. About 104 m of new guide, partly shared with other instruments, will have to be installed for IN12.

Due to geometrical constraints the new guide will have a similar S-shaped curvature like the present one. The new guide will have a radius of 4 km (present 2.7 km) for about 22 m, followed by a radius of -2.0 km for 82 m (present -2.7 km for 75 m). The new dimensions are 45x105 mm (now 30x120 mm).

The overall coating of the guide will be m=2 (present m=1 for the last 80 m) fitting the already earlier renewed in-pile part further upstream.

For a better performance at lower wavelengths the outer part of the curved guide will get a higher coating of m=2.4. For a schematic drawing of the guide see also Fig. 3. The focusing end part will be horizontally focused down to 20 mm and will have an increased coating up to m=3.2. Simultaneously it will be vertically widened up to 140 mm to better match the mosaicity of the monochromator crystals leading to an intensity gain of 15-20% at the sample position.

The shutdown of the present spectrometer is planned for mid October 2010. The mounting of the new components at the new guide end position is foreseen for summer 2011.

[1] W. Schmidt et al., Physica B **356**, 192 (2005)

[2] W. Schmidt et al., Physica B **350**, e849 (2004)

[3] W. Schmidt et al., Physica B **385-386**, 1073 (2006)

NSE at SNS: completion

M. Ohl[1], M. Monkenbusch[1], T. Kozielewski[1], N. Arend[1], M. Sharp[4], G. Vehres[1], D. Richter[1], M. Butzek[2], C. Thiemann[2], R. Achten[2], B. Laatsch[2], H. Soltner[2], U. Pabst[2], B. Lindenau[2], M. Leyendecker[2], H. Stelzer[2], H. Kleines[3], P. Kämmerling[3], M. Wagener[3], M. Drochner[3], R. Möller[3], S. Schmidt[5]

[1] IFF-5: Neutron Scattering
[2] ZAT: Central Technology Division
[3] ZEL: Central Institute for Electronics
[4] European Spallation Source, Lund, Sweden
[5] Forschungszentrum Jülich

In Spring 2009 the instrument readiness took place and after successfully fulfilling all requirements first neutron had been applied to the NSE. The flux resulting from this first measurement were comparable to the predicted flux from MC simulation. In fall 2009 the first echo has been measured at the NSE spectrometer especially with the superconducting coils showing that also the magnetic part of the spectrometer principally works as it should. With these results we were able to successfully perform a first measurement with a test sample polystyrene in d-Toluol including all correction measurement with an elastic scatter in a Fouriertime range between 100ps$<\tau<$10ns and around Q=0.1nm^{-1}. Commissioning is still going on and especially data treatment has to take place for the first official friendly user experiments in the first half of this year.

Neutron spin-echo spectroscopy (NSE) is the only inelastic neutron scattering technique that significantly overcomes the resolution limit of $\sim 1\mu$eV of the crystal (backscattering) or conventional time-of flight spectrometers. However, NSE is a Fourier method and yields S(Q,t) instead of S(Q,ω). An energy transfer resolution of 0.7μeV corresponds to a Fourier time of 1ns, the new NSE spectrometer is designed to reach times of about 1μs i.e. corresponding to a resolution of 0.7neV. This is achieved by a combined utilization of high field integral, J ($>$1Tm) in the precession coils and long neutron wavelength λ; t/ns$\cong$0.2$\times$J/(Tm)$\times(\lambda$/Å$)^3$. On the other hand use of short wavelengths in combination with short precession coils times down to 1ps will result in a dynamic range of 1:10^6, see Figure 1.

NSE spectroscopy is especially well suited to identify and measure motions respectively mobility in the nanoscopic domain. That extends from polymer dynamics in the scale between single segments to macromolecules in solution or melts to the internal domain motions of proteins. Slow diffusion processes of small and mesoscopic objects can be investigated.

The layout of the spectrometer comprises a system of 4 choppers and a polarizing solid state bender to prepare the neutron beam and select the proper wavelength frame. The beam then enters a magnetically shielded enclosure that hosts the proper spectrometer consisting mainly of two superconducting precession coils and analyzer and a detector. The whole secondary spectrometer can be positioned at different moderator-detector distances between 18m and 27m. The former supplying the largest wavelength frame whereas the latter has the larges scattering angle range (up to 60^0). Figure 2 shows the layout with the spectrometer at the 21m position.

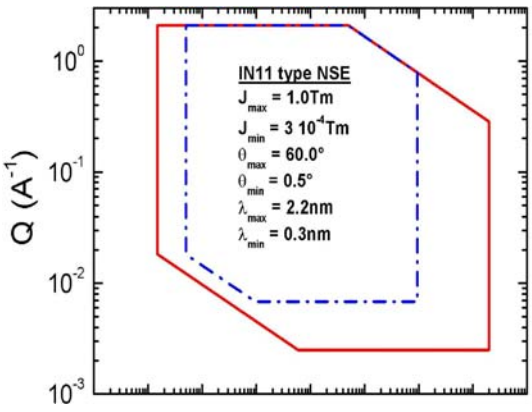

FIG. 1: Expected coverage of (Q,t) range (just for 60° scattering angle).

FIG. 2: shows the secondary spectrometer in its operational stage at the small scattering angle position.

The first big milestone had been achieved in spring 2009 with the successful completion of the instrument readiness review. Here all safety requirements and further aspects of possible general user opera-

tion had been checked. The list of revisions was minor and could be done within 2 weeks. Subsequently first neutrons were applied to the instrument in April 2009 (see Fig. 3 and 4).

FIG. 3: The instrument team receiving first neutrons after successfully completing the instrument readiness review (just 3years 1month and 24days after signing the Memorandum of Understanding between ORNL and FZJ which gave the starting point for the investments, manufacturing, etc.).

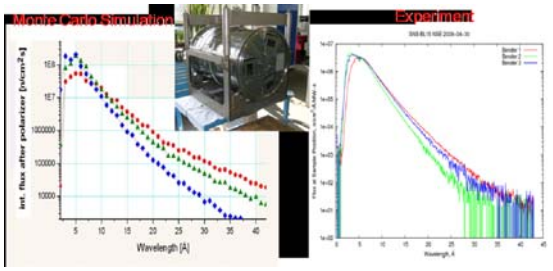

FIG. 4: Shows the Monte Carlo simulations (left) and the experimental results (right).

With the successful fixation of the moderator for our beamline we were able to perform first test measurements (see right plot on Fig. 4) for flux evaluation and especially to compare to the first Monte Carlo simulation (see left plot of Fig. 4). First the results indicate that all three polarizer working in the wavelength band between 0.2nm$<\lambda<$0.5nm, 0.5nm$<\lambda<$1.0nm and 1.0nm$<\lambda<\ldots$ principally cover the own wavelength band correct. Second the measured flux at lower wavelength is up to 8% higher than expected and third the flux at higher wavelengths is up to 18% lower than expected.

After the flux had been measured a couple of additional installation tasks like the superconducting coils had to take place before one could move over to the magnetic measurements of the instrument especially the echo.

So the remaining components like the superconducting coils, correction elements, shifter etc. had been installed. Additional adjustments of the coils took place, too. The instrument setup had been entered in the software with most of the components being controllable through the instrument control software now.

So after careful adjustment of the principal components and checking of the polarization of the beamline itself the first echo had been measured (see Fig.5) and principal functionality had been shown.

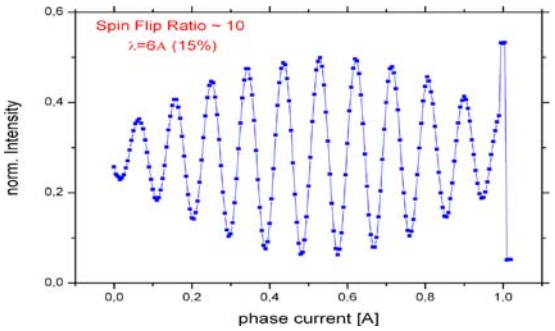

FIG. 5: First echo measured in Fall 2009 with a spin flip ratio of 10 and $\Delta\lambda v\lambda$=15% at λ=6A.

In one of the subsequent measurements before Christmas were able to perform measurements at polystyrene in d-toluol between 100ps and 10ns and around 0.1nm^{-1}. The echos itself are very muzch comparable to the echo above but the time of flight evaluation is still pending and shall be done beginning of 2010 to see if the instrument behaves similar to other instruments worldwide. In one next step the reliability of several components has to be improved, instrument control software has to be documented and evaluation software has to be written to perform first friendly user experiments in spring 2010.

To summarize, with the year 2009 the instrument has been installed and is completed so far. The first experiment had been done and shows principal operation at the instrument is possible. The near future will be covered by further long term testing of the hardware, completing of the software to control and evaluate the data and performing first friendly user experiments in spring 2010. With the completion of this instrument it has been build in time (just 3y7m9d after signing the Memorandum of Understanding between ORNL and FZJ) and in budget and now we will show that the instrument was also built in its specification culminating in an spin echo at about τ=1μs.

We thank SNS for the fruitful cooperation and especially again the central departments of the FZJ for their outstanding performance during the design and erection of this instrument despite all additional complications to build such and instrument on another continent.

In 2009, scientists of the IFF have published numerous scientific articles, hold lectures and educated young researches. Please find details on the following pages.

Appendix

Part 1: publications and activities

Part 2: people

Publications in refereed journals

Akola, J.; Jones, R. O.
Experimentally constrained density-functional calculations of the amorphous structure of the prototypical phase-change material $Ge_2Sb_2Te_5$
Physical Review B, 80 (2009) 2, 020201

Akola, J.; Jones, R. O.
Structure of amorphous $Ge_8Sb_2Te_{11}$: GeTe-Sb_2Te_3 alloys and optical storage
Physical Review B, 79 (2009) 13, 134118-1-8

Akola, J.; Jones, R. O.
Structure of liquid phase change material AgInSbTe from density functional/molecular dynamics simulations
Applied Physics Letters, 94 (2009) 251905-1-3

Aliouane, N.; Schmalzl, K.; Senff, D.; Maljuk, A.; Prokes, K.; Braden, M.; Argyriou, D. N.
Flop of electric polarization driven by the flop of the Mn spin cycloid in multiferroic $TbMnO_3$
Physical Review Letters, 102 (2009), 207205 1 – 4

Appavou, M. S.; Gibrat, G.; Bellissent-Funel, M. C.
Temperature dependence on structure and dynamics of Bovine Pancreatic Trypsin Inhibitor (BPTI) – A neutron scattering study
Biochimica et Biophysica Acta, 1794 (2009) 10, 1398 – 1406

Arndt, J.; Stockert, O.; Borth, R.; Faulhaber, E.; Schmalzl, K.; Schneidewind, A.; Jeevan, H. S.; Geibel, C.; Loewenhaupt, M.; Steglich, F.
Do antiferromagnetism and superconductivity coexist in 2% and 10% Ge doped $CeCu_2Si_2$?
Journal of Physics: Conference Series, 150 (2009), 042008: 1 – 4

Atodiresei, N.; Caciuc, V.; Lazic, P.; Blügel, S.
Chemical versus van der Waals Interaction: The Role of the Heteroatom in the Flat Absorption of Aromatic Molecules C_6H_6, C_5NH_5, and $C_4N_2H_4$ on the Cu(110) Surface
Physical Review Letters, 102 (2009) 13, 136809

Auth, T.; Gompper, G.
Budding and vesiculation induced by conical membrane inclusions
Physical Review E, 80 (2009) 3, 031901-1 - 031901-10

Auth, T.; Gov, N. S.
Diffusion in a fluid membrane with a flexible cortical cytoskeleton
Biophysical Journal, 96 (2009) 3, 818 – 830

Balanetskyy, S.; Kowalski, W.; Grushko, B.
Liquidus, solidus and reaction scheme of the Al-rich part of AlCr-Mn
Journal of Alloys and Compounds, 474 (2009) 1/2, 147 - 151

Banachowicz, E.; Kozak, M.; Patkowski, A.; Meier, G.; Kohlbrecher, J.
High-pressure small-angle neutron scattering studies of glucose isomerase conformation in solution
Journal of Applied Crystallography, 42 (2009), 461 – 468

Bannykh, A. A.; Pfeiffer, J.; Solyarov, V. S.; Batov, I. E.; Ryazanov, V. V.; Weides, M.
Josephson tunnel junctions with strong ferromagnetic interlayer
Physical Review B, 79 (2009), 054501

Bar-Sadan, M.; Heidelmann, M.; Houben, L.; Tenne, R.
Inorganic WS_2 nanotubes revealed atom by atom using ultra-high-resolution transmission electron microscopy
Applied Physics A, 96 (2009), 343 – 348

Baumgaertner, A.
Fast-ion transport in peptide nanochannels
Materials Science and Engineering B, 165 (2009) 3, 261 – 265

Belushkin, M.; Gompper, G.
Twist grain boundaries in cubic surfactant phases
Journal of Chemical Physics, 130 (2009), 134712

Bentmann, H.; Forster, F.; Bihlmayer, G.; Chulkov, E. V.; Moreschini, L.; Grioni, M.; Reinert, F.
Origin and manipulation of the Rashba splitting in surface alloys
Europhysics Letters, 87 (2009) 37003,

Biehl, R.; Richter, D.
Protein in action gefilmt
Physik in unserer Zeit, 40 (2009), 9 – 10

Bobisch, C. A.; Bannani, A.; Koroteev, Y. M.; Bihlmayer, G.; Chulkov, E. V.; Möller, R.
Conservation of the lateral electron momentum at a metal semiconductor interface studied by ballistic electron emission microscopy
Physical Review Letters, 102 (2009) 13, 136807

Borghols, W. J. H.; Wagemaker, M.; Lafont, U.; Kelder, E. M.; Mulder, F. M.
Size Effects in the $Li_{4+x}Ti_5O_{12}$ Spinel
Journal of the American Chemical Society, 17786 (2009) 131, 17786 – 17792

Bosenberg, U.; Vainio, U.; Pranzas, P. K.; von Colbe, J. M. B.; Goerigk, G.; Welter, E.; Dornheim, M.; Schreyer, A.; Bormann, R.
On the chemical state and distribution of Zr- and V-based additives in reactive hydride composites
Nanotechnology, 20 (2009) 20, 204003

Botar, B.; Ellern, A.; Hermann, R.; Kögerler, P.
Electronic control of spin coupling in Keplerate-type polyoxomolybdates
Angewandte Chemie-International Edition, 48 (2009) 48, 9080 – 9083

Botar, B.; Ellern, A.; Hermann, R.; Kögerler, P.
Removing compositional boundaries in mixed-linker Keplerate clusters
European Journal of Inorganic Chemistry, 7 (2009) 34, 5071 – 5074

Botar, B.; Ellern, A.; Kögerler, P.
Acetate-controlled demetalion in multiiron polyoxometalates: A triiron cluster trapped between beta- and gamma-Keggin isomers
Dalton Transactions, 7 (2009), 5606 – 5608

Brener, E. A.; Boussinot, G.; Hüter, C.; Fleck, M.; Pilipenko, D.; Spatschek, R.; Temkin, D. E.
Pattern formation during diffusional transformations in the presence of triple junctions and elastic effects
Journal of Physics: Condensed Matter, 21 (2009), 464106

Brener, E. A.; Marchenko, V. I.
Nonlinear Green's Functions in Smectics
JETP Letters, 90 (2009) 2, 143 – 145

Brener, E. A.; Marchenko, V. I.; Pilipenko, D. A.
Nonlinear Two-Dimensional Green's Function in Smectics
JETP Letters, 90 (2009) 10, 688 – 689

Brodeck, M.; Alvarez, F.; Arbe, A.; Juranyi, F.; Unruh, T.; Holderer, O.; Colmenero, J.; Richter, D.
Study of the dynamics of poly(ethylene oxide) by combining molecular dynamics simulations and neutron scattering experiments
Journal of Chemical Physics, 130 (2009), 094908

Brommer, P.; de Boissieu, M.; Euchner, H.; Francoual, S.; Gähler, F.; Johnson, M.; Parlinski, K.; Schmalzl, K.
Vibrational properties of $MgZn_2$
Zeitschrift für Kristallographie, 224 (2009), 97 – 100

Bruchhaus, R.; Honal, M.; Symanczyk, R.; Kund, M.
Selection of optimized materials for CBRAM based on HT-XRD and electrical test results
Journal of the Electrochemical Society, 156 (2009) 9, H729 – H 733

Buchmeier, M.; Schreiber, R.; Bürgler, D. E.; Schneider, C. M.
Thickness dependence of linear and quadratic magneto-optical Kerr effects in ultrathin Fe(001) films
Physical Review B, 79 (2009) 6, 064402

Carbone, G.; Lorenz, B.; Persson, B. N. J.
Contact mechanics and rubber friction for randomly rough surfaces with anisotropic statistical properties
European Physical Journal E, 29 (2009) 3, 275 – 284

Chang, L. J.; Su, Y.; Schweika, W.; Brückel, T.; Chen, Y. Y.; Jang, D. S.; Liu, R. S.
Neutron polarization analysis on the multiferroic $TbMn_2O_5$
Physica B: Condensed Matter, 404 (2009) 17, 2517 – 2519

Chatterjee, S.; Schütz, G. M.
Diffusion of hydrocarbon mixture in one-dimensional zeolite channel: an exclusion model approach
Microporous and Mesoporous Materials, 125 (2009) 1/2, 143 – 148

Chatterji, T.; Freeman, P. G.; Jimenez-Ruiz, M.; Mittal, R.; Chaplot, S. L.
Pressure- and temperature-induced M3 phonon softening in ReO_3
Physical Review B, 79 (2009) 18, 184302

Chatterji, T.; Hansen, T. C.; Brunelli, M.; Henry, P. F.
Negative thermal expansion of ReO_3 in the extended temperature range
Applied Physics Letters, 94 (2009), 241902

Chatterji, T.; McIntyre, G. J.; Lindgard, P. A.
Antiferromagnetic phase transition and spin correlations in NiO
Physical Review B, 79 (2009) 17, 172403

Chatterji, T.; Ouladdiaf, B.; Bhattacharya, D.
Neutron diffraction investigation of the magnetic structure and magnetoelastic effects $NdMnO_3$
Journal of Physics: Condensed Matter, 21 (2009), 306001

Chatterji, T.; Schneider, G. J.
Anomalous hyperfine interaction in CoF_2 investigated by high resolution neutron spectroscopy
Journal of Physics: Condensed Matter, 21 (2009) 43, 436008: 1 – 5

Chatterji, T.; Schneider, G. J.
Low-energy nuclear spin excitations in CoO
Physical Review B, 79 (2009), 212409: 1 – 3

Chatterji, T.; Schneider, G. J.; Perßon, J.
Low-energy nuclear spin excitations in $NdAl_2$
Physical Review B, 79 (2009) 13, 132408

Chatterji, T.; Schneider, G. J.; van Eijck, L.; Frick, B.; Bhattacharya, D.
Direct evidence for the Nd magnetic ordering in $NdMnO_3$ from the hyperfine field splitting of Nd nuclear level
Journal of Physics: Condensed Matter, 21 (2009), 126003-1 – 126003-6

Chatterji, T.; Schneider, G. J.
Anomalous hyperfine interaction in CoF_2 investigated by high resolution neutron spectroscopy
Journal of Physics: Condensed Matter, 21 (2009), 436008

Chatterji, T.; Schneider, G. J.
Low-energy nuclear spin excitations in Co0
Physical Review B, 79 (2009), 212409

Chatterji, T.; Schneider, G. J.; Persson, J.
Low-energy nuclear spin excitations in NdA_{12}
Physical Review B, 79 (2009) 13, 132408

Chatterji, T.; Schneider, G. J.; van Eijck, L.; Frick, B.; Bhattacharya, D.
Direct evidence for the Nd magnetic ordering in $NdMnO_3$ from the hyperfine field splitting of Nd nuclear levels
Journal of Physics: Condensed Matter, 21 (2009), 126003

Chelakkot, R.; Lipowsky, R.; Gruhn, T.
Self-assembling network and bundle structures in systems of rods and crosslinkers – A Monte Carlo study
Soft Matter, 5 (2009) 5, 1504 – 1513

Chen, J.; Köhler, R.; Gutberlet, T.; Möhwald, H.; Krastev, R.
Asymmetric lipid bilayer sandwiched in polyelectrolyte multilayer films through layer-by-layer assembly
Soft Matter, 5 (2009) 1, 228 – 233

Cherstvy, A. G.
Positively Charged Residues in DNA-Binding Domains of S tructural Proteins Follow Sequence-specific Positions in DNA Phosphate Groups
Journal of Physical Chemistry B, 113 (2009) 13, 4242 – 4247

Cherstvy, A. G.
Probing DNA-DNA Electrostatic Friction in Tight Superhelical DNA Plies
Journal of Physical Chemistry B, 113 (2009) 16, 5350 – 5355

Comets, F.; Popov, S.; Schütz, G. M.; Vachkovskaia, M.
Billiards in a General Domain with Random Reflections
Archive for Rational Mechanics and Analysis, 191 (2009) 3, 497 – 537

Costi, T. A.; Bergqvist, L.; Weichselbaum, A.; von Delft, J.; Micklitz, T; Rosch, A.; Mavropoulos, P.; Dederichs, P. H.; Mallet, F.; Saminadayar, L.; Bäuerle, C.
Kondo Decoherence: finding the right spin model for iron impurities in gold and silver
Physical Review Letters, 102 (2009), 056802

Delajon, C.; Gutberlet, T.; Möhwald, H.; Krastev, R.
Absorption of light and heavy water vapours in polyelectrolyte multilayer films
Colloids and Surfaces B: Biointerfaces, 74 (2009), 462 – 467

Delgado, J.; Kriegs, H.; Castillo, R.
Flow velocity profiles and shear banding onset in a semidilute wormlike micellar system under couette flow
Journal of Physical Chemistry B, 113 (2009) 47, 15485 – 15494

Dhont, J. K. G.; Gompper, G.; Richter, D.
Jülich Soft Matter Days 2008 – Conference Report II
Applied Rheology, 19 (2009) 3, 176 – 178

Dietrich, U.; Krüger, P.; Gutberlet, T.; Käs, J. A.
Interaction of the MARCKS peptide with PIP2 in phospholipid monolayers
Biochimica et Biophysica Acta, 1788 (2009) 7, 1474 – 1481

Dolinsek, J.; Feuerbacher, M.; Jagodic, M.; Jaglicic, Z.; Heggen, M.; Urban, K.
A thermal memory cell
Journal of Applied Physics, 106 (2009), 043917

Ebert, Ph.; Ivanova, L.; Borisova, S.; Eisele, H.; Laubsch, A.; Dähne, U.
Electronic properties of dislocations in GaN investigated by scanning tunneling microscopy
Applied Physics Letters, 94 (2009), 062104

Ebert, Ph.; Ivanova, L.; Eisele, H.
Scanning tunneling microscopy on unpinned GaN(1100) surfaces: Invisibility of valence-band states
Physical Review B, 80 (2009) 8, 085316

Ehlers, G.; Mamontov, E.; Zamponi, M.; Kam, K. C.; Gardner, J. S.
Direct observation of a nuclear spin excitation in $Ho_2Ti_2O_7$
Physical Review Letters, 102 (2009), 016405

Eisele, H.; Ivanova, L.; Borisova, S.; Dähne, M.; Winkelnkemper, M.; Ebert, Ph.
Doping modulation in GaN imaged by cross-sectional scanning tunneling microscopy
Applied Physics Letters, 94 (2009) 16, 162110

Eisenriegler, E.
Density profiles around nanoparticles and distant perturbations
Journal of Chemical Physics, 130 (2009) 13, 134902-1 - 134902-

Elgeti, J.; Gompper, G.
Self-Propelled Rods near Surfaces
Europhysics Letters, 85 (2009), 38002

Enyashin, A.; Bar-Sadan, M.; Sloan, J.; Houben, L.; Seifert, G.
Nanoseashells and Nanooctahedra of MoS_2: Routes to Inorganic Fullerenes
Chemistry of Materials, 21 (2009) 23, 5627 – 5636

Fernández, J. F.; Leardini, F.; Bodega, J.; Sánchez, C.; Joubert, J. M.; Cuevas, F.; Leroy, E.; Baricco, M.; Feuerbacher, M.
Interaction of Hydrogen with the Beta-Al_3Mg_2 Complex Metallic Alloy: Experimental Reliability of Theroretical Preditictions
Journal of Alloys and Compounds, 472 (2009) 1/2, 565 – 570

Ferriani, P.; von Bergmann, K.; Vedmedenko, E. Y.; Heinze, S.; Bode, M.; Heide, M.; Bihlmayer, G.; Blügel, S.; Wiesendanger, R.
Erratum: Atomic-Scale Spin Spiral with a Unique Rotational Sense: Mn Monolayer on W(001)
Physical Review Letters, 102 (2009), 019901(E)

Finger, F.; Astakhov, O.; Bronger, T.; Carius, R.; Chen, T.; Dasgupta, A.; Gordijin, A.; Houben, L.; Huang, Y.; Klein, S.; Luysberg, M.; Wang, H.; Xiao, L.
Microcrystalline silicon carbide alloys prepared with HWCVD as highly transparent and conductive window layers for thin film solar cells
Thin Solid Films, 517 (2009) 12, 3507 – 3512

Fornleitner, J.; Lo Verso, F.; Kahl, G.; Likos, C. N.
Ordering in Two-Dimensional Dipolar Mixtures
Langmuir, 25 (2009) 14, 7836 – 7846

Frank, S.; Winkler, R. G.
Mesoscale hydrodynamic simulation of short polyelectrolytes in electric fields
Journal of Chemical Physics, 131 (2009), 234905

Friedrich, C.; Schindlmayr, A.; Blügel, S.
Efficient calculation of the Coulomb matrix and its expansion around k=0 within the FLAPW method
Computer Physics Communications, 180 (2009) 3, 347 – 359

Frielinghaus, H.; Pipich, V.; Radulescu, A.; Heiderich, M.; Hanslik, R.; Dahlhoff, K.; Iwase, H.; Koizumi, S.; Schwahn, D.
Aspherical refractive lenses for small angle neutron scattering
Journal of Applied Crystallography, 42 (2009), 681 – 690

Gapinski, J.; Patkowski, A.; Banchio, A. J.; Buitenhuis, J.; Holmqvist, P.; Lettinga, M. P.; Meier, G.; Nägele, G.
Structure and Short-Time Dynamics in Suspensions of Charged Silica Spheres in the Entire Fluid Regime
Journal of Chemical Physics, 130 (2009), 084503

Goerigk, G.; Mattern, N.
Critical scattering of Ni-Nb-Y metallic glasses probed by quantitative anomalous small-angle X-ray scattering
Acta Materialia, 57 (2009), 3652 – 3661

Gögelein, C.; Nägele, G.; Buitenhuis, J.; Tuinier, R.; Dhont, J. K. G.
Polymer depletion-driven cluster aggregation and initial phase separation in charged nanosized colloids
Journal of Chemical Physics, 130 (2009) 20, 204905

Gompper, G.; Ihle, T.; Kroll, D. M.; Winkler, R. G.
Multi-Particle Collision Dynamics: A Particle-Based Mesoscale Simulation Approach to the Hydrodynamics of Complex Fluids
Advances in Polymer Science, 221 (2009), 1 – 87

Goß, K.; Kamra, A.; Spudat, C.; Meyer, C.; Kögerler, P.; Schneider, C. M.
CVD growth of carbon nanotubes using molecular nanoclusters as catalyst
Physica Status Solidi B, 246 (2009) 11/12, 2494 – 2497

Gottlieb-Schönmeyer, S.; Brühne, S.; Ritter, F.; Assmua, W.; Balanetskyy, S.; Feuerbacher, M.; Weber, Th.; Steurer, W.
Crystal growth of copper-rich ytterbium compounds: The predicted giant unit cell structures $YbCu_{4.4}$ and $YbCu_{4.25}$
Intermetallics, 17 (2009), 1/2, 6 – 10

Gourdon, O.; Izaola, Z.; Elcoro, L.; Petricek, V.; Miller, G. J.
Structure Determination of Two Modulated gamma-Brass Structures in the Zn-Pd System through a (3+1)-Dimensional Space Description
Inorganic Chemistry, 48 (2009) 20, 9715 – 9722

Greedan, J. E.; Gout, D.; Lozano-Gorrin, A. D.; Derahkshan, S.; Proffen, Th.; Kim, H. J.; Bozin, E.; Billinge, S. J. L.
Local and average structures of the spin-glass pyrochlore $Y_2Mo_2O_7$ from neutron diffraction and neutron pair distribution function analysis
Physical Review B, 79 (2009), 014427: 1 – 10

Grushko, B.
X-ray powder diffraction data for high-temperature $Al_4Re(Ni)$
Powder Diffraction, 24 (2009) 1, 29 – 31

Grushko, B.; Kowalski, W.; Balanetskyy, S.
Phase equilibria in the Al-rich region of the Al-Ni-Re alloy system
Journal of Alloys and Compounds, 479 (2009) 1/2, L59 – L61

Grushko, B.; Kowalski, W.; Pavlyuchkov, D.; Balanetskyy, S.; Surowiec, M.
On the constitution of the Al-rich part of the Al-Cr-Mn system
Journal of Alloys and Compounds, 468 (2009) 1/2, 87 – 95

Grushko, B.; Kowalski, W.; Pavlyuchkov, D.; Mi, S.; Surowiec, M.
Al-rich region of the Al-Ni-Cr alloy system below 900°C
Journal of Alloys and Compounds, 485 (2009) 1/2, 132 – 138

Gunnarsson, O.; Sangiovanni, G.; Rösch, O.; Koch, E.; Castellani, C.; Capone, M.
Polaron formation in cuprates
Physica C, 460 (2007) 1, 263 – 266

Guo, X.
Comment on "Colossal ionic conductivity at interfaces of epitaxial ZrO_2:Y_2O_3/$SrTiO_3$ heterostructures"
Science, 324 (2009), 465

Haan, M.; Gwan, J. F.; Baumgaertner, A.
Correlated movements of ions and water in a nanochannel
Molecular Simulations, 35 (2009) 1/2, 13 – 23

Hamley, I. W.; O'Driscoll, B. M. D.; Lotze, G.; Moulton, C.; Allgaier, J.; Frielinghaus, H.
Highly Asymmetric Phase Diagram of a Poly(1,2-octylene oxide)-Poly(ethylene oxide) Diblock Copolymer System Comprising a Brush-Like Poly(1,2-octylene oxide) Block
Macromolecular Rapid Communications, 30 (2009) 24, 2414 – 2146

Hardrat, B.; Al-Zubi, A.; Ferriani, P.; Blügel, S.; Bihlmayer, G.; Heinze, S.
Complex Magnetism of Iron Monolayers on Hexagonal Transition Metal Surfaces from First Principles
Physical Review B, 79 (2009)9, 094411- 094416

Hayashi, M.; Ootsuka, Y.; Paulsson, M.; Persson, B. N. J.; Ueba, H.
Lateral hopping of CO molecules on Pt(111) surface by femtosecond laser pulses
Physical Review B, 80 (2009) 24, 245409

Head, D. A.
Critical Scaling and Aging in Cooling Systems Near the Jamming Transition
Physical Review Letters, 102 (2009) 13, 138001

Headen, T. F.; Boek, E. S.; Stellbrink, J.; Scheven, U. M.
Small Angle Neutron Scattering (SANS and V-SANS) study of asphaltene aggregates in crude oil: Temperature effect and geometric shape analysis
Langmuir, 25 (2009) 1, 422 – 428

Heide, M.; Bihlmayer, G.; Blügel, S.
Describing Dzyaloshinskii-Moriya spirals from first principles
Physica B: Condensed Matter, 404 (2009) 18, 2678 – 2683

Heidelmann, M.; Barthel, J.; Houben, L.
StripeSTEM, a technique for the isochronous acquisition of high angle annular dark-field images and monolayer resolved electron energy loss spectra
Ultramicroscopy, 109 (2009) 12, 1447 – 1452

Heinen, M.; Kull, H. J.
Radiation boundary conditions for the numerical solution of the three-dimensional time-dependent Schrödinger equation with a localized interaction
Physical Review E, 79 (2009) 5, 056709,

Herrero-Martín, J.; Scagnoli, V.; Mazzoli, C.; Su, Y.; Mittal, R.; Xiao, Y.; Brückel, T.; Kumar, N.; Dhar, S.; Thamizhavel, A.; Paolasini, L.
Magnetic structure of $EuFe_2As_2$ as determined by resonant X-ray scattering
Physical Review B, 80 (2009) 13, 134411

Highfield, J.; Liu, T.; Loo, Y. S.; Grushko, B.; Borgna, A.
Skeletal Ru/Cu catalysts prepared from crystalline and quasicrystalline ternary alloy precursors: characterization by X-ray absorption spectroscopy and CO oxidation
Physical Chemistry Chemical Physics, 11 (2009) 8, 1196 – 1208

Hirschberg, O.; Mukamel, D.; Schütz, G. M.
Condensation in Temporally Correlated Zero-Range Dynamics
Physical Review Letters, 103 (2009), 090602

Holmqvist, P.; Ratajczyk, M.; Meier, G.; Wensink, H. H.; Lettinga, M. P.
Supersaturated dispersions of rod-like viruses with added attraction
Physical Review E, 80 (2009) 3, 031402

Hsieh, D.; Xia, Y.; Wray, L.; Qian, D.; Pal, A.; Dil, J. H.; Osterwalder, J.; Meier, F.; Bihlmayer, G.; Kane, C. L.; Hor, Y. S.; Cava, R. J.; Hasan, M. Z.
Observation of unconventional quantum spin textures in topological insulators
Science, 323 (2009), 919 – 922

Huang, B. X.; Malzbender, J.; Steinbrech, R. W.; Grychtol, P.; Schneider, C. M.; Singheiser, L.
Anomalies in the thermomechanical behavior of $Ba_{0.5}Sr_{0.5}Co_{0.8}Fe_{0.2}O_{3-\delta}$ ceramic oxygen conductive membranes at intermediate temperatures
Applied Physics Letters, 95 (2009) 5, 051901

Huang, C. C.; Ryckaert, J. P.; Yu, H.
Structure and dynamics of cylindrical micelles at equilibrium and under shear flow
Physical Review E, 79 (2009) 4, 041501

Huettel, A. K.; Witkamp, B.; Leijnse, M.; Wegewijs, M. R.; van der Zant, H. S. J.
Pumping of vibrational excitations in a Coulomb blockaded suspended carbon nanotube
Physical Review Letters, 102 (2009) 225501,

Ishida, H.; Liebsch, A.
Embedding approach for dynamical mean-field theory of strongly correlated heterostructures
Physical Review B, 79 (2009) 4, 045130

Jagodic, M.; Jaglicic, Z.; Grushko, B.; Balanetskyy, S.; Dolinsek, J.
The influence of thermal annealing on structural order in the i-Al_4Mn complex intermetallic
Zeitschrift für Kristallographie, 224 (2009) 1/2, 42 – 44

Jeong, D. S.; Schroeder, H.; Waser, R.
Abnormal bipolar-like resistance change behavior induced by symmetric electroforming in Pt/TiO_2/Pt resistive switching cells
Nanotechnology, 20 (2009) 375201,

Jeong, D. S.; Schroeder, H.; Waser, R.
Mechanism for bipolar switching in a Pt/TiO_2/Pt resistive switching cell
Physical Review B, 79 (2009) 19, 195317

Jia, C. L.; Mi, S. B.; Faley, M.; Poppe, U.; Schubert, J.; Urban, K.
Oxygen octahedron reconstruction in the $SrTiO_3$/$LaAlO_3$ heterointerfaces investigated using aberration-corrected ultrahigh-resolution transmission electron microscopy
Physical Review B, 79 (2009) 8, 081405(R),

Jia, C. L.; Mi, S. B.; Urban, K.; Vrejoiu, I.; Alexe, M.; Hesse, D.
Effect of a single dislocation in a heterostructure layer on the local polarization of a ferroelectric layer
Physical Review Letters, 102 (2009) 11, 117601

Junghans, C.; Bachmann, M.; Janke, W.
Statistical Mechanics of Aggregation and Crystallization for Semiflexible Polymers
Europhysics Letters, 87 (2009), 40002

Kaiser, A.; Banerjee, D.; Rata, A. D.; Wiemann, C.; Cramm, S.; Schneider, C. M.
Magnetic Microstructure of Candidates for Epitaxial Dual Heusler Magnetic Tunnel Junctions
Journal of Magnetism and Magnetic Materials, 321 (2009), 1182 – 1187

Kaiser, A.; Wiemann, C.; Cramm, S.; Schneider, C. M.
Influence of magnetocrystalline anisotropy on the magnetization dynamics of magnetic microstructures
Journal of Physics: Condensed Matter, 21 (2009), 314008

Kajewski, D.; Ujma, Z.; Szot, K.
Dielectric properties and phase transition in $SrBi_2Nb_2O_9$–$SrBi_2Ta_2O_9$ solid solution
Ceramics International, 35 (2009) 6, 2351 – 2355

Kang, K.; Dhont, J. K. G.
Criticality in a non-equilibrium, driven system: Charged colloidal rods (fd-viruses) in electric fields
European Physical Journal E, 30 (2009) 3, 333 – 340

Kim, S. K.; Hoffmann-Eifert, S.; Mi, S.; Waser, R.
Liquid injection atomic layer deposition of crystalline TiO_2 thin films with a smooth morphology from $Ti(O\text{-}i\text{-}Pr)_2(DPM)_2$
Journal of the Electrochemical Society, 156 (2009) 8, D296 – D300

Kim, S. K.; Hoffmann-Eifert, S.; Waser, R.
Growth of noble metal Ru thin films by liquid injection atomic layer deposition
Journal of Physical Chemistry C, 113 (2009) 26, 11329

Kimber, S. A. J.; Kreyssig, A.; Zhang, Y. Z.; Jeschke, H. O.; Valenti, R.; Yokaichiya, F.; Colombier, E.; Yan, J.; Hansen, T. C.; Chatterji, T.; McQueeney, R. J.; Canfield, P. C.; Goldman, A. I.; Argyriou, D. N.
Similarities between structural distortions under pressure and chemical doping in superconducting $BaFe_2As_2$
Nature Materials, 8 Letters (2009), 471 – 475

Kirstein, O.; Prager, M.; Schneider, G.J.
Rotational dynamics and coupling of methyl group rotations in methyl group rotations in methyl fluoride studied by high resolution inelastic neutron scattering
Journal of Chemical Physics, 130 (2009) 21, 214508

Koehl, D.; Luysberg, M.; Wuttig, M.
Highly textured zinc oxide films by room temperature ion beam assisted deposition
Physica Status Solidi - Rapid Research Letters, 3 (2009)//8, 236 – 238

Kolasinska, M.; Gutberlet, T.; Krastev, R.
Ordering of Fe_30_4 Nanoparticles in Polyelectrolyte Multilayer Films
Langmuir, 25 (2009) 17, 10292 – 10297

Kolasinska, M.; Krastev, R.; Gutberlet, T.; Warszynski, P.
Layer-by-Layer Deposition of Polyelectrolytes. Dipping versus Spraying
Langmuir, 25 (2009) 2, 1224 – 1232

Konstantinidis, N. P.
s=1 / 2 antiferromagnetic Heisenberg model on fullerene-type symmetry clusters
Physical Review B, 80 (2009) 13, 134427

Krauss, G.; Gu, Q. F.; Feuerbacher, M.; Steurer, W.
Compressibility of $Al_{64}Pd_{30.4}Fe_{5.6}$
Zeitschrift für Kristallographie, 224 (2009) 1/2, 119 – 122

Krott, M.; Houben, A.; Müller, P.; Schweika, W.; Dronskowski, R.
Determination of the magnetic structure of manganese carbodiimide with diffraction experiments using polarized neutrons
Physical Review B, 80 (2009) 2, 024117

Krupin, O.; Bihlmayer, G.; Döbrich, K.; Prieto, J. E., Starke, K.; Gorovikov, S.; Blügel, S.; Kevan, S.; Kaindl, G.
Rashba effect at the surfaces of rare-earth metals and their monoxides
New Journal of Physics, 11 (2009), 013035

Krutyeva, M.; Martin, J.; Arbe, A.; Colmenero, J.; Mijangos, C.; Schneider, G.; Unruh, T.; Su, Y.; Richter, D.
Neutron scattering study of the dynamics of a polymer melt under nanoscopic confinement
Journal of Chemical Physics, 131 (2009) 19, 174901

Kügeler, C.; Böttger, U.; Schneller, T.
Electromechanical properties of lanthanum-doped lead hafnate titanate thin films for integrated piezoelectric MEMS applications
Applied Physics A, 94 (2009) 4, 739 – 743

Kügeler, C.; Hennings, A.; Böttger, U.; Waser, R.
An Integrated Microelectromechanical Microwave Switch Based on Piezoelectric Actuation
Journal of Electroceramics, 22 (2009) 1/3, 145 – 149

Kügeler, C.; Meier, M.; Rosezin, R.; Gilles, S.; Waser, R.
High density 3D memory architecture based on the resistive switching effect
Solid-State Electronics, 53 (2009) 12, 1287 – 1292

Landrock, S.; Jiang, Y.; Wu, K. H.; Wang, E. G.; Urban, K.; Ebert, Ph.
Origin of nanoscale potential fluctuations in two-dimensional semiconductors
Applied Physics Letters, 95 (2009) 7, 072107

La-O-Vorakiat, C.; Siemens, M.; Murnane, M. M.; Kapteyn, H. C.; Mathias, S.; Aelischmann, M.; Grychtol, P.; Adam, R.; Schneider, C. M.; Shaw, J. M.; Nembach, H.; Silva, T. J.
Ultrafast demagnetization dynamics at the M edges of magnetic elements observed using a tabletop high-harmonic soft X-ray source
Physical Review Letters, 103 (2009) 25, 257402

Laubsch, A.; Urban, K.; Ebert, Ph.
Three- to two-dimensional transition in electrostatic screening of point charges at semiconductor surfaces studied by scanning tunneling microscopy
Physical Review B, 80 (2009) 24, 245314

Lee, C. H.; Chang, H. H.; Su, H. C.; Wu, Y. H.; Hu, C. W.; Chang, L. J.; Ioffe, A.; Bussmann, K.; Brückel, T.
Neutron depolarization study on the magnetic correlation length of nickel ferrite with different packing densities
Physica B: Condensed Matter, 404 (2009) 17, 2565 – 2567

Lehndorff, R.; Bürgler, D. E.; Gliga, S.; Hertel, R.; Grünberg, P.; Schneider, C. M.
Magnetization dynamics in spin torque nano-oscillators: Vortex state versus uniform state
Physical Review B, 80 (2009) 5, 054412

Leijnse, M.; Wegewijs, M. R.; Hettler, M.
Pair-tunneling resonance in the single-electron transport regime
Physical Review Letters, 103 (2009) 15, 156803

Lennartz, C.; Atodiresei, N.; Müller-Meskamp, L.; Karthäuser, S.; Waser, R.; Blügel, S.
Cu-adatom-mediated bonding in close-packed benzoate/Cu (110)-Systems
Langmuir, 25 (2009), 856 – 864

Lennartz, C. M.; Müller-Meskamp, L.; Karthäuser, S.; Waser, R.
Transitions at domain boundaries in octanethiol monolayers on Au(111)
Surface Science, 603 (2009) 8, 1156 – 1159

Lerch, M.; Janek, J.; Becker, K.D.; Berendts, S.; Boysen, H.; Bredow, T.; Dronskowski, R.; Egginghaus, S.G.; Kilo, M.; Lumey, M.W.; Martin, M.; Reimann, C.; Schweda, E.; Valov, I.; Wiemhöfer, H.D.
Oxide nitrides: From oxides to solids with mobile nitrogen ions
Progress in Solid State Chemistry, 37 (2009) 81

Lettinga, M. P.; Manneville, S.
Competition between shear banding and wall slip in wormlike micelles
Physical Review Letters, 103 (2009) 24, 248302

Li, H. F.; Su, Y.; Xiao, Y. G.; Perßon, J.; Meuffels, P.; Brückel, T.
Crystal and magnetic structure of single-crystal $La_{1-x}SrxMnO_3$ ($x \sim 1/8$)
European Physical Journal B, 67 (2009), 149 – 157

Liebsch, A.; Ishida, H.; Merino, J.
Mott transition in two-dimensional frustrated compounds
Physical Review B, 79 (2009), 195108

Liebsch, A.; Tong, N. H.
Finite-temperature exact diagonalization cluster dynamical mean-field study of the two-dimensional Hubbard model: Pseudogap, non-Fermi-liquid behavior, and particle-hole asymmetry
Physical Review B, 80 (2009) 16, 165126

Liu, Y.; Hou, Z.; Gliga, S.; Hertel, R.
Influence of the dynamic dipolar interaction on the current-induced core switch in vortex pairs
Physical Review B, 79 (2009) 10, 104435

Lopes, J. M. J.; Durgun-Özben, E.; Roeckerath, M.; Littmark, U.; Lupták, R.; Lenk, St.; Luysberg, M.; Besmehn, A.; Breuer, U.; Schubert, J.; Mantl, S.
Amorphous ternary rare-earth gate oxides for future integration in MOSFETs
Microelectronic Engineering, 86 (2009) 7/9, 1646 – 1649

Lorenz, B.; Persson, B. N. J.
Interfacial separation between elastic solids with randomly rough surfaces: comparison of experiment with theory
Journal of Physics: Condensed Matter, 21 (2009) 1, 015003

Lorenz, B.; Persson, B. N. J.
Leak rate of seals: Comparison of theory with experiment
Europhysics Letters, 86 (2009) 4, 44006

Lorenz, W. E. A.; Kuzian, R. O.; Drechsler, S. L.; Stein, W. D.; Wizent, N.; Behr, G.; Málek, J.; Nitzsche, U.; Rosner, H.; Hiess, A.; Schmidt, W.; Klingeler, R.; Loewenhaupt, M.; Büchner, B.
Highly dispersive spin excitations in the chain cuprate Li_2CuO_2
Europhysics Letters, 88 (2009), 37002: 1 – 6

Lund, R.; Willner, L.; Lindner, P.; Richter, D.
Structural properties of weakly segregated PS-PB block copolymer micelles in n-alkanes: solvent entropy effects
Macromolecules, 42 (2009) 7, 2686 – 2695

Lund, R.; Willner, L.; Monkenbusch, M.; Panine, P.; Narayanan, T.; Colmenero, J.; Richter, D.
Structural observation and kinetic pathway in the formation of polymeric micelles
Physical Review Letters, 102 (2009) 18, 188301

Lustfeld, H.; Hirschfeld, J.; Reißel, M.; Steffen, B.
Uniqueness of magnetotomography for fuel cells and fuel cell stacks
Journal of Physics A – Mathematical and Theoretical, 42 (2009), 495205

Lustfeld, H.; Reißel, M.; Schmidt, U.; Steffen, B.
Reconstruction of Electric Currents in a Fuel Cell by Magnetic Field Measurements
Journal of Fuel Cell Science and Technology, 6 (2009) 2, 021012 – 021020

Lustfeld, H.; Reißel, M.; Steffen, B.
Magnetotomography and electric currents in a fuel cell
Fuel Cells: from Fundamentals to Systems, 9 (2009) 4, 474 – 481

Luysberg, M.; Heidelmann, M.; Houben, L.; Boese, M.; Heeg, T.; Roeckerath, M.; Schubert, J.
Atomic scale compositions across $DyScO_3/SrTiO_3$ interfaces
Microscopy and Microanalysis, 15 (2009) S2, 1012

Luysberg, M.; Heidelmann, M.; Houben, L.; Boese, M.; Heeg, T.; Schubert, J.; Roeckerath, M.
Intermixing and charge neutrality at $DyScO_3/SrTiO_3$ interfaces
Acta Materialia, 57 (2009) 11, 3192 – 3198

Luysberg, M.; Sofin, R. G. S.; Arora, S. K.; Shvets, I. V.
Strain relaxation in $Fe_3O_4/MgAl_2O_4$ heterostructures: Mechanism for formation of antiphase boundaries in an epitaxial system with identical symmetries of film and substrate
Physical Review B, 80 (2009) 2, 024111

Lyatti, M.; Divin, Y.; Poppe, U.; Urban, K.
Liquid identification by Hilbert spectroscopy
Superconductor Science and Technology, 22 (2009), 114005

Magno, M.; Tessendorf, R.; Medronho, B.; Miguel, M. G.; Stubenrauch, C.
Gelled polymerizable microemulsions. Part 3 Rheology
Soft Matter, 5 (2009), 4763 – 4772

Martin, M.; Dronskowski, R.; Janek, J.; Becker, K.-D.; Roehrens, D.; Brendt, J.; Lumey, M.W.; Nagarajan, L.; Valov, I.; Börger, A.
Thermodynamics, structure and kinetics in the system Ga-O-N
Progress in Solid State Chemistry, 37 (2009) 132

Mattern, N.; Goerigk, G.; Vainio, U.; Miller, M. K.; Gemming, T.; Eckert, J.
Spinodal decomposition of Ni-Nb-Y metallic glasses
Acta Materialia, 57 (2009) 3, 903 – 908

Mavropoulos, Ph.; Ležaić , M. ; Blügel, S.
Ferromagnetism in nitrogen-doped MgO: Density-functional calculations
Physical Review B, 80 (2009) 18, 184403

McGuire, M. A.; Hermann, R. P.; Sefat, A. S.; Sales, B. C.; Jin, R.; Mandrus, D.; Grandjean, F.; Long, G. J.
Influence of the rare-earth element on the effects of the structural and magnetic phase transitions in CeFeAsO, PrFeAsO, and NdFeAsO
New Journal of Physics, 11 (2009), 025011-1 – 025011-16

McWhirter, J. L.; Noguchi, H.; Gompper, G.
Flow-induced clustering and alignment of vesicles and red blood cells in microcapillaries
Proceedings of the National Academy of Sciences of the United States of America, 106 (2009) 15, 6039 – 6043

Meier, M.; Gilles, S.; Rosezin, R.; Schindler, S; Trellenkamp, S.; Rüdiger, A.; Mayer, D.; Kügeler, C.; Waser, R.
Resistively switching Pt/Spin-on glass/Ag nanocells for non-volatile memories fabricated with UV nanoimprint lithography
Microelectronic Engineering, 86 (2009) 4/6, 1060 – 1062

Meier, M.; Schindler, C.; Gilles, S.; Rosezin, R.; Rüdiger, A.; Kügeler, C.; Waser, R.
A nonvolatile memory with resistively switching methyl-silsesquioxane
IEEE Electron Device Letters, 30 (2009), 8 – 10

Menke, T.; Dittmann, R.; Meuffels, P.; Szot, K.; Waser, R.
Impact of the electroforming process on the device stability of epitaxial Fe-doped $SrTiO_3$ resistive switching cells
Journal of Applied Physics, 106 (2009) 114507

Menke, T.; Meuffels, P.; Dittmann, R.; Szot, K.; Waser, R.
Separation of bulk and interface contributions to electroforming and resistive switching behavior of epitaxial Fe-doped $SrTiO_3$
Journal of Applied Physics, 105 (2009) 6, 066104

Meshi, L.; Grushko, B.; Ezersky, V.
Identification of a new hexagonal phase in the Al–Cu–Re system
Journal of Alloys and Compounds, 488 (2009), 108 – 111

Meßlinger, S.; Schmidt, B.; Noguchi, H.; Gompper, G.
Dynamical regimes and hydrodynamic lift of viscous vesicles under shear
Physical Review E, 80 (2009) 1, 011901

Meyer, C.; Spudat, C.; Houben, L.; Schneider, C. M.
Defects induced on chemical vapour deposition carbon nanotubes during peapod synthesis on substrates
Nanotechnology, 20 (2009), 065603

Mi, S. B.; Jia, C. L.; Zhao, Q. T.; Mantl, S.; Urban, K.
$NiSi_2/Si$ interface chemistry and epitaxial growth mode
Acta Materialia, 57 (2009) 1, 232 – 236

Miao, G. X.; Müller, M.; Moodera, J. S.
Magnetoresistance in double spin filter tunnel junctions with nonmagnetic electrodes and its unconventional bias dependence
Physical Review Letters, 102 (2009) 7, 076601

Mittal, R.; Pintschovius, L.; Öhrn, A.; Lamago, D.; Bohnen, K. P.; Reznik, D.; Chaplot, S. L.; Su, Y.; Kumar, N.; Dhar, S. K.; Thamizhavel, A.; Brückel, T.
Measurement of Anomalous Phonon Dispersion of $CaFe_2As_2$ Single Crystals Using Inelastic Neutron Scattering
Physical Review Letters, 102 (2009) 21, 217001: 1 – 4

Mittal, R.; Rols, S.; Zbiri, M.; Su, Y.; Schober, H.; Chaplot, S. L.; Johnson, M; Tegel, M.; Chatterji, T.; Matsuishi, S.; Hosono, H.; Johrendt, D.; Brückel, T.
Phonon spectra in $CaFe_2As_2$ and $Ca_{0.6}Na_{0.4}Fe_2As_2$: Measurement of the pressure and temperature dependence and comparison with ab initio and shell model calculations
Physical Review B, 79 (2009) 14, 144516

Mittal, R.; Zbiri, M.; Rols, S.; Su, Y.; Xiao, Y.; Schober, H.; Chaplot, S. L.; Johnson, M.; Chatterji, T.; Matsuishi, S.; Hosono, H.; Brückel, T.
Effects of magnetic doping and temperature dependence of phonon dynamics in $CaFe_{1-x}Co_xAsF$ compounds (x=0, 0.06, and 0.12)
Physical Review B, 79 (2009) 21, 214514

Mokrousov, Y.; Thiess, A.; Heinze, S.
Structurally driven magnetic state transition of biatomic Fe chains on Ir(001)
Physical Review B, 80 (2009) 19, 195420

Molak, A.; Pawelczyk, M.; Kubacki, J.; Szot, K.
Nano-scale chemical and structural segregation induced in surface layer of $NaNbO_3$ crystals with thermal treatment at oxidising conditions studied by XPS, AFM, XRD, and electric properties tests
Phase Transitions, 82 (2009) Issue 9, 662 – 682

Molak, A.; Szot, K.
Insulator-semiconductor-metallic state transition induced by electric fields in Mn-doped $NaNbO_3$
Physica Status Solidi - Rapid Research Letters, 3 (2009) 5, 127 – 129

Moras, P.; Topwal, D.; Sheverdyaeva, P. M.; Ferrari, L.; Fujii, J.; Bihlmayer, G.; Blügel, S.; Carbone, C.
Influence of the substrate bands on the sp-levels topology of Ag films on Ge(111)
Physical Review B, 80 (2009) 20, 205418

Müller, M.; Miao, G. X.; Moodera, J. S.
Exchange splitting and bias-dependent transport in EuO spin filter tunnel barriers
Europhysics Letters, 88 (2009), 47006

Müller, M.; Miao, G. X.; Moodera, J. S.
Thickness dependence of ferromagnetic- and metal-insulator transition in thin EuO films
Journal of Applied Physics, 105 (2009) 7, 07C917

Müller, R.; Krebs, C.; Goux, L.; Wouters, D. J.
Bipolar resistive electrical switching of CuTCNQ memories incorporating a dedicated switching layer
IEEE Electron Device Letters, 30 (2009) 6, 620 – 622

Müller-Meskamp, L.; Karthäuser, S.; Waser, R.; Homberger, M.; Wang, Y.; Englert, U.; and Simon, U.
Structural Characterization of w-Ferrocenylalkanethiols on Au(111) by Scanning Tunneling Microscopy
Surface Science, 603 (2009) 4, 716 – 722

Müller-Meskamp, L.; Karthäuser, S.; Zandvliet, H. J. W.; Homberger, M.; Simon, U.; Waser, R.
Field Emission Resonances at Tip/alpha, omega-Mercaptoalkyl-ferrocene/Au Interfaces Studied by STM
Small, 5 (2009) 4, 496 – 502

Nepijko, S. A.; Graff, A.; Schönhense, G.; Schneider, C. M.
Quantitative determination of magnetic fields from iron particles of oblong form encapsulated by carbon nanotubes using electron holography
Applied Physics A, 94 (2009) 3, 543 – 547

Niu, A.; Stellbrink, J.; Allgaier, J.; Richter, D.; Hartmann, R.; Domski, G. J.; Coates, G. W.; Fetters, L. J.
Polymerization of 1-Octene by a Pyridylamidohafnium Catalyst: A SEC, 1H-NMR and Small Angle Neutron Scattering Study
Macromolecules, 42 (2009) 4, 1083 – 1090

Noguchi, H.
Swinging and synchronized rotations of red blood cells in simple shear flow
Physical Review E, 80 (2009) 2, 021902

Nygard, K.; Satapathy, D. K.; Buitenhuis, J.; Perret, E.; Bunk, O.; David, C.; van der Veen, J. F.
Confinement-induced orientational alignment of quasi-2D fluids
EuroPhysics Letters: epl, 86 (2009), 66001

Nygard, K; Satapathy, D. K.; Bunk, O.; Perret, E.; Buitenhuis, J.; David, C.; van der Veen, J. F.
Grating-based holographic X-ray diffraction: theory and application to confined fluids
Journal of Applied Crystallography, 42 (2009) 6, 1129 – 1138

Ozdogan, K.; Sasioglu, E.; Aktas, B.; Galanakis, I.
Erratum: Doping and disorder in the Co_2MnAl and Co_2MnGa half-metallic Heusler alloys
Physical Review B, 80 (2009) 029901, (E)

Özdogan, K.; Sasioglu, E.; Aktas, B.; Galanakis, I.
Erratum: Doping and disorder in the Co_2MnAl and Co_2MnGa half-metallic Heusler alloys
Physical Review B, 80 (2009), 172412

Ozdogan, K.; Sasioglu, E.; Galanakis, I.
Half-metallic ferrimagnetism in the $[Sc_{1-x}V_x]C$ and $[Sc_{1-x}V_x]Si$ alloys adopting the zincblende and wurtzite structures from first-principles
Journal of Magnetism and Magnetic Materials, 322 (2010) 1, 46 – 50

Ozdogan, K.; Sasioglu, E.; Galanakis, I.
Tuning the magnetic properties of half-metallic semi-Heusler alloys by sp-electron substitution: the case of $AuMnSn_{1-x}Sb_x$ quaternary alloys
Journal of Physics D – Applied Physics, 42 (2009), 085003

Paul, A.; Mattauch, S.
Microscopic origin of training in exchange bias system
Applied Physics Letters, 95 (2009), 092502

Pavlyuchkov, D.; Balanetskyy, S.; Kowalski, W.; Surowiec, M.; Grushko, B.
Stable Decagonal Quasicrystals in the Al-Fe-Cr and Al-Fe-Mn Alloy Systems
Journal of Alloys and Compounds, 477 (2009) 1/2, L41 – L44

Pavlyuchkov, D.; Grushko, B.; Velikanova, T. Ya.
An investigation of the high-Al part of the Al-Pd-Ru phase diagram at 790 to 900°C
Journal of Alloys and Compounds, 469 (2009) 1/2, 146 – 151

Peica, N.; Röhrig, S.; Rüdiger, A.; Brose, K.; Thomsen, C.; Maultzsch, J.
Characterization of dye molecules and carbon nanostructures by tip-enhanced Raman spectroscopy
Physica Status Solidi B, 246 (2009) 11/12, 2708 – 2712

Persson, B. N. J.
Theory of powdery rubber wear
Journal of Physics: Condensed Matter, 21 (2009) 48, 485001

Persson, B. N. J.; Scaraggi, M.
On the transition from boundary lubrication to hydrodynamic lubrication in soft contacts
Journal of Physics: Condensed Matter, 21 (2009) 18, 185002

Phan, M. H.; Frey, N. A.; Srikanth, H.; Angst, M.; Sales, B. C.; Mandrus, D.
Magnetism and cluster glass dynamics in geometrically frustrated $LuFe_2O$
Journal of Applied Physics, 105 (2009) 7, 07E308

Polyakov, P.; Rossinsky, E.; Wiegand, S.
Study of the Soret Effect in Hydrocarbon Chain/Aromatic Compound Mixtures
Journal of Physical Chemistry B, 113 (2009) 40, 13308 – 13312

Polyakov, P.; Wiegand, S.
Investigation of the soret effect in aqueous and non-aqueous mixtures by the thermal lens technique
Physical Chemistry Chemical Physics, 11 (2009), 864 – 871

Prado, L. A. S. d. A.; Ponce, M. L.; Goerigk, G.; Funari, S. S.; Garamus, V. M.; Willumeit, R.; Schulte, K.; Nunes, S. P.
Analysis of proton-conducting organic-inorganic hybrid materials based on sulphonated poly(ether ether ketone) and phospho-tungstic acid via ASAXS and WAXS
Journal of Non-Crystalline Solids, 355 (2009) 1, 6 – 11

Rapp, Ö.; Andersson, M.; Feuerbacher, M.
Anomalous transport in rhombohedral Mg_2Al_3
Journal of Physics: Conference Series, 150 (2009) 022070,

Reckermann, F.; Leijnse, M.; Wegewijs, M. R.
Vibrational detection and control of spin in mixed-valence molecular transistors
Physical Review B, 79 (2009) 7, 075313

Rheinstädter, M. C.; Schmalzl, K.; Wood, K.; Strauch, D.
Protein-Protein Interaction in Purple Membrane
Physical Review Letters, 103 (2009) 12, 128104

Riedl, Th.; Gemming, Th.; Dörr, K.; Luysberg, M.; Wetzig, K.
Mn valancy at $La_{0.7}Sr_{0.3}MnO_3/SrTiO_3$ (001) thin film interfaces
Microscopy and Microanalysis, 15 (2009) 3, 213 – 221

Roch, N.; Florens, S.; Costi, T. A.; Wernsdorfer, W.; Balestro, F.
Observation of the underscreened Kondo effect in a molecular transistor
Physical Review Letters, 103 (2009) 19, 197202

Rosezin, R.; Nauenheim, C.; Trellenkamp, S.; Kügeler, C.; Waser, R.
Electrical properties of Pt interconnects for passive crossbar memory arrays
Microelectronic Engineering, 86 (2009) 11, 2275 – 2278

Sasioglu, E.
Nonzero macroscopic magnetization in half-metallic antiferromagnets at finite temperatures
Physical Review B, 79 (2009) 10, 100406

Sasioglu, E.; Caliskan, S.; Kumru, M.
Critical behavior of density of states near Fermi energy in low-dimensional disordered metals
Physical Review B, 79 (2009), 3 035123

Schäpers, Th.; Guzenko, V. A.; Bringer, A.; Akabori, M.; Hagedorn, M.; Hardtdegen, H.
Spin-orbit coupling in $GaxIn_{1-x}As/InP$ two-dimensional electron gases and quantum wire structures
Semiconductor Science and Technology, 24 (2009) 6, 064001

Schindler, C.; Staikov, G.; Waser, R.
Electrode kinetics of Cu-SiO_2-based resistive switching cells: overcoming the voltage-time dilemma of electrochemical metallization memories
Applied Physics Letters, 94 (2009), 072109

Schindler, Ch.; Valov, I.; Waser, R.
Faradaic currents during electroforming of resistively switching Ag-Ge-Se type electrochemical metallization memory cells
Physical Chemistry Chemical Physics, 11(28) (2009), 5974-9

Schmidt, H.; Hüger, E.; Chakravarty, S.; Stahn, J.; Gutberlet, T.; Tietze, U.; Lott, D.
Neutron Reflectometry: A Tool to Investigate Diffusion Processes in Solids on the Nanometer Scale
Advanced Engineering Materials, 11 (2009) 6, 446 – 451

Schnabel, S.; Bachmann, M.; Janke, W.
Elastic Lennard-Jones Polymers Meet Clusters – Differences and Similarities
Journal of Chemical Physics, 131 (2009) 124904

Schnabel, S.; Vogel, T.; Bachmann, M.; Janke, W.
Surface Effects in the Crystallization Process of Elastic Flexible Polymers
Chemical Physics Letters, 476 (2009) 4-6, 201 – 204

Schnabel, S.; Vogel, T.; Bachmann, M.; Janke, W.
Surface Effects in the Crystallization Process of Elastic Flexible Polymers
Chemical Physics Letters, 476 (2009) 4/6, 204 – 210

Schneider, C. M.; Krug, I. P.; Müller, M.; Matthes, F.; Kaiser, A.; Wiemann, C.; Cramm, S.; Wegelin, F.; Krasyuk, A.; Nepijko, S. A.; Schönhense, G.
Investigating spintronic thin film systems with synchrotron radiation
Radiation Physics and Chemistry, 78 (2009) 10, S5 – S10

Schütz, G. M.; Pigeard de Almeida, P.; Harris, R. J.; Belitsky, V.
Short-time behaviour of demand and price viewed through an exactly solvable model for heterogeneous interacting market agents
Physica A, 388 (2009) 19, 4126 – 4144

Shtrikman, H.; Popovitz-Biro, R.; Kretinin, A.; Houben, L.; Heiblum, M.; Bukala, M.; Galicka, M.; Buczko, R.; Kacman, P.
Method for Suppression of Stacking Faults in Wurtzite III-V Nanowires
Nano Letters, 9 (2009) 4, 1506 – 1510

Shukla, A. K.; Dhaka, R. S.; D'Souza, S. W.; Maniraj, M.; Barman, S. R.; Horn, K.; Ebert, Ph.; Urban, K.; Wu, D.; Lograsso, T. A.
Manganese adlayers on i-Al-Pd-Mn quasicrystal: growth and electronic structure
Journal of Physics: Condensed Matter, 21 (2009) 405005, 1-8

Slipukhina, I.; Arras, E.; Mavropoulos, Ph.; Pochet, P.
Simulation of the enhanced Curie temperature in Mn_5Ge_3Cx compounds
Applied Physics Letters, 94 (2009), 192505

Sobczyk, L.; Prager, M.; Sawka-Dobrowolska, W.; Bator, G.; Pawlukojc, A.; Grech, E.; van Eijck, L.; Ivanov, A.; Rols, S.; Wuttke, J.; Unruh, T.
The structure of diaminodurene and the dynamics of the methyl groups
Journal of Physical Chemistry B, 130 (2009), 164519

Soni, R.; Meier, M.; Rüdiger, A.; Holländer, B.; Kügeler, C.; Waser, R.
Integration of "Ge_xSe_{1-x}" in crossbar arrays for non-volatile memory applications
Microelectronic Engineering, 86 (2009), 1054 – 1056

Soni, R.; Meuffels, P.; Kohlstedt, H.; Kügeler, C.; Waser, R.
Reliability analysis of the low resistance state stability of $Ge_{0.3}Se_{0.7}$ based solid electrolyte nonvolatile memory cells
Applied Physics Letters, 94 (2009) 12, 123503

Spatschek, R; Gugenberger, C.; Brener, E. A.
Effective elastic moduli in solids with high density of cracks
Physical Review B, 80 (2009) 144106,

Sprungmann, D.; Westerholt, K.; Zabel, H.; Weides, M.; Kohlstedt, H.
Josephson tunnel junctions with ferromagnetic $Fe_{0.75}Co_{0.25}$ barriers
Journal of Applied Physics, D42 (2009), 075005

Spudat, C.; Meyer, C.; Goß, K.; Schneider, C. M.
Peapod synthesis depending on the number of nanotube sidewalls
Physica Status Solidi B, 246 (2009) 11-12, 2498 – 2501

Stadler, F. J.; Pyckhout-Hintzen, W.; Schumers, J. M.; Fustin, C. A.; Gohy, J. F.; Bailly, C.
Linear viscoelastic rheolgy of moderately entangled telechelic polybutadiene temporary networks
Macromolecules, 42 (2009) 16, 6181 – 6192

Stanic, D.; Ikvov, J.; Smontara, A.; Jaglicic, Z.; Dolinsek, J.; Heggen, M.; Feuerbacher, M.
Hall effect in Taylor-phase and decagonal Al_3(Mn,Fe) complex intermetallics
Zeitschrift für Kristallographie, 224 (2009) 1/2, 49 – 52

Steffens, P.; Farrell, J.; Price, S.; Mackenzie, A. P.; Sidis, Y.; Schmalzl, K.; Braden, M.
Incommensurate magnetic ordering in Ti-doped $Sr_3Ru_2O_7$
Physical Review B, 79 (2009) 5, 054422-1 – 054422-8

Strachan, J. P.; Yang, J. J.; Münstermann, R.; Scholl, A.; Medeiros-Ribeiro, G.; Stewart, D. R.; Williams, R. S.
Structural and chemical characterization of TiO_2 memristive devices by spatially-resolved NEXAFS
Nanotechnology, 20 (2009), 485701

Su, Y.; Link, P.; Schneidewind, A.; Wolf, Th.; Adelmann, P.; Xiao, Y.; Meven, M.; Mittal, R.; Rotter, M.; Johrendt, D.; Brückel, T.; Loewenhaupt, M.
Antiferromagnetic ordering and structural phase transition in $Ba_2Fe_2As_2$ with Sn incorporated from the growth flux
Physical Review B, B79 (2009), 064504

Symanczyk, R.; Bruchhaus, R.; Dittrich, R.; Kund, M.
Investigation of the reliability behavior of conductive-bridging memory cells
IEEE Electron Device Letters, 30 (2009), 876 – 878

Szade, J.; Psiuk, B.; Pilch, M.; Waser, R.; Szot, K.
Self-neutralization via electroreduction in photoemission from $SrTiO_3$ single crystals
Applied Physics A, 97 (2009) 2, 449 – 454

Thiess, A.; Mokrousov, Y.; Heinze, S.; Blügel, S.
Magnetically Hindered Chain Formation in Transition-Metal Break Junctions
Physical Review Letters, 103 (2009) 21, 217201

Thust, A.
High-Resolution Transmission Electron Microscopy on an Absolute Contrast Scale
Physical Review Letters, 102 (2009), 220801

Tripathi, T.; Schütz, G. M.; Chowdhury, D.
RNA polymerase motors: dwell time distribution, velocity and dynamical phases
Journal of Statistical Mechanics: Theory and Experiment, (2009), P08018

Ubic, R.; Subodh, G.; Gout, D.; Sebastian, M.; Proffen, T.
Crystal Structure of $Sr_{0.4}Ce_{0.4}TiO_3$ Ceramics
Chemistry of Materials, 21 (2009), 4706 – 4710

Ubic, R.; Subodh, G.; Gout, D.; Sebastian, M.; Proffen, T.
Effective size of vacancies in the $Sr_{1-3}x/_2CexTiO_3$ Superstructure
Ceramic Transactions, 204 (2009), 177

Urban, K.
Is science prepared for atomic-resolution electron microscopy
Nature Materials, 8 (2009) 4, 260 – 262

Urban, K.; Jia, C. L.; Houben, L.; Lentzen, M.; Mi, S.; Tilmann, K.
Negative spherical abberation ultrahigh-resolution imaging in corrected transmission electron microscopy
Philosophical Transactions of the Royal Society of London Series A, 367 (2009), 3735 – 3753

Vacarro, M.; Magiapia, G.; Radulescu, A.; Schillen, K.; D'Errico, G.; Morelli, G.; Paduano, L.
Colloidal particles composed of amphiphilic molecules binding gadolinium complexes and peptides as tumor-specific contrast agents in MRI: physico-chemical characterization.
Soft Matter, 5 (2009) 5, 2504 – 2512

Valldor, M.; Sanders, Y.; Schweika, W.
High Spin Frustration in Co Based Swedenborgites
Journal of Physics: Conference Series, 145 (2009), 012076-1 – 012076-6

Valov, I.; Rührup, V.; Klein, R.; Rödel, T.-C.; Stork, A.; Berendts, S.; Dogan, M.; Wiemhöfer, H.-D.; Lerch, M.; Janek, J.
Ionic and electronic conductivity of nitrogen-doped YSZ single crystals
Solid State Ionics, 180 (2009) 1463

van Aert, S.; Verbeeck, J.; Erni, R.; Bals, S.; Luysberg, M.; van Dyck, D.; van Tendeloo, G.
Quantitative atomic resolution mapping using high-angle annular dark field scanning transmission electron microscopy
Ultramicroscopy, 109 (2009) 10, 1236 – 1244

Vavrin, R.; Kohlbrecher, J.; Wilk, A.; Ratajczyk, M.; Lettinga, M. P.; Buitenhuis, J.; Meier, G.
Structure and phase diagram of an adhesive colloidal dispersion under high pressure: A small angle neutron scattering, diffusing wave spectroscopy, and light scattering study
Journal of Chemical Physics, 130 (2009), 154903,

Verberck, B.; Vliegenthart, G. A.; Gompper, G.
Orientational ordering in solid C_{60} fullerene-cubane
Journal of Chemical Physics, 130 (2009), 154510-1 – 154510-14

Vogel, T.; Neuhaus, T.; Bachmann, M.; Janke, W.
Ground-state Properties of Tubelike Flexible Polymers
European Physical Journal E, 30 (2009) 1, 7 – 18

Vogel, T.; Neuhaus, T.; Bachmann, M.; Janke, W.
Thermodynamics of tube like flexible polymers
Physical Review E, 80 (2009) 1, 011802

Volkov, O. Yu.; Divin, Y.; Gubankov, V. N.; Gundareva, I. I.; Pavlovskiy, V. V.
Josephson Admittance Spectroscopy of Log-Periodic Antenna at the Submillimeter Wavelength Range
Journal of Communications Technology and Electronics, 54 (2009) 11, 1310 – 1314

Walter, W.; Boffo, C.; Borlein, M.; Kozielewski, T.; Monkenbusch, M.; Ohl, M.; Paul, A.; Schrauth, B.; Sikler, G.; Tiemann, C.
Design, manufacturing and performance of a pair of superconducting solenoids for a neutron spin-echo spectrometer at the SNS
IEEE Transactions on Nuclear Science, 19 (2009) 3, 1320 – 1323

Waser, R.
Resistive non-volatile memory devices
Microelectronic Engineering, 86 (2009) 7/9, 1925 – 1928

Waser, R.; Dittmann, R.; Staikov, G.; Szot, K.
Redox-based resistive switching memories – nanoionic mechanisms, prospects and challenges
Advanced Materials, 21 (2009) 25/26, 2632

Waser, R.; Valov, I.
Electrochemical reactions in nanoionics towards future resistive switching memories
Journal of the Electrochemical Society, 25 (2009) 6, 431 – 437

Weides, M.
Josephson Junctions with Centred Step and Local Variation of Critical Current Density
IEEE Transactions on Applied Superconductivity, 19 (2009) 3, 689 – 692

Weides, M.; Disch, M.; Kohlstedt, H.; Bürgler, D. E.
Observation of Josephson coupling through an interlayer of antiferromagnetically ordered chromium
European Physical Journal B, 80 (2009) 6, 064508

Weismann, A.; Wenderoth, M.; Lounis, S.; Zahn, P.; Quaas, N.; Ulbrich, R. G.; Dederichs, P. H.; Blügel, S.
Seeing the Fermi-surface in Real Space by Nanoscale Electron Focusing
Science, 323 (2009) 5918, 1190 – 1193

Widmer, R.; Groening, P.; Feuerbacher, M.; Groening, O.
Experimental signatures of spicy local density of states in quasicrystals
Physical Review B, 79 (2009) 10, 104202

Winkler, R. G.; Huang, C. C.
Stress Tensors of Multiparticle Collision Dynamics Fluids
Journal of Chemical Physics, 130 (2009), 074907

Wojciechowski, K.; Brzozowska, A.; Cap, S.; Rzodkiewicz, W.; Gutberlet, T.
Adsorption of azacrown ethers at solid-liquid interface. contact angle and neutron reflectivity study
Applied Surface Science, 256 (2009) 1, 274 – 279

Woodford, S. R.
Conservation of angular momentum and the inverse Faraday effect
Physical Review B, 79 (2009) 21, 212412

Wu, H.; Burnus, T.
Spin and orbital states in $La_{1.5}$ $Sr_{0.5}CoO_4$ studied by electronic structure calculations
Physical Review B, 80 (2009) 8, 081105(R),

Wysocki, A.; Royall, C. P.; Winkler, R. G.; Gompper, G.; Tanaka, H.; van Blaaderen, A.; Löwen, H.
Direct observation of hydrodynamic instabilities in a driven non-uniform colloidal dispersion
Soft Matter, 5 (2009), 1340 – 1344

Xiao, Y.; Su, Y.; Meven, M.; Mittal, R.; Kumar, C. M. N.; Chatterji, T.; Price, S.; Perßon, J.; Kumar, N.; Dhar, S. K.; Thamizhavel, A.; Brückel, T.
Magnetic structure of $EuFe_2As_2$ determined by single-crystal neutron diffraction
Physical Review B, 80 (2009), 174424: 1 – 8

Xiao, Y.; Su, Y.; Mittal, R.; Chatterji, T.; Hansen, T.; Kumar, C. M. N.; Matsuishi, S.; Hosono, H.; Brückel, T.
Magnetic order in the $CaFe_{1-x}Co_xAsF$ (x = 0.00, 0.06, 0.12) superconducting compounds
Physical Review B, 79 (2009), 060504-1 - 060504-4 (R)

Yang, L.; Kügeler, C.; Szot, K.; Rüdiger, A.; Waser, R.
The influence of copper top electrode on the resistive switching effect in TiO_2 thin films studied by conductive atomic force microscopy
Applied Physics Letters, 95 (2009) 1, 013109

Yoon, S.; Dornseiffer, J.; Schneller, T.; Henning, D.; Iwaya, S.; Pithan, C.; Waser, R.
Percolative $BaTiO_3$-Ni composite nanopowders from alkoxide-mediated synthesis
Journal of the European Ceramic Society, 30 (2010), 561 – 567

You, T. S.; Lidin, S.; Gourdon, O.; Wu, Y.; Miller, G. J.
To what extent does the Zintl-Klemm formalism work? The Eu $(Zn_{1-x}Ge_x)_2$ series
Inorganic Chemistry, 48 (2009), 6380 – 6390

Zbiri, M.; Schober, H.; Johnson, M. R.; Rols, S.; Mittal, R.; Su, Y.; Rotter, M.; Johrendt, D.
Ab initio lattice dynamics simulations and inelastic neutron scattering spectra for studying phonons in $BaFe_2As_2$: Effect of structural phase transition, structural relaxation and magnetic ordering
Physical Review B, 79 (2009) 6, 064511

Zhang, Z.; Krishna, N.; Lettinga, M. P.; Vermant, J.; Grelet, E.
Reversible gelation of rod-like viruses grafted with thermoresponsive polymers
Langmuir, 25 (2009) 4, 2437 – 2442

Zhao, Q. T.; Mi, S. B; Jia, C. L.; Urban, C.; Sandow, C.; Habicht, S.; Mantl, S.
Epitaxial growth of $NiSi_2$ induced by sulfur segregation at the $NiSi_t$/Si(100) interface
Journal of Materials Research, 24 (2009) 1, 135139

Zorn, R.
On the evaluation of neutron scattering elastic scan data
Nuclear Instruments and Methods in Physics Research Section A, 603 (2009) 3, 439 – 445

Books and proceedings

Akola, J.; Jones, R. O.
Density functional simulations of phase change materials: disordered phases of $Ge_8Sb_2Te_{11}$ and Ag/In/Sb/Te alloys
European Phase Change and Ovonics Symposium. Proceedings, EPCOS 2009/ed.: M. Wuttig, M. Salinga. – (RWTH Aachen University, 06.09. - 08.09.2009). – S. 57 – 63

Bachmann, M.
Statistical Analysis of Structural Transitions in Small Systems
Proceedings of the 22nd Workshop on Recent Developments in Computer Simulation Studies in Condensed Matter Physics, 23 - 27. Feb. 2009. - Athens, Georgia, USA

Bechthold, P. S.
Galvanomagnetic Transport: from Hall Effect in AMR
IFF Spring School ,Forschungszentrum Jülich

Bihlmayer, G.
Electronic States in Solids
Spintronics – From GMR to Quantum Information; lecture manuscripts of the 40th Spring School 2009/ed.: S. Blügel, D. Bürgler, M. Morgenstern, C. M. Schneider, R. Waser. Jülich, Forschungszentrum, Verlag, 2009. Schriften des Forschungszentrum Jülich. Reihe Schlüsseltechnologien/Key Technologies; 10. 978-3-89336-559-3. S. A1.1 - A1.33

Blügel, S.
Magnetism in Reduced Dimensions
Spintronics – From GMR to Quantum Information; lecture manuscripts of the 40th Spring School 2009/ed.: S. Blügel, D. Bürgler, M. Morgenstern, C. M. Schneider, R. Waser . Jülich, Forschungszentrum, Verlag, 2009. Schriften des Forschungszentrum Jülich. Reihe Schlüsseltechnologien/Key Technologies; 10. 978-3-89336-559-3. S. A3.1 – A3.49 P42

Bringer, A.
Spin-orbit coupling in semiconductor devices
Spintronics – From GMR to Quantum Information; lecture manuscripts of the 40th Spring School 2009/ed.: S. Blügel, D. Bürgler, M. Morgenstern, C. M. Schneider, R. Waser. Jülich, Forschungszentrum, Verlag, 2009. Schriften des Forschungszentrum Jülich. Reihe Schlüsseltechnologien/Key Technologies; 10. 978-3-89336-559-3. S. B5.1 – B5.14

Brückel, T.
International Conference "Polarized Neutrons and Synchrotron X-rays for Magnetism: Book of Abstract": 2 – 5 August 2009, Bonn, Germany, 2009, Jülich, Forschungszentrum.

Brückel, T.; Voigt, J.; Ioffe, A.; Manoshin, S.
Diffractometer for non-equilibrium states of condensed matter
International Conference "Polarized Neutrons and Synchrotron X-rays for Magnetism: Book of Abstract": 2 – 5 August 2009, Bonn, Germany, 2009. – S. 95

Bürgler, D. E.
Spin-transfer torque dynamics
Spintronics – From GMR to Quantum Information; lecture manuscripts of the 40th Spring School 2009/ed.: S. Blügel, D. Bürgler, M. Morgenstern, C. M. Schneider, R. Waser . Jülich, Forschungszentrum, Verlag, 2009. Schriften des Forschungszentrum Jülich. Reihe Schlüsseltechnologien/Key Technologies; 10. 978-3-89336-559-3.

Chatterjee, S.; Schütz, G. M.
Diffusion in a one-dimensional zeolite channel: an analytical and numerical study
Diffusion Fundamentals III/ed.: C. Chmelik, N. Kanellopoulos, J. Kärger, D. Theodorou. – Leipziger Universitätsverlag, Leipzig, 2009. – S. 222 – 234

de Groot, J.; Kentzinger, E.; Voigt, J.; Goukassov, A.; Gillon, B.; Brückel, T.
Magnetization density in $TbMnO_3$ single crystals
International Conference "Polarized Neutrons and Synchrotron X-rays for Magnetism: Book of Abstract": 2 – 5 August 2009, Bonn, Germany, 2009. – S. 120

Disch, S.; Hermann, R.; Sager, W.; Brückel, T.
Not so small angle scattering with polarization analysis: Towards the magnetic form factor of nanoparticles
International Conference "Polarized Neutrons and Synchrotron X-rays for Magnetism: Book of Abstract": 2 – 5 August 2009, Bonn, Germany, 2009. - S. 131

Dressen, J.; Bürgler, D. E.; Grünberg, P.
Magneto-electronics
Technology Guide – Principles, Applications, Trends/ed.: H. J. Bullinger, Springer Heidelberg, Germany (2009). – 978-3-540-88545-0. – S. 88 – 91. – 2009

Dronskowski, R.; Schweika, W.; Brückel, T.; Houben, A.
Advanced nitrides and neutrons: New nitridic itinerant ferromagnets and the high-performance time-of-flight neutron diffractometer POWTEX
Mater. Res. Soc. Symp. Proc
Solid-State Chemistry of Inorganic Materials VII, edited by P. Woodward, J. Mitchell, S. Brock, J. Evans , paper 1148-PP15-01. Volume 1148E, Warrendale, PA, 2009

Fenske, J.; Lott, D.; Mankey, G. J.; Schmidt, W.; Schmalzl, K.; Tartakovkaya, E. V.; Klose, F.; Mulders, A. M.; Schreyer, A.
Investigation of the magnetic spin configuration in thin $Fe_{50}Pt_{50}$-x films with polarized neutron diffraction
International Conference "Polarized Neutrons and Synchrotron X-rays for Magnetism: Book of Abstract": 2 – 5 August 2009, Bonn, Germany, 2009. – 2009. – S. 158

Feuerbacher, M.; Heggen, M.
Metadislocations
Invited chapter in Disklocations in Solids Vol. 16 (30th Annniversary Volume dedicated to Frank Nabarro) Elsevier 2009 / ed.: J. P. Hirth, L. Kubin

Glavic, A.; Voigt, J.; Schubert, J.; Su, Y.
Neutron scattering from $TbMnO_3$ deposited on $YAlO_3$
International Conference "Polarized Neutrons and Synchrotron X-rays for Magnetism: Book of Abstract": 2 – 5 August 2009, Bonn, Germany, 2009. – 2009. – S. 122

Herrero-Martin, J.; Paolasini, L.; Mazzoli, C.; Scagnoli, V.; Mittal, R.; Brückel, T.; Su, Y.
Study of magnetic correlations on the iron pnictide $EuFe_2As_2$ by RXS
International Conference "Polarized Neutrons and Synchrotron X-rays for Magnetism: Book of Abstract": 2 – 5 August 2009, Bonn, Germany, 2009. – S. 73

Hermann, R. P.; Möchel, A.; Claudio Weber, T.
Nuclear inelastic scattering by antimony and tellurium in thermoelectric materials
28th International Conference / 7th European Conference on Thermoelectrics ICT/ECT (2009), 100

Hermann, R. P.; Sergueev, I.; Pelzer, U.; Angst, M.; Schweika, W.; McGuire, M.
Nuclear resonance scattering by ^{57}Fe and ^{151}Eu in $EuFe_2As_2$
International Conference on the Applications of the Mössbauer Effect ICAME 2009, Book of Programme and Abstracts (2009), 58

Ishii, F.
Electronic structures of transition-metal oxides
Spintronics – From GMR to Quantum Information; lecture manuscripts of the 40th Spring School 2009/ed.: S. Blügel, D. Bürgler, M. Morgenstern, C. M. Schneider, R. Waser. Jülich, Forschungszentrum, Verlag, 2009. Schriften des Forschungszentrum Jülich. Reihe Schlüsseltechnologien/Key Technologies; 10. 978-3-89336-559-3. S. A5.1 – A5.16 P42

Josten, E.; Rücker, U.; Brückel, T.
Magnetic correlations in laterally patterned magnetic multilayers
International Conference Polarized Neutrons and Synchrotron X-rays for Magnetism: Book of Abstract: 2 – 5 August 2009, Bonn, Germany, 2009. – S. 161

Kentzinger, E.; Mattauch, S.; Korolkov, D.; Rücker, U.; Ioffe, A.; Toperverg, B.; Brückel, T.
Probing lateral correlations in magnetic nanostructures by polarized neutron scattering under grazing incidence
International Conference: Polarized Neutrons and Synchrotron X-rays for Magnetism. Book of Abstract. Bonn, Germany, 2 – 5 August 2009. – S. 104

Kohara, S.; Tanaka, Y.; Fukuyama, Y.; Yasude, N.; Kim, J.; Murayama, H.; Kimura, S.; Kato, K.; Moritomo, Y.; Matsunaga, T.; Kojima, R.; Yamada, N.; Tanaka, H.; Ohshima, T.; Akola, J.; Jones, R. O.; Takata, M.
The amorphous structural basis of the rapid phase-change mechanism in DVD materials
Proceedings E\PCOS 2009, European Phase Change and Ovonics Symposium/ed.: M. Wuttig, M. Salinga (RWTH Aachen University, 2008). – S. 75 – 82

Kügeler, C.; Rosezin, R.; Weng, R.; Menzel, S.; Klopstra, B.; Böttger, U.; Waser, R.
Fast resistive switching in WO_3 thin films for non-volatile memory applications
Proceedings of the 9th IEEE Nanotechnology Conference, 2009, Genova, Switzerland. – S. 1102 – 1105

Kumar, C. M. N.; Xiao, Y.; Su, Y.; Perßon, J.; Brückel, T.
Magnetic structure of hexagonal $DyMnO_3$
International Conference :"Polarized Neutrons and Synchrotron X-rays for Magnetism: Book of Abstract": 2 – 5 August 2009, Bonn, Germany, 2009. – S. 123

Ležaić , M.
Introduction to Multiferroics
Spintronics – From GMR to Quantum Information; lecture manuscripts of the 40th Spring School 2009/ed.: S. Blügel, D. Bürgler, M. Morgenstern, C. M. Schneider, R. Waser . Jülich, Forschungszentrum, Verlag, 2009. Schriften des Forschungszentrum Jülich. Reihe Schlüsseltechnologien/Key Technologies; 10. 978-3-89336-559-3. S. A6.1 – A6.22

Liebsch, A.
Highly Correlated Electron Materials: Dynamical Mean Field Theory
Spintronics – From GMR to Quantum Information; lecture manuscripts of the 40th Spring School 2009/ed.: S. Blügel, D. Bürgler, M. Morgenstern, C. M. Schneider, R. Waser . Jülich, Forschungszentrum, Verlag, 2009. Schriften des Forschungszentrum Jülich. Reihe Schlüsseltechnologien/Key Technologies; 10. 978-3-89336-559-3. S. A4.1 – A4.25

Luysberg, M.; Heidelmann, M.; Houben, L.; Boese, M.; Heeg, T.; Roeckerath, M.; Schubert, J.
Atomic scale compositions across $DyScO_3/SrTiO_3$ interfaces
Proceedings of the Microscopy Conference, Graz, 30. August – 04. September 2009 Vol. 3 Materias Science,/ed.: F. Hofer, P. Pölt, W. Grogger, (2009)

Mattauch, S.; Rücker, U.; Fracassi, V.; Schmitz, R.; Daemen, J.; Babcock, E.; Ioffe, A.; Brückel, T.
MARIA – The new high-intensity polarized neutron reflectometer of JCNS
International Conference "Polarized Neutrons and Synchrotron X-rays for Magnetism: Book of Abstract" : 2 – 5 August 2009, Bonn, 2009. – S. 106

Mavropoulos, P.
Spin relaxation in nonmagnetic metals and semiconductors
Spintronics – From GMR to Quantum Information; lecture manuscripts of the 40th Spring School 2009/ed.: S. Blügel, D. Bürgler, M. Morgenstern, C. M. Schneider, R. Waser . Jülich, Forschungszentrum, Verlag, 2009. Schriften des Forschungszentrum Jülich. Reihe Schlüsseltechnologien/Key Technologies; 10. 978-3-89336-559-3. S. B6.1 – B6.28

Meier, M.; Rosezin, R.; Gilles, S.; Rüdiger, A.; Kügeler, C.; Waser, R.
A multilayer RRAM nanoarchitecture with resistively switching Ag-doped spin-on glass
Proceedings IEEE: International Conference on Ultamate Integration on Silicon (ULIS). – 2009. – S. 147 – 150

Meyer, C.
Quantum computing with semiconductor quantum dots
Spintronics – From GMR to Quantum Information; lecture manuscripts of the 40th Spring School 2009/ed.: S. Blügel, D. Bürgler, M. Morgenstern, C. M. Schneider, R. Waser . Jülich, Forschungszentrum, Verlag, 2009. Schriften des Forschungszentrum Jülich. Reihe Schlüsseltechnologien/Key Technologies; 10. 978-3-89336-559-3. S. E2-1 – E2-22

Mokrousov, Y.
Anomalous Hall Effect
Spintronics – From GMR to Quantum Information; lecture manuscripts of the 40th Spring School 2009/ed.: S. Blügel, D. Bürgler, M. Morgenstern, C. M. Schneider, R. Waser . Jülich, Forschungszentrum, Verlag, 2009. Schriften des Forschungszentrum Jülich. Reihe Schlüsseltechnologien/Key Technologies; 10. 978-3-89336-559-3. S. C2.1 – C2.34

Müller, M.
Spin filter
Spintronics – From GMR to Quantum Information; lecture manuscripts of the 40th Spring School 2009/ed.: S. Blügel, D. Bürgler, M. Morgenstern, C. M. Schneider, R. Waser. Jülich, Forschungszentrum, Verlag, 2009. Schriften des Forschungszentrum Jülich. Reihe Schlüsseltechnologien/Key Technologies; 10. 978-3-89336-559-3. S. B4.1 – B4.18

Nauenheim, C.; Kügeler, C.; Trellenkamp, S.; Rüdiger, A.; Waser, R.
Phenomenological considerations of resistively switching TiO_2 in nano crossbar arrays
Proceedings of the 10th International Conference on Ultimate Itegration on Silicon, March 18-20, 2009, Aachen. – S. 135 – 138

Oberdisse, J.; Pyckhout-Hintzen, W.; Straube, E.
Structure determination of polymer nanocomposites by small-angle scattering
Recent Advances in Polymer Nanocomposites/ed.: S. Thomas, G. E. Zaikov, S. V. Valsaraj. – Koninklijke Brill NV, VSP, Leiden, The Netherlands, 2009. – 978-9-004-16726-1. – S. 397 – 438

Ozdogan, K.; Sasioglu, E.; Galanakis, I.
Fundamentals of Half-Metallic Full-Heusler Alloys
Spintronics: Materials, Applications and Devices/ed.: G. C. Lombardi, G. E. Bianchi, Nova Science Publishers (2009), ISBN 978-1-60456-734-2

Pfuhl, E.; Voigt, J.; Brückel, T.
Proximity effects in Er/Tb multilayers
International Conference: Polarized Neutrons and Synchrotron X-rays for Magnetism: Book of Abstract; Bonn, Germany, 2 – 5 August 2009. – S. 166

Rapp, Ö.; Andersson, M.; Feuerbacher, M.
Anomalous transport in rhombohedral Mg_2Ai_3
Journal of Physics: Conference Series. Vol.150 (2009) S. 022070

Rücker, U.; Toperverg, B.; Ott, F.; Brückel, T.
Zeeman splitting revisited – polarized neutron reflectivity in high magnetic fields
International Conference "Polarized Neutrons and Synchrotron X-rays for Magnetism: Book of Abstract"; 2 – 5 August 2009, Bonn, Germany, 2009. – S. 167

Schumacher, D.; Mattauch, S.; Rücker, U.; Brückel, T.
2-Dimensional magnetism of Fe-Monolayers in Pd
International Conference : "Polarized Neutrons and Synchrotron X-rays for Magnetism": Book of Abstract, 2 – 5 August 2009, Bonn, Germany, 2009. – S. 168

Schweika, W.
Multi-detector polarization analysis development for diffuse magnetic scattering by single crystals
International Conference "Polarized Neutrons and Synchrotron X-rays for Magnetism: Book of Abstract" : 2 – 5 August 2009, Bonn, Germany, 2009. – 2009. – S. 107

Staikov, G.
Electrocrystallization
in: Encyclopedia of Electrochemical Power Sources, Vol. 2, Eds. J. Garche, C. Dyer, P. Moseley, Z. Ogumi, D. Rand and B. Scrosati, Elsevier, Amsterdam, (2009) 32-40

Su, Y.; Schweika, W.; Mittal, R.; Harbott, P.; Küssel, E.; Bussmann, K.; Gossen, F.; Schmitz, B.; Skrobucha, M.; Möller, R.; Wagener, M.; Drochner, M.; Kleines, H.; Ioffe, A.; Brückel, T.
DNS-Diffuse neutron scattering with polarization analysis
International Conference "Polarized Neutrons and Synchrotron X-rays for Magnetism: Book of Abstract" : 2 – 5 August 2009, Bonn, 2009. – S. 110

Voigt, J.; Babcock, E.; Brückel, T.
Polarisation analysis for thermal time-of-flight spectroscopy
International Conference "Polarized Neutrons and Synchrotron X-rays for Magnetism: Book of Abstract": 2 – 5 August 2009, Bonn, 2009. – S. 113

Wortmann, D.
Theory of tunneling magneto resistance
Spintronics – From GMR to Quantum Information; lecture manuscripts of the 40th Spring School 2009/ed.: S. Blügel, D. Bürgler, M. Morgenstern, C. M. Schneider, R. Waser. Jülich, Forschungszentrum, Verlag, 2009. Schriften des Forschungszentrum Jülich. Reihe Schlüsseltechnologien/Key Technologies; 10. 978-3-89336-559-3. S. B2.1 – B2.22

Xiao, Y.; Su, Y.; Kumar, C. M. N.; Li, H. F.; Mittal, R.; Perßon, J.; Senyshyn, A.; Gross, K.; Brückel, T.
Magnetic structure and orbital odering in $KCrF_3$
International Conference on "Polarized Neutrons and Synchrotron X-rays for Magnetism" Book of Abstract; 2 – 5 August 2009, Bonn, Germany, 2009. – S. 148

Ph.D. theses

Brodeck, M.
A study of polymer melts combining MD simulations and neutron scattering experiments
Forschungszentrum Jülich, Institut für Festkörperforschung, 2009
University of Münster, 2009

Clemens, S.
Template-Controlled Integration and Characterization of Bottom-Up Grown Ferroelectric Nanoislands
Forschungszentrum Jülich, Institut für Festkörperforschung, 2009
RWTH Aachen University, 2009

Gliga, S.
Ultrafast vortex core dynamics investigated by finite-element micromagnetic simulations
Forschungszentrum Jülich, Institut für Festkörperforschung, 2009
University of Duisburg-Essen

Jeong, D.S.
Resistive switching in Pt/TiO_2/Pt
Forschungszentrum Jülich, Institut für Festkörperforschung, 2009
Schriften des Forschungszentrums Jülich. Reihe Information/ Information; 6; 978-3-89336-579
RWTH Aachen University, 2009

Kaiser, A.
Magnetization dynamics in magnetically coupled heterostructures
Forschungszentrum Jülich, Institut für Festkörperforschung, 2009
University of Duisburg-Essen

Kever, T.
Resistive Switching in Cu: TCNQ Thin Film Devices
Forschungszentrum Jülich, Institut für Festkörperforschung, 2009
RWTH Aachen University, 2009

Meier, M.
Entwicklung einer Nanotechnologie-Plattform für die Herstellung Crossbar-basierter Speicherarchitekturen
Forschungszentrum Jülich, Institut für Festkörperforschung, 2009
Schriften des Forschungszentrums Jülich. Reihe Schlüsseltechnologien/Key Technologies; 12; 978-3-89336-598
RWTH Aachen University, 2009

Röhrig, S.
Electromechanical force microscopy and tip-enhanced raman spectroscopy on polar oxide nanoparticles
Forschungszentrum Jülich, Institut für Festkörperforschung, 2009
RWTH Aachen University, 2009

Schindler, C.
Resistive switching in electrochemical metallization memory cells
Forschungszentrum Jülich, Institut für Festkörperforschung, 2009
RWTH Aachen University, 2009

Diploma theses

Hirschfeld, J.
Tomographic Problems in the Diagnostics of Fuel Cell Stacks
Forschungszentrum Jülich, 2009
ISSN 0944-2952

Josten, E.
Magnetische Korrelationen in lateral strukturierten Fe/Cr-Schichtsystemen
Forschungszentrum Jülich, Institut für Festkörperforschung, 2009
Bonn University, 2009

Krebs, C.
Schnelle Pulsmessungen an elektrochemischen Metallisierungsspeicherzellen
Forschungszentrum Jülich, Institut für Festkörperforschung, 2009
RWTH Aachen University, 2009

Meyer, M.
Strukturelle Chrarakterisierung von Polymer-beschichteten SiO2-Nanopartikeln in Lösung mittels Kleinwinkel-Streuung
Forschungszentrum Jülich, Institut für Festkörperforschung, 2009
RWTH Aachen University, 2009

Conferences and schools

March 2 – 6	Winter School Multiscale Simulation Methods in Molecular Sciences Forschungszentrum Jülich, Germany
March 9 – 20	40th IFF Spring School Spintronics – From GMR to Quantum Information Forschungszentrum Jülich, Germany
March 18 – 20	MESOSOFT Mesoscale Simulations of Soft Matter Out of Equilibrium Forschungszentrum Jülich, Germany
August 2 – 5	PNSXM 2009 Polarized Neutrons and Synchrotron X-rays for Magnetism 2009 Gustav-Stresemann-Institut Bonn, Germany
September 7 – 18	13th JCNS Laboratory Course – Neutron Scattering Forschungszentrum Jülich, Jülich and Garching, Germany
October 5 – 8	JCNS Workshop 2009 Trends and Perspectives in Neutron Scattering on Soft Matter Tutzing, Germany
November 10 – 13	Jülich Soft Matter Days 2009 Gustav-Stresemann-Institut Bonn, Germany

Kolloquia

February 13	Veronica Vildosola, Argentina CNEA, Buenos Aires Electronic properties of the new high-Tc Fe-based superconductors
May 8	Wulf Wulfhekel Universität Karlsruhe, Germany Inelastic scanning tunnelling spectroscopy: A new tool to probe magnetic excitations of nano-scale magnets
May 11	Knut Urban IFF, Forschungszentrum Jülich, Germany Das neue Paradigma der Elektronenmikroskopie – Materialwissenschaft an den Grenzen der Optik
May 15	Klaus Mecke Universität Erlangen-Nürnberg, Germany Fluids on the nanoscale
May 20	Isaac B. Bersuker University Texas Austin, USA The Jahn-Teller Effect: Novel Findings and Applications
May 29	Daniel Khomskii Universität zu Köln, Germany Spontaneous currents and electronic polarization in Mott insulators: are electrons really localized?
June 26	Ernst Bauer Arizona State University, USA Spin-polarized low energy electron microscopy of ultrathin ferromagnetic films.
July 3	Steve Nagler Oak Ridge National Laboratory, USA Superconductivity and Magnetism in the Iron Age
July 10	Peter Entel Universität Duisburg-Essen, Germany Simulating complex functional magnetic materials on supercomputers
November 6	Michael Bachmann IFF, Forschungszentrum Jülich, Germany Challenges in Computational Biology
November 20	Martin Weinelt Max-Born-Institut Berlin, Germany Ultrafast spin-dependent carrier dynamics in ferromagnetic thin films

Institute of Solid State Research (IFF)

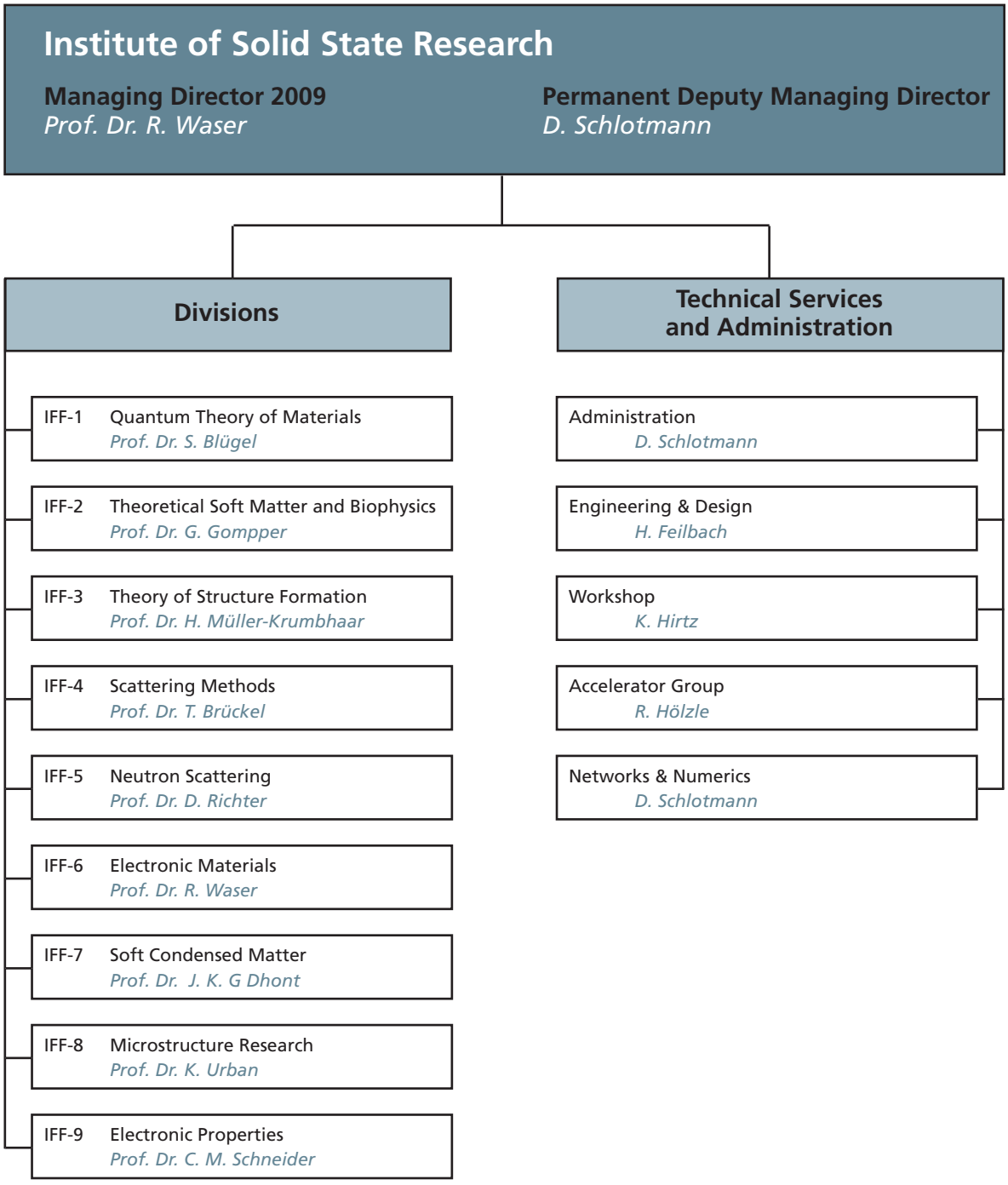

Personnel

Staff members (centrally financial)	
• Scientific Staff	198
Including those funded externally	*44*
• Technical Staff	107
Including those funded externally	*55*
Staff members of service-groups	44
Administrations including Secretaries	20
Graduate students	76
Including those funded externally	*24*
Diploma students	40
Including those funded externally	*7*
Trainees	26
Guests Scientists staying for two weeks or longer	149
Invited lectures	147
Scientists on leave	55

Scientific advisory board

Joint Scientific Council
The joint Scientific Council of the IFF and IBN advises the Institute and the committees of Research Centre Jülich and functions as a supervisory board. The members of the council are leading scientists from research and industry. The council was appointed in 2004 for five years.

Prof. Dr. Georg Bednorz
IBM Research GmbH, Rüschlikon (CH)

Prof. Dr. Wim J. Briels
University Twente, AE Enschede (NL)

Dr. Kurt Clausen
Paul Scherrer Institut, Villingen (CH)

Dr. Manfred Horstmann
AMD Saxony LLC & Co. KG, Dresden (D)

Prof. Dr. Klaus Kern
Max-Planck-Institut, Stuttgart (D)

Prof. Dr. Jürgen Kirschner
Max-Planck-Institut, Halle (D)

Prof. Dr. Beate Klösgen
University of Southern Denmark, Odense (DK)

Prof. Dr. Hilbert von Löhneysen
Forschungszentrum Karlsruhe (D)

Prof. Dr. Werner Press (Chairman)
Christian Alberts-Universität Kiel (D)

Prof. Dr. Friederike Schmid
Universität Bielefeld (D)

Prof. Dr. Herbert Schöller
RWTH Aachen (D)

Prof. Dr. Clivia M. Sotomayor-Torres
University College Cork (IRE)

Prof. Dr. Hans-Rainer Trebin
Universität Stuttgart (D)

Prof. Dr. Gero Vogl
Universität Wien (A)

Scientists

Adam, Roman
Electronic Properties

Allgaier, Jürgen
Neutron Scattering

Al-Zubi, Ali Khlaif Abdullah
Quantum Theory of Materials/Institute for Advanced Simulation 1

Angst, Niklaus Manuel
Scattering Methods

Appavou, Marie-Sousai Deveramban
Jülich Centre for Neutron Science

Arend, Nikolas
Jülich Centre for Neutron Science

Atodiresei, Nicolae
Quantum Theory of Materials/Institute for Advanced Simulation 1

Auth, Thorsten
Theoretical Soft Matter and Biophysics

Babcock, Earl
Jülich Centre for Neutron Science

Bachmann, Michael
Theoretical Soft Matter and Biophysics/Institute for Advanced Simulation 2

Baumgarten, Lutz
Electronic Properties

Baumgärtner, Artur
Theoretical Soft Matter and Biophysics/Institute for Advanced Simulation 2

Bechthold, Paul-Siegfried
Electronic Properties

Beigmohamadi, Maryam
Microstructure Research

Belhadji, Brahim
Theory of Structure Formation

Belushkin, Maxim
Theoretical Soft Matter and Biophysics

Biehl, Ralf
Neutron Scattering

Bihlmayer, Gustav
Quantum Theory of Materials/Institute for Advanced Simulation 1

Blügel, Stefan
Quantum Theory of Materials

Borghols, Wouter Joannes Henrik
Jülich Centre for Neutron Science

Botar, Bogdan
Electronic Properties

Brener, Efim
Theory of Structure Formation

Bruchhaus, Rainer
Electronic Materials

Brückel, Thomas
Scattering Methods

Buitenhuis, Johan
Soft Condensed Matter

Bürgler, Daniel-Emil
Electronic Properties

Burnus, Tobias Patrick
Quantum Theory of Materials/Institute for Advanced Simulation 1

Busch, Peter
Jülich Centre for Neutron Science

Caciuc, Vasile
Quantum Theory of Materials

Carsughi, Flavio
Neutron Scattering

Chatterjee, Sakuntala
Theoretical Soft Matter and Biophysics

Chatterji, Tapan Kumar
Jülich Centre for Neutron Science

Chelakkot Govindalayam, Raghunath
Theoretical Soft Matter and Biophysics

Chelaru, Liviu Ionut
Electronic Properties

Cherstvy, Andrey
Theoretical Soft Matter and Biophysics

Claver-Cabrero, Ana
Neutron Scattering

Conrad, Harald
Scattering Methods

Contreras Aburto, Claudio
Soft Condensed Matter

Costi, Theodoulos
Theory of Structure Formation/Institute for Advanced Simulation 3

Cramm, Stefan
Electronic Properties

Dahbi, Louisa
Neutron Scattering

Das, Sourin
Theory of Structure Formation

de Souza, Nicolas Raphäel Louis
Jülich Centre for Neutron Science

Deac-Renner, Alina Maria
Electronic Properties

Dhont, Jan-Karel
Soft Condensed Matter

Dittmann, Regina
Electronic Materials

Divin, Yuri
Microstructure Research

Ebert, Philipp-Georg
Microstructure Research

Elgeti, Jens
Theoretical Soft Matter and Biophysics

Faley, Mikhail
Microstructure Research

Feuerbacher, Michael
Microstructure Research

Fornleitner, Julia
Theoretical Soft Matter and Biophysics

Freimuth, Frank
Quantum Theory of Materials/Institute for Advanced Simulation 1

Friedrich, Christoph
Quantum Theory of Materials

Frielinghaus, Henrich
Jülich Centre for Neutron Science

Frielinghaus, Xiuli
Neutron Scattering

Gliga, Seastian
Electronic Properties

Goerigk, Günter
Jülich Centre for Neutron Science

Gögelein, Christoph
Soft Condensed Matter

Gompper, Gerhard
Theoretical Soft Matter and Biophysics

Gorelov, Evgeny
Theory of Structure Formation

Götze, Ingo Oliver
Theoretical Soft Matter and Biophysics

Greenall, Martin James
Theoretical Soft Matter and Biophysics

Grushko, Benjamin
Microstructure Research

Guo, Xin
Electronic Materials

Gupta, Sudipta
Neutron Scattering

Gutberlet, Thomas Werner
Jülich Centre for Neutron Science

Harbott, Peter
Scattering Methods

Head, David Andrew
Theoretical Soft Matter and Biophysics

Heggen, Marc
Microstructure Research

Heide, Marcus
Quantum Theory of Materials

Heilmann, David Bernhard
Theory of Structure Formation/Institute for Advanced Simulation 3

Hermann, Raphaël
Scattering Methods

Hertel, Riccardo
Electronic Properties

Hoffmann-Eifert, Susanne
Electronic Materials

Holderer, Olaf
Jülich Centre for Neutron Science

Holmqvist, Jan Peter
Soft Condensed Matter

Houben, Lothar
Microstructure Research

Huang, Chien-Cheng
Theoretical Soft Matter and Biophysics

Hübner, Eike Gerhard
Neutron Scattering

Inoue, Rintaro
Neutron Scattering

Ioffe, Alexander
Jülich Centre for Neutron Science

Ji, Shichen
Theoretical Soft Matter and Biophysics

Jia, Chunlin
Microstructure Research

Jin, Lei
Microstructure Research

Kakay, Attila
Electronic Properties

Kang, Kyong Ok
Soft condensed Matter

Karthäuser, Silvia
Electronic Materials

Kentzinger, Emmanuel
Scattering Methods

Koch, Erik Eduard
Quantum Theory of Materials/Institute for Advanced Simulation 1

Kögerler, Prof. Dr. Paul
Electronic Properties

Kohlstedt, Herbert Hermann
Electronic Materials

Korolkov, Denis
Jülich Centre for Neutron Science

Kriegs, Hartmut Oskar Kurt
Soft Condensed Matter

Krug, Ingo Peter
Electronic Properties

Krutyeva, Margarita
Neutron Scattering

Kügeler, Carsten
Electronic Materials

Kundu, Shyamal Kumar
Neutron Scattering

Kusmin, André
Neutron Scattering

Lang, Peter Robert
Soft Condensed Matter

Lehndorff, Ronald
Electronic Properties

Lentzen, Markus
Microstructure Research

Lettinga, Minne Paul
Soft Condensed Matter

Ležaić, Marjana
Quantum Theory of Materials

Liebsch, Ansgar
Quantum Theory of Materials

Lo Celso, Fabrizio
Neutron Scattering

Lounis, Samir
Quantum Theory of Materials

Lustfeld, Hans
Quantum Theory of Materials

Luysberg, Martina
Microstructure Research

Lyatti, Matvey
Microstructure Research

Malaestean, Iurie Leonid
Electronic Properties

Mattauch, Stefan Hans Josef
Jülich Centre for Neutron Science

Matthes, Frank
Electronic Properties

Mavropoulos, Phivos
Quantum Theory of Materials/Institute for Advanced Simulation 1

Meier, Gerhard
Soft Condensed Matter

Menke, Tobias
Electronic Materials

Meuffels, Paul
Electronic Materials

Meyer, Carola
Electronic Properties

Mi, Shaobo
Microstructure Research

Mittal, Ranjan
Jülich Centre for Neutron Science

Mokrousov, Yuriy
Quantum Theory of Materials/Institute for Advanced Simulation 1

Monkenbusch, Michael
Neutron Scattering

Müller, Martina
Electronic Properties

Müller-Krumbhaar, Heiner
Theory of Structure Formation

Nägele, Gerhard
Soft Condensed Matter

Nauenheim, Christian
Electronic Materials

Ohl, Michael
Jülich Centre for Neutron Science

Pandian, Ramanathaswamy
Electronic Materials

Pavarini, Eva
Theory of Structure Formation/Institute for Advanced Simulation 3

Peltomäki, Matti Paavo Johannes
Theoretical Soft Matter and Biophysics

Persson, Bo
Quantum Theory of Materials

Perßon, Jörg
Scattering Methods

Petraru, Adrian Ion
Electronic Materials

Pilipenko, Denis
Theory of Structure Formation

Pipich, Vitaliy
Jülich Centre for Neutron Science

Pithan, Christian
Electronic Materials

Plucinski, Lukasz
Electronic Properties

Polyakov, Pavel
Soft Condensed Matter

Poppe, Ulrich
Microstructure Research

Pyckhout-Hintzen, Wim
Neutron Scattering

Radulescu, Aurel
Jülich Centre for Neutron Science

Reigh, Shang Yik
Theoretical Soft Matter and Biophysics

Reiners, Marcel
Electronic Materials

Richter, Dieter
Neutron Scattering

Ripoll Hernando, Maria Soledad
Theoretical Soft Matter and Biophysics

Rücker, Ulrich
Scattering Methods

Rushchanskii, Konstantin
Quantum Theory of Materials

Sager, Wiebke
Soft Condensed Matter

Saha, Debasish
Neutron Scattering

Saptsov, Roman
Theory of Structure Formation

Sasioglu, Ersoy
Quantum Theory of Materials

Schiller, Ulf Daniel
Theoretical Soft Matter and Biophysics

Schmalzl, Karin Elisabeth
Jülich Centre for Neutron Science

Schmidt, Wolfgang
Jülich Centre for Neutron Science

Schneider, Claus Michael
Electronic Properties

Schneider, Gerald-Johannes
Jülich Centre for Neutron Science

Schrader, Tobias E.
Jülich Centre for Neutron Science

Schroeder, Herbert
Electronic Materials

Schütz, Gunter-Markus
Theoretical Soft Matter and Biophysics

Schwahn, Dietmar
Neutron Scattering

Schweika, Werner
Scattering Methods

Seemann, Klaus Michael
Electronic Properties

Singh, Sunil Pratap
Theoretical Soft Matter and Biophysics

Slipukhina, Ivetta
Quantum Theory of Materials

Staikov, Georgi Tzvetanov
Electronic Materials

Stellbrink, Jörg
Neutron Scattering

Stiakakis, Emmanuel Ioannis
Soft Condensed Matter

Su, Yixi
Jülich Centre for Neutron Science

Szot, Krzysztof
Electronic Materials

Tessendorf, Renate
Neutron Scattering

Thust, Andreas
Microstructure Research

Tillmann, Karsten
Microstructure Research

Tsukamoto, Shigeru
Quantum Theory of Materials/Institute for Advanced Simulation 1

Urban, Knut
Microstructure Research

Valov, Ilia
Electronic Materials

Vliegenthart, Gerard Adriaan
Theoretical Soft Matter and Biophysics/Institute for Advanced Simulation 2

Vogel, Thomas
Theoretical Soft Matter and Biophysics/Institute for Advanced Simulation 2

Voigt, Jörg Jakob
Jülich Centre for Neutron Science

Waser, Rainer
Electronic Materials

Wegewijs, Maarten Rolf
Theory of Structure Formation

Weides, Martin Peter
Electronic Materials

Wiegand, Simone
Soft Condensed Matter

Wiemann, Carsten
Electronic Properties

Willner, Lutz
Neutron Scattering

Winkler, Roland
Theoretical Soft Matter and Biophysics/Institute for Advanced Simulation 2

Wischnewski, Andreas
Neutron Scattering

Wortmann, Daniel
Quantum Theory of Materials/Institute for Advanced Simulation 1

Wuttke, Joachim
Jülich Centre for Neutron Science

Xiao, Yinguo
Scattering Methods

Yan, Ming
Electronic Properties

Yang, Mingcheng
Theoretical Soft Matter and Biophysics

Yang, Yingzi
Theoretical Soft Matter and Biophysics

Zamponi, Michaela
Jülich Centre for Neutron Science

Zeller, Rudolf
Theory of Structure Formation/Institute for Advanced Simulation 3

Zhang, Hongbin
Quantum Theory of Materials/Institute for Advanced Simulation 1

Zhang, Jing
Soft Condensed Matter

Zlatic, Veljko
Theory of Structure Formation/Institute for Advanced Simulation 3

Zorn, Reiner
Neutron Scattering

Graduate students

Al-Zubi, Ali
Quantum Theory of Materials

Arlt, Bastian
Soft Condensed Matter

Bauer, David Siegfried Georg
Quantum Theory of Materials/Institute for Advanced Simulation 1

Bauer Pereira, Paula
Scattering Methods

Baumeister, Paul Ferdinand
Quantum Theory of Materials/Institute for Advanced Simulation 1

Bessas, Dimitrios
Scattering Methods

Betzinger, Markus
Quantum Theory of Materials/Institute for Advanced Simulation 1

Brodeck, Martin
Neutron Scattering

Chogondahalli Muniraju, Naveen Kumar
Scattering Methods

Claudio Weber, Tania
Scattering Methods

de Groot, Joost
Scattering Methods

Disch, Sabrina
Scattering Methods

Fleck, Michael
Theory of Structure Formation

Flesch, Andreas
Theory of Structure Formation/Institute for Advanced Simulation 3

Freimuth, Frank
Quantum Theory of Materials

Fu, Zhendong
Scattering Methods

Gerstl, Christine Ilona
Neutron Scattering

Gierlich, Andreas Gottfried
Quantum Theory of Materials/Institute for Advanced Simulation 1

Glavic, Artur Gregor
Scattering Methods

Gliga, Sebastian
Electronic Properties

Goß, Karin
Electronic Properties

Gottschlich, Michael
Scattering Methods

Große, Christoph
Electronic Materials

Heers, Swantje
Quantum Theory of Materials/Institute for Advanced Simulation 1

Heidelmann, Markus
Microstructure Research

Heinen, Marco
Soft Condensed Matter

Herdt, Alexej
Electronic Properties

Hermes, Christoph Rudolf
Electronic Materials

Hirschfeld, Julian Arndt
Quantum Theory of Materials/Institute for Advanced Simulation 1

Hüter, Claas
Theory of Structure Formation

Josten, Elisabeth
Scattering Methods

July, Christoph
Soft Condensed Matter

Kerscher, Michael
Neutron Scattering

Kowalzik, Peter
Electronic Materials

Lennartz, Maria Christina
Electronic Materials

Lenser, Christian
Electronic Materials

Lorenz, Boris
Quantum Theory of Materials

Lüsebrink, Daniel Alexander
Theoretical Soft Matter and Biophysics

Manheller, Marcel
Electronic Materials

Marx, Kristian
Theoretical Soft-Matter and Biophysics

Meier, Matthias
Electronic Materials

Menke, Tobias
Electronic Materials

Mennig, Martin Julius
Electronic Properties

Meyer, Mathias
Neutron Scattering

Möchel, Anne
Scattering Methods

Morgan, Caitlin Dunne
Electronic Properties

Münstermann, Ruth Christine
Electronic Materials

Nauenheim, Christian
Electronic Materials

Nusser, Klaus Lothar Josef
Neutron Scattering

Park, Chan-woo
Electronic Materials

Popova, Darya
Quantum Theory of Materials

Price, Stephen
Scattering Methods

Rahmanizadeh, Kourosh
Theory of Structure Formation

Reckermann, Felix David
Theory of Structure Formation

Rosezin, Roland Daniel
Electronic Materials

Schlipf, Martin Ulrich
Quantum Theory of Materials

Schumacher, Daniel
Scattering Methods

Shanmugavadivelu, Gopinath
Soft Condensed Matter

Shen, Wan
Electronic Materials

Sluka, Volker
Electronic Properties

Soltow, Alexander
Electronic Materials

Soni, Rohit
Electronic Materials

Spudat, Christian
Electronic Properties

Steffens, Lars
Electronic Materials

Taslimi, Farzaneh
Theoretical Soft Matter and Biophysics/Institute for Advanced Simulation 2

Thieß, Alexander Reinhold
Quantum Theory of Materials/Institute for Advanced Simulation 1

Tomczyk, Karolina Renata
Soft Condensed Matter

Tranca, Ionut Claudiu
Theory of Structure Formation

Tsigkri, Angeliki
Soft Condensed Matter

Weber, Dieter
Microstructure Research

Weidenbach, Marc
Microstructure Research

Wenig, Robert
Electronic Materials

Wicklein, Sebastian
Electronic Materials

Wu, Bin
Theoretical Soft Matter and Biophysics/Institute for Advanced Simulation 2

Yang, Lin
Electronic Materials

Yang, Yingzi
Theoretical Soft-Matter and Biophysics

Technical staff

Bernard, Norbert Josef
Design/Workshop

Bickmann, Konrad
Electronic Properties

Bläsen, Franz
Networks and Numerical Methods

Bongartz, Dieter
Networks and Numerical Methods

Borowski, René Michael
Electronic Materials

Both, Sabrina-Aloisia
Networks and Numerical Methods

Braun, Waldemar
Design/Workshop

Bremen, Arnd
Design/Workshop

Bünten, Ulrich
Neutron Scattering

Bussmann, Klaus Max
Scattering Methods

Croonenbroeck, Daniel Andreas
Electronic Properties

Cüppers, Tobias
Scattering Methods

de Waal, Sylvia-Maria
Soft Condensed Matter

Doghmi, Jaouad
Networks and Numerical Methods

Emmerich, Hans-Matthias
Design/Workshop

Enns, Andreas
Design/Workshop

Erven, Andreas
Jülich Centre for Neutron Science

Esser, Heinz-Peter
Design/Workshop

Feilbach, Herbert
Design/Workshop

Felder, Christian
Networks and Numerical Methods

Friedrich, Jochen
Electronic Materials

Funk-Kath, Ursula
Networks and Numerical Methods

Gebauer, Manfred
Electronic Materials

Gehlhaar, Reimund Werner
Design/Workshop

Gerst, Marcel
Electronic Materials

Gödel, Marco
Jülich Centre for Neutron Science

Graf, Karl-Heinz
Microstructure Research

Gülak, Fatma
Networks and Numerical Methods

Gurzi, Dennis
Jülich Centre for Neutron Science

Hahn, Christoph
Networks and Numerical Methods

Haselier, Johann
Electronic Materials

Heiderich, Manfred
Neutron Scattering

Heinen, Josef
Networks and Numerical Methods

Henkel, Dorothea
Networks and Numerical Methods

Herrmann, Aileen
Design/Workshop

Hiller, Peter
Scattering Methods

Hintzen, Maria Elisabeth
Neutron Scattering

Hirtz, Kurt
Design/Workshop

Hoffmann, Hans-Jürgen
Soft Condensed Matter

Horriar-Esser, Christel
Scattering Methods

Jansen, Thomas
Electronic Properties

John, Holger
Electronic Materials

Johnen, Karl-Heinz
Design/Workshop

Jungbluth, Heinrich
Scattering Methods

Kinzel, Gernot
Networks and Numerical Methods

Klein, Horst
Administration

Kluck, Günther
Neutron Scattering

Köhne, Franz-Josef
Electronic Properties

Kohnke, Thomas
Jülich Centre for Neutron Science

Korres, Daniela
Design/Workshop

Kozielewski, Tadeusz
Jülich Centre for Neutron Science

Krings, Thorsten
Scattering Methods

Küpper, Bernhard
Electronic Properties

Küppers, Ralf
Neutron Scattering

Kusche, Harald
Jülich Centre for Neutron Science

Lauer, Jürgen
Electronic Properties

Leuchtenberg, Anton
Design/Workshop

Lingenbach, Peter Josef
Design/Workshop

Lipfert, Frederik Nino Julien
Neutron Scattering

Lipp, Alexander
Design/Workshop

Lumma, Nils Friedemann
Design/Workshop

Makovicka, Cerstin Renate
Electronic Materials

Matulewski, Anton
Design/Workshop

Meertens, Doris
Microstructure Research

Nebel, Andreas Fabian
Jülich Centre for Neutron Science

Nguyen, Vu-Thanh
Neutron Scattering

Olefs, Bodo-August
Networks and Numerical Methods

Ossovyi, Vladimir
Jülich Centre for Neutron Science

Peters, Alexander
Networks and Numerical Methods

Pfeifer, Heinz
Electronic Properties

Pickartz, Georg
Electronic Materials

Pieper, Werner
Microstructure Research

Pohl, Maria
Design/Workshop

Radermacher, Bert Hubert
Design/Workshop

Radermacher, Thomas
Scattering Methods

Rehfisch, Jessica
Design/Workshop

Reisen, Christian
Neutron Scattering

Richter, Alfred
Jülich Centre for Neutron Science

Sachsenhausen, Hans-Rudolf
Design/Workshop

Sausen-Malka, Ulrike
Neutron Scattering

Schätzler, Liane
Networks and Numerical Methods

Schätzler, Reinhardt
Neutron Scattering

Schmidt, Marita
Microstructure Research

Schmitz, Berthold-Klaus
Scattering Methods

Schneider, Harald Michael
Jülich Centre for Neutron Science

Schnitzler, Helmut-Hubert
Design/Workshop

Schnitzler, Jens-Willi
Design/Workshop

Schnitzler, Norbert
Electronic Properties

Schramm, Franz-Josef
Design/Workshop

Schreiber, Reinert
Electronic Properties

Sellinghoff, Karin
Soft Condensed Matter

Speen, Hans-Rolf
Microstructure Research

Starc, Thomas
Neutron Scattering

Staringer, Simon
Jülich Centre for Neutron Science

Stefelmanns, Hans-Peter
Design/Workshop

Stollenwerk, Robert
Neutron Scattering

Stronciwilk, Peter
Jülich Centre for Neutron Science

Sybertz, Wilma
Microstructure Research

Telschow, Roger
Networks and Numerical Methods

Thomas, Carsten
Microstructure Research

Thomas, Rita
Networks and Numerical Methods

Triefenbach, Dieter
Soft Condensed Matter

Vehres, Guido
Neutron Scattering

Wassenhoven, Gabriele-Marie
Microstructure Research

Westphal, Elmar
Networks and Numerical Methods

Wingerath, Kurt
Networks and Numerical Methods

Würtz, Eva Maria
Microstructure Research

Administrative staff and secretaries

Borges, Martina
Neutron Scattering

Garcia y Gonzales, Maria
Electronic Materials

Göcking, Marie-Luise
Soft Condensed Matter

Gollnick, Jutta
Electronic Properties

Griesen, Johann Engelbert
Administration

Hölzle, Reiner
Accelerator Group

Köppchen, Barbara-Dorothea
Scattering Methods

Michel, Franziska
Jülich Centre for Neutron Science

Mirea, Elena
Administration

Ockenfels, Silke
Administration

Oubenkhir, Saida
Neutron Scattering

Paffen, Helga
Theoretical Soft Matter and Biophysics

Rische-Radloff, Ingrid
Mictrostructure Research

Schlotmann, Dirk
Administration

Schnitzler, Anna Christine
Neutron Scattering

Sittardt, Hanne
Administration

Snyders, Luise
Theory of Structure Formation

Wassenhoven, Gertrud
Administration

Wenzik, Angela
Technical Services and Administration

Winkler, Ute
Quantum Theory of Materials

Scientists on leave

Bundesministerium für Bildung und Forschung, Bonn, Germany

Wischnewski, Andreas

CEA, Saclay, France

Krug, Ingo-Peter

EFDA CSU, München-Garching, Germany

Lässer, Rainer

Harvard University, Cambridge, USA

Heggen, Marc

Hewlett-Packard Quantum Research Laboratory, Palo Alto, USA

Münstermann, Ruth Christine

Institute Curie, Paris, France

Elgeti, Jens

Institute Laue Langevin, Grenoble France

Chatterji, Tapan Kumar

Schmalzl, Karin Elisabeth

Schmidt, Wolfgang

Jülich Centre for Neutron Science, München, Germany

Appavou, Marie-Sousai Deveram

Babcock, Earl

Borghols, Wouter Joannes Henrik

Busch, Peter

de Souza, Nicolas Raphäel Lounis

Erven, Andreas

Frielinghaus, Henrich

Gerstl, Christine

Goerigk, Günter

Gödel, Marco

Glomann, Thomas Gabriel

Gurzi, Dennis

Gutberlet, Thomas Werner

Holderer, Olaf

Ioffe, Alexander

Kerscher, Michael

Kohnke, Thomas

Korolkov, Denis

Kusche, Harald

Lipfert, Frederik

Mattauch, Stefan Hans Josef

Michel, Franziska

Mittal, Ranjan

Nebel, Andreas Fabian

Neueder, Susann

Nusser, Klaus Lothar Josef

Ossovyi, Vladimir

Pipich, Vitaliy

Price, Stephen

Radulescu, Aurel

Schneider, Gerald-Johannes

Schneider, Harald Michael

Schrader, Tobias E.

Staringer, Simon

Stronciwilk, Peter

Su, Yixi

Wuttke, Joachim

Zitzelsberger, Andreas

Osaka University, Japan

Baumeister, Paul Ferdinand

Spallation Neutron Source , Oak Ridge, USA

Arend, Nikolas

Kozielewski, Tadeusz

Ohl, Michael

Zamponi, Michaela

University of California, Santa Barbara, USA

Weides, Martin Peter

University of Florida, Gainesville, Florida, USA

Schiller, Ulf Daniel

University of New South Wales, Material Science Department, Sydney, Australia

Disch, Mario

Guest scientists

Belgium

Reddy, Naveen Krishna
Soft Condensed Matter
Katholieke Universiteit Leuven

Vermant, Jan Prof. Dr.
Soft Condensed Matter
Katholieke Universiteit Leuven

Vlassopoulos, Prof. Dr., Dimitris
Soft Condensed Matter
Katholieke Universiteit Leuven

Zhang, Zhenkun, Dr.
Soft Condensed Matter
Katholieke Universiteit Leuven

Brasil

Grando Stroppa, Daniel
Microstructure Research
Laboratorio Nacional de Luz Sincrotron

China

Zhang, Wei
Neutron Scattering
China Resaerch Institute of Daily Chemical Industry

Xu, Lingmin
Microstructure Research
Dalian University of Technology, Liaoning Province

Han, Xiujun
Theory of Structure Formation
Northwestern Polytechnical University, Xian

Zheng, Yan-Zhen, Dr.
Electronic Properties
Sun Yat-Sen University

Zhou, Zhiyong
Electronic Materials
Sun Yat-Sen University

Xie, Lin
Microstructure Research
Tsinghua University

Li, Peigang
Electronic Materials
Zhejiang sci-tech University

Croatia

Lazic, Dr., Predag
Quantum Theory of Materials
Ruder Boskovic Institute

Czech. Rep.

Drchal, Vaclav
Quantum Theory of Materials
Academy of Sciences of the Czech Rep.

Finland

Akola Jaakkob Eemeli
Quantum Theory of Materials
Universität Jyväskylä

France

Pouget, Dr., Emilie
Soft Condensed Matter
Centre de Research Paul Pascal

Slipukhina, Ivetta
Quantum Theory of Materials
Commissariat à l'énergie atomique (CEA), Grenoble

Germany

Arunthavarajah, Abiramy
Soft Condensed Matter
Fachhochschule Jülich

Reisen, Andreas
Neutron Scattering
Fachhochschule Jülich

Raad, Charbel
Microstructure Research
FH Aachen

Bohn, Friedrich-Hugo
Neutron Scattering
FHB Consulting

Loosen, Peter
Electronic Materials
Fraunhofer-Institut für Lasertechnik

Hanes, Richard
Soft Condensed Matter
Heinrich-Heine University, Düsseldorf

Kyrkis, Kyriakos
Soft Condensed Matter
Heinrich-Heine University, Düsseldorf

Hennings, Dr. rer. nat., Detlef
Electronic Materials
Philips Forschungslabor Aachen

Spatschek, Dr., Robert
Theory of Structure Formation
Ruhr Universität Bochum

Balan, Aravind
Theory of Structure Formation
RWTH Aachen University

Barthel, Juri
Microstructure Research
RWTH Aachen University

Bauer, David
Quantum Theory of Materials
RWTH Aachen University

Böttger, Dr., Ulrich
Electronic Materials
RWTH Aachen University

Boussinot, Dr., Guillaume
Theory of Structure Formation
RWTH Aachen University

Bräuhaus, Dennis
Electronic Materials
RWTH Aachen University

Brener, Alexey
Theory of Structure Formation
RWTH Aachen University

Burkert, Andreas
Electronic Materials
RWTH Aachen University

Dederichs, Peter-Heinz
Theory of Structure Formation
RWTH Aachen University

Dehoff, Carsten
Electronic Materials
RWTH Aachen University

Dippel, Ann-Christin
Electronic Materials
RWTH Aachen University

Evertz, Udo
Electronic Materials
RWTH Aachen University

Gugenberger, Clemens Matthias
Theory of Structure Formation
RWTH Aachen University

Heins, Martina
Electronic Materials
RWTH Aachen University

Heiss, Wolf-Alexander
Microstructure Research
RWTH Aachen University

Herzog, Stefan
Theory of Structure Formation
RWTH Aachen University

Homberger, Melanie
Electronic Materials
RWTH Aachen University

Houben, Andreas
Scattering Methods
RWTH Aachen University

Karakatsanis, Ioannis
Electronic Materials
RWTH Aachen University

Klopstra, Bart
Electronic Materials
RWTH Aachen University

Knorr, Fabian
Electronic Properties
RWTH Aachen University

Konstantinidis, Nikolaos
Theory of Structure Formation
RWTH Aachen University

Krannich, Sven
Electronic Materials
RWTH Aachen University

Lentz, Florian
Electronic Materials
RWTH Aachen University

Linn, Eike
Electronic Materials
RWTH Aachen University

Marchewka, Astrid
Electronic Materials
RWTH Aachen University

Mayer, Prof. Dr., Joachim
Microstructure Research
RWTH Aachen University

Menzel, Stephan
Electronic Materials
RWTH Aachen University

Morgenstern, Prof., Markus
Electronic Materials
RWTH Aachen University

Noll, Tobias
Electronic Materials
RWTH Aachen University

Park, Daesung
Electronic Materials
RWTH Aachen University

Reichenberg, Bernd
Electronic Materials
RWTH Aachen University

Reinholt, Dr., Alexander
Microstructure Research
RWTH Aachen University

Roitsch, Stefan
Microstructure Research
RWTH Aachen University

Röscher, Mark
Electronic Materials
RWTH Aachen University

Roth, Georg, Prof.
Electronic Materials
RWTH Aachen University

Schmidt, Marita
Electronic Materials
RWTH Aachen University

Schmitz, Thorsten
Microstructure Research
RWTH Aachen University

Simon, Ulrich
Electronic Materials
RWTH Aachen University

Sivebaek, Dr., Ion
Electronic Materials
RWTH Aachen University

Tappertzhofen, Stefan
Electronic Materials
RWTH Aachen University

Timper, Jan
Electronic Materials
RWTH Aachen University

Tong, Ninghua
Microstructure Research
RWTH Aachen University

Van den Hurk, Jan
Electronic Materials
RWTH Aachen University

Xia, Junhai
Electronic Materials
RWTH Aachen University

Zhang, Jiahua
Electronic Materials
RWTH Aachen University

Sicot, Muriel
Electronic Properties
University Konstanz

Weirich, Thomas
Microstructure Research
University of Göttingen

Straube, Prof., Ekkehard
Neutron Scattering
University of Halle

Schubert, Franziska
Quantum Theory of Materials
University of Hamburg

Shen, Wan
Electronic Materials
University of Hamburg

Grychtol, Patrik
Electronic Properties
University of Karlsruhe

Große, Christoph
Electronic Materials
University of Kassel

Möddel, Monika
Theoretical Soft Matter and Biophysics
Institute for Advanced Simulation 2
University of Leipzig

Vass, Szabolcs
Soft Condensed Matter
University of Miskolc

Friedrich, Dr., Christoph
Quantum Theory of Materials
University of Paderborn

Schindlmayr, Prof. Dr., Arno
Quantum Theory of Materials
University of Paderborn

Schmelzer, Sebastian
Electronic Materials
University of Paderborn

Greece

Loppinet, Dr., Benoit
Soft Condensed Matter
FORTH Heraklion

Michailidou, Dr., Vassiliki
Soft Condensed Matter
FORTH Institute of Electronic Structure

Petekidis, Dr., George
Soft Condensed Matter
FORTH Heraklion

Volokitin, Prof., Alexander
Quantum Theory of Materials
FORTH Heraklion

Bessas, Dimitrios
Scattering Methods
National and Kapodistrian University of Athens

India

Mittal, Ranjan
Jülich Centre for Neutron Science
Bhabha Atomic Research Center

Chatterji, Apratim
Theoretical Soft Matter and Biophysics
Indian Institute of Science, Education and Reserch

Adiga, Shilpa
Scattering Methods
Indian Institute of Science, Bangalore

Nair, Sasidharan Harikrishnan
Scattering Methods
Indian Institute of Science, Bangalore

Malhotra, Deepankur
Scattering Methods
Indian Institute of Technology Delhi (IITD)

Yamauchi, Kunihiko
Electronic Materials
Indian Institute of Technology Kanpur

Jayaraman, Rajeswari
Electronic Properties
University of Chennai

Das, Samar K., Prof.
Electronic Properties
University of Hyderabad

Iran

Pourmoosa, Amir Masoud
Theoretical Soft Matter and Biophysics
Sharif University Teheran

Tiedke, Stephan
Theoretical Soft Matter and Biophysics
University of Theheran

Israel

Bar Sadan, Maya
Microstructure Research
Weizmann Institute Rehovot

Italy

Perroni, Dr., Antonio Carmine
Quantum Theory of Materials
Physics Department Napoli

Carbone, Dr., Guiseppe
Quantum Theory of Materials
Politecnico di Bari, Bai

Japan

Ishii, Prof., Fumiyuki
Quantum Theory of Materials
Kanazawa University

Saito, Yukio
Theory of Structure Formation
KEIO University

Katsu, Hayato
Electronic Materials
Murata Manufacturing Co. LtD

Ishida, Hiroshi
Quantum Theory of Materials
Nihon University, Tokyo

Kizaki, Hidetoshi
Quantum Theory of Materials/Institute
for Advanced Simulation 1
Osaka University, Osaka

Sato, Kazunori
Electronic Materials
Osaka University, Osaka

Tartaglino, Dr., Ugo
Quantum Theory of Materials
Osaka University, Osaka

Shibuyaa, Keisuke
Electronic Materials
Universty of Tokyo

Korea

Yoon, Songhak
Electronic Materials
Department of materials

Park, Chanwoo
Electronic Materials
Hanyang University

Kim, Seong Keun
Electronic Materials
Seoul National University

Mexico

Calderon , Hektor
Microstructure Research
ESFM-IPN, Edificio 9, Mexico Department

Netherlands

Briels, Wim
Soft Condensed Matter
Universityof Twente

Poland

Banachowicz, Ewa
Soft Condensed Matter
A. Mlecklewicz University

Gapinski, Jacek
Soft Condensed Matter
Adam Mickiewicz University , Poznan

Patkowski, Prof., Adam
Soft Condensed Matter
Adam Mickiewicz University , Poznan

Ratajczyk, Dr., Monika
Soft Condensed Matter
Adam Mickiewicz University , Poznan

Waligorski, Marek
Soft Condensed Matter
Adam Mickiewicz University , Poznan

Lipinska-Chwalek, Maria
Microstructure Research
AGH University of Science

Kubacki, Jerzy Michal
Electronic Materials
Institute of Physics of Silesian University

Rogala, Maciej
Electronic Materials
Lodz University

Busiakiewicz, Dr., Adam
Electronic Materials
University of Lodz

Kowalski, Wojciech
Microstructure Research
University of Silesia, Katowice

Romania

Botar, Dr., Alexandru
Electronic Properties
JIALEX SRL, Cluj-Napoca

Tranca, Inout
Theory of Structure Formation
University of Craiova

Vamvakaki, Maria
Theory of Structure Formation
University of Craiova

Russia

Gurevich, Vadim, Prof. Dr.
Theory of Structure Formation
A.F. Ioffe Institute, Russian Academy of Sciences

Krichevtsov, Boris, Dr.
Electronic Properties
Ioffe Physico-Techn.

Pertsev, Dr., Nikolay
Electronic Materials
A.F. Ioffe Physico-Techn. Inst.

Samoilov, Prof. Dr., Vladimir
Quantum Theory of Materials/Institute
for Advanced Simulation 1
Moscow State University

Marchenko, Vladimir
Theory of Structure Formation
Russian Academy of Sciences, Chernogolovka

Spain

Barroso-Bujans, Fabienne
Neutron Scattering
Fisica de Materiales

Blanco, Pablo
Soft Condensed Matter
Mondragon University

Krasovskyi, Yevgen
Quantum Theory of Materials
Universidad del Pais Vasco

Sweden

Bergqvist, Lars, Tore
Theory of Structure Formation
Uppsala University

Jacobsson; Adam
Quantum Theory of Materials/Institute
for Advanced Simulation 1
Uppsala University

Switzerland

Kohlbrecher, Dr., Joachim
Soft Condensed Matter
PSI Villigen

Mokthari, Tahreh, Dr.
Soft Condensed Matter
University of Fribourg

Taiwan

Jung-Hsin, Lin
Quantum Theory of Materials
National Taiwan University, Taipei

Lin, Ting-Yi
Electronic Materials
National Tsing Hua University

UK

Dammone, Oliver
Soft Condensed Matter
University College Oxford

Metens, Sebastian
Soft Condensed Matter
University of Oxford

Ukraine

Kapush, Denys
Microstructure Research
Frantsevich Institute for Problems of Materials Science

USA

Fadley, Prof. Dr., Charles
Electronic Properties
ALS Berkeley

Luettmer-Strathmann, Jutta
Soft Condensed Matter
University of Akron

McWhirter, Dr., James Liam Yates
Theoretical Soft Matter and Biophysics
University of Thessaly

IFF scientists teaching at universities

PD Dr. Artur Baumgärtner
Duisburg – Essen

Prof. Dr. Paul-Siegfried Bechthold
Cologne

Prof. Dr. Stefan Blügel
Aachen

Prof. Dr. Thomas Brückel
Aachen

PD Dr. Michael Bachmann
Leipzig

PD Dr. Daniel-Emil Bürgler
Cologne

Prof. Dr. Jan-Karel Dhont
Düsseldorf

PD Dr. Philipp-Georg Ebert
Aachen

Prof. Dr. Gerhard Gompper
Cologne

PD Prof. Dr. Raphaël Hermann
Liège, Belgium

PD Dr. Riccardo Hertel
Duisburg-Essen

Prof. Dr. Erik E. Koch
Aachen

PD Dr. Herbert H. Kohlstedt
Cologne

PD Dr. Peter R. Lang
Düsseldorf

PD Dr. Hans Lustfeld
Duisburg

Prof. Dr. Heiner Müller-Krumbhaar
Aachen

Prof. Dr. Gerhard Nägele
Düsseldorf

Prof. Dr. Eva Pavarini
Aachen

Prof. Dr. Dieter Richter
Münster

Prof. Dr. Claus M. Schneider
Duisburg-Essen

Prof. Dr. Herbert Schroeder
Aachen

Prof. Dr. Gunter-Markus Schütz
Bonn

PD Dr. Werner Schweika
Aachen

Prof. Dr. Krzysztof Szot
Katowice, Poland

Prof. Dr. Knut Urban
Aachen

Prof. Dr. Rainer Waser
Aachen

PD Dr. Simone Wiegand
Cologne

Prof. Dr. Roland Georg Winkler
Aachen

PD Dr. Reiner Zorn
Münster

Imprint

Published by:
Forschungszentrum Jülich GmbH
Institut für Festkörperforschung (IFF)
52425 Jülich, Germany

Phone: +49 2461 61-4465
Fax: +49 2461 61-2410

E-mail: www.iff@fz-juelich.de
Internet: www.fz-juelich.de/iff/e_iff

Published in full on the Internet:
Persistent Identifier: urn:nbn:de:0001-2010051905
Resolving URL: www.persistent-identifier.de/?link=610

June 2010

Conception and editorial:
Angela Wenzik
Claus M. Schneider
IFF

Design and graphics:
Graphic Department
Forschungszentrum Jülich

Layout research reports:
IFF

Pictures:
Forschungszentrum Jülich
except otherwise noted

Print:
Schloemer und Partner GmbH
Düren, Germany

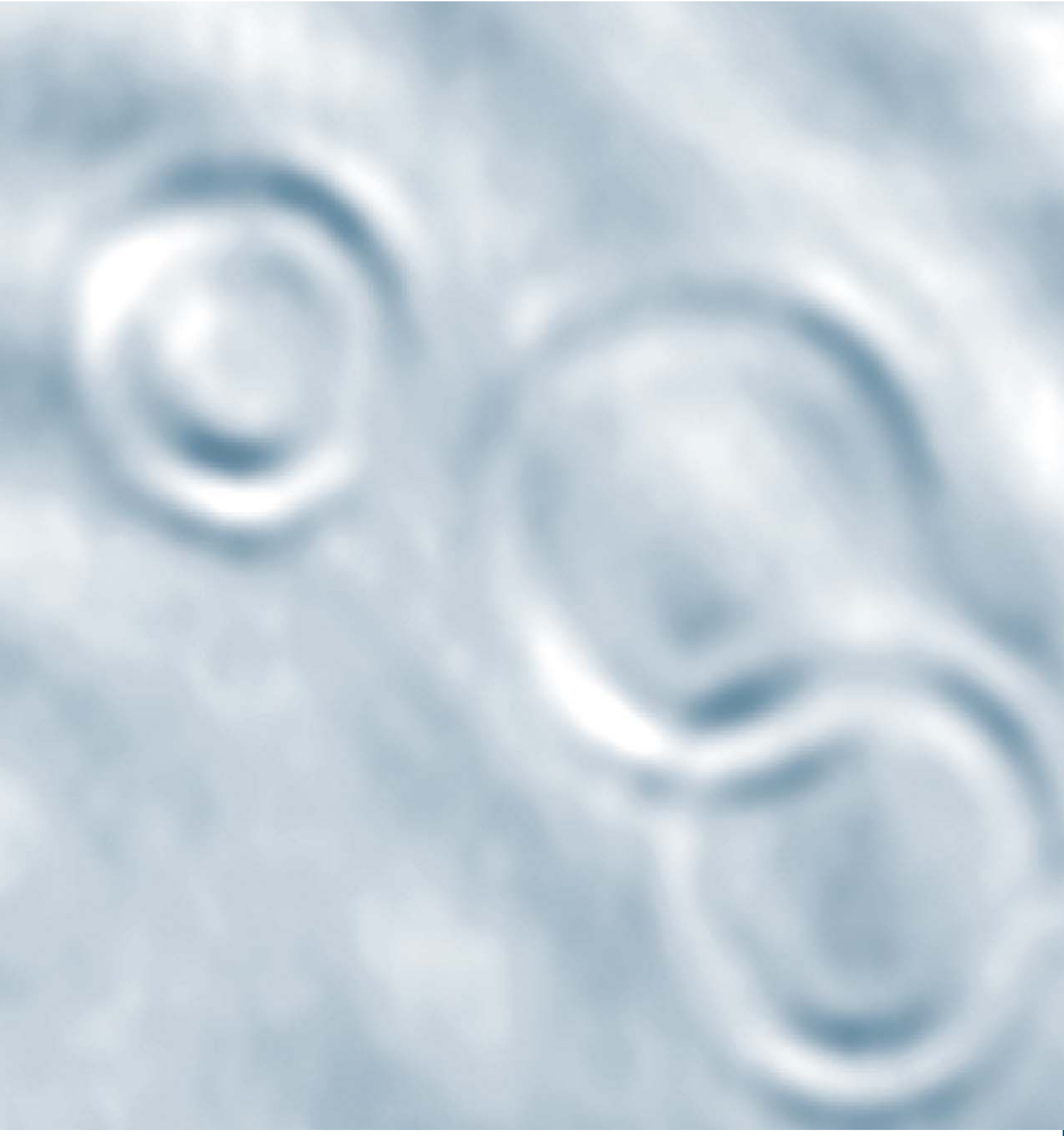

JÜLICH
FORSCHUNGSZENTRUM